Sulfur Isotopic Insights into the Modern and Ancient Marine Sulfur Cycles

Thesis by
Daniel Lee Johnson

In Partial Fulfillment of the Requirements for the
Degree of
Doctor of Philosophy

CALIFORNIA INSTITUTE OF TECHNOLOGY
Pasadena, California

2021
Defended October 13, 2020

Daniel Lee Johnson
ORCID: 0000-0002-7443-1546

ACKNOWLEDGEMENTS

"It takes a village to raise a child." The saying seems to have its origins among several African cultures [153], but in reflecting on my time as a graduate student, I am struck by its parallels with scholarly endeavors. The origins of academic ideas also often become muddled over time and sometimes unexpectedly appear in the scientific literature much earlier than is commonly attributed. But regardless of origin, the idea or sentiment itself remains valid and intriguing. Indeed, it has taken many people for me to successfully complete my PhD thesis. I am especially thankful for all those who have made this thesis possible amidst the ongoing COVID-19 pandemic. I will attempt to mention all of you here, but please know that I appreciate your support regardless of whether or not you are explicitly mentioned.

First and foremost, I would like to thank my PhD advisor, Jess Adkins, for his mentorship. I arrived at Caltech with a lot of enthusiasm for science, but a fair amount of naiveté in critically evaluating scientific results. Jess's contagious curiosity and his desire to understand the methodological details behind every scientific endeavor have helped me develop as a scientist. I am also appreciative of his facilitation of lab camaraderie, his fun sense of humor, and his patience during the times when life got in the way of science.

I have also been fortunate to be guided by three additional members of my thesis advisory committee: Alex Sessions, Woody Fischer, and Yair Rosenthal. Each of these individuals has contributed to my aspirations as a scientist. Alex has taught me the value of hands-on instruction in the lab and of being an effective facilitator of science; Woody, of having a nearly encyclopedic knowledge of Earth history; and Yair, of balancing competing scientific interests and making rigorous science fun. Each of them are outstanding scientists who have contributed to my skills. I am grateful to have had the opportunity to learn from each of you.

As an observational geochemist at heart, my thesis would not have been possible without having interesting samples to study. For this, I owe huge thanks to Ethan Grossman (TAMU), Yanan Shen (USTC), and the International Ocean Discovery Program (IODP). These collaborators have been generous with both their samples and their time, providing me access to hundreds of brachiopods

(EG), bulk rocks (YS), and modern deep marine sediment and pore water samples (IODP). Any errors in this thesis are my own and are not a reflection of these individuals' unsparing efforts.

My time at Caltech would not have been nearly as rewarding without my friends and colleagues within the Adkins lab. I owe an especially large debt of gratitude to Ted Present and Guillaume Paris. Guillaume developed many of the laboratory methods used in this thesis, and Ted helped train me in these methods. I would not be half the scientist I am today without these two. Adam Subhas, Sophie Hines, and Morgan Raven also provided valuable guidance during my first couple of years at Caltech. John Naviaux and Sang Chen started graduate school in the same cohort as me and have been outstanding lab mates, office mates, and friends. I am in awe of their ability to do amazing science while also maintaining good family relationships, sometimes over long distances. Jared Marske, Grecia Lopez Ames, Nathan Dalleska, Fenfang Wu, and Sam Webb also made notable contributions to the work presented here by managing the labs and instruments in which my data were generated. My coding skills and my view of Earth history have been greatly improved with the aid of Preston Kemeny. Melissa Guitierrez and Yashna Peerthum were excellent SURF students and helped generate the data for Sites U1483, U1488, KN223-02, and KN223-16 in Chapter V of this thesis. Alexandra Phillips, Antoine Cremeire, Ren Marquez, Yoni Goldsmith, Paula Mateo, Brad Marske, Frankie Pavia, Daniela Osario, Sijia Dong, Holly Barnhart, Mudit Muraka, Guannan Dong, Min-Sub Sim, Haoyu Li, and Panqing He have also helped make this thesis possible through stimulating discussions and friendships.

The Caltech GPS Division is a remarkable place of work. This is in no small part due to the tireless efforts of the administrative staff to keep the labs running and help scientists like me focus on doing science. Julie Lee, Jen Shechet, Liz Boyd, Marcia Hudson, Nora Oshima, Kathy Young, Bronagh Glaser, Kathy Bravo, Leilani Rivera-Dotson, Julia Zuckerman, Leticia Calderon, Aleen Boladian, Mark Garcia, Janice Grancich, Scott Dungan, and Lisa Christiansen are among the many who have contributed in this respect.

Others within the GPS Division whom I have benefited from interacting with include:

- Faculty - George Rossman, Ken Farley, John Eiler, Joe Kirschvink, Paul

Asimow, John Grotzinger, Andy Thompson, Christian Frankenberg, Claire Bucholz, Rob Clayton, Don Burnett, and Jim Morgan. Thank you for teaching me a lot about geology and about life.

- The Fall 2014 student cohort - Elizabeth Bailey, Austin Chadwick, Sang Chen, Elle Chimiak, Jose Luis Garcia-Reyes, Alistair Hayden, Yuanlong Huang, Voonhui Lai, Ellen Leask, Peter Martin, Kyle Metcalfe, John Naviaux, Leah Sabbath, Nancy Thomas, and Chanel Valiente. You have been some of the greatest friends one could ask for.

- Other postdocs and students - Newton Nyugen, Renee Wang, Jack Muir, Jorge Castillo, Sarah Zeichner, Shaelyn Silverman, Serg Parra, Elliott Mueller, Aida Behmard, Shreyas Vissapragada, Sean Mullin, Hank Yu, Giuliana Viglione, Hao Xie, Nithya Thiagarajan, Nathan Stein, Eryn Eitel, Uri Ryb, Vasilije Dobrosavljevic, Lily Dove, Sara Murphy, Rui Cheng, Mathieu Lapotre, Siraput Jongaramrungruang, Hayden Miller, Reto Wiljker, Max Lloyd, Mike Wong, Stephen Cox, Daven Quinn, Lewis Ward, Jena Johnson, Ho-Hsuan Wei, and Sally Zhang. I am definitely forgetting folks (sorry if I missed you!), but you all have been awesome friends through the good times and the not-so-good ones. Special shout out to Newton for being my running buddy and a constant inspiration to me over these past couple years.

I had the good fortune to serve on the Caltech Graduate Student Council (GSC) for three years during my time at Caltech. This experience complemented my scientific research by giving me new skills in leadership and management plus many additional friends. Thank you to President Tom Rosenbaum, Provost Dave Tirrell, Vice President Joe Shepherd, Dean Doug Rees, Associate Dean Kate McAnulty, Assistant Dean Natalie Gilmore, Angelica Medina-Cuevas, Assistant Vice President Felicia Hunt, Melany Hunt, Matt Orr, Zeynep Turan, Alicia Lanz, Allison Strom, Harpreet Arora, Ivanna Escala, Kenny Buyco, and many others for making this a formative experience for me. I would especially like to thank Dean McAnulty and Alicia for being there for me during some unexpectedly difficult times in my last year on the GSC; you two are role models for me both in professional work and in life more broadly.

Many additional Caltech offices have supported me during my time as a PhD student. Thank you to the Caltech CCID and CTLO for providing me with valu-

able educational opportunities, Caltech Wellness Services for supporting my health, and to Caltech Recreation and Athletics for providing me with a friendly space to exercise.

Other friends I need to thank include Jonathan Herrmann, Emily Stein, Jenny Fung, Monica Meeks, Sarah Negron, Rachel Miller, Zach Hernandez, Sarah Palmer, Samantha Raines, John Wolfe, Ryan Tresemer, Kody Shelley, Aiden Khuiphum, Peng (Brian) He, the IODP Expedition 363 Staff and Scientists, and my friends within the Soka Gakkai International (SGI). Special thanks to Jonathan for his steady friendship and to Jonathan's parents, Barbara and Robert, for serving as my proxy parents during my time here.

The love and support of my family was crucial in my decision to attend graduate school. Thank you to my parents, Kevin and Ellen Johnson, for encouraging me to pursue this big goal and for being understanding each time I came home without a clear answer on when I would be graduating. Thank you also to my brother, Mike, and his partner Kelly. Visiting you in San Francisco during the latter part of my time in Los Angeles has been super fun, and I hope I will be able to do so again soon.

Many of the instructors I had prior to coming to Caltech not only taught me well, but also believed in me long before I believed in myself. Thank you to my high school science teachers, Teri Cox and Lisa Franke, for putting so much effort into my early science education and for making science fun; to my undergraduate academic advisor, Ray Arvidson, for accepting me into the Pathfinder program at WUSTL and showing confidence in me early on; and to Sidney Hemming (Columbia/LDEO), Trevor Williams (IODP), Elizabeth Pierce (Columbia/LDEO), Jen Smith (WUSTL), and David Fike (WUSTL) for introducing me to the joys of research science.

Lastly, I would like to end by acknowledging the friends and family I have lost while in graduate school: Emma Cox, Chance Crompton, Josh Spencer, Lindsey Hedges, Rob Gentry, and Carol Heidenreich. The world lost many of you far too soon, and I dearly miss you. I hope this work and all that will come after in my life has at least a small positive impact in the world in your honor.

ABSTRACT

The marine sulfur cycle plays a key role in regulating Earth's surface oxygen (O_2) levels through its interactions with the carbon and iron cycles. Our understanding of the sulfur cycle has traditionally come from measurements of the sulfur isotopic compositions of marine sulfate (SO_4^{2-}) and sulfur-bearing materials in marine sediments. Because the residence time of SO_4^{2-} in seawater is long (Myr) compared to the mixing time of Earth's oceans (kyr), the concentration and sulfur isotopic composition of marine SO_4^{2-} are homogeneous in modern seawater and are assumed to have been homogeneous throughout most of the Phanerozoic Eon (541 Ma to the present). This assumption of homogeneity, when combined with sulfur isotopic composition measurements, has enabled box model reconstructions of the relative fluxes of oxidized versus reduced sulfur leaving the oceans at times in Earth's past. Such reconstructions have informed our understanding of the interactions between Earth's tectonics, climate, and elemental cycles.

This thesis tests some of the key assumptions made in sulfur cycle box models and attempts to better understand sulfur isotopic variability in geologic archives using a combination of measurements and modeling. Measurements of the sulfur isotopic composition (i.e., $\delta^{34}S$) of SO_4^{2-} in Permo-Carboniferous brachiopod shells demonstrate that more precise records of SO_4^{2-} $\delta^{34}S$ may be generated via careful sampling that avoids diagenetically altered phases (Chapter II). Furthermore, measurements of heterogeneous carbonate associated sulfate (CAS) $\delta^{34}S$ within carbonates deposited across the End-Permian mass extinction (EPME) in South China show that a lack of careful sampling can substantially alter our understanding of the marine sulfur cycle at times in Earth's past (Chapter III). Simple models constructed in each of these studies indicate that changes in the $\delta^{34}S$ of the sulfur input to the ocean, the $\delta^{34}S$ offset (i.e., $\Delta\delta^{34}S$) between the oxidized and reduced sulfur output fluxes, and the amount of SO_4^{2-} incorporated during diagenetic alteration — all assumed to be negligible in many studies of the marine sulfur cycle — may viably explain these data. Development of a sediment diagenesis model that includes sulfur isotopic species demonstrates that variations in organic matter rain rate, ferric iron input, sedimentation rate, bottom water O_2 concentration, and bottom water SO_4^{2-} concentration may all affect $\Delta\delta^{34}S$ in a given sedimentary environment (Chapter IV). Application of

this model to pore water SO_4^{2-} and hydrogen sulfide (H_2S) $\delta^{34}S$ data from International Ocean Discovery Program (IODP) Expedition 361, IODP Expedition 363, and *R.V. Knorr* cruise KN223 sites shows that $\Delta\delta^{34}S$ is ubiquitously large in these deep ocean sedimentary environments (Chapter V). Cluster analysis of pore water [SO_4^{2-}] profiles collected during previous deep ocean cruises successfully extracts and groups profiles that are similar to those observed on these three cruises (Chapter VI). Comparison of cluster data to a compilation of recent marine pyrite (FeS_2) $\delta^{34}S$ data confirms that pyrite burial in shelf sediments constitutes the majority of pyrite burial occurring globally in the modern day. However, changes in sea level or in other variables that affect sediment deposition may plausibly force an increase in deep ocean pyrite burial and a corresponding change in the global $\Delta\delta^{34}S$. Future studies of the modern and ancient marine sulfur cycles must carefully consider the geologic and geochemical context of sulfur isotopic measurements — including sea level changes, sedimentation rate changes, and measured or presumed concentrations of other redox-active species — if interpretations of such data are to be robust.

PUBLISHED CONTENT AND CONTRIBUTIONS

[1] Johnson, D. L. et al. “Brachiopod $\delta^{34}S_{CAS}$ microanalyses indicate a dynamic, climate-influenced Permo-Carboniferous sulfur cycle.” In: Earth and Planetary Science Letters 546 (Sept. 15, 2020).
D.J. participated in the conception of the project, conducted all laboratory preparation and measurements, analyzed and interpreted the data, and helped write the manuscript., p. 116428. ISSN: 0012-821X. DOI: 10.1016/j.epsl.2020.116428. URL: http://www.sciencedirect.com/science/article/pii/S0012821X20303721 (visited on 07/07/2020).

CONTENTS

LIST OF FIGURES

LIST OF TABLES

Chapter I

INTRODUCTION

I.1 Sulfur Isotopes and the Marine Sulfur Cycle

Sulfur (S) is the sixteenth most abundant element in Earth's crust and has four stable isotopes: ^{32}S ($94.99 \pm 0.26\%$), ^{33}S ($0.75 \pm 0.02\%$), ^{34}S ($4.25 \pm 0.24\%$), and ^{36}S ($0.01 \pm 0.01\%$) [138]. It also exists in multiple redox states at Earth's surface ranging from an oxidation number of +6 (e.g. SO_4^{2-}) to -2 (e.g. H_2S). This combination of relatively high abundance and redox chemistry has made S one of the most important elements for electron transfer over the course of Earth's history [137]. Electron transfers between carbon (C), iron (Fe), and S species are thought to have played a key role in maintaining relatively stable atmospheric oxygen concentrations in the Phanerozoic [27, 137].

Most of the redox reactions involving S species preferentially act upon molecules bearing specific isotopes of S. Such isotope discrimination, or "fractionation," is commonly expressed in terms of a fractionation factor α that compares the isotope ratio in a product p to the ratio of the same two isotopes in a reactant r: [75, 79]:

$$^{x}\alpha_{p,r} = \frac{^{x}\mathrm{R}_p}{^{x}\mathrm{R}_r} = \frac{(\frac{\mathrm{X}}{\mathrm{Y}})_p}{(\frac{\mathrm{X}}{\mathrm{Y}})_r}$$

where x is the mass number of isotope X, Y is a second isotope of the same element, $^{x}\mathrm{R}_p$ is the abundance ratio of X to Y in the product, and $^{x}\mathrm{R}_r$ is the same abundance ratio in the reactant. The most abundant isotope is commonly assigned to Y and a more rare isotope to X. For S, ^{32}S is this most common isotope and ^{34}S is most frequently the rare isotope of interest. Commonly, α is recast as a parts per thousand (per mil, ‰) deviation from 1 and communicated as the "isotopic fractionation," ε [75, 79]:

$$^{x}\varepsilon_{p,r}(‰) = (^{x}\alpha_{p,r} - 1) * 1000‰$$

Because the isotope X is typically a rare isotope, differences in isotope ratios among materials are often very small. Thus, isotope ratios are also often recast as a per mil (i.e., parts per thousand) deviation from the isotope ratio of a standard

[75, 79]:

$$\delta^{x}\mathrm{E}\,(‰) = \left(\frac{{}^{x}\mathrm{R}_{\mathrm{sample}}}{{}^{x}\mathrm{R}_{\mathrm{standard}}} - 1\right) * 1000‰$$

where E is the element of interest. For S, the typical standard to which ratios are compared is Vienna Canyon Diablo Troilite (VCDT) [75]. S isotopic compositions are most commonly reported as $\delta^{34}S$ relative to VCDT in the literature, although $\delta^{33}S$ and $\delta^{36}S$ have also been measured in some studies (e.g. [95, 157, 158]).

Marine sediments are the locus of all S burial on Earth today, and the marine S cycle has consequently been a topic of considerable research interest over the past several decades. Sulfate (SO_4^{2-}) is the second most abundant anion in modern seawater ($[SO_4^{2-}] \sim 28$ mM), and under anoxic conditions in water or sediment, it may be reduced to form aqueous sulfide (H_2S). Although most of this H_2S is reoxidized [163], a small fraction is scavenged by metal cations such as ferrous Fe (Fe^{2+}) or by organic matter [274, 355] to form solid S phases. Both H_2S and these solid phases are depleted in rare S isotopes relative to marine SO_4^{2-} due to isotopic fractionations associated with redox reactions involving S species [56, 57]. Microbial sulfate reduction (MSR) is the primary contributor to this depletion [56], but reactions such as H_2S oxidation (e.g. [105, 256]) and S disproportionation (e.g. [60, 164]) may play a role in some settings.

The burial of solid phases depleted in rare S isotopes enriches the remaining marine SO_4^{2-} in these isotopes under steady state conditions, with greater enrichment occurring as the burial flux of these solid phases becomes a larger fraction of the total burial flux. Steady state isotopic box models of the marine S cycle have been constructed by many authors (e.g. [107, 167, 172]) to take advantage of this relationship and interpret variations in marine SO_4^{2-} $\delta^{34}S$ over geologic history ([57, 72, 100, 172, 261]; see Figure II.7). These models are similar to box models of the geologic C cycle (e.g. [190]) and are schematically depicted in Figure I.1. Typically, the models assume that riverine input of SO_4^{2-} derived from continental weathering is the primary input of SO_4^{2-} to seawater; volcanic input is considered negligible [91]. Marine SO_4^{2-} is assumed to leave seawater either as sulfate evaporite minerals (e.g. gypsum, $CaSO_4 \cdot {}_2H_2O$) or in solid phases derived from H_2S — mainly, the disulfide mineral pyrite (FeS_2). If the $\delta^{34}S$ offset ($\Delta\delta^{34}S$) between buried sulfate evaporites and pyrite, the $\delta^{34}S$ of the riverine input ($\delta^{34}S_{in}$), and the size of the seawater SO_4^{2-} reservoir are approximately constant over a time scale of interest — as commonly assumed in steady

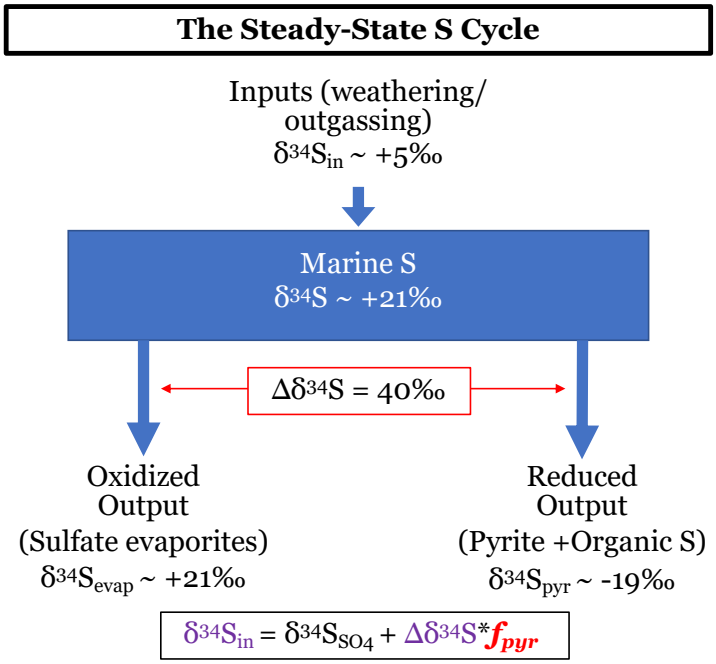

Figure I.1: Box model schematic for the steady state marine S cycle with $\delta^{34}S$ estimates for the modern fluxes. Given a measured seawater sulfate $\delta^{34}S$ (black text) and assumed values for $\delta^{34}S_{in}$ and $\Delta\delta^{34}S$ (purple text), one may solve for f_{py} (red text), the fraction of the total S output flux leaving the ocean as pyrite.

state models of the marine sulfur cycle — the steady state sulfur isotope mass balance equation may be applied ([135]):

$$\delta^{34}S_{in} = \delta^{34}S_{SO4} + \Delta\delta^{34}S * f_{py}$$

where $\delta^{34}S_{SO_4}$ represents the $\delta^{34}S$ of marine SO_4^{2-} and f_{py} is the fraction of the total output flux of S leaving the ocean as pyrite. If the $\delta^{34}S$ of seawater is known, one can solve this equation for f_{py} and gain valuable insight on S cycle dynamics at different times in Earth's past. Such potential has motivated construction of temporal $\delta^{34}S$ records (e.g. [57, 72, 100, 172, 264]) and integration with models of the C cycle (e.g. [25, 199]) to understand the net effects of biogeochemical cycling on Earth's oxygenation and evolution over time. These efforts have proceeded despite significant uncertainties in both the modern values and temporal evolution of $\delta^{34}S_{in}$ and $\delta^{34}S$. Several recent studies (e.g. [52, 126, 195, 342, 369]) have begun to address these uncertainties.

Despite the extensive work done in constructing temporal $\delta^{34}S$ records [57, 72,

100, 172, 264], outstanding questions regarding the history of the marine sulfur cycle still abound. How faithfully do existing sulfate $\delta^{34}S$ records preserve the actual $\delta^{34}S$ of primary seawater sulfate? Could temporal changes in $\delta^{34}S_{in}$ and $\delta^{34}S$ be responsible for some of the seawater $\delta^{34}S$ changes that have traditionally been attributed to changes in the amount of pyrite burial? What other processes (e.g. hydrothermal circulation) may add important complications to the one input, two output topology depicted in Figure I.1? This thesis attempted to address each of these questions through a combination of new sulfur isotope abundance measurements and mathematical modeling. Temporal variation in $\delta^{34}S$ appears to be a particularly significant source of uncertainty that deserves more attention, as changes in both the ε associated with sedimentary sulfur cycling and the role of reactive transport processes (i.e., diffusion, advection, and reaction) in translating ε into a $\delta^{34}S$ within a given environment have not been constant in either space or time. This work identifies some of the processes that may be important in forcing temporal change in these parameters. In the following, we have briefly reviewed the geologic archives that are measured as records of sulfur cycle processes. We have also identified the methods that have been developed for making sulfur isotope abundance measurements. Descriptions of the benefits and shortcomings of each archive and measurement method are followed by an outline of the remainder of this thesis.

I.2 Geologic Archives of the Ancient Marine Sulfur Cycle

Based on the potential for the S isotopic composition of sedimentary materials to reflect important changes in the Earth system, many different geologic materials have had their $\delta^{34}S$ measured by geochemists to document changes in the marine S cycle over Earth history. These geologic archives of the marine S cycle include S in both oxidized and reduced redox states. The archives may occur as pure S-bearing minerals or may instead preserve S as a minor constituent. While oxidized materials are typically targeted as archives of marine $\delta^{34}S$, reduced materials often preserve information on local depositional conditions [100, 246] and are useful for reconstructions of $\Delta\delta^{34}S$ (e.g. [195, 369]).

I.2.1 Sulfate S archives

I.2.1.1 Sulfate minerals

Sulfate evaporite minerals are found in the geologic record across much of Earth history (e.g. [33, 72]) and were a target for many of the earliest studies of S isotopic variation among geologic materials [11, 337, 338]. Such minerals — mainly gypsum and anhydrite ($CaSO_4$) — are attractive given their high S content and their deposition with little to no S isotopic fractionation relative to marine SO_4^{2-} [268]. However, precipitation of evaporite minerals is mostly limited to restricted basins in which evaporation exceeds precipitation. Such basins have not been constant in their abundance throughout geologic time [72, 126] and may experience $\delta^{34}S$ variations reflecting local influences rather than global S cycle changes (e.g. [99]). Evaporite deposits are also often difficult to date due to a lack of diagnostic biostratigraphic markers. These factors have led to temporal records that demonstrate substantial ($> 20‰$) Phanerozoic $\delta^{34}S$ variability, but with gaps and uncertainties in the timing and global significance of variation.

Barite ($BaSO_4$) is found in recent marine sediments and has also been targeted in studies of marine SO_4^{2-} $\delta^{34}S$ variations [252, 254]. Records generated from this archive [252, 254] are notable for their precision and stratigraphic continuity, but are limited in their temporal extent. Barite begins to dissolve upon quantitative consumption of SO_4^{2-} (e.g. [290]) and is only consistently preserved in sediments that have been too organic-poor for complete pore water SO_4^{2-} consumption throughout their histories. This dissolution has allowed marine barite $\delta^{34}S$ records to be extended from the present only to the mid-Cretaceous [254]. Open questions regarding the microenvironments in which barite forms in seawater [253] and the degree to which these microenvironments are altered from seawater in their fluid composition (e.g. [29]) have also limited detailed evaluation of the accuracy of these records.

I.2.1.2 Minor / trace components of other minerals

In addition to precipitating as sulfate minerals, SO_4^{2-} ion may substitute for other polyatomic anions (e.g. CO_3^{2-}, PO_4^{3-}) in mineral lattices. Calcite ($CaCO_3$), an ubiquitous mineral present in marine rocks throughout geologic

time, has been the most commonly targeted mineral in studies of this substituted SO_4^{2-}. Early studies demonstrated the presence of sulfate at 1000+ ppm (w/w) abundances in inorganic calcites [53, 330], calcitic and aragonitic skeletons [318], and bulk ancient carbonates [106]. Pioneering works by Popp (1985) [259] and Burdett, Arthur, and Richardson (1989) [49] also established the potential for the $\delta^{34}S$ of this carbonate associated sulfate (CAS) to reflect the $\delta^{34}S$ of contemporaneous marine SO_4^{2-}. Stratigraphic continuity and easy biostratigraphic correlation have enabled $\delta^{34}S$ records of impressive temporal resolution and extent (e.g. [172, 279]) to be generated in the several decades since these studies. However, recent works [262, 263, 278] have also demonstrated potential for CAS abundance and $\delta^{34}S$ to be altered during burial recrystallization. Great care must be taken to identify and sample phases thought to contain CAS derived from unaltered seawater to ensure the accuracy of such records (e.g. [262, 263]). Offsets in $\delta^{34}S$ related to equilibrium and kinetic fractionations [15, 243, 244] may add further complications.

Sulfate present as a minor component in the calcium phosphate mineral apatite ($Ca_5(PO_4)_3(OH,F,Cl)$) has also been targeted as a potential archive of marine SO_4^{2-} $\delta^{34}S$ [16, 34, 74, 114, 216, 235, 258, 307, 368]. Sedimentary apatite is precipitated by biomineralizing organisms to form bones, teeth, and skeletons (e.g. [113]) and may additionally precipitate authigenically during early diagenesis, sometimes in large quantities (e.g. phosphorites; [216]). Although sulfate is present at significant concentrations (up to several wt%) in phosphorites [16, 34, 74, 114, 216, 235, 258], isotopic studies have shown that the $\delta^{34}S$ of phosphate associated sulfate (PAS) is frequently enriched in ^{34}S relative to seawater SO_4^{2-} due to incorporation of pore water SO_4^{2-} in sulfate-reducing environments [16, 74, 216, 235, 258]. Lower sulfate abundances (typically < 1 wt%) have limited S isotopic studies of biogenic apatites [113]. Studies targeting such samples [113, 368] are too few in number to draw robust conclusions, but have been at least moderately successful in producing PAS $\delta^{34}S$ measurements close to the $\delta^{34}S$ of coeval biogenic CAS [368].

I.2.2 Sulfide S archives

I.2.2.1 Sulfide and disulfide minerals

S cycling in marine sediments produces solid phases that are extremely variable in their $\delta^{34}S$ across modern environments (e.g. [59]). Consequently, the information gathered from the $\delta^{34}S$ of solid phases at a given site is typically local in its relevance, though compilations of data from many environments [56, 57, 58, 100] may facilitate an understanding of global trends (e.g. [195, 369]).

Pyrite is the most common H_2S-derived phase targeted for $\delta^{34}S$ measurements and often constitutes the majority of the solid phase S present in marine sediments (e.g. [149, 311, 336]). This mineral is formed via the authigenic precipitation of iron monosulfide (FeS) from dissolved Fe^{2+} and H_2S, plus a subsequent reaction of FeS with another S species (e.g. S^0) to form pyrite [217, 285]. Pyrite is ubiquitous in sedimentary rocks and is typically extracted from sediments using strong reducing agents to form H_2S that can be collected in a chemical trap (e.g. [61]), though strong oxidizing agents may also be used if quantitative extraction is not crucial (e.g. [274]). Temporal pyrite $\delta^{34}S$ records are generated with ease, but again, high pyrite $\delta^{34}S$ variability exists at spatial scales ranging from individual grains (e.g. [46]) to different depositional environments (e.g. [59]). This, combined with the potential for late diagenetic and/or metamorphic pyrite formation (e.g. [193]) generally limits the utility of data from a given site to understanding local processes.

I.2.2.2 Organic S

Organic S is an understudied component of the marine S cycle. Though studies of its concentration and isotopic composition date back to some of the earliest S isotopic studies (e.g. [336]), only recently have concentrated efforts started to unravel the controls on its composition [273, 274, 303, 354, 355, 356]. The relative dearth of studies is surprising given the significance of organic S as a solid phase S output in sediments that are particularly organic-rich and/or Fe-poor (e.g. [275, 303]). Existing studies suggest that organic S is typically enriched in ^{34}S relative to codepositional pyrite [149, 274, 275] and may reflect longer-term sulfurization reactions between organic matter and pore water H_2S during burial (e.g. [272]). More work is required to understand the quantitative im-

portance of this flux throughout Earth history and its potential effects on the marine S cycle (esp. the $\delta^{34}S$ of seawater).

I.3 Methods of S Isotope Analysis

S isotope abundances are measured using a wide variety of methods. Traditionally, measurements have been made through combustion of samples under a stream of oxygen to yield sulfur dioxide (SO_2) gas suitable for measurement on a gas source isotope ratio mass spectrometer (IRMS) [98, 336, 337, 338]. Measurements made using variants of this method continue to the present day and are included as part of this thesis (see Chapter V). However, a number of new methods for S isotope abundance measurements have been developed over the past 20 years. These methods are often advantageous for specific applications, especially in measuring multiple rare S isotopes. Such methods have also enabled new studies of the archives mentioned above at finer spatial resolution or with improved precision (e.g. [46, 94, 244]). A solid understanding the benefits and drawbacks associated with each method must be garnered to evaluate the utility of the method for studying a specific question related to the S cycle. Brief descriptions of these benefits and drawbacks are included below.

I.3.1 SF_6 *gas source IRMS*

The sulfur hexafluoride (SF_6) method was initially developed by Hulston and Thode (1965) [150]. This method enables precise measurement of the abundances of the rare S isotopes ^{33}S and ^{36}S through fluorination of S-bearing samples to volatile SF_6 and S isotope ratio measurement on a gas source IRMS; because fluorine has only one stable isotope, all variations in the mass of SF_6 are due to S isotopic variation. Difficulties associated with the fluorination process [150] inhibited widespread initial adoption of this method, but methodological improvements by several authors [13, 267, 335] and the discovery of mass-independent fractionation (MIF) of S isotopes in Archean rocks [94] have made the method more common in recent years. Sample requirements (100s to 1000s of S nanomoles) for sub-0.1‰ uncertainty in $\delta^{34}S$ are similar to those required for traditional SO_2 gas source IRMS, albeit with lower sample throughput (e.g. [241]).

I.3.2 Secondary ionization mass spectrometry (SIMS)

Secondary ionization mass spectrometry (SIMS) involves the bombardment of a surface with an ion beam and abundance measurements of the secondary ions expelled from the surface. Such instruments have existed since the late 1960s [67], but have only been commonly used in geologic studies of S isotope abundances since the 1990s (e.g. [284]). SIMS instruments are powerful tools for measuring S isotopic variability at the spatial scale of tens of microns. Studies have successfully used these instruments to measure $\frac{^{34}S}{^{32}S}$ ratios (e.g. [46]) and mass independent S isotope signatures (e.g. [345]) in pyrite grains with short (minutes) analytical times. However, development of standards that are isotopically homogeneous at the micron scale is often challenging, and analytical times are much longer when measuring materials in which S is a minor component (e.g. carbonates).

I.3.3 Orbitrap mass spectrometry

Orbitrap mass spectrometry is a relatively new ($\sim$15 years old) variety of Fourier transform mass spectrometry. Here, ions of different masses are distinguished based on the frequency of their axial oscillations within an electric field [374]. Although the technology has primarily been used for biological applications (e.g. proteomics) thus far, several pioneering studies have begun to explore applications within isotope geochemistry. Neubauer et al. (2018) [237] demonstrated the potential for site-specific isotopic compositions in organic compounds to be measured using Orbitrap mass spectrometry, and a follow up paper [238] reported an initial application of the technology for measurement of S and oxygen (O) isotope ratios in dissolved SO_4^{2-}. Notably, only nanomoles of analyte are currently necessary to constrain uncertainties to sub-‰ levels within tens of minutes; improvements in the technology could reduce this sample requirement by an additional order of magnitude or more [238]. The promise of these initial studies motivates further exploration of the technology for S isotope abundance measurements.

I.3.4 Multicollector inductively coupled plasma mass spectrometry (MC-ICP-MS)

Multicollector inductively coupled plasma mass spectrometry (MC-ICP-MS) has revolutionized the field of isotope geochemistry since the first commercial

MC-ICP-MS instruments were introduced in the early 1990s [88]. Amrani, Sessions, and Adkins (2009) showed that these instruments could be used to make compound-specific $\delta^{34}S$ measurements on relatively small amounts of organic S-bearing compounds. Although these instruments have not historically been used to measure S isotope abundances in aqueous solutions due to large interferences from O_2 and hydrides, Paris et al. (2013) [242] overcame this obstacle by removing solvent vapor using a desolvating membrane and introducing analyte to the plasma as a dry gas. They demonstrated that $\delta^{34}S$ measurements could be made with sub-0.1‰ precision on as little as five nanomoles of S using this method. Subsequent studies [52, 243, 244, 262, 279] have applied this method toward several aspects of the marine S cycle. Extending these efforts is a primary focus of this thesis.

I.4 Strategy and Structure of the Thesis

The recent advancements in mass spectrometry methods described above have expanded the feasibility of precisely measuring the S isotopic composition of geologic materials, especially for S-poor materials (e.g., Archean carbonates; [244, 245]). The full utility of these advancements to improve S isotopic records and answer outstanding questions concerning the global marine S cycle remains untapped in many cases. For example, long-term (100+ Myr) Paleozoic records of marine SO_4^{2-} $\delta^{34}S$ remain relatively imprecise, and the hypothesized effects of sea level on fluxes within the S cycle (e.g. [344]) have not been quantitatively interrogated. Application of new methods toward answering these outstanding questions is imperative.

In this thesis, we attempted to better understand $\delta^{34}S$ variability in geologic archives and the controls upon that variability with measurements and mathematical modeling. We focused on utilizing MC-ICP-MS to measure smaller, more targeted samples than is typically allowed by traditional EA-IRMS and with better precision than is possible over comparable measurement times with SIMS and Orbitrap mass spectrometry. We started by applying this tool towards geologic archives of the marine S cycle. Later, we turned our focus to modern processes that may have been at play in generating past changes in seawater $\delta^{34}S$.

Chapter II began the process of generating a new record of marine $\delta^{34}S$ variation during the Paleozoic with MC-ICP-MS measurements of CAS $\delta^{34}S$ (i.e.,

$\delta^{34}S_{CAS}$) in Permo-Carboniferous brachiopods. In this new record, we observed a novel 3–5‰ increase in $\delta^{34}S_{CAS}$ near the Serpukhovian-Bashkirian boundary (323.4 Ma). We also found that $\delta^{34}S_{CAS}$ within individual brachiopod specimens and among different specimens deposited in the same sediment horizon is only a minor source of $\delta^{34}S_{CAS}$ variability. Mathematical modeling of the Permo-Carboniferous C and S cycles suggests that changes in $\delta^{34}S_{in}$ and/or $\Delta\delta^{34}S$ are necessary to replicate the observed carbonate $\delta^{13}C$ and $\delta^{34}S$ records.

In Chapter III, we attempted to extend the record of Chapter II by documenting $\delta^{34}S_{CAS}$ variations across the End-Permian Mass Extinction (EPME) in South China. The $\delta^{34}S_{CAS}$ within single hand samples is highly heterogenous and sometimes spans a range of nearly 20‰. Plots of CAS abundance versus $\delta^{34}S_{CAS}$ suggest that this variation results from mixing between low CAS abundance, high $\delta^{34}S$ and high CAS abundance, low $\delta^{34}S$ phases. We hypothesized that the low $\delta^{34}S_{CAS}$ end member results from incorporation of SO_4^{2-} derived from sulfide oxidation during oscillations in sedimentary redox conditions near the Permian-Triassic boundary. Mixing calculations show that these low $\delta^{34}S_{CAS}$ values may be generated with oxidation of only a small fraction of the solid phase S that is present in these rocks. However, additional study is necessary to rule out oxidation of solid S phases during laboratory processing of the samples.

Chapter IV outlines the development of a new model of early diagenesis for understanding S isotopic variation in modern sediments. This time-dependent model includes S isotopic species and is one of the first to include both organic matter sulfurization and realistic pyrite formation processes. Model sensitivity tests suggest that organic matter rain rate, porosity, and sedimentation rate are the strongest controls on the S isotopic composition of buried pyrite in marine sediments. The model also indicates that variations in organic matter input and the physical parameters of sedimentary systems (esp. sedimentation rate) can entirely account for the heterogeneity in $\Delta\delta^{34}S$ across depositional environments globally; no variations in the $^{34}\varepsilon$ associated with reactions involving S species are necessary.

In Chapter V, we applied the new model from Chapter IV toward a wealth of new $\delta^{34}S$ data generated from deep ocean sediments cored on IODP Expedition 361, IODP Expedition 363, and *R.V. Knorr* cruise KN223. These sites exhibit a wide range of characteristics in terms of their $[SO_4^{2-}]$ depth profiles, but the new data here suggest they are unified in featuring high (> 40‰) $^{34}\varepsilon$'s associated with

sedimentary sulfur cycling. We found that most of the observed $[SO_4^{2-}]$ and SO_4^{2-} $\delta^{34}S$ depth profiles can be closely replicated under steady state conditions with the new diagenetic model. Such results have important implications for the $\delta^{34}S$ of pyrite that is buried in deep ocean sediments.

Chapter VI takes a broader view of S cycling in modern deep ocean sediments by examining $[SO_4^{2-}]$ profiles collected from past deep sea drilling expeditions. Using k-means clustering, we found that profiles can be broadly allocated into different groups that are distinct in terms of their global spatial distributions. The characteristics of the sites within each group indicate that organic carbon content is the primary control upon the type of profile that a given site will exhibit, with water depth and $CaCO_3$ content serving as secondary influences. In comparing estimated net sulfate reduction rates (nSRRs) to estimated pyrite S accumulation rates derived from a literature compilation of pyrite $\delta^{34}S$ measurements, we found that existing data appear to be biased toward regions with relatively high nSRRs and sedimentary S contents. Finally, we explored the effects of augmenting the deep ocean pyrite burial flux via isotope mass balance calculations. Our calculations suggest that steady state marine $\delta^{34}S$ perturbations of 6‰ or more are possible. These results argue for additional efforts to create unbiased estimates of fluxes within the global marine S cycle and further examination of the effects of past global-scale sedimentation and/or seafloor hypsometry changes on the S cycle.

Chapter II

BRACHIOPOD $\delta^{34}S_{CAS}$ MICROANALYSES INDICATE A DYNAMIC, CLIMATE-INFLUENCED PERMO-CARBONIFEROUS SULFUR CYCLE

The content of this chapter has been published as cited below. When appropriate, the text and figures have been slightly modified to improve clarity and coherence with the remainder of the thesis.

Johnson, D. L. et al. "Brachiopod $\delta^{34}S_{CAS}$ microanalyses indicate a dynamic, climate-influenced Permo-Carboniferous sulfur cycle." In: *Earth and Planetary Science Letters* 546 (Sept. 15, 2020).
D.J. participated in the conception of the project, conducted all laboratory preparation and measurements, analyzed and interpreted the data, and helped write the manuscript., p. 116428. ISSN: 0012-821X. DOI: 10.1016/j.epsl.2020.116428. URL: http://www.sciencedirect.com/science/article/pii/S0012821X20303721 (visited on 07/07/2020)

II.1 Abstract

Early isotopic studies of sulfate in carbonate minerals (carbonate associated sulfate; CAS) suggested that carbonates can provide a reliable, well-dated archive of the marine sulfur cycle through time. However, subsequent research has shown that diagenetic alteration can impose highly heterogeneous CAS sulfur isotopic compositions ($\delta^{34}S_{CAS}$) among different carbonate phases within sediments. Such alteration necessitates targeted sampling of well-preserved, primary carbonate phases. Here, we present a new record of Carboniferous and Early Permian brachiopod $\delta^{34}S_{CAS}$ generated from over 130 measurements of microsampled brachiopod shells. Our record refines existing brachiopod $\delta^{34}S_{CAS}$ records and confirms a large, $\sim$6.5‰ $\delta^{34}S_{CAS}$ decrease in the Early Carboniferous. Importantly, the record also features a novel 2-5‰ increase in $\delta^{34}S_{CAS}$ near the Serpukhovian-Bashkirian boundary (323.4 Ma) that coincides with carbonate $\delta^{13}C$ and $\delta^{18}O$ increases. Variability in $\delta^{34}S_{CAS}$ is minor both within ($<$ 0.3‰) and among ($<$ 2‰) individual co-depositional brachiopod specimens.

A taxon-specific $\delta^{34}S_{CAS}$ offset is present in one species (*Composita subtilita*) that also exhibits a $\delta^{13}C$ offset, supporting the existence of biological "vital effects" on $\delta^{34}S_{CAS}$. Geologic evidence and mathematical modeling of the Permo-Carboniferous carbon and sulfur cycles suggest that changes in the burial ratio of organic carbon to pyrite sulfur ($R_{C:S}$) are insufficient to explain the observed mid-Carboniferous $\delta^{34}S_{CAS}$ record. We found that changes in the ^{34}S depletion of pyrite relative to seawater sulfate ($\Delta\delta^{34}S$) or in the $\delta^{34}S$ of the input to the ocean ($\delta^{34}S_{in}$) are also needed. Large additions of O_2 from organic carbon burial during the Permo-Carboniferous cannot be entirely compensated for with sulfur cycle changes; lower than modern late Visean pO_2 and/or additional O_2 sinks are needed to keep pO_2 at plausible levels. Based on the geologic context surrounding our record's mid-Carboniferous $\delta^{34}S_{CAS}$ increase, our results argue for simultaneous changes in pyrite burial, $\Delta\delta^{34}S$, and $\delta^{34}S_{in}$, driven by sea level or tectonically induced changes in environments of sulfur burial, as a viable mechanism to produce rapid seawater $\delta^{34}S$ changes.

II.2 Introduction

The global marine sulfur cycle plays a key role in regulating the oxygenation of Earth's ocean and atmosphere. This regulation occurs through linkages between the sulfur and carbon cycles via processes like microbial sulfate reduction (e.g. [195]) and oxidative weathering of sulfide minerals (e.g. [341]). A closely balanced transfer of electrons between the carbon and sulfur cycles is often invoked in explaining relatively stable Phanerozoic surface O_2 concentrations (e.g. [107, 347]). However, Berner and Raiswell (1983) note that changes in the sedimentary burial ratio of organic carbon to pyrite sulfur may cause imbalances in this coupled redox system and result in changes in O_2 concentration, suggesting the possibility of a dynamic coupling between the carbon and sulfur cycles.

Previous work has demonstrated dynamic behavior of the carbon and sulfur cycles during the Carboniferous (359.3-298.9 Ma) and Permian (298.9-251.9 Ma; [171, 320, 368, 369, and references within]. These periods constitute the last "icehouse" interval prior to the modern one [232]. Coal deposits (e.g. [236]), ^{13}C-enriched marine carbonate fossils [123], and box modeling efforts (e.g. [26]) suggest voluminous organic carbon burial and an associated atmospheric pO_2 increase during this time. Early analyses of the sulfur isotopic composition of sulfate evaporites [320, and references within] showed substan-

tial age-dependent differences in the $\delta^{34}S$ of Carboniferous evaporites, but low temporal resolution hampered precise correlation with changes in the carbon cycle. Kampschulte, Bruckschen, and Strauss (2001) improved upon these data using measurements of the $\delta^{34}S$ of carbonate-associated sulfate (CAS) in brachiopods. Their study documented a large ($\sim$7‰) decrease in $\delta^{34}S_{CAS}$ during the Tournaisian and early Visean, a modest 2-3‰ increase during the mid-Carboniferous, and a subsequent decrease during the mid- to late Carboniferous [171]. Later brachiopod and conodont $\delta^{34}S$ measurements by Wu and colleagues (2013, 2014) confirmed the trends in the early and latest Carboniferous portions of this record. Maharjan et al. (2018) have argued for the existence of an additional positive $\delta^{34}S$ excursion in the mid-Tournaisian based on whole rock CAS $\delta^{34}S$ (i.e., $\delta^{34}S_{CAS}$) measurements, but previous work [262, 263, 281, 282, 289] suggests that diagenetic alteration may prevent whole rock measurements from reliably recording seawater $\delta^{34}S$. Additional work utilizing diagenetically-resistant phases such as brachiopod secondary and tertiary layer calcite (e.g. [66, 121, 283]) is needed to resolve uncertainties in existing records and improve correlation with the carbonate $\delta^{13}C$ record (e.g. [123]).

Here, we present a new $\delta^{34}S_{CAS}$ record for the Permo-Carboniferous derived from individual well-preserved impunctate brachiopods. Our record allowed us to test the reproducibility of existing Permo-Carboniferous brachiopod $\delta^{34}S_{CAS}$ records [171, 172, 368, 369]. We also evaluated the influence of interspecimen and interspecies $\delta^{34}S_{CAS}$ differences on the variance observed in long-term temporal records. Our data reveal a novel 3-5‰ $\delta^{34}S_{CAS}$ increase at the Serpukhovian-Bashkirian boundary ($\sim$323.4 Ma) and demonstrate that the combination of careful diagenetic screening, analysis of individual brachiopods, and taxonomic classification can substantially improve the precision of temporal $\delta^{34}S_{CAS}$ records. Subsequent box modeling successfully replicates these data through large carbon and sulfur cycle perturbations and supports a large atmospheric pO_2 increase. Our results further cement the Permo-Carboniferous as an important transitional period in Earth history.

II.3 Sample localities

Samples for this study were collected in previous studies [102, 120, 121, 122, 123, 223, 224, 225, 226, 287] from several regions located at tropical and subtropical latitudes during the Carboniferous and Permian (Figure II.1), with the major-

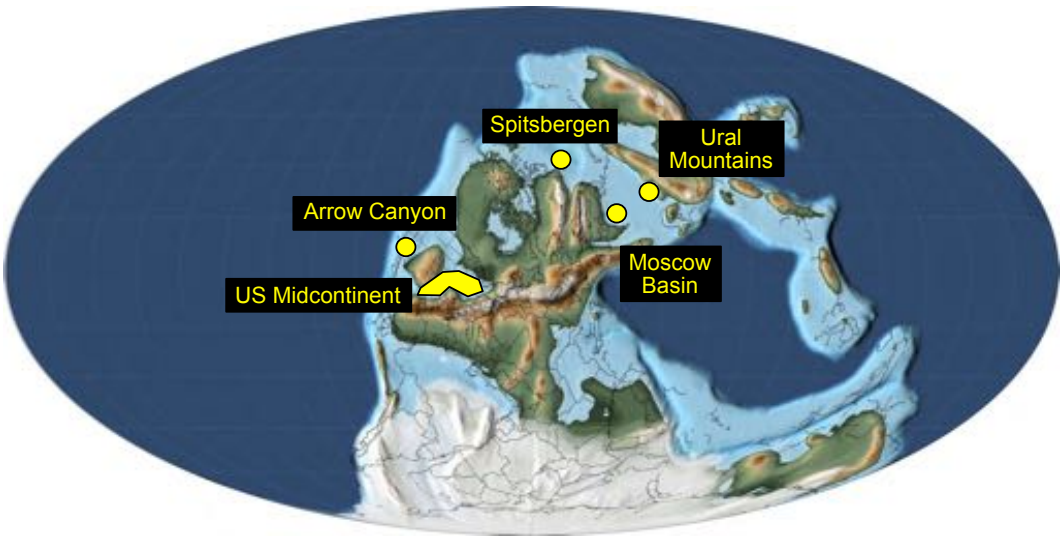

Figure II.1: Paleogeographic map depicting brachiopod sample localities (filled yellow regions) as situated at a maximum flooding surface during the Kasimovian stage of the late Carboniferous (∼305.3 Ma). Map is derived from the PALEOMAP project and modified after Scotese (2014) [298].

ity coming from the US Midcontinent, Moscow Basin, and the Ural Mountains. Additional samples were collected at Arrow Canyon, Nevada (USA) and on the island of Spitsbergen. Each locality is described in brief in Appendix A. Sample ages are derived from biostratigraphy; references may be found in the supplementary information for Grossman et al. (2008) [123].

II.4 Methods

II.4.1 Sample characterization and drilling

Detailed descriptions of sample collection and preparation may be found in previous studies [102, 123, 287, and references within]. In brief, collected brachiopods were removed from their sedimentary matrix, embedded in epoxy, and thin-sectioned. Thin sections were subsequently viewed and photographed under plane-polarized light with an optical microscope to characterize the microstructural preservation of the shells. Thin sections were also subjected to cathodoluminescence microscopy to identify shell regions with diagenetically added Mn.

Based on the above characterization, powders for this study were drilled from the billet corresponding to each thin section using a handheld dental drill or a Dremel tool. Photomicrographs were used as a guide to target non-luminescent,

optically transparent areas of the secondary and tertiary shell layers during drilling. These areas — especially the prismatic tertiary layer — have been previously identified (e.g. [121, 122]) as the most likely to be unaltered and thereby yield a primary geochemical composition. Powders were drilled from material within ∼2 mm of the billet surface for most samples to avoid the possibility of drilling into diagenetically altered regions at depth; however, we detect no obvious decrease in data quality for samples where we explicitly noted drilling beyond this depth. A total of 0.2 to 10 mg of powder was collected to yield enough S (10+ nanomoles) for precise $\frac{^{34}S}{^{32}S}$ ratio measurement depending on expected CAS abundance. Any explicit drilling of material from texturally or geochemically altered regions was noted to enable removal of these data from the final compilation.

To evaluate $\delta^{34}S_{CAS}$ variability within individual specimens, triplicate samples were drilled from well-preserved areas of three large brachiopod specimens (two *Neospirifer sp.* from the US Midcontinent and one *Choristites sp.* from the Russian Platform). In addition, replicate specimens from the same sediment horizon were sampled in 39 different instances to evaluate interspecimen and interspecies variability in $\delta^{34}S_{CAS}$.

II.4.2 Laboratory processing, CAS abundances, and $\delta^{34}S$ measurements

As in previous studies [243, 244, 262], sample powders underwent a thorough cleaning and column purification process to isolate CAS for mass spectrometry. Powders were submerged in 1 mL 10% (w/w) NaCl solution under sonication for at least four hours to remove soluble sulfate unassociated with the carbonate crystal lattice and were subsequently rinsed five times with 18.2 MΩ Millipore Milli-Q water. Powders were then transferred to pre-weighed microcentrifuge tubes, dried down in a laminar flow bench, and weighed on a microbalance. Samples were dissolved in a small excess of 0.5 N Seastar® HCl (300-500 μL), dried down, and taken up in 0.5% (v/v) Seastar® HCl. Sulfate from each sample was isolated on an anion exchange column containing 0.8 mL of Bio-Rad® AG1-X8 resin preconditioned with 2 x 8 mL 10% (v/v) reagent grade HNO_3, 2 x 8 mL 33% (v/v) reagent grade HCl, and 2 x 8 mL 0.5% Seastar® HCl. Following 3 x 8 mL rinses of the column with 18.2 MΩ water, retained sulfate was eluted with 3 x 1.6 mL 0.45 N Seastar® HNO_3. Samples were then dried down on a hot plate in a PicoTrace hood. Quality control was maintained by running at least one

seawater sample, one deep sea coral consistency standard, and two blanks with each batch of columns (10-20 in each batch).

To quantify CAS abundances, purified samples were re-dissolved in 18.2 MΩ water and an aliquot removed for concentration measurements. Sulfate concentrations were measured on a Dionex® ICS-3000 ion chromatography system equipped with a 2 mm AS4A-SC column using a 1.8 mM Na_2CO_3 / 1.7 mM $NaHCO_3$ eluent. Based on the measured sulfate concentrations, samples were dried down, re-dissolved a final time in 5% (v/v) Seastar® HNO_3, and diluted in 2 mL autosampler vials to attain a sulfate concentration matching that of a Na_2SO_4 bracketing standard (either 10 μM or 20 μM). Sulfur isotope ratios were measured on a Neptune Plus multi-collector inductively coupled plasma mass spectrometer (MC-ICP-MS) equipped with a CETAC® Aridus II desolvating nebulizer system at Caltech using the method of Paris et al. (2013). Accuracy was monitored by including at least two seawater standards and a deep sea coral consistency standard in each Neptune run (12-30 samples). Average across all runs was $+21.03 \pm 0.02‰$ for seawater ($n = 46$), $+22.13 \pm 0.03‰$ for the deep sea coral standard ($n = 15$), and $+3.0 \pm 3.3‰$ for procedural blanks ($n = 34$). Average procedural blank size was 0.28 ± 0.05 nanomoles of S. All listed uncertainties are 1σ population standard errors unless otherwise stated. Typical blank-corrected values have a 1σ standard error of the mean of 0.12‰ or less based on replicate 50-measurement blocks of the same sample solution.

II.4.3 Synchrotron X-ray fluorescence (XRF) mapping and X-ray absorption near-edge structure (XANES) spectroscopy

To better understand the distribution of sulfur and other elements within brachiopod specimens, we generated micro-XRF maps of elemental distributions for a small subset of sample thin sections (four in total) on beamline 14-3 at the Stanford Synchrotron Radiation Lightsource (SSRL). Maps were generated by rastering a five micron x-ray beam across each thin section using a Newport sample stage kept under a He atmosphere to reduce x-ray attenuation in air at "tender" (1-5 keV) x-ray energies. Incident beam energy was controlled with a Si 111 $\phi = 90$ crystal monochromator and calibrated using an internal sodium thiosulfate standard defining the thiol peak as 2472.02 eV. Sulfur distribution data were collected at an energy of 2482.5 eV using a Vortex fluorescence detector. Several XANES points per sample were also collected, with multiple repeats

for points with low sulfur fluorescence intensity to increase the signal to noise ratio of the resulting spectra.

II.5 Results

CAS abundance and $\delta^{34}S$ data for all brachiopod samples that contained at least four nanomoles of S and exhibited no evidence of diagenetic alteration are listed in Table A.1. Data for samples containing less than four nanomoles total of sulfur were discarded due to unreasonably large standard errors and inaccuracy resulting from a large blank contribution to the total S. Samples that showed evidence of poor preservation during sample characterization (e.g., brightly luminescent regions) have also been excluded from this table and subsequent figures, but are listed in Table A.2. This table includes two samples with unusually low (<6‰) $\delta^{34}S_{CAS}$ and one additional outlier of +18.47‰ at 297.4 Ma. The two unusually low samples (TUW050 replicate and WP62a KL-1) were noted as containing slightly luminescent fibrous material in the drilled area. We did not observe any evidence of alteration in the additional outlier sample (RAK38-1); perhaps this sample was contaminated by matrix material or by diagenetically altered material present below the surface of the sample billet. Importantly, the $\delta^{34}S$ time series we present and our conclusions regarding the data are largely unaltered by the inclusion or exclusion of these data.

II.5.1 Intraspecimen CAS abundances and $\delta^{34}S$ variability

One goal of this study was to evaluate the contribution of intraspecimen $\delta^{34}S_{CAS}$ variation to the precision and accuracy of temporal records. Brachiopods RU165-1 (a *Choristites sp.* specimen from the Moscow Basin in Russia), KSN18, and KSN19 (*Neospirifer dunbari* specimens from Kansas) were each sufficiently large for unaltered regions to be sampled in triplicate to probe within-brachiopod variation. CAS abundance varies by at least 20% within each specimen, with a mean CAS abundance and 1σ standard deviation of 639 $\pm$ 65 ppm for RU165; 10152 $\pm$ 2481 ppm for KSN18; and 9864 $\pm$ 3386 ppm for KSN19. Despite this significant variability in CAS abundance, $\delta^{34}S_{CAS}$ varies by $\leq$ 0.3‰ within specimen. The mean $\delta^{34}S$ and 1σ standard deviation were 12.01 $\pm$ 0.14‰ for RU165; 12.56 $\pm$ 0.04‰ for KSN18; and 12.55 $\pm$ 0.10‰ for KSN19. These results suggest that intraspecimen variation is a trivial source of scatter within temporal brachiopod $\delta^{34}S_{CAS}$ records so long as well-preserved secondary

and tertiary layers are sampled.

Micro-XRF mapping and XANES spectroscopy of thin sections also confirm substantial variation in CAS abundance within individual brachiopod specimens. XANES spectra typically lack the characteristic 2481 eV "shoulder" of organic sulfate esters and include a post-edge feature at 2484.9 eV (Figure II.2), suggesting that the sulfur present is dominantly inorganic sulfate [283]. Figure II.3 displays micro-XRF maps of the CAS distribution within sample KSN18. This thin section was previously mapped by Mii and Grossman (1994) [223] using an electron microprobe at discrete points. Continuous mapping at high (10 μm) resolution demonstrates $\sim$150% variation in CAS abundance based on the minimum and maximum fluorescence intensities measured at different pixels within the shell. This is consistent with the $\sim$160% variation in CAS abundance among powders drilled from this sample for $\delta^{34}S$ measurements. Maps of the three additional thin sections also featured variations in CAS abundance near this level, with the most variable sample (TWS43, a *Composita subtilita* specimen) exhibiting $\sim$190% variation. Secondary fibrous material shows elevated CAS contents relative to prismatic material within this specimen, consistent with electron microprobe spot analyses by Grossman et al. (1996) [122] showing higher $\frac{S}{Ca}$ ratios in fibrous *Composita* material.

II.5.2 Interspecimen CAS abundance and variability

We additionally interrogated variation among co-depositional brachiopods. Extensive collection of brachiopods for previous studies [123, and references within] enabled us to measure multiple brachiopods from the same sediment horizon in 39 different instances. Ranges in $\delta^{34}S_{CAS}$ among brachiopods specimens within individual horizons are small (Figure A.1), with over half (22 of 39) of the differences 1‰ or less, and approximately 90% (35 of 39) 2‰ or less. The 95% confidence interval (CI) calculated in 0.1 Myr time steps from a restricted cubic spline through our data (see Appendix A, section A.3) confirms this degree of confidence, with 76.1% of the time steps having a CI spanning 2‰ or less and 92.8% spanning 2.5‰ or less. Variation among some taxa is systematic; for example, *Composita sp.* within the late Carboniferous and early Permian is 1-2‰ higher in $\delta^{34}S_{CAS}$ relative to co-depositional specimens from other taxa (Figure II.4).

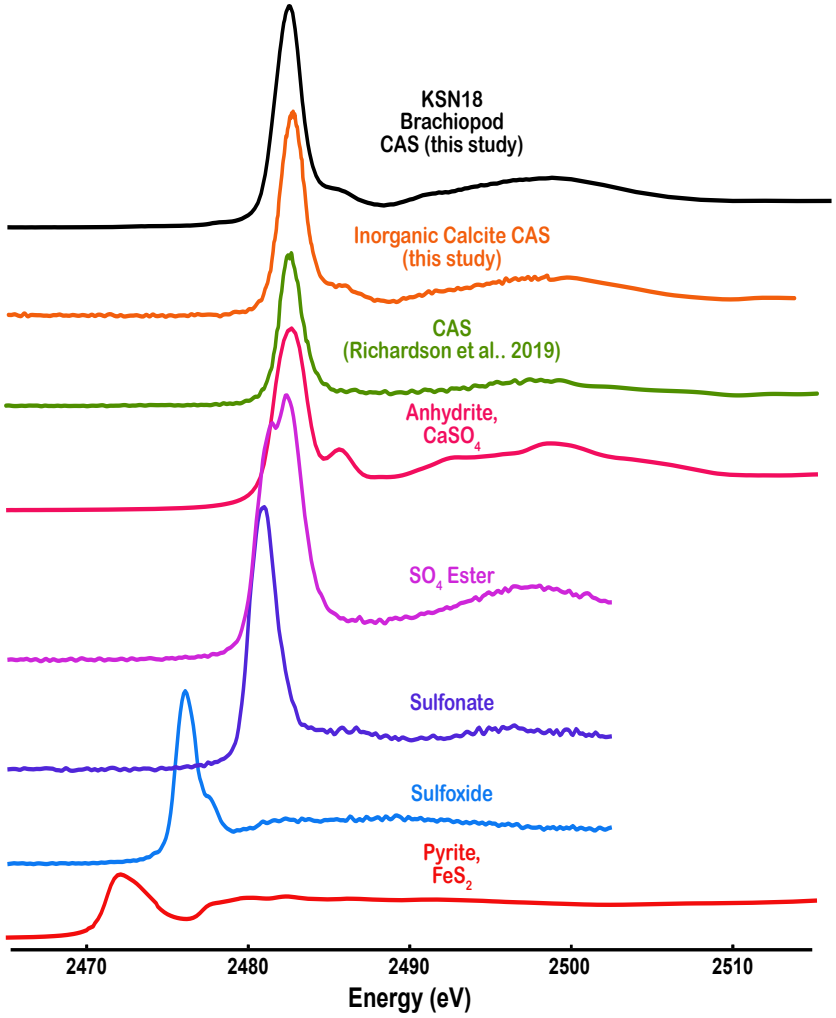

Figure II.2: Background-corrected and averaged X-ray absorption near-edge (XANES) spectra for sample KSN18 (top, black line) compared against reference spectra for inorganic and organic sulfur compounds (colored lines). Spectra have been vertically offset for ease of visualization. The KSN18 CAS trace averages measurements obtained from 15 unique points within the sample thin section to improve the signal to noise ratio and demonstrates a dominance of inorganic CAS over other sulfur phases. Although very small peaks are present in the pre-edge region of the spectra at several points used in this composite trace, the ~2482 eV peak characteristic of SO_4 dominates in intensity in all cases. The composite trace does not have a prominent pre-edge shoulder on the main ~2482 eV peak like the SO_4 ester and has none of the post-edge secondary peaks characteristic of anhydrite. The lack of these features strongly suggests that the sulfur present is inorganic, lattice-bound sulfate [283]. Reference spectra have been collected at SSRL (sulfoxide, sulfonate, SO_4 ester), obtained from the European Synchotron's ID21 Sulfur XANES spectra database, or obtained from previous studies [283].

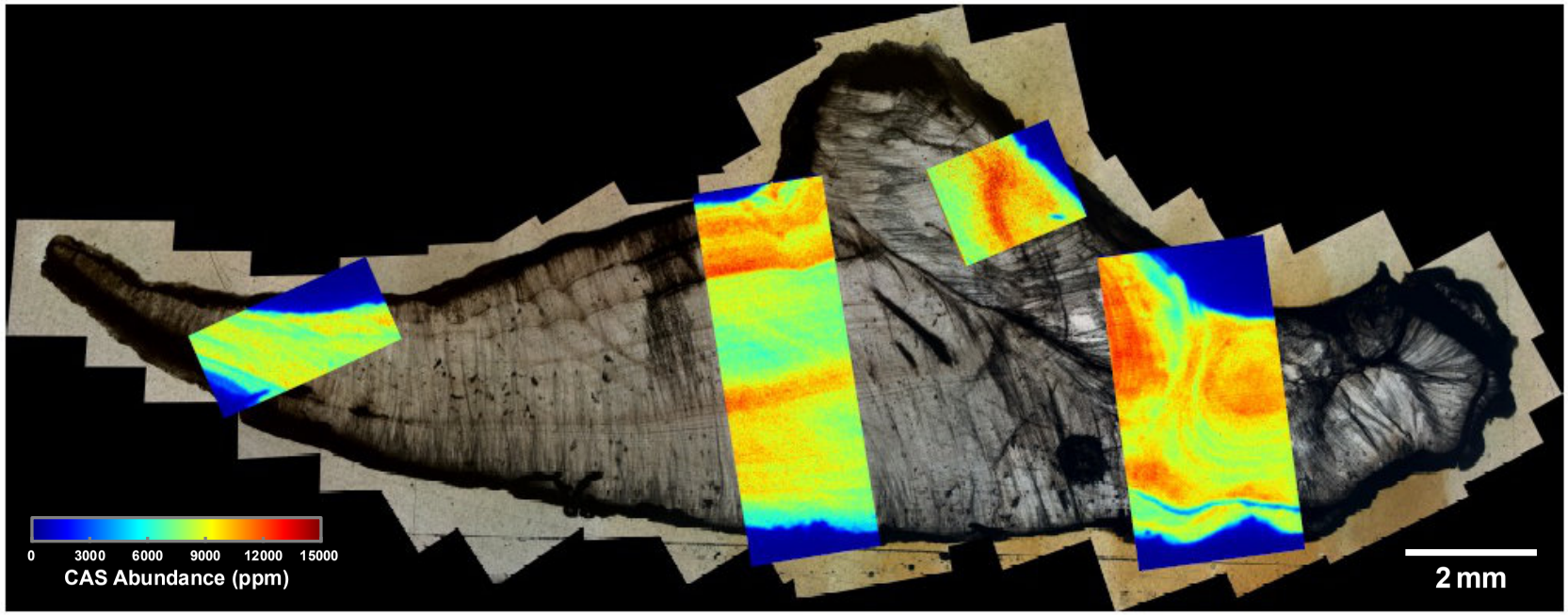

Figure II.3: Transmitted light image of the thin section for sample KSN18 with XRF maps of CAS distribution overlain over mapped regions. XRF maps were captured at 2482.5 eV using a 10 micron step size. Color bar (bottom left) denotes approximate CAS abundance based on calibration with measurements of CAS abundance in sample powders drilled from multiple regions within the thin section billet.

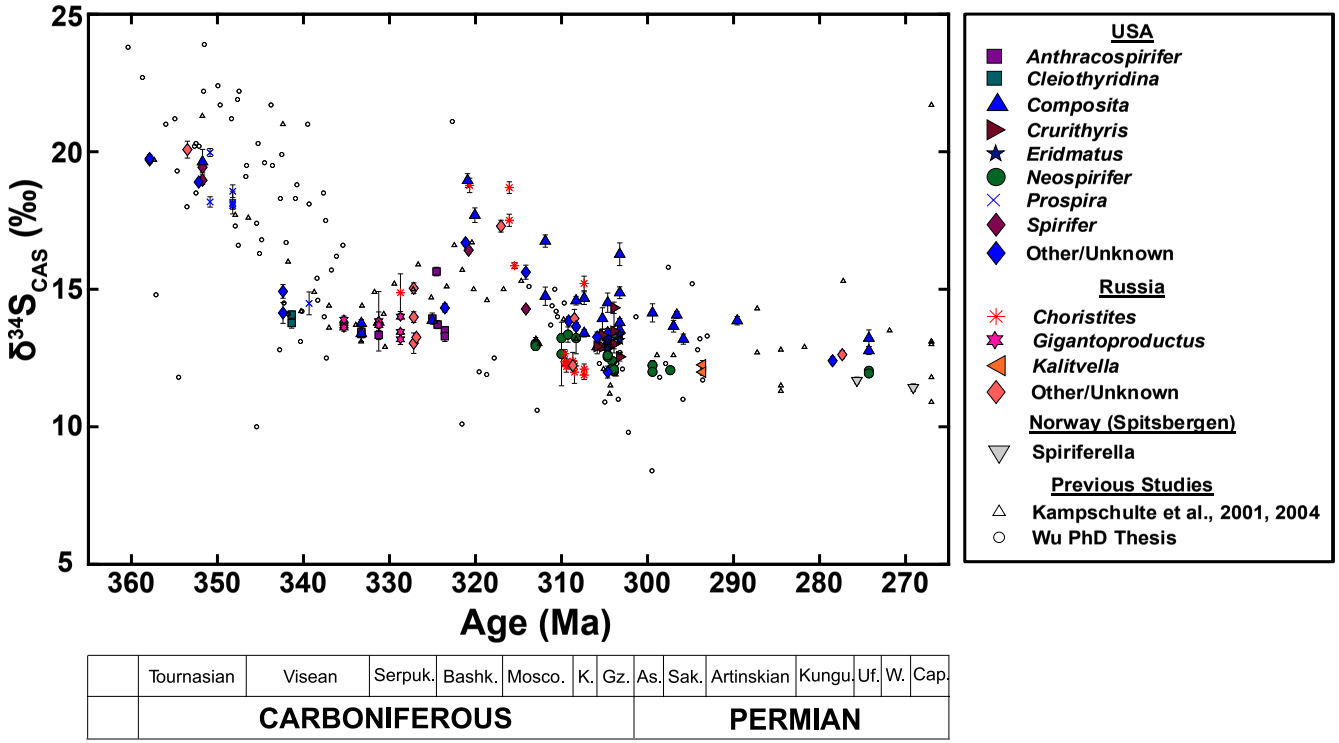

Figure II.4: $\delta^{34}S_{CAS}$ plotted against sample age (GTS 2020 timescale; [117]) for brachiopod specimens measured in this study (large filled symbols). Each unique symbol denotes data collected from a different brachiopod genus. Error bars denote 2σ standard errors. Data from multiple previous brachiopod-based studies [171, 172, 259, 368] are plotted as small hollow symbols to provide a basis for comparison. Note the offset of late Carboniferous *Composita* data points toward higher $\delta^{34}S_{CAS}$ values.

II.5.3 Temporal $\delta^{34}S$ variability

Our new record of $\delta^{34}S_{CAS}$ variation in the Carboniferous and the Early Permian (Figure II.4) displays substantial temporal variability and is mostly consistent with previous brachiopod-based $\delta^{34}S_{CAS}$ records [171, 172, 259, 368]. The earliest Carboniferous features an approximately 6.5‰ decrease in $\delta^{34}S_{CAS}$ from values of ∼+20‰ at the start of the Tournaisian (359.3 Ma) to ∼+13.5‰ in the early to middle Visean (∼338 Ma). Stasis near this +13.5‰ value is punctuated by a sharp increase in $\delta^{34}S_{CAS}$ near the Serpukhovian-Bashkirian boundary (323.4 Ma). $\delta^{34}S_{CAS}$ increases 2‰ to 5‰ within about 2.4 Myr. Peak values of ∼+17‰ in the Bashkirian (∼320 Ma) gradually decline over ∼15 Myr and reach average values near +13‰ by 305 Ma. This decline reaches values as low as +12‰ if the non-*Composita* values are used. Following the Moscovian (315.2-307.0 Ma), $\delta^{34}S_{CAS}$ remains approximately constant through the end Carboniferous (298.9 Ma) into the early Permian. Minimum $\delta^{34}S_{CAS}$ values near +11.5‰ at ∼269 Ma perhaps indicate a small and gradual seawater $\delta^{34}S$ decline over ∼35 Myr.

II.6 Discussion

II.6.1 Sources of variability in CAS abundance

CAS abundance shows a high degree of variability in our study, with up to a factor of two variation within individual specimens and an order of magnitude variation (< 1000 ppm to > 10000 ppm) among specimens from different taxa. The source of this variability within biogenic carbonates has not been robustly constrained. Previous research has shown that CAS abundance within carbonates may be a function of the SO_4^{2-} to CO_3^{2-} activity ratio in the precipitating solution [53], the kinetics of carbonate precipitation (i.e., growth rate; [53]), and the distribution of organic matrix within the shell structure [80, 83]. Diagenetic alteration could also affect CAS abundance, but is an unlikely explanation given our screening for well-preserved samples. Variations are also much too large to be explained by changes in the SO_4^{2-} to CO_3^{2-} activity ratio given the long timescales for changes in seawater $[SO_4^{2-}]$ and $[CO_3^{2-}]$ relative to brachiopod lifespans. Richardson et al. (2019) [283] proposed two likely sources of CAS abundance variations in brachiopods: (1) changes in shell growth rate and (2) oxidation of heterogeneously-distributed organic sulfur compounds. Given the dominance of inorganic CAS in our specimens, we view growth rate variations

as the primary control upon variations in CAS. A growth rate influence is supported by covariance of sulfur abundance with other geochemical data like $\frac{Mg}{Ca}$, $\delta^{13}C_{carb}$, and $\delta^{18}O_{carb}$ in brachiopods (e.g. [223]) and other biogenic carbonates (e.g. [243]). However, oxidized organic compounds could play a minor role in controlling CAS abundance and may be responsible for some of the variability we observe within individual specimens and among co-depositional specimens.

II.6.2 Sources of variability in temporal $\delta^{34}S$ records

To the best of our knowledge, this study represents the first systematic look at $\delta^{34}S_{CAS}$ variation within and among co-depositional, well-preserved brachiopod specimens. Our small-sample approach (0.2-10 mg) has allowed us to probe subtle differences in $\delta^{34}S_{CAS}$ that may have been obscured through mixing of powders from multiple brachiopods (e.g. [172]) or from multiple carbonate components within whole rocks (e.g. [205]). Many specimens measured here were too small to meet the sample requirements of traditional gas source mass spectrometry.

Variation in $\delta^{34}S_{CAS}$ among co-depositional brachiopods within this study is small. The majority of horizons from which multiple brachiopods were sampled show a $\delta^{34}S_{CAS}$ range $\leq 2‰$ in magnitude. This is consistent with the $\sim$2‰ range in brachiopod $\delta^{34}S_{CAS}$ observed at single timepoints by Present et al. (2015) [262] and Kampschulte, Bruckschen, and Strauss (2001) [171]. In studies with comparable measurement precision, our data suggest that one may invoke a change in the $\delta^{34}S$ of seawater sulfate with 68% confidence if the difference between two chronologically successive $\delta^{34}S_{CAS}$ data points is larger than $\sim$0.9‰ and with over 95% confidence if larger than $\sim$1.7‰ (see Appendix A, A.3). Variability among contemporaneous specimens is a more likely explanation for differences smaller than these thresholds. Data quantity, preservation differences, and other relevant factors should also be considered in linking apparent temporal trends in $\delta^{34}S_{CAS}$ to changes in seawater $\delta^{34}S$.

Our data hint that further improvement in the precision of $\delta^{34}S_{CAS}$ records may be possible with careful attention to brachiopod taxonomy. For example, $\delta^{34}S_{CAS}$ in *Composita subtilita* is 1-2‰ higher than $\delta^{34}S_{CAS}$ in co-occurring taxa (*Crurithyris*, *Eridmatus*, and *Neospirifer*). All our *Composita* $\delta^{34}S_{CAS}$ data younger than $\sim$311 Ma were collected from *Composita subtilita* specimens, while earlier *Composita* data come from other species. Note that Grossman, Zhang, and

Yancey (1991) found a $\sim$+1‰ offset in $\delta^{13}C$ in *Composita subtilita* compared with co-occurring taxa. Grossman, Zhang, and Yancey (1991) interpreted this offset as reflecting either a unique, attached life habit minimally affected by sediment pore waters or a species-specific "vital effect" (e.g. [69]). While we cannot rule out a diagenetic origin for these offsets, we favor a species-specific "vital effect" on $\delta^{34}S_{CAS}$ for *Composita subtilita* based on the relatively consistent magnitude of these offsets and the low Na and S abundances for this species [122]. The low and variable Na abundances within *Composita subtilita* ($\frac{Na}{Ca}$ $\sim$2-7 in one measured specimen; [122]) cannot be explained by a lack of pore water chemistry influence. A vital effect is consistent with small offsets in $\delta^{34}S_{CAS}$ from seawater $\delta^{34}S$ in foraminifera [243, 279], deep sea corals [244], and modern brachiopods [262, 283].

II.6.3 Comparison with published CAS $\delta^{34}S$ records

Our new data confirm many observations in the brachiopod $\delta^{34}S_{CAS}$ records generated by Kampschulte, Bruckschen, and Strauss (2001) [171] and Wu (2013) [368], but also diverge from these records in important ways. First, our data feature much less $\delta^{34}S_{CAS}$ scatter during the Tournaisian (359.3-346.7 Ma) and Visean (346.7-330.3 Ma), especially compared with the dataset of Wu (2013) [368] (Figure II.4). In some instances, the new data constrain $\delta^{34}S_{CAS}$ to within 2‰ where existing data spanned over 5‰. Our data agree better with the Kampschulte, Bruckschen, and Strauss (2001) [171] data than the Wu (2013) [368] data, in part because of the samples analyzed. Both Kampschulte, Bruckschen, and Strauss (2001) [171] and our study primarily analyzed samples from the US Midcontinent in the Tournaisian and Visean portions of the $\delta^{34}S_{CAS}$ record, including several samples shared between the studies. In contrast, most of Wu's (2013) [368] samples came from northern Europe. The Wu (2013) [368] $\delta^{34}S_{CAS}$ data are more varied and often high. This may reflect addition of diagenetic pore-fluid sulfate that has been enriched in ^{34}S through microbial sulfate reduction. The brachiopod shells analyzed by Wu (2013) [368] were "routinely checked" for diagenesis in previous studies [44, 348] using optical microscopy, scanning electron microscopy, and Mn contents. However, these methods have been shown to be less effective in avoiding diagenetic calcite with low $\delta^{13}C$ and $\delta^{18}O$ values than the methods used in this study [123]. Overall, our observations are consistent with early diagenetic alteration of the Wu (2013) [368] samples

through carbonate recrystallization or cementation. We favor a diagenetic explanation over possible geographic variability in seawater $\delta^{34}S$ due to similar scatter in the Wu (2013) [368] data collected from other localities (see Appendix A, section A.5).

In addition, our data reveal a notable increase in $\delta^{34}S_{CAS}$ at the Serpukhovian-Bashkirian boundary. Although this increase is present in the Kampschulte, Bruckschen, and Strauss (2001) [171] data, our results show a larger and more rapid increase ($\sim$3 versus $\sim$10 Myr, and up to 5‰ versus as little as 2‰). We suspect that the more gradual $\delta^{34}S_{CAS}$ increase observed by Kampschulte, Bruckschen, and Strauss (2001) [171] results from mixing brachiopods with disparate $\delta^{34}S_{CAS}$ values (see Appendix A, section A.4).

II.6.4 Isotopic co-variation within the Permo-Carboniferous

S, C, O, and Sr isotope records show compelling covariation during the Permo-Carboniferous (Figure II.5). This was first noted by Kampschulte, Bruckschen, and Strauss (2001) [171] and suggests an overarching tectonic control on all four systems. Exploring mechanisms that could generate these changes requires consideration of the major fluxes affecting each of these isotope systems. Thus, we constructed an isotopic box model of the Permo-Carboniferous carbon and sulfur cycles to test different mechanisms that could explain the observed variations in carbonate $\delta^{13}C$ and $\delta^{34}S_{CAS}$. We will focus on the period of contemporaneous increases in $\delta^{13}C$, $\delta^{18}O$, and $\delta^{34}S$ between 325 and 320 Ma.

II.6.4.1 Box modeling introduction

Our coupled one-box model of the carbon and sulfur cycles is described in detail in Appendix A (section A.7). Seawater $\delta^{34}S$ changes in our model may be driven by changes in the magnitude of the pyrite burial flux, changes in the isotopic offset ($\Delta\delta^{34}S$) between the pyrite burial flux and seawater, and/or changes in the $\delta^{34}S$ of the input flux (i.e., $\delta^{34}S_{in}$). Given a constant input flux of sulfur to the ocean, seawater $\delta^{34}S$ may rise due to an increase in the pyrite burial flux, an increase in $\Delta\delta^{34}S$, or an increase in $\delta^{34}S_{in}$. Of these three mechanisms, only pyrite burial has a direct effect on modeled atmospheric pO_2 if the fraction of sulfur input derived from oxidative weathering is constant. We force changes in pyrite burial in our model by coupling it to organic carbon burial via an as-

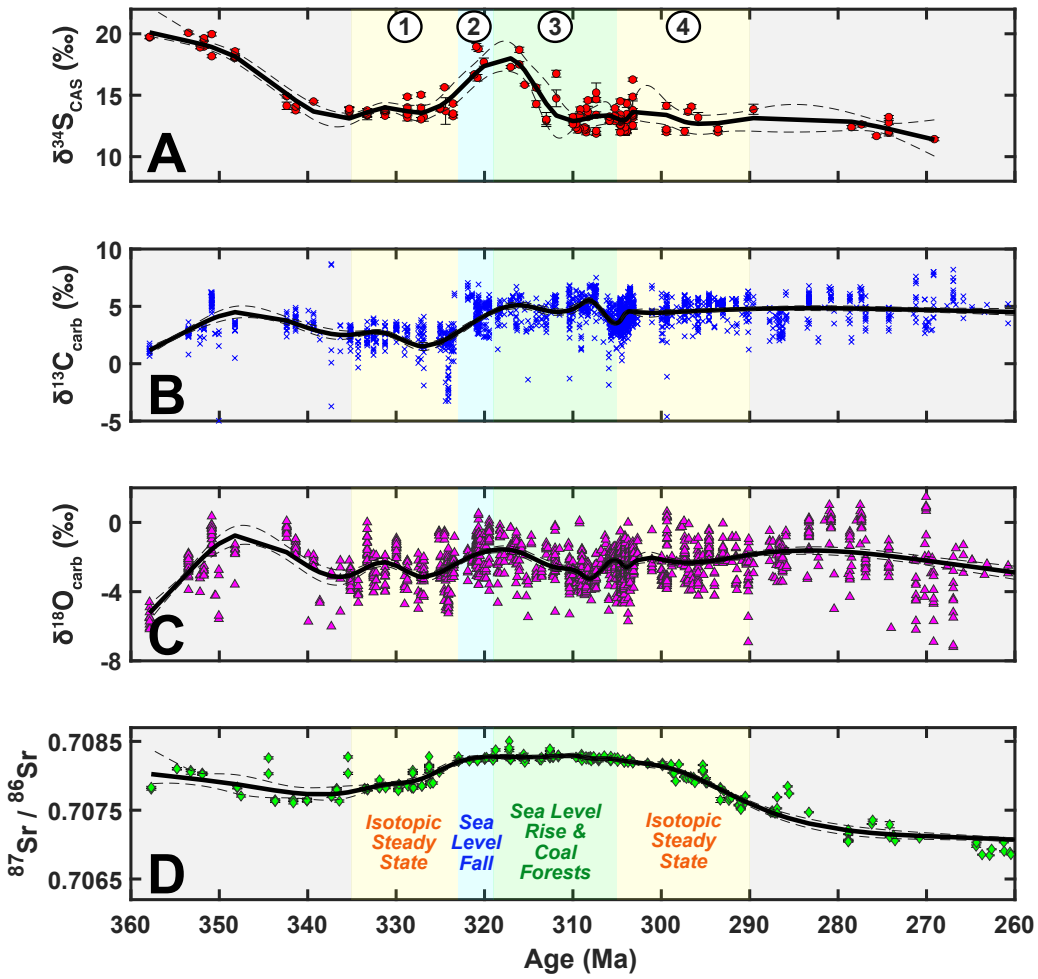

Figure II.5: Stacked plots of $\delta^{34}S_{CAS}$ (A; this study), carbonate $\delta^{13}C$ (B; [123]), carbonate $\delta^{18}O$ (C; [123]), and $\frac{^{87}Sr}{^{86}Sr}$ (D; [44, 45, 265, 348]) plotted against sample age (GTS 2020 timescale; [117]) for the Carboniferous and Early Permian. The black line in each plot denotes a restricted cubic spline through the data (see Appendix A, section A.3 for methods). Dark gray dashed lines represent 95% confidence interval bounds for each restricted cubic spline. Numbered, shaded boxes denote the driving events for the observed isotopic changes as described in detail in Discussion subsection II.6.4.2.

cribed burial ratio, $R_{C:S}$, and driving changes in organic carbon burial with the carbonate $\delta^{13}C$ data of Grossman et al. (2008). Step-function changes in $R_{C:S}$, $\Delta\delta^{34}S$, and/or $\delta^{34}S_{in}$ are allowed to occur at two time points, 325 Ma and 319 Ma, in order to generate model $\delta^{34}S$ curves that yield good matches to our $\delta^{34}S_{CAS}$ data (Appendix A, section A.7). Although such step-function changes may not be realistic, we use this approach to achieve the maximum rate of change in seawater $\delta^{34}S$ that a parameter change of a given magnitude could force. Our approach produces model results that yield the minimum magnitude of changes necessary to reproduce our data. More gradual changes in parameter values are possible, but such changes must be larger in absolute magnitude to reproduce the rate of change attained using step-function forcing.

II.6.4.2 Box modeling results

Berner and Raiswell (1983) [27] proposed that an increase in $R_{C:S}$ associated with an expanded Carboniferous terrestrial biosphere arises naturally from the Permo-Carboniferous carbon and sulfur isotopic records. This idea still works at the broadest scale of our new record, but at ∼323 Ma, both carbonate $\delta^{13}C$ and $\delta^{34}S_{CAS}$ clearly increase. These increases imply both a higher fraction of organic carbon burial and a higher fraction of pyrite burial at the onset of peak Carboniferous glaciation. We find that model runs driven by the carbonate $\delta^{13}C$ curve alone — i.e., with constant $R_{C:S}$, $\Delta\delta^{34}S$, and $\delta^{34}S_{in}$ — fail to adequately fit our data (Appendix A, Figure A.4). In addition, model runs in which just one of these three parameters is changed generally require parameter values that are inconsistent with geologic evidence. Most notably, $R_{C:S}$ must decrease at 325 Ma to values more representative of euxinic environments [27] to generate an adequately large mid-Carboniferous peak (Appendix A, Figure A.5). The $R_{C:S}$ decrease arises from a need for a transient increase in pyrite burial to drive up marine SO_4^{2-} $\delta^{34}S$, but the geologic record instead shows an increase in terrestrial organic sedimentation at this time [236] consistent with a $R_{C:S}$ increase. Variation of at least one additional parameter — $\Delta\delta^{34}S$ or $\delta^{34}S_{in}$ — is needed to maximize model-data fit quality while producing agreement with the geologic record.

Results from the model scenario that best concords with our data and the geologic record are shown in Figure II.6. We impose a permanent increase in $R_{C:S}$ at 325 Ma (Figure II.6D) and allow changes in $\Delta\delta^{34}S$ and $\delta^{34}S_{in}$ (Figures II.6E,F)

to force additional temporal variation in seawater $\delta^{34}S$. Best fit results under this scenario occur when (1) $R_{C:S}$ increases from 3.0 to 4.4 - 4.8 at 325 Ma, (2) $\Delta\delta^{34}S$ undergoes a 12‰- 20‰ increase (to 47‰- 55‰) at 325 Ma and a subsequent decrease to 25‰- 27‰at 319 Ma, and (3) $\delta^{34}S_{in}$ increases by 4‰- 6‰(to +8‰- +10‰) at 325 Ma and later decreases to +6‰ at 319 Ma. The potential mechanisms behind these changes in parameter values are discussed below. Although these changes in $\Delta\delta^{34}S$ are large, substantial variations in the biological isotopic fractionation ($^{34}\varepsilon$) associated with sulfur cycling occur due to variables like cell-specific sulfate reduction rate (e.g. [195, 313]) and sulfur metabolism (e.g. [60]). Differences in iron input (e.g. [303]) and physical depositional parameters (e.g. [246]) also affect the net $\delta^{34}S$ offset between seawater sulfate and sedimentary sulfides. These sources of variability lead to highly disparate $\Delta\delta^{34}S$ among modern environments [59] and suggest that changes of the magnitude required by these model runs may be plausible. Enhanced erosion of sulfate evaporites — possibly, the thick evaporite accumulations within the Windsor Group of the Maritimes Basin [352] — is a potentially viable mechanism of $\delta^{34}S_{in}$ increase (e.g. [309]).

We envision a sequence of events to drive these changes as follows and as numbered in Figure II.5. (1) Isotopic steady state within the marine sulfur cycle was maintained from 335 to 325 Ma, and seawater $\delta^{34}S$ remained nearly constant at ∼+13.5‰ during this period. (2) This isotopic steady state was interrupted by a 100+ m fall in eustatic sea level due to a combination of tectonics and the onset of peak Carboniferous glaciation [123, 232, 291]. Aerial exposure of shallow shelf environments promoted expansion of coal forests [236], an increase in $R_{C:S}$ [27], and an increase in carbonate $\delta^{13}C$ [123]. Loss of shelf environments increased $\Delta\delta^{34}S$ by forcing a higher fraction of pyrite burial in deep marine environments with high $\Delta\delta^{34}S$ (e.g. [279]), and erosion of sulfate evaporites (e.g. [309]) drove a correlative increase in $\delta^{34}S_{in}$. Seawater $\delta^{34}S$ rose rapidly to ∼+17‰ in response. (3) Long-term (i.e., second-order) sea level rose ∼50 m beginning around 319 Ma as indicated by sequence stratigraphy [291]. Coal forests [236] and high carbonate $\delta^{13}C$ [123] suggest that terrestrial organic carbon burial remained high throughout this time. Continental shelf environments increased in abundance with this sea level rise, re-invigorating shelf pyrite burial and decreasing $\Delta\delta^{34}S$ to near-initial values. $\delta^{34}S_{in}$ also decreased as evaporite erosion waned in intensity, possibly due to renewed sediment deposition [352]. Seawater $\delta^{34}S$ declined to ∼+13‰ over ∼15 Myr. (4) Isotopic steady state was re-

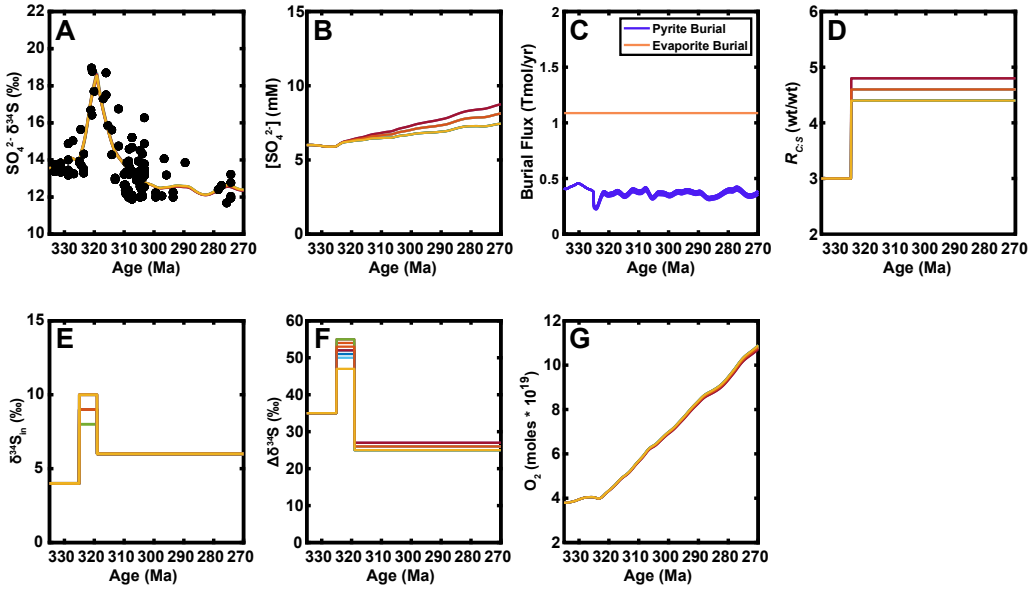

Figure II.6: Plots of (A) SO_4^{2-} $\delta^{34}S$, (B) $[SO_4^{2-}]$, (C) pyrite and evaporite burial fluxes, (D) $R_{C:S}$, (E) $\delta^{34}S_{in}$, (F) $\Delta\delta^{34}S$, and (G) O_2 reservoir size associated with the multi-variable parameter model runs in which $R_{C:S}$ was forced to increase at 325 Ma and both $\delta^{34}S_{in}$ and $\Delta\delta^{34}S$ were allowed to vary with time. Each colored line in the SO_4^{2-} $\delta^{34}S$ and $[SO_4^{2-}]$ plots represents a different model run; the ten best model-data fit runs are shown.

established at ∼305 Ma. Glacial deposits [97, 151, 232] and widespread, correlatable cyclothems with Milankovitch cycle-like periodicities [140] suggest that glacial cycles continued into the Permian. Higher long-term sea level [291] during the early Permian limited perturbations to the fraction of pyrite burial occurring on the shelf and the global $\Delta\delta^{34}S$. High $R_{C:S}$ was maintained via abundant deposition of organic-rich sediments through the earliest Permian [236].

II.6.4.3 Model implications for pO_2 and marine $[SO_4^{2-}]$

Our model results have important implications for past atmospheric oxygen levels. The final pO_2 in each of our model runs exceeds the initial pO_2 (assumed to be modern) by > 3x. However, the sulfur cycle perturbations make a minimal contribution to this pO_2 increase. In all model scenarios we explored, high Permo-Carboniferous carbonate $\delta^{13}C$ values demand a large increase in pO_2 due to a high organic carbon burial flux. The implausibly high final pO_2 values can be ameliorated in two ways: (1) starting the model with a lower initial pO_2 and/or (2) reducing the rise in pO_2 (see Appendix A, subsection A.8). An

implausibly large modeled pO_2 increase across the mid-Carboniferous is difficult to avoid unless a carbon input flux much lower than the modern value is assumed or an additional large sink for O_2 is imposed. Such results generally require pO_2 at 335 Ma to be much lower than modern pO_2 to keep Early Permian pO_2 levels below implausibly high levels. The sulfur cycle can reduce the amount of pO_2 increase through a reduction in pyrite burial, but it cannot entirely prevent too large of an increase in pO_2 on its own.

The rapid $\delta^{34}S$ increase at the Serpukhovian-Bashkirian boundary also provides insight into marine SO_4^{2-} concentrations during the Carboniferous. Our best fit model runs suggest that SO_4^{2-} concentrations of 5-10 mM are necessary for an excursion of appropriate magnitude and rapidity to occur. The best fit SO_4^{2-} concentration scales with the magnitude of changes in $R_{C:S}$, $\Delta\delta^{34}S$, and/or $\delta^{34}S_{in}$; i.e., smaller changes in these parameters require lower SO_4^{2-} concentrations for the model output to adequately fit the data. The 5-10 mM SO_4^{2-} concentration values are more consistent with the Late Devonian estimates of Lowenstein et al. (2003) (5-12 mM) than the Early Permian values (18-26 mM) from the same authors. If our data and the associated excursion timescale are accurate, our modeling suggests that the increase in the size of the marine SO_4^{2-} reservoir must have occurred primarily in the Late Carboniferous. The magnitude of the modeled $[SO_4^{2-}]$ increase is very sensitive to the imposed S input flux and the evaporite output flux; an imbalance of just a few percent results in $[SO_4^{2-}]$ changes of several mM when extrapolated over tens of Myr.

II.6.5 Mechanisms behind the Paleozoic $\delta^{34}S$ decrease

The early Carboniferous $\delta^{34}S$ decrease represents one of the largest changes in seawater $\delta^{34}S$ in the entire Phanerozoic record (Figure II.7). This change is part of a broader long-term decrease in $\delta^{34}S$ from the early Cambrian to the late Permian [172, 261]. Previous studies have interpreted this change as reflecting a long-term decrease in the relative fraction of sulfur leaving the ocean via pyrite burial (e.g. [98, 172]) or as a decrease in subduction flux of ^{34}S-depleted pyrite [57]. Our results are consistent with either of these interpretations. However, decreases in $\delta^{34}S_{in}$ and $\Delta\delta^{34}S$ are also capable of contributing to this decrease. A dominance of pyrite burial over these additional mechanisms of seawater $\delta^{34}S$ change requires that changes in $\delta^{34}S_{in}$ and $\Delta\delta^{34}S$ across this time be negligible or of inappropriate direction.

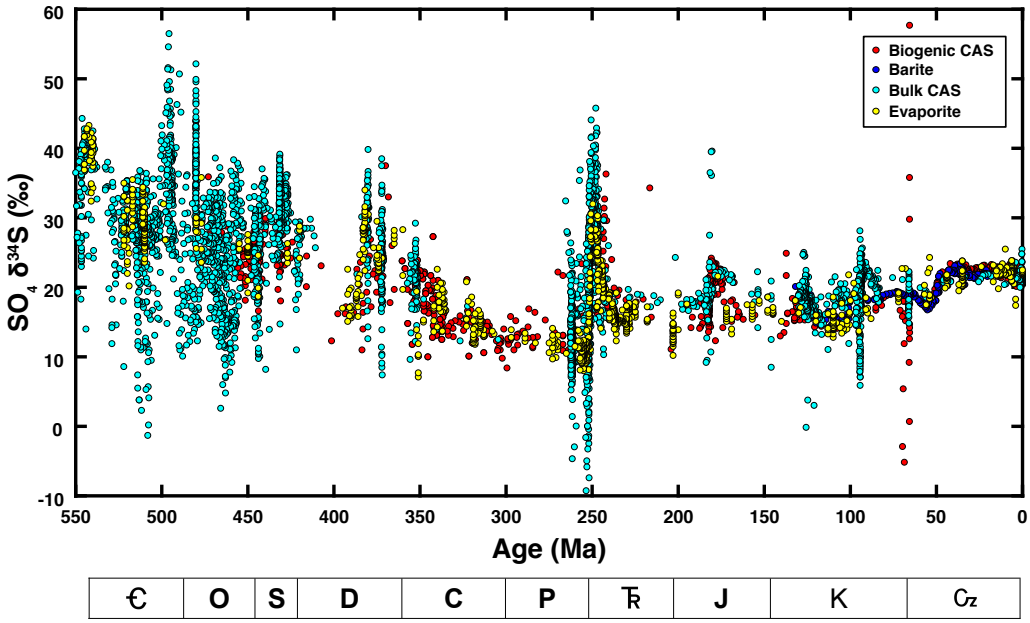

Figure II.7: Plot of sulfate $\delta^{34}S$ against age for biogenic carbonate CAS (red), barite (blue), bulk rock CAS (cyan), and evaporites (yellow). Additional bulk rock CAS data approaching $\delta^{34}S$ values as high as +70‰ during the Cambrian and as low as -40‰ during the latest Permian have been cut off by the axis limits. Data plotted on GTS2012 timescale [116]. Figure after Present, Adkins, and Fischer (2020) [261].

Reconstructions of the global $\Delta\delta^{34}S$ are typically made using the arithmetic difference between the $\delta^{34}S$ of seawater and the mean $\delta^{34}S$ of buried pyrite. Such reconstructions (e.g. [195, 369]) are obscured by a lack of accurate, high-resolution biogenic $\delta^{34}S_{CAS}$ records and a bias of the pyrite $\delta^{34}S$ record toward shallow shelf settings. Deep-ocean pyrite burial constitutes as much as half of the modern global pyrite burial flux [43] and could have been more important under lower Paleozoic deep ocean O_2 concentrations [319]. We tentatively label $\Delta\delta^{34}S$ change as an unimportant factor in the Paleozoic seawater $\delta^{34}S$ decrease given current evidence, but further investigation is warranted.

No geologic archives allow for direct reconstructions of the global $\delta^{34}S_{in}$ through time. However, modeling efforts by Halevy, Peters, and Fischer (2012) and Wu, Farquhar, and Strauss (2014) have suggested a long-term decline in $\delta^{34}S_{in}$ during the Paleozoic, especially following the first major Phanerozoic glaciation in the latest Ordovician (e.g. [204]; Figure II.7). We hypothesize that increased physical erosion rates associated with glaciation enhanced oxidative weathering

of pyrite (OWP; [341]) and gradually decreased $\delta^{34}S_{in}$. Regardless of cause (cf. [1]), OWP enhancement would consume some of the O_2 flux added by organic carbon burial and reduce the pO_2 increase observed in our modeling scenarios (see Appendix A, subsection A.8). We suggest that a $\delta^{34}S_{in}$ decrease is likely to have been important in decreasing Paleozoic seawater $\delta^{34}S$ given these considerations.

II.6.6 A mechanism for rapid changes in the marine S cycle

Previous studies of the Cretaceous and Cenozoic seawater $\delta^{34}S$ record [252, 254, 279] have revealed the potential for rapid ($> 0.5‰$ per Myr) changes in the marine sulfur cycle to occur on timescales of several Myr. Our new Permo-Carboniferous $\delta^{34}S_{CAS}$ record includes similarly rapid changes and indicates that they may be an inherent feature of the marine sulfur cycle (Figure II.8). Notably, rapid changes in these records are commonly separated by periods of stability in which $\delta^{34}S$ varies by $<2‰$ over 10+ Myr. Relatively low marine $[{SO_4}^{2-}]$ may enhance the potential for rapid changes in seawater $\delta^{34}S$ to occur. However, periods of long-term stability bracketing many of these rapid changes suggest threshold-like character within the marine sulfur cycle; i.e., a small change in the Earth system may yield either a large or small change in the marine sulfur cycle depending on the initial state of the system.

Following observations by other authors (e.g. [195, 246, 279]), we suggest that sea level and shelf area influence the marine sulfur cycle and are a key component of this threshold-like character. We envision that changes in the abundance of depositional environments distinct in their sulfur isotopic characteristics — e.g., shallow shelf versus deep marine environments — may simultaneously alter the pyrite burial flux, the $\Delta\delta^{34}S$ associated with global sulfur cycling, and $\delta^{34}S_{in}$. Although limited in scope, existing pyrite $\delta^{34}S$ records from Carboniferous marine sediments (e.g. [78, 166, 212, 310]) support an association of higher $\Delta\delta^{34}S$ with more distal marine environments in which pyrite forms under more open system conditions (e.g. [246]). Special emphasis is placed on simultaneous changes in the pyrite burial flux and $\Delta\delta^{34}S$, as the interaction of these terms may enable particularly rapid changes in seawater $\delta^{34}S$. Tectonics can play a key role in generating these changes and may be especially important in generating changes in $\delta^{34}S_{in}$ (e.g. [309]). Future work should more carefully consider $\Delta\delta^{34}S$ and $\delta^{34}S_{in}$ as significant drivers of seawater $\delta^{34}S$ change within the geo-

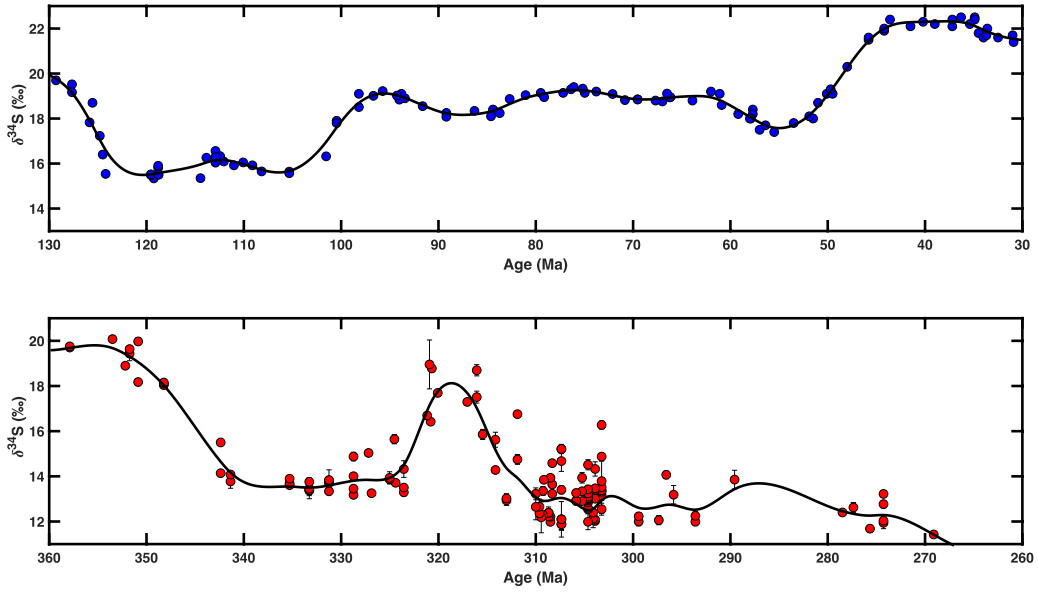

Figure II.8: Comparison of a 100 Myr interval of the marine barite $\delta^{34}S$ record [252, 254] spanning the Early Cretaceous through the Middle Cenozoic (top) and this study's biogenic CAS $\delta^{34}S$ record across the Carboniferous and Early Permian (bottom). The black line in each plot denotes a smoothing spline through the data. Ages are plotted on the GTS2012 timescale [116]. Periods of relative stability exceeding 10 Myr in duration are punctuated by intervals of rapid $\delta^{34}S$ change in both records, suggesting threshold-like behavior in the marine sulfur cycle.

logic record.

II.7 Conclusions

Here, we have reported a new Permo-Carboniferous $\delta^{34}S_{CAS}$ record generated exclusively from measurements of individual brachiopods. Our results indicate that $\delta^{34}S_{CAS}$ variation within and among well-preserved co-depositional brachiopod specimens is small ($< 0.3‰$ and $< 2‰$, respectively). Our results also suggest that single brachiopod $\delta^{34}S_{CAS}$ measurements can significantly improve the precision of existing Paleozoic $\delta^{34}S_{CAS}$ records. Our new record of Permo-Carboniferous $\delta^{34}S_{CAS}$ confirms trends seen in existing brachiopod $\delta^{34}S_{CAS}$ datasets [171, 368], but substantially improves upon the precision of these records. We resolved several changes that were ambiguous in their timing

and magnitude in these previous datasets. Most notably, we found a relatively sharp, 2-5‰ $\delta^{34}S_{CAS}$ increase near the Serpukovian-Bashkirian boundary coinciding with sea level fall and an expansion of continental glaciation. Systematic offsets in $\delta^{34}S_{CAS}$ for at least one species (*Composita subtilita*) suggest the possibility of taxon-specific brachiopod $\delta^{34}S_{CAS}$ vital effects. Future work to better understand these offsets may further improve the precision attainable in temporal $\delta^{34}S_{CAS}$ records.

Geologic evidence and box modeling indicate that changes in $\Delta\delta^{34}S$ and/or $\delta^{34}S_{in}$ are needed in addition to changes in pyrite burial to explain the mid-Carboniferous $\delta^{34}S_{CAS}$ record. Although Berner and Raiswell's (1983) [27] inference of an increase in the reduced C:S burial ratio appears robust, transient increases in $\Delta\delta^{34}S$ and/or $\delta^{34}S_{in}$ must be called upon to account for the mid-Carboniferous peak in $\delta^{34}S$. Large increases in pO_2 driven by organic carbon burial cannot be balanced by sulfur cycle perturbations. These increases necessitate that early to mid-Carboniferous pO_2 be much lower than modern pO_2 or that additional O_2 sinks be considered. We suggest that combined changes in pyrite burial, $\Delta\delta^{34}S$, and $\delta^{34}S_{in}$ should be considered more seriously as drivers of rapid changes in the $\delta^{34}S$ of seawater. Changes in shelf area may alter the relative proportions of isotopically distinct depositional environments and viably force these combined changes. Tectonics can play a key role in generating these shelf area changes and may also influence $\delta^{34}S_{in}$ via uplift and erosion. Improved Paleozoic biogenic $\delta^{34}S_{CAS}$ records will enable more accurate assessment of the timing of seawater $\delta^{34}S$ changes and provide fruitful avenues for future study.

Chapter III

$\delta^{34}S_{CAS}$ HETEROGENEITY ACROSS THE END-PERMIAN MASS EXTINCTION (EPME) IN SOUTH CHINA

III.1 Abstract

The End-Permian Mass Extinction (EPME) represents the largest known extinction in Earth's history. The dynamics of the marine sulfur cycle across this important event have been obscured by disagreement between sulfur isotopic records derived from CAS and sulfate evaporites. Here, we attempted to resolve this disagreement through new measurements of CAS $\delta^{34}S$ (i.e., $\delta^{34}S_{CAS}$) in subsampled carbonates collected from Permian-Triassic boundary (PTB) sections at Meishan and Yudongzi in South China. We observed substantial $\delta^{34}S_{CAS}$ variation within single hand samples from both of these sections, with most samples having a range in $\delta^{34}S_{CAS}$ exceeding 5‰ and some reaching nearly 20‰. We also found evidence for mixing between low CAS abundance, high $\delta^{34}S_{CAS}$ and high CAS abundance, low $\delta^{34}S_{CAS}$ phases in these rocks. A simple model of reduced sulfur oxidation and incorporation into carbonates as CAS suggests that oscillating sedimentary redox conditions may plausibly explain the $\delta^{34}S_{CAS}$ heterogeneity within many EPME carbonates amidst the relative lack of such variation in sulfate evaporite $\delta^{34}S$ data. Future work should test this hypothesis and better evaluate the role of the marine sulfur cycle as a primary versus secondary influence in the EPME.

III.2 Introduction

The End-Permian Mass Extinction (EPME) is the largest known mass extinction event in Earth's history [299]. Paleobiological datasets suggest that nearly 80% of genera went extinct during this event, with losses particularly concentrated in marine invertebrates such as rugose corals, trilobites, brachiopods, and foraminifera [248]. Geochronological studies [50, 51, 304, 305] have revealed that this extinction was also incredibly rapid; recent zircon U-Pb age measurements by Burgess, Bowring, and Shen (2014) [50] have constrained the duration of the extinction in South China to 60 ± 48 kyr, i.e., between 251.941 ± 0.037 Ma and 251.880 ± 0.031 Ma. Strata across the globe show

large diversity losses during this interval [248] that are synchronous on at least a regional scale (e.g. [304]). Catastrophic extinction mechanisms were proposed based on the rapidity of the extinction, and more recent work [71, 183] has suggested a massive influx of carbon to the ocean-atmosphere system as a primary causal factor in the extinction based on preferential loss of heavily calcified taxa.

Geochemical studies have shown that large marine chemistry perturbations were associated with the EPME. Early observations of laminated, pyrite-rich sediments in Permian-Triassic boundary (PTB) strata suggested widespread ocean anoxia and euxinia during the extinction interval [152, 359, 360, 361]. Carbon isotope studies (e.g. [63, 145, 147, 148, 189, 250]) also identified a gradual late Permian carbonate $\delta^{13}C$ decline punctuated by a rapid, large (3-4‰) negative excursion across the extinction event. Similarly dramatic changes occur in strontium [186, 316], calcium [144, 251], osmium [109, 296], lithium [325], selenium [321], uranium [194], and nitrogen [64, 296, 370] isotopic signatures in sedimentary materials. The combination of biostratigraphy, geochronology [50, 277], and geochemistry points to the eruption of the Siberian Traps large igneous province as the source of the environmental and climatic disturbance that caused the EPME. Although volcanic emissions from this eruption cannot account for the large negative carbon isotope excursion on their own [24], volatilization of organic carbon within organic-rich sediments intruded by the eruption [327] may have augmented the magnitude of the eruptions's CO_2 release and its ^{13}C depletion.

Numerous studies have measured the sulfur (S) isotopic composition of carbonate associated sulfate (CAS) in an attempt to study varibility in the global marine S cycle across the EPME (Figure III.1). These studies have documented a huge range in CAS $\delta^{34}S$ (i.e., $\delta^{34}S_{CAS}$), leading some authors (e.g. [203, 317]) to argue for very low (< 5 mM) seawater sulfate (SO_4^{2-}) concentrations at the time of the EPME. Some studies have alternatively suggested mixing of isotopically disparate reservoirs of S (e.g. [169, 239, 280]). Although both CAS (e.g. [209, 239]) and evaporite [17, 76, 366] $\delta^{34}S$ records indicate a large increase in seawater $\delta^{34}S$ from the Late Permian to the Early Triassic, disagreement between records on the character of the $\delta^{34}S$ increase has inhibited a better understanding of marine S cycle behavior across the EPME.

The combination of disagreement among existing records and relatively low CAS abundances in end-Permian carbonates (e.g. [209]) makes the EPME a

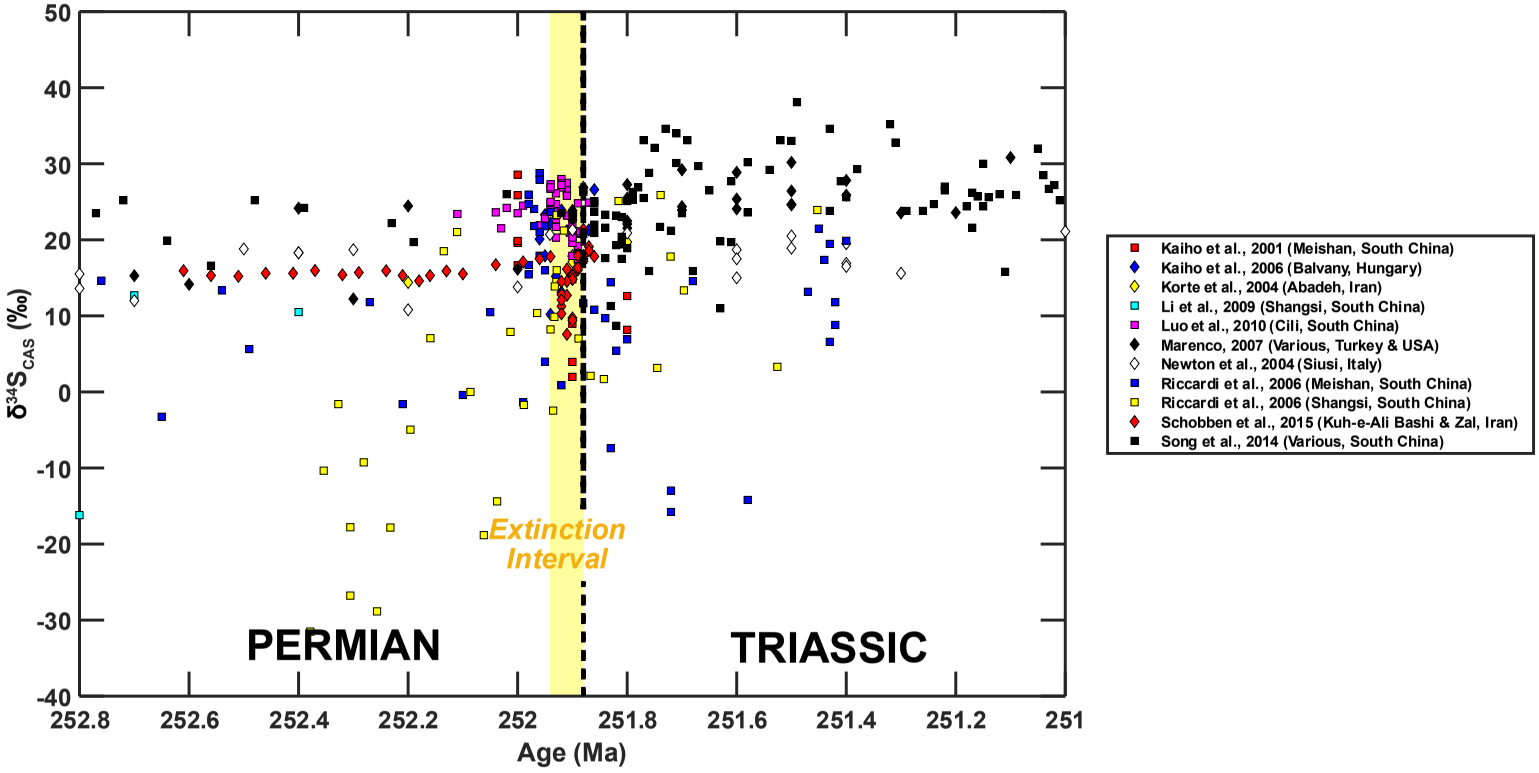

Figure III.1: Plot of CAS $\delta^{34}S$ versus sample age for previous studies focused on the EPME. Sample ages for pre-2012 studies have been updated to the 2012 Geologic Time Scale [116]. Data have been correlated with each other based on stage boundaries published in the studies and the absolute age constraints of Burgess et al. (2014) [50]. Sedimentation rates have been assumed to be constant between age control points. When necessary, sedimentation rates have been extrapolated beyond age control points to estimate ages for samples older or younger than the controls.

Figure III.2: Paleogeographic map of the world at the end of the Permian. Red stars and text denote the approximate paleolocations of the two EPME sections sampled as part of this study. Smaller yellow stars and blue text denote approximate locations from which other EPME $\delta^{34}S_{CAS}$ data have been collected. Map after Scotese (2014) [298].

prime target for S isotopic studies utilizing methods with minimal sample requirements. Here, we present new multicollector inductively coupled plasma mass spectrometry (MC-ICP-MS) $\delta^{34}S_{CAS}$ data from EPME sections at Meishan and Yudongzi in South China. Using a novel micro-X-ray fluorescence (μ-XRF) screening method to target disparate regions of hand samples, we found that $\delta^{34}S_{CAS}$ heterogeneity within single hand samples typically exceeds 5‰ and sometimes reaches nearly 20‰. Cross plots of $\delta^{34}S_{CAS}$ versus the inverse of CAS abundance suggest that this heterogeneity results from mixing between low CAS abundance, high $\delta^{34}S_{CAS}$ and high CAS abundance, low $\delta^{34}S_{CAS}$ phases. In light of other proxy records, the disagreement between evaporite $\delta^{34}S$ and $\delta^{34}S_{CAS}$ records likely indicates carbonate recrystallization and authigenic carbonate precipitation in the presence of SO_4^{2-} derived from oxidation of solid S phases; i.e., the $\delta^{34}S_{CAS}$ variability within prior studies reflects diagenetic alteration rather than primary variation in the $\delta^{34}S$ of a small marine SO_4^{2-} reservoir.

III.3 Sample Localities

Samples for this study were collected from two carbonate sections in South China at Meishan and Yudongzi (Figure III.2). Each of these sections is located

within the Yangtze Platform, an extensive and long-lived (Late Proterozoic through Late Triassic) carbonate platform at the eastern margin of the Paleo-Tethys Ocean [92].

Meishan is the location of the Global Boundary Stratotype Section and Point (GSSP) for the Permian-Triassic boundary [146] and has been extensively targeted for geochemical studies (e.g. [50, 63, 64, 168, 277, 280]). Here, carbonate sediments were deposited in a carbonate ramp setting within a local topographic depression between fair weather and storm wave base [70, 146]. Facies include bioclastic micrite, wackestones, packstones, and grainstones containing abundant pyrite and fossils of brachiopods, crinoids, conodonts, foraminifera, and other calcified organisms [70, 146, 373]. The section is highly condensed and includes multiple ash beds that have been precisely dated through U-Pb zircon geochronology (e.g. [50]); estimated sedimentation rates based on current age constraints range from $< 0.1 \frac{\text{m}}{\text{Myr}}$ to $0.68 \frac{\text{m}}{\text{Myr}}$ [50]. Data presented in this study come from beds 24 through 29 [146], an interval in which the estimated sedimentation rates do not exceed $0.26 \frac{\text{m}}{\text{Myr}}$.

Yudongzi is situated to the west of Meishan in the Sichuan Basin. Here, sediments were deposited on the continental shelf, likely near the margin of a rimmed carbonate platform [331]. The section is relatively unstudied, although recent work [178, 331, 372] has begun to characterize the biostratigraphy and lithofacies of the site. The stratigraphy includes boundstones and skeletal grainstones within the latest Permian Changxing Formation and thrombolitic microbialites, lime mudstones, and grainstones in the earliest Triassic Feixianguan Formation [178, 331, 372]. The exact position of the Permian-Triassic boundary at the site is uncertain; the first appearance datum (FAD) of the conodont *H. parvus* is 0.5 m above the base of the Feixianguan Formation, but the boundary may be at the Changxing-Feixianguan contact. A prominent erosional disconformity is evident at the contact between the Changxing and Feixianguan formations, with an unknown amount of material missing [331]. Absolute ages at the site are not well constrained, but the occurrence of a thick ($\sim$11 m) section of microbialite suggests that the section is highly expanded [331]. Correlation of the extinction interval at the site with that at Meishan [50] indicates that absolute sedimentation rates at Yudongzi are at least an order of magnitude higher ($> 100 \frac{\text{m}}{\text{Myr}}$) than the lowest sedimentation rates at Meishan.

III.4 Methods

Hand samples were collected in the field prior to this study. To enable visual sample assessment, hand samples were cut using a rock saw to expose fresh surfaces and polished on a Covington vibratory lathe using 240-grit silicon carbide, 600-grit aluminum oxide, and 9.5 micron aluminum oxide in sequence. Polished surfaces were imaged under an optical microscope and examined for grain size, pyrite abundance, and biogenic contents. Following optical imaging, a representative subset of samples were selected for μ-XRF microscopy characterization and imaged using a Bruker M4 Tornado μ-XRF spectrometer. Images were typically collected under vacuum with a 240 μA, 50 keV X-ray beam using a 10 ms dwell time and 20 μm spot size.

After imaging, XRF data were exported and loaded into MATLAB® for a principal component analysis (PCA) to identify distinct phases. Counts data for all elements (Al, Ba, Ca, Fe, K, Mg, Mn, Na, P, Rh, S, Si, Sr, and Ti) at each pixel were imported into a single matrix and subjected to PCA using MATLAB®'s built-in pca function. Maps of the first three principle components were visually inspected and used to identify regions for targeted sampling.

Samples were drilled with dental burs using a Dremel tool. Areas were targeted for sampling such that each of the main principal components evident from the PCA analysis was sampled at least once. Either two or three distinct areas were drilled from each hand sample. Collected powders (3 to 15 mg in mass) were subsequently cleaned and subjected to column chemistry using the methods outlined in Chapter II. Quality control was again maintained by including at least one seawater, one deep sea coral, and one procedural blank within each set of columns. After column chemistry, samples were dried down, re-diluted, and an aliquot measured for SO_4^{2-} concentration using a Dionex ICS-3000 ion chromatography system.

S isotope ratios were measured on a Thermo-Fischer Neptune Plus MC-ICP-MS following the methods of Chapter II. SO_4^{2-} concentration measurements were used to ensure that sample concentrations matched the bracketing standard concentration (10 μM Na_2SO_4) as closely as possible. Average procedural blank ($n = 6$) size and $\delta^{34}S$ were 0.39 ± 0.21 nanomoles and $4.3 \pm 3.2‰$, respectively. The average seawater $\delta^{34}S$ ($n = 4$) was $21.05 \pm 0.02‰$, and the average deep sea coral $\delta^{34}S_{CAS}$ ($n = 3$) was $22.7 \pm 0.5‰$.

III.5 Results

III.5.1 μ-XRF mapping

Example μ-XRF elemental maps and PCA maps are depicted in Figures III.3 and III.4, respectively. Although the elemental maps display some variability in elemental count intensities, the PCA maps are more effective in assigning this variation to different components. The first principle component in the example depicted in Figure III.4 (sample YDS 32.5) shows a strong positive association with Ca, and the second component a strong association with Fe and S. These two components are ubiquitous throughout all samples. Cross plots of elemental counts also commonly demonstrate positive correlations between Fe and S and between Al and Si (Figure III.5). Other elemental cross plots either show no correlation or have too few counts of at least one element for the correlation to be robust.

III.5.2 $\delta^{34}S_{CAS}$ measurements

Our $\delta^{34}S_{CAS}$ measurements at Meishan and Yudongzi are plotted as a function of stratigraphic height in Figures III.6 and III.7; data are also listed in Table III.1. Data points located at the same height in each plot indicate data obtained from different locations within the same hand sample.

CAS abundance and $\delta^{34}S_{CAS}$ vary widely within individual hand samples, particularly at Meishan. Across all samples, CAS abundance varies from a minimum of 32 ± 3 ppm to a maximum of 1787 ± 195 ppm. Abundances within hand samples in some cases range over a factor of two or more. $\delta^{34}S_{CAS}$ is similarly variable; the average range of $\delta^{34}S_{CAS}$ within individual hand samples is 6.9‰ and the median range is 3.0‰. Four samples (23-1-up-B, 24-A-down, 29-1, and YDS 31.5) feature $\delta^{34}S_{CAS}$ heterogeneity that exceeds 10‰, with two (29-1 and YDS 31.5) reaching nearly 20‰. Such variation does not appear to be associated with stratigraphic height or with particular features in the carbonate $\delta^{13}C$ profiles collected by other authors at each site [63, 306].

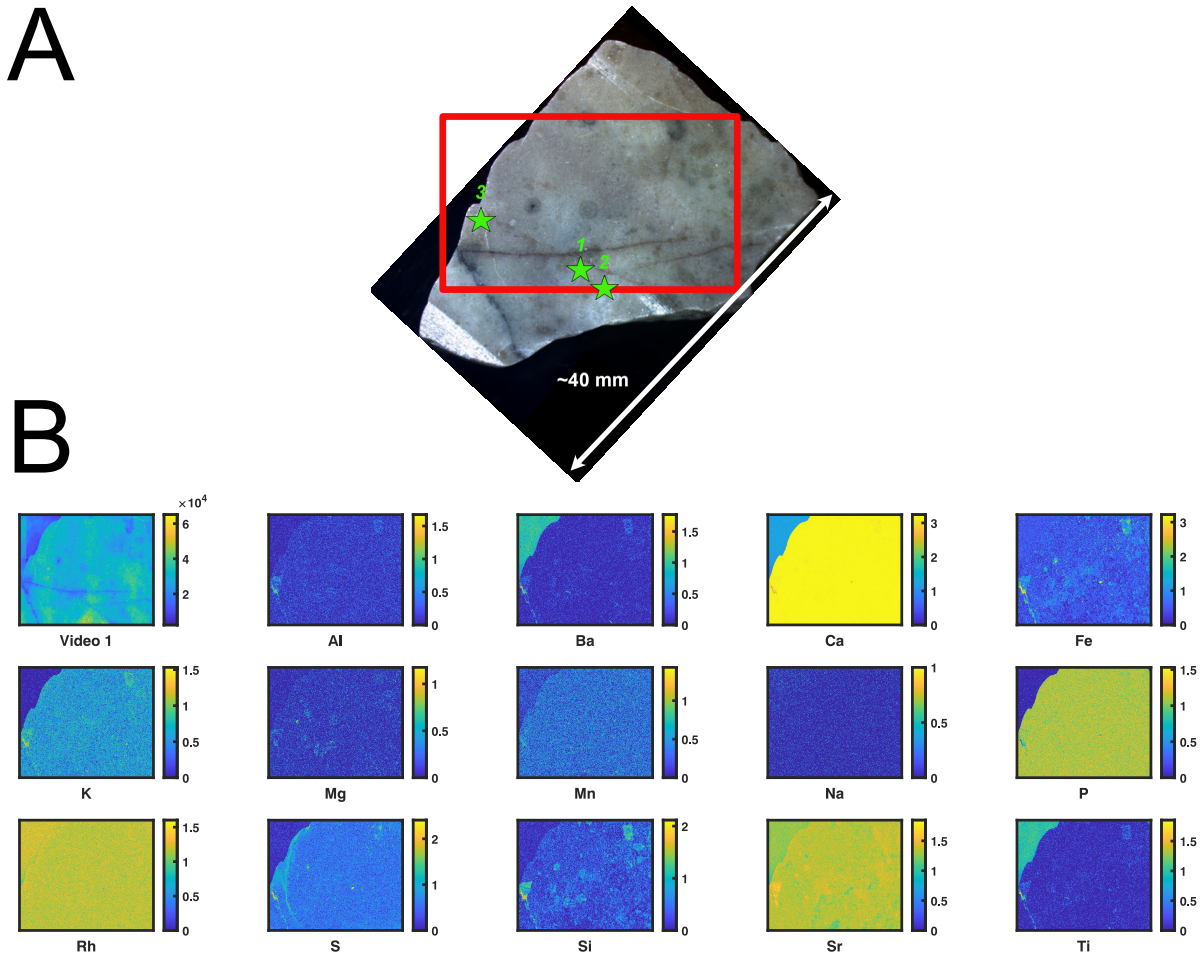

Figure III.3: XRF screening example. (A) Optical image of surface of hand sample YDS 32.5, a wackestone with some zones of calcite spar, veins rich in pyrite and siliclastic material, and disseminated pyrite throughout the sample. Red box denotes approximate area imaged with μ-XRF microscopy; numbered green stars denote areas drilled and sampled for $\delta^{34}S_{CAS}$ measurements. (B) XRF elemental counts maps for sample YDS 32.5; colorbar denotes number of counts. Video image is based on optical brightness and is included for relation of geochemical features to optical ones. Elemental counts in all maps except the video image are displayed as the base ten logarithm of count intensity. The upper left part of the elemental maps is off the edge of the sample.

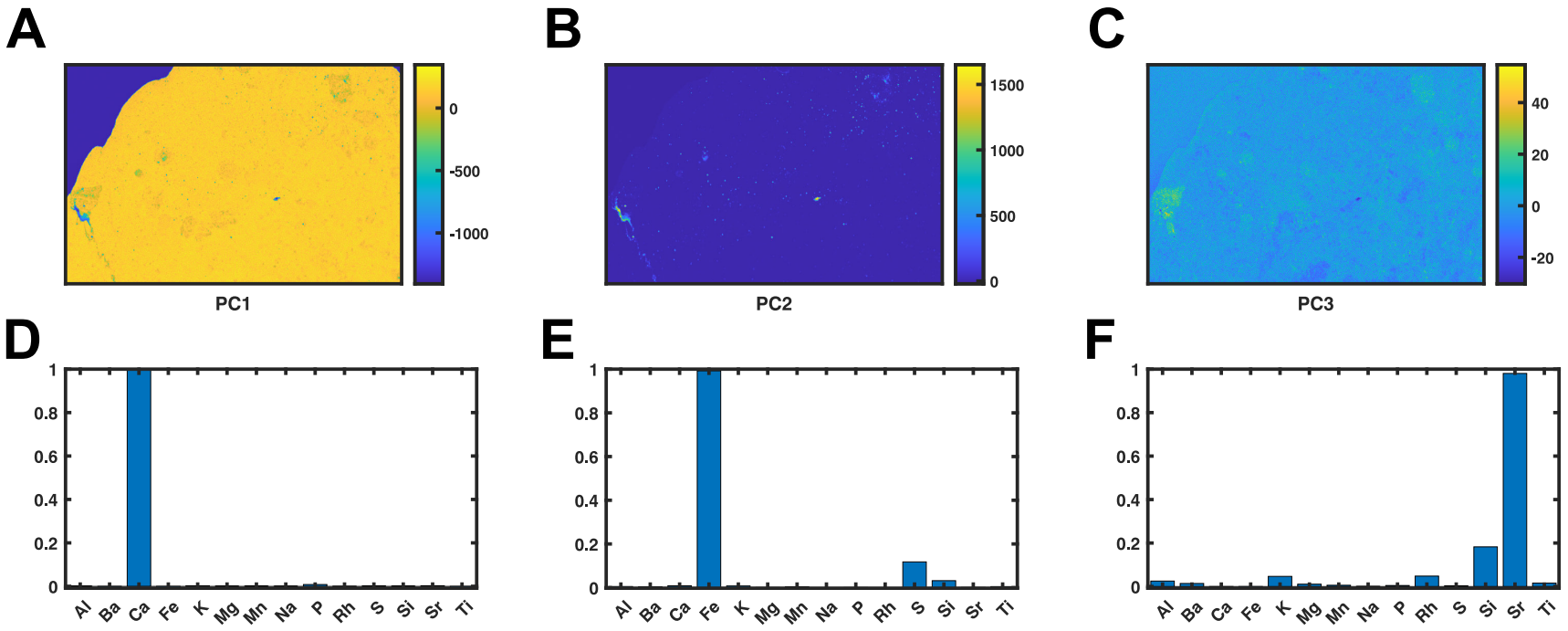

Figure III.4: Principle component analysis example. (A-C) Maps of principal component scores for principal components 1 (A), 2 (B), and 3 (C) for sample YDS 32.5. The upper left part of the PCA maps is off the edge of the sample. (D-F) Principal component coefficients associated with each element for principal components 1 (D), 2 (E), and 3 (F).

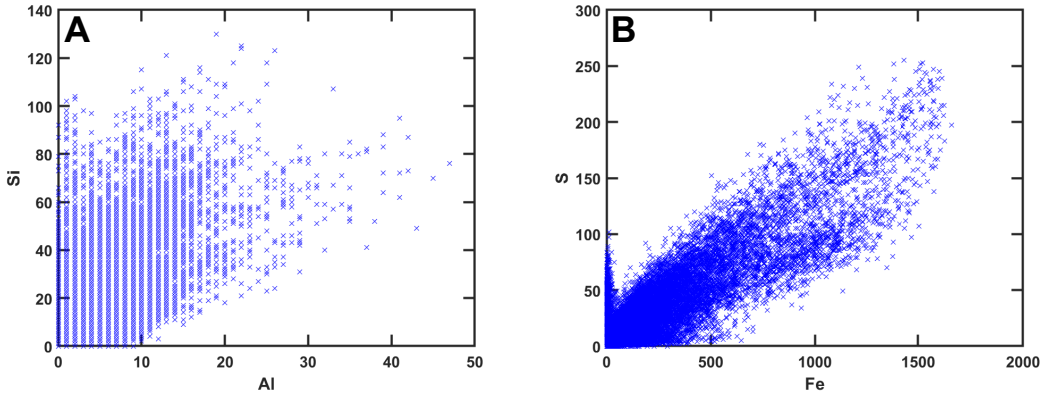

Figure III.5: Crossplots of XRF counts at each pixel for (A) Si versus Al and (B) S versus Fe for sample YDS 32-5. There is slight positive correlation between Si and Al counts plus strong correlation between Fe and S counts. Also note the secondary trend on the S versus Fe plot (B) suggesting the presence of some S unassociated with Fe; the pixels within this trend are all located at the edge of the sample and appear to be a topographic artifact.

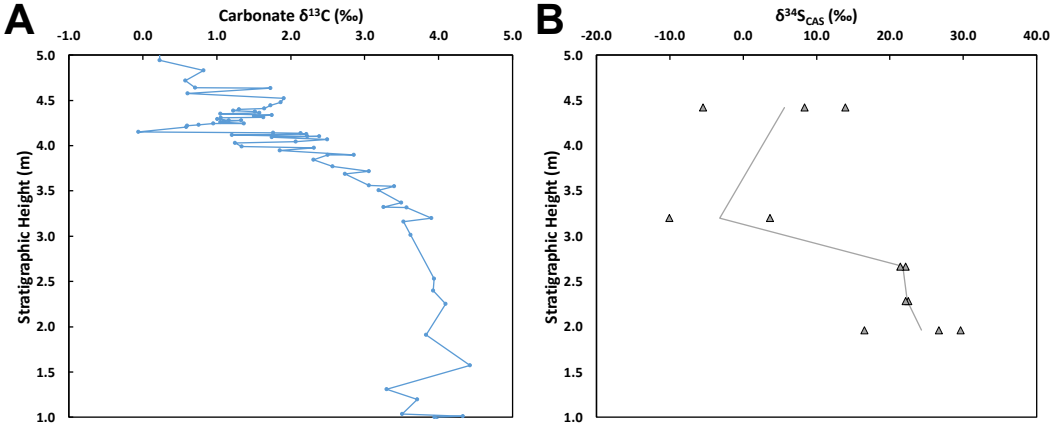

Figure III.6: Plots of (A) carbonate $\delta^{13}C$ and (B) $\delta^{34}S_{CAS}$ from Meishan. Carbonate $\delta^{13}C$ data from Cao et al. (2002) [63].

Table III.1: $\delta^{34}S_{CAS}$ data.

Locality	Sample ID	Height (m)	Description	CAS #1 (ppm)	Error (2σ)	CAS #2 (ppm)	Error (2σ)	CAS #3 (ppm)	Error (2σ)	$\delta^{34}S_{CAS}$ #1 (‰)	Error (2σ)	$\delta^{34}S_{CAS}$ #2 (‰)	Error (2σ)	$\delta^{34}S_{CAS}$ #3 (‰)	Error (2σ)
Meishan	29-1	4.42	grayish-green calcareous mudstone, few to no bioclasts [146, 373]	1551	189	837	94	1100	143	-5.4	0.2	13.9	0.4	8.4	0.6
Meishan	24-A-down	3.2	dark grey bioclastic wackestone [146, 373]	819	88	1787	195			3.7	0.2	-10.1	0.2		
Meishan	23-5	2.665	dark grey bioclastic mudstone [146, 373]	795	82	1130	117			22.2	0.2	21.4	0.2		
Meishan	23-2-up	2.285	dark grey bioclastic mudstone [146, 373]	928	95	869	89			22.6	0.2	22.2	0.2		
Meishan	23-1-up-B	1.963	dark grey bioclastic mudstone [146, 373]	620	64	761	78	458	48	29.7	0.2	16.6	0.3	26.7	0.3
Yudongzi	YDS 34.5	34.5	wackestone with few of identifiable biogenic clasts and sparry matrix	65	7	88	9	62	6	20.7	0.5	19.5	0.5	20.1	0.4
Yudongzi	YDS 32.5	32.5	wackestone with calcite spar, veins rich in pyrite and siliclastic material, and disseminated pyrite	345	37	292	30	301	31	21.3	0.5	22.0	0.3	19.8	0.3
Yudongzi	YDS 31.5	31.5	microbialitic packstone with many well-preserved biogenic grains, including brachiopod fragments and forams; weathered and recrystallized near top of sample with many sparry/recrystallized veins	242	25	545	55	211	22	17.2	0.4	-1.4	0.2	15.7	0.7
Yudongzi	YDS 21	21	microbialitic wackestone w/some brachiopod fragments, thin veins of spar and pyrite	748	77	741	78			12.5	0.2	10.2	0.5		
Yudongzi	YDS 13	13	wackestone w/many mm-width veins of spar/recrystallized carbonate	46	5	95	10			27.5	1.0	21.7	0.6		
Yudongzi	YDS 1.5	1.5	mudstone w/o obvious biogenic grains; zones of spar, dissolution, and abundant pyrite	57	6	42	4	32	3	21.2	-	20.6	0.7	22.2	1.0
Yudongzi	YDS 0	0	mudstone w/o obvious biogenic grains; zones of spar, dissolution, and abundant pyrite	65	7	64	7			15.7	-	19.4	0.5		

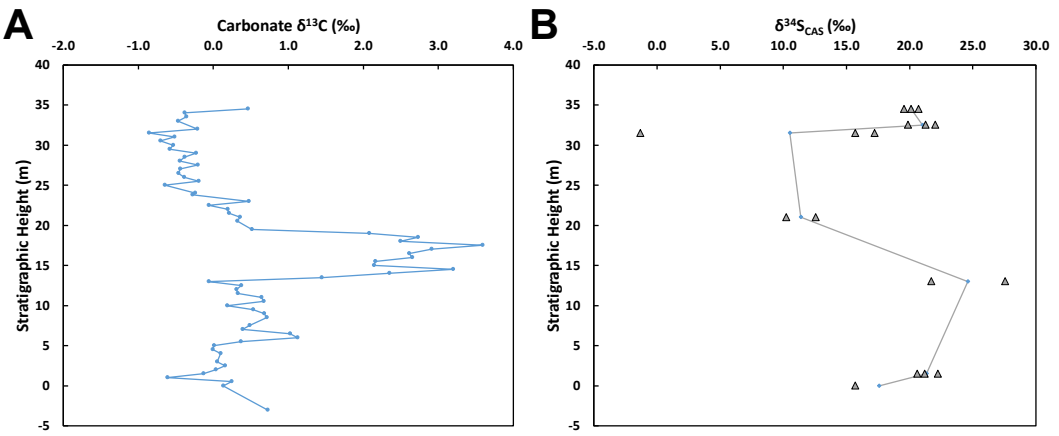

Figure III.7: Plots of (A) carbonate $\delta^{13}C$ and (B) $\delta^{34}S_{CAS}$ from Yudongzi. Carbonate $\delta^{13}C$ data from Yanan Shen (unpublished) [306].

III.6 Discussion

III.6.1 Utility of μ-XRF mapping

Most prior studies of the geochemistry of carbonates have used diagenetic screening methods that are qualitative (e.g. optical microscopy) or are limited to discrete points within samples (e.g. ICP-MS elemental abundance measurements) [120, 121, 348]. Although such methods are important for interpreting isotopic variation within samples, they are often laborious and may provide little context about chemical variation within the sample beyond the area selected for measurement. The results presented here show μ-XRF microscropy to be a powerful tool that can provide information similar to that offered by traditional methods in a less laborious, more spatially extensive, and non-destructive manner. Principle component analysis on elemental counts data effectively identifies different dominant phases within cut and polished hand samples. The method is especially effective for identifying pyrite that may be difficult to observe under optical microscopy (e.g. Figure III.5B); this is important for minimizing the risk of contamination of CAS measurements by sulfur derived from reduced phases.

While we did not attempt to make quantitative abundance estimates here, there is significant potential to use μ-XRF microscopy as a substitute for more traditional chemical methods of quantifying elemental abundances. Careful calibration with standards and longer dwell times would be required to quantify abundances for trace components of carbonates; still, the non-destructive nature of

μ-XRF microscopy makes it particularly advantageous for screening samples for diagenetic alteration. Future work should test the accuracy and precision of abundance quantification with this method and compare analytical times to the time required for traditional chemical measurements to evaluate whether replacement of chemical (e.g. ICP-OES) measurements with μ-XRF measurements may be possible.

III.6.2 $\delta^{34}S_{CAS}$ heterogeneity

Previous studies [262, 263] have found wide variability in $\delta^{34}S_{CAS}$ to occur among the different carbonate phases within bulk carbonate rocks. Our measurements of South China end-Permian carbonates support these findings, with $\delta^{34}S_{CAS}$ variation commonly exceeding 2‰ and sometimes exceeding 10‰ in the samples measured here. What is the source of such large isotopic variation in these rocks?

Plots of $\delta^{34}S_{CAS}$ versus $\frac{1}{CAS}$ provide a clue regarding the origin of $\delta^{34}S_{CAS}$ variation (Figures III.8 and III.9). Samples from Meishan (Figure III.8) show a strong correlation between $\delta^{34}S_{CAS}$ and $\frac{1}{CAS}$, with higher CAS abundances associated with lower $\delta^{34}S_{CAS}$ values. This trend is much weaker and potentially nonexistent at Yudongzi (Figure III.9), though the three samples with the highest CAS abundances show anomalously low $\delta^{34}S_{CAS}$ values. The existence of trends in $\delta^{34}S_{CAS}$ versus inverse abundance space strongly suggests that the observed S isotopic variation is due to mixing between one or more low CAS abundance, high $\delta^{34}S$ and high CAS abundance, low $\delta^{34}S$ phases.

Several possibilities regarding the identity of the high $\delta^{34}S_{CAS}$ phase(s) exist. Sulfate evaporite $\delta^{34}S$ data do not exist at sufficiently high resolution to distinguish precise variation across the EPME. However, existing data suggest that seawater SO_4^{2-} $\delta^{34}S$ was approximately 10 ± 1‰ around 1 Myr prior to the PTB [17]. These data and the corresponding age model [17] indicate that seawater SO_4^{2-} $\delta^{34}S$ underwent a rapid, ~20‰ increase across the PTB over about 2 Myr; approximately $\frac{1}{4}$ to $\frac{1}{3}$ of this increase occurs prior to the PTB. Conservatively, this suggests that the seawater-derived CAS end member should have a $\delta^{34}S_{CAS}$ of 10-22‰, though temporal variation of marine SO_4^{2-} $\delta^{34}S$ across the interval of interest here seems likely. If we treat the upper limit of this range (22‰) as the seawater $\delta^{34}S$ value, our data are reasonably well explained by two end member mixing between CAS unaltered from seawater SO_4^{2-} in its $\delta^{34}S$ and a

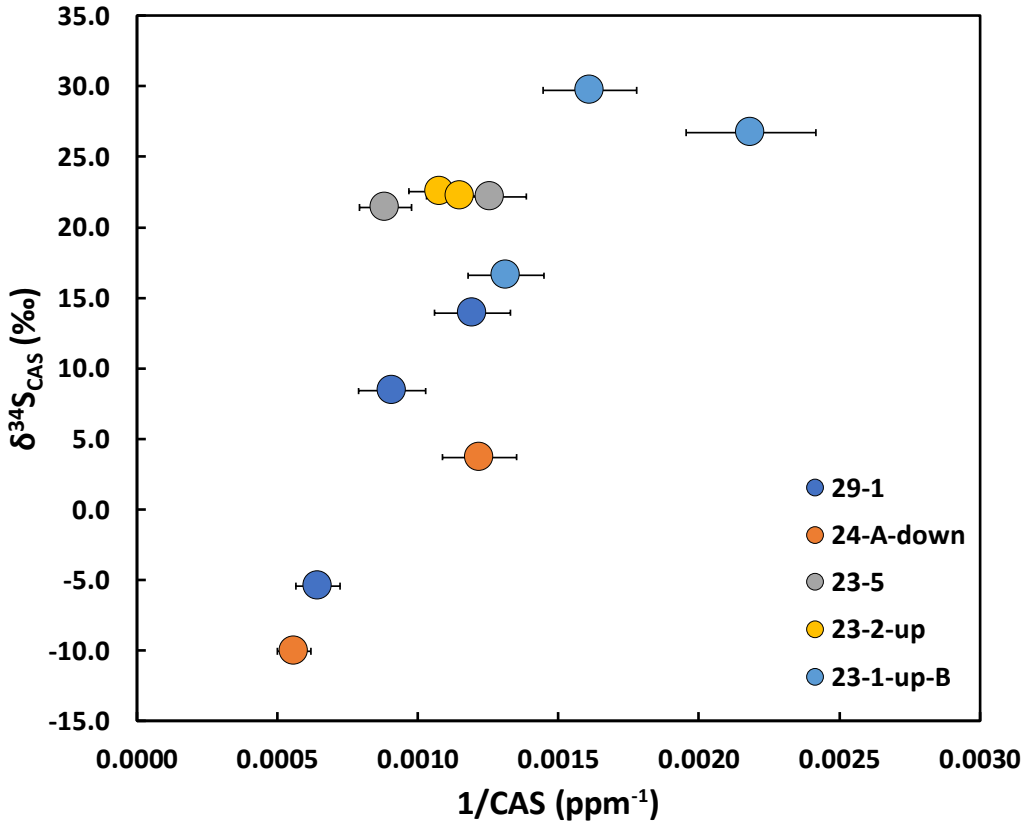

Figure III.8: Plot of $\delta^{34}S_{CAS}$ versus $\frac{1}{CAS}$ (ppm^{-1}) for samples from Meishan. Color denotes hand sample from which each measurement was taken.

low $\delta^{34}S$, high CAS abundance phase. However, a lower $\delta^{34}S$ for seawater would necessitate that most of the data be affected by significant incorporation of ^{34}S-enriched SO_4^{2-}. Such incorporation could occur via carbonate recrystallization and authigenic carbonate precipitation in the presence of pore water SO_4^{2-} that has been partially consumed by microbial SO_4^{2-} reduction (MSR).

The high CAS abundance, low $\delta^{34}S_{CAS}$ end member(s) inferred from our mixing plots also could come from multiple different sources. Both aqueous and mineral sulfides are typically depleted in ^{34}S due to the normal isotope effect associated with MSR. Under the relatively low (< 1000 ppm) CAS abundances typically observed here, oxidation of reduced sulfur to SO_4^{2-} and incorporation of this SO_4^{2-} into our measured CAS could easily skew our CAS measurements toward higher abundances and lower $\delta^{34}S$ values. Alternatively, temporal variation in the concentration and $\delta^{34}S$ of seawater SO_4^{2-} — specifically, an increase in $[SO_4^{2-}]$ and decrease in SO_4^{2-} $\delta^{34}S$ — could also explain this trend. Existing seawater $[SO_4^{2-}]$ would have to be very low and the flux of new SO_4^{2-}

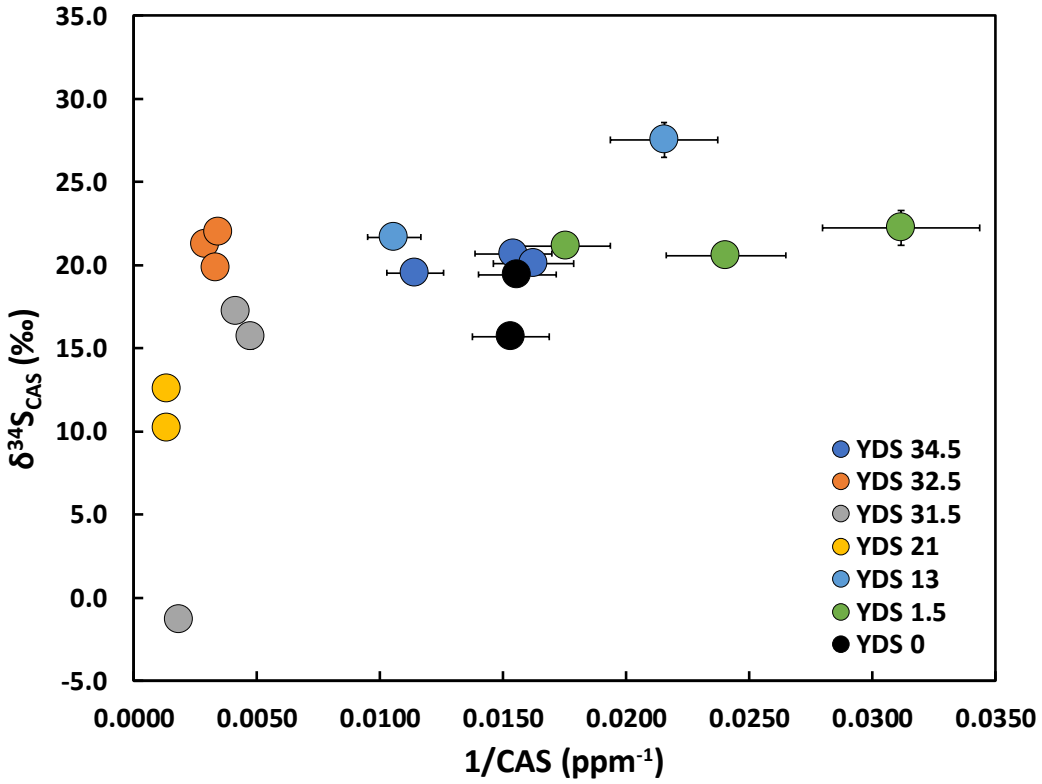

Figure III.9: Plot of $\delta^{34}S_{CAS}$ versus $\frac{1}{CAS}$ (ppm^{-1}) for samples from Yudongzi. Color denotes hand sample from which each measurement was taken.

into seawater incredibly depleted in ^{34}S for this alternate explanation to account for the apparent mixing trend. Carbonate and evaporite mineralogy [132] and evaporite fluid inclusion compositions [202] argue against low $[SO_4^{2-}]$ at this time. Based on this conflicting evidence and the $\delta^{34}S_{CAS}$ heterogeneity we observe within single hand samples, we favor incorporation of SO_4^{2-} derived from reduced S oxidation as the explanation for the mixing trend in our data. We cannot a priori determine if such oxidation occurred during laboratory processing of the samples, in-situ during deposition, or in-situ after lithification (e.g., during weathering), but we discuss the possibility of in-situ oxidation in the section below.

III.6.3 Implications for prior EPME $\delta^{34}S_{CAS}$ records

An updated plot of $\delta^{34}S$ with time with our data is shown in Figure III.10. Here, we have estimated absolute ages for our samples by assigning an age of 251.88 Ma to the PTB at each site and correlating conodont zone transitions to the well-

dated transitions at Meishan [50]. We assume constant sediment accumulation rates between age control points. We expect that our age estimates and correlations with the data of previous studies are not precisely correct, but are accurate enough to yield useful insight into global trends in $\delta^{34}S$ records across the EPME.

Previous work [17, 239, 295] has noted a substantial decrease in SO_4^{2-} $\delta^{34}S$ associated with the extinction interval for the EPME. Although the decrease is more pronounced in CAS $\delta^{34}S$ records (e.g. [168, 295]), it is present to a lesser degree in evaporite $\delta^{34}S$ data [17]. Our $\delta^{34}S_{CAS}$ results here also include anomalously low $\delta^{34}S_{CAS}$ values near and within the extinction interval (Figure III.10). Uncertainties in correlations complicate our temporal $\delta^{34}S_{CAS}$ record, but at each site, the lowest $\delta^{34}S_{CAS}$ values appear to occur just before or within the extinction interval. Unpublished data [260] from the rapidly deposited Penglaitan section [304] are particularly ^{34}S depleted. The rough temporal correlation of very low $\delta^{34}S_{CAS}$ across multiple sections is striking. Is there a mechanism that can explain such low $\delta^{34}S_{CAS}$ values amid comparatively invariant sulfate evaporite $\delta^{34}S$?

Several lines of evidence have suggested oscillating redox conditions in shallow EPME sections across the globe. This evidence includes variations in the mean size of pyrite framboids [36, 240], triple sulfur isotopic compositions of sedimentary pyrite [308], and changing total organic carbon abundance and isotopic composition [119]. Deep ocean stratigraphic sections in Japan [152, 177], British Columbia [152], and the Sverdrup Basin [118] have also found evidence for declining deep ocean oxygen concentrations in the lead up to the EPME. Although uranium abundance and isotopic composition data from carbonates have been used to argue for a modern-like fraction of oxygenated seafloor in the Late Permian [194], the data as a whole suggest widespread occurrence of oxygen-poor waters in the Late Permian and Early Triassic oceans.

Changing sedimentary redox conditions can have a potentially large effect on $\delta^{34}S_{CAS}$; in particular, more extensive penetration of oxygen into the sediments and oxidation of solid S phases like pyrite and organic S could result in a large decrease in $\delta^{34}S_{CAS}$ if some oxidation-derived SO_4^{2-} were incorporated into carbonates. To quantitatively test this hypothesis for the generation of low $\delta^{34}S_{CAS}$, we created a simple model in which carbonates of assigned pre-existing CAS abundance, $\delta^{34}S_{CAS}$, pyrite abundance, and pyrite $\delta^{34}S$ are subjected to various degrees of pyrite oxidation, with all of the oxidized pyrite becoming incorpo-

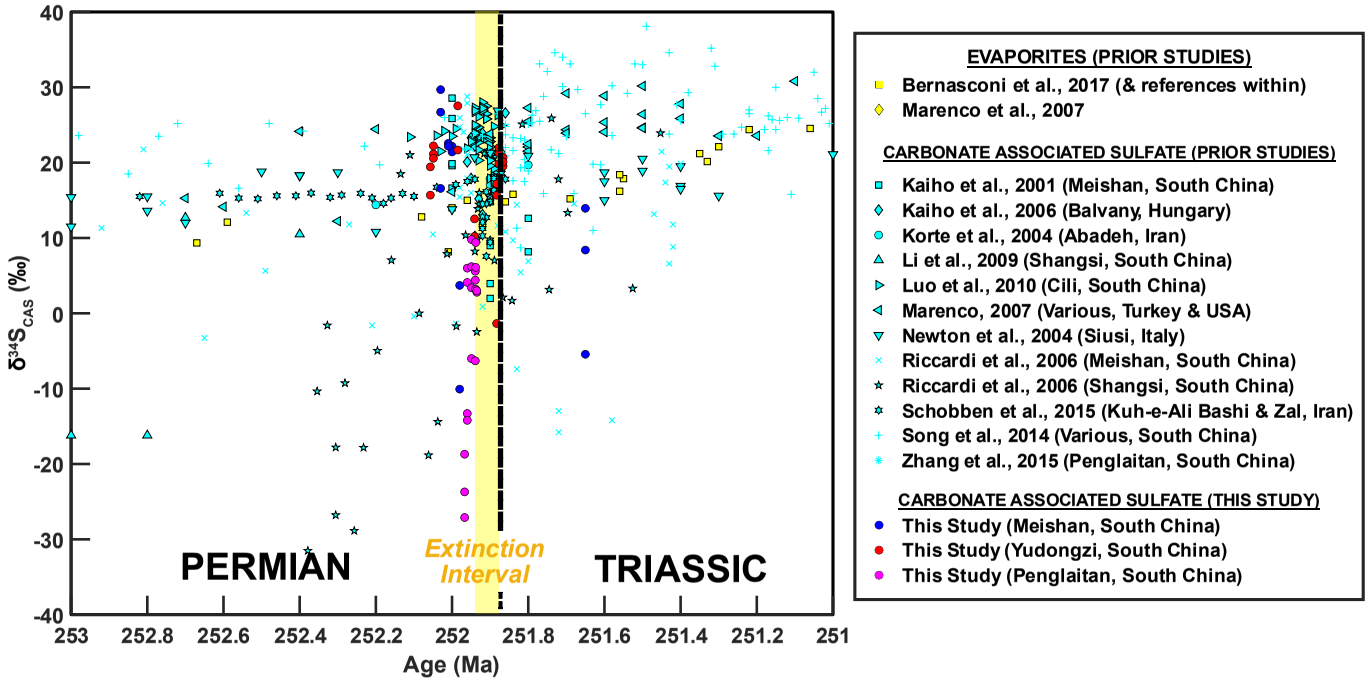

Figure III.10: Plot of $\delta^{34}S$ versus sample age for our data plus the data of previous studies. Sample ages for pre-2012 studies have been updated to the 2012 Geologic Time Scale [116]. Data have been correlated with each other based on stage boundaries published in the studies and the absolute age constraints of Burgess et al. (2014) [50]. Sedimentation rates have been assumed to be constant between age control points. When necessary, sedimentation rates have been extrapolated beyond age control points to estimate ages for samples older or younger than the controls. Data from sulfate evaporites (yellow symbols) and data from carbonate associated sulfate (cyan symbols) collected in previous studies are shown with unique symbols indicating the study in which each data point was collected. Data from this study are shown as opaque circles and are colored based on locality.

rated into the rock as CAS. Although we assume pyrite to be the reservoir subject to oxidation, other sources of S (e.g. elemental S [280]) could also contribute without invalidating the model. Results from the model for the Meishan samples are shown in Figure III.11. Iterating over various degrees of oxidation of a S pool with a $\delta^{34}S$ of -30‰, we find that all our data fall within a CAS abundance - $\delta^{34}S_{CAS}$ space in which up to 0.2 wt% S has been oxidized and incorporated as CAS into a carbonate with initial CAS abundances ranging from 400 to 1000 ppm (Figure III.11). The initial $\delta^{34}S_{CAS}$ in the model was +30‰. Clustering of the data toward the upper left of the plot indicates that most data can be generated via oxidation of far lower amounts of S (< 0.1 wt%). Our model can fit the Yudongzi sample data similarly well if the maximum amount of S that is oxidized is lowered to 0.04 wt% and the initial CAS abundance range lowered to 10 to 600 ppm (Figure III.12). Note that the +30‰ initial $\delta^{34}S_{CAS}$ value is substantially higher than the end-Permian evaporite $\delta^{34}S$ of $\sim$10‰ [17]; this suggests that the initial CAS incorporated into the carbonates at Meishan and Yudongzi was significantly altered by MSR. We also note that these calculations do not require such oxidation to have occurred during deposition; such mixing scenarios could also reflect post-lithification or laboratory oxidation of solid S phases.

Although the data from Penglaitan (Present, unpublished) [260] fall within a compositional space that can be explained by models with an initial $\delta^{34}S_{CAS}$ of +30‰, the much lower maximum $\delta^{34}S_{CAS}$ value exhibited by these data suggests that the initial CAS at this site may have been less influenced by MSR. We ran an additional model with an initial $\delta^{34}S_{CAS}$ of +10‰ and show the results in Figure III.13. Indeed, the data at Penglaitan fully fall in a compositional space in which the starting $\delta^{34}S_{CAS}$ was +10‰. The strikingly close match between the highest $\delta^{34}S_{CAS}$ observed at this site and the $\delta^{34}S$ of end-Permian evaporites [17] may indicate that the CAS initially incorporated into the Penglaitan carbonates was unaltered from seawater SO_4^{2-} in its isotopic composition. Though incorporation of oxidized sulfur into carbonate as CAS requires additional alkalinity-generating reactions to maintain carbonate saturation, the compatibility of these models with our data motivates further study of this scenario. In particular, study of CAS within organic-rich, deep Pacific carbonate sediments from the last glacial maximum (LGM) to the present could serve as a more recent analog given the substantial increase in bottom water oxygen concentrations from the LGM to the present in this region (e.g. [8]).

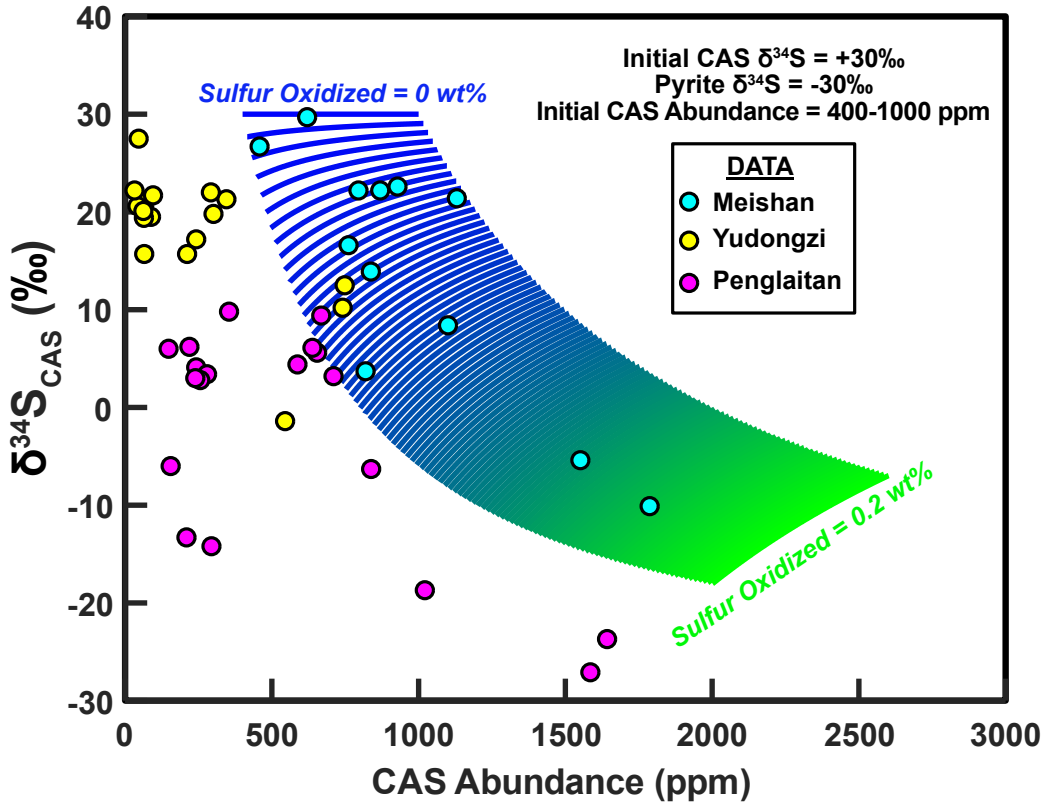

Figure III.11: Plot of final $\delta^{34}S_{CAS}$ versus CAS abundance for models in which pyrite (or other solid phase S) with a bulk $\delta^{34}S$ of -30‰ initially present in a carbonate rock has been completely oxidized and incorporated as CAS. Different lines represent different amounts of oxidized sulfur, with dark blue (top left) indicating no oxidation and lime green (lower right) indicating 0.2 wt% of oxidized S. Colored circles indicate $\delta^{34}S_{CAS}$ and CAS abundance data points for Meishan (cyan), Yudongzi (yellow), and Penglaitan (magenta; Present, unpublished data).

What processes could be responsible for oscillating redox during the EPME, assuming these model trends reflect in-situ oxidation during deposition? Riccardi, Arthur, and Kump (2006) [280] also observed highly variable $\delta^{34}S_{CAS}$ in EPME sections at Meishan and Shangsi in South China. They invoked periodic upwelling of euxinic waters through a shallow chemocline and subsequent oxidation of solid phase sulfur species (esp. elemental S) formed by phototrophic S oxidizing bacteria to explain this significant variability [280]. We agree that processes related to ocean circulation are most likely at play, as continental weathering processes operate on too long of timescales (Myr [143]) to facilitate rapid changes in productivity and seawater oxygenation. Temporally distinct accu-

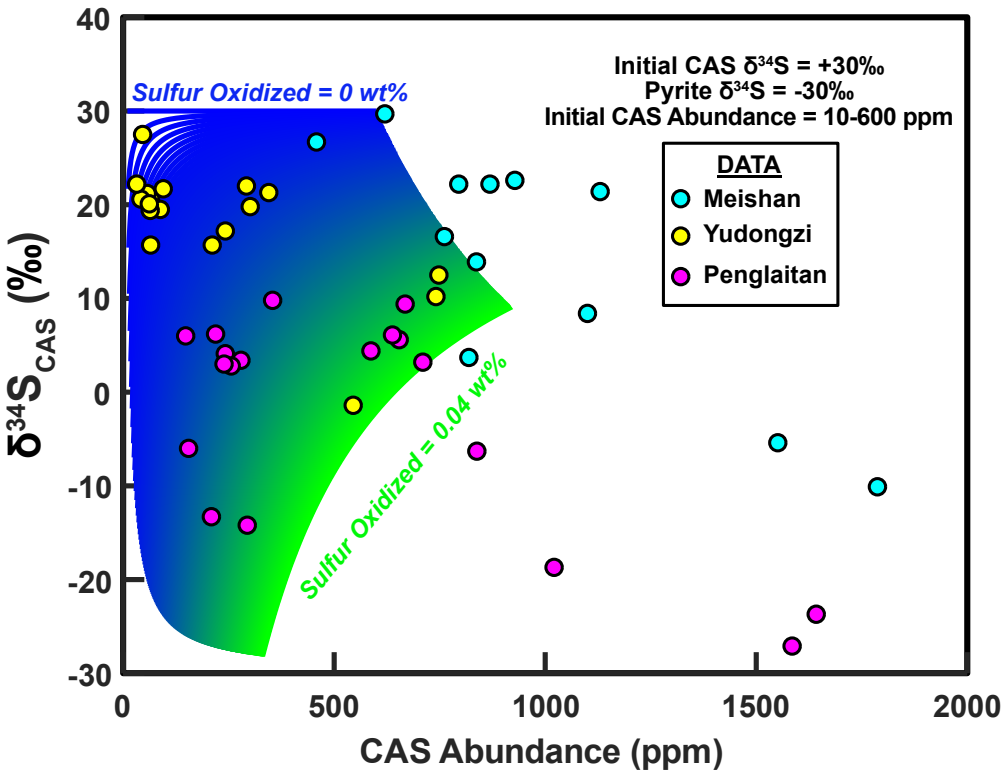

Figure III.12: Plot of final $\delta^{34}S_{CAS}$ versus CAS abundance for models in which pyrite (or other solid phase S) with a bulk $\delta^{34}S$ of -30‰ initially present in a carbonate rock has been completely oxidized and incorporated as CAS. Different lines represent different amounts of sulfur oxidized, with dark blue (top left) indicating no oxidation and lime green (lower right) indicating 0.04 wt% of oxidized S. Colored circles indicate $\delta^{34}S_{CAS}$ and CAS abundance data points for Meishan (cyan), Yudongzi (yellow), and Penglaitan (magenta; Present, unpublished data).

mulation and oxidation of solid phase S species also seem to be necessary to generate the highly negative $\delta^{34}S_{CAS}$ values we observe, but we disagree with Riccardi, Arthur, and Kump (2006) [280] that the S must have been formed in the water column. Our estimates for the amount of S oxidation needed to generate the observed $\delta^{34}S_{CAS}$ data are generally similar to or lower than the amount of pyrite S currently preserved in these rocks (e.g. [280]). In addition, pyrite multiple S isotope data suggest that some of the pyrite present at Meishan was formed through mixing between H_2S produced from a combination of MSR and S disproportionation and H_2S produced from nearly quantitative reduction of SO_4^{2-} (i.e., H_2S identical to seawater SO_4^{2-} in its S isotopic composition) [308]. In the conceptual model associated with these data, Shen et al. (2011) [308] en-

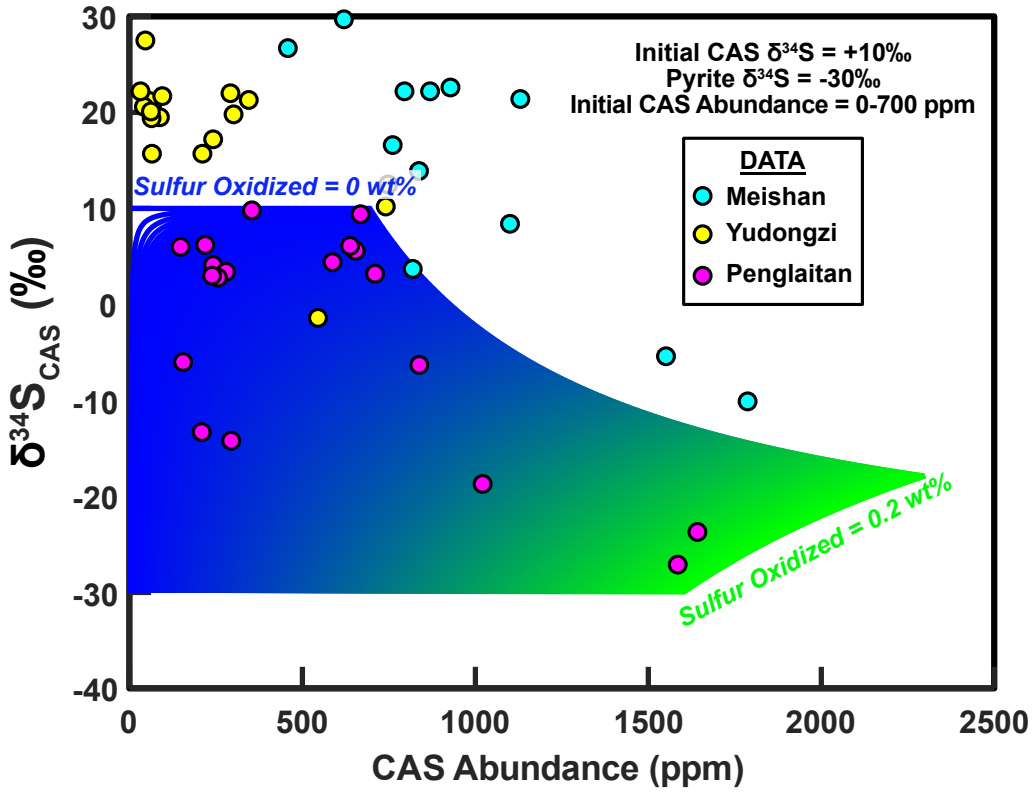

Figure III.13: Plot of final $\delta^{34}S_{CAS}$ versus CAS abundance for model in which pyrite (or other solid phase S) with a bulk $\delta^{34}S$ of -30‰ has been oxidized and incorporated as CAS. Initial $\delta^{34}S_{CAS}$ in this case was +10‰; all other aspects of the figure are as in Figures III.11 and III.12.

visioned both of these variants of pyrite to form in the sediments, albeit under differing bottom water oxygenation conditions. Pyrite trace element contents (e.g. [28]) may be a viable way to distinguish whether pyrite formed in the water column constitutes a significant component of the pyrite present in these sediments. Additional studies of the biomarker contents of shallow water sediments (e.g. [119]) may also yield valuable data to distinguish water column versus pore water redox variations.

Overall, geologic and geochemical records suggest a dynamic marine system during the EPME. Eruption of the Siberian Traps (e.g. [277]) and associated injection of large amounts of ^{13}C-depleted carbon (e.g. [249]) likely initiated rapid global warming [68, 326] that exerted extreme stress on many marine organisms (e.g. [**penn_tEPMErature-dependent_2018**]). Development of anoxic deep ocean waters (e.g. [152]) and periodic incursion of these waters into shallow

environments (e.g. [36]) was a key part of this warming-related stress. Such incursions and related oscillations in sedimentary redox can explain the widely variable $\delta^{34}S_{CAS}$ across the EPME despite relatively invariant sulfate evaporite $\delta^{34}S$; an extremely low size for the seawater SO_4^{2-} reservoir (e.g. [317]) is neither necessary nor likely. The extinction event culminated in a massive ocean acidification event (e.g. [144, 251, 312]) coinciding with a large negative carbon isotope excursion (e.g. [185]) across global environments. Persistently low seawater oxygenation may have prevented ecologic recovery until several Myr into the Triassic (e.g. [194, 239]). Additional careful geochemical work (e.g. triple oxygen isotope measurements of marine SO_4^{2-} [351]) may allow the role of the S cycle as an active driver of the extinction (e.g. [183]) versus a passive responder to other perturbations to be better evaluated.

III.7 Conclusions

The EPME remains Earth's most severe extinction to date, but the behavior of the marine S cycle during this event has been obscured by conflicting S isotopic records. Here, we attempted to resolve this conflict by measuring $\delta^{34}S_{CAS}$ variation within single hand samples and across time for EPME samples deposited in South China at Meishan and Yudongzi. We found substantial variability in $\delta^{34}S_{CAS}$ within single hand samples that in some cases reaches nearly 20‰. Plots of $\delta^{34}S_{CAS}$ versus $\frac{1}{CAS}$ suggest that much of this variability can be explained by mixing between high CAS abundance, low $\delta^{34}S_{CAS}$ and low CAS abundance, high $\delta^{34}S_{CAS}$ phases. Geologic evidence and a simple model of solid phase S oxidation and incorporation as CAS suggest that diagenetic alteration of carbonates under oscillating redox conditions can viably explain our data, supporting the earlier hypothesis of Riccardi, Arthur, and Kump (2006) [280]. Additional work is required to disentangle the role of marine S cycle dynamics as a direct driver of the EPME versus a passive follower of other Earth system changes occurring in the late Permian and early Triassic.

Chapter IV

A NEW REACTIVE TRANSPORT MODEL OF SULFUR CYCLING IN DEEP MARINE SEDIMENTS

IV.1 Abstract

A mechanistic understanding of the links between diagenetic reactions and depositional variables such as organic matter rain rate, sedimentation rate, and particle size is required to better predict the sulfur isotopic composition of sedimentary phases. We constructed a time-dependent reactive transport model for early diagenesis that includes sulfur isotopic species to facilitate this understanding. Our model includes organic matter sulfurization and realistic pyrite formation processes that produce pyrite through reactions of iron monosulfide with aqueous sulfide or elemental sulfur. Model sensitivity tests suggest that organic matter rain rate, porosity, and sedimentation rate act as the strongest controls on the sulfur isotopic composition of buried pyrite in marine sediments through their ability to greatly perturb the relative balance between diffusion, burial advection, and reaction of sedimentary constituents. In particular, these variables modulate the influence of diffusive sulfate fluxes on a given diagenetic system (i.e., how "open" versus "closed" the system is) and constrain the maximum ^{34}S−enrichment that sedimentary pyrite in the system may attain. Our tests also support the recent assertion [127] that variations in organic matter input and the physical parameters of sedimentary systems (esp. sedimentation rate) can entirely account for the heterogeneity in sulfur isotopic offsets between marine sulfate and buried pyrite in environments globally; no variations in sulfur isotopic fractionation ($^{34}\varepsilon$) are necessary. These results demonstrate the utility of our diagenetic model for modeling processes across multiple spatiotemporal scales and motivate further application of the model toward outstanding questions in the marine sulfur cycle.

IV.2 Background

Chapters I, II, and III of this thesis alluded to the important role of diagenetic reactions in altering the sulfur (S) isotopic composition of geologic archives. Such alteration impedes reconstruction of the δ^{34}S of seawater sulfate, but may

still yield valuable information on local or even global depositional conditions. For example, typical isotopic box models of the marine S cycle rely on microbial sulfate reduction and its associated S isotopic fractionation during sedimentary diagenesis to yield estimates of relative S burial fluxes throughout Earth history [57, 167, 172].

S cycling within marine sediments is ultimately driven by the production of organic matter at Earth's surface. Most of this organic matter is oxidized by O_2 within the water column, though dissolved NO_3^- and SO_4^{2-} may play a small role in oxidation within particle microenvironments [29] and highly productive or restricted regions [62, 159, 274]. In most environments, only a small proportion of the organic matter survives transit through the water column to marine sediments [154]. Within the sediments, this organic matter fuels a cascade of biologically-catalyzed chemical reactions. Organic matter is oxidized using available electron acceptors based on free energy yield [104]. Typically, consumption of dissolved oxygen (O_2) occurs first and is followed by the progressive consumption of dissolved nitrate (NO_3^-), solid phase manganese(IV), solid phase iron(III), and dissolved sulfate (SO_4^{2-}). Methanogenesis takes place once electron acceptors have been exhausted. SO_4^{2-} dominates in abundance over the other electron acceptors in modern marine sediments and is responsible for over 50% of organic matter degradation locally [165] and as much as 29% globally [43]. In turn, the products of these organic matter degradation reactions can react with each other via numerous secondary reactions, forming a complex sedimentary diagenetic system.

Previous studies have attempted to model sedimentary diagenesis with varying detail. Early efforts by Berner [20, 21, 22] established the conceptual framework for representing sedimentary diagenesis in mathematical form. Subsequent studies have layered complexity upon this framework by including multiple organic matter fractions [357] or a single fraction of variable reactivity [218], additional organic matter degradation reactions [40, 65, 85, 270, 315], and isotopic species [127, 162, 324]. These studies have also differed in the numerical schemes used to run their models, with some only solving for steady state profiles (e.g. [162, 218]) and others yielding time-dependent outputs (e.g. [65, 362]).

Despite the abundance of sedimentary diagenetic models, few have included S isotopic species or realistic formation mechanisms for solid phase S species.

Jørgensen (1979) [162] made one of the first attempts to model the S isotopic composition of S species during sedimentary diagenesis. He simply removed a set fraction f of the aqueous sulfide (H_2S) generated at each depth as pyrite (FeS_2), with no intermediate iron monosulfide (FeS) phase. More recently, Masterson et. al (2018) [211] modeled the abundances of ^{32}S, ^{33}S, and ^{34}S in pore water SO_4^{2-} during the diagenesis of marine sediments in the Gulf of California, but did not include any aqueous H_2S or solid phase S species in their model. Only recently have modelers begun to incorporate more realistic reaction mechanisms for pyrite formation [127, 217]. Notably, just one of these models [127] has included organic matter sulfurization among its reactions, a potentially significant oversight given the importance of this process as an H_2S sink in some environments [275].

To better understand the controls upon the concentration and S isotopic composition of S phases in marine sediments, we developed a new reactive transport model to simulate S cycling and sedimentary diagenesis in deep marine sediments. This model uses more realistic pyrite formation mechanisms than most previous models and is one of the first to include organic matter sulfurization as an explicit process. Here, we describe the details of the model and its sensitivity to different variables.

IV.3 Model Construction

To simulate the evolution of the concentrations and isotopic compositions of sedimentary species, a time-dependent 1-D reactive transport model was constructed in MATLAB®. The model was inspired by several previous models for diagenetic reactions in shallow sediments [40, 65, 269, 270, 315, 362]. The model uses the method-of-lines approach of Boudreau's (1996) "Carbon and Nutrient Diagenesis" (CANDI) model [40] to solve for the concentration within each depth box at each time point and MATLAB®'s `ode15s` solver to allow for variable time steps. We include several modifications to this model, as described in the following paragraphs. Most notably, we add S isotopic species to our model to simulate $\delta^{34}S$ profiles; isotopic species of other elements may also be easily added. We christen this model "Isotope-enabled Carbon and Nutrient Diagenesis", or "I-CANDI", based on this distinction. A basic schematic of the model is shown in Figure IV.1.

Unlike previous models that have focused on diagenetic reactions in shallow

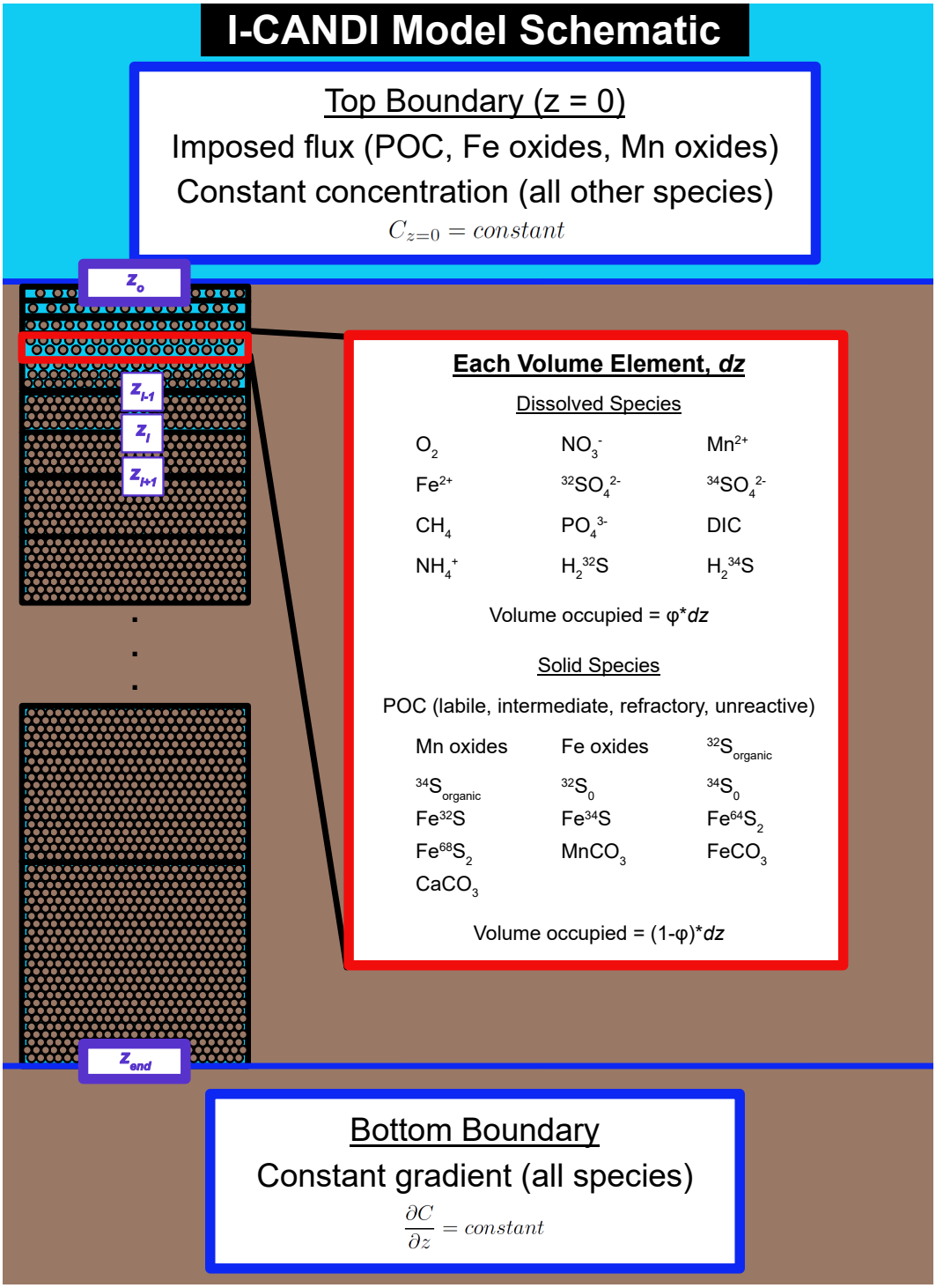

Figure IV.1: Schematic of the I-CANDI sediment diagenesis model. The model explicitly tracks the concentrations of 12 dissolved species and 17 solid species in its current form. The change in the concentration of each species at each time step is calculated using discretized versions of the diagenetic equation as written by Berner (1980) [22] and shown in equations IV.4 and IV.5. See the text for additional details.

sediments, our model is targeted toward deep ocean sedimentary profiles spanning 10s to 100s of meters. Simulating changes across such a large depth range presents a challenge; the depth resolution in the model must be fine enough to accurately capture rapid profile changes in shallow sediments, but not so fine that the computational time required to run the model becomes prohibitive. To combat this challenge, we follow Boudreau (1997) [41] and implement the ability to use an uneven grid into our model. We create an initial depth grid Z from the top of the depth domain (z_o) to the bottom of the domain (z_{end}) with a constant depth increment dz. We then transform this grid to a new grid Z_{new} using an equation of the following form [41]:

$$Z_{new} = z_{end}^{-n} * z^{n+1}$$

where z is each individual depth within the initial grid Z and n is an arbitrary positive value. Such a transformation results in depth increments dz that increase from small values at the top of the domain to large values near the end of the domain; this limits the total number of discretized depth boxes needed to adequately simulate reactions in both the shallow and deep portions of the sedimentary profile. Furthermore, regularly transformed grids of this nature have been found by other authors [41, 207] to yield model results of equivalent accuracy to results obtained with even grids (i.e., grids with depth-invariant dz). The exponent n may be increased as needed to more finely discretize shallow depths at the expense of larger dz near the bottom of the depth domain.

Modeling pH is both computationally difficult and fraught with uncertainty given the large number of reactions that can affect pH in sedimentary pore waters [40, 65, 362]. To reduce computational time, we follow Wijsman et al. (2002) [362] and impose a sedimentary pH profile instead of modeling pH as a reaction-dependent output. This imposed profile is used to speciate dissolved inorganic carbon (DIC) into carbonic acid (H_2CO_3), bicarbonate (HCO_3^-), and carbonate ion (CO_3^{2-}) at each time step. We do not include alkalinity as a variable and assume that the imposed pH profile already incorporates changes in DIC speciation due to sedimentary chemical reactions. Acid dissociation constants are calculated at the beginning of the model run using CO2SYS [346]. Inputs to CO2SYS for the pressure and temperature of measurement were 0 bar and 25 °C, respectively. The CO2SYS output temperature was assigned to be 2 °C at the the sediment-water interface and to increase with sedimentary depth at

a geothermal gradient of 30 $\frac{°C}{km}$. The output pressure was estimated assuming a water depth of 3000 m and a sediment density of 2.7 $\frac{g}{cm^3}$.

As mentioned earlier, we additionally add isotopic species to the model. Separate species for ^{32}S- and ^{34}S-bearing aqueous SO_4^{2-}, aqueous H_2S, solid phase elemental S (S^0), solid phase FeS, solid phase organic S, and pyrite (FeS_2) are included in the model. Species bearing the minor S isotopes ^{33}S and ^{36}S are ignored. Each ^{32}S- and ^{34}S-bearing species is tracked independently. Reactions are scaled for each isotopic species by multiplying an overall reaction rate by the fraction of total reactant represented by the species [89], i.e.:

$$^{32}R = {}^{32}\mathrm{X} * R \qquad \text{(IV.1a)} \qquad\qquad {}^{34}R = {}^{34}\ {}^{34}\mathrm{X} * R \qquad \text{(IV.1b)}$$

where ^{32}R is the reaction rate of the ^{32}S-bearing species, ^{34}R is the reaction rate of the ^{34}S-bearing species, R is the overall reaction rate, ^{32}X is the mole fraction for the ^{32}S-bearing species, and ^{34}X is the mole fraction for the ^{34}S-bearing species. An isotopic fractionation for a reaction, $^{34}\alpha$, is defined as follows:

$$^{34}\alpha = \frac{\frac{^{34}\mathrm{X}}{^{32}\mathrm{X}}_{product}}{\frac{^{34}\mathrm{X}}{^{32}\mathrm{X}}_{reactant}} \qquad \text{(IV.2)}$$

where $\frac{^{34}\mathrm{X}}{^{32}\mathrm{X}}_{product}$ is the ratio of mole fractions for the instantaneous product. Rearranging to solve for $\frac{^{34}\mathrm{X}}{^{32}\mathrm{X}}_{product}$ and substituting for $^{32}\mathrm{X}_{product}$ and $^{34}\mathrm{X}_{product}$ using equations IV.1a and IV.1b, we get:

$$\frac{^{34}R}{^{32}R} = {}^{34}\alpha * \frac{^{34}\mathrm{X}}{^{32}\mathrm{X}}_{reactant} \qquad \text{(IV.3)}$$

Comparison of this result to equations IV.1a and IV.1b shows that an isotopic fractionation for a reaction may be implemented simply by multiplying equation IV.1b by $^{34}\alpha$. Although equations IV.1a and IV.1b do not add to exactly R if $^{34}\alpha \neq 1$, the effect on the magnitude of R is trivial. Isotopic species for additional model constituents are not included here, but may easily be added if required for future applications. Transport mechanisms, reactions, and numerical methods for the model are described below.

IV.3.1 Transport Mechanisms

I-CANDI includes four mechanisms of transport: free diffusion, biodiffusion, (bio)irrigation, and advection. Free diffusion coefficients (D_o) are calculated at

each model depth z with the equations of Boudreau (1997) [41] using the imposed temperature at each depth. The dynamic viscosity of water (μ) is calculated using the Vogel equation [350]. We assume that the same free diffusion coefficient applies for different isotopologues of the same species. A user-defined porosity profile is used to calculate sedimentary diffusion coefficients (D_s) for aqueous phases as follows:

$$D_{s_{i,z}} = \frac{D_{o_{i,z}}}{\phi_z^{1-m}}$$

where $D_{s_{i,z}}$ is the sedimentary diffusion coefficient for species i at depth z, $D_{o_{i,z}}$ is the free diffusion coefficient for species i at depth z, and ϕ_z is the porosity at depth z. The denominator ϕ_z^{1-m} approximates the square of the tortuosity (θ) of the sediment; we follow Berner (1980) and assume $m = 1.8$ based on the average value from many Deep Sea Drilling Project (DSDP) sites [22]. All diffusion equations are summarized in Table IV.1.

Biodiffusion of solid phases (i.e., mixing through bioturbation) in I-CANDI is dependent on sedimentation rate (ω) and is parameterized using the pseudo-two-layer scheme of Boudreau (1996) [40]. In this scheme, the biodiffusion coefficient (D_b) for each solid phase remains constant from the sediment-water interface to a depth z_a and gradually decreases to 0 between depths z_a and z_b. These parameterizations are also summarized in Table IV.1. Aqueous phases are not affected by this process.

Bioirrigation affects only dissolved phases and is assumed to be non-zero down to a depth z_γ. We assign a value of $9.51 * 10^{-7}$ s^{-1} to the bioirrigation coefficient γ based on previous studies [40, 41], though we expect the effect of including this value to be negligible in deep ocean sediments [10]. This constant is multiplied by the difference in concentration between the initial concentration (C_0) and the concentration at the depth of interest (C) for depths $\leq z_\gamma$, i.e.:

$$\text{Irrigation component} = \gamma * (C_0 - C)$$

Finally, advection within I-CANDI occurs as a result of sedimentation and compaction. We assume steady state compaction and calculate solid phase advection rates at each depth as follows [22]:

$$\omega_z = \frac{1 - \phi_{end}}{1 - \phi_z} * \omega_{end}$$

where ω_z is the advection rate at depth z, ϕ_{end} is the porosity at the depth where compaction becomes negligible, ϕ_z is the porosity at depth z, and ω_{end} is the

Table IV.1: Equations used to calculate diffusion and irrigation coefficients in I-CANDI.

Free Diffusion Coefficients			
Species	**Equation**	**Units**	**Reference**
O_2	$D_o = 4.72 * 10^{-9} * \frac{T+273.15}{\mu * 27.9^{0.6}}$	$\frac{cm^2}{s}$	[41]
NO_3^-	$D_o = 9.50 + 0.388 * T$	$\frac{cm^2}{s}$	[41]
Mn^{2+}	$D_o = 3.18 + 0.155 * T$	$\frac{cm^2}{s}$	[41]
Fe^{2+}	$D_o = 3.31 + 0.150 * T$	$\frac{cm^2}{s}$	[41]
SO_4^{2-}	$D_o = 4.88 + 0.232 * T$	$\frac{cm^2}{s}$	[41]
CH_4	$D_o = 4.72 * 10^{-9} * \frac{T+273.15}{\mu * 37.7^{0.6}}$	$\frac{cm^2}{s}$	[41]
HS^-	$D_o = 10.4 + 0.273 * T$	$\frac{cm^2}{s}$	[41]
DIC	$D_o = 5.06 + 0.275 * T$	$\frac{cm^2}{s}$	[41]
PO_4^{3-}	$D_o = 2.62 + 0.143 * T$	$\frac{cm^2}{s}$	[41]
NH_4^+	$D_o = 9.50 + 0.413 * T$	$\frac{cm^2}{s}$	[41]
Sedimentary Diffusion Coefficients			
Symbol	**Equation**	**Units**	**Reference**
D_s	$D_s = \frac{D_o}{\phi^{1-m}}$ (for each species)	$\frac{cm^2}{s}$	[22]
Biodiffusion & Bioirrigation Coefficients			
Symbol	**Equation**	**Units**	**Reference**
D_{b_o}	$D_{b_o} = 15.7 * \omega^{0.7}$	$\frac{cm^2}{s}$	[39]
D_b	$D_b = \begin{cases} D_{b_o}, & 0 \leq z \leq z_a \\ D_{b_o} \frac{z_b - z}{z_b - z_a}, & z_a \leq z \leq z_b \\ 0, & z \geq z_b \end{cases}$	$\frac{cm^2}{s}$	[40]
γ	$\gamma = \begin{cases} 9.51 * 10^{-7}, & 0 \leq z \leq z_\gamma \\ 0, & z \geq z_\gamma \end{cases}$	s^{-1}	[41]

Table IV.2: Transport parameter values in I-CANDI.

Symbol	Description	Value	Units	Reference
ω	Sedimentation rate for solid phases (corrected for compaction)	variable	$\frac{m}{yr}$	
ν	Sedimentation rate for dissolved phases (corrected for compaction)	variable	$\frac{m}{yr}$	
ϕ	Porosity	variable	unitless	
ϕ_{end}	Porosity at depth where compaction becomes negligible	user-defined	unitless	
m	Exponential factor for estimating tortuosity from porosity	1.8	unitless	[22]
μ	Dynamic viscosity of water	variable	poise	
z_a	Bottom boundary of first biodiffusion layer	0.08	m	[39]
z_b	Bottom boundary of second biodiffusion layer	0.1	m	[39]

sedimentation rate at depths where compaction becomes negligible. The pore water advection rate ν_z at depth z is calculated in a similar manner [22]:

$$\nu_z = \frac{\phi_{end}}{\phi_z} * \omega_{end}$$

A summary of the parameter values associated with the transport mechanisms describe above may be found in Table IV.2.

IV.3.2 Reactions

Reactions included within I-CANDI are summarized in Tables IV.3, IV.4, and IV.5. Based on the data of Redfield (1963) [276], we assume a simple molar C:N:P ratio of 106:16:1 for organic matter in I-CANDI. The moles of each of these elements per mole of organic matter are defined as model inputs in Table IV.6. A more reduced composition that better reflects the stoichiometry of marine organic matter [7] will be explored in future studies.

Reactive organic matter within the model is divided into three different fractions that degrade at rates R_{POC_i} based on rate laws of the following form:

$$R_{POC_i} = k_i G_i f_{ox}$$

where k_i is the first-order rate constant for the oxidation of organic matter fraction i, G_i is the amount of organic carbon within fraction i, and f_{ox} is the sum of the fractional contributions of each organic matter oxidation reaction, i.e.:

$$f_{ox} = \sum f_j$$

Here, f_j is the fractional contribution of organic matter oxidation reaction j. Organic matter fractions are divided such that $i = 1$ for highly reactive (labile) organic matter, $i = 2$ for moderately reactive organic matter, and $i = 3$ for slightly reactive organic matter. An unreactive organic matter fraction ($i = 4$) is also included in the model to account for organic compounds that do not degrade on

early diagenetic timescales (see Table IV.6). For organic matter and all other solid phases in the model, we assume that the modeled abundance of the solid phase (in $\frac{\text{mol}}{\text{m}^3}$) is linearly proportional to the activity of the phase and can be used to define rate laws for chemical reactions in I-CANDI. Non-unity activity coefficients are implicitly incorporated into the rate constants for reactions involving these phases.

Organic matter oxidation consumes electron acceptors in order of decreasing free energy yield [104] and is partitioned among different electron acceptors using Monod (a.k.a. Michaelis-Menten) functions to describe oxidant limitation [231]:

$$R_{POC_{i,j}} = k_i G_i f_{ox} f_j$$

$$f_j = \frac{C_j}{K_j + Cj} * (\text{inhibition expressions})$$

where K_j is the half-saturation constant for a given oxidation process and C_j is the concentration of the corresponding electron acceptor. Inhibition expressions are of the form:

$$\frac{K_{j,inhib}}{K_{j,inhib} + C_j}$$

where $K_{inhib,j}$ is the inhibition constant for organic matter oxidation reactions of lower free energy yield in the presence of a given electron acceptor. Given the formulation of the Monod and inhibition expressions, higher half-saturation constants result in lower f_j values and higher inhibition constants result in higher f_j values. Monod terms equal one-half when $C_j = K_j$, and inhibition terms equal one-half when $C_j = K_{j,inhib}$; when $C_j = 0$, Monod terms equal zero and inhibition terms equal one. Values used for each of the half-saturation and inhibition constants in I-CANDI are shown in Table IV.7. Full Monod formulations for the f of each organic matter degradation reaction in a given depth box are shown in Table IV.8. Reactions in the model include oxic respiration, nitrate reduction, manganese reduction, iron reduction, sulfate reduction, and methanogenesis; intermediate fermentation of organic matter (e.g. [201]) is implicitly included in these reactions.

Following the production of species via organic matter oxidation, secondary reactions may occur among these species. These secondary reactions are assumed to follow first-order kinetics with respect to each species and are listed in Table IV.4; in general, rate laws and rate constants for these reactions have been empirically demonstrated or have been assigned based on fits to data from other

Table IV.3: Reaction rate laws for organic matter degradation reactions included in I-CANDI.

Organic Matter Degradation Reactions			
Reaction	**Chemical Equation**	**Kinetic Formulation**	**Reference**
Oxic Respiration	$(CH_2O)_A(NH_3)_B(H_3PO_4)_C + (A + 2\,B)O_2 \longrightarrow A\,CO_2 + B\,HNO_3 + C\,H_3PO_4$	$R_{POC,O_2} = \sum k_i G_i f_{O_2}$	[40]
Nitrate Reduction	$(CH_2O)_A(NH_3)_B(H_3PO_4)_C + \frac{4}{5}A\,NO_3^- \longrightarrow \frac{1}{5}A\,CO_2 + \frac{4}{5}A\,HCO_3^- + \frac{2}{5}A\,N_2 + \frac{1}{5}B\,NH_3 + \frac{1}{5}C\,H_3PO_4$	$R_{POC,NO_3^-} = \sum k_i G_i f_{NO_3^-}$	[40]
Manganese Reduction	$(CH_2O)_A(NH_3)_B(H_3PO_4)_C + 2\,A\,MnO_2 + 3\,A\,CO_2 \longrightarrow 4\,A\,HCO_3^- + 2\,A\,Mn^{2+} + B\,NH_3 + C\,H_3PO_4$	$R_{POC,MnO_2} = \sum k_i G_i f_{MnO_2}$	[40]
Iron Reduction	$(CH_2O)_A(NH_3)_B(H_3PO_4)_C + 4\,A\,Fe(III)_{solid} + 7\,A\,CO_2 \longrightarrow 8\,A\,HCO_3^- + 4\,A\,Fe^{2+} + B\,NH_3 + C\,H_3PO_4$	$R_{POC,Fe(III)} = \sum k_i G_i f_{Fe(III)}$	[40]
Sulfate Reduction	$(CH_2O)_A(NH_3)_B(H_3PO_4)_C + \frac{1}{2}A\,SO_4^{2-} \longrightarrow A\,HCO_3^- + \frac{1}{2}A\,H_2S + B\,NH_3 + C\,H_3PO_4$	$R_{POC,SO_4^{2-}} = \sum k_i G_i f_{SO_4^{2-}}$	[40]
Methanogenesis	$(CH_2O)_A(NH_3)_B(H_3PO_4)_C \longrightarrow \frac{1}{2}A\,CO_2 + \frac{1}{2}A\,CH_4 + B\,NH_3 + C\,H_3PO_4$	$R_{POC,CH_4} = \sum k_i G_i f_{CH_4}$	[40]

Table IV.4: Reaction rate laws for secondary reactions included in I-CANDI.

Secondary Reactions			
Reaction	**Chemical Equation**	**Kinetic Formulation**	**Reference**
Ammonium Oxidation by O_2	$NH_4^+ + 2\,O_2 + 2\,HCO_3^- \longrightarrow NO_3^- + 2\,CO_2 + 3\,H_2O$	$R_{NH_4Ox} = k_{NH_4Ox}[NH_4^+]_T[O_2]$	[40]
Manganese Oxidation by O_2	$2\,Mn^{2+} + O_2 + 4\,HCO_3^- \longrightarrow 2\,MnO_2 + 4\,CO_2 + 2\,H_2O$	$R_{MnOx} = k_{MnOx}[Mn^{2+}][O_2]$	[40]
Iron Oxidation byO_2	$4\,Fe^{2+} + O_2 + 8\,HCO_3^- \longrightarrow Fe(III)_{solid} + 8\,CO_2 + 2\,H_2O$	$R_{FeOx} = k_{FeOx}[Fe^{2+}][O_2]$	[40]
Iron Oxidation by MnO_2	$2\,Fe^{2+} + MnO_2 + 3\,HCO_3^- + 2\,H_2O \longrightarrow 2\,Fe(III)_{solid} + Mn^{2+} + 4\,CO_2$	$R_{FeMn} = k_{FeMn}[Fe^{2+}][MnO_2]$	[40]
Aqueous Sulfide Oxidation by O_2	$H_2S + O_2 + 2\,HCO_3^- \longrightarrow SO_4^{2-} + 2\,CO_2 + 2\,H_2O$	$R_{H_2SOx} = k_{H_2SOx}[H_2S]_T[O_2]$	[40]
Aqueous Sulfide Oxidation by MnO_2	$H_2S + MnO_2 + 2\,CO_2 \longrightarrow S_0 + Mn^{2+} + 2\,HCO_3^-$	$R_{MnO_2TS} = k_{MnO_2TS}[H_2S]_T[MnO_2]$	[40]
Aqueous Sulfide Oxidation by $Fe(III)_{solid}$	$H_2S + 2\,Fe(III)_{solid} + 4\,CO_2 \longrightarrow S_0 + 2\,Fe^{2+} + 4\,HCO_3^- + 2\,H_2O$	$R_{Fe(III)TS} = k_{Fe(III)TS}[H_2S]_T[Fe(III)_{solid}]$	[40]
Methane Oxidation by O_2	$CH_4 + O_2 \longrightarrow CO_2 + 2\,H_2O$	$R_{CH_4Ox} = k_{CH_4Ox}[CH_4][O_2]$	[40]
Methane Oxidation by Sulfate (AOM)	$CH_4 + SO_4^{2-} + CO_2 \longrightarrow 2\,HCO_3^- + H_2S$	$R_{CH_4SO_4} = k_{CH_4SO_4}[CH_4][SO_4^{2-}]$	[40]
Iron Monosulfide Oxidation by O_2	$FeS + 2\,O_2 \longrightarrow Fe^{2+} + SO_4^{2-}$	$R_{FeSOx} = k_{FeSOx}[FeS][O_2]$	[40]
Iron Monosulfide Oxidation by MnO_2	$FeS + MnO_2 + 4\,CO_2 + 2\,H_2O \longrightarrow Mn^{2+} + Fe^{2+} + S_0 + 4\,HCO_3^-$	$R_{FeSMnO_2} = k_{FeSMnO_2}[FeS][MnO_2]$	[40]
Iron Monosulfide Oxidation by $Fe(III)_{solid}$	$FeS + {}_2Fe(III)_{solid} + 4\,CO_2 \longrightarrow 2\,Fe^{2+} + S_0 + 4\,HCO_3^- + 2\,H_2O$	$R_{FeSFe(III)} = k_{FeSFe(III)}[FeS][Fe(III)_{solid}]$	[40]
Organic Matter Sulfurization	$C:S_{OMsulf}\cdot(CH_2O)_A(NH_3)_B(H_3PO_4)_C + H_2S \longrightarrow C:S_{OMsulf}\cdot S(CH_2O)_A(NH_3)_B(H_3PO_4)_C$	$R_{OM_{sulf}} = k_{OMsulf}[POC]_T[H_2S]_T$	

Table IV.5: Reaction rate laws for precipitation reactions included in I-CANDI.

Precipitation Reactions			
Reaction	**Chemical Equation**	**Kinetic Formulation**	**Reference**
Calcium Carbonate Precipitation	$Ca^{2+} + CO_3^{2-} \longrightarrow CaCO_3$	$R_{CaCO_3ppt} = k_{CaCO_3ppt}(\Omega_{CaCO_3} - 1) * \frac{1}{1+10^6 * e^{-k_{log}(\Omega_{CaCO_3}{}^{-1})}}$	[40]
Manganese Carbonate Precipitation	$Mn^{2+} + CO_3^{2-} \longrightarrow MnCO_3$	$R_{MnCO_3ppt} = k_{MnCO_3ppt}(\Omega_{MnCO_3} - 1) * \frac{1}{1+10^6 * e^{-k_{log}(\Omega_{MnCO_3}{}^{-1})}}$	[65]
Iron Carbonate Precipitation	$Fe^{2+} + CO_3^{2-} \longrightarrow FeCO_3$	$R_{FeCO_3ppt} = k_{FeCO_3ppt}(\Omega_{FeCO_3} - 1) * \frac{1}{1+10^6 * e^{-k_{log}(\Omega_{FeCO_3}{}^{-1})}}$	[65]
Iron Monosulfide Precipitation	$Fe^{2+} + HS^- + HCO_3^- \longrightarrow FeS + CO_2 + H_2O$	$R_{FeSppt} = k_{FeS3ppt}(\Omega_{FeS} - 1) * \frac{1}{1+10^6 * e^{-k_{log}(\Omega_{FeS}{}^{-1})}}$	[40]
Pyrite Formation via Elemental S	$FeS + S_0 \longrightarrow FeS_2$	$R_{FeS_2S^0} = k_{FeS_2S^0}[FeS][S_0]$	[217]
Pyrite Formation via Aqueous Sulfide and Aqueous Fe^{2+}	$FeS + H_2S \longrightarrow FeS_2 + H_2$	$R_{FeS_2H_2S,Fe} = k_{FeS_2H_2S,Fe}[FeS][H_2S]_T$	[217]
Pyrite Formation via Aqueous Sulfide and $FeCO_3$	$FeCO_3 + 2\,HS^- \longrightarrow FeS_2 + CO_3^{2-} + H_2$	$R_{FeS_2H_2S,FeCO_3} = k_{FeS_2H_2S,FeCO_3}[FeCO_3][HS^-]$	[217]

Table IV.6: Reaction parameter values used in I-CANDI.

Symbol	Description	Value	Units	Reference
f_{k_1}	Fraction of total organic matter flux with fast degradation rate	variable	unitless	
f_{k_2}	Fraction of total organic matter flux with intermediate degradation rate	variable	unitless	
f_{k_3}	Fraction of total organic matter flux with slow degradation rate	variable	unitless	
f_{k_4}	Fraction of total organic matter flux that is unreactive	variable	unitless	
A	Moles of C per mole of organic matter	106	moles	[276]
B	Moles of N per mole of organic matter	16	moles	[276]
C	Moles of P per mole of organic matter	1	moles	[276]
$C : S_{OM_{sulf}}$	Moles of organic C per mole of S in sulfurized organic matter	15	moles	[108]
k_{log}	logistic growth rate for logistic equation term in precipitation reactions	10^3	(unitless)	
${}^{34}\alpha_{MSR}$	Fractionation factor for sulfur isotopes during microbial sulfate reduction	0.930	(unitless)	
${}^{34}\alpha_{reox}$	Fractionation factor for sulfur isotopes during sulfide and elemental sulfur reoxidation	0.930	(unitless)	

Table IV.7: Half-saturation and inhibition constants used in I-CANDI.

Symbol	Description	Value	Units	Reference
K_{O_2}	Monod constant for degradation of organic matter with O_2	0.003	$\frac{\text{mol}}{\text{m}^3}$ (mM)	[315]
$K_{O_2,inhib}$	Inhibition constant associated with presence of O_2	0.01	$\frac{\text{mol}}{\text{m}^3}$ (mM)	[315]
$K_{NO_3^-}$	Monod constant for degradation of organic matter with NO_3^-	0.03	$\frac{\text{mol}}{\text{m}^3}$ (mM)	[315]
$K_{NO_3^-,inhib}$	Inhibition constant associated with presence of NO_3^-	0.005	$\frac{\text{mol}}{\text{m}^3}$ (mM)	[315]
K_{MnO_2}	Monod constant for degradation of organic matter with MnO_2	42.4	$\frac{\text{mol}}{\text{m}^3}$	[65]
$K_{MnO_2,inhib}$	Inhibition constant associated with presence of MnO_2	42.4	$\frac{\text{mol}}{\text{m}^3}$	[65]
$K_{Fe(III)}$	Monod constant for degradation of organic matter with $Fe(III)_{solid}$	265	$\frac{\text{mol}}{\text{m}^3}$	[65]
$K_{Fe(III),inhib}$	Inhibition constant associated with presence of $Fe(III)_{solid}$	265	$\frac{\text{mol}}{\text{m}^3}$	[65]
$K_{SO_4^{2-}}$	Monod constant for degradation of organic matter with SO_4^{2-}	1.6	$\frac{\text{mol}}{\text{m}^3}$ (mM)	[65]
$K_{SO_4^{2-},inhib}$	Inhibition constant associated with presence of SO_4^{2-}	1.6	$\frac{\text{mol}}{\text{m}^3}$ (mM)	[65]

Table IV.8: Monod formulations for organic matter oxidation reactions included in the model.

Reaction	Symbol	Equation	Units	Reference
Oxic Respiration	f_{O_2}	$f_{O_2} = \frac{[\mathrm{O_2}]}{K_{O_2}+[\mathrm{O_2}]}$	unitless	[324]
Nitrate Reduction	$f_{NO_3^-}$	$f_{NO_3^-} = \frac{[\mathrm{NO_3^-}]}{K_{NO_3^-}+[\mathrm{NO_3^-}]} \frac{K_{O_2,inhib}}{K_{O_2,inhib}+[\mathrm{O_2}]}$	unitless	[324]
Manganese Reduction	f_{MnO_2}	$f_{MnO_2} = \frac{[\mathrm{MnO_2}]}{K_{MnO_2}+[\mathrm{MnO_2}]} \cdot \frac{K_{NO_3^-,inhib}}{K_{NO_3^-,inhib}+[\mathrm{NO_3^-}]} \cdot \frac{K_{O_2,inhib}}{K_{O_2,inhib}+[\mathrm{O_2}]}$	unitless	[324]
Iron Reduction	$f_{Fe(III)}$	$f_{Fe(III)} = \frac{[\mathrm{Fe(III)_{solid}}]}{K_{Fe(III)}+[\mathrm{Fe(III)_{solid}}]} \cdot \frac{K_{MnO_2,inhib}}{K_{MnO_2,inhib}+[\mathrm{MnO_2}]} \cdot \frac{K_{NO_3^-,inhib}}{K_{NO_3^-,inhib}+[\mathrm{NO_3^-}]} \cdot \frac{K_{O_2,inhib}}{K_{O_2,inhib}+[\mathrm{O_2}]}$	unitless	[324]
Sulfate Reduction	$f_{SO_4^{2-}}$	$f_{SO_4^{2-}} = \frac{[\mathrm{SO_4^{2-}}]}{K_{SO_4^{2-}}+[\mathrm{SO_4^{2-}}]} \cdot \frac{K_{Fe(III),inhib}}{K_{Fe(III),inhib}+[\mathrm{Fe(III)_{solid}}]} \cdot \frac{K_{MnO_2,inhib}}{K_{MnO_2,inhib}+[\mathrm{MnO_2}]} \cdot \frac{K_{NO_3^-,inhib}}{K_{NO_3^-,inhib}+[\mathrm{NO_3^-}]} \cdot \frac{K_{O_2,inhib}}{K_{O_2,inhib}+[\mathrm{O_2}]}$	unitless	[324]
Methanogenesis	f_{CH_4}	$f_{CH_4} = \frac{[\mathrm{CH_4}]}{K_{CH_4}+[\mathrm{CH_4}]} \cdot \frac{K_{SO_4^{2-},inhib}}{K_{SO_4^{2-},inhib}+[\mathrm{SO_4^{2-}}]} \cdot \frac{K_{Fe(III),inhib}}{K_{Fe(III),inhib}+[\mathrm{Fe(III)_{solid}}]} \cdot \frac{K_{MnO_2,inhib}}{K_{MnO_2,inhib}+[\mathrm{MnO_2}]} \cdot \frac{K_{NO_3^-,inhib}}{K_{NO_3^-,inhib}+[\mathrm{NO_3^-}]} \cdot \frac{K_{O_2,inhib}}{K_{O_2,inhib}+[\mathrm{O_2}]}$	unitless	[324]

sedimentary profiles [65]. Reactions include numerous reoxidation reactions, anaerobic oxidation of methane (AOM) by sulfate, and the sulfurization of organic matter by aqueous sulfide.

Saturation for various chemical precipitates may also be reached through the accumulation of diagenetic reaction products within sedimentary pore waters. We include precipitation reactions for calcium carbonate (calcite, $CaCO_3$), manganese carbonate (rhodochrosite, $MnCO_3$), iron carbonate (siderite, $FeCO_3$), iron monosulfide (amorphous, FeS), and iron disulfide (pyrite, FeS_2) in I-CANDI and list them in Table IV.5. We do not include a precipitation reaction for manganese sulfide (rambergite, MnS) due to its orders-of-magnitude lower solubility product than that of FeS [322]. Precipitation rate laws for $CaCO_3$, $MnCO_3$, $FeCO_3$, and FeS are each dependent on saturation state:

$$R_{ppt} = k_{ppt} * (\Omega - 1)^m * \frac{1}{1 + 10^6 * e^{-k_{log} * (\Omega - 1)}} \text{ where } \Omega = \frac{\text{Reaction Quotient}}{K_{sp_{ppt}}}$$

Here, R_{ppt} is the precipitation rate, k_{ppt} is the rate constant for the precipitation reaction, $K_{sp_{ppt}}$ is the solubility product for the precipitate, and k_{log} is the logistic growth rate. The logistic term smooths the precipitation rate increase during the transition from $\Omega < 1$ to $\Omega > 1$; this substantially improves computational speed with a minimal impact on model results. We assume that $m = 1$, i.e., all precipitation rates scale linearly with $(\Omega - 1)$. Solubility products and full Ω formulas for $CaCO_3$, $MnCO_3$, $FeCO_3$, and FeS are listed in Table IV.9. The solubility product for calcite is calculated as a function of temperature and pressure using the data of Mucci (1983) [233]. Acid dissociation constants are used to speciate dissolved inorganic carbon (DIC) and are calculated as a function of temperature, pressure, and salinity using CO2SYS [346]. The first acid dissociation constant for H_2S is calculated as a function of temperature and pressure following Millero et al. (1988) [229]. The second acid dissociation constant for H_2S is highly uncertain [285] and is ignored in I-CANDI. Included acid dissociation constants are summarized in Table IV.10. Rate constants for all reactions are listed in Table IV.11.

In addition, I-CANDI allows pyrite to be formed through several competing mechanisms [217] (Table IV.5). The first mechanism involves the oxidation of FeS by H_2S to produce FeS_2 and H_2, whereas the second mechanism instead oxidizes FeS with S^0 to produce FeS_2. We view these mechanisms as computationally necessary simplifications of the more complicated spectrum of pyrite

formation mechanisms that have been studied in the literature (especially those involving polysulfides) [54, 285]. As a computationally efficient alternative to $FeCO_3$ dissolution and sulfide precipitation, we also allow $FeCO_3$ and HS^- to directly react to form FeS_2, H_2, and CO_3^{2-}. We test the sensitivity of the model results to each of these pyrite formation mechanisms later in the chapter.

Organic matter sulfurization [184, 274, 356] serves as an additional solid phase sink for aqueous H_2S in I-CANDI. In the current formulation of I-CANDI, it is included primarily to prevent H_2S from accumulating in pore waters in instances in which data observations do not indicate H_2S accumulation. Laboratory experiments have found a C:S molar ratio of approximately 30-50 for lipids [108] and as low as $\sim$15 for carbohydrates [87]. We assume a carbohydrate-like C:S ratio of 15:1 for the process of organic matter sulfurization in I-CANDI. We also limit sulfurization here to the otherwise unreactive organic matter fraction (f_{k_4}). This limitation prevents competition between organic matter degradation and sulfurization for organic matter consumption, thereby reducing computational time. Although unrealistic, these simplifications may easily be modified in future applications of I-CANDI that are more focused on the dynamics of organic matter sulfurization.

Many of the reactions included within I-CANDI involve transfer of atoms between solid phases and dissolved phases. Given that the solid phase volume $1-\phi$ and the dissolved phase volume ϕ are generally not equal, such transfers require conversion factors to ensure that the total number of moles subtracted from one phase equals the total number of moles added to the other. For dissolved phases that react with solid phases or react to form solid phases, we multiply the dissolved phase reaction term(s) by $\frac{(1-\phi)}{\phi}$ to account for the volume difference.

IV.3.3 Diagenetic Equations & Boundary Conditions

I-CANDI emulates the original CANDI model [40] in the differential equations and boundary conditions it uses to represent sedimentary diagenesis. For each solute, the general diagenetic equation (with derivative terms expanded) solved at each depth z is as follows [41]:

$$\left.\frac{dC}{dt}\right|_z = D_{s_z}\left.\frac{dC^2}{d^2z}\right|_z - \left(\nu_z - \left.\frac{D_{s_z}}{\phi_z}\frac{d\phi}{dz}\right|_z - \left.\frac{dD_s}{dz}\right|_z\right)\left.\frac{dC}{dz}\right|_z + \gamma_z(C_0-C) + \sum R|_z \tag{IV.4}$$

Table IV.9: Solubility products and saturation state formulas used in I-CANDI.

Symbol	Description	Value / Formula	Units	Reference
$K_{sp,MnCO_3}$	Solubility product for $MnCO_3$	$3.16 * 10^{-9}$	$\frac{mol^2}{L^2}$	[65]
$K_{sp,FeCO_3}$	Solubility product for $FeCO_3$	$3.98 * 10^{-9}$	$\frac{mol^2}{L^2}$	[65]
$K_{sp,CaCO_3}$	Solubility product for calcite	variable	$\frac{mol^2}{L^2}$	[233]
$K_{sp,FeS}$	Solubility product for FeS	$6.31 * 10^{-3}$	$\frac{mol}{L}$	[362]
$MnCO_3$	Saturation state for $MnCO_3$	$MnCO_3 = \frac{[Mn^{2+}][CO_3^{2-}]}{K_{sp,MnCO_3}}$	unitless	
$FeCO_3$	Saturation state for $FeCO_3$	$FeCO_3 = \frac{[Fe^{2+}][CO_3^{2-}]}{K_{sp,FeCO_3}}$	unitless	
$CaCO_3$	Saturation state for calcite	$CaCO_3 = \frac{[Ca^{2+}][CO_3^{2-}]}{K_{sp,CaCO_3}}$	unitless	
FeS	Saturation state for FeS	$FeS = \frac{[Fe^{2+}][HS^-]}{[H^+]K_{sp,FeS}}$	unitless	[362]

Table IV.10: Acid dissociation constants included in I-CANDI.

Symbol	Description	Value	Units	Reference
$K_{a_1,DIC}$	First acid dissociation constant for DIC system	variable	unitless	[228]
$K_{a_2,DIC}$	Second acid dissociation constant for DIC system	variable	unitless	[228]
K_{a_1,H_2S}	First acid dissociation constant for aqueous sulfide system	variable	unitless	[229]

where C is the concentration at depth z, and all other variables are as previously defined. Subscripted z's denote "at depth z". For solids, this equation becomes [41]:

$$\left.\frac{dC}{dt}\right|_z = D_{b_z}\left.\frac{dC^2}{d^2z}\right|_z - \left(\omega_z - \frac{D_{b_z}}{(1-\phi_z)}\left.\frac{d(1-\phi_z)}{dz}\right|_z - \left.\frac{dD_b}{dz}\right|_z\right)\left.\frac{dC}{dz}\right|_z + \sum R|_z \tag{IV.5}$$

I-CANDI implements central differences for all derivatives except the first order spatial derivative for solid phases; a backwards difference is implemented for this derivative. With uneven grid spacing, the central difference formula for the first concentration derivative is [41]:

$$\left.\frac{\partial C}{\partial z}\right|_{z_l} \approx -\frac{\Delta z_{l+1}}{\Delta z_l(\Delta z_l + \Delta z_{l+1})}C_{l-1} + \frac{\Delta z_{l+1} - \Delta z_l}{\Delta z_{l+1}\Delta z_l}C_l + \frac{\Delta z_l}{\Delta z_{l+1}(\Delta z_l + \Delta z_{l+1})}C_{l+1} \tag{IV.6}$$

Table IV.11: Rate constants for all reactions in I-CANDI.

Symbol	Description	Value	Units	Reference
k_1	Rate constant for fast organic matter degradation	3.17×10^{-13}	s^{-1}	
k_2	Rate constant for intermediate organic matter degradation	3.17×10^{-14}	s^{-1}	
k_3	Rate constant for slow organic matter degradation	3.17×10^{-15}	s^{-1}	
k_4	Rate constant for unreactive organic matter degradation	0	s^{-1}	
k_{NH_4Ox}	Rate constant for ammonium oxidation by O_2	2.31×10^{-4}	$\frac{m^3}{mol^{-1} s^{-1}}$	[362]
k_{MnOx}	Rate constant for manganese oxidation by O_2	1.59×10^{-4}	$\frac{m^3}{mol^{-1} s^{-1}}$	[362]
k_{FeOx}	Rate constant for iron oxidation by O_2	3.40×10^{-5}	$\frac{m^3}{mol^{-1} s^{-1}}$	[362]
k_{FeMn}	Rate constant for iron oxidation by MnO_2	9.51×10^{-5}	$\frac{m^3}{mol^{-1} s^{-1}}$	[362]
k_{H_2SOx}	Rate constant for aqueous sulfide oxidation by O_2	5.07×10^{-6}	$\frac{m^3}{mol^{-1} s^{-1}}$	[362]
k_{MnO_2TS}	Rate constant for aqueous sulfide oxidation by O_2	6.34×10^{-10}	$\frac{m^3}{mol^{-1} s^{-1}}$	[362]
$k_{Fe(III)TS}$	Rate constant for aqueous sulfide oxidation by $Fe(III)_{solid}$	1.16×10^{-12}	$\frac{m^3}{mol^{-1} s^{-1}}$	[362]
k_{CH_4Ox}	Rate constant for methane oxidation by O_2	3.17×10^{-1}	$\frac{m^3}{mol^{-1} s^{-1}}$	[362]
$k_{CH_4SO_4}$	Rate constant for methane oxidation by SO_4^{2-} (AOM)	3.17×10^{-7}	$\frac{m^3}{mol^{-1} s^{-1}}$	[362]
k_{FeSOx}	Rate constant for iron monosulfide oxidation by O_2	9.51×10^{-6}	$\frac{m^3}{mol^{-1} s^{-1}}$	[362]
k_{FeSMn}	Rate constant for iron monosulfide oxidation by MnO_2	0	$\frac{m^3}{mol^{-1} s^{-1}}$	[362]
$k_{FeSFe(III)}$	Rate constant for iron monosulfide oxidation by $Fe(III)_{solid}$	0	$\frac{m^3}{mol^{-1} s^{-1}}$	[362]
$k_{OM_{sulf}}$	Rate constant for organic matter sulfurization	1×10^{-13}	$\frac{m^3}{mol^{-1} s^{-1}}$	
k_{MnCO_3ppt}	Rate constant for $MnCO_3$ precipitation	8.56×10^{-6}	$\frac{m^3}{mol^{-1} s^{-1}}$	[65]
k_{FeCO_3ppt}	Rate constant for $FeCO_3$ precipitation	3.85×10^{-13}	$\frac{m^3}{mol^{-1} s^{-1}}$	
k_{CaCO_3ppt}	Rate constant for $CaCO_3$ precipitation	3.85×10^{-5}	$\frac{m^3}{mol^{-1} s^{-1}}$	
k_{FeSppt}	Rate constant for FeS precipitation	1×10^{-7}	$\frac{m^3}{mol^{-1} s^{-1}}$	
$k_{FeS_2S^0ppt}$	Rate constant for FeS_2 precipitation via FeS + S_0	1.16×10^{-5}	$\frac{m^3}{mol^{-1} s^{-1}}$	
$k_{FeS_2H_2Sppt}$	Rate constant for FeS_2 precipitation via FeS + H_2S	1.16×10^{-5}	$\frac{m^3}{mol^{-1} s^{-1}}$	
$k_{FeS_2FeCO_3}$	Rate constant for FeS_2 precipitation via $FeCO_3$ + $_2HS^-$	1×10^{-5}	$\frac{m^3}{mol^{-1} s^{-1}}$	

where z_l is the depth at point l, Δz_l is the difference in z between point l and the preceding point $l-1$ (i.e., $z_l - z_{l-1}$), and Δz_{l+1} is the difference in z between the subsequent point $l+1$ and point l (i.e., $z_{l+1} - z_l$). C_{l-1}, C_l, and C_{l+1} are the corresponding concentrations at points $l-1$, l, and $l+1$, respectively. The backwards difference formula used for the first concentration derivative for solids is [41]:

$$\left.\frac{\partial C}{\partial z}\right|_{z_l} \approx \frac{C_l - C_{l-1}}{\Delta z_l} \tag{IV.7}$$

and central difference formula for the second concentration derivative is [41]:

$$\left.\frac{\partial^2 C}{\partial z^2}\right|_{z_l} \approx \frac{2}{\Delta z_l(\Delta z_l + \Delta z_{l+1})} C_{l-1} \; - \; \frac{2}{\Delta z_{l+1}\Delta z_l} C_l \; + \; \frac{2}{\Delta z_{l+1}(\Delta z_l + \Delta z_{l+1})} C_{l+1} \tag{IV.8}$$

Substituting equations IV.6 and IV.8 into the general diagenetic equation for solutes (equation IV.4), we get:

$$\begin{aligned}\left.\frac{dC}{dt}\right|_{z_l} =& D_{s_{z_l}} \Bigg(\frac{2}{\Delta z_l(\Delta z_l + \Delta z_{l+1})} C_{l-1} \; - \; \frac{2}{\Delta z_{l+1}\Delta z_l} C_l \; + \\ & \frac{2}{\Delta z_{l+1}(\Delta z_l + \Delta z_{l+1})} C_{l+1} \Bigg) \; - \; \left(\nu_z \; - \; \frac{D_{s_{z_l}}}{\phi_{z_l}} \left.\frac{d\phi}{dz}\right|_{z_l} \; - \; \left.\frac{dD_s}{dz}\right|_{z_l} \right) \\ & \Bigg(\; - \frac{\Delta z_{l+1}}{\Delta z_l(\Delta z_l + \Delta z_{l+1})} C_{l-1} \; + \; \frac{\Delta z_{l+1} - \Delta z_l}{\Delta z_{l+1}\Delta z_l} C_l \\ & + \; \frac{\Delta z_l}{\Delta z_{l+1}(\Delta z_l + \Delta z_{l+1})} C_{l+1} \Bigg) + \; \gamma(z_l)(C_0 - C) \; + \; \sum R|_{z_l}\end{aligned} \tag{IV.9}$$

Similarly, substituting equations IV.7 and IV.8 into the general diagenetic equation for solids (equation IV.5) yields:

$$\begin{aligned}\left.\frac{dC}{dt}\right|_{z_l} =& D_{b_{z_l}} \Bigg(\frac{2}{\Delta z_l(\Delta z_l + \Delta z_{l+1})} C_{l-1} \; - \; \frac{2}{\Delta z_{l+1}\Delta z_l} C_l \; + \\ & \frac{2}{\Delta z_{l+1}(\Delta z_l + \Delta z_{l+1})} C_{l+1} \Bigg) \\ & - \; \left(\omega_{z_l} \; - \; \frac{D_{b_{z_l}}}{(1-\phi_{z_l})} \left.\frac{d(1-\phi_{z_l})}{dz}\right|_{z_l} \; - \; \left.\frac{dD_b}{dz}\right|_{z_l} \right) \left(\frac{C_l - C_{l-1}}{\Delta z_l} \right) \\ & + \; \sum R|_{z_l}\end{aligned} \tag{IV.10}$$

Boundary conditions must be imposed to account for the non-existent C_{l-1} at the top boundary of the z domain and C_{l+1} at the bottom of the domain. We use a constant concentration (Dirichlet) boundary condition at the top boundary (z_o) for solutes:

$$\frac{dC}{dt} = 0 \qquad \text{or} \qquad C_{z=0} = C_0 \tag{IV.11}$$

where C_0 is the initial concentration at the top boundary. For solids, we impose a flux boundary condition at the top of the domain by calculating a non-existent C_{l-1} value based on an ascribed flux [40, 41], i.e.:

$$C_{-1} = C_1 + \frac{2\Delta z_0}{D_b(0)}\left(\frac{F_{top}}{(1-\phi_0)} - \omega_0 C_0 \right) \tag{IV.12}$$

where F_{top} is the depositional flux of the solid species of interest. This C_{-1} value is substituted into equation IV.5 to calculate $\frac{dC}{dt}$ at $z = 0$. At the bottom of the domain, we ascribe a constant gradient boundary condition (i.e., $\frac{d^2C}{dz^2} = 0$) by default and use backwards differencing to estimate the first derivative for both solutes and solids. We assume $\Delta z_{end} = \Delta z_{end-1}$ in this instance. For solutes:

$$\left.\frac{dC}{dt}\right|_{z_{end}} = -\left(\nu_{z_{end}} - \frac{D_{s_{z_{end}}}}{\phi_{z_{end}}}\left.\frac{d\phi}{dz}\right|_{z_{end}} - \left.\frac{dD_s}{dz}\right|_{z_{end}} \right)\left(\frac{C_{z_{end}} - C_{z_{end-1}}}{\Delta z_{end}} \right) + \gamma(z_{end})(C_0 - C_{z_{end}}) + \sum R|_{z_{end}} \tag{IV.13}$$

and for solids:

$$\left.\frac{dC}{dt}\right|_{z_{end}} = -\left(\omega_{z_{end}} - \frac{D_{b_{z_{end}}}}{(1-\phi_{z_{end}})}\left.\frac{d(1-\phi_{z_{end}})}{dz}\right|_{z_{end}} - \left.\frac{dD_b}{dz}\right|_{z_{end}} \right) * \left(\frac{C_{z_{end}} - C_{z_{end-1}}}{\Delta z_{end}} \right) + \sum R|_{z_{end}} \tag{IV.14}$$

If desired, a flux bottom boundary condition may instead be imposed to simulate a source of solute below the bottom of the z domain. In this case, a value for $C_{z_{end+1}}$ is calculated as follows [41]:

$$C_{z_{end+1}} = C_{z_{end-1}} - \frac{2\Delta z_{end}}{D_{s_{z_{end}}}}\left(\frac{F_{bottom}}{\phi_{z_{end}}} - \nu_{z_{end}} C_{z_{end}} \right) \tag{IV.15}$$

where F_{bottom} is the ascribed bottom flux. This $C_{z_{end+1}}$ value is then substituted into equation IV.4 to calculate $\frac{dC}{dt}$ at the bottom boundary.

IV.3.4 Numerical Methods

I-CANDI utilizes a scheme similar to the Method of Lines in the original CANDI model [40] to set up its differential equations, but allows for variable time steps in evaluating changes in concentration with time. A general diagenetic equation for each species is constructed at each depth to yield a system of (# of species) x (# of discrete depths z) differential equations. MATLAB®'s built in stiff ode solver $\mathrm{ode15s}$ [302] is used to step forward in time and evaluate the system of equations at each time step. To improve computational speed, MATLAB®'s Symbolic Math Toolbox™ is used to calculate the sparsity pattern of the Jacobian for the system of differential equations and supply the sparsity pattern as an optional input to the solver. Model concentrations were calculated in units of $\frac{\mathrm{mol}}{\mathrm{m}^3}$. We specified an absolute error tolerance of $1\mathrm{e}\text{-}8$ and a relative error tolerance of $1\mathrm{e}\text{-}3$ as additional solver inputs.

For steady state model simulations, we calculate the amount of time necessary for a sediment parcel to advect from the top boundary to the bottom boundary based on the ascribed sedimentation rate at the sediment-water interface. The end time is then set to 10 times this length of time, i.e.:

$$t_{end} = \frac{(\text{length of } z \text{ domain})}{\omega_{end}} * 10 \tag{IV.16}$$

I-CANDI outputs model results at user-defined time points and saves all results to a MATLAB® structure. Steady-state and mass conservation are confirmed by calculating the definite integral of the general diagenetic equation for each species from the top boundary to the bottom boundary. Typical model runs conserve > 99.9% of C, Fe, and S on an atom basis and are similarly robust in conserving individual species.

IV.4 Results

IV.4.1 Numerical model validation

To confirm proper functioning of the model and mass balance in the absence of reactive fluxes, we ran several tests. First, we initiated the model with zero input fluxes for organic matter, iron, and manganese, and ran the model without any reactive fluxes. Bottom water dissolved phase concentrations were set to 1 mM. The resulting model output shows concentration profiles that are invariant with depth for all constituents, as expected in the absence of reactive fluxes (Figure

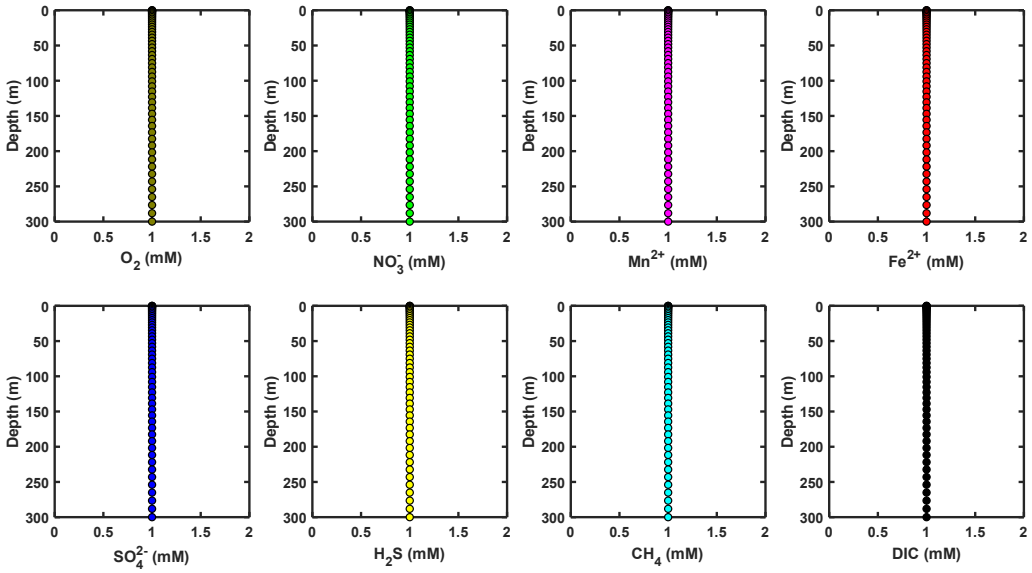

Figure IV.2: Concentration profiles for an assortment of dissolved phases in I-CANDI without any solid inputs or reactive fluxes. As expected, concentrations are invariant with depth at values equal to the bottom water concentration.

IV.2). Additional model runs with non-zero reactive fluxes and different values for dz demonstrated an insensitivity of the model results to the depth discretization so long as the depth resolution is sufficiently high that no constituents are consumed to zero concentration within the first depth box.

IV.4.2 Model sensitivity

After confirming proper model function, we performed sensitivity tests to determine the response of the model output to changing model parameters. Initial conditions and parameters common across all sensitivity tests are listed in Table IV.12. We follow Rabouille and Gaillard (1991) and impose an exponential function to describe the decrease in porosity with depth:

$$\phi(z) = (\phi_0 - \phi_{end})e^{-\frac{z}{\zeta}} + \phi_{end} \tag{IV.17}$$

where ϕ_0 is the initial sediment porosity at $z = 0$, ζ is the depth constant for the porosity decrease, and z is depth in the sediment. To appropriately resolve AOM, all model sensitivity experiments were run with an even depth grid instead of an uneven grid, though uneven grid runs can also successfully resolve AOM with finer discretization of the depth domain and longer computational

times. The following discussion focuses upon (1) the percentage of total organic matter flux degraded using a given pathway, and (2) the concentration and $\delta^{34}S$ of the pyrite flux out the bottom of the model domain. In our accounting, sulfate reduction refers solely to organoclastic sulfate reduction and does not include AOM; sulfate reduced through AOM is attributed to the methanogenesis pathway. Wijsman et al. (2002) [362] previously found a rapid, threshold-like trade-off between iron reduction and sulfate reduction in remineralizing organic matter as organic matter flux increases. Our goal in maintaining the stated foci was to determine whether such a trade-off also exists in I-CANDI and, if so, whether the trade-off is similarly manifest in the $\delta^{34}S$ of buried pyrite. We include mostly summary and comparison figures in the results below; additional figures depicting more detailed results from each model experiment may be found in Appendix B.

IV.4.2.1 Model sensitivity to organic carbon and Fe fluxes

We first tested the sensitivity of the steady-state model results to the rain rate of particulate organic carbon (RRPOC) at a constant Fe(III) rain rate of 1.375 $\frac{\mu mol}{m^2\,day}$ (Figure IV.3). Varying RRPOC from near-zero values to values up to 0.5 $\frac{mmol}{m^2\,day}$ (i.e., an initial sedimentary POC abundance range from < 0.01 to > 10 wt%) results in a progressive transition from oxygen-dominated organic matter degradation to methanogenesis-dominated degradation (Figure IV.3A,C). Oxic degradation constitutes over 90% of the total organic matter degradation so long as RRPOC remains below 0.0015 $\frac{mmol}{m^2\,day}$ ($\sim$0.035 wt%). As the POC flux increases, denitrification begins to consume available nitrogen and is the dominant mode of degradation for a very narrow range of RRPOC ($\sim$0.025 to 0.03 $\frac{mmol}{m^2\,day}$, or $\sim$0.06 to 0.075 wt%). Further increases in RRPOC result in transition to iron and sulfate reduction as the dominant degradation pathways. The manganese rain rate is sufficiently low to render manganese reduction nearly negligible ($< 0.7\%$ of total degradation). In addition, the imposed Fe(III) rain rate is small enough that little inhibition of the sulfate reduction pathway occurs. Iron reduction briefly accounts for over 10% of all organic matter degradation, and Fe^{2+} becomes high enough at these RRPOCs to support substantial reoxidation by O_2. However, the diffusive supply of sulfate from seawater allows sulfate reduction to account for a greater proportion of the total degradation at all tested organic matter fluxes for this Fe(III) rain rate.

Table IV.12: Conditions common across all I-CANDI sensitivity tests (unless otherwise noted in the text). Symbols are as defined and described earlier in the text.

Parameter	Value	Units
ω_{end}	1.0	$\frac{\text{cm}}{\text{kyr}}$
ϕ_0	0.8	unitless
ϕ_{end}	0.4	unitless
ζ	250	m
Water depth	3000	m
Bottom water temperature	2.0	°C
Geothermal gradient	30	$\frac{\text{°C}}{\text{km}}$
dz	1	m
z_{end}	50	m
Bottom water $[O_2]$	150	μM
Bottom water $[NO_3^-]$	40	μM
Bottom water $[SO_4^{2-}]$	28.2	mM
Mn^{2+} rain rate	0.25	$\frac{\mu\text{mol}}{\text{m}^2\text{day}}$
Fe^{3+} rain rate	1.375	$\frac{\mu\text{mol}}{\text{m}^2\text{day}}$
Bottom water SO_4^{2-} $\delta^{34}S$	+21	‰

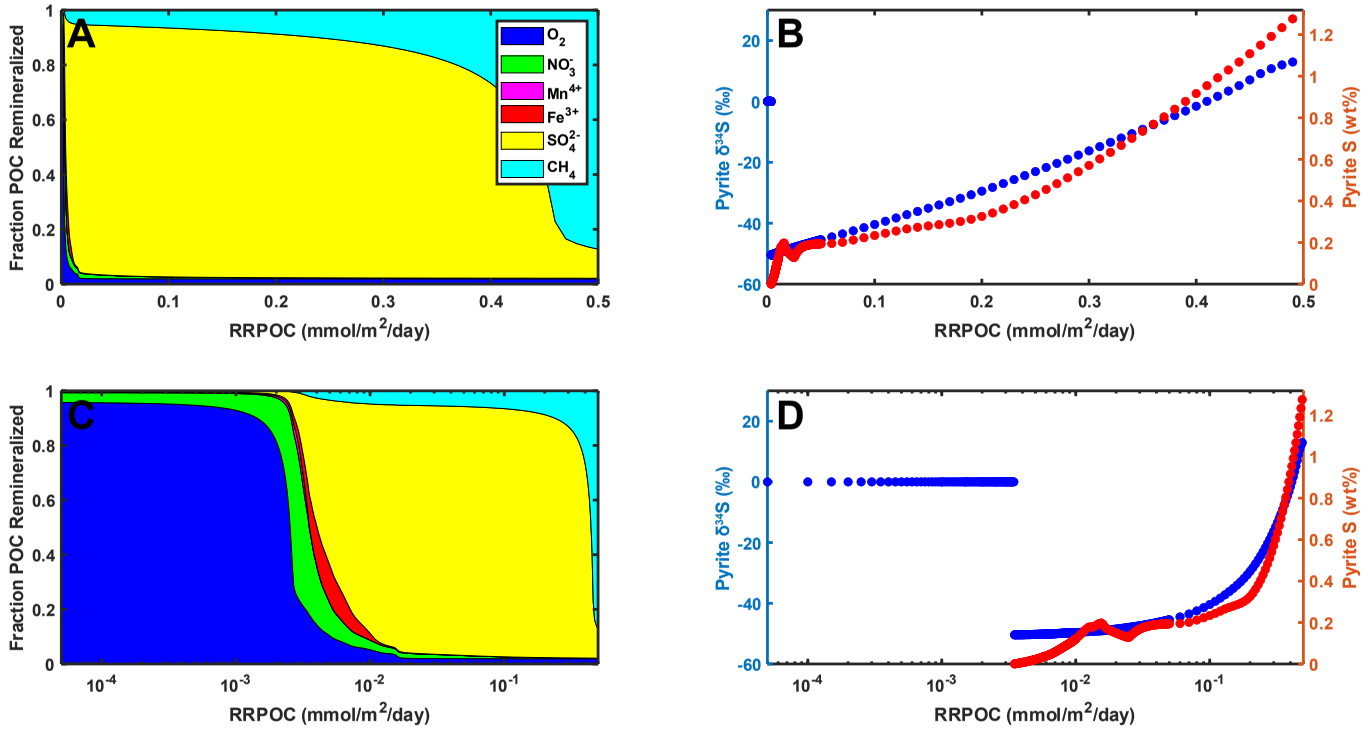

Figure IV.3: Initial model experiment. (A) Area plot of the fractional contribution of different electron acceptors to organic carbon degradation at different initial sedimentary POC concentrations. Shaded areas represent the fractional contributions of oxic respiration (dark blue), denitrification (green), manganese reduction (magenta), iron reduction (red), sulfate reduction (yellow), and methanogenesis (cyan) to overall POC degradation. (B) Plot of pyrite δ^{34}S (left axis; blue circles) and pyrite sulfur abundance (right axis; red circles) for buried pyrite exiting the bottom of the model domain as a funtion of POC rain rate. (C) and (D) are replicate plots of (A) and (B), respectively, with the initial POC plotted on a log scale instead of a linear scale. Note in this and all following figures that 0‰ is the default δ^{34}S value for pyrite abundances that are below the ascribed absolute error tolerance for the model (1e-8 $\frac{\text{mol}}{\text{m}^3}$).

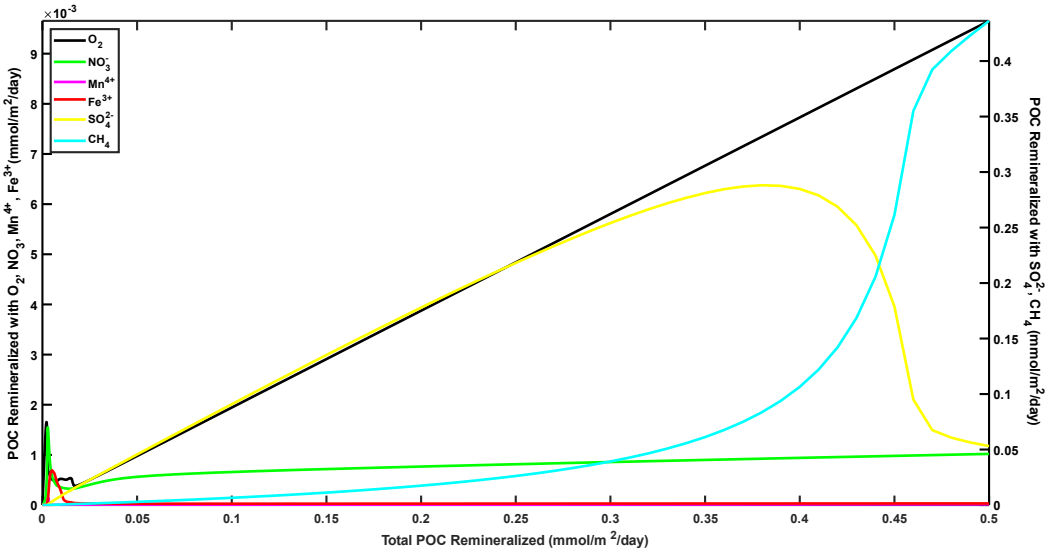

Figure IV.4: Line plot of the absolute amount of POC degraded using different electron acceptors plotted against the total amount of POC degraded. Lines for oxic respiration (black), denitrification (green), mangenese reduction (magenta), and iron reduction (red) are plotted on the left axis, whereas those for sulfate reduction (yellow) and methanogenesis (cyan) are plotted on the right axis. Note the rapid switch from a sulfate reduction dominance to a methanogenesis dominance.

Sulfate reduction is dominant enough to titrate all dissolved Fe^{2+} out of pore waters once RRPOC reaches $\sim$0.013 $\frac{\text{mmol}}{\text{m}^2\,\text{day}}$ ($\sim$0.32 wt%). At this point, the iron reduction contribution decreases below 0.5% of the total amount of POC degraded. Sulfate reduction remains the dominant pathway for POC degradation until RRPOC increases by well over an order of magnitude. Only once RRPOC exceeds 0.35 $\frac{\text{mmol}}{\text{m}^2\,\text{day}}$ ($\sim$8.7 wt% POC) does sulfate reduction account for less than $\sim$80% of total degradation. At this point, sulfate reduction rapidly declines to $<$ 20% of total degradation at RRPOC = 0.46 $\frac{\text{mmol}}{\text{m}^2\,\text{day}}$ ($\sim$11.4 wt% POC), and methanogenesis becomes the dominant mode of degradation. The rapid transition from sulfate reduction dominance to methanogenesis dominance is also clearly seen if the data are plotted in terms of the absolute amount of POC degraded (Figure IV.4). However, we note that sulfate remains the ultimate sink for electrons initially transferred to methane due to the consumption of methane through anaerobic oxidation with sulfate. The δ^{34}S of buried pyrite also changes as RRPOC increases. The pyrite exiting the bottom of the model has an initial δ^{34}S of $\sim$-50‰ when sulfate reduction begins. A rapid increase in pyrite abundance occurs as the POC abundance at the sediment-water interface

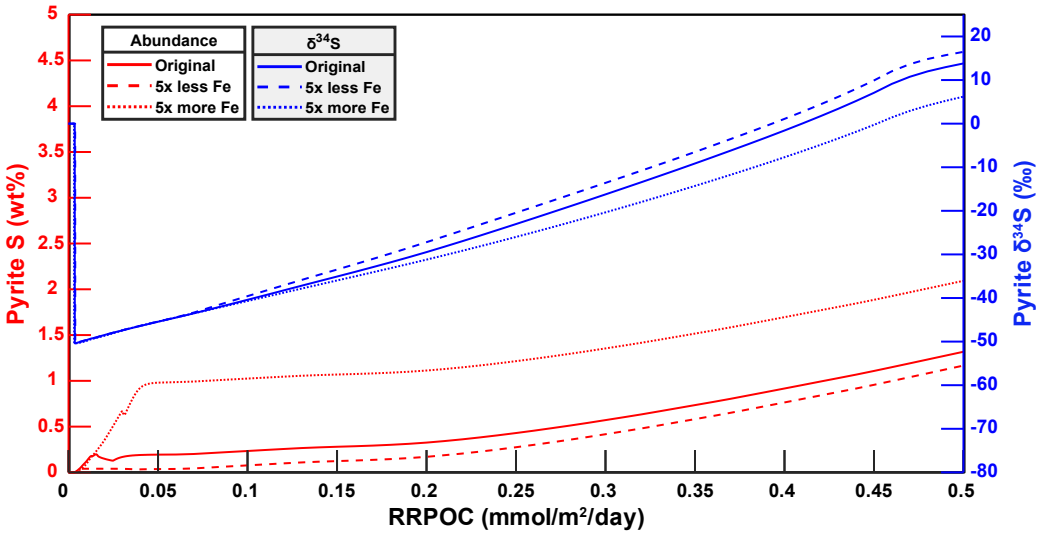

Figure IV.5: Plot of pyrite sulfur abundance (left axis, red lines) and $\delta^{34}S$ (right axis; blue lines) for buried pyrite exiting the bottom of the model domain as a function of POC rain rate for model experiments in which the Fe(III) rain rate was varied. Line style denotes model experiment.

increases from ∼0.1 to ∼0.3 wt%; this increase corresponds to the titration of aqueous Fe^{2+} by H_2S. Pyrite $\delta^{34}S$ remains low (< -49‰) during this increase due to H_2S limitation of pyrite formation. Only with further enhancements in RRPOC does pyrite formation become iron limited; pyrite $\delta^{34}S$ values begin to linearly increase with RRPOC at this point. Still, pyrite remains highly depleted in ^{34}S ($\delta^{34}S \leq -40$ ‰) until RRPOC exceeds 0.35 $\frac{\text{mmol}}{\text{m}^2\,\text{day}}$ (∼2.5 wt% POC). Additional RRPOC increases push the system toward methanogenesis-dominated degradation. The rate of pyrite $\delta^{34}S$ increase slows once methanogenesis becomes dominant and pyrite $\delta^{34}S$ exceeds ∼+10‰.

Varying the solid phase Fe^{3+} rain rate (RRFe) also significantly impacts the model results, especially in terms of buried pyrite abundance (Figure IV.5; see also Figures IV.3, B.1, and B.2). If all other model parameters are kept constant, decreasing RRFe by a factor of five reduces the final pyrite abundance by ∼11% at the highest RRPOC. This reduction is amplified to a factor of two or more at lower RRPOCs. The $\delta^{34}S$ of the buried pyrite is slightly elevated at a given RRPOC when RRFe is reduced; modeled $\delta^{34}S$ is 0.07‰ higher at the initiation of pyrite formation and 2.66‰ higher at the highest modeled RRPOC. Similar behavior occurs if RRFe is increased by a factor of five. Buried pyrite abundances in this case are substantially elevated at low organic matter rain rates

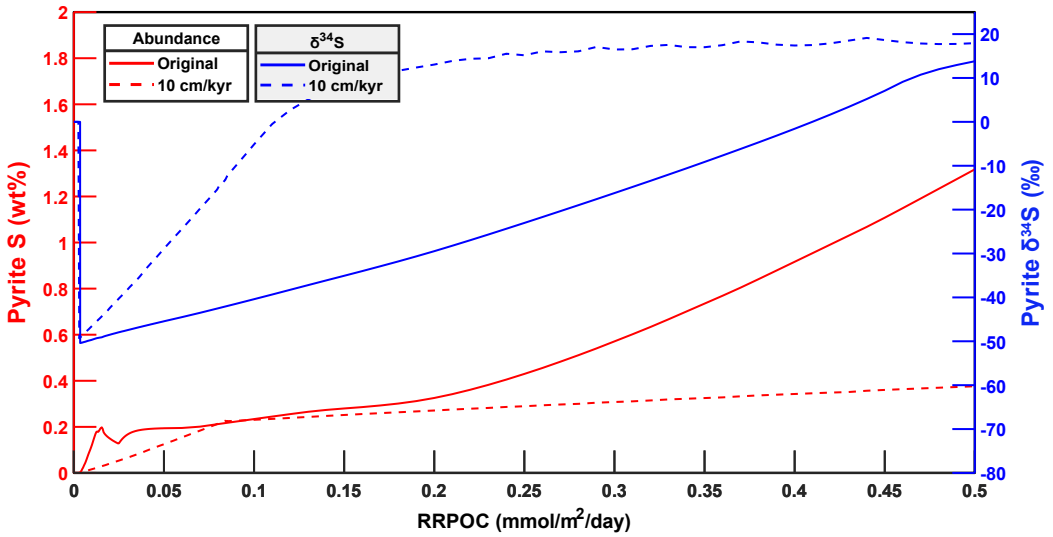

Figure IV.6: Plot of pyrite sulfur abundance (left axis, red lines) and $\delta^{34}S$ (right axis; blue lines) for buried pyrite exiting the bottom of the model domain as a function of POC rain rate for model experiments in which the sedimentation rate was varied by an order of magnitude. Line style denotes model experiment.

and are less elevated at high rain rates, with lower pyrite $\delta^{34}S$ at a given RRPOC.

IV.4.2.2 Model sensitivity to sedimentation rate

Sedimentation rates in the modern ocean vary over several orders of magnitude [219]. To examine the effect of sedimentation rate on our model results, we increase the model sedimentation rate and RRPOC by an order of magnitude while holding all other parameters constant. Results are depicted in Figures B.3 and B.4. The increase in the sedimentation rate from 1 $\frac{cm}{kyr}$ to 10 $\frac{cm}{kyr}$ reduces the POC rain rate at which the model transitions from sulfate reduction-dominated degradation to methanogenesis-dominated degradation. This transition occurs at a POC rain rate of $\sim$0.44 $\frac{mmol}{m^2 day}$ for a 1 $\frac{cm}{kyr}$ sedimentation rate and $\sim$0.11 $\frac{mmol}{m^2 day}$ for a 10 $\frac{cm}{kyr}$ rate. Simultaneously, the pyrite $\delta^{34}S$ at a given RRPOC is higher for the 10 $\frac{cm}{kyr}$ model runs, in some cases dramatically so (Figure IV.6). For example, the $\delta^{34}S$ of buried pyrite at an RRPOC of 0.1 $\frac{mmol}{m^2 day}$ is -3.7‰ at a sedimentation rate of 10 $\frac{cm}{kyr}$ versus -40.4‰ at the original sedimentation rate of 1 $\frac{cm}{kyr}$. This disparity lessens as RRPOC increases; at an RRPOC of 0.5 $\frac{mmol}{m^2 day}$, buried pyrite has a $\delta^{34}S$ of +18.7‰ in the 10 $\frac{cm}{kyr}$ model run and +13.8‰ in the original 1 $\frac{cm}{kyr}$ run. We discuss the reasons for this disparity later in this chapter.

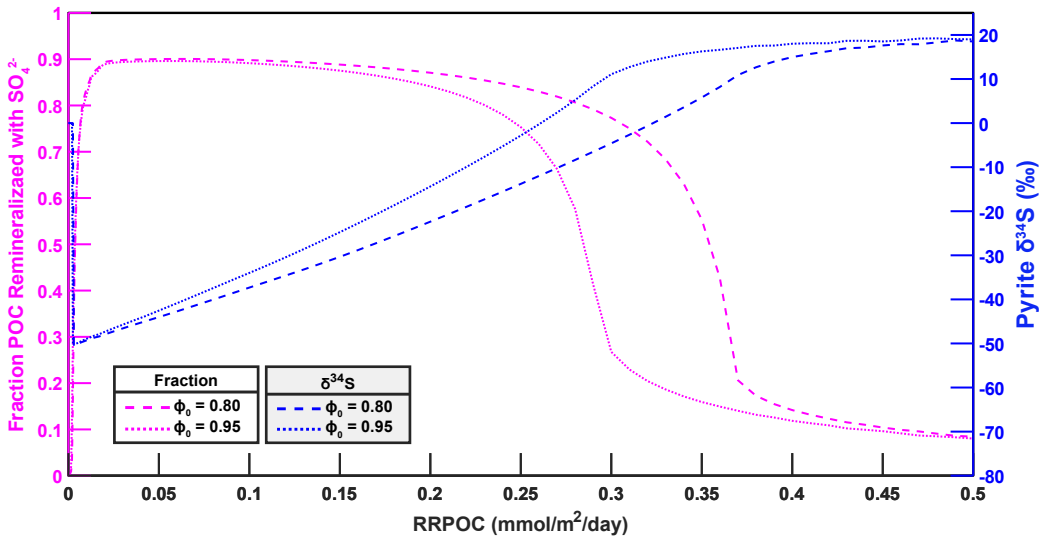

Figure IV.7: Plot of the fraction of POC degradation attributable to sulfate reduction (left axis, magenta lines) and the $\delta^{34}S$ (right axis; blue lines) of buried pyrite exiting the bottom of the model domain as a function of POC rain rate. Line style denotes model experiments with initial porosities of 0.80 and 0.95.

IV.4.2.3 Model sensitivity to porosity

In natural environments, the porosity of sediments may vary as a function of sedimentation rate and authigenic precipitation reactions [269]. To test the effect of porosity on the model results, we varied both the initial porosity ϕ_0 and the depth constant ζ for the decrease in porosity with depth. The final porosity (ϕ_{end}) was kept constant at a value of 0.6, slightly higher than the 0.4 value in the baseline model runs. We find that changes in the porosity profile have a substantial effect on the model results, particularly with respect to the fraction of POC degraded via a given pathway. For a ϕ_0 of 0.8, model runs fail to transition to methanogenesis-dominated degradation until RRPOC exceeds at least 0.5 $\frac{\text{mmol}}{\text{m}^2\,\text{day}}$, or initial POC ~17.2 wt% (Figure B.5). This is true regardless of the ζ used for the decrease in ϕ with depth (5 m, 50 m, or 250 m). In contrast, setting ϕ_{z_0} to 0.95 results in a transition to methanogenesis-dominated degradation well below RRPOC = 0.5 $\frac{\text{mmol}}{\text{m}^2\,\text{day}}$ for two of the three ζ's tested; the transition occurs at a RRPOC ~0.29 $\frac{\text{mmol}}{\text{m}^2\,\text{day}}$ (initial POC ~11.5 wt%) for ζ = 250 m (Figure B.6) and ~0.36 $\frac{\text{mmol}}{\text{m}^2\,\text{day}}$ (initial POC ~14.4 wt%) for ζ = 50 m (not shown). The $\delta^{34}S$ of buried pyrite shifts in these runs as well; at a given RRPOC, $\delta^{34}S$ is lower for model runs with a higher fraction of POC degradation attributable to sulfate reduction (Figure IV.7). We also note that the initial POC abundance at a given

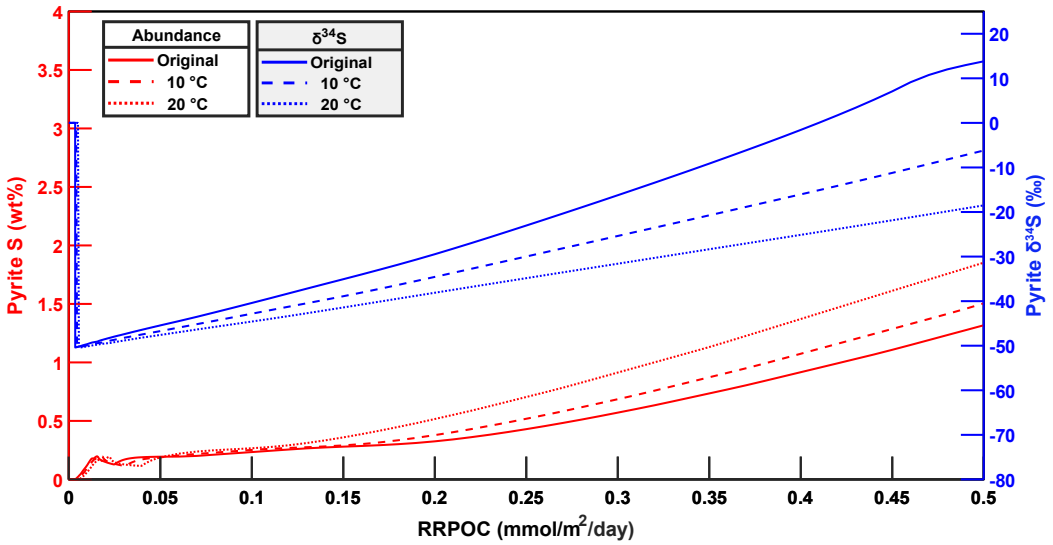

Figure IV.8: Plot of pyrite sulfur abundance (left axis, red lines) and $\delta^{34}S$ (right axis; blue lines) for buried pyrite exiting the bottom of the model domain as a function of POC rain rate for model experiments in which the bottom water temperature was varied. Line style denotes model experiment.

RRPOC value is higher in model runs with $\phi_{z_0} = 0.95$. We comment on this in more detail in the Discussion section.

IV.4.2.4 Model sensitivity to bottom water temperature

Temperature also can alter diagenetic profiles by modifying the diffusion coefficents of chemical species [41] and rates of microbial metabolism (e.g. [339]). We tested the effect of temperature on our model results by repeating the baseline set of model runs at bottom water temperatures of 10 °C and 20 °C (versus 2 °C for the original runs). Rates of POC degradation were kept constant, but diffusion coefficients were modified according to the equations listed in Table IV.2. Results for each of these runs are shown in Figures B.7 and B.8. Compared to the original set of runs (Figure IV.3), the runs at higher bottom water temperatures show a shift in the transition points between dominant modes of organic matter degradation toward higher RRPOCs. For example, the shift from oxic degradation dominance to nitrate reduction dominance occurs at RRPOC $\sim$0.0025 $\frac{\text{mmol}}{\text{m}^2\,\text{day}}$ in the original runs, $\sim$0.0032 $\frac{\text{mmol}}{\text{m}^2\,\text{day}}$ in the 10 °C runs, and $\sim$0.0045 $\frac{\text{mmol}}{\text{m}^2\,\text{day}}$ in the 20 °C runs. This shift also results in changes in the abundance and isotopic composition of buried pyrite: pyrite is less abundant and $\sim$1‰ lower in $\delta^{34}S$ at a given RRPOC when RRPOC is relatively low ($< \sim$0.05 $\frac{\text{mmol}}{\text{m}^2\,\text{day}}$) in the el-

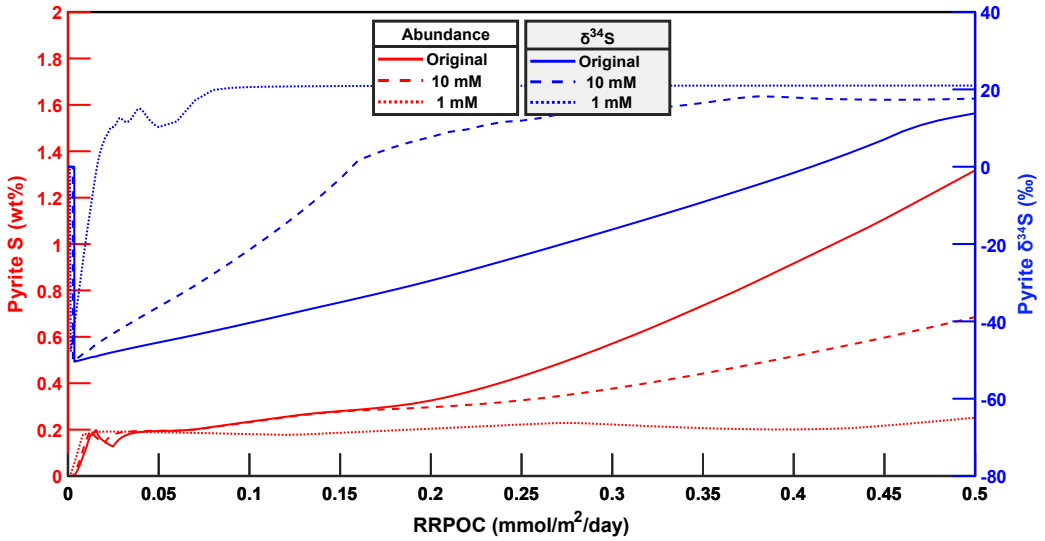

Figure IV.9: Plot of pyrite sulfur abundance (left axis, red lines) and $\delta^{34}S$ (right axis; blue lines) for buried pyrite exiting the bottom of the model domain as a function of POC rain rate for model experiments in which the bottom water sulfate concentration was varied. Line style denotes model experiment.

evated temperature runs (Figure IV.8). This depletion in ^{34}S becomes more pronounced as RRPOC increases; for example, the buried pyrite $\delta^{34}S$ is +13.8‰ at RRPOC $= 0.5 \frac{\text{mmol}}{\text{m}^2\,\text{day}}$ in the original runs and -18.5‰ at the same RRPOC in the 20 °C runs. The depletion remains despite an increase in the amount of pyrite buried at high RRPOC in the higher bottom water temperature runs relative to the original runs.

IV.4.2.5 Model sensitivity to bottom water concentrations

Fluid inclusions in halite evaporites suggest that seawater sulfate concentrations have varied by nearly an order of magnitude during the Phanerozoic [202]. To simulate the effect of changing seawater chemistry on our model results, we ran additional runs of I-CANDI at different bottom water sulfate and oxygen concentrations. Results from model runs with 10 mM $[SO_4{}^{2-}]$, 100 μM $[O_2]$ and 1 mM $[SO_4{}^{2-}]$, 10 μM $[O_2]$ are shown in Figures B.9 and B.10, respectively. As expected based on the sulfate concentration decrease, the transition between sulfate reduction-dominated POC degradation to methanogenesis-dominated degradation occurs at a lower RRPOC in the 10 mM $[SO_4{}^{2-}]$ runs compared to the original 28.2 mM runs ($\sim$0.15 versus $\sim$0.44 $\frac{\text{mmol}}{\text{m}^2\,\text{day}}$ POC). The $\delta^{34}S$ of buried pyrite is also higher at a given RRPOC and reaches a maximal asymptote more

quickly as RRPOC increases (Figure IV.9). However, the overall character of the results is similar. In contrast, the results from the 1 mM $[SO_4^{2-}]$ runs are substantially different. The $\delta^{34}S$ of buried pyrite is higher still at a given RRPOC and plateaus to a value nearly equal to the $\delta^{34}S$ of seawater sulfate ($\sim$+20.8‰ versus +21‰). But here, the pyrite $\delta^{34}S$ shows no "plateau" of highly negative values when it starts accumulating to abundances above I-CANDI's absolute error tolerance. Instead, the pyrite $\delta^{34}S$ starts to rise immediately and continues to do so as RRPOC increases. Methanogenesis also accounts for a larger proportion of POC degradation than sulfate reduction at all RRPOCs. This unusual character stems from a seawater $[SO_4^{2-}]$ that is lower than the imposed sulfate reduction inhibition constant (1.6 mM), preventing effective inhibition of methanogenesis. We delve more deeply into the sensitivity of the model results to the values of the half-saturation and inhibition constants below.

IV.4.2.6 Model sensitivity to half-saturation and inhibition constants

Half-saturation and inhibition constants have varied substantially in previous diagenetic models [40, 315, 362] and are even disparate among modern taxa that utilize the same metabolism to survive (e.g. [196]). Here, we examine the sensitivity of our model results to the imposed values for these constants. We reduced the magnitude of the half-saturation and inhibition constants in I-CANDI by one, two, and three orders of magnitude and plot the results of the one order of magnitude runs in Figure B.11. For a seawater chemistry identical to that used in the original runs, decreasing the half-saturation and inhibition constants by an order of magnitude increases the sharpness of the transitions between the zones of dominance for different degradation pathways. The change in constants also decreases the contribution of methanogenesis to POC degradation for RRPOCs that are too low to consume all sulfate. Methanogenesis accounts for over 1% of all POC degradation for initial POC concentrations above $\sim$0.075 wt% in the original runs, but only concentrations above $\sim$5.25 wt% yield a methanogenesis contribution $\geq$ 1% when the half-saturation and inhibition constants are reduced by an order of magnitude. Despite this difference, the abundance and $\delta^{34}S$ of buried pyrite are nearly identical between the two cases. At the highest tested RRPOC, the buried pyrite abundance is $\sim$0.8% higher and its $\delta^{34}S$ $\sim$0.15‰ lower in the reduced constants case than in the original runs.

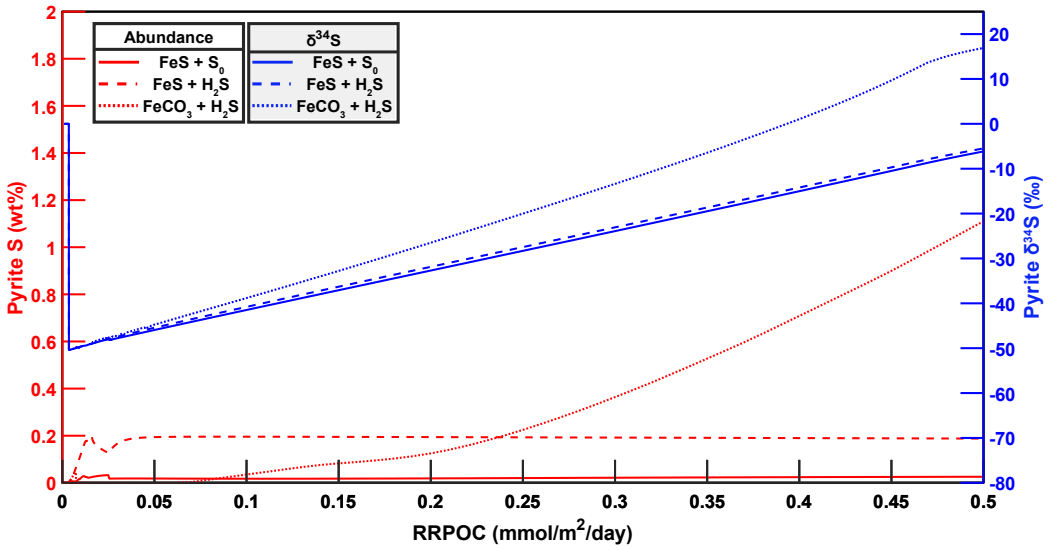

Figure IV.10: Plot of pyrite sulfur abundance (left axis, red lines) and $\delta^{34}S$ (right axis; blue lines) for buried pyrite exiting the bottom of the model domain as a function of POC rain rate for model experiments in which the pyrite formation mechanism was varied. Line style denotes model experiment.

IV.4.2.7 Model sensitivity to pyrite formation mechanism

As mentioned in the Methods section, I-CANDI includes three different pyrite formation mechanisms. To determine the influence of pyrite formation mechanism on the results, we ran I-CANDI three additional times, each including one of the pyrite formation mechanisms in isolation with the other two mechanisms set to zero (Figures B.12, B.13, and B.14). Model pyrite concentrations were lowest ($\sim$0.032 wt% S) when only FeS and S^0 could combine to form pyrite (Figure IV.10). Concentrations were nearly an order of magnitude higher ($\sim$0.197 wt% S) when the FeS+H_2S mechanism was active and $\sim$5 times higher still when the $FeCO_3$ + H_2S mechanism was active. Despite differences in concentration, the $\delta^{34}S$ of buried pyrite is essentially identical when either the FeS+S^0 or FeS+H_2S mechanisms are used. The buried pyrite in the $FeCO_3$+H_2S mechanism runs, in contrast, becomes substantially more enriched in ^{34}S at high (≥ 0.04 $\frac{\text{mmol}}{\text{m}^2\text{ day}}$) POC rain rates. The $\delta^{34}S$ of buried pyrite at the highest tested RRPOC is +16.9‰ in this case versus $\sim$-6‰ for each of the other two mechanisms.

IV.5 Discussion

IV.5.1 Controls upon POC degradation processes and $[SO_4^{2-}]$ *profiles*

We have examined the sensitivity of I-CANDI model outputs to a wide variety of variables. These sensitivity tests have shown that organic matter input, sedimentation rate, and porosity are the biggest influences on the dominant POC degradation pathways in I-CANDI. In turn, the dominant degradation pathways exert a fundamental control on the concentration profiles of SO_4^{2-} and other species with depth (e.g. Figure IV.11). Bottom water chemistry, bottom water temperature, Fe^{3+} rain rate, and half-saturation and inhibition constants are of secondary importance, though each may yield important changes if varied dramatically.

POC degradation in I-CANDI proceeds through a consistent sequence as RRPOC increases: oxic respiration, nitrate reduction, manganese reduction, iron reduction, sulfate reduction, and methanogenesis. Although many factors influence the absolute amount of POC degradation contributed by each of these pathways, our results make clear that sedimentation rate plays a critical role in forcing changes in the dominant degradation pathways for a given initial POC concentration. This finding is consistent with previous work [134, 141] demonstrating an association between sedimentation rate and "oxygen exposure time," or the amount of time that organic matter is exposed to oxic conditions in seawater and sediments. Just as lower sedimentation rate results in greater degradation of organic matter through oxic degradation in natural sediments [134, 141], lower sedimentation rates in I-CANDI result in a larger fraction of POC consumed through oxic degradation and through degradation with dissolved electron acceptors in general (e.g. NO_3^-, SO_4^{2-}). This association results from a greater ability of diffusion to supply dissolved constituents from seawater to sedimentary pore waters at lower sedimentation rates.

Compaction results in differences between dissolved and solid phase burial rates (e.g. [22]) and complicates comparisons of the relative influence of diffusion versus burial advection at different sites. However, we can conceptually think about these influences through a Peclét number (Pe):

$$Pe = \frac{\omega}{D_s L} \tag{IV.18}$$

Here, ω is the sedimentation rate at depths where compaction becomes negligible, D_s is the sedimentary diffusion coefficient for the dissolved constituent of

interest, and L is the characteristic length. This Peclét number ratios the rate of advective transport of pore water via burial (once compaction ceases) to the rate of diffusive transport of an aqueous species of interest. Given the presence of sulfate ion and other dissolved species within this advecting pore water and the ability of diffusion to supply fresh ions from seawater, we can usefully apply this ratio to understand how changes in transport processes might effect the δ^{34}S of sedimentary phases. As ω increases or D_s decreases, advective transport increases in its relative influence on the concentration profiles of the dissolved constituents. Although the sedimentary diffusion coefficients for the dissolved-phase electron acceptors (O_2, NO_3^-, and SO_4^{2-}) may vary by several factors as a function of temperature, ionic strength, and tortuosity (e.g. [41]), sedimentation rate ranges over several orders of magnitude in the modern ocean [219]. We thereby expect changes in ω to be the biggest influence upon Pe variability across modern sedimentary environments.

Under a low sedimentation rate of 1 $\frac{\text{cm}}{\text{kyr}}$ and a correspondingly low Pe, diffusion plays an important role by supplying fresh SO_4^{2-} from seawater. At the highest tested RRPOC, the diffusive flux of SO_4^{2-} into the sediments is around two orders of magnitude larger than the corresponding advective flux from pore water burial, and the initial POC abundance at which methanogenesis becomes the dominant mode of degradation is $\sim$11.2 wt%. Increasing the sedimentation rate to 10 $\frac{\text{cm}}{\text{kyr}}$ lowers the ratio of the diffusive SO_4^{2-} flux to the advective flux by over an order of magnitude; in turn, the initial POC abundance at which methanogenesis becomes the dominant mode of degradation is reduced to $\sim$0.3 wt%. This decrease is present even when the effect of dilution by inorganic sediments is removed and POC abundance is recast in terms of RRPOC, a more direct measure of the absolute moles of organic matter available. The transition to methanogenesis-dominated degradation occurs at a net POC degradation rate of $\sim$0.44 $\frac{\text{mmol}}{\text{m}^2\,\text{day}}$ in the 1 $\frac{\text{cm}}{\text{kyr}}$ runs and $\sim$0.11 $\frac{\text{mmol}}{\text{m}^2\,\text{day}}$ in the 10 $\frac{\text{cm}}{\text{kyr}}$ runs. The primary reason for this nonlinear response to increasing sedimentation rate lies in the physical nature of diffusion. Diffusive flux into a given parcel of sediment within I-CANDI is a linear function of the curvature (second derivative) of the depth profile of a chemical constituent's concentration. Increasing the sedimentation rate while holding the initial sedimentary POC abundance constant increases the advective burial flux without any corresponding increase in the rate of POC consumption. As a result, the concentration gradient in I-CANDI is reduced, and the corresponding diffusive flux of dissolved electron accep-

tors (O_2, NO_3^-, SO_4^{2-}) decreases. These results exemplify the "closed" versus "open" system behavior of sedimentary systems (e.g. [42]): as Pe increases and advection dominates transport, the systems become closed to ongoing diffusive contributions from seawater.

Porosity also exerts a huge influence on the results of I-CANDI model runs, mainly by modulating the amount of POC per volume of solid phase. POC degradation reactions within I-CANDI are cast with first-order kinetics with respect to the POC abundance per volume of solid. For a constant sedimentation rate and RRPOC, this abundance goes up as the porosity increases — i.e., as the POC present is forced to inhabit a smaller solid phase volume. This results in a doubling of POC degradation rates each time the volume taken up by solid phases is halved (e.g. in going from $\phi_0 = 0.90$ to $\phi_0 = 0.95$). The applicability of such a relationship to natural environments is uncertain. Although an empirical study of soil organic matter degradation [230] found a correlation between porosity and initial organic matter degradation rates, we are unaware of similar studies focused on marine sedimentary systems. Disentangling this potential physical influence on organic matter degradation from chemical influences (e.g. organic matter lability) is an enticing avenue for research.

Although sedimentation rate, organic carbon rain rate, porosity, and other variables are treated as independent in our model sensitivity tests, many of these parameters covary in natural environments. Most notably, Hedges and Keil (1995) [141] found a log-log relationship between the sedimentation rate and organic carbon content of sediments across a range of depositional environments, and Martin, Wood, and Becker (2015) [210] more recently identified an inverse correlation between porosity and sedimentation rate using a machine learning approach. The effect of these correlations on pyrite $\delta^{34}S$ is likely multiplicative in most cases: in shallow water environments proximal to the continents, higher sedimentation rates, higher organic matter rain rates, and lower porosities all promote the burial of pyrite with higher $\delta^{34}S$ via faster sulfate reduction rates and a decreased ability of diffusion to supply fresh seawater sulfate to the zone of pyrite formation. Precise sensitivity of pyrite $\delta^{34}S$ to changes in multiple depositional environment parameters is presumably complex and has likely varied over time through changes in global bottom water temperatures and productivity. We leave such multi-parameter exploration of this sensitivity to future study.

We earlier noted the threshold-like trade-off between iron reduction and sulfate

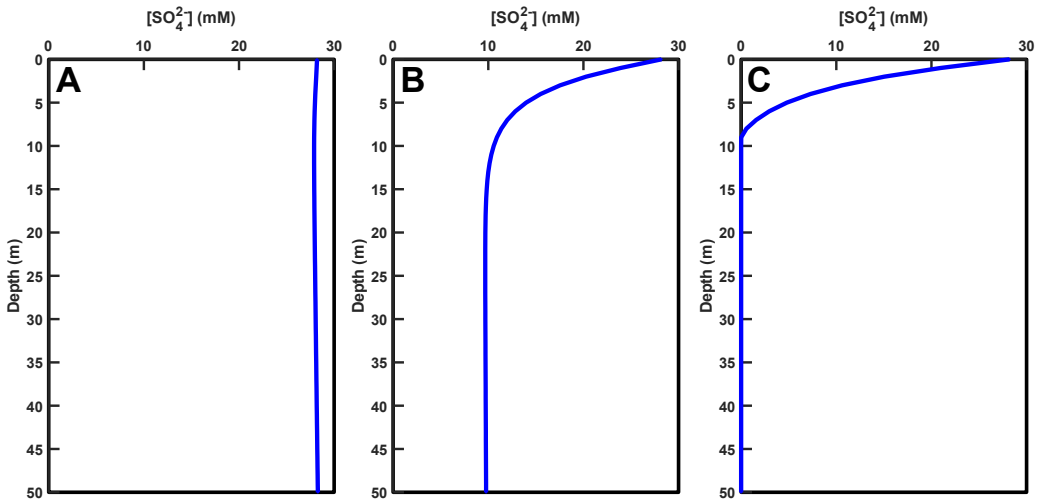

Figure IV.11: I-CANDI model outputs of $[SO_4{}^{2-}]$ versus depth for (A) RRPOC $= 0.01\ \frac{\text{mmol}}{\text{m}^2\text{day}}$, (B) RRPOC $= 0.3\ \frac{\text{mmol}}{\text{m}^2\text{day}}$, and (C) high RRPOC $= 0.5\ \frac{\text{mmol}}{\text{m}^2\text{day}}$. Each of the concentration profiles depicted here resembles measured profiles observed under low, intermediate, and high organic matter input in deep ocean sedimentary settings.

reduction in Wijsman et al.'s (2002) [362] diagenetic model. Based on our sensitivity tests, the abruptness of the switch between these two modes of degradation is primarily a function of the half-saturation and inhibition constants applied in the model. Our original model runs failed to yield an abrupt transition between iron reduction-dominated degradation and sulfate reduction-dominated degradation as RRPOC increased; we instead observed a more gradual transition with much overlap (Figure IV.3). Notably, our half-saturation and inhibition constants for iron and manganese reduction were roughly an order of magnitude higher than those used by Wijsman et al. (2002) [362]. Reducing all half-saturation and inhibition constants in our model by an order of magnitude resulted in much more abrupt transitions between modes of degradation (Figure B.11). The switch between SO_4^{2-} reduction and methanogenesis, however, is relatively abrupt regardless of the half-saturation and inhibition constants. This abrupt switch primarily results from the fast kinetics of AOM in I-CANDI, though the inhibition constant limiting methanogenesis in the presence of SO_4^{2-} also has some influence.

Finally, we found that I-CANDI can successfully produce SO_4^{2-} concentration profiles as diverse as those found in natural sedimentary settings (Figure IV.11). As exemplified by data shown in later chapters of this thesis, SO_4^{2-} concen-

tration profiles exist in several distinct variants in deep ocean settings. These variants include profiles in which $[SO_4^{2-}]$ is nearly invariant with depth, profiles in which $[SO_4^{2-}]$ exhibits an exponential decay with depth, and profiles in which $[SO_4^{2-}]$ declines in quasi-linear fashion to nearly zero concentration at a sulfate-methane transition (SMT). I-CANDI demonstrates that these variants are characteristic of oxic/suboxic POC degradation, SO_4^{2-} reduction-dominated POC degradation, and methanogenesis-dominated POC degradation, respectively. The implications of these variants for the S isotopic composition of sedimentary phases are discussed below.

IV.5.2 Controls upon sedimentary $\delta^{34}S$ profiles

The $\delta^{34}S$ of sedimentary pyrite is an important input to isotopic box models of the marine S cycle. These box models commonly assume a constant offset between the $\delta^{34}S$ of buried pyrite and that of seawater SO_4^{2-} (e.g. [58, 167]). However, data compilations [59, 127, 220] demonstrate that this offset is extremely variable ($\sim$0-80‰) across modern depositional environments. Previous studies [176, 195, 313] have shown that S isotopic fractionation ($^{34}\varepsilon$) during microbial sulfate reduction (MSR) varies as a function of cell-specific sulfate reduction rate (csSRR), potentially explaining some of this sulfide $\delta^{34}S$ variability. Halevy and colleagues [127] have instead argued that nearly all MSR in nature occurs at thermodynamic equilibrium with maximal ($\sim$70+‰) $^{34}\varepsilon$. These authors contend that variation in the physical parameters of depositional environments (e.g. sedimentation rate and porosity) can entirely account for the pyrite $\delta^{34}S$ heterogeneity seen in modern environments. What does I-CANDI have to say about each of these hypotheses? Are any of the threshold-like transitions in POC degradation reflected in the $\delta^{34}S$ of buried pyrite?

Our results confirm that nearly the entire range of pyrite $\delta^{34}S$ seen in modern environments can be explained without invoking changes in $^{34}\varepsilon$; such changes in $^{34}\varepsilon$ are still a *possible* explanation for pyrite $\delta^{34}S$ differences, but are not *required* to generate the differences. Despite the application of a constant $^{34}\alpha$ in all model iterations shown here, we observe offsets ($\Delta\delta^{34}S$) between the $\delta^{34}S$ of buried pyrite and that of seawater SO_4^{2-} ranging from over 70‰ to nearly 0‰ (Figure IV.12). This offset varies primarily as a function of organic matter degradation rate and sedimentation rate; these parameters, in turn, are influenced by RRPOC and porosity. There are similar trends in the relationship

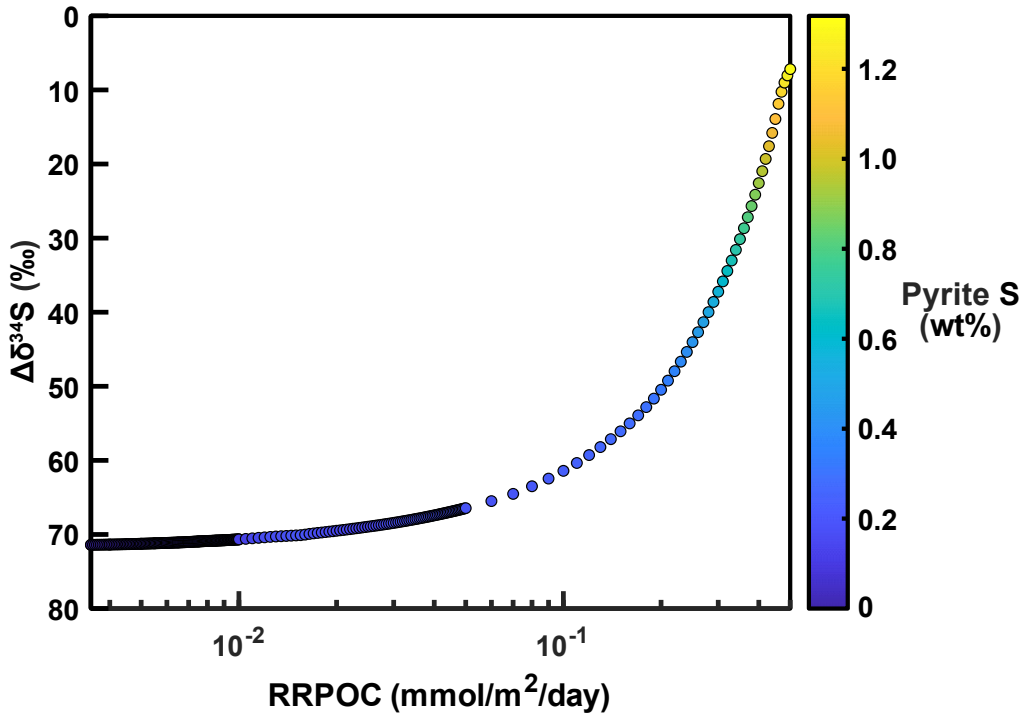

Figure IV.12: Plot of the $\Delta\delta^{34}S$ between seawater SO_4^{2-} and buried pyrite in the baseline I-CANDI model experiment as a function of RRPOC. The isotope fractionation associated with MSR was kept constant at ${}^{34}\varepsilon = 70‰$ across all model runs. Symbol color denotes the absolute amount of pyrite buried in each model iteration.

between pyrite $\delta^{34}S$ and RRPOC across all runs: regardless of the applied parameters, pyrite $\delta^{34}S$ is highly negative across all RRPOCs for which methanogenesis makes a negligible contribution to POC degradation. Pyrite $\delta^{34}S$ is near minimum values when oxic/suboxic POC degradation dominates and remains highly negative when SO_4^{2-} reduction dominates. Only once methanogenesis begins to constitute a substantial portion of POC degradation does pyrite $\delta^{34}S$ rapidly increase and approach a maximal value. This effect occurs due to the rapid AOM kinetics in I-CANDI: as methanogenesis becomes dominant, sulfate reduction is quickly condensed into a much shorter depth interval, and rates of diffusion from seawater become too slow to effectively offset the increase in SO_4^{2-} $\delta^{34}S$ resulting from sulfate reduction within the zone of pyrite formation.

In their recent work, Halevy et al. [127] assert that sedimentation rate and porosity act as key controls on the $\delta^{34}S$ of pyrite by modulating the relative influence of diffusion versus advection on the supply of SO_4^{2-} to the system. Our

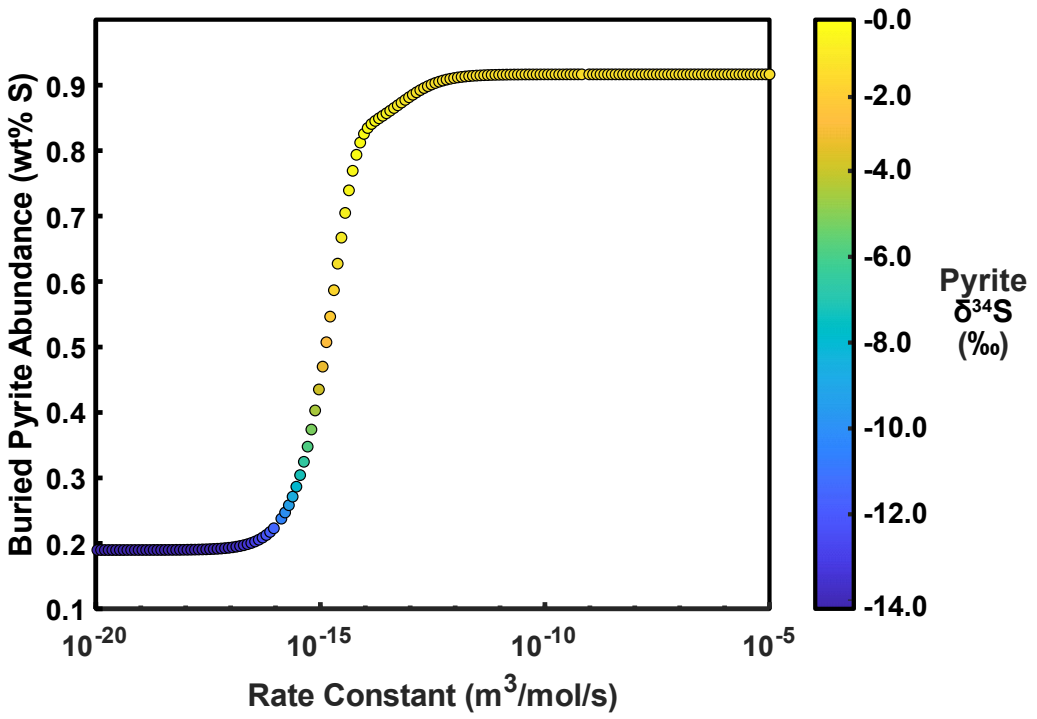

Figure IV.13: Plot of the concentration of buried pyrite versus the rate constant assigned to the $FeCO_3 + H_2S$ pyrite precipitation mechanism. Model experiment was run with the two other pyrite formation mechanisms active at their standard values. RRPOC and RRFe were kept constant at 0.4 $\frac{\text{mmol}}{\text{m}^2\text{day}}$ and 1.375 $\frac{\mu\text{mol}}{\text{m}^2\text{day}}$, respectively.

results concur with this assertion, but provide a more nuanced view. The Pe in a given depositional setting limits the maximal $\delta^{34}S$ value that pyrite may attain; i.e., even at relatively quick rates of SO_4^{2-} consumption, diffusive transfer of S species between the sediments and seawater prevents the sedimentary system from becoming completely closed. As Pe decreases, the maximal pyrite $\delta^{34}S$ that can be obtained also decreases. Pyrite $\delta^{34}S$ at lower RRPOCs also decreases as Pe is lowered, but such pyrite remains depleted in ^{34}S relative to seawater SO_4^{2-} at levels near the SO_4^{2-}-H2S thermodynamic equilibrium so long as methanogenesis is not the dominant mode of POC degradation. The implications of this finding are vast: if the equilibrium $^{34}\varepsilon$ in a given depositional environment can be constrained, the $\delta^{34}S$ of buried pyrite can be predicted with good accuracy (within $\sim$5‰) when methanogenesis is not a dominant mode of POC degradation.

The effect of pyrite formation mechanism on pyrite $\delta^{34}S$ in I-CANDI depends

on the strength of reversible ferrous iron sequestering mechanisms like siderite ($FeCO_3$) precipitation and surface absorption. All solid S phases in I-CANDI are ultimately derived from H_2S, and rates of H_2S consumption are quick enough that little transport occurs before scavenging as solids. As a result, we observe very little difference in pyrite $\delta^{34}S$ between the $FeS + S_0$ and $FeS + H_2S$ formation mechanisms. However, a large increase in $\delta^{34}S$ occurs at high organic matter rain rates if the $FeCO_3 + H_2S$ formation mechanism is enabled (Figure IV.13). This increase results from the availability of Fe^{2+} that can capture and sequester H_2S in the sediments. Much dissolved Fe^{2+} escapes from the sediments to seawater at high RRPOC in the absence of any siderite precipitation or iron sorption reactions, as aqueous H_2S cannot diffuse and react with it quickly enough to capture it quantitatively. Only additional reactions that capture iron prior to its diffusive escape to seawater can make it available for later pyrite precipitation in this case. Studies integrating pyrite $\delta^{34}S$ measurements with measurements of benthic iron fluxes [301] and iron partitioning among sedimentary phases [187] may yield more insight into the relevance of such iron sequestration in natural settings.

IV.5.3 Implications for Earth history

Our I-CANDI sensitivity tests have confirmed the results of Halevy and colleagues' [127] finding that large perturbations to pyrite $\delta^{34}S$ may occur through changes in the physical parameters of depositional environments; changes in csSRR, temperature, microbial community composition, or other parameters influencing $^{34}\varepsilon$ during sedimentary S cycling are not required. How does such a finding impact our interpretation of S isotope records over different timescales across Earth history?

Several authors (e.g. [19, 246, 344]) have discussed the possibility of changes in the marine S cycle on glacial-interglacial timescales during the Pleistocene. These studies have primarily focused on the global continental weathering flux [344] and the $\delta^{34}S$ of pyrite buried in specific localities [246]. Our work supports Pasquier and colleagues' (2017) assertion that changes in sedimentation rate may yield substantial changes in pyrite $\delta^{34}S$ locally. Although these hypothesized glacial-interglacial changes have occurred over too short of timescales relative to the 10+ Myr residence time of sulfur in seawater ($\sim$10 Myr; [18]) to force significant change in seawater $\delta^{34}S$, such changes could provide a nega-

tive feedback that acts to stabilize pyrite $\delta^{34}S$ amid oscillations in sea level on longer timescales. Seawater SO_4^{2-} $\delta^{34}S$ was nearly constant at $\sim$+22‰ for most of the past 45 Myr [252, 279] despite substantial changes in eustatic sea level, including a large (100+ m) decrease at the Eocene-Oligocene boundary [129]. Although transfer of sediment from the shelf to the deep ocean under lower eustatic sea level presumably would have increased the Pe in deep ocean settings, a net decrease in the $\delta^{34}S$ of the global pyrite burial flux may still have occurred (e.g. [279]). This change would have opposed any decrease in the $\delta^{34}S$ of the input flux from enhanced oxidative weathering of pyrite [344] by increasing the $\Delta\delta^{34}S$ between seawater SO_4^{2-} and buried pyrite. For example, steady state seawater $\delta^{34}S$ calculations for a range of $\Delta\delta^{34}S$ and $\delta^{34}S_{in}$ values (Figure IV.14) suggest that a 1‰ decrease in $\delta^{34}S_{in}$ could be compensated by a $\sim$2‰ increase in $\Delta\delta^{34}S$ to maintain a constant seawater $\delta^{34}S$. The potential influence of sea level on $\Delta\delta^{34}S$ is explored in more detail in Chapter VI of this thesis.

Our findings also impact our understanding of the marine S cycle on longer timescales. For example, Halevy and colleagues [127] have postulated that more positive pyrite $\delta^{34}S$ during the Archean and Proterozoic resulted from a decrease in the diffusive SO_4^{2-} flux into the sediments under lower seawater SO_4^{2-} concentrations. I-CANDI model runs under lower bottom water SO_4^{2-} concentrations support this possibility, but also provide mechanisms through which this effect could be ameliorated. Previous studies have suggested that the Archean was characterized by lower weathering rates (e.g. [130]) and higher global temperatures (e.g. [181]). Decreases in sedimentation rate and increases in bottom water temperature each would lower the Pe in depositional environments globally and oppose any increase in pyrite $\delta^{34}S$ resulting from lower seawater $[SO_4^{2-}]$. Although neither of these conditions *must* co-occur with a decrease in seawater $[SO_4^{2-}]$, such conditions could apply to much of the Archean and Proterozoic and may help explain the persistent depletion of pyrite in ^{34}S despite lower marine $[SO_4^{2-}]$.

Lastly, I-CANDI reveals that methanogenesis becomes the dominant mode of POC degradation at much lower RRPOCs when marine $[SO_4^{2-}]$ is lower. Although lower SO_4^{2-} reduction half-saturation and methanogenesis inhibition constants (e.g. [196]) could partially compensate for this effect, an increase in the importance of methanogenesis as a POC degradation pathway under lower $[SO_4^{2-}]$ seems highly likely. Such an effect could help explain the maintenance

of warmer climate states under lower marine [SO_4^{2-}] conditions during the Cretaceous and the early Paleozoic [142, 202]. Methanogenesis accounts for only a few percent of the POC degraded in modern ocean sediments [90], but its product methane (CH_4) forces ∼16% of greenhouse warming on modern Earth [9]. Egger et al. (2018) [90] have estimated that ∼3 Tmol of methane (CH_4) are oxidized by SO_4^{2-} through AOM each year. This estimate is surprisingly close to estimates of the modern riverine input flux of SO_4^{2-} to seawater, 2.8 ± 0.4 Tmol/yr [52] — of particular note given the 1:1 stoichiometry of CH_4:SO_4^{2-} consumption in AOM. If the amount of SO_4^{2-} reduced through AOM in sediments were decreased by an order of magnitude from Egger and colleagues' (2018) estimates without any corresponding change in CH_4 production, the amount of CH_4 required to be consumed by other oxidants would be ∼2 Tmol/yr. The similarity in the magnitude of this flux to the modern riverine SO_4^{2-} input flux suggests that SOM could have played a critical role in maintaining lower marine [SO_4^{2-}] [202] and/or increasing the $\delta^{34}S$ of pyrite buried globally (e.g. [195]). Escape of any portion of this flux to the atmosphere (e.g., through shallow water CH_4 release or destabilization of methane hydrates [86]) would also help maintain a greenhouse climate state.

IV.6 Conclusions

A mechanistic understanding of the processes affecting sedimentary S cycling is necessary to accurately predict the effects of Earth system changes on the marine S cycle. Here, we have constructed a diagenetic model, I-CANDI, that simulates time-dependent transport and reaction processes in one-dimension. Our model includes isotopic species for S-bearing compounds to allow sedimentary $\delta^{34}S$ profiles to be simulated. Through myriad sensitivity tests, we find that organic matter input, porosity, and sedimentation rate are the strongest controls on the dominant organic matter degradation processes and the $\delta^{34}S$ of buried pyrite in I-CANDI. I-CANDI also reveals that maximal pyrite $\delta^{34}S$ values in a local sedimentary system are not reached until methanogenesis becomes the dominant degradation process. The physical parameters of the system and the organic matter rain rate modulate pyrite $\delta^{34}S$ and can adequately account for the $\delta^{34}S$ heterogeneity observed in natural sediments; no changes in $^{34}\varepsilon$ are necessary. These findings have significant implications for our interpretation of the ancient marine S cycle and motivate additional applications of I-CANDI.

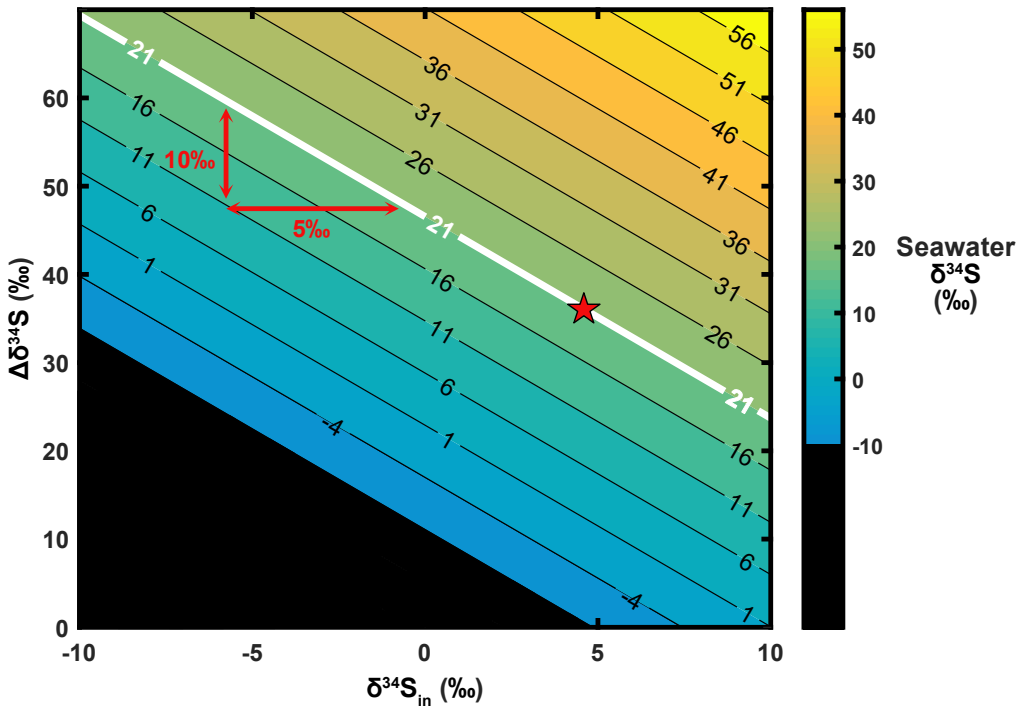

Figure IV.14: Contour plot of the steady state seawater $\delta^{34}S$ as a function of the $\Delta\delta^{34}S$ between seawater SO_4^{2-} and buried pyrite plus the $\delta^{34}S$ of the weathering input ($\delta^{34}S_{in}$). Calculations assume a constant magnitude for the weathering input flux and two burial fluxes (pyrite and sulfate evaporites) with no S isotopic fractionation during evaporite precipitation. The red star denotes the approximate solution for modern seawater given the global $\delta^{34}S_{in}$ estimate of [52]. Note that the slope of $\sim \frac{1}{2}$ in this space indicates that a 1‰ change in $\delta^{34}S_{in}$ could be compensated by a 2‰ opposing change in $\Delta\delta^{34}S$ to maintain approximately constant seawater $\delta^{34}S$. Results yielding a seawater $\delta^{34}S$ less than the minimum $\delta^{34}S_{in}$ value tested (-10‰) require negative burial fluxes and have been blacked out as implausible.

Chapter V

SULFUR CYCLING IN DEEP MARINE OXYGENATED SETTINGS: INSIGHTS FROM IODP EXPEDITION 361, IODP EXPEDITION 363, AND *R.V. KNORR* CRUISE KN223

V.1 Abstract

Understanding the magnitude and S isotopic composition of fluxes within the S cycle is critical for interpreting seawater $\delta^{34}S$ variations in Earth's past. Deep ocean sedimentary S cycling remains a particularly understudied component of the S cycle, and studies of cycling below the uppermost several meters of sediment are rare. We undertook a study of deep ocean sedimentary S cycling by analyzing pore water and solid phase samples from 11 sites cored on Integrated Ocean Discovery Program (IODP) Expedition 361, IODP Expedition 363, and *R.V. Knorr* cruise KN223. We observed a diverse array of sedimentary S cycling at these sites, with total organic carbon (TOC) content and mean net sulfate reduction rate (nSRR) each varying by over an order of magnitude among the different sites. Closed and open system modeling indicate that large ($> 45‰$) S isotopic fractionations are an ubiquitous feature of sedimentary S cycling at these sites. We also found that the $\delta^{34}S$ of pyrite buried at these sites depends crucially on the degree to which sulfate (SO_4^{2-}) reduction goes to completion and on the rapidity with which other electron acceptors (e.g. O_2) are exhausted. SO_4^{2-} reduction at sites with quasi-linear $[SO_4^{2-}]$ profiles and with profiles indicating a source of SO_4^{2-} at depth have been overlooked in previous studies estimating global SO_4^{2-} reduction rates (e.g. [43]), but yield significantly higher mean nSRRs here than sites with exponentially-decreasing $[SO_4^{2-}]$. Our results suggest that accounting for these sites could lead to significant changes and improvements in our understanding of S isotopic mass balance within the modern marine S cycle.

V.2 Background

Chapter II of this thesis demonstrated a potentially significant role for $\Delta\delta^{34}S$ and $\delta^{34}S_{in}$ in forcing changes in seawater $\delta^{34}S$ at times in Earth's past. Although our box model suggests that these parameters can affect seawater $\delta^{34}S$, the plausi-

bility of changes in these parameters requires that the effects on other biogeochemical cycles also be considered. For example, what are the implications of a 10‰ decrease in $\delta^{34}S_{in}$ for atmospheric pO_2? Can a $\Delta\delta^{34}S$ change of 20‰ still be considered plausible once all effects are considered in detail? We must elucidate the controls on the concentration and isotopic composition of seawater SO_4^{2-} to begin to answer these questions.

Historically, values for the globally integrated $\delta^{34}S_{in}$ and $\Delta\delta^{34}S$ have not been well constrained due to high local variability in each of these parameters [52, 59]. Box models of the marine S cycle have typically used estimates of these values derived from limited data sets (e.g. [72]). Recent studies [52, 127] have improved our understanding of the modern values of these parameters with larger data sets [52, 127] and predictive modeling [127]. However, additional data are needed to refine and verify these estimates. Studies that begin to parse out the influence of variations in sulfur isotopic fractionation ($^{34}\varepsilon$) versus variations in other sedimentary parameters on $\Delta\delta^{34}S$ are particularly necessary.

Sulfur cycling in deep ocean sediments — and particularly, deep ocean $\Delta\delta^{34}S$ — remains an understudied component of the global S cycle. Previous studies (e.g. [19]) have trivialized the importance of pyrite burial in deep ocean sediments given these sediments' low rates of sedimentation and SO_4^{2-} reduction — i.e., the net pyrite burial flux in these sediments is low. This neglect of deep ocean pyrite burial has occurred despite the fact that these deep environments constitute over 90% of the modern seafloor in terms of surface area [5] and are an important source of sulfur that gets recycled to the mantle via subduction (e.g. [57]). However, several more recent studies [43, 165] have suggested that SO_4^{2-} reduction in these environments comprises as much as half of the SO_4^{2-} reduction occurring in marine sediments globally. Lower oxygenation of the deep ocean [319] may have allowed this flux to be even larger at times in Earth's past. Existing pyrite $\delta^{34}S$ data from deep ocean sediments [4, 37, 38, 115, 158, 188, 197, 220, 222, 266, 293, 329] have demonstrated a high frequency of very negative (< -30‰) pyrite $\delta^{34}S$ values in these sediments that are disparate from the more positive pyrite $\delta^{34}S$ values observed in shelf sediments (e.g. [363]). This suggests that $^{34}\varepsilon$ is very large in deep ocean sediments and that the deep ocean pyrite burial flux could have an outsize influence on the global pyrite burial $\delta^{34}S$ value. Better constraints on the magnitude of this pyrite flux and the controls upon its sulfur isotopic composition are needed to assess the potential role of

deep ocean pyrite burial in modifying S cycle isotope mass balance.

Here, we undertake a study of S cycling in oxygenated deep ocean environments. We do so through the lens of sites cored on IODP Expedition 361 [128], IODP Expedition 363 [290], and *R.V. Knorr* Cruise KN223 [234]. Extensive shipboard and shore-based chemical analyses make these sites prime candidates to determine the influence of different sedimentary variables on S cycling in deep ocean sediments. In the following, we estimate the S isotopic fractionation associated with S cycling at an array of sites using closed system Rayleigh distillation models and our new open-system model, I-CANDI (Chapter IV). We show that large ($> 45‰$) S isotopic fractionations are an ubiquitious feature of deep ocean sedimentary sulfur cycling. We also examine the sensitivity of the I-CANDI model results to the input fluxes of organic matter, iron, and other chemical constituents.

V.3 Site Locations

Samples for this study were collected as part of ocean drilling campaigns in the Atlantic, Indian, and Pacific Ocean basins. Location, depth, and selected shipboard data for each site included in this study are listed in Table V.1. Maps of the site locations are depicted in Figure V.1. Sites for our study were chosen based on their water depth, sedimentation rate, organic carbon content, and $[{SO_4}^{2-}]$ data. Sites that were sampled at high (1.5 m) depth resolution for interstitial water (IW) and that captured unique combinations of these characteristics were prioritized for sampling over sites that closely duplicated a combination already chosen. This strategy resulted in the measurement of ${SO_4}^{2-}$ $\delta^{34}S$ profiles at 11 different sites spanning a wide range of water depths (488 to 5465 meters below sea level), sedimentation rates (< 3 to > 60 $\frac{cm}{kyr}$), and mean total organic carbon (TOC) contents (< 0.5 to $\sim$1 wt%). Each of these sites is briefly described below.

IODP Expedition 361 Sites U1474 and U1478 were drilled in the Natal Valley off the coast of Mozambique in the Indian Ocean. These sites are both heavily influenced by terrigenous input from the Limpopo River [128]. Site U1475 was cored to the south off the southwestern flank of the Agulhas Plateau [128].

Expedition 363 Sites U1482 and U1483 were drilled on the opposite side of the Indian Ocean basin off the northwest coast of Australia. These two sites are located at intermediate water depths ($\sim$1600 mbsl) and are sensitive to inputs of windblown dust blown off the Australian desert [290].

Table V.1: Site location and geochemistry details for samples analyzed in this study. Shipboard sedimentation rate denotes the sedimentation rate estimated for the uppermost portion of the sediments based on the shipboard age model. mbsl = meters below sea level. Data from [128, 234, 290].

Site	Latitude	Longitude	Water Depth (mbsl)	Shipboard Sedimentation Rate ($\frac{cm}{kyr}$)	Mean TOC (wt%)	Mean $CaCO_3$ (wt%)
U1474	31° 13.00' S	31° 32.71' E	3045	3.7	0.4	37
U1475	41° 25.61' S	25° 15.64' E	2669	2.8	0.4	80
U1478	25° 49.26' S	34° 46.16' E	488	9	0.4	30
U1482	15° 03.32' S	120° 16.10' E	1466	7	0.7	60
U1483	13° 05.24' S	121° 48.25' E	1733	10	0.9	59
U1485	03° 06.16' S	142° 47.59' E	1145	62.5	1.0	9
U1486	02° 22.34' S	144° 36.08' E	1332	6	0.5	40.5
U1487	02° 20.00' S	144° 49.17' E	874	3.5	-	37.6
U1488	02° 02.59' S	141° 45.29' E	2604	3	0.5	83.5
KN223-02	15° 50.90' N	52° 00.00' W	5465	-	-	-
KN223-16	35° 42.60' N	57° 36.90' W	4575	-	-	-

Sites U1485-8 were drilled in the Pacific Ocean north of Papua New Guinea (PNG); Site U1485 is located on the PNG continental slope, Sites U1486 and U1487 in the Manus Basin, and Site U1488 on the Euaripik Rise [290].

KN223 Sites 02 and 16 were drilled in the North Atlantic near Researcher Ridge and on the Bermuda Rise, respectively. These are abyssal sites and represent the two deepest sites targeted by this study.

V.4 Methods

V.4.1 Shipboard data collection

Detailed sampling methods were documented in cruise reports [128, 234, 290] and are briefly described below. For IODP Expedition 361 and 363 sites, pore water was extracted from 5-10 cm long whole round sediment sections by removing cut and capped sediment samples from the core liner, scraping off the outer $\sim$0.5 cm of the whole round, and compressing the whole round in a Manheim titanium squeezer with a Carver hydraulic press [206]. Pressures up to 35,000 lbs gauge force were applied with the press. Water was filtered through a pre-washed Whatman No. 1 filter and collected in an acid-cleaned plastic syringe. Extracted IW (i.e., pore water) was filtered using a 0.45 μm polysulfone syringe filter and aliquoted for shipboard and shore-based analyses. Shipboard SO_4^{2-} concentrations were measured using a Metrohm 850 professional ion chromatography system (ICS) with an 858 professional sample processor.

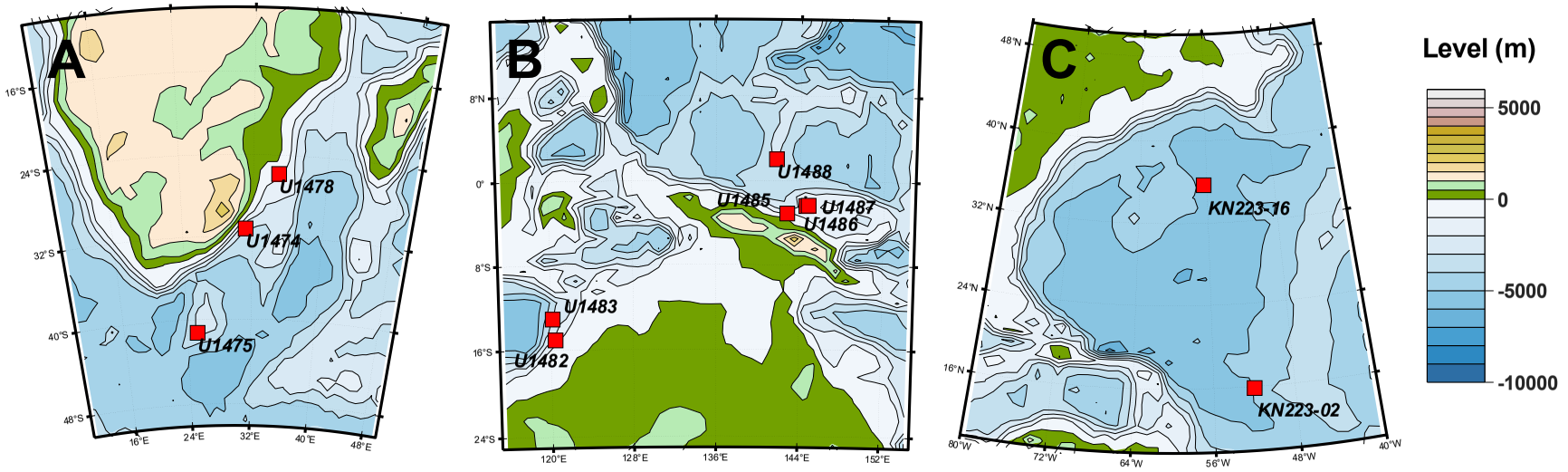

Figure V.1: Maps of locations from which samples for this study were collected on (A) IODP Expedition 361, (B) IODP Expedition 363, and (C) *R.V. Knorr* cruise KN223. Maps were created using the M_Map Mapping Toolbox [247].

Samples were diluted 100x with 18.2 MΩ nanopure water for $[SO_4^{2-}]$ measurements. The IAPSO seawater standard was diluted 20x to 500x to create a five-point standard calibration curve for the set of concentration measurements at each site, and a 150x dilution of IAPSO was run every ∼10 samples as a consistency standard. Precision (1σ relative standard deviation) was 0.98% ($n = 44$) on Expedition 363 based on all measurements of this consistency standard.

For *R.V. Knorr* Cruise KN223, whole rounds cut from long cores were squeezed using Manheim squeezers to extract IW. Pressures up to 35,000 lbs gauge force were applied. SO_4^{2-} concentrations were measured on the ship using a Metrohm 861 Advanced Compact IC. Dilutions of a secondary standard calibrated against IAPSO were used to create a calibration curve for quantifying concentrations. Five IAPSO samples were also measured in each run of 36 analyses as a consistency check. The standard deviation of the drift-corrected IAPSO $[SO_4^{2-}]/[Cl^-]$ ratios and samples analyzed in duplicate was better than 0.21‰.

V.4.2 Shore-based data collection

Samples of both pore water and sediment were aliquoted for shore-based S isotopic measurements while on the ship. Pore water aliquoted for SO_4^{2-} and H_2S $\delta^{34}S$ analyses was fixed with 500 μL 1 M zinc acetate to preserve H_2S as ZnS. These samples were shipped and stored frozen for shore-based laboratory processing. Once ready for laboratory processing, samples were thawed and centrifugated to separate the aqueous phase from any solid precipitates. The aqueous phase was decanted into an acid-cleaned 15 mL centrifuge tube and saved. Solid phase (if present) was rinsed five times with milliQ water to remove residual SO_4^{2-} and dried down at 60 °C in a laminar flow bench.

For aqueous SO_4^{2-} $\delta^{34}S$ measurements, aliquots of aqueous phase were pipetted into PFA vials, dried down, diluted in weak (0.5% v/v) HCl, and loaded onto 10 mL Bio-Rad® disposable HDPE columns containing 0.8 mL AGI-X8 anion exchange resin. Column chromatography and mass spectrometry methods for these samples were identical to those used in Chapter II. Repeated analyses of a seawater consistency standard ($n = 39$) yielded a mean $\delta^{34}S$ of +21.03 ± 0.12‰ (1σ standard deviation). Procedural blanks ($n = 33$) yielded a $\delta^{34}S$ of +16 ± 14‰ (1σ standard deviation) and contained 1.0 ± 2.2 S nanomoles. Note that this mean blank size is reduced to 0.4 ± 0.3 S nanomoles if two unusually

large blanks containing 5-15 S nanomoles are excluded. Given that most samples measured contained at least 100 nanomoles S, the size of the procedural blank correction was very small ($\leq 0.05‰$) for all but the most sulfur-poor samples — mainly, those samples taken at or below a sulfate-methane transition (SMT).

For aqueous H_2S $\delta^{34}S$ measurements, ZnS was converted to Ag_2S using $AgNO_3$. HNO_3 was added immediately after conversion to remove any $ZnCO_3$ present. Samples were centrifugated and the supernant removed immediately after centrifugation to limit oxidation of the Ag_2S by NO_3^-. Remaining solid phase was rinsed five times with milliQ water and dried down on a 60 °C hot plate in a laminar flow bench. For mass spectrometry, the solid phase was crushed and aliqouts weighed for measurement on a Thermo Scientific™ EA Isolink™ IRMS System. Many samples were run with several replicates due to $\delta^{34}S$ heterogeneity within the sample powders. For smaller samples, we avoided this problem by measuring the entire sample in a single measurement.

V.5 Results

V.5.1 Sulfate concentration and $\delta^{34}S$

Shipboard concentration and $\delta^{34}S$ data for pore water SO_4^{2-} are summarized in Table C.1 in Appendix C. For the purpose of presenting results, we group sites with similar depth profiles together in our descriptions below. We note that one outlying shipboard $[SO_4^{2-}]$ measurement at 1.45 mbsf for Site U1482 was treated as erroneous and has been removed in our analysis of the data. In addition, data from cruise KN223 were reported as SO_4^{2-}/Cl^- ratio deviations from seawater (in %). These data have been converted to estimated $[SO_4^{2-}]$ assuming a constant $[Cl^-]$ and a seawater $[SO_4^{2-}]$ of 28.2 mM.

V.5.1.1 Sites U1474 and U1475

Sulfate concentration and $\delta^{34}S$ profiles for Sites U1474 and U1475 are depicted in Figure V.2. At both sites, $[SO_4^{2-}]$ decreases exponentially with depth, but the rate of decrease is faster overall at Site U1474 than U1475. The U1474 $[SO_4^{2-}]$ profile becomes nearly invariant at $>$ 200 m depth. In contrast, $[SO_4^{2-}]$ at U1475 is still decreasing at the lowest depths sampled.

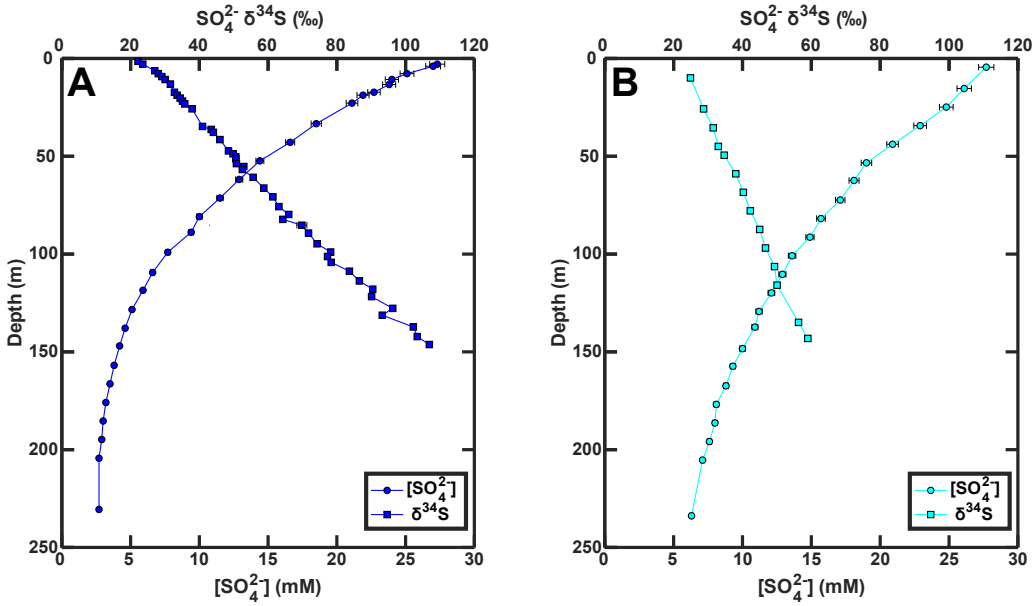

Figure V.2: Sulfate concentration (circular symbols, bottom horizontal axis) and sulfur isotopic composition (square symbols, top axis) for (A) IODP Site U1474 and (B) IODP Site U1475. Sulfate concentration data from [128].

SO_4^{2-} $\delta^{34}S$ increases in a quasi-linear fashion with depth at both Sites U1474 and U1475. The gradient of the $\delta^{34}S$ increase is lower at Site U1475 than Site U1474, as expected from the lower rate of $[SO_4^{2-}]$ decrease. Although samples for $\delta^{34}S$ were not collected below 150 mbsf at either of these sites, the $\delta^{34}S$ at Site U1474 nonetheless reaches incredibly high values (+106.9‰ at 146.24 mbsf). The maximum SO_4^{2-} $\delta^{34}S$ measured at Site U1475 is much lower (∼+59‰ at 143.14 mbsf).

V.5.1.2 Sites U1478, U1482, U1483, U1485, and KN223-16

Sites U1478, U1482, U1483, U1485, and KN223-16 are disparate in terms of geographic location (Figure V.1) and some sedimentary parameters (Table V.1), but all feature quantitative consumption of SO_4^{2-} (Figure V.3). SO_4^{2-} is consumed to near-zero levels by ∼70 mbsf at Site U1478, ∼120 mbsf at Site U1482, ∼55 mbsf at Site U1483, ∼8 mbsf at Site U1485, and ∼39 mbsf at Site KN223-16. Shipboard measurements for the IODP sites confirm the onset of significant concentrations of CH_4 near these depths and indicate the presence of a SMT. Although there are notable variations in the gradient of SO_4^{2-} depletion among the sites, $[SO_4^{2-}]$ decreases in a more linear manner at these sites than at Sites

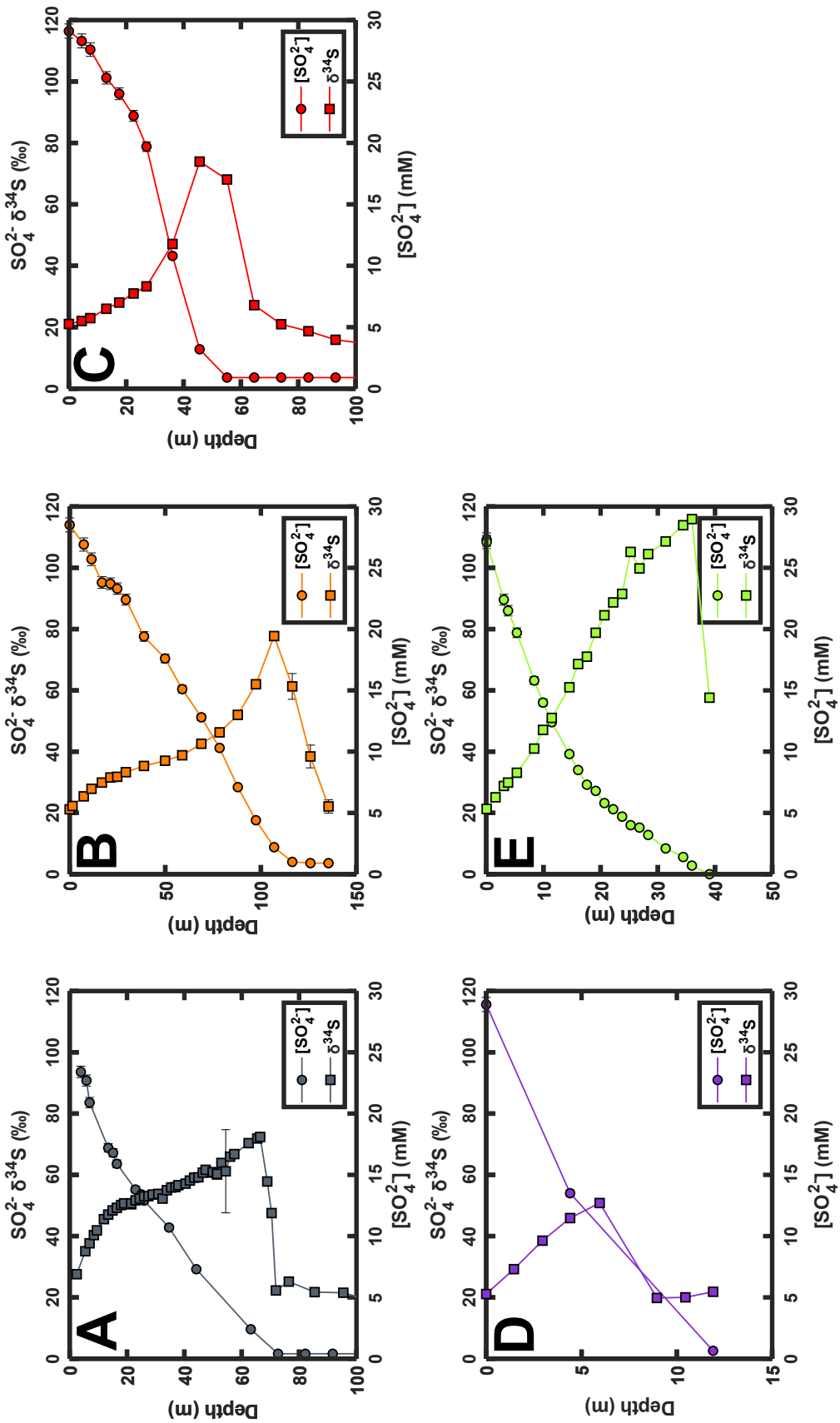

Figure V.3: Sulfate concentration (circular symbols, bottom horizontal axis) and sulfur isotopic composition (square symbols, top axis) for (A) IODP Site U1478, (B) IODP Site U1482, (C) IODP Site U1483, (D) IODP Site U1485, and (E) Site KN223-16. Sulfate concentration data from [128, 234, 290].

U1474 and U1475.

The sulfate $\delta^{34}S$ depth profiles at these sites exhibit changes that reflect the gradient in their corresponding $[SO_4^{2-}]$ profiles; as the $[SO_4^{2-}]$ gradient increases in magnitude, the rate of $\delta^{34}S$ change also increases. This is most apparent at Sites U1478 and U1483. At Site U1478, a high rate of $[SO_4^{2-}]$ decrease above $\sim$10 mbsf is accompanied by the most rapid increase in its $\delta^{34}S$ profile. Site U1483 instead exhibits its most rapid decrease in $[SO_4^{2-}]$ below $\sim$35 mbsf, with $\delta^{34}S$ increasing more quickly in tandem. At all these sites, an abrupt decrease in SO_4^{2-} $\delta^{34}S$ occurs at the SMT. This decrease exceeds 30‰ in magnitude at each site and returns SO_4^{2-} $\delta^{34}S$ to seawater-like $\delta^{34}S$ values ($\sim$+21‰) at sites with multiple measurements below the SMT.

V.5.1.3 Sites U1486, U1487, and U1488

A smaller subset of sites — Sites U1486, U1487, and U1488 — were cored north of Papua New Guinea and differ from all others in terms of their profiles (Figure V.4). These sites do not exhibit a monotonic decrease in $[SO_4^{2-}]$ with depth, but instead feature an initial decrease followed by increasing $[SO_4^{2-}]$ (Sites U1486 and U1488) or invariant $[SO_4^{2-}]$ (Site U1487) at greater depths. This reversal in gradient occurs at $\sim$50 mbsf at Site U1486 and $\sim$100 mbsf at Site U1488. Minimum $[SO_4^{2-}]$ near these depths is 19.8 mM at Site U1486 and 21.8 mM at Site U1488. Following these minima, $[SO_4^{2-}]$ increases in quasi-linear fashion with depth to concentrations exceeding 22 mM at Site U1486 and 24 mM at Site U1488. $[SO_4^{2-}]$ is mostly invariant ($\sim$24.2 mM) below the sediment-water interface at Site U1487.

SO_4^{2-} $\delta^{34}S$ depth profiles at Sites U1486-8 are nearly mirror images of their corresponding $[SO_4^{2-}]$ profiles; i.e., $\delta^{34}S$ increases across depths where $[SO_4^{2-}]$ is decreasing, reaches an asymptote at depths where $[SO_4^{2-}]$ stops decreasing, and decreases as $[SO_4^{2-}]$ begins increasing again. Maximum $\delta^{34}S$ is +45.5‰ at Site U1486, +28.7‰ at Site U1487, and $\sim$+30‰ (excluding one outlier) at Site U1488. Sulfate $\delta^{34}S$ decreases at depths below these maxima to +27.6‰ at Site U1486, +28.2‰ at Site U1487, and +26.7‰ at Site U1488.

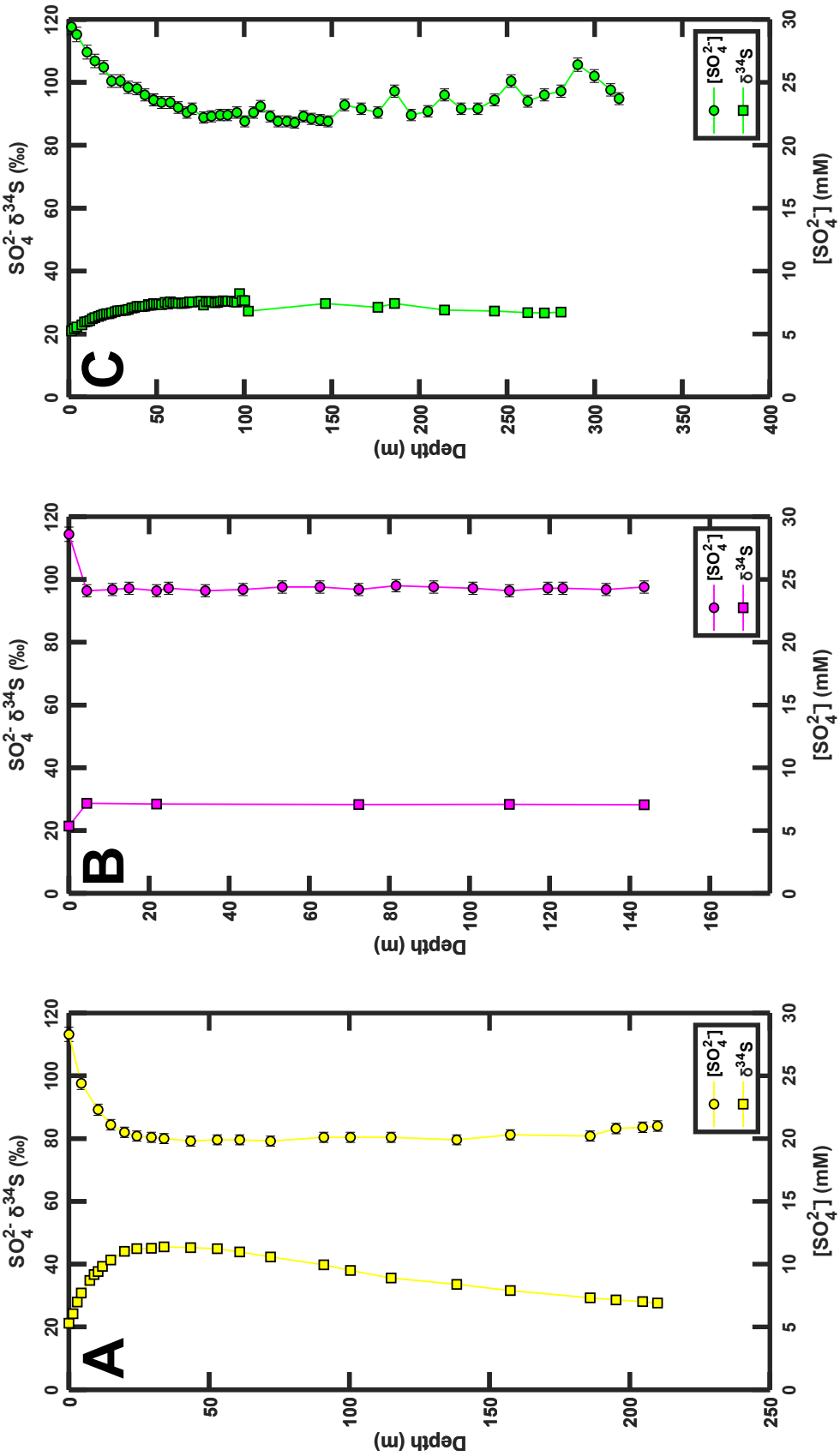

Figure V.4: Sulfate concentration (circular symbols, bottom horizontal axis) and sulfur isotopic composition (square symbols, top axis) for (A) IODP Site U1486, (B) IODP Site U1487, and (C) IODP Site U1488. Sulfate concentration data from [290].

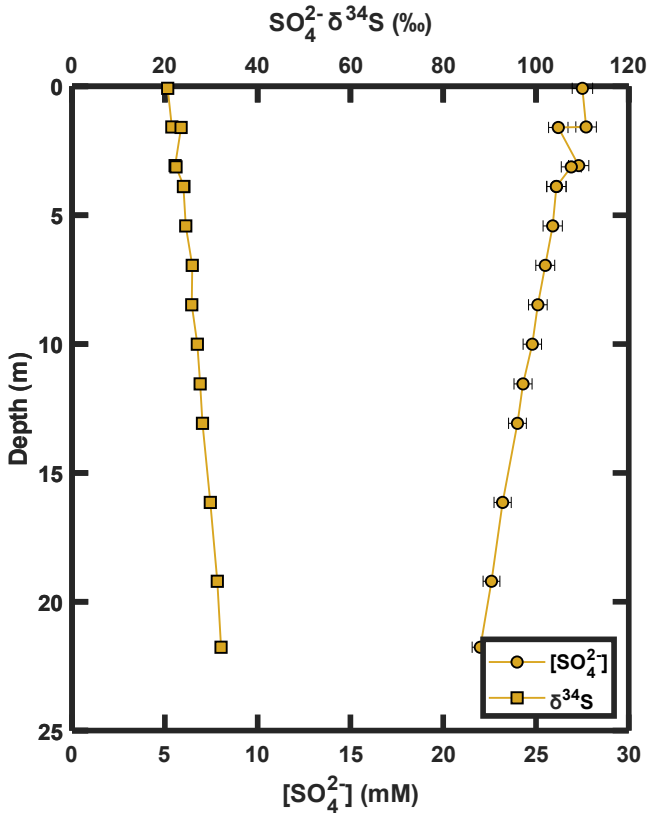

Figure V.5: Sulfate concentration (circular symbols, bottom horizontal axis) and sulfur isotopic composition (square symbols, top axis) for KN223 Site 02. Sulfate concentration data from [234].

V.5.1.4 Site KN223-02

Site KN223-02 was cored over too short a depth interval (∼22 mbsf) to permit classification with any of the above groups; its $[SO_4^{2-}]$ and $\delta^{34}S$ profiles are depicted in Figure V.5. Here, $[SO_4^{2-}]$ decreases in a quasi-linear fashion from the sediment-seawater interface to the deepest sampled depth. The lowest $[SO_4^{2-}]$ (22.0 mM) occurs at the deepest sampled depth (21.8 mbsf). SO_4^{2-} $\delta^{34}S$ increases in a similar manner from +20.6‰ at the sediment-seawater interface to +32.1‰ at 21.8 mbsf.

V.5.2 Aqueous sulfide $\delta^{34}S$

Aqueous sulfide was present at high enough concentrations to enable H_2S $\delta^{34}S$ measurements at two sites thus far, Sites U1482 and U1483 (Figure V.6). At both of these sites, H_2S $\delta^{34}S$ closely follows SO_4^{2-} $\delta^{34}S$, but is offset toward lower

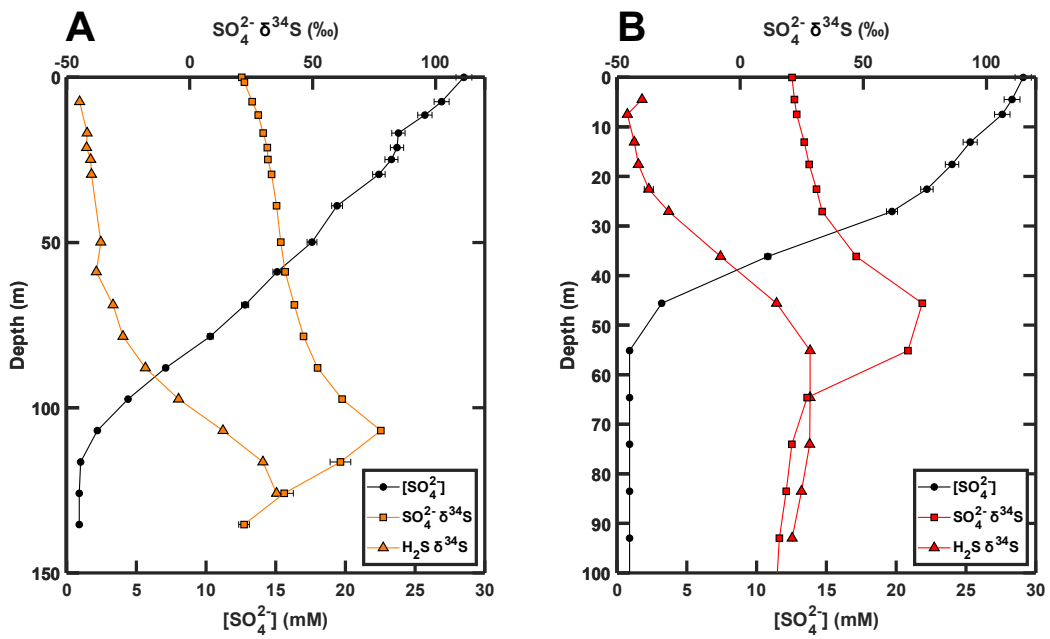

Figure V.6: Sulfate concentration (black circles, bottom horizontal axis) and sulfur isotopic composition for sulfate (square symbols, top axis) and aqueous sulfide (triangle symbols, top axis) at (A) Site U1482 and (B) Site U1483. Sulfate concentration data from [290].

absolute values at most depths. H_2S is initially highly depleted in ^{34}S ($\delta^{34}S$ ∼-40‰) and becomes progressively enriched with depth as $[SO_4{}^{2-}]$ decreases. H_2S $\delta^{34}S$ maintains a large offset from SO_4^{2-} $\delta^{34}S$ to a depth of ∼90 mbsf at Site U1482 and ∼30 mbsf at Site U1483. Here, the offset gradually decreases with depth until becoming nearly zero by 125.9 mbsf at Site U1482 and even reversing in sign below 60 mbsf at Site U1483. We discuss some possible reasons for this reversal later in this chapter.

V.6 Discussion

V.6.1 Diversity in deep ocean sulfur cycling

Viewed through the lens of our results, the character of S cycling in deep marine sedimentary settings is highly diverse. Sites may feature the complete consumption of $SO_4{}^{2-}$ at depth within the sediments (Sites U1478, U1482, U1483, U1485, and KN223-16), an exponential decline in $[SO_4{}^{2-}]$ to non-zero values at depth (Sites U1474 and U1475), or even an initial decrease in $[SO_4{}^{2-}]$ followed by a gradual increase with depth (Sites U1486-8). What controls the character manifested at an individual site?

Previous work (e.g. [134]) has demonstrated a strong association between organic matter preservation and the amount of time organic matter is exposed to oxic seawater. Sedimentation rate is one of the key controls on this amount of time [134] and may effect SO_4^{2-} reduction rates by modulating the lability of organic matter available for SO_4^{2-} reduction (e.g. [195, 313]). Our results confirm a strong association between sedimentation rate and total organic carbon (TOC) content at the sites studied on IODP Expeditions 361 and 363 (Figure V.7A). Sedimentation rate, in turn, correlates well with water depth at these sites (Figure V.7B) as well as on a broader global scale (e.g. [219, 343]. Visual inspection of our results suggests that sites with relatively high TOC (e.g. U1482, U1483, and U1485) are associated with the complete consumption of SO_4^{2-} at depth, while those with lower TOC (e.g. U1474, U1475, and U1488) do not have enough reactive organic matter available for complete SO_4^{2-} consumption.

Our results also indicate that advective and/or diffusive supply of SO_4^{2-} from deep fluids plays an important role in some depositional environments. Sites U1486, U1487, and U1488 all feature intervals of increasing $[SO_4^{2-}]$ with depth or, in the case of U1487, invariant $[SO_4^{2-}]$ at a value below seawater $[SO_4^{2-}]$ ($\sim$22 mM). Given the short timescale of diffusion relative to the Myr+ age of these sediments [290], such profiles are not possible without a supply of SO_4^{2-} below the sediment-seawater interface. D'Hondt et al. (2004) previously documented similar $[SO_4^{2-}]$ profiles at several Ocean Drilling Program (ODP) Leg 201 sites. They attributed the profiles to diffusion of SO_4^{2-} from fluids at depth [81]. Although the invariant profile at Site U1487 implies an advective fluid source, similar diffusive processes are likely responsible for the SO_4^{2-} profiles at Sites U1486 and U1488. The proximity of Sites U1486 and U1487 to several hydrothermal vent fields in the Manus Basin [180] suggests that hydrothermal circulation could influence the pore water profiles at these two sites.

The magnitude of $^{34}\varepsilon$ associated with sulfur cycling in our deep ocean sediments is difficult to glean visually from out data. However, our H_2S $\delta^{34}S$ data from Sites U1482 and U1483 suggest that $^{34}\varepsilon$ — a key prerequisite for large $\Delta\delta^{34}S$ — does indeed occur at a couple sites (Figure V.8). The maximum $\Delta\delta^{34}S$ between SO_4^{2-} and H_2S from the same pore water sample reaches 73.7‰ at Site U1482 and 69.4‰ at Site U1483, equivalent to fractionations of 76‰ and 72.3‰ (respectively) after correcting for non-linearities in δ notation space. These are *minimum* constraints on the $^{34}\varepsilon$ associated with S cycling at these sites due to the role of dif-

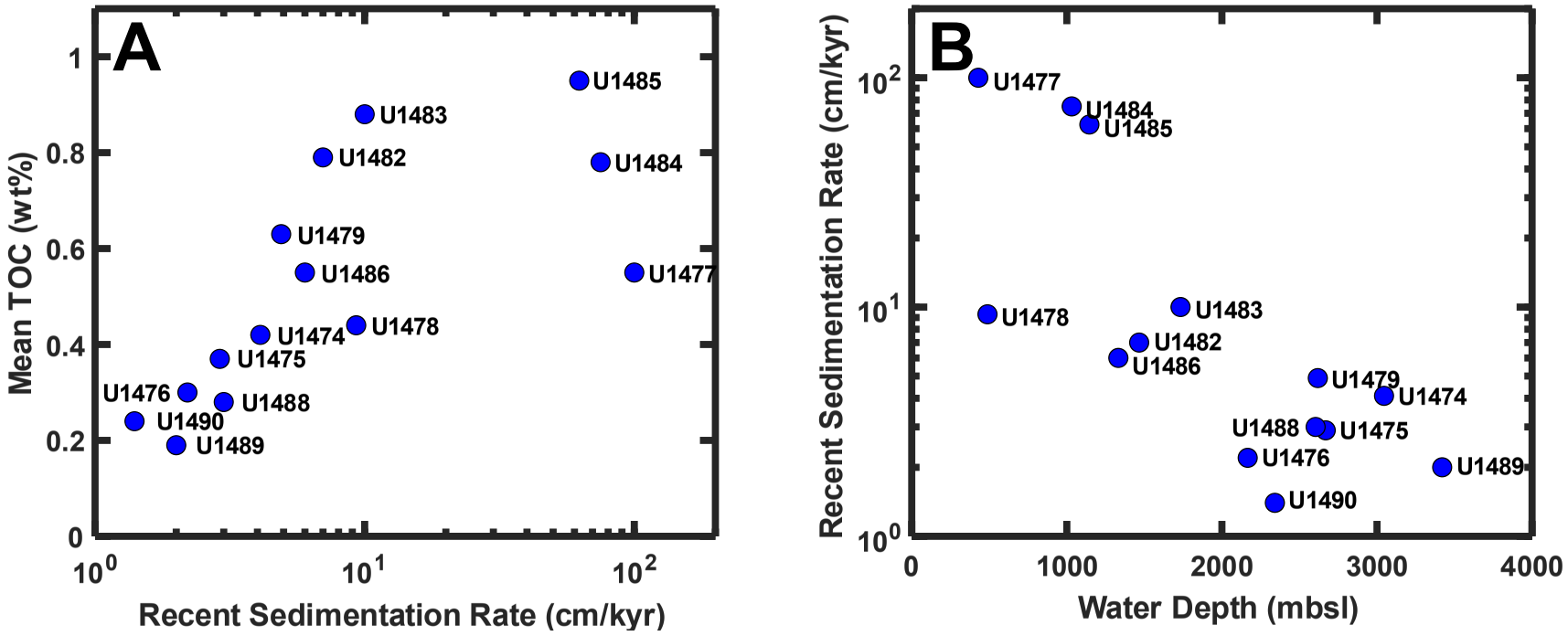

Figure V.7: Relationships among IODP Expeditions 361 and 363 mean total organic carbon, water depth, and sedimentation rate. (Left) Scatter plot of the mean total organic carbon (TOC) content versus the sedimentation rate for the uppermost portion of the sediments cored at IODP Expedition 361 and 363 sites. TOC and sedimentation rate data are from [128, 290]. (Right) Scatter plot of sedimentation rate versus the water depth for hole A at each site.

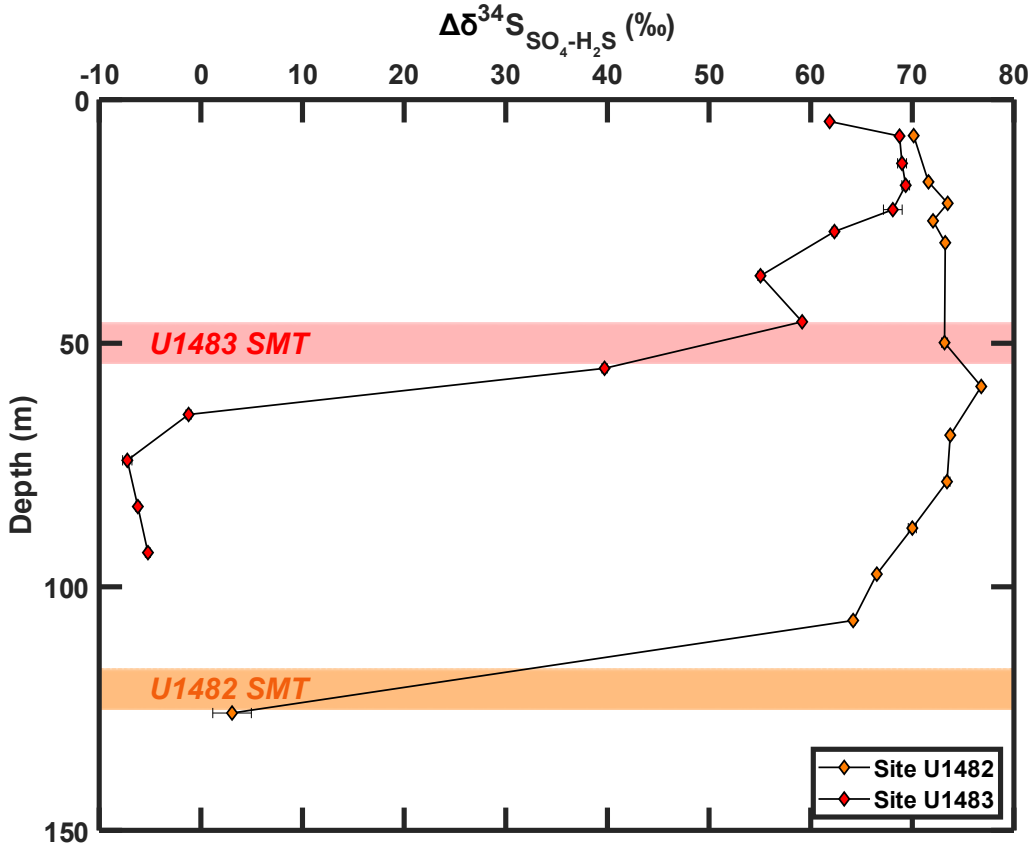

Figure V.8: $\Delta\delta^{34}S_{SO4-H2S}$ (i.e., $\delta^{34}S_{SO42-}$ - $\delta^{34}S_{H2S}$) for Site U1482 (orange diamonds) and Site U1483 (red diamonds). Shaded orange and red boxes denote the approximate location of the sulfate-methane transition at Sites U1482 and U1483, respectively. 1σ uncertainties have been assigned a value of 1‰ in instances in which the uncertainty on H_2S $\delta^{34}S$ was not determined through replicate measurements.

fusion in reducing gradients. Note that Sites U1482 and U1483 are also two of the sites featuring complete consumption of SO_4^{2-} at depth; other sites featuring lower nSRRs are likely to exhibit similarly large $^{34}\varepsilon$. The translation of these large $^{34}\varepsilon$'s into large $\Delta\delta^{34}S$ between seawater SO_4^{2-} and pyrite depends on other sedimentary parameters like iron input, sedimentary porosity, and other variables that influence the balance among rates of diffusion, advection, and reaction in sediments (e.g. Chapter IV Discussion).

Although high $^{34}\varepsilon$ values at other sites seem plausible based on our limited H_2S $\delta^{34}S$ data, additional constraints are needed to make this assertion robust. Our $[SO_4^{2-}]$ and $\delta^{34}S$ data from other sites, in combination with estimated sedimentation rates and known bottom water conditions, fortunately provide constraints

to enable this assertion to be tested. In the following, we refine our $^{34}\varepsilon$ estimates by constructing closed system and open system models of S cycling at our deep ocean sites using a Rayleigh distillation model and our I-CANDI diagenetic model, respectively. We also use I-CANDI to understand the chemical fluxes required to replicate the pore water data available for each site and the sensitivity of the pyrite $\delta^{34}S$ at each site to various sedimentary parameters (especially Fe flux).

V.6.2 Closed system modeling

To provide an initial estimate of $^{34}\varepsilon$ at all sites, we constructed a Rayleigh distillation model of SO_4^{2-} consumption in a manner similar to prior studies (e.g. [162]). We plot our data and the expected model curves in Figure V.9. We estimated $^{34}\varepsilon$ for the uppermost portion of the sediments at each site using the slope of linear trends through the data; these estimates are summarized in Table V.2. Despite the somewhat rapid depletion of SO_4^{2-} with depth at several sites, each estimated $^{34}\varepsilon$ exceeds 30‰ in magnitude, and all except three exceed 40‰. We note again that these are *minimum* estimates of the actual isotopic fractionation, as our Rayleigh distillation model does not account for the effects of diffusion on the profiles. Our H_2S $\delta^{34}S$ data at Sites U1482 and U1483 confirm that the actual $^{34}\varepsilon$ values are larger: the maximum $\Delta\delta^{34}S$ between aqueous SO_4^{2-} and H_2S at these sites exceeds their estimated $^{34}\varepsilon$ values by 30‰ and 34‰, respectively. These large model-data disagreements demonstrate the important influence of diffusion on the pore water profiles at deep ocean sites with relatively low sedimentation rates. Open system models that account for diffusion are clearly needed to improve the accuracy of our $^{34}\varepsilon$ estimates.

V.6.3 Open system modeling

To obtain more accurate estimates of $^{34}\varepsilon$, we used our new reactive transport model for sedimentary diagenesis (I-CANDI) to replicate the $[SO_4^{2-}]$ and SO_4^{2-} $\delta^{34}S$ profiles at each site. We refer the reader to Chapter IV of this thesis for a detailed description of the I-CANDI model. The depth domains, depth discretization, and boundary conditions for the model runs at each site are summarized in Appendix C, Table C.2. In-situ temperatures and pressures were estimated based on water depth, World Ocean Atlas bottom water temperature [200], sediment depth, and an imposed geothermal gradient. Bottom

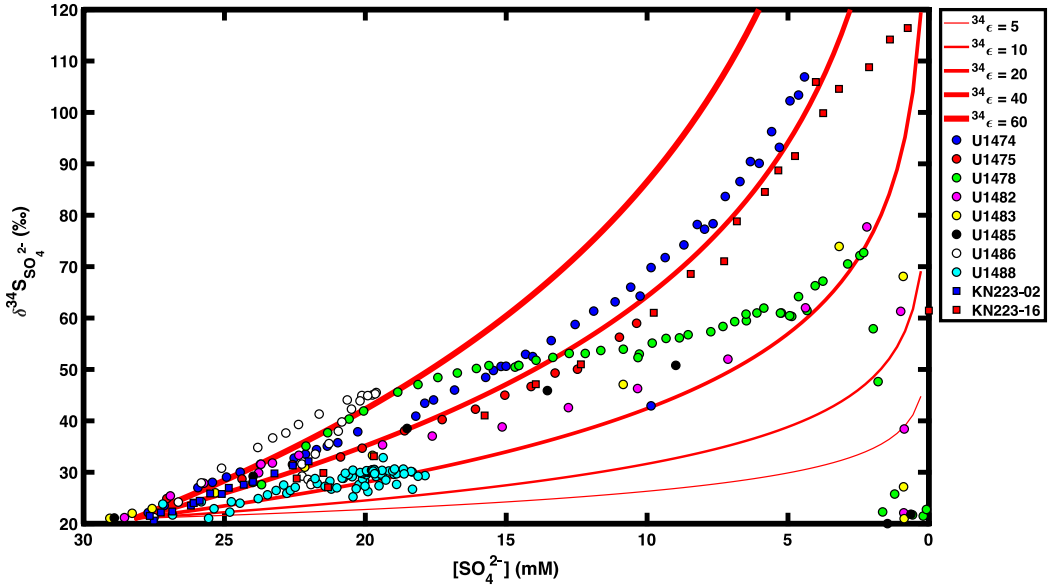

Figure V.9: Rayleigh plot of SO_4^{2-} concentration and $\delta^{34}S$. Red lines of variable thickness denote the trends expected for SO_4^{2-} consumption with a constant isotope fractionation $^{34}\varepsilon$ in a closed system. Trends were constructed assuming an initial $[SO_4^{2-}]$ of 28.2 mM and an initial SO_4^{2-} $\delta^{34}S$ of +21‰.

Table V.2: Rayleigh model initial $^{34}\varepsilon$ estimates for all sites. Table includes the estimated $^{34}\varepsilon$, the lower depth bound for the estimate (in meters below seafloor, mbsf), and the number of concentration/$\delta^{34}S$ data points used to make the estimate. An estimate for Site U1487 was not possible due to the strong influence of fluid advection on the pore water profiles at this site.

Site	Estimated minimum initial $^{34}\varepsilon$ (‰)	Bottom depth for estimate (mbsf)	# of points
U1474	49	20	10
U1475	43	40	3
U1478	52	20	11
U1482	46	20	4
U1483	35	20	5
U1485	31	5	4
U1486	78	20	10
U1487	-	-	-
U1488	63	20	14
KN223-02	49	20	14
KN223-16	39	20	12

water chemistry data were estimated from World Ocean Atlas [200], World Ocean Circulation Experiment [294], and shipboard interstitial water [128, 290] geochemical data. Dissolved inorganic carbon (DIC) and aqueous H_2S were partitioned into their constituent species using shipboard pH measurements [128, 290] (when available) and CO2SYS [346]. At Site KN223-02, we used shipboard alkalinity and DIC measurements [234] for this purpose. Site KN223-16 DIC data were erroneous, and we simplisticly assume a constant pH to calculate acid dissociation constants and partition aqueous species at this site. To ensure steady state, each model iteration was run for a duration equal to 10 times the amount of time required for a sediment parcel to traverse the entire depth domain based on the site's sedimentation rate.

Model fits for the data at each site were obtained by iteratively varying the organic matter rain rate, organic matter reactivity, $^{34}\varepsilon$, and Fe(III) rain rate at each site. Model-data fits were evaluated based on the average least squares offset between fits to the model estimated [SO_4^{2-}] and SO_4^{2-} $\delta^{34}S$ and the real data at each site; lower averages indicated better model fits to the data. We also implemented bottom boundary fluxes of CH_4 and/or SO_4^{2-} to adequately fit the data at some sites. After obtaining a visually good fit between the model output and the site data, we subsequently tested the sensitivity of the model output to particulate organic matter rain rate (RRPOC), Fe(III) rain rate (RRFe), CH_4 flux (if non-zero), and $^{34}\varepsilon$. We ran an additional set of model iterations that varied organic matter and Fe rain rates to $\pm$10%, 5%, and 1% of their original best fit values; CH_4 flux was varied to $\pm$10% of its best fit value when non-zero, and $^{34}\varepsilon$ was modified by $\pm$10‰, 5‰, 2‰, and 1‰. We also tested the sensitivity of the $\delta^{34}S$ of buried pyrite to the Fe(III) rain rate by doing an additional set of runs in which the Fe rain rate was varied from approximately zero up to values equal to or slightly exceeding the initial best fit Fe rain rate.

In the following, we briefly describe and depict our best model-data fits for the [SO_4^{2-}] and SO_4^{2-} $\delta^{34}S$ at each site. We also discuss the sensitivity of modeled pyrite $\delta^{34}S$ to RRPOC and RRFe. We do not depict model profiles from suboptimal RRPOC, RRFe, and $^{34}\varepsilon$ value runs, but briefly note that such runs result in worse model-data fits than those displayed in the figures here; in general, $^{34}\varepsilon$ values that differ by more than 5‰ from the best fit model value conspicuously deviate from our data. Model results are further detailed in Appendix C with Table C.2, Table C.3, and additional sensitivity test figures.

V.6.3.1 Site U1474

Site U1474 best fit model results are show in Figure V.10. A modeled reactive POC rain rate of $\sim$20 $\frac{\mu mol}{m^2 day}$ fuels relatively slow, but steady organic matter remineralization and SO_4^{2-} reduction. The rate constant for the intermediate lability organic matter fraction (k_2) was increased by 50% to yield a better fit than was possible with mixing of multiple fractions in this instance. The model Fe(III) rain rate (6.1 $\frac{\mu mol}{m^2 day}$) is sufficient to produce pyrite at an abundance of $\sim$0.21 wt% (0.11 S wt%) at depth. The mean nSRR with depth is 47.6 $\frac{\mu mol}{m^3 yr}$. A best fit to the SO_4^{2-} $\delta^{34}S$ data is achieved with a very high initial $^{34}\varepsilon$ of 88‰ and a decrease in $^{34}\varepsilon$ to 59‰ below 55 m depth; this step-function decrease in $^{34}\varepsilon$, combined with extremely low aqueous sulfide concentrations, is responsible for the large jump in H_2S $\delta^{34}S$ seen at 55 m depth (Figure V.10). Model underestimates of SO_4^{2-} $\delta^{34}S$ above 30 m depth suggests that the shipboard $[SO_4^{2-}]$ data may be slightly too high and yield nSRRs that are lower than the true initial rates of SO_4^{2-} consumption. The final buried pyrite $\delta^{34}S$ is -17‰, and its abundance is 0.21 wt% (0.11 S wt%). Sensitivity tests suggest that substantially lower ($\geq$ 10‰) final pyrite $\delta^{34}S$ is possible if both RRPOC and RRFe are lowered, although slight decreases are also possible with dramatic increases in RRFe (Figure V.11).

V.6.3.2 Site U1475

Best fit model results for S species at Site U1475 are shown in Figure V.12. The modeled reactive POC rain rate of $\sim$14 $\frac{\mu mol}{m^2 day}$ is lower than that at U1474; some unreactive POC is also included in the overall rain rate of $\sim$90 $\frac{\mu mol}{m^2 day}$ to better match observed shipboard POC abundance measurements ($\leq$ 0.5 wt% [128]). The modeled Fe(III) rain rate is 2.8 $\frac{\mu mol}{m^2 day}$, and the final buried pyrite abundance at depth is $\sim$0.18 wt% (0.09 S wt%). Mean nSRR is slightly lower (40 $\frac{\mu mol}{m^3 yr}$) than at Site U1474, and the modeled $^{34}\varepsilon$ is also lower (57‰). Slight underestimation of $[SO_4^{2-}]$ by the model relative to the data above 50 m depth suggests that this model $^{34}\varepsilon$ underestimates the actual $^{34}\varepsilon$ by several per mil at shallow depths. The final buried pyrite $\delta^{34}S$ at the bottom boundary of the model is -13.8‰; the true pyrite $\delta^{34}S$ is likely lower based on the underestimated $^{34}\varepsilon$ just described. Sensitivity tests suggest that lowering or substantially increasing the Fe(III) rain rate can lower pyrite $\delta^{34}S$ to more negative values (Figure C.1).

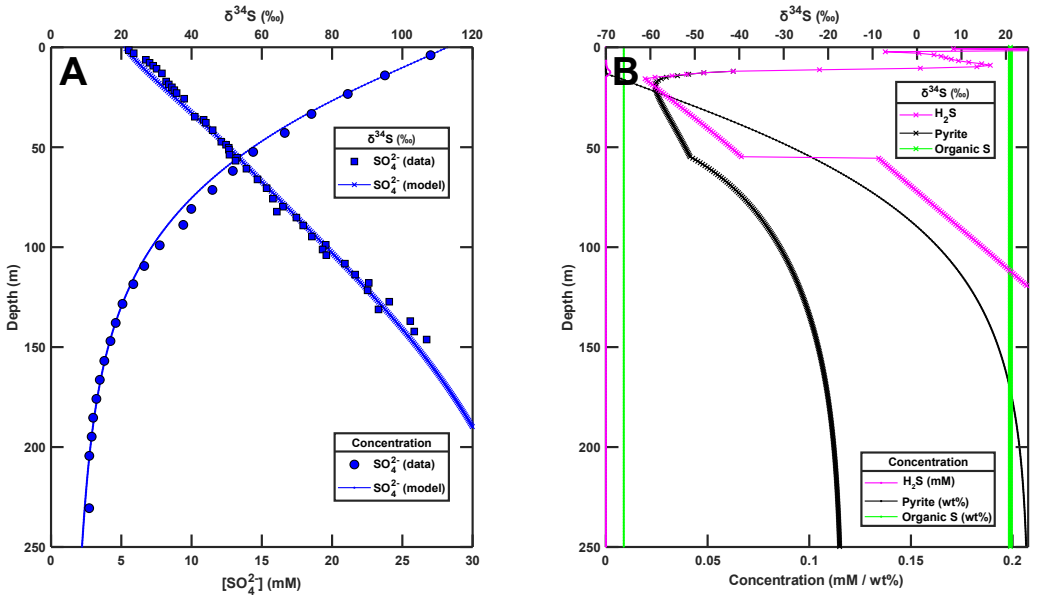

Figure V.10: Site U1474 best fit model results for S species. (A) Data (filled markers) and best fit model results (blue lines) for SO_4^{2-} concentration and $\delta^{34}S$ with depth at Site U1474. (B) Best fit model concentrations (lines with "." markers) and $\delta^{34}S$ (lines with "x" markers) for H_2S, pyrite, and organic S at Site U1474. The step-function increase in H_2S $\delta^{34}S$ at 55 m depth results from the combination of aqueous sulfide concentrations below the I-CANDI absolute error tolerance and an ascribed 29‰increase in $^{34}\varepsilon$ at this depth.

V.6.3.3 Site U1478

Best fit model results for the main S species at Site U1478 are depicted in Figure V.13. Our model fit is imperfect and slightly underestimates the decrease in $[SO_4^{2-}]$ with depth between 10 m and 30 m depth; this also results in an underestimate of SO_4^{2-} $\delta^{34}S$ at these depths. Still, the model fit requires a very large $^{34}\varepsilon$ of 84‰ to adequately fit the data. We also apply a methane flux of 4.5 $\frac{\mu mol}{m^2 day}$ at the bottom boundary to attain a SMT depth consistent with shipboard observations. The Fe rain rate imposed in this model run is 40.5 $\frac{\mu mol}{m^2 day}$ and results in a final pyrite abundance of ~0.55 wt% (0.29 S wt%) at depth. Mean nSRR is 2500 $\frac{\mu mol}{m^3 yr}$ and is over an order of magnitude higher than at Sites U1474 and U1475. Pyrite $\delta^{34}S$ is highly depleted (< -50‰) until the SMT, at which point a jump in pyrite abundance and $\delta^{34}S$ occurs. The final pyrite $\delta^{34}S$ at depth remains quite ^{34}S-depleted at a $\delta^{34}S$ of -38.2‰ and an abundance of 0.55 wt% (0.29 S wt%). Sensitivity studies in which the POC and Fe rain rates were varied indicate that this final pyrite $\delta^{34}S$ is most sensitive to the Fe rain rate, with lower final pyrite

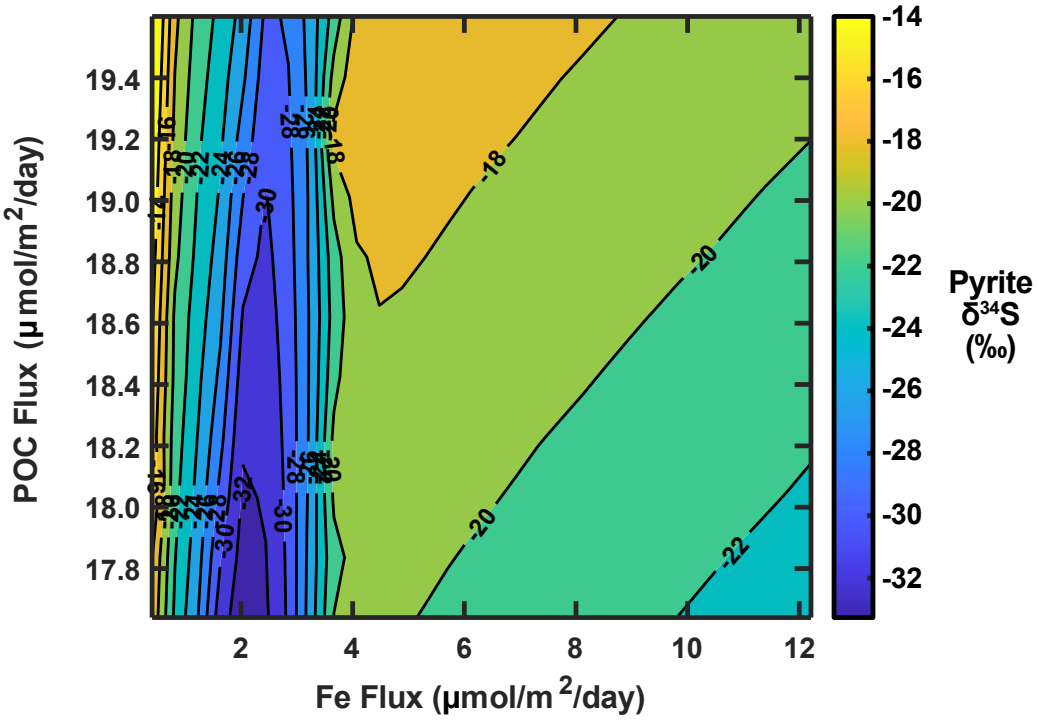

Figure V.11: Contour plot for the $\delta^{34}S$ of pyrite exiting the bottom of the model as a function of POC rain rate (vertical axis) and Fe(III) rain rate (horizontal axis) at Site U1474.

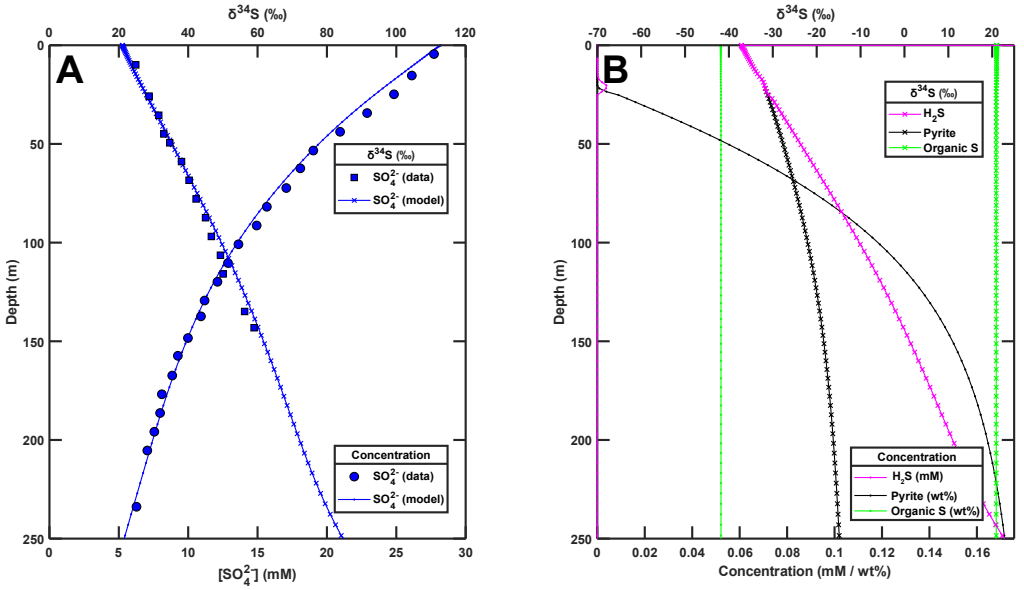

Figure V.12: Site U1475 best fit model results for S species. (A) Data (filled markers) and best fit model results (blue lines) for SO_4^{2-} concentration and $\delta^{34}S$ with depth at Site U1475. (B) Best fit model concentrations (lines with "." markers) and $\delta^{34}S$ (lines with "x" markers) for H_2S, pyrite, and organic S at Site U1475.

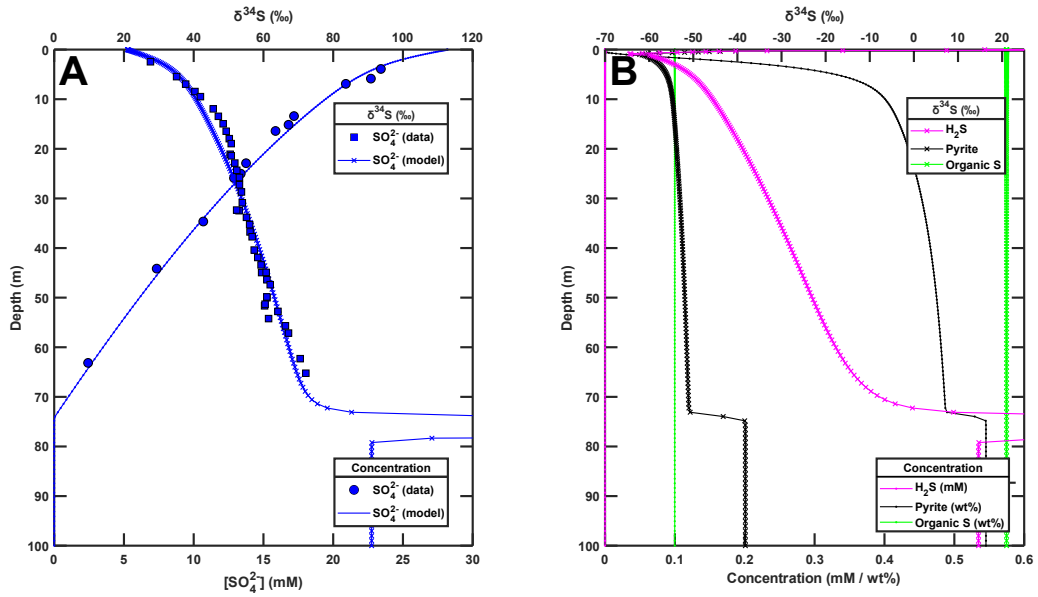

Figure V.13: Site U1478 best fit model results for S species. (A) Data (filled markers) and best fit model results (blue lines) for SO_4^{2-} concentration and $\delta^{34}S$ with depth at Site U1478. (B) Best fit model concentrations (lines with "." markers) and $\delta^{34}S$ (lines with "x" markers) for H_2S, pyrite, and organic S at Site U1478.

$\delta^{34}S$ possible at lower Fe rain rates (Figure C.2). However, H_2S begins to accumulate to mM levels at Fe rain rates $\leq\sim 35\ \frac{\mu mol}{m^2 day}$, a result inconsistent with shipboard reports that make no mention of sulfidic pore waters [128].

V.6.3.4 Site U1482

Site U1482 is the first of several sites for which we had significant difficulties obtaining good model-data fits; our best fit result thus far is shown in Figure V.14. The nearly linear nature of the $[SO_4^{2-}]$ profile dictates that most SO_4^{2-} reduction at the site either occurs at the SMT or is closely balanced by sulfide reoxidation. Here, we model the profiles by forcing most SO_4^{2-} reduction to occur at the SMT and apply a methane flux of 2.2 $\frac{\mu mol}{m^2 day}$ plus a reactive POC rain rate of 222 $\frac{\mu mol}{m^2 day}$. Still, the model fit underestimates SO_4^{2-} $\delta^{34}S$ above 20 m depth and depletes SO_4^{2-} too quickly at intermediate (20 to 100 m) depths. Attempting to fit the profile through increased sulfide reoxidation requires that Fe(III) abundances and the rate constant for sulfide oxidation by Fe(III) both be several orders of magnitude higher than the values used in other studies [40, 65]. The best fit $^{34}\varepsilon$ is 68‰. The applied Fe(III) rain rate of 7.7 $\frac{\mu mol}{m^2 day}$ yields a

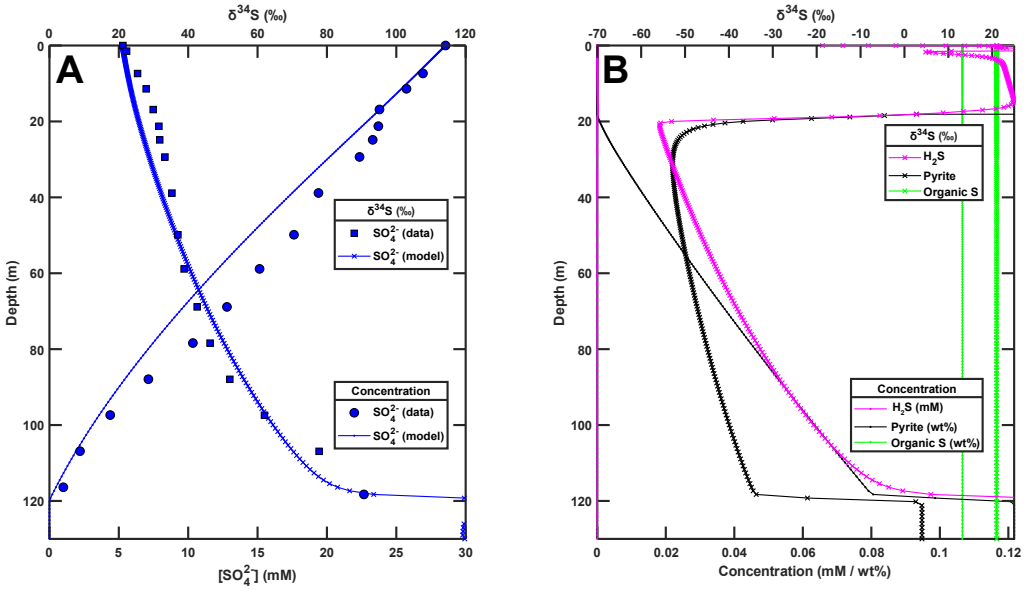

Figure V.14: Site U1482 best fit model results for S species. (A) Data (filled markers) and best fit model results (blue lines) for SO_4^{2-} concentration and $\delta^{34}S$ with depth at Site U1482. (B) Best fit model concentrations (lines with "." markers) and $\delta^{34}S$ (lines with "x" markers) for H_2S, pyrite, and organic S at Site U1482.

final pyrite abundance of 0.11 wt% (0.06 S wt%) with a $\delta^{34}S$ of 2.4‰. Sensitivity tests show a similar relationship of pyrite $\delta^{34}S$ with RRPOC and RRFe as at Site U1474 (Figure C.3).

V.6.3.5 Site U1483

Site U1483 model fits feature shortcomings similar to those at Site U1482 (Figure V.15). Here, we are unable to replicate the curvature of the $[SO_4^{2-}]$ profile under steady state model runs; the increase in the $[SO_4^{2-}]$ gradient below 20 m depth should not be stable over time and may reflect a recent change in the flux of methane diffusing from deeper sediments. We apply a methane flux of 12.1 $\frac{\mu mol}{m^2 day}$ and a reactive POC rain rate of 105 $\frac{\mu mol}{m^2 day}$ to attain the depicted model profiles. These model results match the SO_4^{2-} $\delta^{34}S$ reasonably well, but predict too large a $[SO_4^{2-}]$ decrease at all depths above the SMT. The best fit $^{34}\varepsilon$ of 75‰ is reasonably consistent with the H_2S $\delta^{34}S$ data that we have collected. The final abundance of buried pyrite at depth is 0.08 wt% (0.04 S wt%). The $\delta^{34}S$ of buried pyrite (1.4‰) is relatively insensitive to RRPOC, but quite sensitive to changes in RRFe (Figure C.4). We also note that organic sulfur is a significant sink for

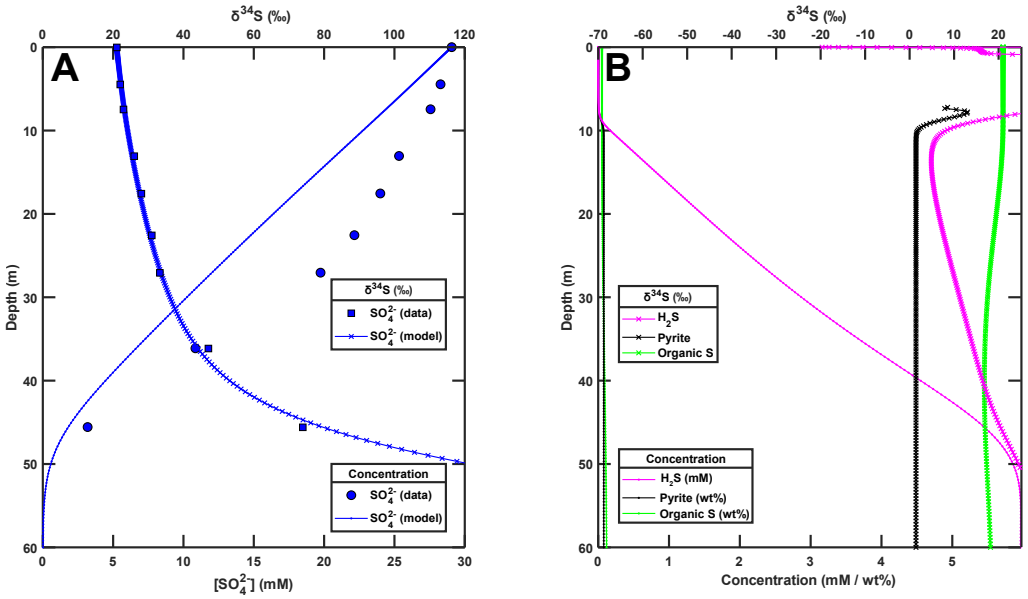

Figure V.15: Site U1483 best fit model results for S species. (A) Data (filled markers) and best fit model results (blue lines) for SO_4^{2-} concentration and $\delta^{34}S$ with depth at Site U1483. (B) Best fit model concentrations (lines with "." markers) and $\delta^{34}S$ (lines with "x" markers) for H_2S, pyrite, and organic S at Site U1483.

sulfur at this site; sulfurization causes the organic matter to become S-enriched and deviate from seawater SO_4^{2-} in its $\delta^{34}S$ by a few per mil at depth.

V.6.3.6 Site U1485

Site U1485 features the highest sedimentation rates of any of the sites studied here, and both RRPOC and nSRR are correspondingly high (Figure V.16). The modeled reactive POC rain rate is 682 $\frac{\mu mol}{m^2 day}$, and the resulting mean nSRR is 19500 $\frac{\mu mol}{m^3 yr}$. The model once again predicts too much SO_4^{2-} consumption above the SMT; the estimated $^{34}\varepsilon$ of 66‰ is therefore a minimum estimate on the true fractionation associated with sedimentary S cycling at this site. The applied Fe(III) rain rate (82.5 $\frac{\mu mol}{m^2 day}$) yields a final pyrite abundance of 0.23 wt% (0.12 S wt%) and a final pyrite $\delta^{34}S$ of +3.3‰. Sensitivity tests (Figure C.5) demonstrate similar relationships between RRPOC, RRFe, and pyrite $\delta^{34}S$ to those at Site U1474.

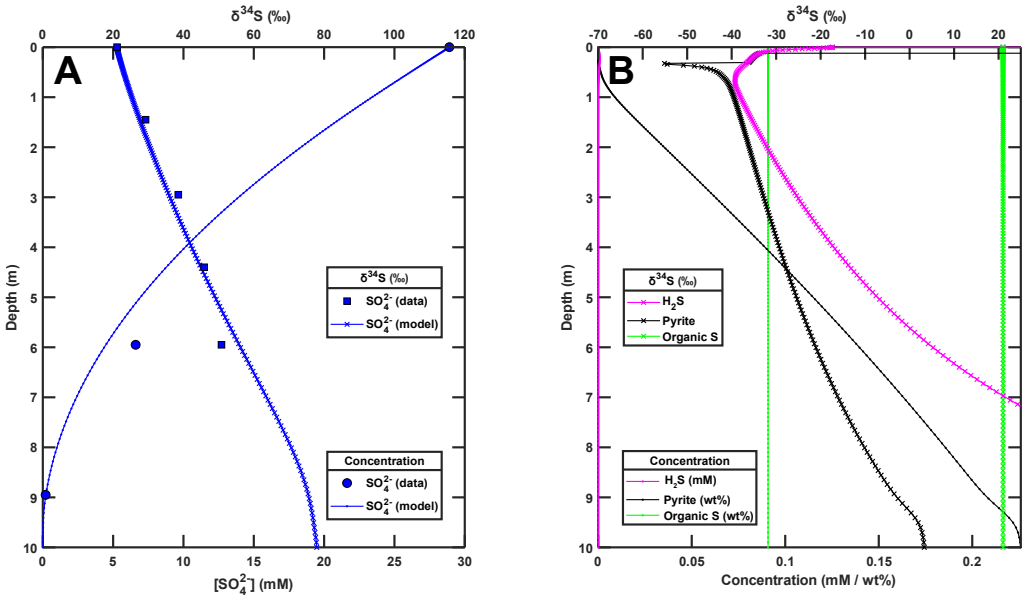

Figure V.16: Site U1485 best fit model results for S species. (A) Data (filled markers) and best fit model results (blue lines) for SO_4^{2-} concentration and $\delta^{34}S$ with depth at Site U1485. (B) Best fit model concentrations (lines with "." markers) and $\delta^{34}S$ (lines with "x" markers) for H_2S, pyrite, and organic S at Site U1485.

V.6.3.7 Site U1486

Model best fits at Site U1486 were attained using a constant concentration bottom bound for SO_4^{2-}, as the base of the profile at this site is thought to have been the basement [290]. This SO_4^{2-} was assigned a concentration of 23.5 mM with a $\delta^{34}S$ of 27‰. The modeled reactive POC rain rate is 77 $\frac{\mu mol}{m^2 day}$ with a mean nSRR of 1100 $\frac{\mu mol}{m^3 yr}$; this nSRR is higher than might otherwise be expected due to the diffusive flux of SO_4^{2-} emanating from the basement. The estimated $^{34}\varepsilon$ of 74‰ and applied Fe(III) rain rate of ~25 $\frac{\mu mol}{m^2 day}$ collectively result in burial of pyrite at a final abundance of 0.26 wt% (0.49 S wt%) with a $\delta^{34}S$ of -41.7‰. Pyrite even more depleted in ^{34}S is possible at lower RRFe (Figure C.6).

V.6.3.8 Site U1487

Site U1487's relatively invariant depth profiles for most pore water constituents [290] strongly suggest a dominance of advection on the profiles. However, our efforts to replicate the profiles at this site were unsuccessful; applying a flux of SO_4^{2-} at the bottom boundary results in a profile with a local minimum in $[SO_4^{2-}]$

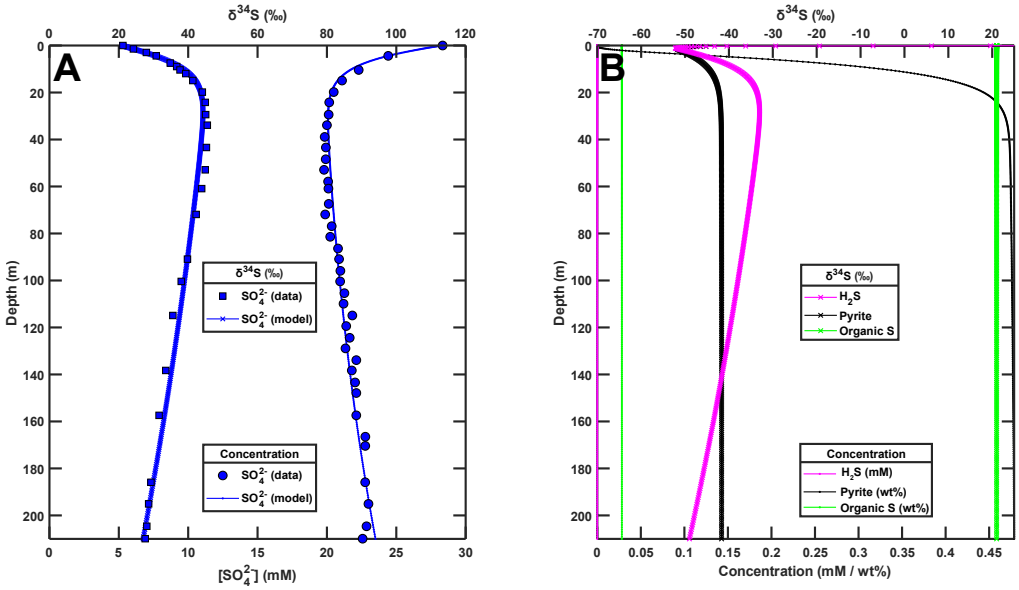

Figure V.17: Site U1486 best fit model results for S species. (A) Data (filled markers) and best fit model results (blue lines) for SO_4^{2-} concentration and $\delta^{34}S$ with depth at Site U1486. (B) Best fit model concentrations (lines with "." markers) and $\delta^{34}S$ (lines with "x" markers) for H_2S, pyrite, and organic S at Site U1486.

akin to those at Sites U1486 and U1488. This suggests that the pore water at Site U1487 is advecting too quickly for any reaction-driven chemical gradients to be maintained and/or that the advection is primarily lateral. Violation of I-CANDI's assumption of 1-D (vertical) motion negates any model results for this site, and we exclude them here.

V.6.3.9 Site U1488

Best fit model results for Site U1488 are depicted in Figure V.18. We must apply a SO_4^{2-} flux at the bottom boundary to replicate the reversal in gradient seen in the $[SO_4^{2-}]$ profile; we here apply a flux of 0.3 $\frac{\mu mol}{m^2 day}$ and assign the flux a mantle-like $\delta^{34}S$ of 0‰. A higher, seawater-like $\delta^{34}S$ for this flux may be possible, but would require a much higher magnitude for the flux and proportionally higher nSRR at depth. Alternatively, a diffusive flux from basement like that used to model Site U1486 could also yield a good fit. A reactive POC rain rate of 24 $\frac{\mu mol}{m^2 day}$ supports a mean nSRR of 147 $\frac{\mu mol}{m^3 yr}$, and the best fit $^{34}\varepsilon$ is 48‰. The applied Fe(III) rain rate is 3.3 $\frac{\mu mol}{m^2 day}$ and yields a final buried pyrite abundance of 0.23 wt% (0.12 S wt%). The final pyrite $\delta^{34}S$ is -21.7‰. Sensitivity studies demonstrate relatively

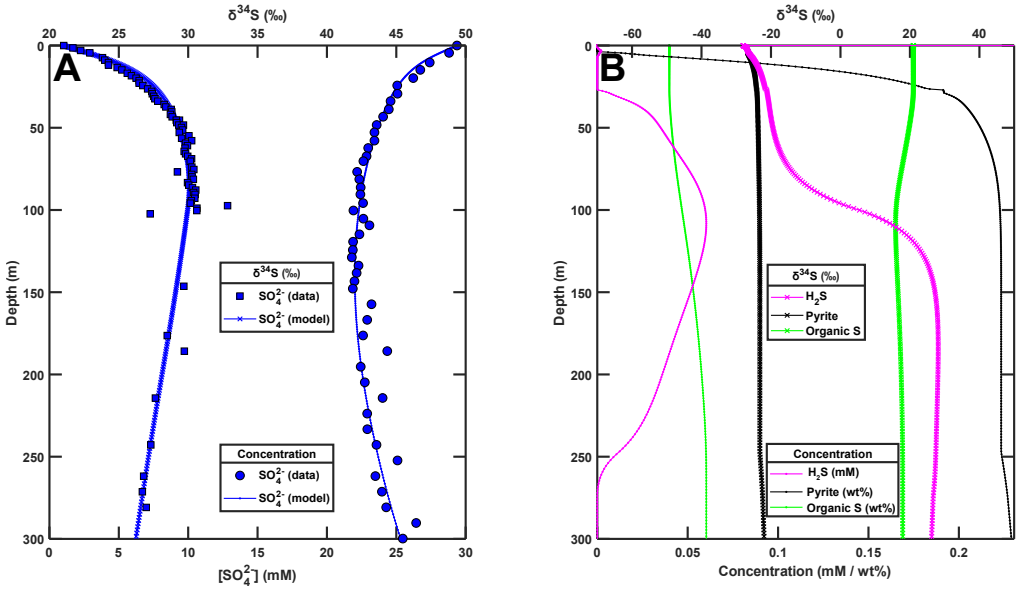

Figure V.18: Site U1488 best fit model results for S species. (A) Data (filled markers) and best fit model results (blue lines) for SO_4^{2-} concentration and $\delta^{34}S$ with depth at Site U1488. (B) Best fit model concentrations (lines with "." markers) and $\delta^{34}S$ (lines with "x" markers) for H_2S, pyrite, and organic S at Site U1488.

little dependence of this value on RRPOC and a stronger dependence on RRFe (Figure C.7).

V.6.3.10 Site KN223-02

Site KN223-02 data are available only down to around 20 m depth, but can be fit reasonably well with I-CANDI (Figure V.19) assuming a relatively low sedimentation rate of 2 $\frac{\text{cm}}{\text{kyr}}$ — sedimentation rate for this site was not estimated in shipboard studies [234]. The best fit was attained with a reactive POC rain rate of 7.9 $\frac{\mu\text{mol}}{\text{m}^2\text{day}}$, a Fe(III) rain rate of 1.65 $\frac{\mu\text{mol}}{\text{m}^2\text{day}}$, and a $^{34}\varepsilon$ of 57‰. Mean nSRR over the cored interval is 56.2 $\frac{\mu\text{mol}}{\text{m}^3\text{yr}}$. Pyrite is buried at the lowest modeled depth (30 m) with an abundance of 0.06 wt% (0.03 S wt%) and a $\delta^{34}S$ of -30.4‰. Model results can likely be considered lower bounds on the actual pyrite abundance assuming that SO_4^{2-} reduction continues below the lowermost cored depth at the site. Sensitivity of pyrite $\delta^{34}S$ to RRPOC and RRFe is similar to that at Site U1474 (Figure C.8).

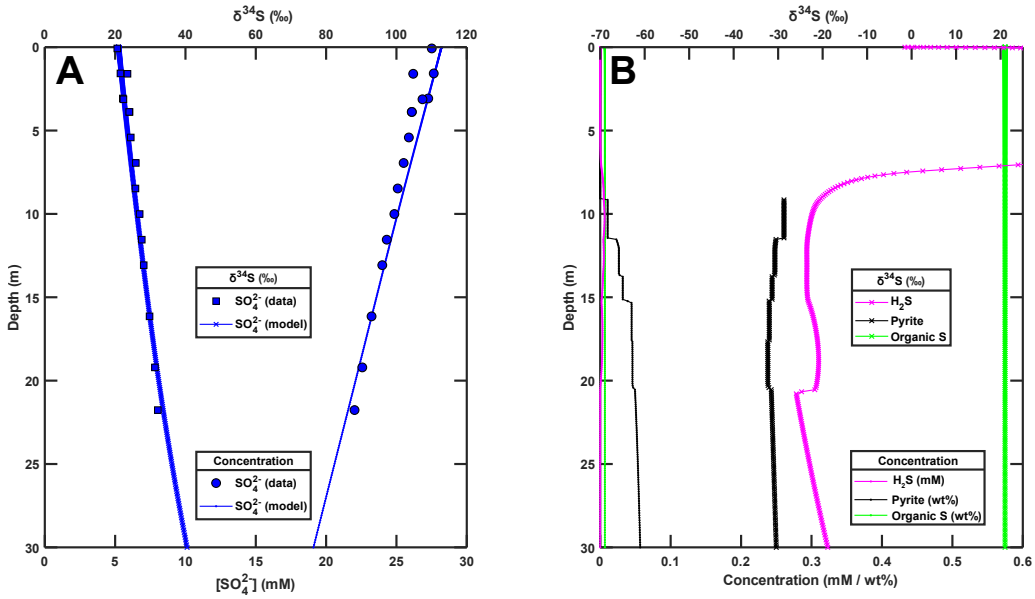

Figure V.19: Site KN223-02 best fit model results for S species. (A) Data (filled markers) and best fit model results (blue lines) for SO_4^{2-} concentration and $\delta^{34}S$ with depth at Site KN223-02. (B) Best fit model concentrations (lines with "." markers) and $\delta^{34}S$ (lines with "x" markers) for H_2S, pyrite, and organic S at Site KN223-02.

V.6.3.11 Site KN223-16

The sedimentation rate at Site KN223-16 is also uncertain. However, we are able to attain a relatively good model-data fit if a rate similar to that at other sites on the Bermuda Rise [12] is applied (Figure V.20). The best fit features a reactive POC rain rate of 162 $\frac{\mu mol}{m^2 day}$ and a Fe(III) rain rate of 29.7 $\frac{\mu mol}{m^2 day}$. Mean nSRR is 1900 $\frac{\mu mol}{m^3 yr}$ and occurs with a $^{34}\varepsilon$ of 79‰. Buried pyrite exiting the model has an abundance of 0.12 wt% (0.06 S wt%) and a $\delta^{34}S$ of -13.9‰. Lower pyrite $\delta^{34}S$ is possible if RRPOC is reduced and/or RRFe is either increased or dramatically lowered (Figure C.9).

V.6.3.12 Summary and comparison with closed system results

The open system modeling described above has shown that accounting for diffusion indeed alters $^{34}\varepsilon$ estimates to higher values than those attained via closed system modeling. In most cases, the values estimated from I-CANDI model fits are higher than the closed system estimates by at least 20‰ (Table V.3). Only

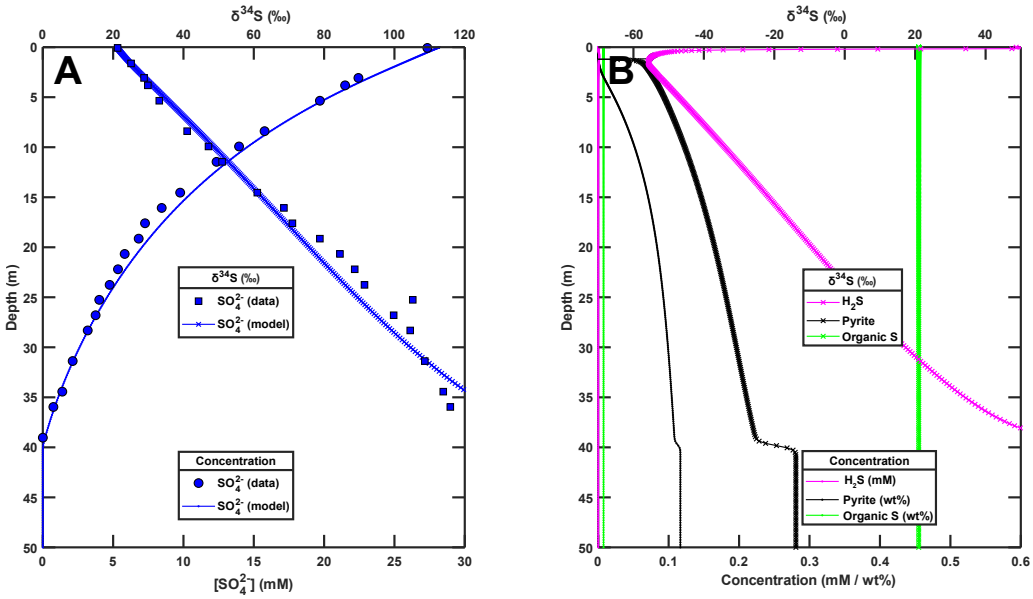

Figure V.20: Site KN223-16 best fit model results for S species. (A) Data (filled markers) and best fit model results (blue lines) for SO_4^{2-} concentration and $\delta^{34}S$ with depth at Site KN223-16. (B) Best fit model concentrations (lines with "." markers) and $\delta^{34}S$ (lines with "x" markers) for H_2S, pyrite, and organic S at Site KN223-16.

Sites U1486 and U1488 feature lower estimates, presumably due to the influence of the bottom flux of SO_4^{2-} at these sites.

Interestingly, the modeled $\delta^{34}S$ of pyrite at these sites is often substantially higher than the estimated $^{34}\varepsilon$ would predict. This ^{34}S enrichment is expected with the distillation of SO_4^{2-} and aqueous H_2S from pore waters, but is still higher in the models than observed in many deep ocean pyrite $\delta^{34}S$ measurements [4, 37, 38, 115, 158, 188, 197, 220, 222, 266, 293, 329]. Although shipboard geochemical data [128, 290] do not constrain oxygen penetration depth or the locations of sedimentary redox boundaries at the IODP sites, Murray et al. (2014) [234] measured dissolved oxygen profiles at Sites KN223-02 and KN223-16. These data demonstrate oxygen penetration depth to be $\sim$2 m at Site KN223-02 and $<$ 5 cm at Site KN223-16; our best fit model runs, in contrast, yield oxygen penetration depths of $\sim$1.8 m and $\sim$0.3 m (respectively) at these two sites. Based on the large disparity between the data and the model at Site KN223-16, we suspect that I-CANDI is overestimating the depths of the oxic-suboxic and suboxic-anoxic redox boundaries at most of the sites modeled here. Such overestimates would result in a decrease in the ability of diffusion to supply fresh

Table V.3: Comparison of I-CANDI open system model and Rayleigh model initial $^{34}\varepsilon$ estimates for all sites.

Site	I-CANDI initial $^{34}\varepsilon$ (‰)	Rayleigh model $^{34}\varepsilon$ (‰)	Difference (‰)
U1474	88	49	39
U1475	57	43	14
U1478	84	52	32
U1482	68	46	22
U1483	75	35	40
U1485	66	31	34
U1486	74	78	-4
U1488	48	63	-15
KN223-02	57	49	8
KN223-16	79	39	40

seawater SO_4^{2-} to the zone of SO_4^{2-} reduction in the sediments and a more "closed" system in the model than in reality. Additional runs at Site U1478 with an added, extremely labile organic matter fraction tentatively confirm this hypothesis and show that final pyrite $\delta^{34}S$ can vary by over 15‰ with relatively little observable effects on the modeled SO_4^{2-} concentration and $\delta^{34}S$ profiles (Figure C.10). However, more work is needed to tease apart this relationship in detail.

V.6.4 The Fe dependence of buried pyrite abundance and $\delta^{34}S$

The $\delta^{34}S$ of buried pyrite exhibits a complex relationship with total Fe input among the sites examined in this study, but a few general trends exist among sites where an upward flux of SO_4^{2-} is not important. To illustrate these trends, we will walk through the contour plot of pyrite $\delta^{34}S$ as a function of RRPOC and RRFe at Site U1474 (Figure V.21) in more detail.

At an RRPOC of 19.6 $\frac{\mu mol}{m^2 day}$, pyrite $\delta^{34}S$ exhibits a decrease as RRFe increases from 0 to $\sim$2.5 $\frac{\mu mol}{m^2 day}$ (Figure V.21). Examination of depth profiles of the concentration and $\delta^{34}S$ of S phases for the first non-zero RRFe run (Figure V.22) and the minimum $\delta^{34}S$ run (Figure V.23) shows that this initial decrease results from increased scavenging of ^{34}S-depleted aqueous sulfide at depth. Note that H_2S $\delta^{34}S$ initially decreases from an imposed boundary condition value of

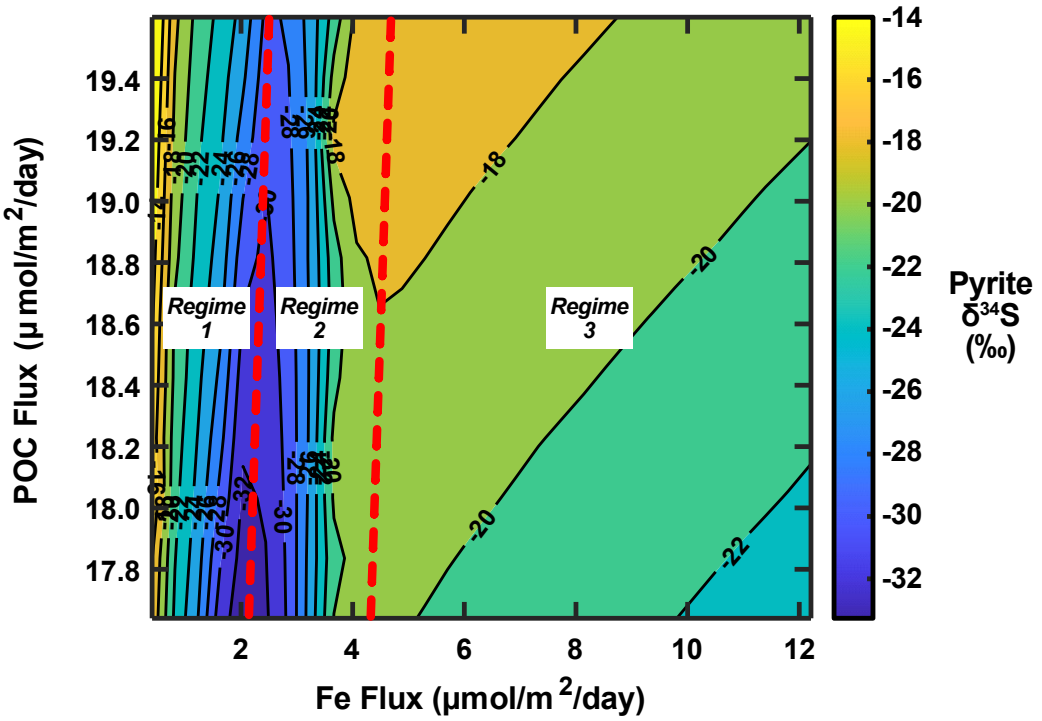

Figure V.21: Replicate of Figure V.11, now with different pyrite $\delta^{34}S$ regimes labeled. The characteristics of each regime are described in the text. Red dashed lines denote boundaries between successive regimes.

+21‰ at the sediment-water interface to a minimum of about -19‰ at ∼12 m depth. Within the upper ∼12 m of sediment, the net pyrite precipitation flux increases from about 2.1 x $10^{-11}\,\frac{\text{mol}}{\text{m}^2\text{s}}$ upon the initial addition of Fe to 1.2 x $10^{-10}\,\frac{\text{mol}}{\text{m}^2\text{s}}$ when RRFe = ∼2.5 $\frac{\mu\text{mol}}{\text{m}^2\text{day}}$; the depth of the maximum rate of pyrite precipitation also increases from ∼3.75 m to ∼5.25 m. Rates of pyrite formation higher than $10^{-15}\,\frac{\text{mol}}{\text{m}^2\text{s}}$ persist down to only 13 m depth in the former run and to 16 m depth in the latter; thus, very little H_2S of higher $\delta^{34}S$ below these depths is scavenged. Although the decrease in H_2S $\delta^{34}S$ is largely imposed by the top boundary condition in this case, a similar decrease could occur in natural sediments if initial, rapid microbial sulfate reduction (MSR) with labile organic matter substrate were characterized by a lower $^{34}\varepsilon$ (e.g. [195, 313]). This regime, "Regime 1," may not exist in natural sediments in which no initial increase in the magnitude of $^{34}\varepsilon$ with depth occurs.

Following this initial decrease in pyrite $\delta^{34}S$, further increases in RRFe result in a steady increase in pyrite $\delta^{34}S$ until a maximum is reached at an RRFe of ∼4.5 $\frac{\mu\text{mol}}{\text{m}^2\text{day}}$. This interval is characterized by slight declines in $[H_2S]$ as Fe additions

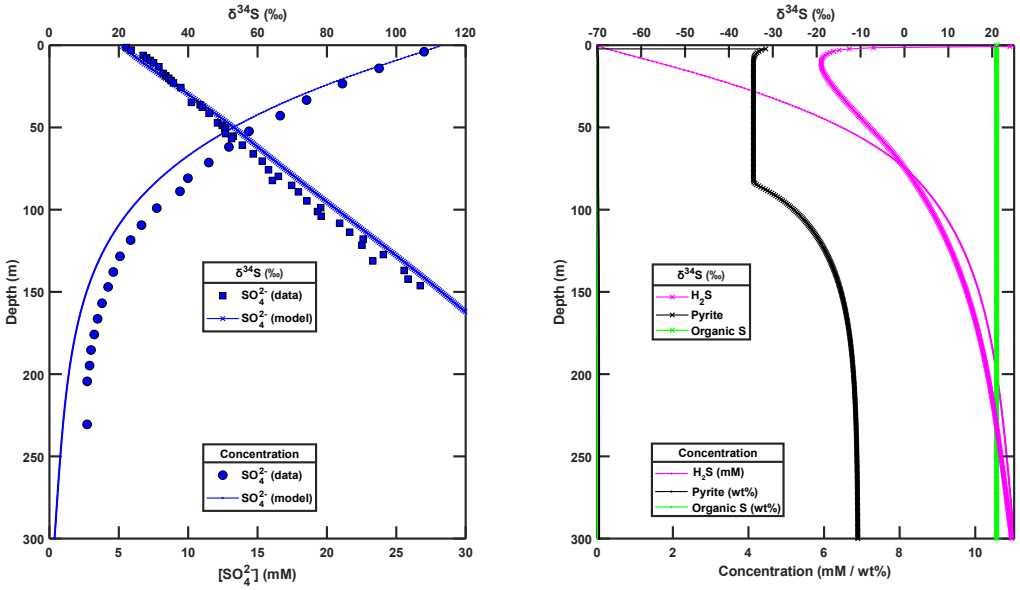

Figure V.22: Site U1474 model results for first non-zero RRFe run. (A) Data (filled markers) and model results (blue lines) for SO_4^{2-} concentration and $\delta^{34}S$ with depth at Site U1474 for a RRFe of $\sim$0.41 $\frac{\mu mol}{m^2 day}$ (B) Model concentrations (lines with "." markers) and $\delta^{34}S$ (lines with "x" markers) for H_2S, pyrite, and organic S.

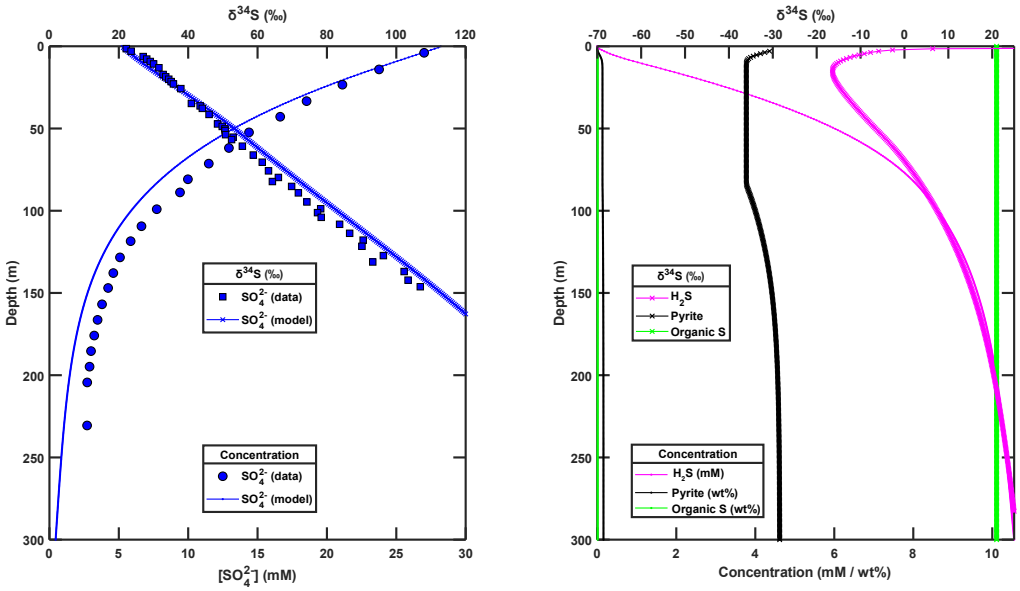

Figure V.23: Site U1474 model results for minimum pyrite $\delta^{34}S$ run. (A) Data (filled markers) and model results (blue lines) for SO_4^{2-} concentration and $\delta^{34}S$ with depth at Site U1474 for a RRFe of $\sim$2.44 $\frac{\mu mol}{m^2 day}$ (B) Model concentrations (lines with "." markers) and $\delta^{34}S$ (lines with "x" markers) for H_2S, pyrite, and organic S.

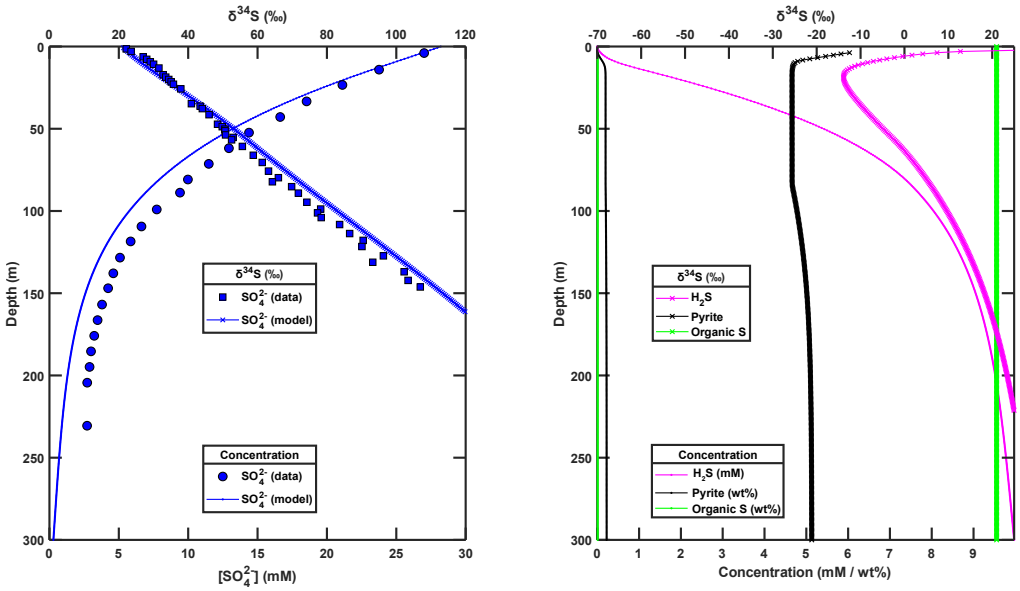

Figure V.24: Site U1474 model results for model run with RRFe just below the pyrite $\delta^{34}S$ maximum. (A) Data (filled markers) and model results (blue lines) for SO_4^{2-} concentration and $\delta^{34}S$ with depth at Site U1474 for a RRFe of $\sim$3.66 $\frac{\mu mol}{m^2 day}$ (B) Model concentrations (lines with "." markers) and $\delta^{34}S$ (lines with "x" markers) for H_2S, pyrite, and organic S.

allow more H_2S to be scavenged. Such scavenging is illustrated by the depth profiles of S species from a model run just prior to the $\delta^{34}S$ maximum (Figure V.24). Here, the flux of pyrite formation in the upper 12 m is even higher at 1.7 x $10^{-10} \frac{mol}{m^2 s}$, and the depth of the maximum rate of pyrite formation is $\sim$8.25 m. Rates of pyrite formation higher than $10^{-15} \frac{mol}{m^2 s}$ persist down to 20 m depth, thereby capturing more H_2S of elevated $\delta^{34}S$. H_2S remains present at high (mM) concentrations. At the maximum, a sudden switch in the character of the depth profiles occurs (Figure V.25): H_2S is nearly fully consumed by Fe and is present at only μM levels. This switch is associated with an RRFe threshold at which Fe(III) becomes abundant enough to persist at depth in the sediment (Figures C.11 and C.12); i.e., there is insufficient labile organic matter to facilitate complete Fe(III) consumption. Buried pyrite abundance also increases in step with RRFe in this regime (until the maximum $\delta^{34}S$ is reached) and in Regime 1, indicating an Fe limitation on pyrite formation. This regime, "Regime 2," is akin to a transition from carbonate-dominated system with very little siliciclastic/Fe(III) input to a system with moderate siliclastic input.

Pyrite $\delta^{34}S$ begins to slowly decrease again with additional increases in RRFe beyond the $\delta^{34}S$ maximum at $\sim$4.5 $\frac{\mu mol}{m^2 day}$. Depth profiles of S-bearing species

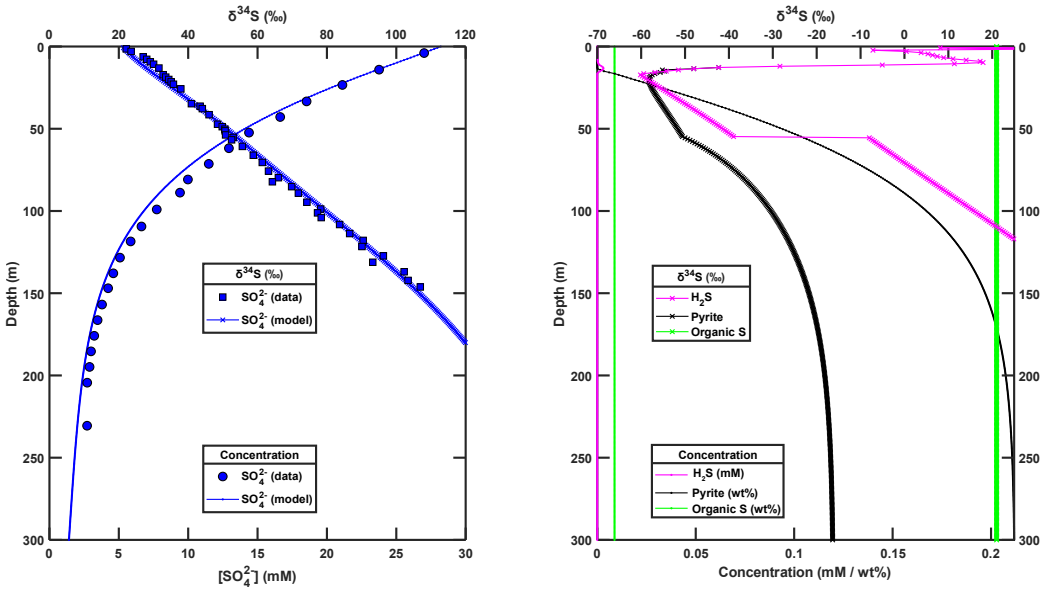

Figure V.25: Site U1474 model results for model run at the pyrite $\delta^{34}S$ maximum. (A) Data (filled markers) and model results (blue lines) for SO_4^{2-} concentration and $\delta^{34}S$ with depth at Site U1474 for a RRFe of $\sim$4.48 $\frac{\mu mol}{m^2 day}$ (B) Model concentrations (lines with "." markers) and $\delta^{34}S$ (lines with "x" markers) for H_2S, pyrite, and organic S.

(Figure V.26) and of dissolved constituents (Figure C.13) suggest that this decrease results from a combination of more complete scavenging of aqueous H_2S at relatively shallow (< 20 m) sediment depths and a decrease in the net amount of SO_4^{2-} reduction; i.e., the final $[SO_4^{2-}]$ at the model bottom boundary (300 m depth) becomes higher as RRFe increases. Final buried pyrite abundances decrease with increasing RRFe, and dissolved Fe^{2+} accumulates in sedimentary pore waters at depth. These trends indicate a transition to sulfide limitation of pyrite burial, with increasing RRFe causing a progressively greater contribution of Fe reduction to POC remineralization at the expense of SO_4^{2-} reduction. The slope of the contour lines in Figure V.21 indicates that addition of POC could facilitate more SO_4^{2-} reduction and force the diagenetic regime back toward Fe limitation of pyrite burial. This regime, "Regime 3," describes sites in which SO_4^{2-} reduction creates an insufficient amount of H_2S to scavenge all of the Fe^{2+} generated through Fe reduction. Regime 3 presumably characterizes most of the deep ocean.

Based on our analysis here and in Chapter IV, we can conceptually summarize the effects of various processes on the $\delta^{34}S$ of pyrite buried within a given

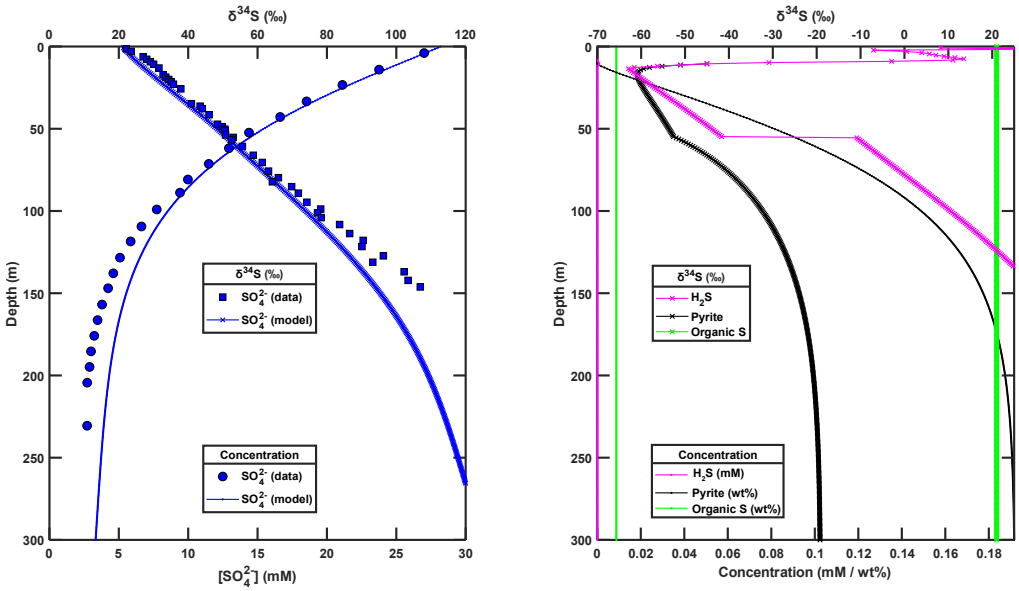

Figure V.26: Site U1474 model results for model run with RRFe higher than that at the pyrite $\delta^{34}S$ maximum. (A) Data (filled markers) and model results (blue lines) for SO_4^{2-} concentration and $\delta^{34}S$ with depth at Site U1474 for a RRFe of $\sim$12.21 $\frac{\mu mol}{m^2 day}$ (B) Model concentrations (lines with "." markers) and $\delta^{34}S$ (lines with "x" markers) for H_2S, pyrite, and organic S.

environment using a plot of pyrite $\delta^{34}S$ versus Fe(III) rain rate (Figure V.27). Here, we have drawn a pyrite $\delta^{34}S$ trajectory for a constant RRPOC as a blue arrow. Additional parameter changes that may act to increase pyrite $\delta^{34}S$ (upward brown arrow, upper left) or decrease pyrite $\delta^{34}S$ (downward brown arrow, lower right) have been listed above and below this trajectory, respectively. At a constant RRPOC and $^{34}\varepsilon$, pyrite $\delta^{34}S$ will rise with increasing RRFe as H_2S is progressively scavenged. Here, pyrite burial is iron limited, and sediments are characterized by depth profiles similar to those in our Regimes 1 and 2. Pyrite $\delta^{34}S$ reaches a maximum just as the fraction of POC remineralization attributable to SO_4^{2-} reduction is maximized. As RRFe increases further, SO_4^{2-} reduction decreases in its overall contribution toward organic matter remineralization, and pyrite formation becomes limited by sulfide production. We again note that spatial (i.e., with depth) and/or temporal changes in parameter values may alter the trajectory of pyrite $\delta^{34}S$ in this space by perturbing the ability of diffusion to influence the diagenetic system (as with sedimentation rate, bottom water concentrations, porosity, and temperature) or by modifying reaction rates directly (as with RRPOC and $^{34}\varepsilon$). For example, an increase in the magnitude of $^{34}\varepsilon$ as RRFe initially increases would counteract the scavenging of increas-

ingly ^{34}S-enriched H_2S and replicate the "Regime 1" behavior of our model in this space.

V.6.5 The relationship between nSRR and $^{34}\varepsilon$

Laboratory culture studies of MSR have found an inverse correlation between $^{34}\varepsilon$ and cell-specific SO_4^{2-} reduction rate (csSRR) [176, 195, 313] wherein higher csSRR is associated with lower $^{34}\varepsilon$. To investigate whether a similar relationship between $^{34}\varepsilon$ and nSRR exists in natural environments, we plot I-CANDI model estimates for the $^{34}\varepsilon$ and nSRR at each site in Figure V.28A. Surprisingly, we observe a relationship opposite to the one expected: higher nSRR is generally associated with larger $^{34}\varepsilon$ — not smaller $^{34}\varepsilon$ — at these sites. Larger numbers of active SO_4^{2-}-reducing microbial cells at the sites with higher nSRRs could be one possible explanation for this trend; if relative growth in the number of active SO_4^{2-}-reducing microbial cells outpaces growth in nSRR among these sites, sites with higher nSRRs could feature lower csSRRs despite their quicker rates of SO_4^{2-} consumption.

Kallmeyer et al. (2012) [170] have shown that the abundance of microbial cells in sediments shows a strong correlation with mean sedimentation rate at marine sites. Given the association between estimated nSRR and sedimentation rate at the sites in this study (Figure V.28B), it is likely that the total number of microbial cells is larger in the sediments at our relatively high nSRR sites compared to our low nSRR sites. However, we are unaware of studies specifically addressing SO_4^{2-}-reducing cell abundances in marine sediments on a global scale, though some studies have quantified abundances in the water column (e.g. [333]) and in sediments (e.g. [182]) within local environments. Further investigation into the relationship between sulfate-reducing cell abundances and nSRR in marine sediments is needed to better constrain csSRR in natural environments and evaluate the origin of this trend.

V.6.6 Mechanisms for $\Delta\delta^{34}S_{SO_4^{2-}-H_2S}$ reversal

MSR and S disproportionation feature S isotope fractionations that deplete the product H_2S relative to SO_4^{2-} (e.g. [60, 176]). Enrichment of H_2S in ^{34}S should not be possible if only these reactions are occurring; however, we observe such enrichment in samples below the SMT at Site U1483 (Figure V.8). There are several potential explanations for this enrichment. Multiple studies (e.g. [105,

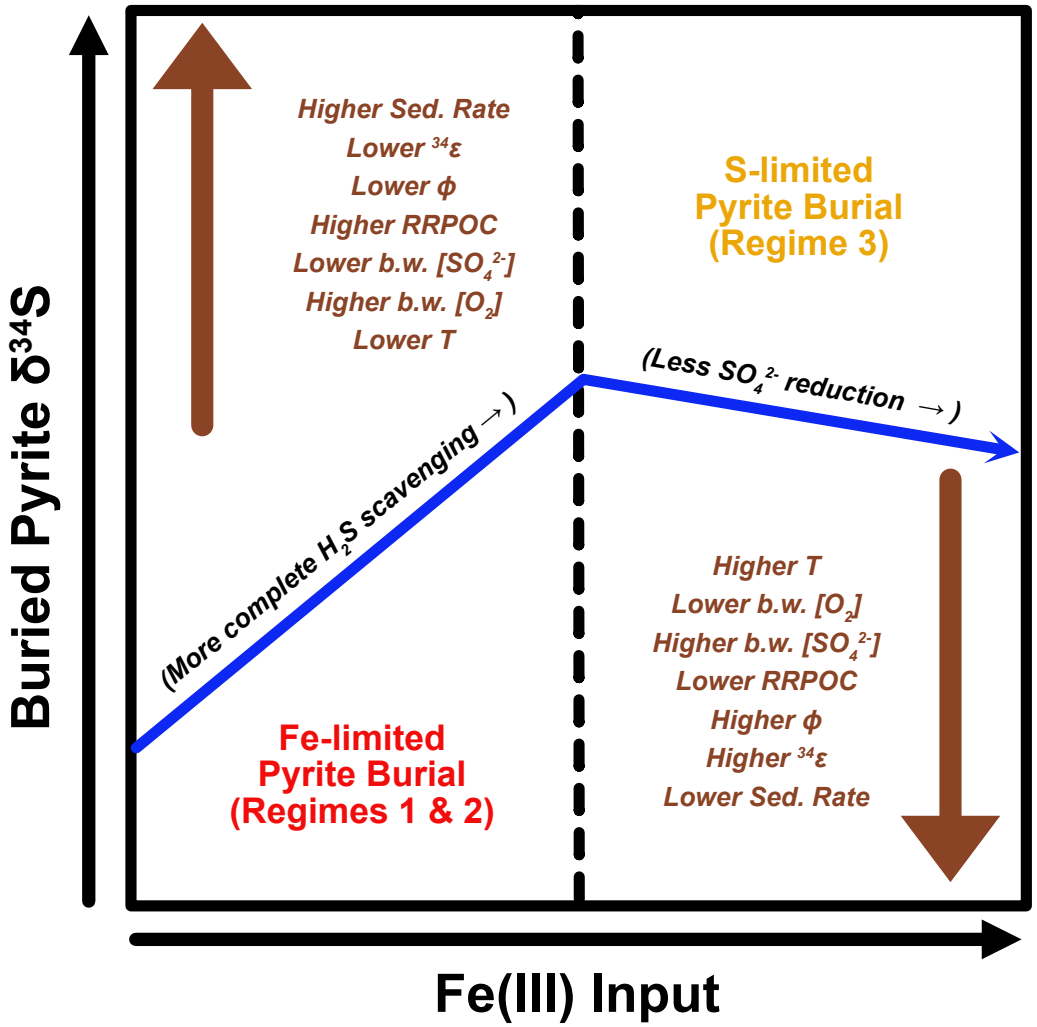

Figure V.27: Schematic depiction of the final $\delta^{34}S$ of buried pyrite as a function of the Fe(III) rate in a given depositional environment. Blue arrow defines the expected trajectory if all other variables (e.g. RRPOC) remain constant. Brown arrows denote the direction of the expected pyrite $\delta^{34}S$ response to the listed perturbations; perturbations are roughly listed such that those likely to result in greater pyrite $\delta^{34}S$ changes are located closer to the tips of the arrows. Dashed black vertical line denotes the boundary between Fe limitation of pyrite burial (left) and sulfur limitation of pyrite burial (right). Note that this schematic assumes no change in reaction kinetics associated with any of the listed perturbations; e.g., reaction rate constants are invariant with temperature.

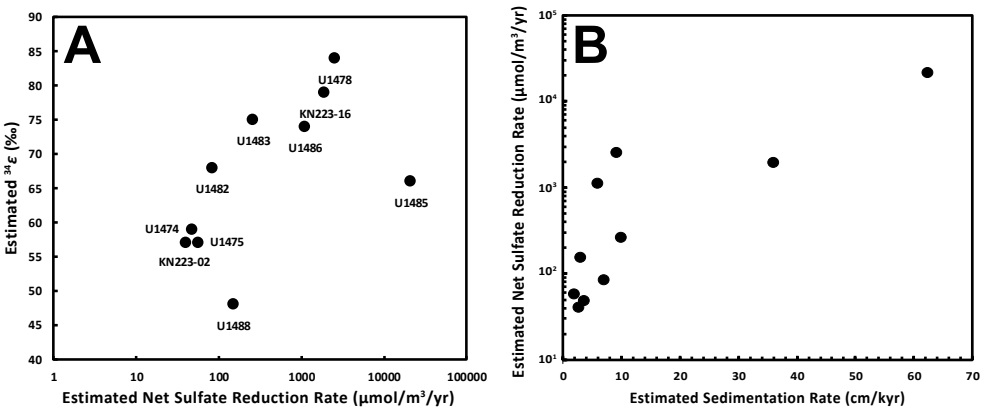

Figure V.28: Relationships among mean nSRR, sedimentation rate, and $^{34}\varepsilon$. (A) Scatter plot of I-CANDI model estimates of $^{34}\varepsilon$ (vertical axis) versus net sulfate reduction rate (nSRR; horizontal axis) for each of the sites modeled in this study. Note that nSRR is plotted on a logarithmic scale. (B) Scatter plot of estimated nSRR versus estimated sedimentation rate for each of the sites in this study.

256]) have observed H_2S oxidation that creates SO_4^{2-} depleted in ^{34}S. Such oxidation could account for the $\Delta\delta^{34}S$ reversal if SO_4^{2-} derived from oxidation is the dominant component of the ambient SO_4^{2-} pool. Small amounts of solid phase S oxidation or of blank contamination could also skew the SO_4^{2-} $\delta^{34}S$ data toward lower values under these conditions.

Although we do not have H_2S $\delta^{34}S$ data from any sites beyond Sites U1482 and U1483, we consistently observe a return of SO_4^{2-} $\delta^{34}S$ to seawater-like values ($\sim$+21‰) below the SMT at all sites where we have data. This consistency in SO_4^{2-} $\delta^{34}S$ below the SMT suggests that a common process is responsible. Notably, the amount of SO_4^{2-} in these post-SMT samples is vanishingly small in our data as well as in other studies [255]. Based on these considerations, we favor blank contamination as the source of this $\Delta\delta^{34}S$ reversal. We are currently unable to distinguish whether such contamination occurred during shipboard processes (e.g. small amounts of contamination with seawater during coring plus some sulfide oxidation) or during shore-based laboratory processing. Analysis of pore water species that are differentially sensitive to each of these contamination sources is needed to resolve this uncertainty.

V.6.7 Implications for the global marine sulfur cycle

Our results demonstrate that high $^{34}\varepsilon$ is an ubiquitous feature of sulfur cycling in modern deep marine sediments. Although the physical parameters of depositional environments [127, 246] and the amount of iron and labile organic matter input may modulate the $\delta^{34}S$ of pyrite that is buried in these sediments, past observations [4, 37, 38, 115, 158, 188, 197, 220, 222, 266, 293, 329] and our modeling show that the depletion of this deep ocean pyrite in ^{34}S relative to pyrite in shelf sediments is robust.

Previous efforts to characterize global nSRRs (e.g. [43]) have often ignored sites that are not well characterized by an exponential decrease in $[SO_4^{2-}]$ with depth. Such filtering of sites eliminates inclusion of many continental slope sites with relatively linear $[SO_4^{2-}]$ profiles (e.g. Sites U1482 and U1483 in this study) or with upward fluxes of SO_4^{2-} from sources at depth (e.g., Sites U1486 and U1488). Our modeling shows that such exclusion probably imparts a substantial bias in global nSRR estimates; both of these varieties of sites display elevated nSRRs compared to sites with exponential $[SO_4^{2-}]$ decreases (e.g. Sites U1474 and U1475) in our study. Preferential sampling of high nSRR sites and other sources of bias prevent us from concluding that the global nSRR estimate of Bowles et al. (2014) [43] is too low; in fact, their estimate of 11.3 x $10^{12}\,\frac{mol}{yr}$ is already four times higher than a recent estimate of the pre-anthropogenic riverine SO_4^{2-} input flux [52]. However, our analysis does show that a more serious accounting of these sites may be necessary to bring estimates of the net input and output fluxes in the modern marine S cycle into better agreement.

We can roughly constrain the size of the bias that may be present in current global nSRR estimates based on the exclusion of the sites with a SO_4^{2-} source at depth. Although global fluxes of S to and from the crust due to hydrothermal activity remain poorly constrained, prior studies [2, 3, 358] have estimated the flux of S out of seawater through circulating fluids to be in the range of 0.3 to 2.5 $\frac{Tmol}{yr}$. Most of this flux is removed via the precipitation of anhydrite that later dissolves under cooler off-axis temperatures [2, 3]. For comparison, the amount of SO_4^{2-} reduction estimated by Bowles et al. (2014) [43] to occur in sites below 2000 m water depth is about 2.9 $\frac{Tmol}{yr}$; most spreading centers are within this depth range. If 100% of the anhydrite that dissolves from cooling crust is removed via SO_4^{2-} reduction in the sediments and does not re-enter seawater, this additional SO_4^{2-} flux would increase the amount of SO_4^{2-} reduc-

tion occurring in these deep environments by 10 to 86%. These numbers are admittedly an upper limit on the contribution of SO_4^{2-} from bottom fluids to global SO_4^{2-} reduction if the Bowles et al. (2014) [43] model is accurate, but the contribution could be even more significant if the model overestimates global SO_4^{2-} reduction rates (see Chapter VI).

Finally, Figure V.27 presents a useful framework for interpreting the influence of past Earth system changes on the S isotopic composition of pyrite buried globally. For example, Jones and Fike (2013) [160] observed an increase in pyrite $\delta^{34}S$ in end-Ordovician sediments without any corresponding increase in the $\delta^{34}S$ of seawater SO_4^{2-} proxies. This decrease in $\Delta\delta^{34}S$ was attributed to a decrease in $^{34}\varepsilon$, but our analysis suggests that a decrease in ambient water temperatures [101] and higher bottom water oxygen concentrations could also contribute to this change. Halevy et al. (*submitted*) [127] have also recently argued that a decrease in seawater $[SO_4^{2-}]$ and the corresponding diffusive flux of SO_4^{2-} to sediments can explain the lower $\Delta\delta^{34}S$ values observed in Archean and Proterozoic sediments. While this could be true, our model indications that lower bottom water O_2 concentrations (e.g. [58, 94, 167]), lower RRPOCs (e.g. [32]), higher temperatures (e.g. [181]), and lower sedimentation rates (e.g. [130]) all force pyrite $\delta^{34}S$ towards *lower* values (i.e., higher $\Delta\delta^{34}S$) complicate this picture. More extensive sensitivity studies with these variables — as well as Fe(III) mineral fractions of differing reactivities [47] — are needed to fully evaluate the net effect of these competing influences on $\Delta\delta^{34}S$ through time.

V.7 Conclusions

Here, we have undertaken a study of sedimentary S cycling in deep ocean sediments through measurements and modeling of S geochemical profiles at 11 sites cored on IODP Expedition 361, IODP Expedition 363, and *R.V. Knorr* cruise KN223. We find high diversity in the character of the $[SO_4^{2-}]$ and $\delta^{34}S$ profiles across the different sites. However, all are united by large ($> 45‰$) $^{34}\varepsilon$ estimates based on closed system and open system modeling of their profiles. The modeled $\delta^{34}S$ of the pyrite buried at each of these sites is quite depleted in ^{34}S relative to pyrite buried in shallow shelf sediments, but exhibits a complicated dependence on POC rain rate, Fe(III) rain rate, and oxygen penetration depth. Notably, nSRRs are higher among the sites with quasi-linear $[SO_4^{2-}]$ profiles and with $[SO_4^{2-}]$ profiles indicating a deep source of SO_4^{2-} than at sites with a tradi-

tional exponential decrease in $[SO_4^{2-}]$. Ignorance of such sites in estimates of the global nSRR likely biases these estimates, and accounting for the sites could help future estimates resolve isotope mass balance within the modern marine S cycle. In addition, better understanding of the effects of non-S species on the $\delta^{34}S$ of pyrite preserved in marine sediments is needed. These considerations motivate continued investigation into the controls on pyrite $\delta^{34}S$ in marine sediments.

Chapter VI

GLOBAL TRENDS IN SEDIMENTARY SULFUR CYCLING WITHIN DEEP MARINE SEDIMENTS

VI.1 Abstract

Recent studies [43, 165] have suggested that SO_4^{2-} reduction in deep marine sediments constitutes a significant portion of SO_4^{2-} reduction globally. However, at least one of these studies [43] yields a global net SO_4^{2-} reduction rate (nSRR) that far exceeds recent estimates of the riverine input of S to seawater [52]. Such a disparity suggests that these prior studies have not captured the full diversity of sulfur inputs to seawater or marine sedimentary S cycling in an unbiased manner. Here, we re-examined sulfur cycling in deep ocean sediments with cluster analysis. Using pore water $[SO_4^{2-}]$ data collected from over 700 DSDP, ODP, and IODP sites, we show that k-means clustering can identify groups (clusters) of $[SO_4^{2-}]$ depth profiles that are disparate in terms of SO_4^{2-} reduction rate and inclusion versus exclusion of a sulfate-methane transition (SMT). We also show that the geographic distributions of the sites within each identified cluster are distinct: sites in clusters with relatively low SO_4^{2-} reduction rates (SRRs) are predominantly located on the continental rise and in the abyss, whereas clusters with higher SRRs are located almost exclusively in more shallow coastal regions. Examination of the sedimentary total organic carbon (TOC) contents, $CaCO_3$ contents, and water depths of the sites within each cluster show that TOC content is the strongest control on the character of the $[SO_4^{2-}]$ profiles; water depth and $CaCO_3$ content act as secondary influences. These findings confirm similar conclusions made with smaller deep ocean data sets [55]. Comparison of estimated nSRRs to pyrite S accumulation rates calculated from a literature compilation of over 300 pyrite $\delta^{34}S$ measurements suggests that sediments of relatively high pyrite content are over-represented in current data relative to their actual global abundance. This compilation confirms that shelf pyrite burial constitutes the majority of pyrite buried globally, though additional studies of deltaic sediments are needed to better constrain the magnitude of the shelf burial flux. Considerations of sulfur isotope mass balance in the modern marine sulfur cycle indicate that variation in the amount of deep ocean (> 200

m water depth) pyrite burial can alter the steady state $\delta^{34}S$ of seawater SO_4^{2-} by several per mil if such variation is unaccompanied by changes in the $\Delta\delta^{34}S$ between seawater SO_4^{2-} and buried pyrite.

VI.2 Introduction

The previous chapter of this thesis (Chapter V) discussed sedimentary sulfur cycling across 11 deep ocean sites cored on three cruises. Data at these sites revealed a high diversity in the character of S cycling within deep ocean sediments. Is such diversity common when viewed in the broader context of deep ocean sedimentary S cycling globally? What are the implications of this cycling for the magnitude and S isotopic composition of output fluxes within the modern marine S cycle?

Many prior studies (e.g. [4, 37, 38, 115, 133, 158, 174, 175, 188, 197, 198, 220, 221, 222, 266, 293, 328, 329, 336, 349, 371]) have sought to better understand the controls upon the S contents of deep marine sediments. These studies have often included S isotope analysis of solid phases and/or pore water SO_4^{2-} in samples collected through the Deep Sea Drilling Program (DSDP), the Ocean Drilling Program (ODP), and the International Ocean Discovery Program (IODP). However, most of these efforts have focused on samples collected from a narrow geographic region within the modern ocean. Few studies have attempted to integrate global data and make inferences about the broader marine S cycle.

Recently, Bowles et al. (2014) [43] made one of the first attempts to integrate a wealth of global deep ocean pore water $[SO_4^{2-}]$ data and make a new estimate of the global net SO_4^{2-} reduction rate (nSRR). Using 199 DSDP, ODP, and IODP $[SO_4^{2-}]$ depth profiles, these authors trained an artificial neural network to predict nSRRs in different regions across the globe based on water depth, surface productivity, distance to the coast, and a range of oceanographic parameters [43]. Their model predicted a global nSRR of 11.3 $\frac{\text{Tmol}}{\text{yr}}$ based on a training data set of $[SO_4^{2-}]$ profiles that could be described with an exponential curve. This number is about four times higher than the pre-anthropogenic riverine S input flux estimated by Burke et al. (2018) [52] and nearly an order of magnitude higher than Berner's (1982) [19] estimate of the global pyrite burial flux [43]. Such a disparity suggests that (1) the nSRR estimate of Bowles et al. (2014) [43] is too high, (2) the Burke et al. (2018) [52] riverine flux estimate is too low, (3) one or more S input fluxes are missing or grossly underestimated in the modern

global S cycle, or (4) some combination of these three possibilities.

Here, we have re-examined S cycling in deep ocean sediments by applying cluster analysis to pore water $[SO_4^{2-}]$ profiles collected from over 700 DSDP, ODP, and IODP sites. We show that k-means clustering can successfully identify and group $[SO_4^{2-}]$ depth profiles of different character. We also have built a literature compilation of over 300 pyrite $\delta^{34}S$ measurements from recent marine sediments. We found that sites with relatively high S content seem to be overrepresented in both solid phase and pore water data. The implications of an increase in the amount of pyrite buried in deep marine sediments for isotope mass balance in the modern marine S cycle are considered at the conclusion of our study.

VI.2.1 K-means cluster analysis

Cluster analysis is a method of grouping data that are quantitatively "similar" to each other and is commonly used to identify features common among observations within large sets of data. Typically, algorithms used to perform cluster analysis use a distance metric (often, Euclidean distance) to determine how alike two observations are to each other [112, 173]. *K*-means refers to a specific type of clustering algorithm in which the number of clusters, *k*, is predetermined by the user [173]. In detail, the algorithm functions by looping over each observation and assigning it to the nearest cluster based on the distance from the observation to the cluster centroid (i.e., the mean of the observations within the cluster), calculating the mean (centroid) of the observations within the cluster, and repeating the algorithm until the distance between the centroids among the *k* different clusters and the distance between the observations within each cluster are minimized [173]. The results of the algorithm are dependent upon the initial cluster assignments such that the algorithm finds only a local minimum in distances; i.e., running the algorithm multiple times on the same data set may yield slightly different results [112]. In our experience, however, the *k*-means algorithm identifies the same cluster variants when the analysis is repeated with the same data set even if individual observations sometimes shift among the clusters.

Although sulfate reduction rates in deep ocean sediments tend to covary with water depth (e.g. [219]), variations in sedimentation rate and organic matter input at a given water depth (e.g. [55, 219]) prevent water depth from being used

as an precise predictor of sedimentary sulfate reduction rate on its own. Cluster analysis, however, assumes nothing about variations in parameters that are not included as part of the algorithm; i.e., if only sulfate concentration depth profiles are provided as observations within the algorithm, the algorithm clusters observations based exclusively on those concentration profiles. This provides a powerful means of identifying trends in the sulfate concentration profiles collected from deep ocean sediments while assuming no a priori associations with other parameter values. We have explored the ability of cluster analysis to provide information about the controls upon S cycling within deep ocean sediments in the following.

VI.3 Methods

To examine S cycling in deep ocean sediments across the globe, we downloaded data collected during previous DSDP, ODP, and IODP cruises from the JANUS and LIMS databases; sites for which data were downloaded are listed in Table D.2. These data included all available geochemical data on interstitial waters, gases, and solid phases, as well as physical properties data on sedimentary porosity. Once downloaded, all data were imported into MATLAB® from the original .csv files and saved into MATLAB® structures.

To enable cluster analysis, pore water $[SO_4^{2-}]$ data were extracted from the structures and interpolated to an identical depth resolution of 1 m across all sites. Interpolated data were then inserted into a master array in which each row represented data collected from a different site and each column data from a specific depth (i.e., column 1 houses all $[SO_4^{2-}]$ interpolated to 0 mbsf at different sites, column 2 houses 1 mbsf data, etc.). For each iteration of cluster analysis, we chose a bottom boundary depth below which interpolated $[SO_4^{2-}]$ data were not included in the analysis. This depth was increased from 10 mbsf to 400 mbsf in increments of 10 m to examine the sensitivity of our clustering results to the number of included $[SO_4^{2-}]$ observations at each site. In all iterations, sites with fewer than five pre-interpolation $[SO_4^{2-}]$ data points were excluded from our analysis. Sites with no $[SO_4^{2-}]$ data below the chosen bottom boundary depth were also excluded. The number of included sites in the analysis decreases from 788 for a bottom depth of 10 mbsf to 235 for a bottom depth of 400 mbsf.

After creation of the master $[SO_4^{2-}]$ array, we used MATLAB®'s evalclusters function to evaluate the optimal number of clusters based on the entries in the

$[SO_4^{2-}]$ array. We choose the optimal number of clusters based on the Calinski-Harabasz Index (also known as the variance ratio index). This index ratios the overall variance (sum of the squares) of observations between clusters to the variance within the clusters:

$$\text{Calinski-Harabasz Index} = \frac{SS_B}{SS_W} \text{ x } \frac{N-k}{k-1} \tag{VI.1}$$

where SS_B is the variance between the clusters, SS_W is the variance within the clusters, N is the number of observations (sites, in this case), and k is the number of clusters. The number of clusters is optimized when the Calinski-Harabasz Index in minimized.

Clustering was accomplished using k-means clustering with MATLAB®'s kmeans function. Squared Euclidian distance was used as the distance metric, and the maximum number of iterations was set to 1000. In all of the iterations we report, the clusters have been numbered such that the cluster with the most sites was designated to be Cluster 1 and clusters containing progressively smaller numbers of sites were assigned chronologically increasing cluster numbers. Clustering results were saved to a separate MATLAB structure.

Following clustering, we extracted and examined additional data from the deep ocean drilling databases to better understand the controls on the $[SO_4^{2-}]$ profiles across all sites. Water depth, porosity, total organic carbon (TOC) content, and calcium carbonate ($CaCO_3$) content were among the data we extracted. We also estimated the mean nSRR at all sites by fitting an exponential curve to the extracted porosity data, fitting a cubic spline to the $[SO_4^{2-}]$ data, and solving for the reaction term in the general diagenetic equation (see Chapter IV). Aerial nSRR was estimated using the method of Canfield (1991) [55]. Sedimentation rates at each site were estimated based on water depth using the relationship between water depth and sedimentation rate observed by Middelburg, Soetaert, and Herman (1997) [219].

VI.4 Results

VI.4.1 Sensitivity analysis

In examining the sensitivity of our cluster analysis results to the bottom boundary depth chosen for clustering, we find that the optimal number of clusters varies between three and six throughout all iterations, with five being the most

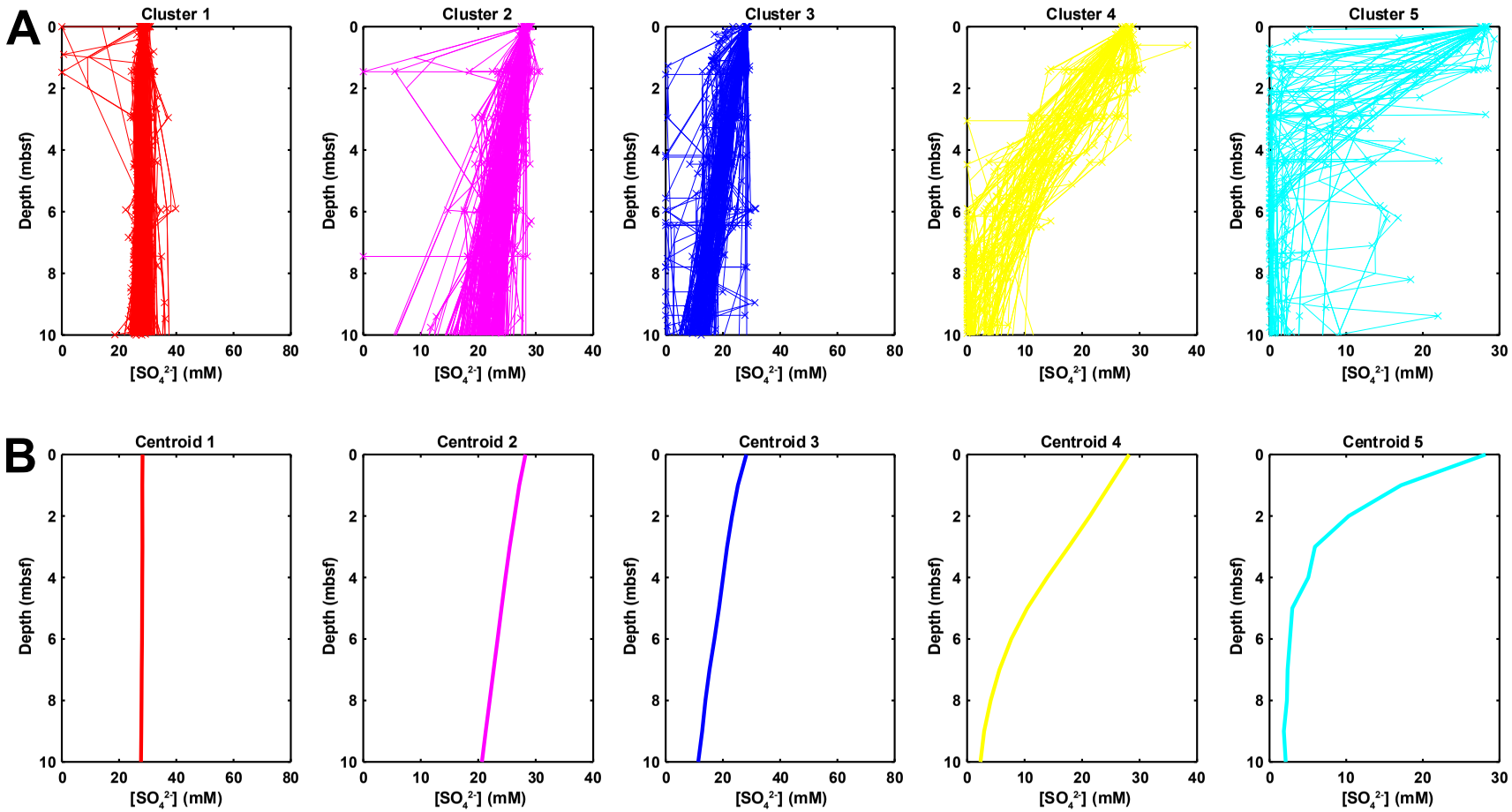

Figure VI.1: Cluster analysis results for 10 mbsf bottom boundary with five clusters. (A) Observed $[SO_4{}^{2-}]$ depth profiles for 0 to 10 mbsf for sites within Clusters 1 (far left) through 5 (far right). (B) Cluster centroids (i.e., the average $[SO_4{}^{2-}]$ depth profiles for the sites within the cluster) for Clusters 1 (far left) through 5 (far right).

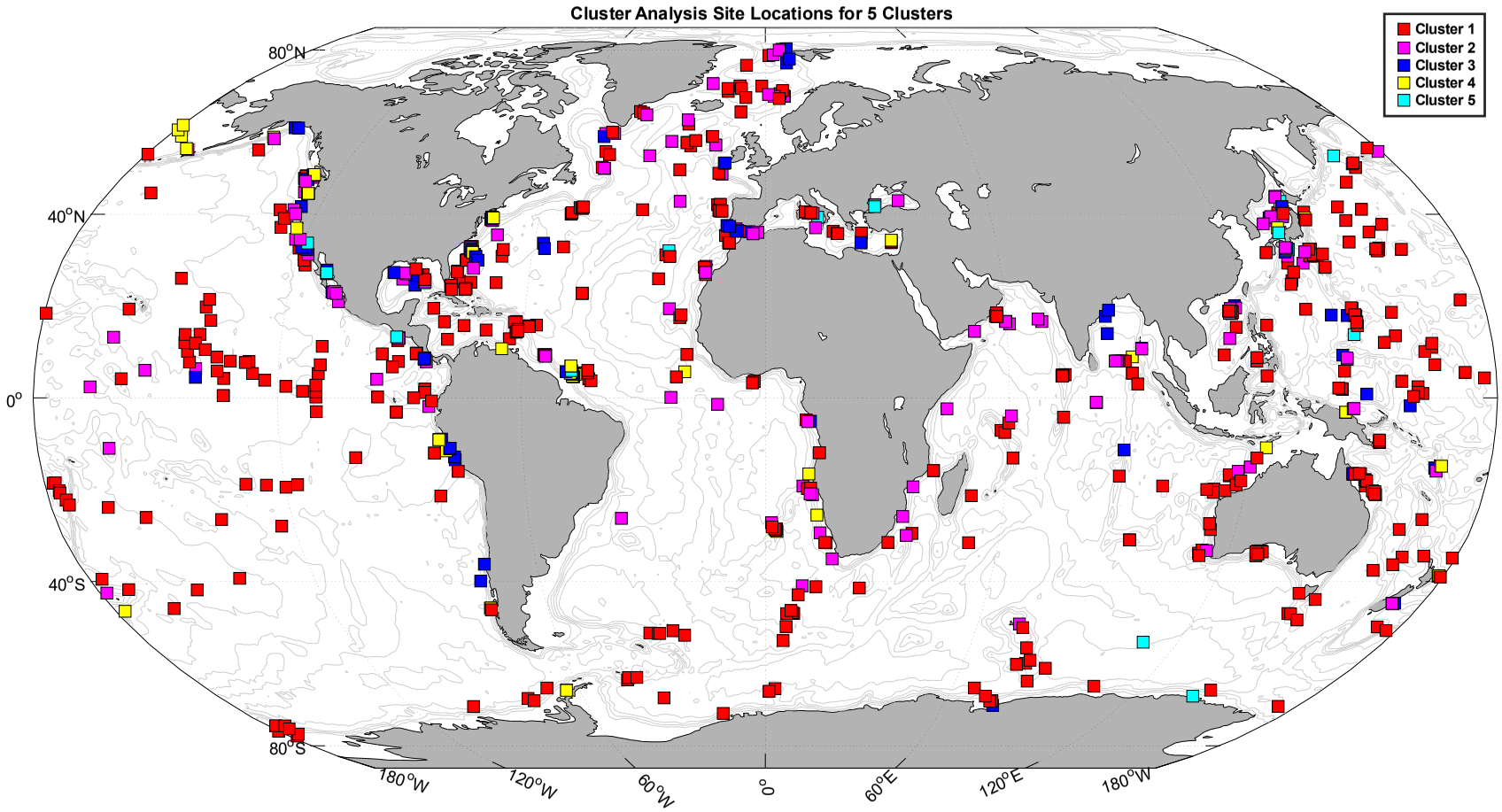

Figure VI.2: Global map of the distribution of sites included within the cluster analysis for a bottom boundary depth of 10 mbsf. The color of the symbol denoting site location corresponds to the cluster assignment and matches the colors of the profiles in Figure VI.1; i.e., Cluster 1 sites are shown with red squares, Cluster 2 sites with magenta squares, Cluster 3 sites with blue squares, Cluster 4 sites with yellow squares, and Cluster 5 sites with cyan squares. Map created using the M _Map mapping package [247].

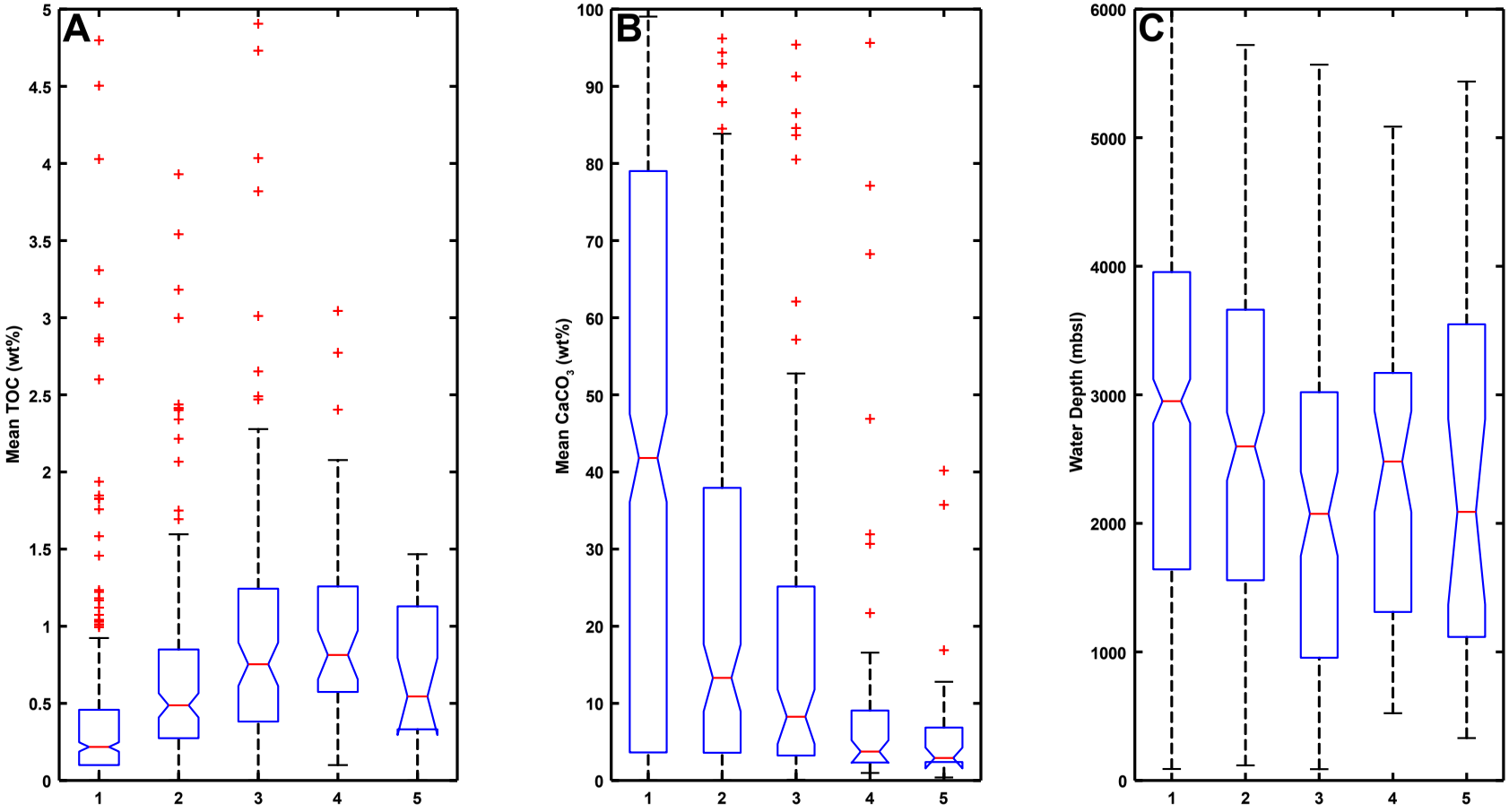

Figure VI.3: Box and whisker plots of (A) mean TOC content, (B) mean $CaCO_3$ content, and (C) water depth for the sites included within each cluster for a bottom boundary of 10 mbsf. Red horizontal lines denote the medians for each cluster, and the blue indented notches in the boxes denote the 95% confidence interval bounds for the median value. The top and bottom edges of the blue boxes denote the 25th and 75th percentile ranges for the data within each cluster. Whiskers (capped dashed lines) are depicted with lengths equal to 2σ (95%) coverage of the data within each cluster; outliers are depicted as red "+" symbols.

common optimal number of clusters. Example clustering results for a bottom depth of 10 mbsf are depicted in Figure VI.1. Even at a bottom depth of 10 meters, clusters are already fairly distinct in character. Clusters 1 and 2, which feature essentially no decrease in $[SO_4^{2-}]$ with depth (Cluster 1, $n = 450$) or a small decrease with depth (Cluster 2, $n = 156$), are dominant in the open ocean (Figure VI.2). Clusters 3, 4, and 5 ($n = 93$, 54, and 27, respectively) show stronger decreases in $[SO_4^{2-}]$ with depth and are located almost exclusively along the coasts of continents. Box plots of the mean TOC content, mean $CaCO_3$ content, and water depth for the sites within each cluster are shown in Figure VI.3. These plots demonstrate that sites within Cluster 1 have statistically lower mean TOC content, higher $CaCO_3$ content, and deeper water depth than the sites within Clusters 3 through 5. Cluster 2 data are intermediate between those of Cluster 1 and those of Clusters 3-5.

Extending the bottom boundary to deeper depths results in the refinement of clusters and more visually clear differences. The optimal number of clusters also varies from four for a 50 mbsf bottom boundary (Figure D.1), to six for a 100 mbsf bottom boundary (Figure VI.4) and back to five for a 200 mbsf bottom boundary (Figure D.4). The number of sites included in the clustering for these three bottom boundary depths are 727, 681, and 506, respectively. In the following, we focus on describing the cluster analysis results for a 100 mbsf bottom boundary in detail. We include profiles, maps, and box plots for the 50 mbsf and 200 mbsf bottom boundary depth iterations in Appendix D.

VI.4.2 Cluster analysis results for 100 mbsf bottom boundary

Depth profiles of $[SO_4^{2-}]$ for each of the six clusters in the optimal 100 mbsf cluster analysis iteration are shown in Figure VI.4. Here, Cluster 1 ($n = 232$) is similar to the first cluster in the 10 mbsf iteration and shows little decrease in $[SO_4^{2-}]$ with depth. Plotting of the locations of the sites within this cluster (Figure VI.5) shows that sites within this cluster are predominantly located in the open ocean. Box and whisker plots (Figure VI.6) also demonstrate the median value for mean TOC at these sites to be very low (0.17 wt%). Median values for both mean $CaCO_3$ content and water depth are relatively high (55.1 wt% and 2962 meters below sea level, respectively).

In contrast with Cluster 1, Cluster 2 contains sites ($n = 133$) in which SO_4^{2-} is depleted relatively quickly with depth; the centroid for the cluster shows that

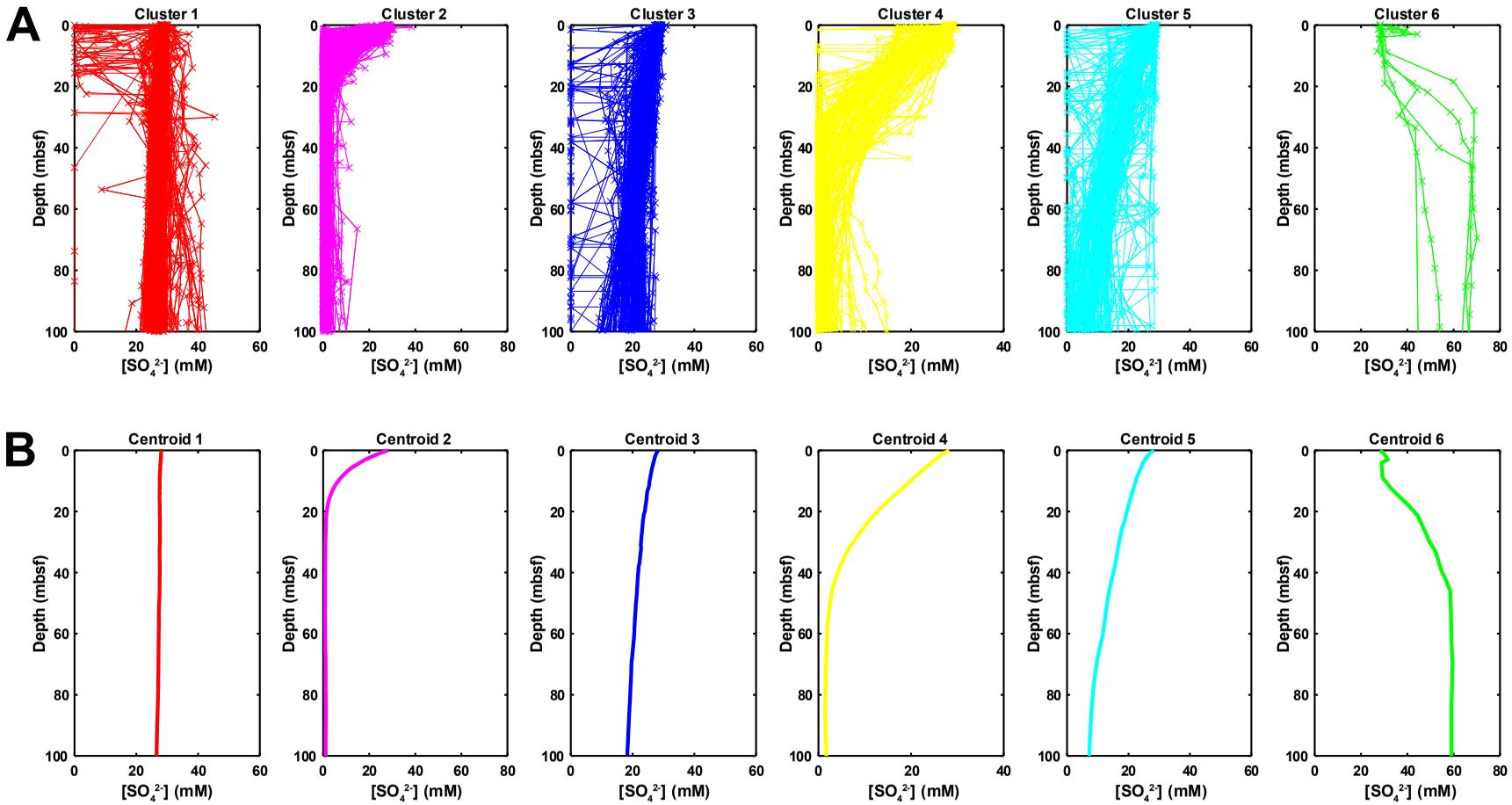

Figure VI.4: Cluster analysis results for 100 mbsf bottom boundary with six clusters. (A) Observed $[SO_4^{2-}]$ depth profiles for 0 to 100 mbsf for sites within Clusters 1 (far left) through 6 (far right). (B) Cluster centroids (i.e., the average $[SO_4^{2-}]$ depth profiles for the sites within the cluster) for Clusters 1 (far left) through 6 (far right).

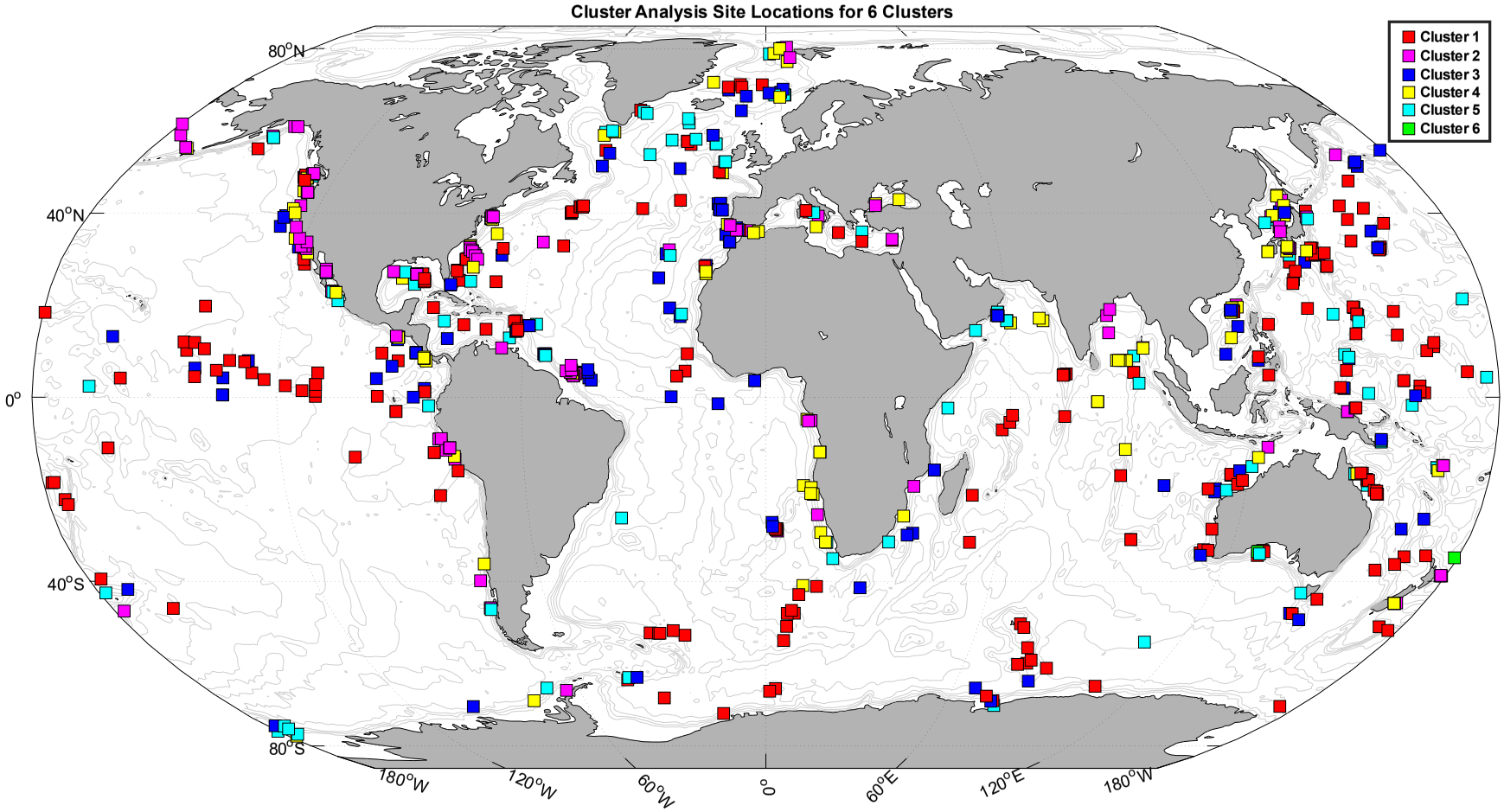

Figure VI.5: Global map of the distribution of sites included within the cluster analysis for a bottom boundary depth of 100 mbsf. The color of the symbol denoting site location corresponds to the cluster assignment and matches the colors of the profiles in Figure VI.1; i.e., Cluster 1 sites are shown with red squares, Cluster 2 sites with magenta squares, Cluster 3 sites with blue squares, Cluster 4 sites with yellow squares, Cluster 5 sites with cyan squares, and Cluster 6 sites with lime green squares. Map created using the M _Map mapping package [247].

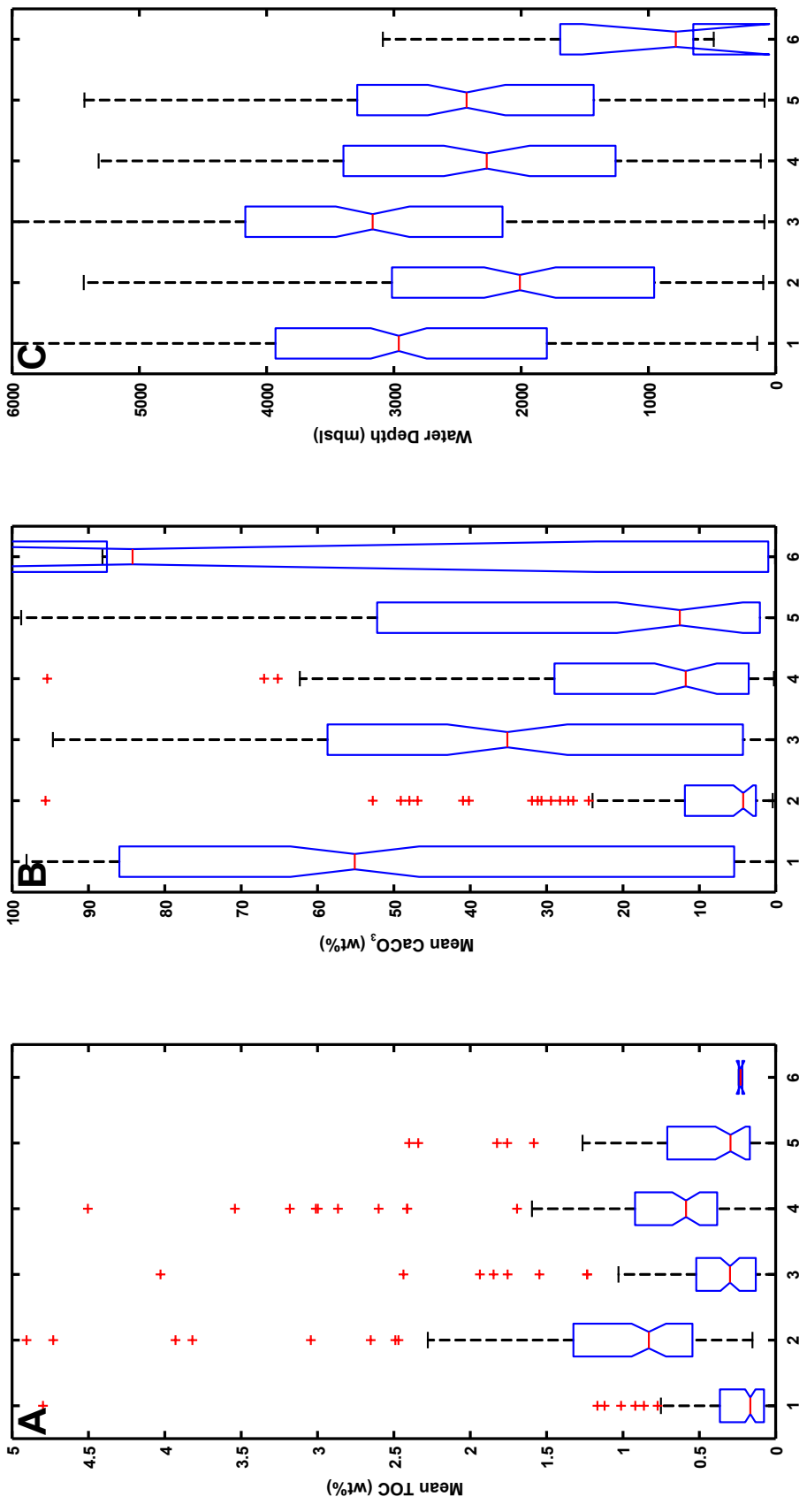

Figure VI.6: Box and whisker plots of (A) mean TOC content, (B) mean $CaCO_3$ content, and (C) water depth for the sites included within each cluster for a bottom boundary of 100 mbsf. Red horizontal lines denote the medians for each cluster, and the blue indented notches in the boxes denote the 95% confidence interval bounds for the median value. The top and bottom edges of the blue boxes denote the 25th and 75th percentile ranges for the data within each cluster. Whiskers (capped dashed lines) are depicted with lengths equal to 2σ (95%) coverage of the data within each cluster; outliers are depicted as red "+" symbols.

the average depth of complete SO_4^{2-} consumption at these sites is ~20 mbsf. Examination of Figure VI.5 reveals these sites to be located exclusively near coasts. The median value for mean TOC content at these sites (0.83 wt%) is nearly a factor of five higher than that for Cluster 1. Both the median value for mean $CaCO_3$ content (4.3%) and the median water depth (2010 meters below sea level, or mbsl) are lower.

Clusters 3, 4, and 5 (n = 120, 99, and 92, respectively) are intermediate in character between Clusters 1 and 2. Cluster 3 sites generally feature a slight $[SO_4^{2-}]$ decrease with depth, with $[SO_4^{2-}]$ remaining well above zero. Cluster 5 sites have a stronger decrease with depth, but still do not have a sulfate-methane transition (SMT) within the upper 100 m of sediment. Cluster 4 sites do reach a SMT, but at greater depths (~30 to 60 mbsf) than at Cluster 2 sites. These trends are again reflected in terms of distance from landmasses in Figure VI.5: with few exceptions, sites within Cluster 4 are concentrated along coasts, whereas sites within Clusters 3 and 5 are more heterogeneously distributed between coastal regions and the open ocean. The faster rates of SO_4^{2-} consumption at Cluster 4 sites are consistent with higher mean TOC contents and shallower water depths than for the sites within Clusters 3 and 5 (Figure VI.6).

Finally, Cluster 6 features sites (n = 5) that have a substantial increase in $[SO_4^{2-}]$ within the upper 100 m of sediment. $[SO_4^{2-}]$ is somewhat invariant in the upper 10 m before increasing by at least 10 mM over the next 30 to 80 m; some sites reach $[SO_4^{2-}]$ as high as 65 mM. Figure VI.5 shows that these sites are generally limited in their geographic distribution to shallow water depths to the south of Australia and north of New Zealand.

VI.5 Discussion

VI.5.1 k-means clustering

Our application of cluster analysis to deep sea drilling data has demonstrated k-means clustering to be a simple, but powerful tool for finding trends among large data sets. With a relatively small amount of effort, this clustering algorithm has been able to distinguish sites from around the globe based on the presence of a shallow SMT, a deeper SMT, or no SMT whatsoever. Such capability presents an opportunity to ascertain relationships in the global marine S cycle in a manner that is less computationally complex than predictive models like artificial neural

networks (e.g. [43]).

In comparing the clusters identified in this chapter to our groupings of sites in Chapter V, we find that cluster analysis is able to successfully distinguish at least two of the three groupings: sites with an SMT and sites featuring neither an SMT nor a source of SO_4^{2-} at depth. Our third grouping — sites with a source of SO_4^{2-} below cored depths — is apparently not numerous enough to be identified as a unique cluster. However, our analysis with a 100 mbsf bottom boundary does identify sites with a more shallow SO_4^{2-} source within the sediments (Cluster 6, Figure VI.4). Reports describing the interstitial water geochemistry at these sites (e.g. [96, 323]) attribute these increases to evaporite dissolution, brine generation, and/or fluid flow from evaporitic systems on nearby landmasses. The small number of sites included in this cluster suggests that the global significance of this type of $[SO_4^{2-}]$ profile is minimal. Still, measurement of nSRRs in continental shelf and slope environments proximal to evaporitic systems should carefully account for brine addition as a potential source of SO_4^{2-} to ensure accurate results.

The geographic locations (Figure VI.5) and geochemical statistics (e.g. Figure VI.6) associated with the k-means clusters underscore the strong influence of terrigenous input on the strength of microbial sulfate reduction (MSR) at a given site. Clusters with higher nSRRs are associated with higher TOC content, lower $CaCO_3$ content, and closer proximity to land than those with relatively low nSRRs. This set of relationships is consistent with high productivity sustained by nutrient input from continental weathering (e.g. [314]) in coastal regions and enhanced opportunity for organic matter to survive water column transport with the aid of mineral protection (e.g. [14]). We also note that the overlap between clusters is much lower for TOC content than for $CaCO_3$ content and water depth (Figure VI.6). This suggests that the abundance of TOC in the sediment is the primary control on the $[SO_4^{2-}]$ profile that a given site exhibits; $CaCO_3$ content and water depth serve as secondary influences through their ability to alter TOC abundance.

VI.5.1.1 Implications for nSRR prediction

Disparate mean TOC contents among the clusters in our analysis suggest a compelling possibility: can we predict the mean nSRR that a given site will exhibit

data based on mean TOC content and sedimentation rate alone, in the absence of any $[SO_4^{2-}]$ data? Furthermore, can TOC content be estimated in regions of the seafloor without any TOC data based on influencing variables that are well constrained?

To answer the latter question, we begin by plotting the mean TOC content for deep ocean sites with data available from the JANUS and LIMS databases as a function of modern water depth (Figure VI.7). Although the data can be fit with an exponential relationship wherein TOC (wt%) $= 0.63 * 0.9998^d$ (with d equal to the water depth in meters below sea level), the high amount of variance about this line indicates that TOC content predictions could be inaccurate by an order of magnitude or more for any given site. Such variance is presumably due to differences in sedimentation rate and oxygen exposure time among sites situated at the same water depth; prior studies [134, 141] have found that these two variables in particular are much better predictors of organic matter preservation. A similar situation results if we estimate mean nSRR and plot it against mean TOC for these sites (Figure VI.8). The log-log plot in this figure suggests a power law relationship in which mean nSRR $= 10^{-7.6} *$ mean TOC$^{0.745}$, but the high amount of scatter ($R^2 \sim 0.15$) again indicates that estimates at any given site could be highly inaccurate.

Fundamentally, the accuracy of our estimates of organic matter accumulation rates (a more raw indicator of sedimentary organic matter input than TOC wt%) and of nSRRs are limited by the accuracy of our sedimentation rate estimates. Both here and in Bowles et al. (2014) [43], we have estimated sedimentation rate through a functional relationship with water depth (as well as productivity in [43]). We have made no attempt to incorporate sedimentation rate estimates from site-specific age models, though such an task could be accomplished with much effort. The choice to use a functional relationship introduces a large amount of imprecision into our nSRR estimates, as Middelburg, Soetaert, and Herman (1997) [219] have shown that sedimentation rate can vary by two orders of magnitude or more at a given water depth. Such variation can crucially alter the organic carbon remineralization dynamics and $[SO_4^{2-}]$ profiles that develop at a given site by modifying diffusive supply of dissolved electron acceptors from seawater (see Chapter IV). Development and application of better-constrained sedimentation rate estimates to global nSRR models should be of high priority for future studies.

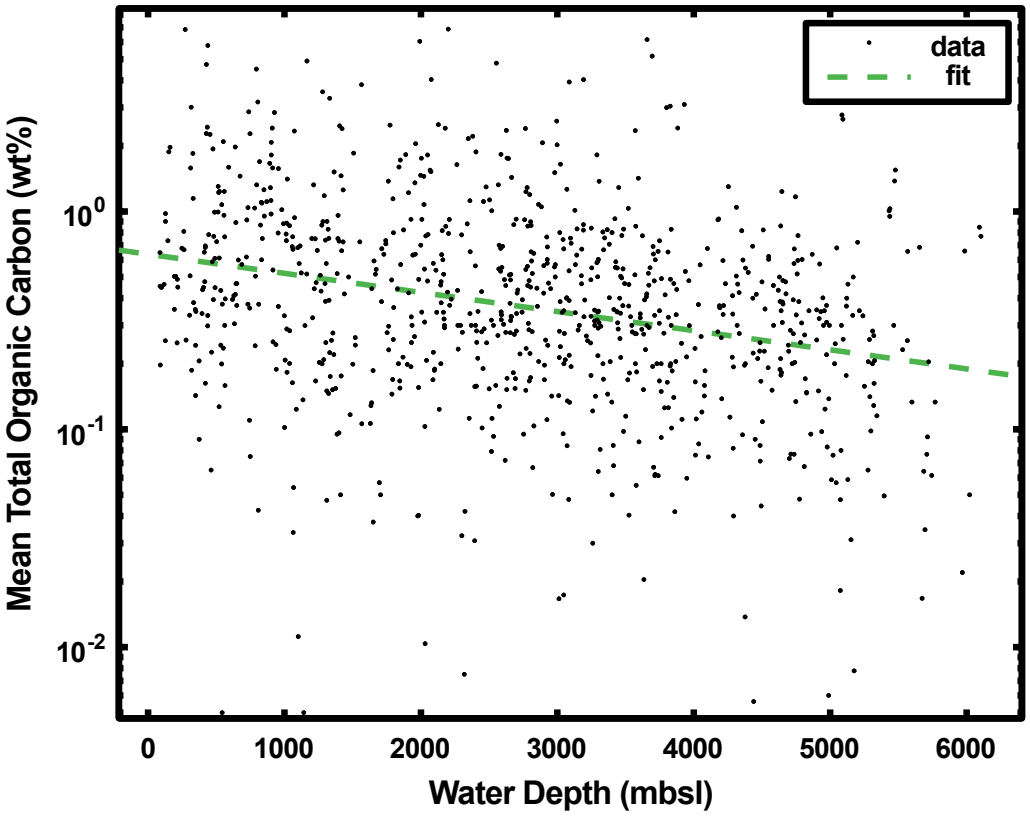

Figure VI.7: Mean sedimentary total organic carbon (TOC) plotted against modern water depth for a compilation of 601 DSDP, ODP, and IODP sites. The dashed green line denotes an exponential fit to the data wherein TOC (wt%) $= 0.63 * 0.9998^{d}$, with d being the water depth in meters below sea level.

VI.5.2 Modern marine S isotope mass balance

VI.5.2.1 Reconciliation of global nSRR and pyrite burial estimates

Uncertainties in the nSRR associated with deep marine sediments have important consequences for our understanding of S isotope mass balance within the modern marine S cycle. A literature compilation of 343 measurements of pyrite $\delta^{34}S$ (Figure VI.9; Table D.2) in modern marine sediments plotted as a function of estimated pyrite S accumulation rate shows over 70‰ variation. We also plot these data in terms of pyrite S accumulation rate versus water depth in Figure D.7. This compilation is clearly biased toward relatively productive coastal regions (Figure D.8); still, measurements on the continental slope and rise often feature lower pyrite $\delta^{34}S$ than sites on the continental shelf (Figure VI.9). Examination of pyrite $\delta^{34}S$ as a function of water depth on the shelf demonstrates

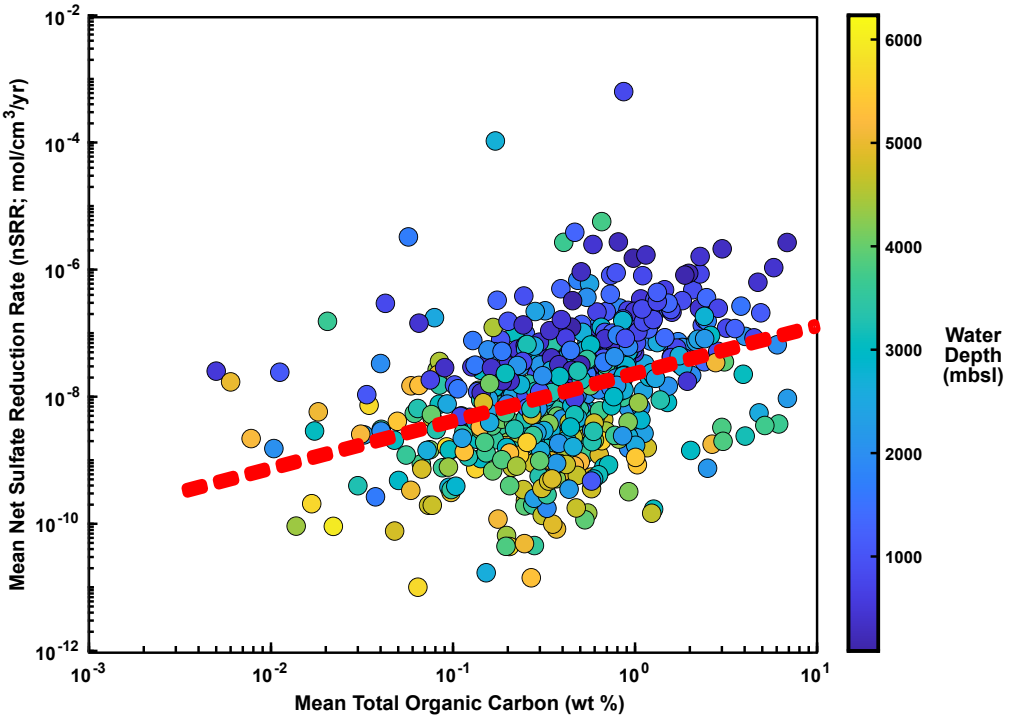

Figure VI.8: Mean nSRR plotted against mean sedimentary total organic carbon (TOC) for a compilation of 601 DSDP, ODP, and IODP sites. Mean nSRR was estimated by assuming steady state and solving for the reaction term in the general diagenetic equation using a curve fit (polynomial or exponential) to the $[SO_4^{2-}]$ and porosity data. Only intervals with positive nSRRs (i.e., SO_4^{2-} consumption) were considered in calculating the mean to avoid any bias introduced by SO_4^{2-} sources at depth or extended depth intervals of no SO_4^{2-} reduction (e.g., below the SMT). The red dashed line denotes a power law fit to the data where mean nSRR $= 10^{-7.6} * \text{mean TOC}^{0.745}$.

that only sites in < 50 m water depth tend to feature pyrite at high (> 1 wt% S) abundances and with $\delta^{34}S$ above 0‰ (Figure VI.10) in our compilation. The average pyrite $\delta^{34}S$ in these sediments weighted based on S accumulation rate is -14.5‰, while the average in 50 to 200 m water depth sediments is -24.6‰. The variance in the pyrite $\delta^{34}S$ data is larger in deeper marine environments, but a recent study [127] suggests a mean pyrite $\Delta\delta^{34}S$ of ~60‰ for sites in > 1000 m water depth. The greater area of the seafloor encompassed by the slope and rise compared to the continental shelf (~92 x 10^6 km^2 versus ~21 x 10^6 km^2 [43]) partially compensates for lower pyrite accumulation rates and allows these regions to contribute significantly to S isotope mass balance given their distinct

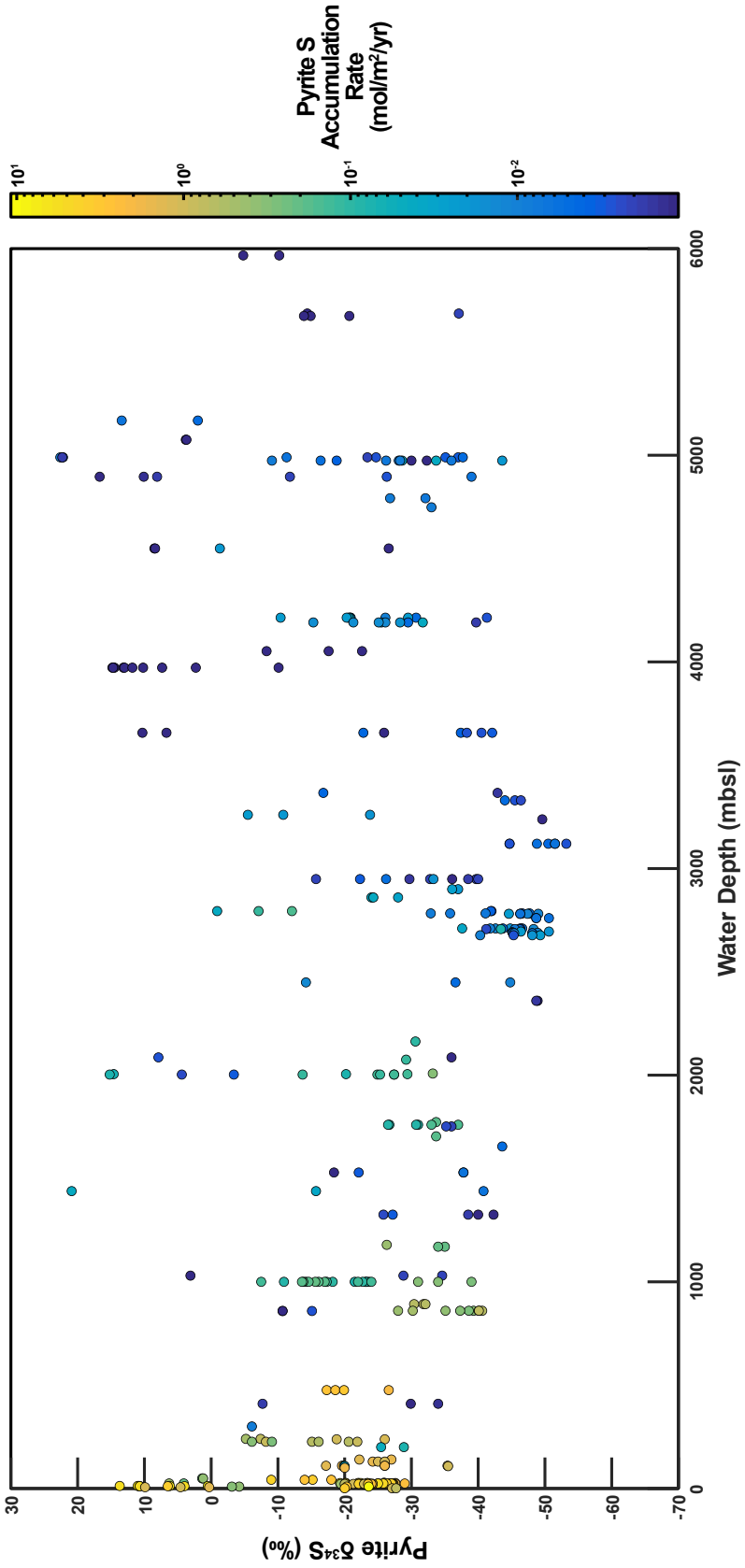

Figure VI.9: Literature compilation of 343 measurements (colored circles) of pyrite $\delta^{34}S$ plotted against modern water depth (meters below sea level). Color of symbols denotes the estimated pyrite S accumulation rate based on the measured pyrite S content of the sediment sample and sedimentation rate. Sedimentation rates were taken from literature estimates or were estimated from water depth based on the relationship of [219]. Data from [4, 37, 38, 115, 133, 158, 174, 175, 188, 197, 198, 220, 221, 222, 266, 293, 328, 329, 336, 349, 371].

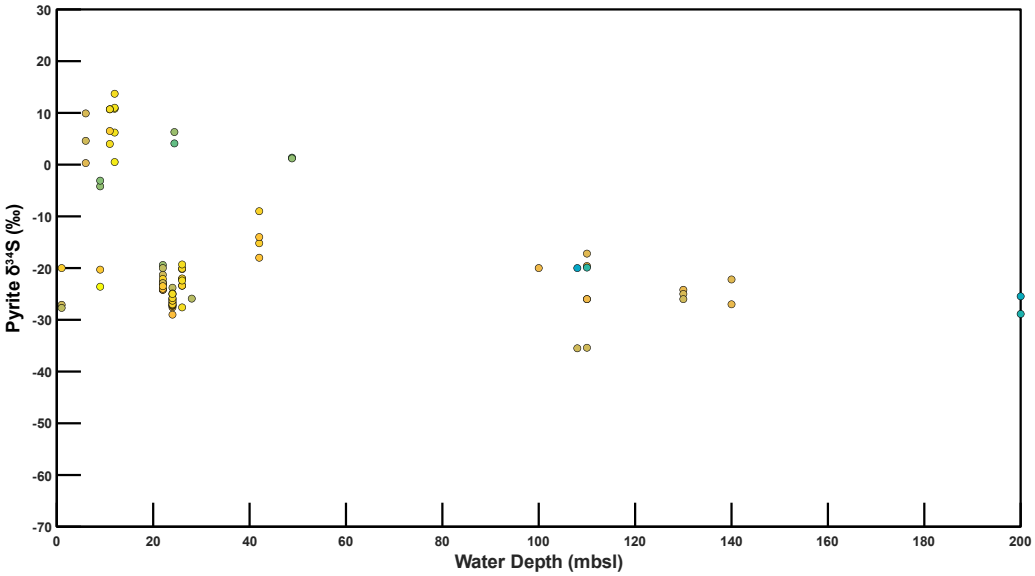

Figure VI.10: Subset of compilation depicted in Figure VI.9 showing only data collected from water depths $\leq$ 200 mbsl. Color of symbols denotes the estimated pyrite S accumulation rate based on the scale shown in Figure VI.9. Sedimentation rates were taken from literature estimates or were estimated from water depth based on the relationship of [219]. Data from [4, 37, 38, 115, 133, 158, 174, 175, 188, 197, 198, 220, 221, 222, 266, 293, 328, 329, 336, 349, 371].

pyrite δ^{34}S. How sensitive is our understanding of isotope mass balance to these deep ocean sites?

We can test the sensitivity of S isotope mass balance to pyrite burial in different ocean regions by experimenting with the following equation:

$$\delta^{34}S_{in} = \delta^{34}S_{evap}(1 - f_{py,tot}) - (\Delta\delta^{34}S_{py,shelf}f_{py,shelf} + \Delta\delta^{34}S_{py,slope}f_{py,slope} + \Delta\delta^{34}S_{py,rise}f_{py,rise} + \Delta\delta^{34}S_{py,abyss}f_{py,abyss}) \quad \text{(VI.2)}$$

where $\delta^{34}S_{in}$ is the δ^{34}S of the weathering input, $\delta^{34}S_{evap}$ is the δ^{34}S of buried sulfate evaporites (assumed to equal $\delta^{34}S_{sea}$, the δ^{34}S of seawater here), $f_{py,tot}$ is the total fraction of the input flux buried as pyrite, and the remaining terms are the $\Delta\delta^{34}$S and pyrite burial fractions associated with shelf, slope, rise, and abyss sediments.

In a recent study of the S isotopic composition of modern seawater, Tostevin et al. (2014) [342] used the abundances of multiple rare sulfur isotopes in seawater SO_4^{2-} to constrain the fraction of S leaving the modern ocean as pyrite. They

found this fraction to be between 0.1 and 0.45, with a more probable range of 0.2 to 0.35 [342]. If we assume a global pyrite S burial flux of 1.22 $\frac{\text{Tmol}}{\text{yr}}$ based on Berner's (1982) [19] analysis of global sedimentary reduced C:S ratios and a partitioning of global pyrite burial in proportion to the sedimentation estimates of Middelburg, Soetaert, and Herman (1997) [219] (i.e., 56% on the shelf, 30% on the slope, 13% on the rise, and 1% in the abyss), we find that Tostevin's seawater $\delta^{34}S = \sim 21.2‰$ can be matched by assigning a $\Delta\delta^{34}S$ of 25‰ to pyrite buried on the shelf, 45‰ to pyrite on the slope, and 60‰ to pyrite on the rise and in the abyss; these assigned values are informed by our pyrite $\delta^{34}S$ compilation. The fraction of S leaving seawater as pyrite in this scenario is 0.44, the globally integrated pyrite $\Delta\delta^{34}S$ is 35.9‰, and the weathering input flux matches the pre-anthropogenic flux estimate of Burke et al. (2018) [52] in its magnitude and $\delta^{34}S$.

Alternatively, we can also use the pyrite S accumulation rate estimates from the pyrite compilation to estimate S isotope mass balance. If we treat the S accumulation data in Figure D.7 as being biased toward high values and assign mean pyrite S accumulation rates of 0.05 $\frac{\text{mol}}{\text{m}^2\text{yr}}$ to the shelf (< 200 mbsl), 0.005 $\frac{\text{mol}}{\text{m}^2\text{yr}}$ to the slope (200-2000 mbsl), and 0.0005 $\frac{\text{mol}}{\text{m}^2\text{yr}}$ to the rise and abyss (> 2000 mbsl), extrapolating over the seafloor areas encompassed by these depth intervals [5, 43] yields a total pyrite S burial rate of $\sim 1.34 \frac{\text{Tmol}}{\text{yr}}$. This burial rate is of the same order of magnitude as both the riverine input flux [52] and Berner's (1982) [19] pyrite burial flux estimate; however, the proportion of pyrite burial that occurs on the shelf (78%) is much higher than that assumed based on the distribution of global sedimentation [219] or the results of Bowles et al. (2014) [43]. This distribution of pyrite burial can yield a steady state seawater $\delta^{34}S$ matching the modern one [342] if the $\Delta\delta^{34}S$ of shelf pyrite burial is increased from 25‰ to ~27‰with all other $\Delta\delta^{34}S$ values identical to those in the previous scenario. We note that the total pyrite burial flux in this model is highly sensitive to the mean pyrite S accumulation rate assumed for shelf sediments; increasing the mean accumulation rate for these sediments by an order of magnitude or more quickly yields total pyrite burial fluxes that exceed even the relatively high global nSRR estimate of Bowles et al. (2014) [43].

A major caveat to both of these reconstructions is the lack of data from deltaic sediments. Berner (1982) [19] has estimated that deltaic shelf sediments account for over 80% of the organic carbon buried in sediments in the modern ocean. Although this estimate is well constrained by extensive measurement

of the organic carbon content of deltaic sediments, such studies have not routinely measured the abundance of pyrite sulfur in these same sediments; instead, Berner's (1982) [19] pyrite burial flux estimate relies on the average ratio of organic carbon to sulfur by weight in marine sediments. We have not distinguished continental shelf environments from deltaic environments in our data compilation efforts, and whether each of these environments has a similar effect on the $\delta^{34}S$ of the global pyrite burial flux is uncertain. Additional studies should explore this open question in more detail.

Finally, the pore water $[SO_4{}^{2-}]$ profiles included in our cluster analysis can be used to provide a sanity check on the pyrite S accumulation rates assigned to different regions in the latter of the above two mass balance estimates. Using the method of Canfield (1991) [55] to roughly estimate the aerial nSRR for each site included in our analysis, we find the median aerial nSRRs for clusters 1, 3, and 5 to be 0.0013, 0.0018, and 0.0043 $\frac{mol}{m^2 yr}$, respectively. These median nSRR values fall between our assumed pyrite S accumulation rate values for the slope and the rise + abyss; this is consistent with the geographic distribution of the sites within these clusters being skewed toward the continental slope/rise and the abyss. Clusters 2 and 4 have higher median aerial nSRR values of 0.0099 and 0.0065 $\frac{mol}{m^2 yr}$, respectively. These values are slightly larger than the pyrite S accumulation rate we assumed for the slope (0.005 $\frac{mol}{m^2 yr}$) in the above scenario, consistent with the distribution of the sites within these clusters in relatively shallow coastal areas. The pore water $[SO_4{}^{2-}]$ profiles included in our cluster analysis thus are in general agreement with our relatively low S accumulation rate assignments above and appear to confirm that sites with high sedimentary S contents are over-represented in our compilation — and likely, in marine pyrite $\delta^{34}S$ data in general. Our observation of slightly higher median aerial nSRR values within the clusters than the values we assume for our mass balance calculations suggests that the pore water data may also be slightly biased toward regions with relatively high nSRR. Future comparison of these site locations with surface productivity and oxygen exposure time estimates [134] will test this hypothesis.

VI.5.2.2 Sensitivity of seawater $\delta^{34}S$ to the deep ocean pyrite burial flux

Neither of the mass balance calculations in the preceding section considered the isotope mass balance effects of $SO_4{}^{2-}$ sequestered as hydrothermal anhy-

drite and later released through off-axis dissolution [2, 3, 358]. Addition of this SO_4^{2-} to sediments has the potential to substantially augment the amount of pyrite buried in deep ocean sediments if it is sequestered as sulfide rather than returned to seawater. If we assume the lowest estimate of S removal via hydrothermal circulation in Alt (1995) [2] (0.3 $\frac{\text{Tmol}}{\text{yr}}$) to be accurate and estimate that half of this removal occurs as anhydrite, the resulting anhydrite S dissolution flux (0.15 $\frac{\text{Tmol}}{\text{yr}}$) would augment the total amount of pyrite formed outside of shelf sediments by $\sim$28% and $\sim$51% in the above two mass balance scenarios (respectively) if the entire dissolution flux were preserved as pyrite. Notably, the magnitude of this dissolution flux is smaller than the uncertainty in the Burke et al. (2018) [52] riverine input estimate. If we increase both the magnitude of the input flux and the magnitude of the continental rise pyrite burial flux by 0.15 $\frac{\text{Tmol}}{\text{yr}}$ while changing nothing else, the resulting steady state seawater δ^{34}S becomes 25.8‰ and 26.2‰ in the aforementioned scenarios. Reducing the $\Delta\delta^{34}$S for pyrite burial by nearly 10‰ on the shelf or the slope and rise would be required to return the steady state seawater δ^{34}S to $\sim$21‰ in the former scenario; a reduction in the shelf $\Delta\delta^{34}$S by $\sim$6‰ or the slope and rise $\Delta\delta^{34}$S by $\sim$15‰ would be needed in the latter scenario.

In both of the mass balance scenarios considered here, the majority of pyrite burial in the modern ocean occurs in shelf sediments. However, Berner (1982) [19] has discussed the possibility of a transfer of some sedimentation from the shelf to the deep ocean in conjunction with lower sea levels during the last glacial period. Burial of pyrite in proportion to sedimentation would result in a concomitant shift of some shelf pyrite burial to the slope and deeper environments. How would such a transfer affect S isotope mass balance?

To estimate the sensitivity of seawater δ^{34}S to sedimentation shifts driven by changes in shelf area, we downloaded the ice surface ETOPO1 arc-minute global relief model [5] and estimated the change in shelf area (0-200 mbsl) for changes in sea level ranging from -150 m to +100 m (Figure VI.11). We then transferred sedimentation between the continental shelf and the continental slope in proportion to the relative change in shelf area. The Bowles et al. (2014) [43] nSRR estimates were used to distribute pyrite burial among different global environments at modern sea level, and the relative amount of pyrite burial in each environment was shifted to match the relative sedimentation change while keeping the total pyrite burial flux constant. Note that modern global hypsometry is

dominated by topography near sea level: a sea level decrease of just 50 m halves the amount of shelf area, while an increase of 50 m increases shelf area by about 50%. Our calculations show that shifting pyrite burial without any concomitant changes in shelf or slope $\Delta\delta^{34}S$ causes the steady state seawater $\delta^{34}S$ to increase by over 6‰ for a 150 m drop in sea level or to decrease by nearly 5‰ for a 100 m rise (Figure VI.11C). Initiating the numerical experiment with pyrite burial concentrated on the shelf to a greater degree results in more dramatic pyrite burial shifts and even larger seawater $\delta^{34}S$ changes. In reality, changes in $\Delta\delta^{34}S$ associated with sedimentation shifts may partially offset such shelf-area related effects (see Chapter IV discussion). The rate of Pleistocene glacial-interglacial sea level changes is far too rapid for this mechanism to force substantial changes in seawater $\delta^{34}S$ on this timescale given the 10+ Myr residence time of seawater SO_4^{2-} in the modern ocean [353]. However, it may be a plausible mechanism for altering seawater $\delta^{34}S$ on longer (1 Myr+), tectonic timescales ([195]; see Chapter II) or at times when seawater $[SO_4^{2-}]$ was much lower.

VI.6 Conclusions

Here, we have undertaken a new analysis of S cycling in deep marine sediments by subjecting global deep ocean pore water $[SO_4^{2-}]$ profiles to cluster analysis. We find that k-means clustering can successfully group sites with distinct variants of $[SO_4^{2-}]$ profiles; in turn, these groups of sites have differing geographic distributions. Organic carbon content is the strongest determinant of the type of $[SO_4^{2-}]$ profile that a given site will exhibit, although water depth and $CaCO_3$ content exert secondary influences. Comparison of estimated nSRRs to estimated pyrite S accumulation rates derived from a literature compilation of pyrite $\delta^{34}S$ measurements suggests that the compiled data are biased toward regions with relatively high sedimentary S contents. Isotope mass balance calculations indicate that augmentation of the pyrite burial flux in deep marine sediments, whether it be due to a reduction in shelf area or via another mechanism, may perturb the steady state $\delta^{34}S$ of seawater SO_4^{2-} by 6‰ or more if unaccompanied by synchronous changes in $\Delta\delta^{34}S$. These findings motivate further efforts toward making unbiased estimates of global S cycle fluxes and reconciling current disagreements between input and output flux estimates.

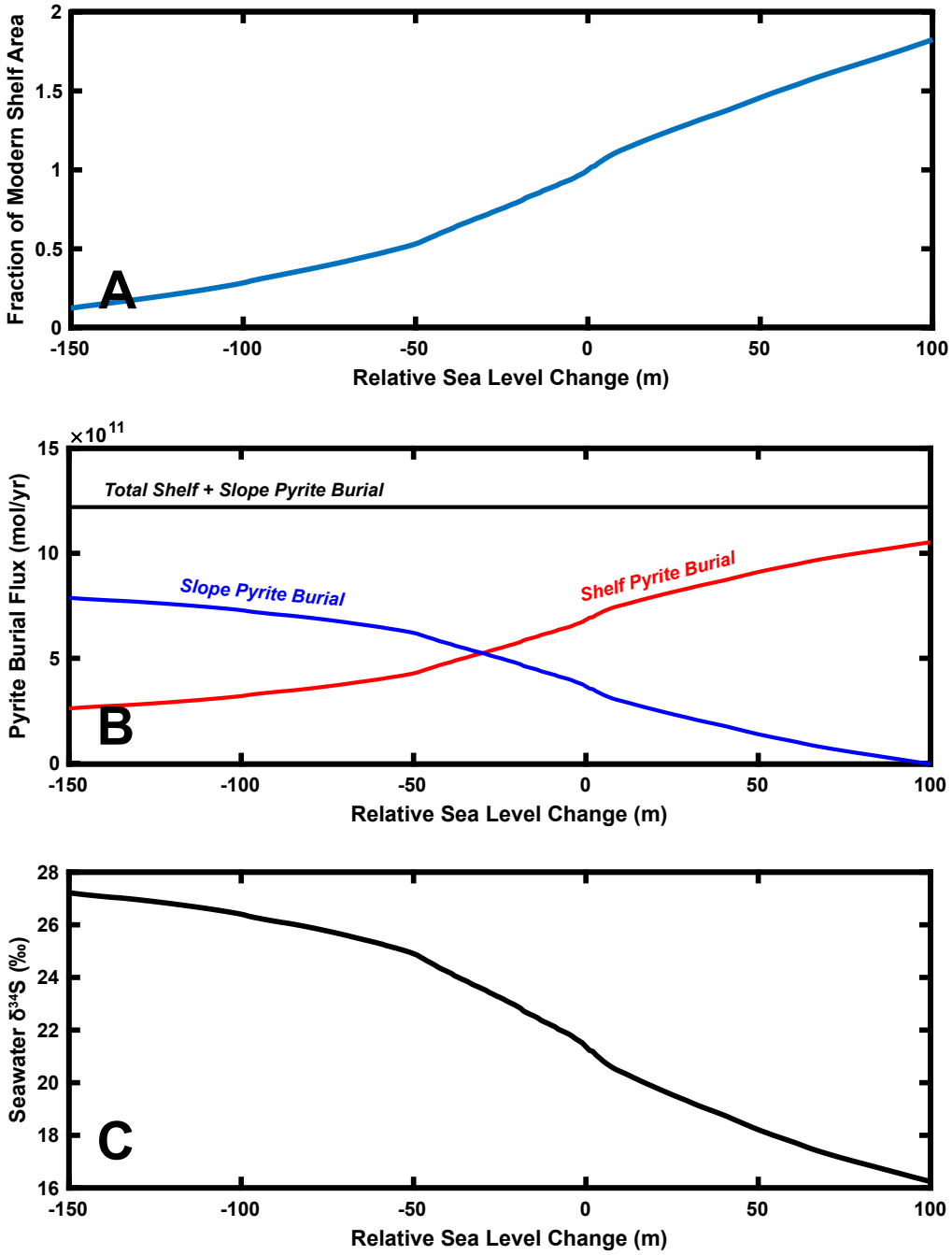

Figure VI.11: Sea level / shelf area numerical experiment results. (A) Calculated change in the amount of submerged shelf area (0-200 mbsl) relative to modern for a given change in sea level. Area was calculated using the ice surface version of the ETOPO1 global topography [5]. (B) Continental shelf and continental slope pyrite burial flux. If total pyrite burial is unchanged and shelf burial is proportional to shelf area, sea level fall results in a transfer of pyrite burial from the shelf to the slope. (C) Calculated steady-state seawater $\delta^{34}S$ for shelf $\Delta\delta^{34}S = 25‰$ and slope $\Delta\delta^{34}S = 45‰$.

BIBLIOGRAPHY

[1] Algeo, T. J. and Sheckler, S. E. "Terrestrial-marine teleconnections in the Devonian: Links between the evolution of land plants, weathering processes, and marine anoxic events." In: *Philosophical Transactions of the Royal Society of London. Series B: Biological Sciences* 353.1365 (Jan. 29, 1998), pp. 113–130. DOI: 10.1098/rstb.1998.0195. URL: https://royalsocietypublishing.org/doi/abs/10.1098/rstb.1998.0195 (visited on 04/23/2019).

[2] Alt, J. C. "Sulfur isotopic profile through the oceanic crust: Sulfur mobility and seawater-crustal sulfur exchange during hydrothermal alteration." In: *Geology* 23.7 (July 1, 1995). Publisher: GeoScienceWorld, pp. 585–588. ISSN: 0091-7613. DOI: 10.1130/0091-7613(1995)023<0585:SIPTTO>2.3.CO;2. URL: https://pubs.geoscienceworld.org/gsa/geology/article/23/7/585/206332/Sulfur-isotopic-profile-through-the-oceanic-crust (visited on 09/05/2020).

[3] Alt, J. C., Anderson, T. F., and Bonnell, L. "The geochemistry of sulfur in a 1.3 km section of hydrothermally altered oceanic crust, DSDP Hole 504B." In: *Geochimica et Cosmochimica Acta* 53.5 (1989). ISBN: 0016-7037 Publisher: Pergamon, pp. 1011–1023. DOI: 10.1016/0016-7037(89)90206-8.

[4] Alt, J. C. and Burdett, J. W. "Sulfur in Pacific deep-sea sediments (Leg 129) and implications for cycling of sediment in subduction zones." In: *Proceedings of the Ocean Drilling Program, Scientific Results*. Vol. 129. College Station, TX (Ocean Drilling Program), 1992, pp. 283–294. DOI: 10.2973/odp.proc.sr.129.125.1992.

[5] Amante, C. and Eakins, B. W. "ETOPO1 arc-minute global relief model: Procedures, data sources and analysis." In: (2009). DOI: 10.7289/V5C8276M.

[6] Amrani, A., Sessions, A. L., and Adkins, J. F. "Compound-specific $\delta^{34}S$ analysis of volatile organics by coupled GC/multicollector-ICPMS." In: *Analytical Chemistry* 81.21 (Nov. 1, 2009). Publisher: American Chemical Society, pp. 9027–9034. ISSN: 0003-2700. DOI: 10.1021/ac9016538. URL: https://doi.org/10.1021/ac9016538 (visited on 08/07/2020).

[7] Anderson, L. A. "On the hydrogen and oxygen content of marine phytoplankton." In: *Deep Sea Research Part I: Oceanographic Research Papers* 42.9 (Sept. 1, 1995), pp. 1675–1680. ISSN: 0967-0637. DOI: 10.1016/0967-0637(95)00072-E. URL: http://www.

sciencedirect.com/science/article/pii/096706379500072E (visited on 10/16/2020).

[8] Anderson, R. F. et al. “Deep-sea oxygen depletion and ocean carbon sequestration during the last ice age.” In: *Global Biogeochemical Cycles* 33.3 (2019), pp. 301–317. ISSN: 1944-9224. DOI: 10.1029/2018GB006049. URL: https://agupubs.onlinelibrary.wiley.com/doi/abs/10.1029/2018GB006049 (visited on 11/18/2019).

[9] *AR5 Climate Change 2014: Mitigation of Climate Change — IPCC*. Library Catalog: www.ipcc.ch. 2014. URL: https://www.ipcc.ch/report/ar5/wg3/ (visited on 07/04/2020).

[10] Archer, D. and Devol, A. “Benthic oxygen fluxes on the Washington shelf and slope: A comparison of in situ microelectrode and chamber flux measurements.” In: *Limnology and Oceanography* 37.3 (May 1, 1992), pp. 614–629. ISSN: 1939-5590. DOI: 10.4319/lo.1992.37.3.0614. URL: https://aslopubs.onlinelibrary.wiley.com/doi/abs/10.4319/lo.1992.37.3.0614 (visited on 10/05/2018).

[11] Ault, W. U. and Kulp, J. L. “Isotopic geochemistry of sulphur.” In: *Geochimica et Cosmochimica Acta* 16.4 (July 1, 1959), pp. 201–235. ISSN: 0016-7037. DOI: 10.1016/0016-7037(59)90112-7. URL: http://www.sciencedirect.com/science/article/pii/0016703759901127.

[12] Bacon, M. P. and Rosholt, J. N. “Accumulation rates of Th-230, Pa-231, and some transition metals on the Bermuda Rise.” In: *Geochimica et Cosmochimica Acta* 46.4 (Apr. 1, 1982), pp. 651–666. ISSN: 0016-7037. DOI: 10.1016/0016-7037(82)90166-1. URL: http://www.sciencedirect.com/science/article/pii/0016703782901661 (visited on 07/26/2020).

[13] Bains-Sahota, S. K. and Thiemens, M. H. “Fluorination of sulfur tetrafluoride, pentafluorosulfur chloride and disulfur decafluoride to sulfur hexafluoride for mass spectrometric isotope ratio analysis.” In: *Analytical Chemistry* 60.10 (May 15, 1988). Publisher: American Chemical Society, pp. 1084–1086. ISSN: 0003-2700. DOI: 10.1021/ac00161a029. URL: https://doi.org/10.1021/ac00161a029 (visited on 08/06/2020).

[14] Baldock, J. A. and Skjemstad, J. O. “Role of the soil matrix and minerals in protecting natural organic materials against biological attack.” In: *Organic Geochemistry* 31.7 (July 1, 2000), pp. 697–710. ISSN: 0146-6380. DOI: 10.1016/S0146-6380(00)00049-8. URL: http://www.sciencedirect.com/science/article/pii/S0146638000000498 (visited on 09/07/2020).

[15] Barkan, Y. et al. “Sulfur isotope fractionation between aqueous and carbonate-associated sulfate in abiotic calcite and aragonite.” In: *Geochimica et Cosmochimica Acta* (Mar. 24, 2020). ISSN: 0016-7037. DOI: 10.1016/j.gca.2020.03.022. URL: http://www.sciencedirect.com/science/article/pii/S0016703720301939 (visited on 04/06/2020).

[16] Benmore, R. A., Coleman, M. L., and McArthur, J. M. “Origin of sedimentary francolite from its sulphur and carbon isotope composition.” In: *Nature* 302.5908 (Apr. 1983). Number: 5908 Publisher: Nature Publishing Group, pp. 516–518. ISSN: 1476-4687. DOI: 10.1038/302516a0. URL: https://www.nature.com/articles/302516a0 (visited on 07/30/2020).

[17] Bernasconi, S. M. et al. “An evaporite-based high-resolution sulfur isotope record of Late Permian and Triassic seawater sulfate.” In: *Geochimica et Cosmochimica Acta* 204 (2017), pp. 331–349. ISSN: 0016-7037. DOI: 10.1016/j.gca.2017.01.047. URL: http://www.sciencedirect.com/science/article/pii/S0016703717300716.

[18] Berner, E. K. and Berner, R. A. *Global environment: Water, air, and geochemical cycles*. Princeton University Press, 2012. ISBN: 0-691-13678-5. URL: https://press.princeton.edu/books/hardcover/9780691136783/global-environment.

[19] Berner, R. A. “Burial of organic carbon and pyrite sulfur in the modern ocean: Its geochemical and environmental significance.” In: *American Journal of Science* 282.4 (1982), pp. 451–473. DOI: 10.2475/ajs.282.4.451.

[20] Berner, R. A. “An idealized model of dissolved sulfate distribution in recent sediments.” In: *Geochimica et Cosmochimica Acta* 28.9 (Sept. 1, 1964), pp. 1497–1503. ISSN: 0016-7037. DOI: 10.1016/0016-7037(64)90164-4. URL: http://www.sciencedirect.com/science/article/pii/0016703764901644 (visited on 05/11/2020).

[21] Berner, R. A. “Diagenetic models of dissolved species in the interstitial waters of compacting sediments.” In: *American Journal of Science* 275.1 (Jan. 1, 1975), pp. 88–96. DOI: 10.2475/ajs.275.1.88. URL: http://www.ajsonline.org/content/275/1/88.short%20http://www.ajsonline.org/content/275/1/88.full.pdf.

[22] Berner, R. A. *Early diagenesis: A theoretical approach*. Princeton University Press, 1980. URL: https://press.princeton.edu/titles/121.html (visited on 12/03/2017).

[23] Berner, R. A. “Sedimentary pyrite formation: An update.” In: *Geochimica et Cosmochimica Acta* 48.4 (1984), pp. 605–615. ISSN: 0016-7037. DOI: 10.1016/0016-7037(84)90089-9. URL: http://www.sciencedirect.com/science/article/pii/0016703784900899%20http://ac.els-cdn.com/0016703784900899/1-s2.0-0016703784900899-main.pdf?_tid=db620d40-3fc7-11e4-a15b-00000aacb361&acdnat=1411109014_c733f335afe8789d8515aececeb55cd8.

[24] Berner, R. A. “Examination of hypotheses for the Permo–Triassic boundary extinction by carbon cycle modeling.” In: *Proceedings of the National Academy of Sciences* 99.7 (Apr. 2, 2002). Publisher: National Academy of Sciences Section: Physical Sciences, pp. 4172–4177. ISSN: 0027-8424, 1091-6490. DOI: 10.1073/pnas.032095199. URL: https://www.pnas.org/content/99/7/4172 (visited on 08/13/2020).

[25] Berner, R. A. “GEOCARBSULF: A combined model for Phanerozoic atmospheric O2 and CO2.” In: *Geochimica et Cosmochimica Acta* 70.23 (2006), pp. 5653–5664. ISSN: 0016-7037. DOI: 10.1016/j.gca.2005.11.032. URL: http://www.sciencedirect.com/science/article/pii/S0016703706002031%20http://ac.els-cdn.com/S0016703706002031/1-s2.0-S0016703706002031-main.pdf?_tid=da30d6f2-ee56-11e4-b55c-00000aacb362&acdnat=1430301932_38a92ba964326d6de763bac14ea5fdf0.

[26] Berner, R. A. and Canfield, D. E. “A new model for atmospheric oxygen over Phanerozoic time.” In: *American Journal of Science* 289.4 (Apr. 1, 1989), pp. 333–361. ISSN: 0002-9599, 1945-452X. DOI: 10.2475/ajs.289.4.333. URL: http://www.ajsonline.org/content/289/4/333 (visited on 06/21/2018).

[27] Berner, R. A. and Raiswell, R. “Burial of organic carbon and pyrite sulfur in sediments over phanerozoic time: A new theory.” In: *Geochimica et Cosmochimica Acta* 47.5 (1983), pp. 855–862. ISSN: 0016-7037. DOI: 10.1016/0016-7037(83)90151-5. URL: http://www.sciencedirect.com/science/article/pii/0016703783901515%20http://ac.els-cdn.com/0016703783901515/1-s2.0-0016703783901515-main.pdf?_tid=d85a2286-3fc7-11e4-becd-00000aab0f02&acdnat=1411109008_c185311082fe8f48dbb1f596c2057444.

[28] Berner, Z. A. et al. “Pyrite geochemistry in the Toarcian Posidonia Shale of south-west Germany: Evidence for contrasting trace-element patterns of diagenetic and syngenetic pyrites.” In: *Sedimentology* 60.2 (2013). _eprint: https://onlinelibrary.wiley.com/doi/pdf/10.1111/j.1365-3091.2012.01350.x, pp. 548–573. ISSN: 1365-3091. DOI:

10.1111/j.1365-3091.2012.01350.x. URL: https://onlinelibrary.wiley.com/doi/abs/10.1111/j.1365-3091.2012.01350.x (visited on 08/30/2020).

[29] Bianchi, D. et al. “Global niche of marine anaerobic metabolisms expanded by particle microenvironments.” In: *Nature Geoscience* 11.4 (Apr. 2018). Number: 4 Publisher: Nature Publishing Group, pp. 263–268. ISSN: 1752-0908. DOI: 10.1038/s41561-018-0081-0. URL: https://www.nature.com/articles/s41561-018-0081-0 (visited on 07/30/2020).

[30] Bishop, J. W., Montañez, I. P., and Osleger, D. A. “Dynamic Carboniferous climate change, Arrow Canyon, Nevada.” In: *Geosphere* 6.1 (Feb. 1, 2010), pp. 1–34. DOI: 10.1130/ges00192.1. URL: http://geosphere.gsapubs.org/content/6/1/1.abstract.

[31] Bishop, J. W. et al. “The onset of mid-Carboniferous glacio-eustasy: Sedimentologic and diagenetic constraints, Arrow Canyon, Nevada.” In: *Palaeogeography, Palaeoclimatology, Palaeoecology* 276.1 (May 15, 2009), pp. 217–243. ISSN: 0031-0182. DOI: 10.1016/j.palaeo.2009.02.019. URL: http://www.sciencedirect.com/science/article/pii/S0031018209000492%20http://ac.els-cdn.com/S0031018209000492/1-s2.0-S0031018209000492-main.pdf?_tid=5ca899ee-611e-11e7-a2cf-00000aab0f6b&acdnat=1499217049_b32bbfbeb7a4283861fb57cece120ca1.

[32] Bjerrum, C. J. and Canfield, D. E. “Ocean productivity before about 1.9 Gyr ago limited by phosphorus adsorption onto iron oxides.” In: *Nature* 417.6885 (2002), pp. 159–162. ISSN: 0028-0836. DOI: 10.1038/417159a. URL: http://dx.doi.org/10.1038/417159a%20http://www.nature.com/nature/journal/v417/n6885/pdf/417159a.pdf.

[33] Blättler, C. L. et al. “Two-billion-year-old evaporites capture Earth’s great oxidation.” In: *Science* (Mar. 22, 2018), eaar2687. ISSN: 0036-8075, 1095-9203. DOI: 10.1126/science.aar2687. URL: http://science.sciencemag.org/content/early/2018/03/21/science.aar2687 (visited on 04/05/2018).

[34] Bliskovskiy, V. Z. et al. “Sulfur isotopic composition of the minerals of phosphorites.” In: *Geokhimiya* 8 (1977), pp. 1208–1216.

[35] Blomeier, D. et al. “Environmental change in the Early Permian of NE Svalbard: from a warm-water carbonate platform (Gipshuken Formation) to a temperate, mixed siliciclastic-carbonate ramp (Kapp Starostin Formation).” In: *Facies* 57.3 (July 1, 2011), pp. 493–523. ISSN: 1612-4820. DOI: 10.1007/s10347-010-0243-z. URL:

https://doi.org/10.1007/s10347-010-0243-z (visited on 12/20/2018).

[36] Bond, D. P. G. and Wignall, P. B. “Pyrite framboid study of marine Permian–Triassic boundary sections: A complex anoxic event and its relationship to contemporaneous mass extinction.” In: *GSA Bulletin* 122.7 (July 1, 2010), pp. 1265–1279. ISSN: 0016-7606. DOI: 10.1130/B30042.1. URL: https://pubs.geoscienceworld.org/gsa/gsabulletin/article/122/7-8/1265/125592/pyrite-framboid-study-of-marine-permian-triassic (visited on 10/19/2018).

[37] Bonnell, L. M. and Anderson, T. F. “Sulfur isotopic variations in dodular and disseminated pyrite - Hole 603B.” In: *Initial Reports of the Deep Sea Drilling Project* 93 (1987), pp. 1257–1262. DOI: 10.2973/dsdp.proc.93.157.1987.

[38] Böttcher, M. E. et al. “Microbial sulfate reduction in deep sediments of the Southwest Pacific (ODP Leg 181, Sites 1119–1125): evidence from stable sulfur isotope fractionation and pore water modeling.” In: *Marine Geology*. Cenozoic Oceanographic Evolution of the Southwest Pacific Gateway, ODP Leg 181 205.1 (Apr. 30, 2004), pp. 249–260. ISSN: 0025-3227. DOI: 10.1016/S0025-3227(04)00026-X. URL: http://www.sciencedirect.com/science/article/pii/S002532270400026X.

[39] Boudreau, B. P. “Is burial velocity a master parameter for bioturbation?” In: *Geochimica et Cosmochimica Acta* 58.4 (Feb. 1, 1994), pp. 1243–1249. ISSN: 0016-7037. DOI: 10.1016/0016-7037(94)90378-6. URL: http://www.sciencedirect.com/science/article/pii/0016703794903786 (visited on 04/05/2020).

[40] Boudreau, B. P. “A method-of-lines code for carbon and nutrient diagenesis in aquatic sediments.” In: *Computers & Geosciences* 22.5 (June 1, 1996), pp. 479–496. ISSN: 0098-3004. DOI: 10.1016/0098-3004(95)00115-8. URL: http://www.sciencedirect.com/science/article/pii/0098300495001158 (visited on 09/24/2018).

[41] Boudreau, B. P. *Diagenetic models and their implementation*. Vol. 505. Springer Berlin, 1997. URL: https://www.researchgate.net/profile/Bernard_Boudreau/publication/235335761_Diagenetic_models_and_their_implementation_modelling_transport_and_reactions_in_aquatic_sediments/links/0fcfd510fd916cfdde000000/Diagenetic-models-and-their-implementation-modelling-transport-and-reactions-in-aquatic-sediments.pdf.

[42] Boudreau, B. P. and Canfield, D. E. “A comparison of closed- and open-system models for porewater pH and calcite-saturation state.” In: *Geochimica et Cosmochimica Acta* 57.2 (Jan. 1, 1993), pp. 317–334. ISSN: 0016-7037. DOI: 10.1016/0016-7037(93)90434-X. URL: http://www.sciencedirect.com/science/article/pii/001670379390434X (visited on 10/08/2018).

[43] Bowles, M. W. et al. “Global rates of marine sulfate reduction and implications for sub–sea-floor metabolic activities.” In: *Science* 344.6186 (May 23, 2014), pp. 889–891. DOI: 10.1126/science.1249213. URL: http://www.sciencemag.org/content/344/6186/889.abstract%20http://www.sciencemag.org/content/344/6186/889.full.pdf.

[44] Bruckschen, P., Oesmann, S., and Veizer, J. “Isotope stratigraphy of the European Carboniferous: Proxy signals for ocean chemistry, climate and tectonics.” In: *Chemical Geology* 161.1 (1999), pp. 127–163. ISSN: 0009-2541. DOI: 10.1016/S0009-2541(99)00084-4. URL: http://www.sciencedirect.com/science/article/pii/S0009254199000844.

[45] Bruckschen, P. et al. “$^{87}Sr/^{86}Sr$ isotopic evolution of Lower Carboniferous seawater: Dinantian of western Europe.” In: *Sedimentary Geology* 100.1 (Dec. 1, 1995), pp. 63–81. ISSN: 0037-0738. DOI: 10.1016/0037-0738(95)00103-4. URL: http://www.sciencedirect.com/science/article/pii/0037073895001034.

[46] Bryant, R. N. et al. “Sulfur isotope analysis of microcrystalline iron sulfides using secondary ion mass spectrometry imaging: Extracting local paleo-environmental information from modern and ancient sediments.” In: *Rapid Communications in Mass Spectrometry: RCM* 33.5 (Mar. 15, 2019). Publisher: John Wiley & Sons, Inc., pp. 491–502. ISSN: 09514198. DOI: 10.1002/rcm.8375. URL: http://search.ebscohost.com/login.aspx?direct=true&db=cxh&AN=134930929&site=eds-live (visited on 08/06/2020).

[47] Bryant, R. N. et al. “Shifting modes of iron sulfidization at the onset of OAE-2 drive regional shifts in pyrite $\delta^{34}S$ records.” In: *Chemical Geology* 553 (Oct. 20, 2020), p. 119808. ISSN: 0009-2541. DOI: 10.1016/j.chemgeo.2020.119808. URL: http://www.sciencedirect.com/science/article/pii/S0009254120303478 (visited on 08/14/2020).

[48] Budil, P. and Hoerbinger, F. “Exoskeletal structures and ultrastructures in Lower Devonian dalmanitid trilobites of the Prague Basin (Czech Republic).” In: *Bulletin of Geosciences* 82.1 (2007), pp. 27–36. DOI: 10.3140/bull.geosci.2007.01.27.

[49] Burdett, J. W., Arthur, M. A., and Richardson, M. “A Neogene seawater sulfur isotope age curve from calcareous pelagic microfossils.” In: *Earth and Planetary Science Letters* 94.3 (1989), pp. 189–198. ISSN: 0012-821X. DOI: 10.1016/0012-821X(89)90138-6. URL: http://www.sciencedirect.com/science/article/pii/0012821X89901386%20http://ac.els-cdn.com/0012821X89901386/1-s2.0-0012821X89901386-main.pdf?_tid=fd0b94e0-3f70-11e4-9394-00000aab0f6c&acdnat=1411071704_56ff1ab1782821f52b2e4e8b3ec9dc48.

[50] Burgess, S. D., Bowring, S., and Shen, S.-z. “High-precision timeline for Earth’s most severe extinction.” In: *Proceedings of the National Academy of Sciences* 111.9 (Mar. 4, 2014), pp. 3316–3321. DOI: 10.1073/pnas.1317692111. URL: http://www.pnas.org/content/111/9/3316.abstract%20http://www.pnas.org/content/111/9/3316.full.pdf.

[51] Burgess, S. D. and Bowring, S. A. “High-precision geochronology confirms voluminous magmatism before, during, and after Earth’s most severe extinction.” In: *Science Advances* 1.7 (2015). DOI: 10.1126/sciadv.1500470. URL: http://advances.sciencemag.org/content/advances/1/7/e1500470.full.pdf.

[52] Burke, A. et al. “Sulfur isotopes in rivers: Insights into global weathering budgets, pyrite oxidation, and the modern sulfur cycle.” In: *Earth and Planetary Science Letters* 496 (Aug. 15, 2018), pp. 168–177. ISSN: 0012-821X. DOI: 10.1016/j.epsl.2018.05.022. URL: http://www.sciencedirect.com/science/article/pii/S0012821X18302991 (visited on 06/22/2018).

[53] Busenberg, E. and Plummer, N. L. “Kinetic and thermodynamic factors controlling the distribution of SO42- and Na+ in calcites and selected aragonites.” In: *Geochimica et Cosmochimica Acta* 49.3 (1985), pp. 713–725. ISSN: 0016-7037. DOI: 10.1016/0016-7037(85)90166-8. URL: http://www.sciencedirect.com/science/article/pii/0016703785901668.

[54] Butler, I. B. et al. “Sulfur isotope partitioning during experimental formation of pyrite via the polysulfide and hydrogen sulfide pathways: Implications for the interpretation of sedimentary and hydrothermal pyrite isotope records.” In: *Earth and Planetary Science Letters* 228.3 (2004), pp. 495–509. ISSN: 0012-821X. DOI: 10.1016/j.epsl.2004.10.005. URL: http://www.sciencedirect.com/science/article/pii/S0012821X04006107%20http://ac.els-cdn.com/S0012821X04006107/1-s2.0-S0012821X04006107-main.pdf?_tid=373c4a1e-06fa-11e5-89ef-00000aacb362&acdnat=1433010924_18f021eb41058378fe30f8649a86a2ae.

[55] Canfield, D. E. “Sulfate reduction in deep-sea sediments.” In: *American Journal of Science* 291.2 (Feb. 1991), pp. 177–188. ISSN: 0002-9599. DOI: 10.2475/ajs.291.2.177. PMID: 11538491. URL: http://europepmc.org/abstract/MED/11538491%20http://www.ajsonline.org/cgi/content/abstract/291/2/177%20http://dx.doi.org/10.2475/ajs.291.2.177%20http://www.ajsonline.org/cgi/reprint/291/2/177.pdf%20http://www.ajsonline.org/content/291/2/177.full.pdf.

[56] Canfield, D. E. “Biogeochemistry of sulfur isotopes.” In: *Reviews in mineralogy and geochemistry* 43.1 (2001), pp. 607–636. ISSN: 1529-6466. URL: http://sfx.caltech.edu:8088/caltech?sid=google&auinit=DE&aulast=Canfield&atitle=Biogeochemistry%20of%20sulfur%20isotopes&id=doi%3A10.2138%2Fgsrmg.43.1.607&title=Reviews%20in%20mineralogy%20and%20geochemistry&volume=43&issue=1&date=2001&spage=607&issn=1529-6466.

[57] Canfield, D. E. “The evolution of the Earth surface sulfur reservoir.” In: *American Journal of Science* 304.10 (Dec. 1, 2004), pp. 839–861. DOI: 10.2475/ajs.304.10.839. URL: http://www.ajsonline.org/content/304/10/839.abstract%20http://www.ajsonline.org/content/304/10/839.full.pdf.

[58] Canfield, D. E. and Farquhar, J. “Animal evolution, bioturbation, and the sulfate concentration of the oceans.” In: *Proceedings of the National Academy of Sciences* 106.20 (May 19, 2009), pp. 8123–8127. DOI: 10.1073/pnas.0902037106. URL: http://www.pnas.org/content/106/20/8123.abstract%20http://www.pnas.org/content/106/20/8123.full.pdf.

[59] Canfield, D. E. and Teske, A. “Late Proterozoic rise in atmospheric oxygen concentration inferred from phylogenetic and sulphur-isotope studies.” In: *Nature* 382.6587 (1996), pp. 127–132. DOI: 10.1038/382127a0. URL: http://dx.doi.org/10.1038/382127a0%20http://www.nature.com/nature/journal/v382/n6587/pdf/382127a0.pdf.

[60] Canfield, D. E. and Thamdrup, B. “The production of ^{34}S-depleted sulfide during bacterial disproportionation of elemental sulfur.” In: *Science* 266.5193 (Dec. 23, 1994), pp. 1973–1975. ISSN: 0036-8075, 1095-9203. DOI: 10.1126/science.11540246. URL: https://science.sciencemag.org/content/266/5193/1973 (visited on 06/08/2019).

[61] Canfield, D. E. et al. “The use of chromium reduction in the analysis of reduced inorganic sulfur in sediments and shales.” In: *Chemical Geology* 54.1 (Jan. 30, 1986), pp. 149–155. ISSN: 0009-2541. DOI:

10.1016/0009-2541(86)90078-1. URL: http://www.sciencedirect.com/science/article/pii/0009254186900781.

[62] Canfield, D. E. et al. “A cryptic sulfur cycle in oxygen-minimum–zone waters off the Chilean coast.” In: *Science* 330.6009 (Dec. 3, 2010), pp. 1375–1378. DOI: 10.1126/science.1196889. URL: http://www.sciencemag.org/content/330/6009/1375.abstract%20http://www.sciencemag.org/content/330/6009/1375.

[63] Cao, C., Wang, W., and Jin, Y. “Carbon isotope excursions across the Permian-Triassic boundary in the Meishan section, Zhejiang Province, China.” In: *Chinese Science Bulletin* 47.13 (July 1, 2002), p. 1125. ISSN: 1861-9541. DOI: 10.1360/02tb9252. URL: https://doi.org/10.1360/02tb9252 (visited on 12/17/2018).

[64] Cao, C. et al. “Biogeochemical evidence for euxinic oceans and ecological disturbance presaging the end-Permian mass extinction event.” In: *Earth and Planetary Science Letters* 281.3 (May 15, 2009), pp. 188–201. ISSN: 0012-821X. DOI: 10.1016/j.epsl.2009.02.012. URL: http://www.sciencedirect.com/science/article/pii/S0012821X09001083 (visited on 08/13/2020).

[65] Cappellen, P. V. and Wang, Y. “Cycling of iron and manganese in surface sediments: A general theory for the coupled transport and reaction of carbon, oxygen, nitrogen, sulfur, iron, and manganese.” In: *American Journal of Science* 296.3 (Mar. 1, 1996), pp. 197–243. ISSN: 0002-9599, 1945-452X. DOI: 10.2475/ajs.296.3.197. URL: http://www.ajsonline.org/content/296/3/197 (visited on 09/20/2019).

[66] Casella, L. A. et al. “Micro- and nanostructures reflect the degree of diagenetic alteration in modern and fossil brachiopod shell calcite: A multi-analytical screening approach (CL, FE-SEM, AFM, EBSD).” In: *Palaeogeography, Palaeoclimatology, Palaeoecology* 502 (Aug. 1, 2018), pp. 13–30. ISSN: 0031-0182. DOI: 10.1016/j.palaeo.2018.03.011. URL: http://www.sciencedirect.com/science/article/pii/S0031018217307939 (visited on 05/22/2018).

[67] Chambost, E. de. “A history of cameca (1954–2009).” In: *Advances in Imaging and Electron Physics*. Vol. 167. Elsevier, 2011, pp. 1–119. ISBN: 1076-5670. DOI: 10.1016/B978-0-12-385985-3.00001-8.

[68] Chen, J. et al. “High-resolution SIMS oxygen isotope analysis on conodont apatite from South China and implications for the end-Permian mass extinction.” In: *Palaeogeography, Palaeoclimatology, Palaeoecology*. Ecosystem evolution in deep time: Evidence from the rich Palaeozoic fossil records of China 448 (Apr. 15, 2016), pp. 26–38. ISSN: 0031-0182. DOI: 10.1016/j.palaeo.2015.11.025. URL:

http://www.sciencedirect.com/science/article/pii/S0031018215006914 (visited on 08/13/2020).

[69] Chen, S., Gagnon, A. C., and Adkins, J. F. "Carbonic anhydrase, coral calcification and a new model of stable isotope vital effects." In: *Geochimica et Cosmochimica Acta*. Chemistry of oceans past and present: A Special Issue in tribute to Harry Elderfield 236 (Sept. 1, 2018), pp. 179–197. ISSN: 0016-7037. DOI: 10.1016/j.gca.2018.02.032. URL: http://www.sciencedirect.com/science/article/pii/S0016703718301145 (visited on 07/31/2018).

[70] Chen, Z.-Q. et al. "Complete biotic and sedimentary records of the Permian–Triassic transition from Meishan section, South China: Ecologically assessing mass extinction and its aftermath." In: *Earth-Science Reviews*. Global review of the Permian-Triassic mass extinction and subsequent recovery: Part II 149 (Oct. 1, 2015), pp. 67–107. ISSN: 0012-8252. DOI: 10.1016/j.earscirev.2014.10.005. URL: http://www.sciencedirect.com/science/article/pii/S0012825214001846 (visited on 08/17/2020).

[71] Clapham, M. E. and Payne, J. L. "Acidification, anoxia, and extinction: A multiple logistic regression analysis of extinction selectivity during the Middle and Late Permian." In: *Geology* 39.11 (Nov. 1, 2011). Publisher: GeoScienceWorld, pp. 1059–1062. ISSN: 0091-7613. DOI: 10.1130/G32230.1. URL: http://pubs.geoscienceworld.org/gsa/geology/article/39/11/1059/130447/Acidification-anoxia-and-extinction-A-multiple (visited on 08/14/2020).

[72] Claypool, G. E. et al. "The age curves of sulfur and oxygen isotopes in marine sulfate and their mutual interpretation." In: *Chemical Geology* 28.0 (1980), pp. 199–260. ISSN: 0009-2541. DOI: 10.1016/0009-2541(80)90047-9. URL: http://www.sciencedirect.com/science/article/pii/0009254180900479.

[73] Cleal, C. J. and Thomas, B. A. "Palaeozoic tropical rainforests and their effect on global climates: Is the past the key to the present?" In: *Geobiology* 3.1 (2005), pp. 13–31. ISSN: 1472-4669. DOI: 10.1111/j.1472-4669.2005.00043.x. URL: https://onlinelibrary.wiley.com/doi/abs/10.1111/j.1472-4669.2005.00043.x (visited on 07/25/2018).

[74] Compton, J. S. et al. "Origin and age of phosphorite from the south-central Florida Platform: Relation of phosphogenesis to sea-level fluctuations and $\delta^{13}C$ excursions." In: *Geochimica et Cosmochimica Acta* 57.1 (Jan. 1, 1993), pp. 131–146. ISSN: 0016-7037. DOI:

10.1016/0016-7037(93)90474-B. URL: http://www.sciencedirect.com/science/article/pii/001670379390474B.

[75] Coplen, T. B. et al. “Isotope-abundance variations of selected elements (IUPAC Technical Report).” In: *Pure and Applied Chemistry* 74.10 (Jan. 1, 2002). Publisher: De Gruyter Section: Pure and Applied Chemistry, pp. 1987–2017. ISSN: 0033-4545, 1365-3075. DOI: 10.1351/pac200274101987. URL: https://www.degruyter.com/view/journals/pac/74/10/article-p1987.xml (visited on 08/04/2020).

[76] Cortecci, G. et al. “Sulfur and oxygen isotopes in Italian marine sulfates of Permian and Triassic ages.” In: *Chemical Geology* 34.1 (Nov. 1, 1981), pp. 65–79. ISSN: 0009-2541. DOI: 10.1016/0009-2541(81)90072-3. URL: http://www.sciencedirect.com/science/article/pii/0009254181900723 (visited on 09/16/2018).

[77] Courtillot, V. E. and Renne, P. R. “On the ages of flood basalt events.” In: *Comptes Rendus Geoscience* 335.1 (Jan. 1, 2003), pp. 113–140. ISSN: 1631-0713. DOI: 10.1016/S1631-0713(03)00006-3. URL: http://www.sciencedirect.com/science/article/pii/S1631071303000063 (visited on 02/14/2019).

[78] Coveney, R. M. and Shaffer, N. R. “Sulfur-isotope variations in Pennsylvanian shales of the midwestern United States.” In: *Geology* 16.1 (Jan. 1, 1988). Publisher: GeoScienceWorld, pp. 18–21. ISSN: 0091-7613. DOI: 10.1130/0091-7613(1988)016<0018:SIVIPS>2.3.CO;2. URL: https://pubs.geoscienceworld.org/geology/article/16/1/18/204522/Sulfur-isotope-variations-in-Pennsylvanian-shales (visited on 03/10/2020).

[79] Criss, R. E. *Principles of stable isotope distribution*. Oxford University Press on Demand, 1999. ISBN: 0-19-511775-1. URL: https://global.oup.com/academic/product/principles-of-stable-isotope-distribution-9780195117752?cc=us&lang=en&#.

[80] Cusack, M. et al. “Micro-XANES mapping of sulphur and its association with magnesium and phosphorus in the shell of the brachiopod, Terebratulina retusa.” In: *Chemical Geology* 253.3 (2008), pp. 172–179. ISSN: 0009-2541. DOI: 10.1016/j.chemgeo.2008.05.007. URL: http://www.sciencedirect.com/science/article/pii/S0009254108001812%20http://ac.els-cdn.com/S0009254108001812/1-s2.0-S0009254108001812-main.pdf?_tid=8d25fb50-6092-11e4-932b-00000aab0f02&acdnat=1414714507_4e932aafbfcef190a777b12814f64ea2.

[81] D'Hondt, S. et al. "Distributions of Microbial Activities in Deep Subseafloor Sediments." In: *Science* 306.5705 (Dec. 24, 2004), pp. 2216–2221. ISSN: 0036-8075, 1095-9203. DOI: 10.1126/science.1101155. URL: http://science.sciencemag.org/content/306/5705/2216 (visited on 08/12/2018).

[82] Dalingwater, J. E. "Trilobite cuticle microstructure and composition." In: *Palaeontology* 16 (1973), pp. 827–839. URL: https://www.palass.org/sites/default/files/media/publications/palaeontology/volume_16/vol16_part4_pp827-839.pdf.

[83] Dauphin, Y. et al. "Speciation and distribution of sulfur in a mollusk shell as revealed by in situ maps using X-ray absorption near-edge structure (XANES) spectroscopy at the S K-edge." In: *American Mineralogist* 90.11 (Nov. 1, 2005), pp. 1748–1758. DOI: 10.2138/am.2005.1640. URL: http://ammin.geoscienceworld.org/content/90/11-12/1748.abstract%20http://ammin.geoscienceworld.org/content/90/11-12/1748.full.pdf.

[84] Desrochers, A. et al. "A far-field record of the end Ordovician glaciation: The Ellis Bay Formation, Anticosti Island, Eastern Canada." In: *Palaeogeography, Palaeoclimatology, Palaeoecology* 296.3 (2010), pp. 248–263. ISSN: 0031-0182. DOI: 10.1016/j.palaeo.2010.02.017. URL: http://www.sciencedirect.com/science/article/pii/S0031018210000891%20http://ac.els-cdn.com/S0031018210000891/1-s2.0-S0031018210000891-main.pdf?_tid=a9c775ee-3f9f-11e5-9e22-00000aacb35e&acdnat=1439239248_9970471344a39dda845abe75150014af.

[85] Dhakar, S. P. and Burdige, D. J. "A coupled, non-linear, steady-state model for early diagenetic processes in pelagic sediments." In: *American Journal of Science* 296.3 (Mar. 1, 1996), pp. 296–330. ISSN: 0002-9599, 1945-452X. DOI: 10.2475/ajs.296.3.296. URL: http://www.ajsonline.org/content/296/3/296 (visited on 10/08/2018).

[86] Dickens, G. R. "Rethinking the global carbon cycle with a large, dynamic and microbially mediated gas hydrate capacitor." In: *Earth and Planetary Science Letters* 213.3 (Aug. 25, 2003), pp. 169–183. ISSN: 0012-821X. DOI: 10.1016/S0012-821X(03)00325-X. URL: http://www.sciencedirect.com/science/article/pii/S0012821X0300325X (visited on 02/13/2019).

[87] Dongen, B. E. van et al. "An experimental study of the low-temperature sulfurization of carbohydrates." In: *Organic Geochemistry* 34.8 (Aug. 1,

2003), pp. 1129–1144. ISSN: 0146-6380. DOI: 10.1016/S0146-6380(03)00060-3. URL: http://www.sciencedirect.com/science/article/pii/S0146638003000603 (visited on 04/15/2020).

[88] Douthitt, C. B. "The evolution and applications of multicollector ICPMS (MC-ICPMS)." In: *Analytical and Bioanalytical Chemistry* 390.2 (Jan. 1, 2008), pp. 437–440. ISSN: 1618-2650. DOI: 10.1007/s00216-007-1660-x. URL: https://doi.org/10.1007/s00216-007-1660-x (visited on 08/07/2020).

[89] Druhan, J. L. et al. "Timing the onset of sulfate reduction over multiple subsurface acetate amendments by measurement and modeling of sulfur isotope fractionation." In: *Environmental Science & Technology* 46.16 (Aug. 21, 2012), pp. 8895–8902. ISSN: 0013-936X. DOI: 10.1021/es302016p. URL: https://doi.org/10.1021/es302016p (visited on 11/09/2018).

[90] Egger, M. et al. "Global diffusive fluxes of methane in marine sediments." In: *Nature Geoscience* 11.6 (June 2018), p. 421. ISSN: 1752-0908. DOI: 10.1038/s41561-018-0122-8. URL: https://www.nature.com/articles/s41561-018-0122-8 (visited on 05/28/2019).

[91] Elderfield, H. and Schultz, A. "Mid-ocean ridge hydrothermal fluxes and the chemical composition of the ocean." In: *Annual Review of Earth and Planetary Sciences* 24.1 (May 1, 1996), pp. 191–224. ISSN: 0084-6597. DOI: 10.1146/annurev.earth.24.1.191. URL: http://dx.doi.org/10.1146/annurev.earth.24.1.191%20http://www.annualreviews.org/doi/pdf/10.1146/annurev.earth.24.1.191 (visited on 04/07/2015).

[92] Enos, P., Wei Jiayong, and Lehrmann, D. J. "Death in Guizhou — Late Triassic drowning of the Yangtze carbonate platform." In: *Sedimentary Geology* 118.1 (June 1, 1998), pp. 55–76. ISSN: 0037-0738. DOI: 10.1016/S0037-0738(98)00005-0. URL: http://www.sciencedirect.com/science/article/pii/S0037073898000050 (visited on 08/17/2020).

[93] Eynor, O. L., Bel'govskiy, G. L., and Smirnov, G. A. "Carboniferous geology and paleogeography of the USSR." In: *International Geology Review* 12.2 (Feb. 1, 1970), pp. 105–113. ISSN: 0020-6814. DOI: 10.1080/00206817009475215. URL: https://doi.org/10.1080/00206817009475215 (visited on 12/20/2018).

[94] Farquhar, J., Bao, H., and Thiemens, M. “Atmospheric influence of Earth’s earliest sulfur cycle.” In: *Science* 289.5480 (Aug. 4, 2000), pp. 756–758. DOI: 10.1126/science.289.5480.756. URL: http://www.sciencemag.org/content/289/5480/756.abstract%20http://www.sciencemag.org/content/289/5480/756.full.pdf.

[95] Farquhar, J. and Wing, B. A. “Multiple sulfur isotopes and the evolution of the atmosphere.” In: *Earth and Planetary Science Letters* 213.1 (2003), pp. 1–13. ISSN: 0012-821X. DOI: 10.1016/S0012-821X(03)00296-6.

[96] Feary, D. A. et al. “Leg 182 synthesis: Exposed secrets of the Great Australian Bight.” In: *Proceedings of the ocean drilling program, scientific results*. Vol. 182. 2004, pp. 1–30. DOI: 10.2973/odp.proc.sr.182.017.2004.

[97] Fielding, C. R. et al. “Stratigraphic imprint of the Late Palaeozoic Ice Age in eastern Australia: A record of alternating glacial and nonglacial climate regime.” In: *Journal of the Geological Society* 165.1 (Jan. 1, 2008), pp. 129–140. ISSN: 0016-7649, 2041-479X. DOI: 10.1144/0016-76492007-036. URL: http://jgs.lyellcollection.org/content/165/1/129 (visited on 12/19/2017).

[98] Fike, D. A. and Grotzinger, J. P. “A paired sulfate–pyrite δ^{34}S approach to understanding the evolution of the Ediacaran–Cambrian sulfur cycle.” In: *Geochimica et Cosmochimica Acta* 72.11 (June 1, 2008), pp. 2636–2648. ISSN: 0016-7037. DOI: 10.1016/j.gca.2008.03.021. URL: http://www.sciencedirect.com/science/article/pii/S0016703708001749 (visited on 03/18/2020).

[99] Fike, D. A. and Grotzinger, J. P. “A δ^{34}SSO4 approach to reconstructing biogenic pyrite burial in carbonate-evaporite basins: An example from the Ara Group, Sultanate of Oman.” In: *Geology* 38.4 (Apr. 1, 2010). Publisher: GeoScienceWorld, pp. 371–374. ISSN: 0091-7613. DOI: 10.1130/G30230.1. URL: http://pubs.geoscienceworld.org/gsa/geology/article/38/4/371/130255/A-34SSO4-approach-to-reconstructing-biogenic (visited on 08/05/2020).

[100] Fike, D. A., Bradley, A. S., and Rose, C. V. “Rethinking the ancient sulfur cycle.” In: *Annual Review of Earth and Planetary Sciences* 43.1 (2015), null. DOI: 10.1146/annurev-earth-060313-054802. URL: http://www.annualreviews.org/doi/abs/10.1146/annurev-earth-060313-054802%20http://www.annualreviews.org/doi/pdf/10.1146/annurev-earth-060313-054802.

[101] Finnegan, S. et al. “The magnitude and duration of late Ordovician–early Silurian glaciation.” In: *Science* 331.6019 (Feb. 18, 2011), pp. 903–906. DOI: 10.1126/science.1200803. URL: http://www.sciencemag.org/content/331/6019/903.abstract%20http://www.sciencemag.org/content/331/6019/903.full.pdf.

[102] Flake, R. C. “Circulation of North American epicontinental seas during the Carboniferous using stable isotope and trace element analyses of brachiopod shells.” In: *Texas, Texas A&M University* (2011). URL: http://hdl.handle.net/1969.1/ETD-TAMU-2011-05-9365.

[103] Fortey, R. “The palaeoecology of trilobites.” In: *Journal of Zoology* 292.4 (2014), pp. 250–259. ISSN: 1469-7998. DOI: 10.1111/jzo.12108. URL: http://dx.doi.org/10.1111/jzo.12108%20http://onlinelibrary.wiley.com/doi/10.1111/jzo.12108/abstract.

[104] Froelich, P. N. et al. “Early oxidation of organic matter in pelagic sediments of the eastern equatorial Atlantic: Suboxic diagenesis.” In: *Geochimica et Cosmochimica Acta* 43.7 (1979), pp. 1075–1090. ISSN: 0016-7037. DOI: 10.1016/0016-7037(79)90095-4. URL: http://www.sciencedirect.com/science/article/pii/0016703779900954.

[105] Fry, B. et al. “Sulfur isotope effects associated with oxidation of sulfide by O2 in aqueous solution.” In: *Chemical Geology: Isotope Geoscience section* 73.3 (1988), pp. 205–210. ISSN: 0168-9622. DOI: 10.1016/0168-9622(88)90001-2. URL: http://www.sciencedirect.com/science/article/pii/0168962288900012%20http://ac.els-cdn.com/0168962288900012/1-s2.0-0168962288900012-main.pdf?_tid=5d57c6d8-3eb4-11e4-b166-00000aacb35f&acdnat=1410990690_d220a636940eab8687575b69a36301fb.

[106] Galle, O. K. “Chemical analysis of some standard carbonate rocks.” In: *Chemical Geology* 5.2 (Nov. 1, 1969), pp. 143–146. ISSN: 0009-2541. DOI: 10.1016/0009-2541(69)90030-8. URL: http://www.sciencedirect.com/science/article/pii/0009254169900308 (visited on 08/05/2020).

[107] Garrels, R. M. and Lerman, A. “Phanerozoic cycles of sedimentary carbon and sulfur.” In: *Proceedings of the National Academy of Sciences* 78.8 (Aug. 1, 1981), pp. 4652–4656. URL: http://www.pnas.org/content/78/8/4652.abstract.

[108] Gelin, F. et al. “Laboratory sulfurisation of the marine microalga Nannochloropsis salina.” In: *Organic Geochemistry* 29.8 (Dec. 1, 1998), pp. 1837–1848. ISSN: 0146-6380. DOI: 10.1016/S0146-6380(98)00171-5. URL: http://www.

sciencedirect.com/science/article/pii/S0146638098001715 (visited on 04/15/2020).

[109] Georgiev, S. V. et al. “Enhanced recycling of organic matter and Os-isotopic evidence for multiple magmatic or meteoritic inputs to the Late Permian Panthalassic Ocean, Opal Creek, Canada.” In: *Geochimica et Cosmochimica Acta* 150 (Feb. 1, 2015), pp. 192–210. ISSN: 0016-7037. DOI: 10.1016/j.gca.2014.11.019. URL: http://www.sciencedirect.com/science/article/pii/S0016703714006899 (visited on 08/13/2020).

[110] Geyman, E. C. and Maloof, A. C. “A diurnal carbon engine explains 13C-enriched carbonates without increasing the global production of oxygen.” In: *Proceedings of the National Academy of Sciences* (Nov. 8, 2019). ISSN: 0027-8424, 1091-6490. DOI: 10.1073/pnas.1908783116. URL: https://www.pnas.org/content/early/2019/11/07/1908783116 (visited on 11/15/2019).

[111] Gibling, M. R. et al. “The Maritimes Basin of Atlantic Canada: Basin creation and destruction in the collisional zone of Pangea.” In: *Sedimentary basins of the world* 5 (2008), pp. 211–244. DOI: 10.1016/S1874-5997(08)00006-3.

[112] “Principal component and factor analysis.” In: *Modeling Methods for Marine Science*. Ed. by D. M. Glover, S. C. Doney, and W. J. Jenkins. Cambridge: Cambridge University Press, 2011, pp. 75–119. ISBN: 978-0-521-86783-2. DOI: 10.1017/CBO9780511975721.005. URL: https://www.cambridge.org/core/books/modeling-methods-for-marine-science/principal-component-and-factor-analysis/43950883E93848E687D0C24B85577ACE.

[113] Goedert, J. et al. “High-precision 34S/32S measurements in vertebrate bioapatites using purge-and-trap elemental analyser/isotope ratio mass spectrometry technology.” In: *Rapid Communications in Mass Spectrometry* 30.18 (2016), pp. 2002–2008. ISSN: 1097-0231. DOI: 10.1002/rcm.7690. URL: https://onlinelibrary.wiley.com/doi/abs/10.1002/rcm.7690 (visited on 05/01/2019).

[114] Goldberg, T., Shields, G. A., and Newton, R. J. “Analytical constraints on the measurement of the sulfur isotopic composition and concentration of trace sulfate in phosphorites: Implications for sulfur isotope studies of carbonate and phosphate rocks.” In: *Geostandards and Geoanalytical Research* 35.2 (2011), pp. 161–174. ISSN: 1751-908X. DOI: 10.1111/j.1751-908X.2010.00102.x. URL: http://dx.doi.org/10.1111/j.1751-908X.2010.00102.x%20http://onlinelibrary.wiley.com/store/10.1111/j.1751-

908X.2010.00102.x/asset/j.1751-908X.2010.00102.x.pdf?v=1&t=i7xsblhg&s=fa80f9ed3ea4f2b226e2a1a5f208e0efc907c69a.

[115] Goldhaber, M. B. and Kaplan, I. R. “The Sulfur Cycle.” In: *The Sea*. Ed. by E. D. Goldberg. Vol. 5. New York, NY: Wiley, 1974, pp. 569–655.

[116] Gradstein, F. M. et al. *The geologic time scale 2012*. Elsevier, 2012. ISBN: 0-444-59448-5. URL: https://www.elsevier.com/books/the-geologic-time-scale-2012/gradstein/978-0-444-59425-9.

[117] Gradstein, F. M. et al. *Geologic Time Scale 2020 - 2nd Edition*. Elsevier, 2020. 1300 pp. ISBN: 978-0-444-63798-7. URL: https://www.elsevier.com/books/geologic-time-scale-2020/gradstein/978-0-444-63798-7 (visited on 03/17/2020).

[118] Grasby, S. E. and Beauchamp, B. “Latest Permian to Early Triassic basin-to-shelf anoxia in the Sverdrup Basin, Arctic Canada.” In: *Chemical Geology* 264.1 (June 30, 2009), pp. 232–246. ISSN: 0009-2541. DOI: 10.1016/j.chemgeo.2009.03.009. URL: http://www.sciencedirect.com/science/article/pii/S0009254109001181 (visited on 08/26/2020).

[119] Grice, K. et al. “Photic zone euxinia during the Permian-Triassic superanoxic event.” In: *Science* 307.5710 (Feb. 4, 2005), pp. 706–709. ISSN: 0036-8075, 1095-9203. DOI: 10.1126/science.1104323. URL: http://science.sciencemag.org/content/307/5710/706 (visited on 01/16/2018).

[120] Grossman, E. L., Mii, H.-S., and Yancey, T. E. “Stable isotopes in Late Pennsylvanian brachiopods from the United States: Implications for Carboniferous paleoceanography.” In: *Geological Society of America Bulletin* 105.10 (1993), pp. 1284–1296. ISSN: 0016-7606. DOI: 10.1130/0016-7606(1993)105<1284:SIILPB>2.3.CO;2.

[121] Grossman, E. L., Zhang, C., and Yancey, T. E. “Stable-isotope stratigraphy of brachiopods from Pennsylvanian shales in Texas.” In: *Geological Society of America Bulletin* 103.7 (1991), pp. 953–965. ISSN: 0016-7606. DOI: 10.1130/0016-7606(1991)103<0953:SISOBF>2.3.CO;2.

[122] Grossman, E. L. et al. “Chemical variation in Pennsylvanian brachiopod shells; Diagenetic, taxonomic, microstructural, and seasonal effects.” In: *Journal of Sedimentary Research* 66.5 (1996), pp. 1011–1022. DOI: 10.1306/d4268469-2b26-11d7-8648000102c1865d.

[123] Grossman, E. L. et al. “Glaciation, aridification, and carbon sequestration in the Permo-Carboniferous: The isotopic record from low latitudes.” In: *Palaeogeography, Palaeoclimatology, Palaeoecology* 268.3 (2008), pp. 222–233. ISSN: 0031-0182. DOI:

10.1016/j.palaeo.2008.03.053. URL: http://www.sciencedirect.com/science/article/pii/S0031018208003027.

[124] Gruszczynski, M. et al. “A brachiopod calcite record of the oceanic carbon and oxygen isotope shifts at the Permian/Triassic transition.” In: *Nature* 337.6202 (Jan. 1989), pp. 64–68. ISSN: 1476-4687. DOI: 10.1038/337064a0. URL: https://www.nature.com/articles/337064a0 (visited on 12/20/2018).

[125] Habicht, K. S. and Canfield, D. E. “Sulfur isotope fractionation during bacterial sulfate reduction in organic-rich sediments.” In: *Geochimica et Cosmochimica Acta* 61.24 (Dec. 1, 1997), pp. 5351–5361. ISSN: 0016-7037. DOI: 10.1016/S0016-7037(97)00311-6. URL: http://www.sciencedirect.com/science/article/pii/S0016703797003116.

[126] Halevy, I., Peters, S. E., and Fischer, W. W. “Sulfate burial constraints on the Phanerozoic sulfur cycle.” In: *Science* 337.6092 (July 20, 2012), pp. 331–334. DOI: 10.1126/science.1220224. URL: http://www.sciencemag.org/content/337/6092/331.abstract%20http://www.sciencemag.org/content/337/6092/331.full.pdf.

[127] Halevy, I. et al. “Sedimentary parameters control the sulfur isotope composition of marine pyrite (submitted to *Science*).” In: (). URL: https://johnstonlab.fas.harvard.edu/publications/sedimentary-parameters-control-sulfur-isotope-composition-marine-pyrite.

[128] Hall, I. R. *South African Climates (Agulhas LGM Density Profile)*. Ed. by S. R. Hemming et al. Vol. 361. Proceedings of the International Ocean Discovery Program; Place: Washington, DC, United States Publisher: International Ocean Discovery Program. College Station, TX: International Ocean Discovery Program, 2017. DOI: 10.14379/iodp.proc.361.2017.

[129] Hallam, A. “Pre-Quaternary Sea-Level Changes.” In: *Annual Review of Earth and Planetary Sciences* 12.1 (May 1, 1984), pp. 205–243. ISSN: 0084-6597. DOI: 10.1146/annurev.ea.12.050184.001225. URL: https://www.annualreviews.org/doi/10.1146/annurev.ea.12.050184.001225 (visited on 04/13/2019).

[130] Hao, J. et al. “Cycling phosphorus on the Archean Earth: Part I. Continental weathering and riverine transport of phosphorus.” In: *Geochimica et Cosmochimica Acta* 273 (Mar. 15, 2020), pp. 70–84. ISSN: 0016-7037. DOI: 10.1016/j.gca.2020.01.027. URL: http://www.sciencedirect.com/science/article/pii/S001670372030048X (visited on 09/12/2020).

[131] Haq, B. U. and Schutter, S. R. “A chronology of Paleozoic sea-level changes.” In: *Science* 322.5898 (Oct. 3, 2008), pp. 64–68. ISSN: 0036-8075, 1095-9203. DOI: 10.1126/science.1161648. URL: https://science.sciencemag.org/content/322/5898/64 (visited on 09/27/2019).

[132] Hardie, L. A. “Secular variation in seawater chemistry: An explanation for the coupled secular variation in the mineralogies of marine limestones and potash evaporites over the past 600 m.y.” In: *Geology* 24.3 (Mar. 1, 1996), pp. 279–283. ISSN: 0091-7613. DOI: 10.1130/0091-7613(1996)024<0279:SVISCA>2.3.CO;2. URL: https://pubs.geoscienceworld.org/gsa/geology/article/24/3/279/206498/secular-variation-in-seawater-chemistry-an (visited on 04/23/2019).

[133] Hartmann, M. and Nielsen, H. “δ^{34}S values in recent sea sediments and their significance using several sediment profiles from the western Baltic Sea.” In: *Isotopes in Environmental and Health Studies* 48.1 (Mar. 1, 2012), pp. 7–32. ISSN: 1025-6016. DOI: 10.1080/10256016.2012.660528. URL: https://doi.org/10.1080/10256016.2012.660528 (visited on 08/15/2018).

[134] Hartnett, H. E. et al. “Influence of oxygen exposure time on organic carbon preservation in continental margin sediments.” In: *Nature* 391.6667 (1998), pp. 572–575. ISSN: 0028-0836. DOI: 10.1038/35351. URL: http://dx.doi.org/10.1038/35351.

[135] Hayes, J. M. “An introduction to isotopic calculations.” In: 2543 (2004). URL: https://www.whoi.edu/cms/files/jhayes/2005/9/IsoCalcs30Sept04_5183.pdf.

[136] Hayes, J. M., Strauss, H., and Kaufman, A. J. “The abundance of 13C in marine organic matter and isotopic fractionation in the global biogeochemical cycle of carbon during the past 800 Ma.” In: *Chemical Geology* 161.1 (Sept. 30, 1999), pp. 103–125. ISSN: 0009-2541. DOI: 10.1016/S0009-2541(99)00083-2. URL: http://www.sciencedirect.com/science/article/pii/S0009254199000832 (visited on 06/26/2018).

[137] Hayes, J. M. and Waldbauer, J. R. “The carbon cycle and associated redox processes through time.” In: *Philosophical Transactions of the Royal Society B: Biological Sciences* 361.1470 (2006), pp. 931–950. ISSN: 0962-8436. URL: http://www.ncbi.nlm.nih.gov/pmc/articles/PMC1578725/pdf/rstb20061840.pdf.

[138] Haynes, W. M. *CRC Handbook of Chemistry and Physics*. Google-Books-ID: VVezDAAAQBAJ. CRC Press, June 22, 2016. 2643 pp. ISBN: 978-1-4987-5429-3.

[139] Hays, J. D. and Pitman, W. C. “Lithospheric plate motion, sea level changes and climatic and ecological consequences.” In: *Nature* 246.5427 (Nov. 1973), pp. 18–22. ISSN: 1476-4687. DOI: 10.1038/246018a0. URL: https://www.nature.com/articles/246018a0 (visited on 09/27/2019).

[140] Heckel, P. H. “Evidence for global (glacial-eustatic) control over upper Carboniferous (Pennsylvanian) cyclothems in midcontinent North America.” In: *Geological Society, London, Special Publications* 55.1 (Jan. 1, 1990), pp. 35–47. ISSN: 0305-8719, 2041-4927. DOI: 10.1144/GSL.SP.1990.055.01.02. URL: http://sp.lyellcollection.org/content/55/1/35 (visited on 06/20/2018).

[141] Hedges, J. I. and Keil, R. G. “Sedimentary organic matter preservation: an assessment and speculative synthesis.” In: *Marine Chemistry* 49.2 (1995), pp. 81–115. ISSN: 0304-4203. DOI: 10.1016/0304-4203(95)00008-F. URL: http://www.sciencedirect.com/science/article/pii/030442039500008F%20http://ac.els-cdn.com/030442039500008F/1-s2.0-030442039500008F-main.pdf?_tid=2c412bc4-3f6e-11e4-9265-00000aacb35f&acdnat=1411070495_96ddccd1fc6f4f91b99398c04bd05595.

[142] Henkes, G. A. et al. “Temperature evolution and the oxygen isotope composition of Phanerozoic oceans from carbonate clumped isotope thermometry.” In: *Earth and Planetary Science Letters* 490 (May 15, 2018), pp. 40–50. ISSN: 0012-821X. DOI: 10.1016/j.epsl.2018.02.001. URL: https://www.sciencedirect.com/science/article/pii/S0012821X18300578.

[143] Hilley, G. E. et al. “Competition between erosion and reaction kinetics in controlling silicate-weathering rates.” In: *Earth and Planetary Science Letters* 293.1 (Apr. 15, 2010), pp. 191–199. ISSN: 0012-821X. DOI: 10.1016/j.epsl.2010.01.008. URL: http://www.sciencedirect.com/science/article/pii/S0012821X10000270 (visited on 08/30/2020).

[144] Hinojosa, J. L. et al. “Evidence for end-Permian ocean acidification from calcium isotopes in biogenic apatite.” In: *Geology* 40.8 (Aug. 1, 2012), pp. 743–746. ISSN: 0091-7613. DOI: 10.1130/G33048.1. URL: https://pubs.geoscienceworld.org/gsa/geology/article/40/8/743/130993/evidence-for-end-permian-ocean-acidification-from (visited on 01/15/2018).

[145] Holser, W. T. et al. “A unique geochemical record at the Permian/Triassic boundary.” In: *Nature* 337.6202 (Jan. 1989). Number:

6202 Publisher: Nature Publishing Group, pp. 39–44. ISSN: 1476-4687. DOI: 10.1038/337039a0. URL: https://www.nature.com/articles/337039a0 (visited on 08/14/2020).

[146] Hongfu, Y. et al. "The global stratotype section and point (GSSP) of the Permian-Triassic boundary." In: *Episodes* 24.2 (2001). ISBN: 0705-3797 Publisher: International Union of Geological Sciences, pp. 102–114. DOI: 10.18814/epiiugs/2001/v24i2/004.

[147] Horacek, M., Brandner, R., and Abart, R. "Carbon isotope record of the P/T boundary and the Lower Triassic in the Southern Alps: Evidence for rapid changes in storage of organic carbon." In: *Palaeogeography, Palaeoclimatology, Palaeoecology*. The Permian-Triassic Boundary Crisis and Early Triassic Biotic Recovery 252.1 (Aug. 20, 2007), pp. 347–354. ISSN: 0031-0182. DOI: 10.1016/j.palaeo.2006.11.049. URL: http://www.sciencedirect.com/science/article/pii/S0031018207001277 (visited on 09/16/2018).

[148] Horacek, M. et al. "High-resolution carbon isotope changes, litho- and magnetostratigraphy across Permian-Triassic Boundary sections in the Dolomites, N-Italy. New constraints for global correlation." In: *Palaeogeography, Palaeoclimatology, Palaeoecology*. Triassic climates 290.1 (Apr. 15, 2010), pp. 58–64. ISSN: 0031-0182. DOI: 10.1016/j.palaeo.2010.01.007. URL: http://www.sciencedirect.com/science/article/pii/S0031018210000088 (visited on 09/16/2018).

[149] Hughes, E. et al. *Sulfur Isotope Composition of Pyrite and Organic Matter from the Monterey Formation: Implications for $\delta^{34}S$ as a Paleoenvironmental Proxy*. Earth and Space Science Open Archive. Dec. 12, 2018. DOI: 10.1002/essoar.10500121.1. URL: http://www.essoar.org/doi/10.1002/essoar.10500121.1 (visited on 08/06/2020).

[150] Hulston, J. R. and Thode, H. G. "Variations in the S33, S34, and S36 contents of meteorites and their relation to chemical and nuclear effects." In: *Journal of Geophysical Research* 70.14 (1965), pp. 3475–3484. ISSN: 2156-2202. DOI: 10.1029/JZ070i014p03475. URL: http://dx.doi.org/10.1029/JZ070i014p03475%20http://onlinelibrary.wiley.com/store/10.1029/JZ070i014p03475/asset/jgr4358.pdf?v=1&t=j0vt3my3&s=c2ab344e05146f0d90c155df5fa0f462519351c7.

[151] Isbell, J. L. et al. "Timing of late Paleozoic glaciation in Gondwana: Was glaciation responsible for the development of Northern Hemisphere cyclothems?" In: *Special Paper 370: Extreme depositional environments: Mega end members in geologic time*. Vol. 370. Geological Society of

America, 2003, pp. 5–24. ISBN: 978-0-8137-2370-9. DOI: 10.1130/0-8137-2370-1.5. URL: https://pubs.geoscienceworld.org/books/book/519/chapter/3801135/.

[152] Isozaki, Y. "Permo-Triassic boundary superanoxia and stratified superocean: Records from lost seep sea." In: *Science* 276.5310 (Apr. 11, 1997). Publisher: American Association for the Advancement of Science Section: Report, pp. 235–238. ISSN: 0036-8075, 1095-9203. DOI: 10.1126/science.276.5310.235. URL: http://science.sciencemag.org/content/276/5310/235 (visited on 08/26/2020).

[153] *It takes a village to determine the origins of an African proverb*. NPR.org. Library Catalog: www.npr.org. July 30, 2016. URL: https://www.npr.org/sections/goatsandsoda/2016/07/30/487925796/it-takes-a-village-to-determine-the-origins-of-an-african-proverb (visited on 08/07/2020).

[154] Jahnke, R. A. "The global ocean flux of particulate organic carbon: Areal distribution and magnitude." In: *Global Biogeochemical Cycles* 10.1 (1996). _eprint: https://onlinelibrary.wiley.com/doi/pdf/10.1029/95GB03525, pp. 71–88. ISSN: 1944-9224. DOI: 10.1029/95GB03525. URL: http://agupubs.onlinelibrary.wiley.com/doi/abs/10.1029/95GB03525 (visited on 07/06/2020).

[155] John, S. G. and Adkins, J. F. "Analysis of dissolved iron isotopes in seawater." In: *Marine Chemistry* 119.1 (2010), pp. 65–76. ISSN: 0304-4203. DOI: 10.1016/j.marchem.2010.01.001. URL: http://www.sciencedirect.com/science/article/pii/S0304420310000022%20http://ac.els-cdn.com/S0304420310000022/1-s2.0-S0304420310000022-main.pdf?_tid=5f4cf124-24e2-11e5-8e2e-00000aacb362&acdnat=1436299218_2fb428adb4190079a5e15063d583de63.

[156] Johnson, D. L. et al. "Brachiopod $\delta^{34}S_{CAS}$ microanalyses indicate a dynamic, climate-influenced Permo-Carboniferous sulfur cycle." In: *Earth and Planetary Science Letters* 546 (Sept. 15, 2020). D.J. participated in the conception of the project, conducted all laboratory preparation and measurements, analyzed and interpreted the data, and helped write the manuscript., p. 116428. ISSN: 0012-821X. DOI: 10.1016/j.epsl.2020.116428. URL: http://www.sciencedirect.com/science/article/pii/S0012821X20303721 (visited on 07/07/2020).

[157] Johnston, D. T., Farquhar, J., and Canfield, D. E. "Sulfur isotope insights into microbial sulfate reduction: When microbes meet models." In: *Geochimica et Cosmochimica Acta* 71.16 (2007),

pp. 3929–3947. ISSN: 0016-7037. DOI: 10.1016/j.gca.2007.05.008. URL: http://www.sciencedirect.com/science/article/pii/S0016703707002487%20http://ac.els-cdn.com/S0016703707002487/1-s2.0-S0016703707002487-main.pdf?_tid=39660ddc-3eb6-11e4-8631-00000aab0f27&acdnat=1410991489_fb7b173b808f8f513ef41b603cb9e594.

[158] Johnston, D. T. et al. "Sulphur isotopes and the search for life: strategies for identifying sulphur metabolisms in the rock record and beyond." In: *Geobiology* 6.5 (2008), pp. 425–435. ISSN: 1472-4669. DOI: 10.1111/j.1472-4669.2008.00171.x. URL: https://onlinelibrary.wiley.com/doi/abs/10.1111/j.1472-4669.2008.00171.x (visited on 07/09/2018).

[159] Johnston, D. T. et al. "Placing an upper limit on cryptic marine sulphur cycling." In: *Nature* 513.7519 (2014), pp. 530–533. ISSN: 0028-0836. DOI: 10.1038/nature13698. URL: http://dx.doi.org/10.1038/nature13698.

[160] Jones, D. S. and Fike, D. A. "Dynamic sulfur and carbon cycling through the end-Ordovician extinction revealed by paired sulfate–pyrite δ^{34}S." In: *Earth and Planetary Science Letters* 363.0 (2013), pp. 144–155. ISSN: 0012-821X. DOI: 10.1016/j.epsl.2012.12.015. URL: http://www.sciencedirect.com/science/article/pii/S0012821X12007017%20http://ac.els-cdn.com/S0012821X12007017/1-s2.0-S0012821X12007017-main.pdf?_tid=72b14134-3e9c-11e4-b2fa-00000aacb360&acdnat=1410980418_f8b644acdc1f2ee87fe02b5c93a754a5.

[161] Jones, D. S. et al. "Terminal Ordovician carbon isotope stratigraphy and glacioeustatic sea-level change across Anticosti Island (Québec, Canada)." In: *Geological Society of America Bulletin* 123.7 (July 1, 2011), pp. 1645–1664. DOI: 10.1130/b30323.1. URL: http://gsabulletin.gsapubs.org/content/123/7-8/1645.abstract.

[162] Jørgensen, B. B. "A theoretical model of the stable sulfur isotope distribution in marine sediments." In: *Geochimica et Cosmochimica Acta* 43.3 (1979), pp. 363–374. ISSN: 0016-7037. DOI: 10.1016/0016-7037(79)90201-1. URL: http://www.sciencedirect.com/science/article/pii/0016703779902011.

[163] Jørgensen, B. B. "Mineralization of organic matter in the sea bed – the role of sulphate reduction." In: *Nature* 296.5858 (1982), pp. 643–645. DOI: 10.1038/296643a0. URL: http://dx.doi.org/10.1038/296643a0.

[164] Jørgensen, B. B. "A thiosulfate shunt in the sulfur cycle of marine sediments." In: *Science* 249.4965 (July 13, 1990), pp. 152–154. DOI: 10.1126/science.249.4965.152. URL: http:

//science.sciencemag.org/sci/249/4965/152.full.pdf%20http://science.sciencemag.org/content/249/4965/152.

[165] Jørgensen, B. B. and Kasten, S. “Sulfur cycling and methane oxidation.” In: *Marine Geochemistry*. Springer, Berlin, Heidelberg, 2006, pp. 271–309. ISBN: 978-3-540-32143-9 978-3-540-32144-6. DOI: 10.1007/3-540-32144-6_8. URL: https://link.springer.com/chapter/10.1007/3-540-32144-6_8 (visited on 08/12/2018).

[166] Jowett, E. C. et al. “‘Background’ δ^{34}S values of Kupferschiefer sulphides in Poland: Pyrite-marcasite nodules.” In: *Mineralium Deposita* 26.2 (Apr. 1, 1991), pp. 89–98. ISSN: 1432-1866. DOI: 10.1007/BF00195254. URL: https://doi.org/10.1007/BF00195254 (visited on 03/10/2020).

[167] Kah, L. C., Lyons, T. W., and Frank, T. D. “Low marine sulphate and protracted oxygenation of the Proterozoic biosphere.” In: *Nature* 431.7010 (Oct. 2004). Number: 7010 Publisher: Nature Publishing Group, pp. 834–838. ISSN: 1476-4687. DOI: 10.1038/nature02974. URL: https://www.nature.com/articles/nature02974 (visited on 03/15/2020).

[168] Kaiho, K. et al. “End-Permian catastrophe by a bolide impact: Evidence of a gigantic release of sulfur from the mantle.” In: *Geology* 29.9 (Sept. 1, 2001), pp. 815–818. ISSN: 0091-7613. DOI: 10.1130/0091-7613(2001)029<0815:EPCBAB>2.0.CO;2. URL: https://pubs.geoscienceworld.org/gsa/geology/article/29/9/815/191819/end-permian-catastrophe-by-a-bolide-impact (visited on 01/16/2018).

[169] Kaiho, K. et al. “A sulfur isotope event at the end of the Permian.” In: *Chemical Geology* 235.1 (Nov. 30, 2006), pp. 33–47. ISSN: 0009-2541. DOI: 10.1016/j.chemgeo.2006.06.001. URL: http://www.sciencedirect.com/science/article/pii/S0009254106002786.

[170] Kallmeyer, J. et al. “Global distribution of microbial abundance and biomass in subseafloor sediment.” In: *Proceedings of the National Academy of Sciences* 109.40 (Oct. 2, 2012), pp. 16213–16216. ISSN: 0027-8424, 1091-6490. DOI: 10.1073/pnas.1203849109. URL: http://www.pnas.org/content/109/40/16213 (visited on 08/12/2018).

[171] Kampschulte, A., Bruckschen, P., and Strauss, H. “The sulphur isotopic composition of trace sulphates in Carboniferous brachiopods: Implications for coeval seawater, correlation with other geochemical cycles and isotope stratigraphy.” In: *Chemical Geology* 175.1 (2001), pp. 149–173. ISSN: 0009-2541. DOI: 10.1016/S0009-2541(00)00367-3. URL:

http://www.sciencedirect.com/science/article/pii/S0009254100003673%20http://ac.els-cdn.com/S0009254100003673/1-s2.0-S0009254100003673-main.pdf?_tid=c301f142-c7c5-11e6-9919-00000aab0f6b&acdnat=1482356467_4d471b00ba43207c30238f72da0441ca.

[172] Kampschulte, A. and Strauss, H. "The sulfur isotopic evolution of Phanerozoic seawater based on the analysis of structurally substituted sulfate in carbonates." In: *Chemical Geology* 204.3 (2004), pp. 255–286. ISSN: 0009-2541. DOI: 10.1016/j.chemgeo.2003.11.013. URL: http://www.sciencedirect.com/science/article/pii/S0009254103003747%20http://ac.els-cdn.com/S0009254103003747/1-s2.0-S0009254103003747-main.pdf?_tid=4c8c7d50-3e8f-11e4-99f8-00000aab0f01&acdnat=1410974771_d9c820b720005816b666f68d8d9245f7%20http://ac.els-cdn.com/S0009254103003747/1-s2.0-S0009254103003747-main.pdf?_tid=d58ccd76-eee3-11e4-b8e7-00000aab0f27&acdnat=1430362483_2890e4c59cfbdee9094655020ac04f2d.

[173] Kanungo, T. et al. "An efficient k-means clustering algorithm: analysis and implementation." In: *IEEE Transactions on Pattern Analysis and Machine Intelligence* 24.7 (July 2002). Conference Name: IEEE Transactions on Pattern Analysis and Machine Intelligence, pp. 881–892. ISSN: 1939-3539. DOI: 10.1109/TPAMI.2002.1017616.

[174] Kaplan, I. R., Rafter, T. A., and Hulston, J. R. "Sulphur isotopic variations in nature, part 8: application to some biogeochemical problems." In: *New Zealand J. Sci.* 3 (1960).

[175] Kaplan, I. R., Emery, K. O., and Rittenberg, S. C. "The distribution and isotopic abundance of sulphur in recent marine sediments off southern California." In: *Geochimica et Cosmochimica Acta* 27.4 (Apr. 1, 1963), pp. 297–331. ISSN: 0016-7037. DOI: 10.1016/0016-7037(63)90074-7. URL: http://www.sciencedirect.com/science/article/pii/0016703763900747.

[176] Kaplan, I. R. and Rittenberg, S. C. "Microbiological Fractionation of Sulphur Isotopes." In: *Journal of General Microbiology* 34.2 (Feb. 1, 1964), pp. 195–212. DOI: 10.1099/00221287-34-2-195. URL: http://mic.sgmjournals.org/content/34/2/195.abstract%20http://mic.sgmjournals.org/content/34/2/195.full.pdf.

[177] Kato, Y., Nakao, K., and Isozaki, Y. "Geochemistry of Late Permian to Early Triassic pelagic cherts from southwest Japan: Implications for an oceanic redox change." In: *Chemical Geology* 182.1 (Jan. 1, 2002), pp. 15–34. ISSN: 0009-2541. DOI: 10.1016/S0009-2541(01)00273-X.

URL: http://www.sciencedirect.com/science/article/pii/S000925410100273X (visited on 08/26/2020).

[178] Kershaw, S. et al. “Microbialites and global environmental change across the Permian–Triassic boundary: A synthesis.” In: *Geobiology* 10.1 (2012), pp. 25–47. ISSN: 1472-4669. DOI: 10.1111/j.1472-4669.2011.00302.x. URL: http://onlinelibrary.wiley.com/doi/abs/10.1111/j.1472-4669.2011.00302.x (visited on 08/14/2020).

[179] Khain, V. E. *Geology of the USSR*. 1985.

[180] Kim, J., Lee, I., and Lee, K.-Y. “S, Sr, and Pb isotopic systematics of hydrothermal chimney precipitates from the Eastern Manus Basin, western Pacific: Evaluation of magmatic contribution to hydrothermal system.” In: *Journal of Geophysical Research: Solid Earth* 109 (B12 2004). _eprint: https://agupubs.onlinelibrary.wiley.com/doi/pdf/10.1029/2003JB002912. ISSN: 2156-2202. DOI: 10.1029/2003JB002912. URL: https://agupubs.onlinelibrary.wiley.com/doi/abs/10.1029/2003JB002912 (visited on 07/27/2020).

[181] Knauth, L. P. and Lowe, D. R. “High Archean climatic temperature inferred from oxygen isotope geochemistry of cherts in the 3.5 Ga Swaziland Supergroup, South Africa.” In: *GSA Bulletin* 115.5 (May 1, 2003), pp. 566–580. ISSN: 0016-7606. DOI: 10.1130/0016-7606(2003)115<0566:HACTIF>2.0.CO;2. URL: http://pubs.geoscienceworld.org/gsabulletin/article/115/5/566/183983/High-Archean-climatic-temperature-inferred-from (visited on 12/26/2019).

[182] Knoblauch, C., Jørgensen, B. B., and Harder, J. “Community size and metabolic rates of psychrophilic sulfate-reducing bacteria in Arctic marine sediments.” In: *Applied and Environmental Microbiology* 65.9 (Sept. 1, 1999). Publisher: American Society for Microbiology Section: GENERAL MICROBIAL ECOLOGY, pp. 4230–4233. ISSN: 0099-2240, 1098-5336. DOI: 10.1128/AEM.65.9.4230-4233.1999. URL: https://aem.asm.org/content/65/9/4230 (visited on 09/05/2020).

[183] Knoll, A. H. et al. “Paleophysiology and end-Permian mass extinction.” In: *Earth and Planetary Science Letters* 256.3 (Apr. 30, 2007), pp. 295–313. ISSN: 0012-821X. DOI: 10.1016/j.epsl.2007.02.018. URL: http://www.sciencedirect.com/science/article/pii/S0012821X07000842 (visited on 08/13/2020).

[184] Kohnen, M. E. L. et al. “Origin and diagenetic transformations of C25 and C30 highly branched isoprenoid sulphur compounds: Further evidence for the formation of organically bound sulphur during early diagenesis.” In: *Geochimica et Cosmochimica Acta* 54.11 (Nov. 1, 1990), pp. 3053–3063. ISSN: 0016-7037. DOI:

10.1016/0016-7037(90)90121-Z. URL: http://www.sciencedirect.com/science/article/pii/001670379090121Z (visited on 04/15/2020).

[185] Korte, C. and Kozur, H. W. "Carbon-isotope stratigraphy across the Permian–Triassic boundary: A review." In: *Journal of Asian Earth Sciences* 39.4 (Sept. 9, 2010), pp. 215–235. ISSN: 1367-9120. DOI: 10.1016/j.jseaes.2010.01.005. URL: http://www.sciencedirect.com/science/article/pii/S1367912010000313 (visited on 08/13/2020).

[186] Korte, C. et al. "Carbon, sulfur, oxygen and strontium isotope records, organic geochemistry and biostratigraphy across the Permian/Triassic boundary in Abadeh, Iran." In: *International Journal of Earth Sciences* 93.4 (Sept. 1, 2004), pp. 565–581. ISSN: 1437-3262. DOI: 10.1007/s00531-004-0406-7. URL: https://doi.org/10.1007/s00531-004-0406-7 (visited on 08/14/2020).

[187] Kostka, J. E. and Luther, G. W. "Partitioning and speciation of solid phase iron in saltmarsh sediments." In: *Geochimica et Cosmochimica Acta* 58.7 (Apr. 1, 1994), pp. 1701–1710. ISSN: 0016-7037. DOI: 10.1016/0016-7037(94)90531-2. URL: http://www.sciencedirect.com/science/article/pii/0016703794905312 (visited on 07/03/2020).

[188] Krouse, H. R., Brown, H. M., and Farquharson, R. B. "Sulphur isotope compositions of sulphides and sulphates, DSDP Leg37." In: *Canadian Journal of Earth Sciences* 14.4 (Apr. 1, 1977), pp. 787–793. ISSN: 0008-4077. DOI: 10.1139/e77-078. URL: http://www.nrcresearchpress.com/doi/abs/10.1139/e77-078 (visited on 06/27/2018).

[189] Krull, E. S. et al. "Stable carbon isotope stratigraphy across the Permian–Triassic boundary in shallow marine carbonate platforms, Nanpanjiang Basin, south China." In: *Palaeogeography, Palaeoclimatology, Palaeoecology* 204.3 (Feb. 25, 2004), pp. 297–315. ISSN: 0031-0182. DOI: 10.1016/S0031-0182(03)00732-6. URL: http://www.sciencedirect.com/science/article/pii/S0031018203007326 (visited on 08/14/2020).

[190] Kump, L. R. and Arthur, M. A. "Interpreting carbon-isotope excursions: carbonates and organic matter." In: *Chemical Geology* 161.1 (Sept. 30, 1999), pp. 181–198. ISSN: 0009-2541. DOI: 10.1016/S0009-2541(99)00086-8. URL: http://www.sciencedirect.com/science/article/pii/S0009254199000868.

[191] Kump, L. R. and Garrels, R. M. “Modeling atmospheric O_2 in the global sedimentary redox cycle.” In: *American Journal of Science* 286.5 (May 1, 1986), pp. 337–360. ISSN: 0002-9599, 1945-452X. DOI: 10.2475/ajs.286.5.337. URL: http://www.ajsonline.org/content/286/5/337 (visited on 06/22/2018).

[192] Laakso, T. A. and Schrag, D. P. “Regulation of atmospheric oxygen during the Proterozoic.” In: *Earth and Planetary Science Letters* 388.0 (2014), pp. 81–91. ISSN: 0012-821X. DOI: 10.1016/j.epsl.2013.11.049. URL: http://www.sciencedirect.com/science/article/pii/S0012821X13006894%20http://ac.els-cdn.com/S0012821X13006894/1-s2.0-S0012821X13006894-main.pdf?_tid=ba1d99ee-e551-11e4-ab12-00000aab0f27&acdnat=1429310170_3220a271ca014a963fd5ab0396e3aa5f.

[193] Large, R. R. et al. “Multistage Sedimentary and Metamorphic Origin of Pyrite and Gold in the Giant Sukhoi Log Deposit, Lena Gold Province, Russia.” In: *Economic Geology* 102.7 (Nov. 1, 2007). Publisher: GeoScienceWorld, pp. 1233–1267. ISSN: 0361-0128. DOI: 10.2113/gsecongeo.102.7.1233. URL: https://pubs.geoscienceworld.org/segweb/economicgeology/article/102/7/1233/127917/Multistage-Sedimentary-and-Metamorphic-Origin-of (visited on 10/14/2020).

[194] Lau, K. V. et al. “Marine anoxia and delayed Earth system recovery after the end-Permian extinction.” In: *Proceedings of the National Academy of Sciences* 113.9 (Mar. 1, 2016). Publisher: National Academy of Sciences Section: Physical Sciences, pp. 2360–2365. ISSN: 0027-8424, 1091-6490. DOI: 10.1073/pnas.1515080113. URL: https://www.pnas.org/content/113/9/2360 (visited on 08/13/2020).

[195] Leavitt, W. et al. “Influence of sulfate reduction rates on the Phanerozoic sulfur isotope record.” In: *Proceedings of the National Academy of Sciences of the United States of America* 110.28 (2013), pp. 11244–9. ISSN: 0027-8424. URL: http://sfx.caltech.edu:8088/caltech?sid=google&auinit=WD&aulast=Leavitt&atitle=Influence%20of%20sulfate%20reduction%20rates%20on%20the%20Phanerozoic%20sulfur%20isotope%20record&id=pmid%3A23733944%20http://www.ncbi.nlm.nih.gov/pmc/articles/PMC3710818/pdf/pnas.201218874.pdf.

[196] Leavitt, W. D. et al. “Proteomic and isotopic response of *Desulfovibrio vulgaris* to DsrC perturbation.” In: *Frontiers in Microbiology* 10 (2019). Publisher: Frontiers. ISSN: 1664-302X. DOI: 10.3389/fmicb.2019.00658. URL: https://www.frontiersin.org/articles/10.3389/fmicb.2019.00658/full (visited on 05/08/2020).

[197] Lein, A. Y. et al. “Isotopic composition of sulfur compounds in sediments of the Pacific.” In: *Biochemistry of Diagenesis of Ocean Sediments, Nauka, Moscow* (1976), pp. 179–185.

[198] Lein, A. Y. “Biogeochemistry of the Anaerobic Diagenesis of Recent Baltic Sea Sediments.” In: *Ecological Bulletins* 35 (1983), pp. 441–461. ISSN: 0346-6868. URL: https://www.jstor.org/stable/20112879 (visited on 09/23/2019).

[199] Lenton, T. M., Daines, S. J., and Mills, B. J. W. “COPSE reloaded: An improved model of biogeochemical cycling over Phanerozoic time.” In: *Earth-Science Reviews* 178 (Mar. 1, 2018), pp. 1–28. ISSN: 0012-8252. DOI: 10.1016/j.earscirev.2017.12.004. URL: http://www.sciencedirect.com/science/article/pii/S0012825217304117 (visited on 07/13/2018).

[200] Locarnini, R. A. et al. “World ocean atlas 2013. Volume 1, Temperature.” In: (2013). URL: https://repository.library.noaa.gov/view/noaa/14847.

[201] Lovley, D. R. and Klug, M. J. “Intermediary Metabolism of Organic Matter in the Sediments of a Eutrophic Lake.” In: *Applied and Environmental Microbiology* 43.3 (Mar. 1, 1982). Publisher: American Society for Microbiology Section: General Microbial Ecology, pp. 552–560. ISSN: 0099-2240, 1098-5336. URL: https://aem.asm.org/content/43/3/552 (visited on 10/16/2020).

[202] Lowenstein, T. K. et al. “Secular variation in seawater chemistry and the origin of calcium chloride basinal brines.” In: *Geology* 31.10 (Oct. 1, 2003), pp. 857–860. DOI: 10.1130/g19728r.1. URL: http://geology.gsapubs.org/content/31/10/857.abstract.

[203] Luo, G. et al. “Isotopic evidence for an anomalously low oceanic sulfate concentration following end-Permian mass extinction.” In: *Earth and Planetary Science Letters* 300.1 (Nov. 15, 2010), pp. 101–111. ISSN: 0012-821X. DOI: 10.1016/j.epsl.2010.09.041. URL: http://www.sciencedirect.com/science/article/pii/S0012821X10006163 (visited on 08/14/2020).

[204] Macdonald, F. A. et al. “Arc-continent collisions in the tropics set Earth’s climate state.” In: *Science* 364.6436 (Apr. 12, 2019), pp. 181–184. ISSN: 0036-8075, 1095-9203. DOI: 10.1126/science.aav5300. URL: https://science.sciencemag.org/content/364/6436/181 (visited on 04/13/2019).

[205] Maharjan, D. et al. “Sulfur isotope change across the Early Mississippian K–O (Kinderhookian–Osagean) $\delta^{13}C$ excursion.” In: *Earth and Planetary Science Letters* 494 (July 15, 2018), pp. 202–215. ISSN: 0012-821X. DOI: 10.1016/j.epsl.2018.04.043. URL:

http://www.sciencedirect.com/science/article/pii/S0012821X18302462 (visited on 05/29/2018).

[206] Manheim, F. T. and Sayles, F. "Composition and origin of interstitial waters of marine sediments, based on deep sea drill cores." In: *Sea, Vol. 5; Marine chemistry; the sedimentary cycle*. Red. by Wiley. Vol. 5. Wiley, 1974, pp. 527–568. URL: http://pubs.er.usgs.gov/publication/70207491.

[207] Manteuffel, T. A. and White, A. B. "The numerical solution of second-order boundary value problems on nonuniform meshes." In: *Mathematics of Computation* 47.176 (1986), 511–535, S53. ISSN: 0025-5718, 1088-6842. DOI: 10.1090/S0025-5718-1986-0856700-3. URL: https://www.ams.org/mcom/1986-47-176/S0025-5718-1986-0856700-3/ (visited on 06/07/2019).

[208] Marenco, P. J. et al. "Oxidation of pyrite during extraction of carbonate associated sulfate." In: *Chemical Geology* 247.1 (2008), pp. 124–132. ISSN: 0009-2541. DOI: 10.1016/j.chemgeo.2007.10.006. URL: http://www.sciencedirect.com/science/article/pii/S0009254107004421%20http://ac.els-cdn.com/S0009254107004421/1-s2.0-S0009254107004421-main.pdf?_tid=b5350720-ddc5-11e4-94cb-00000aacb360&acdnat=1428480374_54cf3158933331039a1fef9744405144.

[209] Marenco, P. J. "Sulfur isotope geochemistry and the End Permian mass extinction." 2007. ISBN: 0-549-25096-4. URL: http://digitallibrary.usc.edu/cdm/ref/collection/p15799coll127/id/524325/.

[210] Martin, K. M., Wood, W. T., and Becker, J. J. "A global prediction of seafloor sediment porosity using machine learning." In: *Geophysical Research Letters* 42.24 (2015). _eprint: https://agupubs.onlinelibrary.wiley.com/doi/pdf/10.1002/2015GL065279, pp. 10, 640–10, 646. ISSN: 1944-8007. DOI: 10.1002/2015GL065279. URL: https://agupubs.onlinelibrary.wiley.com/doi/abs/10.1002/2015GL065279 (visited on 10/18/2020).

[211] Masterson, A. et al. "Interpreting multiple sulfur isotope signals in modern anoxic sediments using a full diagenetic model (California-Mexico margin: Alfonso Basin)." In: *American Journal of Science* 318.5 (May 1, 2018), pp. 459–490. ISSN: 0002-9599, 1945-452X. DOI: 10.2475/05.2018.02. URL: http://www.ajsonline.org/content/318/5/459 (visited on 07/27/2018).

[212] Maynard, J. B. "Sulfur isotopes of iron sulfides in Devonian-Mississippian shales of the Appalachian Basin; control by rate of sedimentation." In: *American Journal of Science* 280.8 (Oct. 1,

1980), pp. 772–786. ISSN: 0002-9599, 1945-452X. DOI: 10.2475/ajs.280.8.772. URL: http://www.ajsonline.org/content/280/8/772 (visited on 10/14/2019).

[213] McAllister, J. E. “Microstructural and geochemical investigation of North American lower-middle Paleozoic trilobites and recent arthropods.” 1989. URL: https://dr.library.brocku.ca/handle/10464/1959.

[214] McAllister, J. E. and Brand, U. “Geochemistry of some Ordovician and Devonian trilobite cuticles from North America.” In: *Chemical Geology* 78.1 (Nov. 15, 1989). Publisher: Elsevier, pp. 51–63. ISSN: 0009-2541. DOI: 10.1016/0009-2541(89)90051-X. URL: http://www.sciencedirect.com/science/article/pii/000925418990051X (visited on 09/14/2020).

[215] McAllister, J. E. and Brand, U. W. E. “Primary and diagenetic microstructures in trilobites.” In: *Lethaia* 22.1 (1989), pp. 101–111. ISSN: 1502-3931. DOI: 10.1111/j.1502-3931.1989.tb01173.x. URL: http://dx.doi.org/10.1111/j.1502-3931.1989.tb01173.x%20http://onlinelibrary.wiley.com/doi/10.1111/j.1502-3931.1989.tb01173.x/abstract.

[216] McArthur, J. M. et al. “Stable isotopic characterisation of francolite formation.” In: *Earth and Planetary Science Letters* 77.1 (1986), pp. 20–34. ISSN: 0012-821X. DOI: 10.1016/0012-821X(86)90129-9. URL: http://www.sciencedirect.com/science/article/pii/0012821X86901299%20http://ac.els-cdn.com/0012821X86901299/1-s2.0-0012821X86901299-main.pdf?_tid=75c2532c-3e9c-11e4-81d4-00000aacb361&acdnat=1410980424_caf67595c6fe2d72c6c09b5f9f9ea1bf.

[217] Meysman, F. J. R. and Middelburg, J. J. “Acid-volatile sulfide (AVS) — A comment.” In: *Marine Chemistry* 97.3 (Dec. 20, 2005), pp. 206–212. ISSN: 0304-4203. DOI: 10.1016/j.marchem.2005.08.005. URL: http://www.sciencedirect.com/science/article/pii/S0304420305001052 (visited on 01/18/2020).

[218] Middelburg, J. J. “A simple rate model for organic matter decomposition in marine sediments.” In: *Geochimica et Cosmochimica Acta* 53.7 (1989), pp. 1577–1581. ISSN: 0016-7037. DOI: 10.1016/0016-7037(89)90239-1. URL: http://www.sciencedirect.com/science/article/pii/0016703789902391%20http://ac.els-cdn.com/0016703789902391/1-s2.0-0016703789902391-

main.pdf?_tid=2779c9a0-3f61-11e4-8eb0-00000aab0f26&acdnat=1411064903_52a34fceb439ae816ed9f70cab8e1e31.

[219] Middelburg, J. J., Soetaert, K., and Herman, P. M. J. "Empirical relationships for use in global diagenetic models." In: *Deep Sea Research Part I: Oceanographic Research Papers* 44.2 (Feb. 1, 1997), pp. 327–344. ISSN: 0967-0637. DOI: 10.1016/S0967-0637(96)00101-X. URL: http://www.sciencedirect.com/science/article/pii/S096706379600101X (visited on 10/15/2019).

[220] Migdisov, A. et al. "Major and minor elements and sulfur isotopes of the Mesozoic and Cenozoic sediments at Sites 415 and 416, Leg 50, Deep Sea Drilling Project." In: (June 1, 1980). DOI: 10.2973/dsdp.proc.50.132.1980.

[221] Migdisov, A. A., Cherkovskiy, S. L., and Grinenko, V. A. "The effects of formation conditions on the sulfur isotopes of aquatic sediments." In: *Geochemistry International* 11 (1974), pp. 1028–1047.

[222] Migdisov, A. A. "The concentration and isotope composition of sulfur from the Galapagos mounds area sediments, Leg 70, Deep Sea Drilling Project." In: *Initial Reports of the Deep Sea Drilling Project*. Initial reports of the Deep Sea Drilling Project covering Leg 70 of the cruises of the drilling vessel Glomar Challenger; Balboa, Panama to Callao, Peru, November-December, 1979 70 (1983). Ed. by V. M. Belyi et al. Place: Ocean Drilling Program, College Station, TX, United States Publisher: Texas A & M University, p. 333. ISSN: 0080-8334. DOI: 10.2973/dsdp.proc.70.118.1983.

[223] Mii, H.-S. and Grossman, E. L. "Late Pennsylvanian seasonality reflected in the 18O and elemental composition of a brachiopod shell." In: *Geology* 22.7 (1994), pp. 661–664. DOI: 10.1130/0091-7613(1994)022<0661:LPSRIT>2.3.CO;2.

[224] Mii, H.-s., Grossman, E. L., and Yancey, T. E. "Stable carbon and oxygen isotope shifts in Permian seas of West Spitsbergen-Global change or diagenetic artifact?" In: *Geology* 25.3 (Mar. 1, 1997), pp. 227–230. DOI: 10.1130/0091-7613(1997)025<0227:scaois>2.3.co;2. URL: http://geology.gsapubs.org/content/25/3/227.abstract.

[225] Mii, H.-s., Grossman, E. L., and Yancey, T. E. "Carboniferous isotope stratigraphies of North America: Implications for Carboniferous paleoceanography and Mississippian glaciation." In: *GSA Bulletin* 111.7 (July 1, 1999), pp. 960–973. ISSN: 0016-7606. DOI: 10.1130/0016-7606(1999)111<0960:CISONA>2.3.CO;2. URL: https://pubs.geoscienceworld.org/gsa/gsabulletin/article/111/7/960/183527/carboniferous-isotope-stratigraphies-of-north (visited on 12/19/2018).

[226] Mii, H.-S. et al. “Isotopic records of brachiopod shells from the Russian Platform — evidence for the onset of mid-Carboniferous glaciation.” In: *Chemical Geology* 175.1 (2001), pp. 133–147. ISSN: 0009-2541. DOI: 10.1016/S0009-2541(00)00366-1. URL: http://www.sciencedirect.com/science/article/pii/S0009254100003661%20http://ac.els-cdn.com/S0009254100003661/1-s2.0-S0009254100003661-main.pdf?_tid=a44f409c-140f-11e7-903d-00000aab0f6b&acdnat=1490744487_01fa8644cc42744626c392f086cf5fe4.

[227] Miller, J. and Clarkson, E. N. K. “The post-ecdysial development of the cuticle and the eye of the Devonian trilobite *Phacops rana milleri* (Stewart, 1927).” In: *Philosophical Transactions of the Royal Society of London. Series B, Biological Sciences* 288.1030 (1980), pp. 461–480. ISSN: 00804622. DOI: 10.2307/2395369. URL: http://www.jstor.org/stable/2395369.

[228] Millero, F. J. “Thermodynamics of the carbon dioxide system in the oceans.” In: *Geochimica et Cosmochimica Acta* 59.4 (1995), pp. 661–677. ISSN: 0016-7037. DOI: 10.1016/0016-7037(94)00354-0. URL: http://www.sciencedirect.com/science/article/pii/0016703794003540.

[229] Millero, F. J., Plese, T., and Fernandez, M. “The dissociation of hydrogen sulfide in seawater1.” In: *Limnology and Oceanography* 33.2 (1988), pp. 269–274. ISSN: 1939-5590. DOI: 10.4319/lo.1988.33.2.0269. URL: https://aslopubs.onlinelibrary.wiley.com/doi/abs/10.4319/lo.1988.33.2.0269 (visited on 10/25/2019).

[230] Monga, O. et al. “Simulating microbial degradation of organic matter in a simple porous system using the 3-D diffusion-based model MOSAIC.” In: *Biogeosciences* 11 (Apr. 22, 2014). Publisher: European Geosciences Union, pp. 2201–2209. ISSN: 1726-4170. DOI: 10.5194/bg-11-2201-2014. URL: https://rke.abertay.ac.uk/en/publications/simulating-microbial-degradation-of-organic-matter-in-a-simple-po (visited on 06/30/2020).

[231] Monod, J. “The growth of bacterial cultures.” In: *Annual Review of Microbiology* 3.1 (Oct. 1, 1949). Publisher: Annual Reviews, pp. 371–394. ISSN: 0066-4227. DOI: 10.1146/annurev.mi.03.100149.002103. URL: http://www.annualreviews.org/doi/10.1146/annurev.mi.03.100149.002103 (visited on 07/06/2020).

[232] Montañez, I. P. and Poulsen, C. J. “The Late Paleozoic Ice Age: An evolving paradigm.” In: *Annual Review of Earth and Planetary Sciences*

41.1 (2013), pp. 629–656. DOI: 10.1146/annurev.earth.031208.100118. URL: https://doi.org/10.1146/annurev.earth.031208.100118.

[233] Mucci, A. "The solubility of calcite and aragonite in seawater at various salinities, temperatures, and one atmosphere total pressure." In: *American Journal of Science* 283.7 (Sept. 1, 1983), pp. 780–799. DOI: 10.2475/ajs.283.7.780. URL: http://www.ajsonline.org/content/283/7/780.short%20http://www.ajsonline.org/content/283/7/780.full.pdf.

[234] Murray, R. et al. *Cruise Report: R/V Knorr, Cruise KN223*. 2014.

[235] Nathan, Y. and Nielsen, H. "Sulfur Isotopes in Phosphorites." In: (1980). Publisher: Special Publications of SEPM. URL: http://archives.datapages.com/data/sepm_sp/SP29/Sulfur_Isotopes_in_Phosphorites.htm (visited on 03/15/2020).

[236] Nelsen, M. P. et al. "Delayed fungal evolution did not cause the Paleozoic peak in coal production." In: *Proceedings of the National Academy of Sciences* 113.9 (Mar. 1, 2016), p. 2442. DOI: 10.1073/pnas.1517943113. URL: http://www.pnas.org/content/113/9/2442.abstract.

[237] Neubauer, C. et al. "Scanning the isotopic structure of molecules by tandem mass spectrometry." In: *International Journal of Mass Spectrometry* 434 (Nov. 1, 2018), pp. 276–286. ISSN: 1387-3806. DOI: 10.1016/j.ijms.2018.08.001. URL: http://www.sciencedirect.com/science/article/pii/S1387380618301076 (visited on 06/11/2020).

[238] Neubauer, C. et al. "Stable isotope analysis of intact oxyanions using electrospray quadrupole-orbitrap mass spectrometry." In: *Analytical Chemistry* (Feb. 3, 2020). ISSN: 0003-2700. DOI: 10.1021/acs.analchem.9b04486. URL: https://doi.org/10.1021/acs.analchem.9b04486 (visited on 02/17/2020).

[239] Newton, R. J. et al. "Large shifts in the isotopic composition of seawater sulphate across the Permo–Triassic boundary in northern Italy." In: *Earth and Planetary Science Letters* 218.3 (Feb. 15, 2004), pp. 331–345. ISSN: 0012-821X. DOI: 10.1016/S0012-821X(03)00676-9. URL: http://www.sciencedirect.com/science/article/pii/S0012821X03006769 (visited on 09/15/2018).

[240] Nielsen, J. K. and Shen, Y. "Evidence for sulfidic deep water during the Late Permian in the East Greenland Basin." In: *Geology* 32.12 (Dec. 1, 2004). Publisher: GeoScienceWorld, pp. 1037–1040. ISSN: 0091-7613. DOI: 10.1130/G20987.1. URL: http://pubs.geoscienceworld.org/

gsa/geology/article/32/12/1037/29377/Evidence-for-sulfidic-deep-water-during-the-Late (visited on 08/13/2020).

[241] Ono, S. et al. “High precision analysis of all four stable isotopes of sulfur (32S, 33S, 34S and 36S) at nanomole levels using a laser fluorination isotope-ratio-monitoring gas chromatography–mass spectrometry.” In: *Chemical Geology* 225.1 (2006), pp. 30–39. ISSN: 0009-2541. DOI: 10.1016/j.chemgeo.2005.08.005. URL: http://www.sciencedirect.com/science/article/pii/S0009254105003177%20http://ac.els-cdn.com/S0009254105003177/1-s2.0-S0009254105003177-main.pdf?_tid=203c0c50-14f4-11e7-ae3e-00000aab0f6c&acdnat=1490842620_d7dd1deef7ec7a94fdcb71b87035681a.

[242] Paris, G. et al. “MC-ICP-MS measurement of δ^{34}S and 33S in small amounts of dissolved sulfate.” In: *Chemical Geology* 345.0 (2013), pp. 50–61. ISSN: 0009-2541. DOI: 10.1016/j.chemgeo.2013.02.022. URL: http://www.sciencedirect.com/science/article/pii/S0009254113000818%20http://ac.els-cdn.com/S0009254113000818/1-s2.0-S0009254113000818-main.pdf?_tid=8ee333fa-5295-11e4-8943-00000aab0f01&acdnat=1413176482_f0e4b5058eb576e22a57b526f2246d6f.

[243] Paris, G. et al. “Experimental determination of carbonate-associated sulfate δ^{34}S in planktonic foraminifera shells.” In: *Geochemistry, Geophysics, Geosystems* 15.4 (2014), pp. 1452–1461. ISSN: 1525-2027. DOI: 10.1002/2014GC005295. URL: http://dx.doi.org/10.1002/2014GC005295%20http://onlinelibrary.wiley.com/store/10.1002/2014GC005295/asset/ggge20437.pdf?v=1&t=i0osz6oz&s=519c2639fe1ce9045c1a6074c03067f7b01a53ca.

[244] Paris, G. et al. “Neoarchean carbonate–associated sulfate records positive δ^{33}S anomalies.” In: *Science* 346.6210 (Nov. 7, 2014), pp. 739–741. DOI: 10.1126/science.1258211. URL: http://www.sciencemag.org/content/346/6210/739.abstract%20http://www.sciencemag.org/content/346/6210/739.full.pdf.

[245] Paris, G. et al. “Deposition of sulfate aerosols with positive δ^{33}S in the Neoarchean.” In: *Geochimica et Cosmochimica Acta* (July 3, 2020). ISSN: 0016-7037. DOI: 10.1016/j.gca.2020.06.028. URL: http://www.sciencedirect.com/science/article/pii/S0016703720304051 (visited on 07/10/2020).

[246] Pasquier, V. et al. “Pyrite sulfur isotopes reveal glacial-interglacial environmental changes.” In: *Proceedings of the National Academy of Sciences* 114.23 (June 6, 2017), pp. 5941–5945. DOI: 10.1073/pnas.1618245114. URL: http://www.pnas.org/content/114/23/5941.abstract.

[247] Pawlowicz, R. *M_Map: A mapping package for MATLAB*. Version 1.4m. 2020. URL: https://www.eoas.ubc.ca/~rich/map.html.

[248] Payne, J. L. and Clapham, M. E. *End-Permian Mass Extinction in the Oceans: An Ancient Analog for the Twenty-First Century?* http://dx.doi.org/10.1146/annurev-earth-042711-105329. May 2, 2012. DOI: 10.1146/annurev-earth-042711-105329. URL: https://www.annualreviews.org/doi/abs/10.1146/annurev-earth-042711-105329 (visited on 04/13/2019).

[249] Payne, J. L. and Kump, L. R. "Evidence for recurrent Early Triassic massive volcanism from quantitative interpretation of carbon isotope fluctuations." In: *Earth and Planetary Science Letters* 256.1 (Apr. 15, 2007), pp. 264–277. ISSN: 0012-821X. DOI: 10.1016/j.epsl.2007.01.034. URL: http://www.sciencedirect.com/science/article/pii/S0012821X07000611 (visited on 10/01/2018).

[250] Payne, J. L. et al. "Large perturbations of the carbon cycle during recovery from the end-Permian extinction." In: *Science* 305.5683 (July 23, 2004). Publisher: American Association for the Advancement of Science Section: Report, pp. 506–509. ISSN: 0036-8075, 1095-9203. DOI: 10.1126/science.1097023. URL: http://science.sciencemag.org/content/305/5683/506 (visited on 08/14/2020).

[251] Payne, J. L. et al. "Calcium isotope constraints on the end-Permian mass extinction." In: *Proceedings of the National Academy of Sciences* 107.19 (May 11, 2010). Publisher: National Academy of Sciences Section: Physical Sciences, pp. 8543–8548. ISSN: 0027-8424, 1091-6490. DOI: 10.1073/pnas.0914065107. URL: https://www.pnas.org/content/107/19/8543 (visited on 08/13/2020).

[252] Paytan, A. et al. "Sulfur isotopic composition of Cenozoic seawater sulfate." In: *Science* 282.5393 (Nov. 20, 1998), pp. 1459–1462. DOI: 10.1126/science.282.5393.1459. URL: http://www.sciencemag.org/content/282/5393/1459.abstract%20http://www.sciencemag.org/content/282/5393/1459.full.pdf.

[253] Paytan, A. et al. "Origin of marine barite deposits: Sr and S isotope characterization." In: *Geology* 30.8 (Aug. 1, 2002), pp. 747–750. DOI: 10.1130/0091-7613(2002)030<0747:oombds>2.0.co;2. URL: http://geology.gsapubs.org/content/30/8/747.abstract.

[254] Paytan, A. et al. "Seawater sulfur isotope fluctuations in the Cretaceous." In: *Science* 304.5677 (2004), pp. 1663–1665. DOI: 10.1126/science.1095258.

[255] Pellerin, A. et al. “The sulfur cycle below the sulfate-methane transition of marine sediments.” In: *Geochimica et Cosmochimica Acta* (July 30, 2018). ISSN: 0016-7037. DOI: 10.1016/j.gca.2018.07.027. URL: http://www.sciencedirect.com/science/article/pii/S0016703718304137 (visited on 08/06/2018).

[256] Pellerin, A. et al. “Large sulfur isotope fractionation by bacterial sulfide oxidation.” In: *Science Advances* 5.7 (July 1, 2019), eaaw1480. ISSN: 2375-2548. DOI: 10.1126/sciadv.aaw1480. URL: https://advances.sciencemag.org/content/5/7/eaaw1480 (visited on 10/23/2019).

[257] Peters, S. E., Husson, J. M., and Czaplewski, J. “Macrostrat: A platform for geological data integration and deep-time earth crust research.” In: *Geochemistry, Geophysics, Geosystems* 19.4 (2018), pp. 1393–1409. ISSN: 1525-2027. DOI: 10.1029/2018GC007467. URL: https://agupubs.onlinelibrary.wiley.com/doi/abs/10.1029/2018GC007467 (visited on 04/22/2019).

[258] Piper, D. Z. and Kolodny, Y. “The stable isotopic composition of a phosphorite deposit: $\delta^{13}C$, $\delta^{34}S$, and $\delta^{18}O$.” In: *Deep Sea Research Part A. Oceanographic Research Papers* 34.5 (May 1, 1987), pp. 897–911. ISSN: 0198-0149. DOI: 10.1016/0198-0149(87)90044-6. URL: http://www.sciencedirect.com/science/article/pii/0198014987900446.

[259] Popp, B. N. “The record of carbon, oxygen, sulfur, and strontium isotopes and trace elements in late Paleozoic brachiopods.” PhD thesis. 1985.

[260] Present, T. M. *Penglaitan CAS $\delta^{34}S$, unpublished data*.

[261] Present, T. M., Adkins, J. F., and Fischer, W. W. “Variability in sulfur isotope records of Phanerozoic seawater sulfate.” In: *Geophysical Research Letters* 47.18 (2020), e2020GL088766. ISSN: 1944-8007. DOI: 10.1029/2020GL088766. URL: https://agupubs.onlinelibrary.wiley.com/doi/abs/10.1029/2020GL088766 (visited on 09/06/2020).

[262] Present, T. M. et al. “Large Carbonate Associated Sulfate isotopic variability between brachiopods, micrite, and other sedimentary components in Late Ordovician strata.” In: *Earth and Planetary Science Letters* 432 (2015), pp. 187–198. ISSN: 0012-821X. DOI: 10.1016/j.epsl.2015.10.005. URL: http://www.sciencedirect.com/science/article/pii/S0012821X15006330%20http://ac.els-cdn.com/S0012821X15006330/1-s2.0-S0012821X15006330-main.pdf?_tid=23faa376-8286-11e5-942e-00000aab0f02&acdnat=1446595014_30724372fa870748887bac37951d491c.

[263] Present, T. M. et al. “Diagenetic controls on the isotopic composition of carbonate-associated sulphate in the Permian Capitan Reef Complex, West Texas.” In: *Sedimentology* 66.7 (2019), pp. 2605–2626. ISSN: 1365-3091. DOI: 10.1111/sed.12615. URL: https://onlinelibrary.wiley.com/doi/abs/10.1111/sed.12615 (visited on 02/21/2020).

[264] Present, T. M. “Controls on the Sulfur Isotopic Composition of Carbonate-Associated Sulfate.” PhD thesis. California Institute of Technology, 2018. DOI: Present,TheodoreMichael(2018) ControlsontheSulfurIsotopicCompositionofCarbonate-AssociatedSulfate.Dissertation(Ph.D.), CaliforniaInstituteofTechnology.doi:10.7907/6SFR-EX25.http://resolver.caltech.edu/CaltechTHESIS:04042018-153105432<http://resolver.caltech.edu/CaltechTHESIS:04042018-153105432>. URL: http://resolver.caltech.edu/CaltechTHESIS:04042018-153105432 (visited on 05/06/2019).

[265] Prokoph, A., Shields, G. A., and Veizer, J. “Compilation and time-series analysis of a marine carbonate $\delta^{18}O$, $\delta^{13}C$, 87Sr/86Sr and $\delta^{34}S$ database through Earth history.” In: *Earth-Science Reviews* 87.3 (2008), pp. 113–133. ISSN: 0012-8252. DOI: 10.1016/j.earscirev.2007.12.003. URL: http://www.sciencedirect.com/science/article/pii/S0012825208000032%20http://ac.els-cdn.com/S0012825208000032/1-s2.0-S0012825208000032-main.pdf?_tid=98a0740e-ee56-11e4-8395-00000aab0f6c&acdnat=1430301822_ebf752d68f6a8f29c78daf19c622b2a1.

[266] Puchelt, H. and Hubberten, H. W. “Preliminary results of sulfur isotope investigations on Deep Sea Drilling Project cores from Legs 52 and 53.” In: *Initial Reports on the Deep Sea Drilling Project*. Vol. 51-53. 1980, pp. 1145–1148. DOI: 10.2973/dsdp.proc.515253.139.1980.

[267] Puchelt, H., Sabels, B. R., and Hoering, T. C. “Preparation of sulfur hexafluoride for isotope geochemical analysis.” In: *Geochimica et Cosmochimica Acta* 35.6 (June 1, 1971), pp. 625–628. ISSN: 0016-7037. DOI: 10.1016/0016-7037(71)90093-7. URL: http://www.sciencedirect.com/science/article/pii/0016703771900937 (visited on 08/06/2020).

[268] Raab, M. and Spiro, B. “Sulfur isotopic variations during seawater evaporation with fractional crystallization.” In: *Chemical Geology: Isotope Geoscience section* 86.4 (Apr. 5, 1991), pp. 323–333. ISSN: 0168-9622. DOI: 10.1016/0168-9622(91)90014-N. URL: http://www.sciencedirect.com/science/article/pii/016896229190014N.

[269] Rabouille, C. and Gaillard, J.-F. “A coupled model representing the deep-sea organic carbon mineralization and oxygen consumption in surficial sediments.” In: *Journal of Geophysical Research: Oceans* 96 (C2 1991). _eprint: https://onlinelibrary.wiley.com/doi/pdf/10.1029/90JC02332, pp. 2761–2776. ISSN: 2156-2202. DOI: 10.1029/90JC02332. URL: http://agupubs.onlinelibrary.wiley.com/doi/abs/10.1029/90JC02332 (visited on 05/17/2020).

[270] Rabouille, C. and Gaillard, J.-F. “Towards the EDGE: Early diagenetic global explanation. A model depicting the early diagenesis of organic matter, O2, NO3, Mn, and PO4.” In: *Geochimica et Cosmochimica Acta* 55.9 (Sept. 1, 1991), pp. 2511–2525. ISSN: 0016-7037. DOI: 10.1016/0016-7037(91)90369-G. URL: http://www.sciencedirect.com/science/article/pii/001670379190369G (visited on 05/17/2020).

[271] Raiswell, R. and Canfield, D. E. “Sources of iron for pyrite formation in marine sediments.” In: *American Journal of Science* 298.3 (Mar. 1, 1998), pp. 219–245. DOI: 10.2475/ajs.298.3.219. URL: http://www.ajsonline.org/content/298/3/219.abstract%20http://www.ajsonline.org/content/298/3/219.full.pdf.

[272] Raven, M. R. “Organic Matter Sulfurization in the Modern Ocean.” PhD thesis. California Institute of Technology, 2016. DOI: Raven,MorganReed(2016) OrganicMatterSulfurizationintheModernOcean. Dissertation(Ph.D.),CaliforniaInstituteofTechnology.doi: 10.7907/Z91Z42B0.https://resolver.caltech.edu/CaltechTHESIS:05262016-125832967<https://resolver.caltech.edu/CaltechTHESIS:05262016-125832967>. URL: https://resolver.caltech.edu/CaltechTHESIS:05262016-125832967 (visited on 02/01/2020).

[273] Raven, M. R. et al. “Sulfur isotopic composition of individual organic compounds from Cariaco Basin sediments.” In: *Organic Geochemistry* 80.0 (2015), pp. 53–59. ISSN: 0146-6380. DOI: 10.1016/j.orggeochem.2015.01.002. URL: http://www.sciencedirect.com/science/article/pii/S0146638015000042%20http://ac.els-cdn.com/S0146638015000042/1-s2.0-S0146638015000042-main.pdf?_tid=8e46d6da-ee54-11e4-ad94-00000aab0f01&acdnat=1430300946_34b227a4345688e7b42d4322fb669e46.

[274] Raven, M. R. et al. “Rapid organic matter sulfurization in sinking particles from the Cariaco Basin water column.” In: *Geochimica et Cosmochimica Acta* 190 (2016), pp. 175–190. ISSN: 0016-7037. DOI:

10.1016/j.gca.2016.06.030. URL: http://www.sciencedirect.com/science/article/pii/S001670371630360X.

[275] Raven, M. R. et al. “Paired organic matter and pyrite δ^{34}S records reveal mechanisms of carbon, sulfur, and iron cycle disruption during Ocean Anoxic Event 2.” In: *Earth and Planetary Science Letters* 512 (Apr. 15, 2019), pp. 27–38. ISSN: 0012-821X. DOI: 10.1016/j.epsl.2019.01.048. URL: http://www.sciencedirect.com/science/article/pii/S0012821X19300743 (visited on 03/07/2019).

[276] Redfield, A. C. “The influence of organisms on the composition of sea-water.” In: *The Sea* (1963), pp. 26–77. URL: http://ci.nii.ac.jp/naid/10003768545/en/.

[277] Renne, P. R. et al. “Synchrony and Causal Relations Between Permian-Triassic Boundary Crises and Siberian Flood Volcanism.” In: *Science* 269.5229 (Sept. 8, 1995). Publisher: American Association for the Advancement of Science Section: Reports, pp. 1413–1416. ISSN: 0036-8075, 1095-9203. DOI: 10.1126/science.269.5229.1413. URL: http://science.sciencemag.org/content/269/5229/1413 (visited on 08/14/2020).

[278] Rennie, V. C. F. and Turchyn, A. V. “The preservation of d34S and d18O in carbonate-associated sulfate during marine diagenesis: A 25 Myr test case using marine sediments.” In: *Earth and Planetary Science Letters* 395.0 (2014), pp. 13–23. ISSN: 0012-821X. DOI: 10.1016/j.epsl.2014.03.025. URL: http://www.sciencedirect.com/science/article/pii/S0012821X14001691%20http://ac.els-cdn.com/S0012821X14001691/1-s2.0-S0012821X14001691-main.pdf?_tid=7b177a8a-2372-11e5-9f22-00000aab0f27&acdnat=1436141210_e0aeca4b2733f111110de5806d3fb8fe.

[279] Rennie, V. C. F. et al. “Cenozoic record of δ 34 S in foraminiferal calcite implies an early Eocene shift to deep-ocean sulfide burial.” In: *Nature Geoscience* 11.10 (Oct. 2018), pp. 761–765. ISSN: 1752-0908. DOI: 10.1038/s41561-018-0200-y. URL: https://www.nature.com/articles/s41561-018-0200-y (visited on 10/01/2018).

[280] Riccardi, A. L., Arthur, M. A., and Kump, L. R. “Sulfur isotopic evidence for chemocline upward excursions during the end-Permian mass extinction.” In: *Geochimica et Cosmochimica Acta* 70.23 (2006), pp. 5740–5752. ISSN: 0016-7037. DOI: 10.1016/j.gca.2006.08.005. URL: http://www.sciencedirect.com/science/article/pii/S0016703706019739%20http://ac.els-cdn.com/S0016703706019739/1-s2.0-S0016703706019739-

main.pdf?_tid=fa45b1ca-06c7-11e7-b4e9-00000aacb35d&acdnat=1489284342_78722d5a2ca1d0776574abf9b358a385.

[281] Richardson, J. A. et al. “Depositional and diagenetic constraints on the abundance and spatial variability of carbonate-associated sulfate.” In: *Chemical Geology* 523 (Sept. 30, 2019), pp. 59–72. ISSN: 0009-2541. DOI: 10.1016/j.chemgeo.2019.05.036. URL: http://www.sciencedirect.com/science/article/pii/S0009254119302682 (visited on 07/17/2019).

[282] Richardson, J. A. et al. “Silurian records of carbon and sulfur cycling from Estonia: The importance of depositional environment on isotopic trends.” In: *Earth and Planetary Science Letters* 512 (Apr. 15, 2019), pp. 71–82. ISSN: 0012-821X. DOI: 10.1016/j.epsl.2019.01.055. URL: http://www.sciencedirect.com/science/article/pii/S0012821X19300871 (visited on 03/07/2019).

[283] Richardson, J. A. et al. “The source of sulfate in brachiopod calcite: Insights from μ-XRF imaging and XANES spectroscopy.” In: *Chemical Geology* 529 (Dec. 20, 2019), p. 119328. ISSN: 0009-2541. DOI: 10.1016/j.chemgeo.2019.119328. URL: http://www.sciencedirect.com/science/article/pii/S0009254119304358 (visited on 02/21/2020).

[284] Riciputi, L. R., Cole, D. R., and Machel, H. G. “Sulfide formation in reservoir carbonates of the Devonian Nisku Formation, Alberta, Canada: An ion microprobe study.” In: *Geochimica et Cosmochimica Acta* 60.2 (Jan. 1, 1996), pp. 325–336. ISSN: 0016-7037. DOI: 10.1016/0016-7037(96)83133-4. URL: http://www.sciencedirect.com/science/article/pii/0016703796831334 (visited on 08/06/2020).

[285] Rickard, D. and Luther, G. W. “Chemistry of Iron Sulfides.” In: *Chemical Reviews* 107.2 (Feb. 1, 2007), pp. 514–562. ISSN: 0009-2665. DOI: 10.1021/cr0503658. URL: http://dx.doi.org/10.1021/cr0503658%20http://pubs.acs.org/doi/pdfplus/10.1021/cr0503658.

[286] Riechelmann, S. et al. “Impact of diagenetic alteration on brachiopod shell magnesium isotope (δ26Mg) signatures: Experimental versus field data.” In: *Chemical Geology* 440 (Nov. 15, 2016), pp. 191–206. ISSN: 0009-2541. DOI: 10.1016/j.chemgeo.2016.07.020. URL: http://www.sciencedirect.com/science/article/pii/S000925411630362X (visited on 09/16/2020).

[287] Roark, A. et al. “Brachiopod geochemical records from across the Carboniferous seas of North America: Evidence for salinity gradients, stratification, and circulation patterns.” In: *Palaeogeography, Palaeoclimatology, Palaeoecology* 485 (Supplement C Nov. 1, 2017),

pp. 136–153. ISSN: 0031-0182. DOI: 10.1016/j.palaeo.2017.06.009. URL: http://www.sciencedirect.com/science/article/pii/S0031018217302419.

[288] Ronov, A. B. et al. “Influence of Tectonic Conditions Upon Concentrations and Isotopic Concentration of Sulfur in Sedimentary-Rocks.” In: *Geokhimiya* 12 (1974), pp. 1772–1798.

[289] Rose, C. V. et al. “Records of carbon and sulfur cycling during the Silurian Ireviken Event in Gotland, Sweden.” In: *Geochimica et Cosmochimica Acta* 246 (Feb. 1, 2019), pp. 299–316. ISSN: 0016-7037. DOI: 10.1016/j.gca.2018.11.030. URL: http://www.sciencedirect.com/science/article/pii/S0016703718306604 (visited on 01/15/2019).

[290] Rosenthal, Y. *Western Pacific Warm Pool*. Ed. by A. E. Holbourn et al. Vol. 363. Proceedings of the International Ocean Discovery Program. Place: Washington, DC, United State Publisher: International Ocean Discovery Progra. College Station, TX: International Ocean Discovery Program, 2018. URL: http://hdl.handle.net/10.14379/iodp.proc.363.201.

[291] Ross, C. A. and Ross, J. R. “Late Paleozoic sea levels and depositional sequences.” In: *Timing and Depositional History of Eustatic Sequences: Constraints on Seismic Stratigraphy*. Ed. by C. A. Ross and D. Haman. Vol. 24. Cushman foundation for foraminiferal research, 1987, pp. 137–149.

[292] Rouxel, O. J., Bekker, A., and Edwards, K. J. “Iron Isotope Constraints on the Archean and Paleoproterozoic Ocean Redox State.” In: *Science* 307.5712 (Feb. 18, 2005), pp. 1088–1091. ISSN: 0036-8075, 1095-9203. DOI: 10.1126/science.1105692. URL: https://science.sciencemag.org/content/307/5712/1088 (visited on 09/27/2019).

[293] Scharff, M. L. “Die Verteilung von Stickstoff, Schwefel, Schwefel-Isotopen sowie Mn, Zn, Fe und Cu in Sedimenten des Atlantischen Ozeans (DSDP-Bohrkerne).” PhD thesis. Uitgever niet vastgesteld, 1980.

[294] Schlitzer, R. “Electronic atlas of WOCE hydrographic and tracer data now available.” In: *Eos, Transactions American Geophysical Union* 81.5 (2000). _eprint: https://onlinelibrary.wiley.com/doi/pdf/10.1029/00EO00028, pp. 45–45. ISSN: 2324-9250. DOI: 10.1029/00EO00028. URL: http://agupubs.onlinelibrary.wiley.com/doi/abs/10.1029/00EO00028 (visited on 07/27/2020).

[295] Schobben, M. et al. “Flourishing ocean drives the end-Permian marine mass extinction.” In: *Proceedings of the National Academy of Sciences* 112.33 (Aug. 18, 2015), pp. 10298–10303. ISSN: 0027-8424, 1091-6490. DOI: 10.1073/pnas.1503755112. URL: http://www.pnas.org/content/112/33/10298 (visited on 09/16/2018).

[296] Schoepfer, S. D. et al. “Termination of a continent-margin upwelling system at the Permian–Triassic boundary (Opal Creek, Alberta, Canada).” In: *Global and Planetary Change*. New developments in Permian-Triassic paleoceanographic and global climate system research 105 (June 1, 2013), pp. 21–35. ISSN: 0921-8181. DOI: 10.1016/j.gloplacha.2012.07.005. URL: http://www.sciencedirect.com/science/article/pii/S0921818112001452 (visited on 08/13/2020).

[297] Schrag, D. P. et al. “Authigenic carbonate and the history of the global carbon cycle.” In: *Science* 339.6119 (Feb. 1, 2013), pp. 540–543. DOI: 10.1126/science.1229578. URL: http://www.sciencemag.org/content/339/6119/540.abstract%20http://www.sciencemag.org/content/339/6119/540.full.pdf.

[298] Scotese, C. R. *Atlas of Permo-Carboniferous Paleogeographic Maps (Mollweide Projection), Maps 53–64, Volumes 4, The Late Paleozoic, PALEOMAP Atlas for ArcGIS, PALEOMAP Project, Evanston, IL*. 2014. DOI: 10.13140/2.1.1837.8244.

[299] Sepkoski, J. J. “A factor analytic description of the Phanerozoic marine fossil record.” In: *Paleobiology* 7.1 (1981). Publisher: Cambridge University Press, pp. 36–53. ISSN: 0094-8373, 1938-5331. DOI: 10.1017/S0094837300003778. URL: http://www.cambridge.org/core/journals/paleobiology/article/factor-analytic-description-of-the-phanerozoic-marine-fossil-record/F2DC148BF90657CC5DF560D8E3A22BF6 (visited on 08/14/2020).

[300] Sepkoski, J. J. “A compendium of fossil marine animal genera.” In: *Bulletins of American paleontology* 363 (2002), pp. 1–560. URL: http://strata.geology.wisc.edu/jack/.

[301] Severmann, S. et al. “The continental shelf benthic iron flux and its isotope composition.” In: *Geochimica et Cosmochimica Acta* 74.14 (July 15, 2010), pp. 3984–4004. ISSN: 0016-7037. DOI: 10.1016/j.gca.2010.04.022. URL: http://www.sciencedirect.com/science/article/pii/S0016703710002073 (visited on 07/03/2020).

[302] Shampine, L. F. and Reichelt, M. W. “The MATLAB ODE Suite.” In: *SIAM Journal on Scientific Computing* 18.1 (Jan. 1, 1997). Publisher: Society for Industrial and Applied Mathematics, pp. 1–22. ISSN: 1064-8275. DOI: 10.1137/S1064827594276424. URL: http://epubs.siam.org/doi/abs/10.1137/s1064827594276424 (visited on 04/17/2020).

[303] Shawar, L. et al. “Dynamics of pyrite formation and organic matter sulfurization in organic-rich carbonate sediments.” In: *Geochimica et Cosmochimica Acta* 241 (Nov. 15, 2018), pp. 219–239. ISSN: 0016-7037. DOI: 10.1016/j.gca.2018.08.048. URL: http://www.sciencedirect.com/science/article/pii/S0016703718305039 (visited on 09/22/2018).

[304] Shen, S.-Z. et al. “A sudden end-Permian mass extinction in South China.” In: *GSA Bulletin* 131.1 (Jan. 1, 2019), pp. 205–223. ISSN: 0016-7606. DOI: 10.1130/B31909.1. URL: https://pubs.geoscienceworld.org/gsa/gsabulletin/article/131/1-2/205/548278/a-sudden-end-permian-mass-extinction-in-south (visited on 03/19/2019).

[305] Shen, S.-z. et al. “Calibrating the end-Permian mass extinction.” In: *Science* 334.6061 (Dec. 9, 2011). Publisher: American Association for the Advancement of Science Section: Research Article, pp. 1367–1372. ISSN: 0036-8075, 1095-9203. DOI: 10.1126/science.1213454. URL: http://science.sciencemag.org/content/334/6061/1367 (visited on 08/13/2020).

[306] Shen, Y. *Yudongzi carbonate $\delta^{13}C$ and $\delta^{18}O$, unpublished data*.

[307] Shen, Y. et al. “The carbon and sulfur isotope signatures in the Precambrian-Cambrian Transition series of the Yangtze Platform.” In: *Precambrian Research* 89.1 (1998), pp. 77–86. ISSN: 0301-9268. DOI: 10.1016/S0301-9268(97)00081-8. URL: http://www.sciencedirect.com/science/article/pii/S0301926897000818.

[308] Shen, Y. et al. “Multiple S-isotopic evidence for episodic shoaling of anoxic water during Late Permian mass extinction.” In: *Nature Communications* 2.1 (Feb. 22, 2011). Number: 1 Publisher: Nature Publishing Group, p. 210. ISSN: 2041-1723. DOI: 10.1038/ncomms1217. URL: https://www.nature.com/articles/ncomms1217 (visited on 08/13/2020).

[309] Shields, G. A. et al. “Unique Neoproterozoic carbon isotope excursions sustained by coupled evaporite dissolution and pyrite burial.” In: *Nature Geoscience* (Sept. 2, 2019), pp. 1–5. ISSN: 1752-0908. DOI: 10.1038/s41561-019-0434-3. URL: https://www.nature.com/articles/s41561-019-0434-3 (visited on 09/10/2019).

[310] Siedenberg, K., Strauss, H., and Littke, R. “Multiple sulfur isotopes ($\delta^{34}S$, $\delta^{33}S$) and trace elements (Mo, U, V) reveal changing palaeoenvironments in the mid-Carboniferous Chokier Formation, Belgium.” In: *Chemical Geology* 441 (Nov. 21, 2016), pp. 47–62. ISSN: 0009-2541. DOI: 10.1016/j.chemgeo.2016.08.017. URL: http://www.sciencedirect.com/science/article/pii/S0009254116303941 (visited on 03/10/2020).

[311] Siedenberg, K. et al. “Multiple sulfur isotopes ($\delta^{34}S$, $\Delta^{33}S$) of organic sulfur and pyrite from Late Cretaceous to Early Eocene oil shales in Jordan.” In: *Organic Geochemistry* 125 (Nov. 1, 2018), pp. 29–40. ISSN: 0146-6380. DOI: 10.1016/j.orggeochem.2018.08.002. URL: http://www.sciencedirect.com/science/article/pii/S0146638018301736 (visited on 10/14/2020).

[312] Silva-Tamayo, J. C. et al. “Global perturbation of the marine calcium cycle during the Permian-Triassic transition.” In: *GSA Bulletin* 130.7 (July 1, 2018). Publisher: GeoScienceWorld, pp. 1323–1338. ISSN: 0016-7606. DOI: 10.1130/B31818.1. URL: http://pubs.geoscienceworld.org/gsa/gsabulletin/article/130/7-8/1323/527060/Global-perturbation-of-the-marine-calcium-cycle (visited on 08/13/2020).

[313] Sim, M. S. et al. “Effect of electron donors on the fractionation of sulfur isotopes by a marine Desulfovibrio sp.” In: *Geochimica et Cosmochimica Acta* 75.15 (2011), pp. 4244–4259. ISSN: 0016-7037. DOI: 10.1016/j.gca.2011.05.021. URL: http://www.sciencedirect.com/science/article/pii/S0016703711002894%20http://ac.els-cdn.com/S0016703711002894/1-s2.0-S0016703711002894-main.pdf?_tid=e49c6dfa-3ea6-11e4-a589-00000aab0f01&acdnat=1410984904_8f5a90d7f4b27c99b5f9a47a8c3e62e4.

[314] Slomp, C. P. and Van Cappellen, P. “Nutrient inputs to the coastal ocean through submarine groundwater discharge: controls and potential impact.” In: *Journal of Hydrology* 295.1 (Aug. 10, 2004), pp. 64–86. ISSN: 0022-1694. DOI: 10.1016/j.jhydrol.2004.02.018. URL: http://www.sciencedirect.com/science/article/pii/S002216940400112X (visited on 09/07/2020).

[315] Soetaert, K., Herman, P. M. J., and Middelburg, J. J. “A model of early diagenetic processes from the shelf to abyssal depths.” In: *Geochimica et Cosmochimica Acta* 60.6 (1996), pp. 1019–1040. ISSN: 0016-7037. DOI: 10.1016/0016-7037(96)00013-0. URL: http://www.sciencedirect.com/science/article/pii/0016703796000130.

[316] Song, H. et al. “Integrated Sr isotope variations and global environmental changes through the Late Permian to early Late Triassic.” In: *Earth and Planetary Science Letters* 424 (Aug. 15, 2015),

pp. 140–147. ISSN: 0012-821X. DOI: 10.1016/j.epsl.2015.05.035. URL: http://www.sciencedirect.com/science/article/pii/S0012821X15003337 (visited on 09/16/2018).

[317] Song, H. et al. “Early Triassic seawater sulfate drawdown.” In: *Geochimica et Cosmochimica Acta* 128 (Mar. 1, 2014), pp. 95–113. ISSN: 0016-7037. DOI: 10.1016/j.gca.2013.12.009. URL: http://www.sciencedirect.com/science/article/pii/S0016703713006935 (visited on 09/14/2018).

[318] Staudt, W. J. and Schoonen, M. A. A. “Sulfate incorporation into sedimentary carbonates.” In: *Geochemical Transformations of Sedimentary Sulfur*. Vol. 612. 0 vols. ACS Symposium Series 612. American Chemical Society, 1995, pp. 332–345. ISBN: 0-8412-3328-4. DOI: 10.1021/bk-1995-0612.ch018. URL: http://dx.doi.org/10.1021/bk-1995-0612.ch018%20http://pubs.acs.org/doi/pdfplus/10.1021/bk-1995-0612.ch018 (visited on 06/04/2017).

[319] Stolper, D. A. and Keller, C. B. “A record of deep-ocean dissolved O_2 from the oxidation state of iron in submarine basalts.” In: *Nature* 553.7688 (Jan. 2018), pp. 323–327. ISSN: 1476-4687. DOI: 10.1038/nature25009. URL: https://www.nature.com/articles/nature25009 (visited on 07/08/2019).

[320] Strauss, H. “The isotopic composition of sedimentary sulfur through time.” In: *Palaeogeography, Palaeoclimatology, Palaeoecology* 132.1 (1997), pp. 97–118. ISSN: 0031-0182. DOI: 10.1016/S0031-0182(97)00067-9. URL: http://www.sciencedirect.com/science/article/pii/S0031018297000679%20http://ac.els-cdn.com/S0031018297000679/1-s2.0-S0031018297000679-main.pdf?_tid=7bbcbe2a-3e9c-11e4-8f58-00000aacb35e&acdnat=1410980434_f11508bb35e6cabfc6983cdee4830e75.

[321] Stüeken, E. E. et al. “Selenium isotope ratios, redox changes and biological productivity across the end-Permian mass extinction.” In: *Chemical Geology* 410 (Sept. 2, 2015), pp. 28–39. ISSN: 0009-2541. DOI: 10.1016/j.chemgeo.2015.05.021. URL: http://www.sciencedirect.com/science/article/pii/S0009254115002843 (visited on 08/13/2020).

[322] Stumm, W. and Morgan, J. J. *Aquatic chemistry: An introduction emphasizing chemical equilibria in natural waters*. New York: John Wiley, 1981. ISBN: 0-471-04831-3.

[323] Suess, E. and Huene, R. v. “Ocean Drilling Program Leg 112, Peru continental margin: Part 2, sedimentary history and diagenesis in a coastal upwelling environment.” In: *Geology* 16.10 (Oct. 1, 1988). Publisher: GeoScienceWorld, pp. 939–943. ISSN: 0091-7613. DOI: 10.1130/0091-7613(1988)016<0939:ODPLPC>2.3.CO;2. URL: https://pubs.geoscienceworld.org/gsa/geology/article/16/10/939/204600/Ocean-Drilling-Program-Leg-112-Peru-continental (visited on 09/07/2020).

[324] Sulpis, O. and Adkins, J. F. “1-D reactive-advection-diffusion-irrigation model with full diagenesis.” In: ().

[325] Sun, H. et al. “Rapid enhancement of chemical weathering recorded by extremely light seawater lithium isotopes at the Permian–Triassic boundary.” In: *Proceedings of the National Academy of Sciences* 115.15 (Apr. 10, 2018). Publisher: National Academy of Sciences Section: Physical Sciences, pp. 3782–3787. ISSN: 0027-8424, 1091-6490. DOI: 10.1073/pnas.1711862115. URL: https://www.pnas.org/content/115/15/3782 (visited on 08/13/2020).

[326] Sun, Y. et al. “Lethally hot temperatures during the Early Triassic greenhouse.” In: *Science* 338.6105 (Oct. 19, 2012), pp. 366–370. ISSN: 0036-8075, 1095-9203. DOI: 10.1126/science.1224126. URL: http://science.sciencemag.org/content/338/6105/366 (visited on 09/16/2018).

[327] Svensen, H. et al. “Siberian gas venting and the end-Permian environmental crisis.” In: *Earth and Planetary Science Letters* 277.3 (Jan. 30, 2009), pp. 490–500. ISSN: 0012-821X. DOI: 10.1016/j.epsl.2008.11.015. URL: http://www.sciencedirect.com/science/article/pii/S0012821X08007292 (visited on 08/14/2020).

[328] Sweeney, R. E. “Pyritization during Diagenesis of Marine Sediments.” PhD thesis. Los Angeles: University of California Los Angeles, 1972.

[329] Sweeney, R. E. and Kaplan, I. R. “Diagenetic sulfate reduction in marine sediments.” In: *Marine Chemistry* 9.3 (June 1, 1980), pp. 165–174. ISSN: 0304-4203. DOI: 10.1016/0304-4203(80)90035-3. URL: http://www.sciencedirect.com/science/article/pii/0304420380900353.

[330] Takano, B. “Geochemical implications of sulfate in sedimentary carbonates.” In: *Chemical Geology* 49.4 (1985), pp. 393–403. ISSN: 0009-2541. DOI: 10.1016/0009-2541(85)90001-4. URL: http://www.sciencedirect.com/science/article/pii/0009254185900014.

[331] Tang, H. et al. “Permian–Triassic boundary microbialites (PTBMs) in southwest China: Implications for paleoenvironment reconstruction.” In: *Facies* 63.1 (Jan. 1, 2017), p. 2. ISSN: 0172-9179, 1612-4820. DOI: 10.1007/s10347-016-0482-8. URL: https://link.springer.com/article/10.1007/s10347-016-0482-8 (visited on 04/18/2018).

[332] Teigler, D. J. and Towe, K. M. “Microstructure and composition of the trilobite exoskeleton.” In: *Fossils and Strata* 4 (1975), pp. 137–149. URL: https://foreninger.uio.no/ngf/FOS/pdfs/F&S_04_p137.pdf.

[333] Teske, A. et al. “Distribution of sulfate-reducing bacteria in a stratified fjord (Mariager Fjord, Denmark) as evaluated by most-probable-number counts and denaturing gradient gel electrophoresis of PCR-amplified ribosomal DNA fragments.” In: *Applied and Environmental Microbiology* 62.4 (Apr. 1, 1996). Publisher: American Society for Microbiology, pp. 1405–1415. ISSN: 0099-2240, 1098-5336. URL: https://aem.asm.org/content/62/4/1405 (visited on 09/05/2020).

[334] Theiling, B. P. and Coleman, M. “Refining the extraction methodology of carbonate associated sulfate: Evidence from synthetic and natural carbonate samples.” In: *Chemical Geology* 411 (2015), pp. 36–48. ISSN: 0009-2541. DOI: 10.1016/j.chemgeo.2015.06.018. URL: http://www.sciencedirect.com/science/article/pii/S000925411500306X%20http://ac.els-cdn.com/S000925411500306X/1-s2.0-S000925411500306X-main.pdf?_tid=e2cc5464-46c4-11e5-a115-00000aacb360&acdnat=1440024893_f5984e4f6b35cf25a1a06075b9680efd.

[335] Thode, H. G. and Rees, C. E. “Measurement of sulphur concentrations and the isotope ratios33S/32S, 34S/32S and36S/32S in Apollo 12 samples.” In: *Earth and Planetary Science Letters* 12.4 (Dec. 1, 1971), pp. 434–438. ISSN: 0012-821X. DOI: 10.1016/0012-821X(71)90029-X. URL: http://www.sciencedirect.com/science/article/pii/0012821X7190029X (visited on 08/06/2020).

[336] Thode, H. G., Harrison, A. G., and Monster, J. “Sulphur isotope fractionation in early diagenesis of recent sediments of northeast Venezuela.” In: *AAPG Bulletin* 44.11 (1960), pp. 1809–1817. ISSN: 0149-1423. URL: http://archives.datapages.com/data/bulletns/1957-60/data/pg/0044/0011/1800/1809.htm (visited on 06/27/2018).

[337] Thode, H. G., Macnamara, J., and Collins, C. B. “Natural variations in the isotopic content of sulphur and their significance.” In: *Canadian Journal of Research* 27b.4 (Apr. 1, 1949), pp. 361–373. ISSN: 1923-4287.

DOI: 10.1139/cjr49b-038. URL: http://www.nrcresearchpress.com/doi/abs/10.1139/cjr49b-038.

[338] Thode, H. G. and Monster, J. "Sulfur-isotope geochemistry of petroleum, evaporites, and ancient seas." In: 71 (1965), pp. 367–377. URL: http://archives.datapages.com/data/specpubs/methodo2/data/a071/a071/0001/0350/0367.htm (visited on 04/06/2018).

[339] Tjoelker, M. G., Oleksyn, J., and Reich, P. B. "Modelling respiration of vegetation: Evidence for a general temperature-dependent Q_{10}." In: *Global Change Biology* 7.2 (Feb. 1, 2001), pp. 223–230. ISSN: 1365-2486. DOI: 10.1046/j.1365-2486.2001.00397.x. URL: https://onlinelibrary.wiley.com/doi/abs/10.1046/j.1365-2486.2001.00397.x (visited on 12/02/2018).

[340] Tomašových, A. and Zuschin, M. "Variation in brachiopod preservation along a carbonate shelf-basin transect (Red Sea and Gulf of Aden): Environmental sensitivity of taphofacies." In: *PALAIOS* 24.10 (Oct. 1, 2009). Publisher: GeoScienceWorld, pp. 697–716. ISSN: 0883-1351. DOI: 10.2110/palo.2009.p09-018r. URL: http://pubs.geoscienceworld.org/sepm/palaios/article/24/10/697/146026/Variation-in-brachiopod-preservation-along-a (visited on 09/16/2020).

[341] Torres, M. A. et al. "Glacial weathering, sulfide oxidation, and global carbon cycle feedbacks." In: *Proceedings of the National Academy of Sciences* 114.33 (Aug. 15, 2017), pp. 8716–8721. ISSN: 0027-8424, 1091-6490. DOI: 10.1073/pnas.1702953114. URL: https://www.pnas.org/content/114/33/8716 (visited on 12/18/2019).

[342] Tostevin, R. et al. "Multiple sulfur isotope constraints on the modern sulfur cycle." In: *Earth and Planetary Science Letters* 396.0 (2014), pp. 14–21. ISSN: 0012-821X. DOI: 10.1016/j.epsl.2014.03.057. URL: http://www.sciencedirect.com/science/article/pii/S0012821X1400209X%20http://ac.els-cdn.com/S0012821X1400209X/1-s2.0-S0012821X1400209X-main.pdf?_tid=df7a2150-8ae6-11e4-bbf0-00000aab0f01&acdnat=1419368672_7edf368fd7843474b99fb40219b21b71.

[343] Tromp, T. K., Van Cappellen, P., and Key, R. M. "A global model for the early diagenesis of organic carbon and organic phosphorus in marine sediments." In: *Geochimica et Cosmochimica Acta* 59.7 (Apr. 1, 1995), pp. 1259–1284. ISSN: 0016-7037. DOI: 10.1016/0016-7037(95)00042-X. URL: http://www.sciencedirect.com/science/article/pii/001670379500042X (visited on 10/08/2018).

[344] Turchyn, A. V. and Schrag, D. P. “Oxygen isotope constraints on the sulfur cycle over the past 10 million years.” In: *Science* 303.5666 (Mar. 26, 2004), pp. 2004–2007. DOI: 10.1126/science.1092296. URL: http://www.sciencemag.org/content/303/5666/2004.abstract%20http://www.sciencemag.org/content/303/5666/2004.full.pdf.

[345] Ushikubo, T. et al. “Development of in situ sulfur four-isotope analysis with multiple Faraday cup detectors by SIMS and application to pyrite grains in a Paleoproterozoic glaciogenic sandstone.” In: *Chemical Geology* 383 (Sept. 15, 2014), pp. 86–99. ISSN: 0009-2541. DOI: 10.1016/j.chemgeo.2014.06.006. URL: http://www.sciencedirect.com/science/article/pii/S0009254114002885 (visited on 03/18/2020).

[346] Van Heuven, S. et al. “MATLAB program developed for CO2 system calculations.” In: *ORNL/CDIAC-105b. Carbon Dioxide Information Analysis Center, Oak Ridge National Laboratory, US Department of Energy, Oak Ridge, Tennessee* 530 (2011). DOI: 10.3334/CDIAC/otg.CO2SYS_MATLAB_v1.1.

[347] Veizer, J., Holser, W. T., and Wilgus, C. K. “Correlation of 13C12C and 34S32S secular variations.” In: *Geochimica et Cosmochimica Acta* 44.4 (Apr. 1, 1980), pp. 579–587. ISSN: 0016-7037. DOI: 10.1016/0016-7037(80)90250-1. URL: http://www.sciencedirect.com/science/article/pii/0016703780902501 (visited on 06/21/2018).

[348] Veizer, J. et al. “87Sr/86Sr, δ^{13}C and δ^{18}O evolution of Phanerozoic seawater.” In: *Chemical Geology* 161.1 (1999), pp. 59–88. ISSN: 0009-2541. DOI: 10.1016/S0009-2541(99)00081-9. URL: http://www.sciencedirect.com/science/article/pii/S0009254199000819%20http://ac.els-cdn.com/S0009254199000819/1-s2.0-S0009254199000819-main.pdf?_tid=f34ad454-06c7-11e7-9b9c-00000aab0f6b&acdnat=1489284330_cb94ac447705fe02e9551f9b475ef970.

[349] Vinogradov, A. P., Grinenko, V. A., and Ustinov, V. I. “Isotopic composition of sulfur compounds in the Black Sea.” In: *Geochemistry* 10 (1962), pp. 973–997.

[350] Vogel, H. “The law of the relation between the viscosity of liquids and the temperature.” In: *Phys. Z* 22 (1921), pp. 645–646.

[351] Waldeck, A. R. et al. “Using triple oxygen isotopes to test Cretaceous/Cenozoic LIP activity as a driver of the marine sulfur cycle.” In: *AGU Fall Meeting Abstracts* 24 (Dec. 1, 2019). URL: http://adsabs.harvard.edu/abs/2019AGUFM.V24A..07W (visited on 08/30/2020).

[352] Waldron, J. W. F. et al. “Evaporite tectonics and the late Paleozoic stratigraphic development of the Cumberland basin, Appalachians of Atlantic Canada.” In: *GSA Bulletin* 125.5 (May 1, 2013), pp. 945–960. ISSN: 0016-7606. DOI: 10.1130/B30718.1. URL: https://pubs.geoscienceworld.org/gsa/gsabulletin/article/125/5-6/945/125936/evaporite-tectonics-and-the-late-paleozoic (visited on 09/30/2019).

[353] Walker, J. C. G. “Global geochemical cycles of carbon, sulfur and oxygen.” In: *Marine Geology* 70.1 (Feb. 1, 1986), pp. 159–174. ISSN: 0025-3227. DOI: 10.1016/0025-3227(86)90093-9. URL: http://www.sciencedirect.com/science/article/pii/0025322786900939.

[354] Werne, J. P. et al. “Reduced sulfur in euxinic sediments of the Cariaco Basin: Sulfur isotope constraints on organic sulfur formation.” In: *Chemical Geology* 195.1 (2003), pp. 159–179. ISSN: 0009-2541. DOI: 10.1016/S0009-2541(02)00393-5. URL: http://www.sciencedirect.com/science/article/pii/S0009254102003935%20http://ac.els-cdn.com/S0009254102003935/1-s2.0-S0009254102003935-main.pdf?_tid=071c3316-6943-11e5-8b78-00000aab0f01&acdnat=1443817410_bf45e8114ba80b8aec067d7b8d5837c5.

[355] Werne, J. P. et al. “Organic sulfur biogeochemistry: Recent advances and future research directions.” In: *Geological Society of America Special Papers* 379 (Jan. 1, 2004), pp. 135–150. DOI: 10.1130/0-8137-2379-5.135. URL: http://specialpapers.gsapubs.org/content/379/135.abstract%20http://specialpapers.gsapubs.org/content/379/135.

[356] Werne, J. P. et al. “Investigating pathways of diagenetic organic matter sulfurization using compound-specific sulfur isotope analysis.” In: *Geochimica et Cosmochimica Acta* 72.14 (July 15, 2008), pp. 3489–3502. ISSN: 0016-7037. DOI: 10.1016/j.gca.2008.04.033. URL: http://www.sciencedirect.com/science/article/pii/S0016703708002494 (visited on 04/15/2020).

[357] Westrich, J. and Berner, R. A. “The role of sedimentary organic matter in bacterial sulfate reduction: The G model tested.” In: *Limnology and oceanography* 29.2 (1984), pp. 236–249. ISSN: 0024-3590. URL: http://sfx.caltech.edu:8088/caltech?sid=google&auinit=JT&aulast=Westrich&atitle=The%20role%20of%20sedimentary%20organic%20matter%20in%20bacterial%20sulfate%20reduction%3A%20The%20G%20model%20tested.&id=doi%3A10.4319%2Flo.1984.29.2.0236&title=Limnology%20and%20oceanography&volume=29&issue=2&date=1984&spage=236&issn=0024-3590.

[358] Wheat, C. G. and Mottl, M. J. “Composition of pore and spring waters from Baby Bare: Global implications of geochemical fluxes from a ridge flank hydrothermal system.” In: *Geochimica et Cosmochimica Acta* 64.4 (Feb. 1, 2000), pp. 629–642. ISSN: 0016-7037. DOI: 10.1016/S0016-7037(99)00347-6. URL: http://www.sciencedirect.com/science/article/pii/S0016703799003476 (visited on 09/05/2020).

[359] Wignall, P. B. and Hallam, A. “Anoxia as a cause of the Permian/Triassic mass extinction: Facies evidence from northern Italy and the western United States.” In: *Palaeogeography, Palaeoclimatology, Palaeoecology* 93.1 (May 1, 1992), pp. 21–46. ISSN: 0031-0182. DOI: 10.1016/0031-0182(92)90182-5. URL: http://www.sciencedirect.com/science/article/pii/0031018292901825 (visited on 08/14/2020).

[360] Wignall, P. B. and Hallam, A. “Griesbachian (Earliest Triassic) palaeoenvironmental changes in the Salt Range, Pakistan and southeast China and their bearing on the Permo-Triassic mass extinction.” In: *Palaeogeography, Palaeoclimatology, Palaeoecology* 102.3 (June 1, 1993), pp. 215–237. ISSN: 0031-0182. DOI: 10.1016/0031-0182(93)90068-T. URL: http://www.sciencedirect.com/science/article/pii/003101829390068T (visited on 08/14/2020).

[361] Wignall, P. B. and Twitchett, R. J. “Oceanic anoxia and the end Permian mass extinction.” In: *Science* 272.5265 (May 24, 1996), pp. 1155–1158. ISSN: 0036-8075, 1095-9203. DOI: 10.1126/science.272.5265.1155. URL: http://science.sciencemag.org/content/272/5265/1155 (visited on 09/28/2018).

[362] Wijsman, J. W. M. et al. “A model for early diagenetic processes in sediments of the continental shelf of the Black Sea.” In: *Estuarine, Coastal and Shelf Science* 54.3 (Mar. 1, 2002), pp. 403–421. ISSN: 0272-7714. DOI: 10.1006/ecss.2000.0655. URL: http://www.sciencedirect.com/science/article/pii/S0272771400906553 (visited on 10/09/2019).

[363] Wijsman, J. W. M. et al. “Sulfur and iron speciation in surface sediments along the northwestern margin of the Black Sea.” In: *Marine Chemistry* 74.4 (June 1, 2001), pp. 261–278. ISSN: 0304-4203. DOI: 10.1016/S0304-4203(01)00019-6. URL: http://www.sciencedirect.com/science/article/pii/S0304420301000196 (visited on 03/21/2020).

[364] Wilmot, N. V. and Fallick, A. E. “Original mineralogy of trilobite exoskeletons.” In: *Palaeontology* 32.2 (1989), p. 297. ISSN: 0031-0239. URL: http://sfx.caltech.edu:8088/caltech?sid=google&

auinit=NV&aulast=Wilmot&atitle=Original%20mineralogy%20of%20trilobite%20exoskeletons&title=Palaeontology&volume=32&issue=2&date=1989&spage=297&issn=0031-0239.

[365] Wing, B. A. and Halevy, I. "Intracellular metabolite levels shape sulfur isotope fractionation during microbial sulfate respiration." In: *Proceedings of the National Academy of Sciences* (Oct. 31, 2014). DOI: 10.1073/pnas.1407502111. URL: http://www.pnas.org/content/early/2014/10/30/1407502111.abstract%20http://www.pnas.org/content/early/2014/10/30/1407502111%20http://www.pnas.org/content/111/51/18116.full.pdf.

[366] Worden, R. H., Smalley, P. C., and Fallick, A. E. "Sulfur cycle in buried evaporites." In: *Geology* 25.7 (July 1, 1997), pp. 643–646. ISSN: 0091-7613. DOI: 10.1130/0091-7613(1997)025<0643:SCIBE>2.3.CO;2. URL: https://pubs.geoscienceworld.org/gsa/geology/article/25/7/643/206711/sulfur-cycle-in-buried-evaporites (visited on 09/16/2018).

[367] Wotte, T., Shields-Zhou, G. A., and Strauss, H. "Carbonate-associated sulfate: Experimental comparisons of common extraction methods and recommendations toward a standard analytical protocol." In: *Chemical Geology* 326–327.0 (), pp. 132–144. ISSN: 0009-2541. DOI: 10.1016/j.chemgeo.2012.07.020. URL: http://www.sciencedirect.com/science/article/pii/S0009254112003269%20http://ac.els-cdn.com/S0009254112003269/1-s2.0-S0009254112003269-main.pdf?_tid=60517476-3dc7-11e4-be24-00000aab0f6b&acdnat=1410888905_e2152b3f9651541e5251a1d952930151.

[368] Wu, N. "Sulfur isotopic evolution of Phanerozoic and Ediacaran seawater sulfate." PhD thesis. 2013. URL: https://drum.lib.umd.edu/handle/1903/14016.

[369] Wu, N., Farquhar, J., and Strauss, H. "$\delta^{34}S$ and $\delta^{33}S$ records of Paleozoic seawater sulfate based on the analysis of carbonate associated sulfate." In: *Earth and Planetary Science Letters* 399.0 (2014), pp. 44–51. ISSN: 0012-821X. DOI: 10.1016/j.epsl.2014.05.004. URL: http://www.sciencedirect.com/science/article/pii/S0012821X14002982%20http://ac.els-cdn.com/S0012821X14002982/1-s2.0-S0012821X14002982-main.pdf?_tid=6d478bf2-4862-11e4-93e0-00000aab0f02&acdnat=1412055010_09a8c5edee21707f00ec160e8807a516.

[370] Xiang, L. et al. "Oceanic redox evolution across the end-Permian mass extinction at Shangsi, South China." In: *Palaeogeography, Palaeoclimatology, Palaeoecology*. Ecosystem evolution in deep time:

evidence from the rich Palaeozoic fossil records of China 448 (Apr. 15, 2016), pp. 59–71. ISSN: 0031-0182. DOI: 10.1016/j.palaeo.2015.10.046. URL: http://www.sciencedirect.com/science/article/pii/S0031018215006082 (visited on 08/13/2020).

[371] Zak, I., Sakai, H., and Kaplan, I. R. "Factors controlling the 18O/16O and 34S/32S isotope ratios of ocean sulfates, evaporites and interstitial sulfates from modern deep sea sediments." In: *Isotope marine chemistry* (1980), pp. 339–373.

[372] Zhang, X.-Y. et al. "Polybessurus-like fossils as key contributors to Permian–Triassic boundary microbialites in South China." In: *Palaeogeography, Palaeoclimatology, Palaeoecology* 552 (Aug. 15, 2020), p. 109770. ISSN: 0031-0182. DOI: 10.1016/j.palaeo.2020.109770. URL: http://www.sciencedirect.com/science/article/pii/S0031018220302157 (visited on 08/16/2020).

[373] Zheng, Q., Cao, C., and Zhang, M. "Sedimentary features of the Permian-Triassic boundary sequence of the Meishan section in Changxing County, Zhejiang Province." In: *Science China Earth Sciences* 56.6 (June 1, 2013), pp. 956–969. ISSN: 1869-1897. DOI: 10.1007/s11430-013-4602-9. URL: https://doi.org/10.1007/s11430-013-4602-9 (visited on 08/16/2020).

[374] Zubarev, R. A. and Makarov, A. "Orbitrap mass spectrometry." In: *Analytical Chemistry* 85.11 (June 4, 2013). Publisher: American Chemical Society, pp. 5288–5296. ISSN: 0003-2700. DOI: 10.1021/ac4001223. URL: https://doi.org/10.1021/ac4001223 (visited on 08/07/2020).

Appendix A

SUPPLEMENTARY MATERIAL FOR CHAPTER II

A.1 Sample Localities

Brachiopod specimens for this study were collected from the sampling regions described below. Additional details on the localities may be found in previous studies [102, 120, 121, 122, 123, 223, 224, 225, 226, 287].

The US Midcontinent samples were collected predominantly from shales and argillaceous (clay-rich) limestones deposited in several areas, including north-central Texas [121]; near Kansas City in Kansas and Missouri [120]; north-central New Mexico [120]; and Nebraska, Oklahoma, Iowa, Illinois, and Indiana [225]. These sediments were deposited on a broad carbonate shelf within epicontinental seas during the Carboniferous, with cyclothem-style deposition occurring during the later Carboniferous and early Permian [225]. Paleogeographic reconstructions suggest deposition near ∼10-15 degS paleolatitude during the earliest Carboniferous and gradual northward migration to ∼5 degN paleolatitude by 270 Ma [298].

Moscow Basin and the Ural Mountains are both part of the Russia Platform, a key area of Carboniferous sedimentation in western Russia [179]. Samples were collected from several different sections containing marine carbonate facies. Early Carboniferous samples come exclusively from Moscow Basin, whereas mid- to late Carboniferous samples were collected from both regions [226]. Fossil assemblages indicate deposition in shallow epicontinental seas [93] that were located at about 0 deg (Moscow Basin) and 10 degN (Ural Mountains) paleolatitude in the early Carboniferous. Plate movement gradually shifted the localities to ∼10 deg farther north at the end of the Carboniferous [298]. Arrow Canyon is located in southeastern Nevada and was the site of a carbonate platform on the western margin of Laurentia during the Carboniferous [30, 31]. Samples included in this study are Bashkirian in age [102] and were deposited near 5 degN paleolatitude [298].

Spitsbergen (formerly known as West Spitsbergen) is an island in northwestern Europe and featured deposition on a mixed siliciclastic-carbonate ramp during

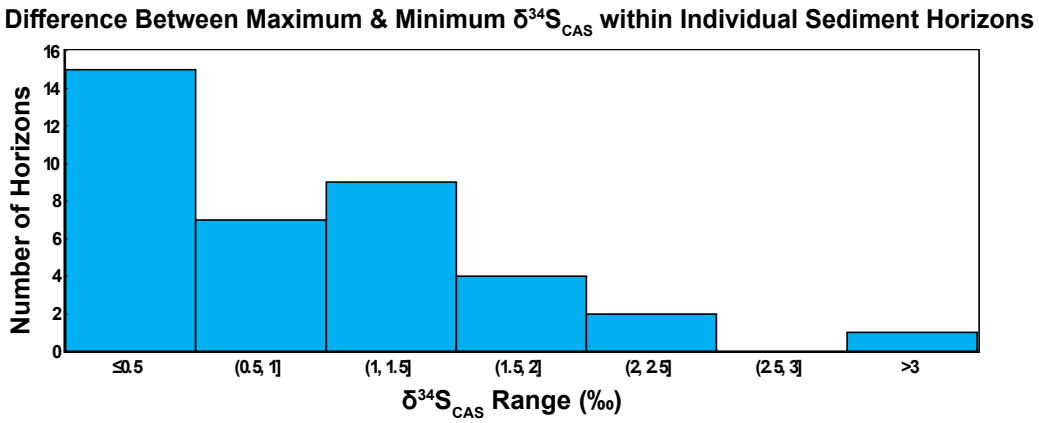

Figure A.1: Histogram of within-horizon $\delta^{34}S_{in}$ range for 39 different sediment horizons in which multiple brachiopod specimens were measured. Over half (22 of 39) of the horizons exhibit a range of $< 1‰$, and nearly all exhibit a range of $< 2‰$.

the mid- to late Permian [35]. Samples measured in this study were collected from the Kapp Starostin Formation and have been previously studied by both Gruszczynski et al. (1989) and Mii, Grossman, and Yancey (1997). Deposition occurred at approximately 45 degN paleolatitude [298].

A.2 Variability in CAS abundance

Variations in CAS abundance against age are plotted in Figure A.2. The overall range of CAS abundances within our data set exceeds two orders of magnitude, spanning from several hundred ppm to well over 10000 ppm. Specimens from the genera *Crurithyris* and *Eridmatus* exhibit very high (> 8000 ppm on average) CAS content (consistent with [122]); *Anthracospirifer*, *Kalitvella*, *Neospirifer*, *Spirifer*, *Spiriferella*, and *Syringothyris* have high abundances (> 4000 ppm on average); and most other genera (including *Composita*, *Choristites*, and *Cleiothyridina*) have intermediate to low CAS abundances (< 4000 ppm on average). Although there is an increase in the frequency of specimens with very high CAS abundance between 325 and 300 Ma, much of this variation is associated with changes in the taxa being measured rather than increases in CAS abundance within individual taxa over time. There is no obvious temporal trend in abundance within our data.

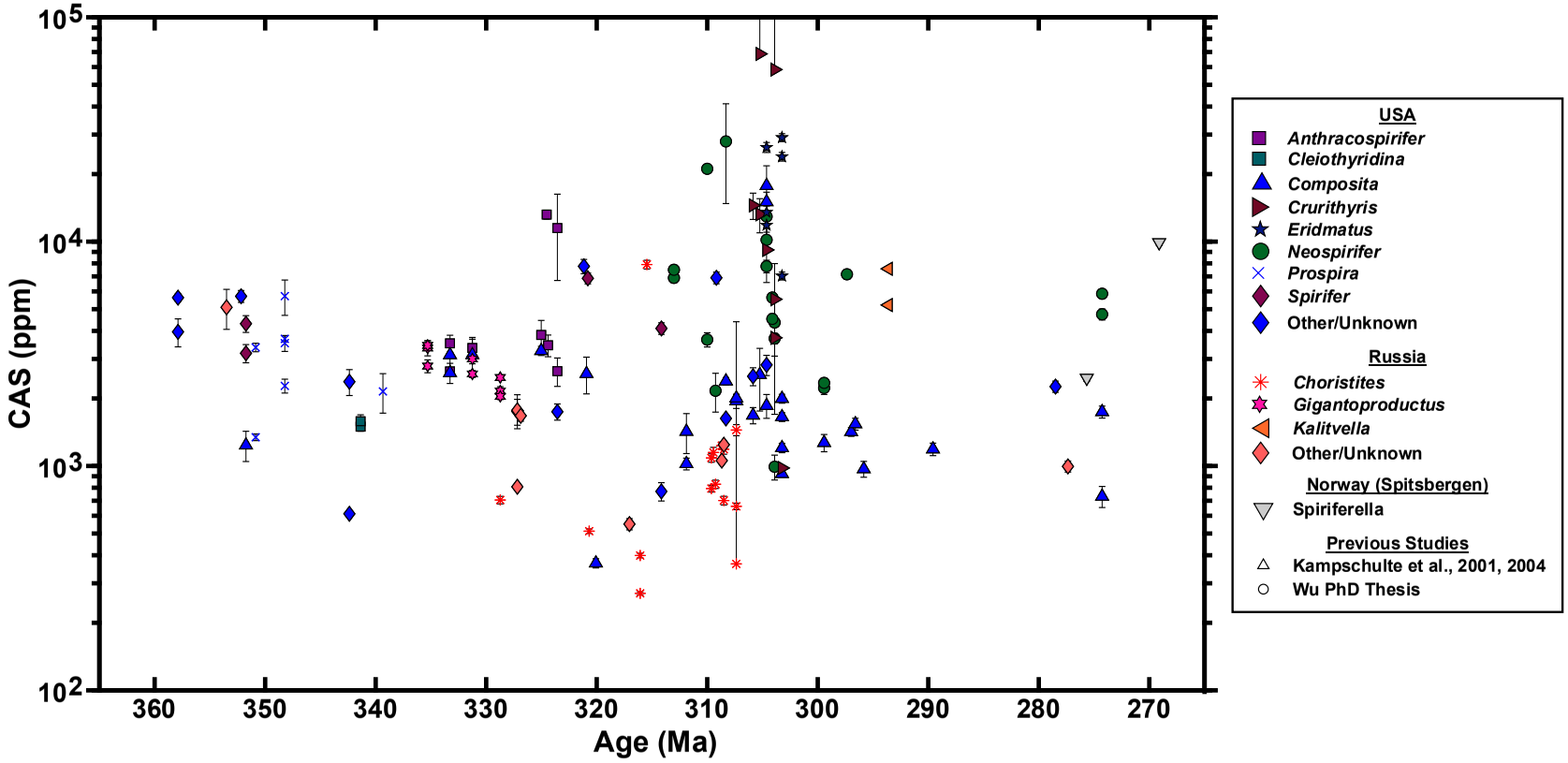

Figure A.2: Brachiopod CAS abundance plotted against age for all unaltered samples. CAS abundance exhibits little to no temporal trend, but displays substantial variation associated with taxonomic diversity. Error bars denote 1σ standard error. Measurements exceeding 40000 ppm are likely erroneous due to anomalous errors associated with measurement of relatively small (< 0.5 mg) sample masses.

A.3 Spline Fitting of Isotopic Data

To determine 95% confidence intervals for our $\delta^{34}S_{in}$ record, we fit a restricted cubic spline with 17 knots to our data using the MATLAB® function rcspline (available at `https://www.mathworks.com/matlabcentral/fileexchange/41241-restricted-cubic-spline`). Knots were chronologically placed at every eighth data point beginning with the oldest $\delta^{34}S_{in}$ age point (357.9 Ma) and continuing to an age of 269.11 Ma. Empirically, this number of knots was found to adequately capture the curvature in the data without dramatically overfitting the data. Confidence intervals were calculated with 100,000 bootstrap samples at 0.1 Myr time increments between the minimum age and the maximum age represented in our $\delta^{34}S_{in}$ data. The maximum span between minimum and maximum 95% confidence interval (CI) bounds for the $\delta^{34}S_{in}$ spline is 3.63‰, with 76.1% of the 0.1 Myr time steps (i.e., 676 of 888) having a span < 2‰ and 92.8% (824 of 888) having a span < 2.5‰. These numbers are further improved if the relatively data-poor time interval after 303 Ma is excluded: 83.2% of the 0.1 Myr time steps (i.e., 457 of 549) have a span < 2‰ and 94.2% (517 of 549) have a span < 2.5‰. We used the same knots and confidence interval time increments in generating restricted cubic splines for the $\delta^{13}C_{carb}$, $\delta^{18}O_{carb}$, and $\frac{^{87}Sr}{^{86}Sr}$ records.

We can also compare pairs of $\delta^{34}S_{in}$ measurements within each horizon to the combined standard error expected based on the standard errors for individual measurements (e.g. [155]). This statistic, termed the "Error Normalized Deviate (END)" by John and Adkins (2010), should be normally distributed with a standard deviation of one if all variability in a population of measurements can be attributed to the variance associated with individual measurements. We calculate ENDs for pairs of specimens within individual horizons, taking care to use each $\delta^{34}S_{in}$ in only one END calculation, except when an odd number of specimens in a horizon required one $\delta^{34}S_{in}$ measurement to be used twice. Among all pairs of measured specimens within individual horizons, the standard deviation of the END is 7.8; i.e., the variability within the population of measurements in each horizon is, on average, over seven times larger than that expected from the variance of each individual measurement. Exclusion of two horizons with abnormally large (> 20) ENDs lowers this standard deviation to 5.9. Given an average error of 0.11‰ associated with individual measurements, the END standard deviation suggests a 68% probability that a given horizon will

constrain $\delta^{34}S_{in}$ to within 0.86‰ and a 95% probability that it will constrain $\delta^{34}S_{in}$ to within 1.72‰.

Comparison among pairs of measurements from only the same taxon demonstrates that a portion of the observed variability is associated with taxonomic differences. The standard deviation of the END population decreases to 5.2 if only same taxon pairs are considered and increases to 10.7 (or 7.1 excluding the two abnormally large ENDs) if only pairs of measurements from different taxa are considered. Exclusion of *Composita subtilita* and the two >20 END pairs from the population lowers the standard deviation from 5.9 to 5.3, supporting the existence of a $\delta^{34}S_{in}$ offset associated with this species. Further efforts to constrain and correct for taxon-associated $\delta^{34}S_{in}$ offsets may thus enable additional improvement in the precision of temporal $\delta^{34}S_{in}$ records generated from brachiopods.

A.4 Effects of mixing brachiopod powders on the Kampschulte et al. (2001) $\delta^{34}S_{in}$ data

A case can be made for diagenetic alteration of $\delta^{34}S_{in}$ in some of Kampschulte, Bruckschen, and Strauss's (2001) samples. Three of the four samples measured by this study and Kampschulte, Bruckschen, and Strauss involved single brachiopods and differed by < 0.2‰. However, two *Cleiothyridina obmaxima* specimens (MO041 and MO001), combined by Kampschulte, Bruckschen, and Strauss (2001) to yield a $\delta^{34}S_{in}$ of $\sim$+16‰, have substantially different $\delta^{34}S_{in}$. MO044 had a value of +13.77‰, whereas MO001 yielded a value of +18.34‰. Visual inspection of MO001 revealed that the area we drilled included some cloudy shell, leading us to exclude this point from our dataset. Since this cloudy shell was drilled adjacent to the area measured by Kampschulte, Bruckschen, and Strauss (2001), we suspect that the Kampschulte, Bruckschen, and Strauss (2001) sample from this shell is also compromised. A replicate sample drilled from an optically transparent portion of the shell yielded a $\delta^{34}S_{in}$ of +14.08‰, similar to the value for MO044. If similarly altered samples are present among the specimens used to generate 13 additional Kampschulte, Bruckschen, and Strauss (2001) data points utilizing multiple brachiopods, the corresponding data points are likely to be inaccurate. We note that six of these 13 additional data points are within 5 Myr of the Serpukhovian-Bashkirian boundary, potentially accounting for the absence of a sharp increase in $\delta^{34}S_{in}$ in the Kampschulte,

Bruckschen, and Strauss (2001) record.

A.5 Geographic variability in $\delta^{34}S_{in}$

Was geographic variability responsible for some of the variation in $\delta^{34}S_{in}$ values between our study and that of Wu (2013)? The majority of Wu's samples were collected in Central Europe, whereas our samples and those of Kampschulte, Bruckschen, and Strauss (2001) were collected mostly from North America and Russia (Figure A.3). There are few intervals of time in which both Wu and our study measured samples collected from the same geographic region. Russian samples dating to ∼345-335 Ma and ∼315-290 Ma were measured in both studies. A comparatively large amount of $\delta^{34}S_{in}$ variability exists in the Wu data compared with both our data and those of Kampschulte, Bruckschen, and Strauss (2001) among the Russian samples in these two time intervals, suggesting that the greater variability in the Wu data may indeed be related to preservation screening methods. The limited (n = 5) $\delta^{34}S_{in}$ data from European samples (excluding Russian samples) reported by Kampschulte, Bruckschen, and Strauss (2001) also show signs of higher variability, but these samples come from the same collection and were screened for preservation using the same methods as the Wu (2013) samples. We thus favor a diagenetic origin for the variability over other explanations.

A.6 The global nature and veracity of the Serpukhovian-Bashkirian $\delta^{34}S_{in}$ increase

The area encompassing eastern Oklahoma and northwest Arkansas is the only area from which we have been able to measure specimens immediately before and soon after the Serpukhovian-Bashkirian boundary collected from sections within ∼100 miles of each other. However, paleogeographic reconstructions (e.g., [298]) suggest that other localities in southwestern Illinois were deposited within the same contiguous water mass. Similarly, Serpukhovian specimens from the Moscow Basin and Bashkirian specimens from the Ural Mountains also have been placed within the same contiguous water mass in paleogeographic reconstructions (e.g.,[298]). We cannot conclusively rule out local depositional effects on the data from each locality, but the presence of an excursion of similar magnitude in two disparate geographic basins suggests that a global sulfur cycle perturbation is the most parsimonious explanation for the

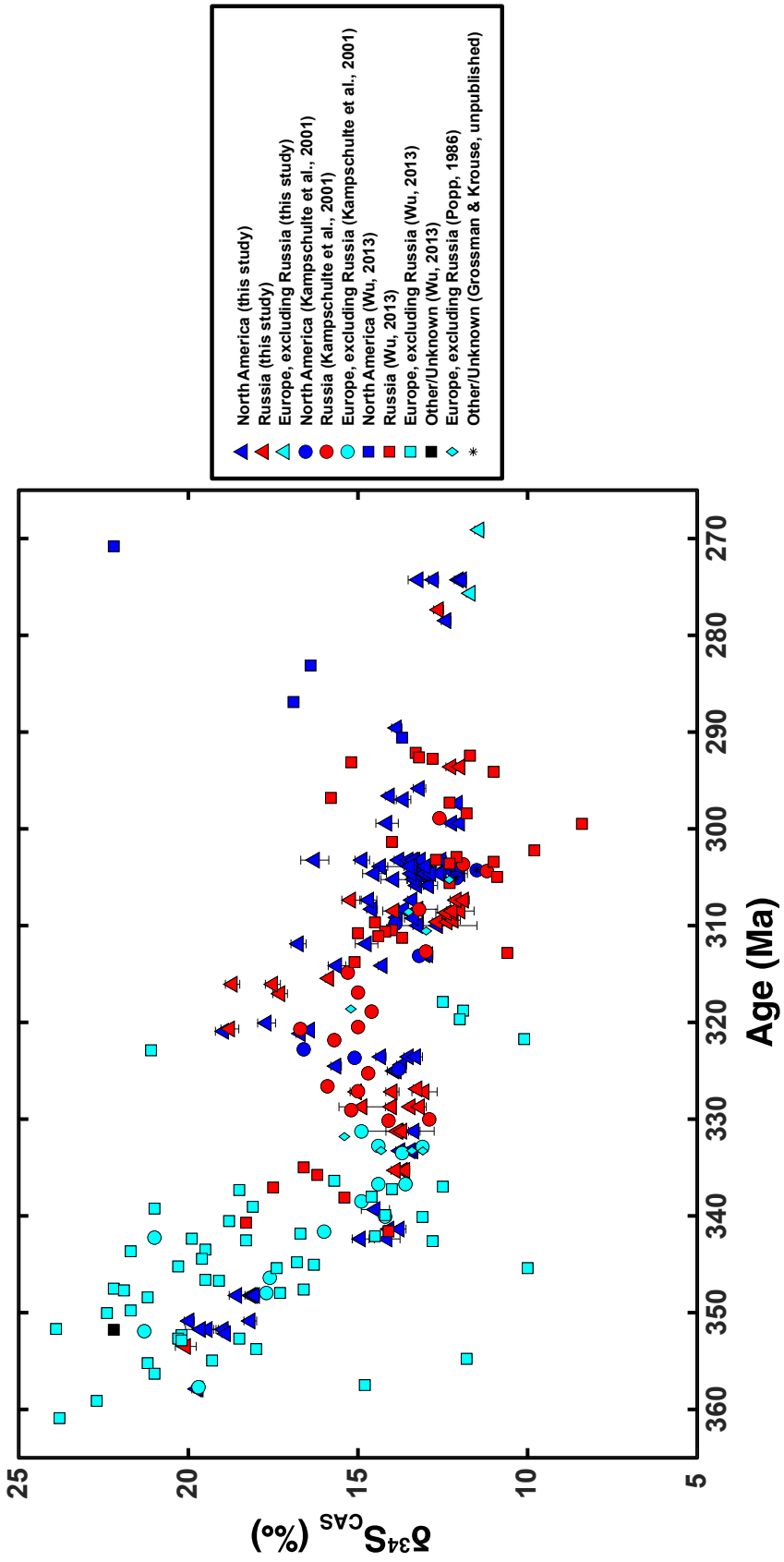

Figure A.3: Plot of $\delta^{34}S_{in}$ against age (Ma). Data point colors denote continent, while shapes denote study.

signal.

A.7 Box modeling

A.7.1 Model details

The change in the size of a reservoir, M, with time, t, is equal to the difference between the net input fluxes (F_in) and output fluxes (F_out) associated with the reservoir:

$$\frac{dM}{dt} = F_{in} - F_{out} \tag{A.1}$$

Treating sulfur (^{32}S, ^{34}S) and carbon (^{12}C, ^{13}C) isotopes independently within our model's reservoirs yields six mass balance equations for each element and thirteen mass balance equations overall when a surficial O_2 reservoir is added. We list each of these mass balance equations, initial conditions, and constant parameter values for the model in Tables A.3, A.4, and A.5. The output flux for each element is partitioned into oxidized and reduced fluxes. Carbonate burial (F_{carb}) and organic carbon burial (F_{org}) represent oxidized and reduced output fluxes (respectively) of carbon from the ocean. For sulfur, evaporite deposition (F_{evap}) is the oxidized output flux and a combined term for pyrite and organic sulfur deposition ($F_{py/org}$) represents the reduced output flux.

Assuming a constant input of carbon to the ocean ($F_{C,in}$) and a steady-state carbon cycle, we calculate F_{carb} at each model time step by solving the following isotope mass balance equation:

$$F_{carb} = F_{C,in} * \left(1 + \frac{\delta^{13}\mathrm{C_{in}} - \delta^{13}\mathrm{C_{carb}}}{\delta^{13}\mathrm{C}}\right) \tag{A.2}$$

where δ^{13}C is the δ^{13}C offset between carbonate and organic carbon. This equation also assumes that the δ^{13}C of carbonate, $\delta^{13}\mathrm{C_{carb}}$, closely approximates the δ^{13}C of contemporaneous seawater. We obtain $\delta^{13}\mathrm{C_{carb}}$ values by fitting a smoothing spline to the data of Grossman et al. (2008) and interpolating spline values to model time points (Figure II.5B). F_{org} at each time step in the model is then calculated by subtracting F_{carb} from $F_{C,in}$ to maintain a concentration steady-state:

$$F_{org} = F_{riv} - F_{carb} \tag{A.3}$$

Table A.1: CAS abundance and $\delta^{34}S$ data.

Sample ID	Alternate Sample ID	GTS2020 Age (Ma)	Period	Stage	Country	Location	Taxon	Reference	CAS (ppm)	Error (1σ)	$\delta^{34}S$ (‰)	Error (1σ)
ILL124-b-1		358.3	Carboniferous	Tournaisian	USA	US Midcontinent (Illinois)	Other/Unknown	[225]	5627	216	19.70	0.07
ILL129-1		358.3	Carboniferous	Tournaisian	USA	US Midcontinent (Illinois)	Other/Unknown	[225]	3961	565	19.75	0.07
RU097-1		353.7	Carboniferous	Tournaisian	Russia	Moscow Basin	Other/Unknown	[226]	5095	1031	20.08	0.15
IA190-1		352.4	Carboniferous	Tournaisian	USA	US Midcontinent (Iowa)	Other/Unknown	[225]	5708	348	18.90	0.06
IA162-1		351.9	Carboniferous	Tournaisian	USA	US Midcontinent (Iowa)	*Spirifer*	[225]	3180	296	18.96	0.08
IA168		351.9	Carboniferous	Tournaisian	USA	US Midcontinent (Iowa)	*Spirifer*	[225]	4308	370	19.43	0.09
IA173-1		351.9	Carboniferous	Tournaisian	USA	US Midcontinent (Iowa)	*Composita*	[225]	1237	191	19.64	0.23
IA112-1		351.0	Carboniferous	Tournaisian	USA	US Midcontinent (Iowa)	*Prospira*	[225]	1343	46	18.17	0.09
IA114		351.0	Carboniferous	Tournaisian	USA	US Midcontinent (Iowa)	*Prospira*	[225]	3377	148	19.97	0.07
MO068-1		348.3	Carboniferous	Tournaisian	USA	US Midcontinent (Missouri)	*Prospira*	[225]	2276	162	18.56	0.12
MO070		348.3	Carboniferous	Tournaisian	USA	US Midcontinent (Missouri)	*Prospira*	[225]	5718	1025	18.15	0.21
MO071		348.3	Carboniferous	Tournaisian	USA	US Midcontinent (Missouri)	*Prospira*	[225]	3528	288	18.11	0.08
MO077		348.3	Carboniferous	Tournaisian	USA	US Midcontinent (Missouri)	*Prospira*	[225]	3687	118	18.04	0.07
IND016-1		342.4	Carboniferous	Visean	USA	US Midcontinent (Indiana)	Other/Unknown	[225]	2375	314	14.92	0.12
IND027-a-1		342.4	Carboniferous	Visean	USA	US Midcontinent (Indiana)	Other/Unknown	[225]	612	18	14.14	0.19
MO001-1		341.4	Carboniferous	Visean	USA	US Midcontinent (Missouri)	*Cleiothyridina*	[225]	1497	69	14.08	0.06
MO044-1		341.4	Carboniferous	Visean	USA	US Midcontinent (Missouri)	*Cleiothyridina*	[225]	1582	109	13.77	0.09
ILL097-1		339.3	Carboniferous	Visean	USA	US Midcontinent (Illinois)	*Prospira*	[225]	2150	430	14.49	0.21
RU228-a-c		335.3	Carboniferous	Visean	Russia	Moscow Basin	*Gigantoproductus*	[226]	3356	260	13.68	0.07
RU229		335.3	Carboniferous	Visean	Russia	Moscow Basin	*Gigantoproductus*	[226]	3447	171	13.61	0.07
RU230		335.3	Carboniferous	Visean	Russia	Moscow Basin	*Gigantoproductus*	[226]	2787	184	13.89	0.07
IA022		333.3	Carboniferous	Visean	USA	US Midcontinent (Iowa)	*Anthracospirifer*	[225]	3520	306	13.37	0.14
IA032-1		333.3	Carboniferous	Visean	USA	US Midcontinent (Iowa)	*Composita*	[225]	2600	268	13.76	0.07
IA034		333.3	Carboniferous	Visean	USA	US Midcontinent (Iowa)	*Composita*	[225]	3125	471	13.39	0.07
IA086		333.3	Carboniferous	Visean	USA	US Midcontinent (Iowa)	*Anthracospirifer*	[225]	2639	93	13.45	0.06
ILL067		331.3	Carboniferous	Visean	USA	US Midcontinent (Illinois)	*Anthracospirifer*	[225]	3357	384	13.34	0.08
ILL074-1		331.3	Carboniferous	Visean	USA	US Midcontinent (Illinois)	*Composita*	[225]	3127	547	13.81	0.18

Sample ID	Alternate Sample ID	GTS2020 Age (Ma)	Period	Stage	Country	Location	Taxon	Reference	CAS (ppm)	Error (1σ)	$\delta^{34}S$ (‰)	Error (1σ)
RU237		331.3	Carboniferous	Visean	Russia	Moscow Basin	*Gigantoproductus*	[226]	2572	93	13.84	0.54
RU238-1,2		331.3	Carboniferous	Visean	Russia	Moscow Basin	*Gigantoproductus*	[226]	2999	144	13.70	0.06
RU065-1		328.4	Carboniferous	Serpukhovian	Russia	Moscow Basin	*Gigantoproductus*	[226]	2159	98	13.45	0.05
RU066-a,b		328.4	Carboniferous	Serpukhovian	Russia	Moscow Basin	*Gigantoproductus*	[226]	2479	59	14.01	0.05
RU068-1,2		328.4	Carboniferous	Serpukhovian	Russia	Moscow Basin	*Gigantoproductus*	[226]	2044	67	13.18	0.09
RU242-1		328.4	Carboniferous	Serpukhovian	Russia	Moscow Basin	*Choristites*	[226]	705	27	14.88	0.34
RU001-1-3		327.0	Carboniferous	Serpukhovian	Russia	Moscow Basin	Other/Unknown	[226]	808	22	13.99	0.10
RU014-1		327.0	Carboniferous	Serpukhovian	Russia	Moscow Basin	Other/Unknown	[226]	1751	232	13.04	0.19
RU026-b-1		327.0	Carboniferous	Serpukhovian	Russia	Moscow Basin	Other/Unknown	[226]	1772	306	15.04	0.10
RU048-1,2		326.7	Carboniferous	Serpukhovian	Russia	Moscow Basin	Other/Unknown	[226]	1674	91	13.25	0.06
ILL036-1		325.0	Carboniferous	Serpukhovian	USA	US Midcontinent (Illinois)	*Anthracospirifer*	[225]	3837	618	13.93	0.10
ILL041-1		325.0	Carboniferous	Serpukhovian	USA	US Midcontinent (Illinois)	*Composita*	[225]	3261	153	13.87	0.05
849		324.6	Carboniferous	Serpukhovian	USA	US Midcontinent (Oklahoma)	*Anthracospirifer*	[123]	13203	605	15.64	0.08
ILL020		324.5	Carboniferous	Serpukhovian	USA	US Midcontinent (Illinois)	*Anthracospirifer*	[225]	3451	383	13.71	0.07
WP58 AS-2		323.7	Carboniferous	Serpukhovian	USA	US Midcontinent (Illinois)	*Anthracospirifer*	[102]	11493	4782	13.50	0.07
WP58 Inf-2		323.7	Carboniferous	Serpukhovian	USA	US Midcontinent (Illinois)	Other/Unknown	[102]	1745	145	14.32	0.08
WP58A AS-1	WP58A Anth-1	323.7	Carboniferous	Serpukhovian	USA	US Midcontinent (Illinois)	*Anthracospirifer*	[102]	2646	383	13.29	0.10
A99 S-1		321.3	Carboniferous	Bashkirian	USA	Arrow Canyon	Other/Unknown	[102]	7763	566	16.69	0.06
OK029-1		321.1	Carboniferous	Bashkirian	USA	US Midcontinent (Oklahoma)	*Composita*	[225]	2576	480	18.95	0.12
OK012-1		320.9	Carboniferous	Bashkirian	USA	US Midcontinent (Oklahoma)	*Spirifer*	[225]	6863	381	16.42	0.06
RU124-1,2		320.8	Carboniferous	Bashkirian	Russia	Ural Mountains	*Choristites*	[226]	512	12	18.78	0.13
813		320.2	Carboniferous	Bashkirian	USA	US Midcontinent (Arkansas)	*Composita*	[123]	369	17	17.69	0.13
RU129-1		317.1	Carboniferous	Bashkirian	Russia	Ural Mountains	Other/Unknown	[226]	551	32	17.29	0.11
RU133-1		316.1	Carboniferous	Bashkirian	Russia	Ural Mountains	*Choristites*	[226]	271	5	18.70	0.11
RU134-1		316.1	Carboniferous	Bashkirian	Russia	Ural Mountains	*Choristites*	[226]	399	9	17.51	0.11
RU131-1		315.5	Carboniferous	Bashkirian	Russia	Ural Mountains	*Choristites*	[226]	7906	351	15.86	0.05
A247 P		314.2	Carboniferous	Moscovian	USA	Arrow Canyon	Other/Unknown	[102]	770	72	15.62	0.13
802		314.1	Carboniferous	Moscovian	USA	US Midcontinent (Illinois)	*Spirifer*	[123]	4103	244	14.28	0.06

Sample ID	Alternate Sample ID	GTS2020 Age (Ma)	Period	Stage	Country	Location	Taxon	Reference	CAS (ppm)	Error (1σ)	δ^{34}S (‰)	Error (1σ)
TXD033-a-1		313.0	Carboniferous	Moscovian	USA	US Midcontinent (Texas)	*Neospirifer*	[225]	6894	327	13.02	0.11
TXD034-a-1		313.0	Carboniferous	Moscovian	USA	US Midcontinent (Texas)	*Neospirifer*	[225]	7490	356	12.94	0.07
TXD022-1		311.9	Carboniferous	Moscovian	USA	US Midcontinent (Texas)	*Composita*	[225]	1022	62	16.75	0.11
TXD029-1		311.9	Carboniferous	Moscovian	USA	US Midcontinent (Texas)	*Composita*	[225]	1424	288	14.75	0.17
TXD009-1		310.0	Carboniferous	Moscovian	USA	US Midcontinent (Texas)	*Neospirifer*	[225]	21115	728	13.22	0.08
TXD013		310.0	Carboniferous	Moscovian	USA	US Midcontinent (Texas)	*Neospirifer*	[225]	3658	266	12.65	0.58
RU144-1,2		309.6	Carboniferous	Moscovian	Russia	Moscow Basin	*Choristites*	[226]	1086	47	12.66	0.08
RU146-1		309.6	Carboniferous	Moscovian	Russia	Moscow Basin	*Choristites*	[226]	793	28	12.36	0.06
RU153-a-1		309.4	Carboniferous	Moscovian	Russia	Moscow Basin	*Choristites*	[226]	1149	62	12.19	0.10
RU141-1		309.2	Carboniferous	Moscovian	Russia	Moscow Basin	*Choristites*	[226]	829	35	12.28	0.09
X198		309.2	Carboniferous	Moscovian	USA	US Midcontinent (Oklahoma)	*Neospirifer*	[225]	2164	426	13.35	0.14
A353 S-2		309.2	Carboniferous	Moscovian	USA	Arrow Canyon	Other/Unknown	[102]	6901	413	13.85	0.08
RU154-1,2		308.7	Carboniferous	Moscovian	Russia	Moscow Basin	Other/Unknown	[226]	1057	37	12.22	0.06
RU156-1		308.7	Carboniferous	Moscovian	Russia	Moscow Basin	*Choristites*	[226]	1232	46	12.39	0.16
RU165-1,2		308.5	Carboniferous	Moscovian	Russia	Moscow Basin	*Choristites*	[226]	702	31	11.99	0.20
									644	32	12.15	0.10
									571	21	11.88	0.11
RU166-1		308.5	Carboniferous	Moscovian	Russia	Moscow Basin	*Choristites*	[226]	1187	59	12.21	0.08
RU169-1		308.5	Carboniferous	Moscovian	Russia	Moscow Basin	Other/Unknown	[226]	1244	36	13.93	0.17
TXD001		308.3	Carboniferous	Moscovian	USA	US Midcontinent (Texas)	*Neospirifer*	[225]			13.23	0.29
TXD005		308.3	Carboniferous	Moscovian	USA	US Midcontinent (Texas)	Other/Unknown	[123]	1629	64	13.64	0.07
TXD006-1		308.3	Carboniferous	Moscovian	USA	US Midcontinent (Texas)	*Composita*	[123]	2388	90	14.58	0.08
RU176-1		307.4	Carboniferous	Moscovian	Russia	Ural Mountains	*Choristites*	[226]	366	4029	15.21	0.13
RU207-1,2		307.4	Carboniferous	Moscovian	Russia	Moscow Basin	*Choristites*	[226]	1446	82	12.10	0.09
RU208-1,2		307.4	Carboniferous	Moscovian	Russia	Moscow Basin	*Choristites*	[226]	661	22	11.88	0.08
Y85		307.4	Carboniferous	Moscovian	USA	US Midcontinent (Iowa)	*Composita*	[225]	1946	142	14.68	0.12

Sample ID	Alternate Sample ID	GTS2020 Age (Ma)	Period	Stage	Country	Location	Taxon	Reference	CAS (ppm)	Error (1σ)	$\delta^{34}S$ (‰)	Error (1σ)
Y86-1		307.4	Carboniferous	Moscovian	USA	US Midcontinent (Iowa)	*Composita*	[225]	2005	78	13.40	0.07
L.S. -3.8m marg A		305.9	Carboniferous	Kasimovian	USA	US Midcontinent (Texas)	Other/Unknown	[120]	2509	231	13.26	0.09
TLS01	L.S. -3.8m crur A	305.9	Carboniferous	Kasimovian	USA	US Midcontinent (Texas)	*Crurithyris*	[120]	14502	1943	12.92	0.07
TLS05	L.S. -3.8m comp B	305.9	Carboniferous	Kasimovian	USA	US Midcontinent (Texas)	*Composita*	[120]	1681	140	12.91	0.13
KCH05	K090PF	305.2	Carboniferous	Kasimovian	USA	US Midcontinent (Kansas)	*Composita*	[225]	2551	793	13.93	0.20
KCH07	K092F	305.2	Carboniferous	Kasimovian	USA	US Midcontinent (Kansas)	*Crurithyris*	[123]	13243	2296	12.91	0.06
KCH08	K093F	305.2	Carboniferous	Kasimovian	USA	US Midcontinent (Kansas)	*Crurithyris*	[123]			13.34	0.11
KSN17	K039P/AP	304.6	Carboniferous	Kasimovian	USA	US Midcontinent (Kansas)	*Composita*	[120]	1857	226	14.51	0.18
KSN18	K042P	304.6	Carboniferous	Kasimovian	USA	US Midcontinent (Kansas)	*Neospirifer*	[120]	12938	1924	12.54	0.06
									9337	1218	12.60	0.09
									8181	537	12.53	0.05
KSN19	K043P	304.6	Carboniferous	Kasimovian	USA	US Midcontinent (Kansas)	*Neospirifer*	[120]	7761	500	12.60	0.08
									8061	585	12.44	0.06
									13770	581	12.61	0.07
KSN20	K044P	304.6	Carboniferous	Kasimovian	USA	US Midcontinent (Kansas)	*Neospirifer*	[120]	10181	482	12.99	0.07
TUW034	TX_UW55, UW 50-60 Composita B	304.6	Carboniferous	Kasimovian	USA	US Midcontinent (Texas)	*Composita*	[121]	15025	1584	13.24	0.06
TUW035	TX_UW55, UW 50-60 Composita D	304.6	Carboniferous	Kasimovian	USA	US Midcontinent (Texas)	*Composita*	[121]	17747	4029	13.42	0.08
TUW049	TX_UW35, UW 30-40 spiri A	304.6	Carboniferous	Kasimovian	USA	US Midcontinent (Texas)	*Eridmatus*	[121]	26315	1352	13.10	0.08
TUW050	TX_UW35, UW 30-40 spiri C	304.6	Carboniferous	Kasimovian	USA	US Midcontinent (Texas)	*Eridmatus*	[121]	13512	894	12.93	0.07
TUW066	TX_UW13, UW 9-16 Crurithyris A	304.6	Carboniferous	Kasimovian	USA	US Midcontinent (Texas)	*Crurithyris*	[121]	9186	2613	13.02	0.07
TUW074	TX_UW13, UW 9-16 spiri C	304.6	Carboniferous	Kasimovian	USA	US Midcontinent (Texas)	*Eridmatus*	[121]	11848	1197	12.85	0.10
TX_UW35, 30-40 Derb		304.6	Carboniferous	Kasimovian	USA	US Midcontinent (Texas)	Other/Unknown	[121]	2821	292	11.99	0.11
KOR16	K016P/PA	304.1	Carboniferous	Kasimovian	USA	US Midcontinent (Kansas)	*Neospirifer*	[120]	5633	257	12.39	0.06
TFS20	F.S. 0.0 neo A	304.1	Carboniferous	Kasimovian	USA	US Midcontinent (Texas)	*Neospirifer*	[121]	4523	242	12.12	0.07
AMA 3-05		303.9	Carboniferous	Kasimovian	USA	US Midcontinent (Ohio)	*Crurithyris*	[102]	5535	2447	14.33	0.10
TFF3		303.9	Carboniferous	Kasimovian	USA	US Midcontinent (Ohio)	*Neospirifer*	[102]	4360	173	12.02	0.06
WP50 NS-3		303.9	Carboniferous	Kasimovian	USA	US Midcontinent (West Virginia)	*Neospirifer*	[102]	992	126	13.40	0.12
WP53 Cr-2		303.9	Carboniferous	Kasimovian	USA	US Midcontinent (West Virginia)	*Crurithyris*	[102]	3727	2028	13.47	0.39
WP53 NS-2		303.9	Carboniferous	Kasimovian	USA	US Midcontinent (West Virginia)	*Neospirifer*	[102]	3702	198	12.08	0.07

Sample ID	Alternate Sample ID	GTS2020 Age (Ma)	Period	Stage	Country	Location	Taxon	Reference	CAS (ppm)	Error (1σ)	δ^{34}S (‰)	Error (1σ)
WP62 Cr-2		303.9	Carboniferous	Kasimovian	USA	US Midcontinent (Illinois)	*Crurithyris*	[102]			13.01	0.09
TWS37	W.F. 0.7 comp B	303.2	Carboniferous	Gzhelian	USA	US Midcontinent (Texas)	*Composita*	[121]	1204	58	14.87	0.11
TWS38	W.F. 0.7 comp C	303.2	Carboniferous	Gzhelian	USA	US Midcontinent (Texas)	*Composita*	[121]	1654	75	16.27	0.21
TWS41	W.F. 0.5 crur C	303.2	Carboniferous	Gzhelian	USA	US Midcontinent (Texas)	*Crurithyris*	[121]	979	0	12.55	0.08
TWS42	W.F. 0.5 comp A	303.2	Carboniferous	Gzhelian	USA	US Midcontinent (Texas)	*Composita*	[121]	923	0	13.79	0.07
TWS43	W.F. 0.5 comp B	303.2	Carboniferous	Gzhelian	USA	US Midcontinent (Texas)	*Composita*	[121]	1996	91	13.52	0.09
TWS45	W.F. 0.5 erid A	303.2	Carboniferous	Gzhelian	USA	US Midcontinent (Texas)	*Eridmatus*	[121]	23917	1065	13.32	0.11
TWS46	W.F. 0.5 erid B	303.2	Carboniferous	Gzhelian	USA	US Midcontinent (Texas)	*Eridmatus*	[121]	29097	1182	13.38	0.07
TWS47	W.F. 0.5 erid C	303.2	Carboniferous	Gzhelian	USA	US Midcontinent (Texas)	*Eridmatus*	[120]	7030	284	13.15	0.06
TXP033		299.4	Carboniferous	Gzhelian	USA	US Midcontinent (Texas)	*Neospirifer*	[123]	2227	144	12.23	0.09
TXP038		299.4	Carboniferous	Gzhelian	USA	US Midcontinent (Texas)	*Composita*	[123]	1269	112	14.14	0.17
TXP044		299.4	Carboniferous	Gzhelian	USA	US Midcontinent (Texas)	*Neospirifer*	[123]	2346	112	12.00	0.05
RAK38-1		296.4	Permian	Asselian	Russia	Ural Mountains	*Kalitvella*	[123]	612	18	18.47	0.16
TXP018		296.4	Permian	Asselian	USA	US Midcontinent (Texas)	*Neospirifer*	[123]	7152	350	12.06	0.07
TXP012		294.0	Permian	Asselian	USA	US Midcontinent (Texas)	*Composita*	[123]	1419	64	13.66	0.11
TXP052		295.2	Permian	Asselian	USA	US Midcontinent (Texas)	*Composita*	[123]	1538	94	14.07	0.06
TXP023		294.0	Permian	Asselian	USA	US Midcontinent (Texas)	*Composita*	[123]	970	79	13.19	0.09
RST27-1		292.4	Permian	Sakmarian	Russia	Ural Mountains	*Kalitvella*	[123]	7569	131	12.25	0.08
RST29-1		292.4	Permian	Sakmarian	Russia	Ural Mountains	*Kalitvella*	[123]	5217	134	11.99	0.06
TXP065		290.1	Permian	Sakmarian	USA	US Midcontinent (Texas)	*Composita*	[123]	1188	76	13.86	0.08
TXP077		282.3	Permian	Kungurian	USA	US Midcontinent (Texas)	Other/Unknown	[123]	2259	130	12.40	0.07
SS6-96-12		280.8	Permian	Kungarian	Russia	Ural Mountains	Other/Unknown	[123]	996	56	12.62	0.07
WSV640-b-1		278.7	Permian	Kungurian	Norway	Spitsbergen	*Spiriferella*	[224]	2467	86	11.68	0.06
TXP001		276.9	Permian	Kungurian	USA	US Midcontinent (Texas)	*Composita*	[123]	1742	107	12.77	0.07
TXP003		276.9	Permian	Kungurian	USA	US Midcontinent (Texas)	*Composita*	[123]	732	79	13.22	0.15
TXP006		276.9	Permian	Kungurian	USA	US Midcontinent (Texas)	*Neospirifer*	[123]	5858	263	12.03	0.06
TXP007		276.9	Permian	Kungurian	USA	US Midcontinent (Texas)	*Neospirifer*	[123]	4743	269	11.94	0.07
J002-a-1		269.7	Permian	Ufimian	Norway	Spitsbergen	*Spiriferella*	[224]	9911	324	11.43	0.07

Table A.2: Additional CAS abundance and $\delta^{34}S$ data for samples with noted evidence of alteration or with outlying $\delta^{34}S$ values.

Sample ID	Alternate Sample ID	GTS2020 Age (Ma)	Period	Stage	Country	Location	Taxon	Reference	CAS (ppm)	Error (1σ)	$\delta^{34}S$ (‰)	Error (1σ)
IA140-1		350.9	Carboniferous	Kinderhookian	USA	US Midcontinent (Iowa)	*Composita*	Mii et al. (1999)	3867	207	20.84	0.06
IND001-a-1		342.4	Carboniferous	Osagian	USA	US Midcontinent (Indiana)	*Composita*	Mii et al. (1999)			15.50	0.08
ILL091		339.3	Carboniferous	Meramecian	USA	US Midcontinent (Illinois)	*Prospira*	Mii et al. (1999)	9771	413	14.83	0.06
ILL065		331.3	Carboniferous	Chesterian	USA	US Midcontinent (Illinois)	*Anthracospirifer*	Mii et al. (1999)	5412	392	13.56	0.07
RU241-1		328.7	Carboniferous	Visean	Russia	Moscow Basin	*Choristites*	Mii et al., 2001	1219	117	13.52	0.12
847		324.5	Carboniferous	Chesterian	USA	US Midcontinent (Oklahoma)	*Composita*	Grossman et al. (2008)	1715	56	13.79	0.05
AC-2	*NV-001*	323.6	Carboniferous	Chesterian	USA	Arrow Canyon	*Composita*	Jones et al. 2003; Flake, 2011	1305	162	17.24	0.25
AC-3	*NV-003*	323.6	Carboniferous	Chesterian	USA	Arrow Canyon	*Anthracospirifer*	Jones et al. 2003; Flake, 2011	4650	693	15.43	0.13
AC-4a	*NV-006*	323.6	Carboniferous	Chesterian	USA	Arrow Canyon	*Other/Unknown*	Jones et al. 2003; Flake, 2011	1870	131	16.86	0.11
WP58A AS-1 (MATRIX)	*WP58A Anth-1 (MATRIX)*	323.6	Carboniferous	Chesterian	USA	US Midcontinent (Illinois)	*Matrix*	Flake, 2011			11.28	0.10
A96 CO-2 (MATRIX)		321.3	Carboniferous	Bashkirian	USA	Arrow Canyon	*Matrix*	Flake, 2011	1124	33	22.95	0.21
812		320.1	Carboniferous	Morrowan	USA	US Midcontinent (Arkansas)	*Spirifer*	Grossman et al. (2008)	2030	242	14.64	0.21
RU127		316.8	Carboniferous	Bashkirian	Russia	Ural Mountains	*Choristites*	Mii et al., 2001	335	9	18.96	0.62
TXD022-1 (MATRIX)		311.9	Carboniferous	Moscovian	USA	US Midcontinent (Texas)	*Matrix*	Mii et al. (1999)	355	20	9.35	0.14
RU153 (MATRIX)		309.4	Carboniferous	Moscovian	Russia	Moscow Basin	*Matrix*	Mii et al., 2001	528	16	12.54	0.08
RU163-1		308.5	Carboniferous	Moscovian	Russia	Moscow Basin	*Choristites*	Mii et al., 2001	1389	55	11.97	0.10
TUW050 (replicate)	*TX_UW35, UW 30-40 spiri C*	304.6	Carboniferous	Missourian	USA	US Midcontinent (Texas)	*Eridmatus*	Grossman et al. (1991)	2883	288	3.82	0.07
WP62a KL-1		303.9	Carboniferous	Virgilian	USA	US Midcontinent (Illinois)	*Other/Unknown*	Flake, 2011	1970	182	5.53	0.23
RAK38-1		297.4	Permian	Asselian	Russia	Ural Mountains	*Kalitvella*	Grossman et al. (2008)	612	18	18.47	0.16
WSV640-b-1 (replicate)		275.7	Permian	Kungurian	Norway	Spitsbergen	*Spiriferella*	Mii et al. (1997)	3250	300	12.52	0.06

Table A.3: Box model parameter values and variable definitions.

Parameter	Value (when held constant)	Units	Description	Reference / Notes
V_{ocean}	1.38×10^{18}	m^3	Volume of the ocean	
$F_{C,in}$	1.5×10^{12}	$\frac{mol}{yr}$	S flux into the ocean	
$F_{S,in}$	1.5×10^{12}	m^3	S flux into the ocean	Similar to value of [191]; lowered slightly to yield F_{evap} values more consistent with the global estimates of [126]
f_{OWOM}	0.192	Unitless	Fraction of C flux into the ocean attributable to the oxidative weathering of organic matter (OWOM)	Calculated assuming an initial condition of isotopic steady state
f_{OWOP}	0.457	Unitless	Fraction of S flux into the ocean attributable to the oxidative weathering of pyrite (OWP)	Calculated using reservoir $\delta^{34}S$ values of [107] to produce an initial steady state S cycle; approximately equals Burke et al. 2018 best estimate of modern f_{OWOP}
$\delta^{13}C_{in}$	-4.4	‰	$\delta^{13}C$ of the C flux into the ocean	[107]
$\delta^{34}S_{in}$	4	‰	$\delta^{34}S$ of the S flux into the ocean	Within error of modern value of [52]
$\delta^{13}C$	30	‰	Isotopic offset between carbonate C (enriched in ^{13}C) and organic C (depleted in ^{13}C) fluxes out of the ocean	[136]
$\Delta\delta^{34}S$	35	‰	Isotopic offset between evaporite S (enriched in ^{34}S) and pyrite/organic (depleted in ^{34}S) fluxes out of the ocean	Calculated assuming an initial condition of isotopic steady state; similar to estimates of [195, 369]
F_{carb}	-	$\frac{mol}{yr}$	Carbonate C flux out of the ocean	Calculated assuming isotopic steady state based on the carbonate $\delta^{13}C$ curve of [123]
F_{evap}	1.09×10^{12}	$\frac{mol}{yr}$	Evaporite S flux out of the ocean	Calculated assuming an initial condition of isotopic steady state
F_{org}	-	$\frac{mol}{yr}$	Organic C flux out of the ocean	Calculated assuming isotopic steady state based on the carbonate $\delta^{13}C$ curve of [123]
$F_{py/org}$	-	$\frac{mol}{yr}$	Pyrite/organic S flux out of the ocean	Calculated from F_{org} using $R_{C:S}$
$R_{C:S}$	3.0	$\frac{wt}{wt}$	Organic C to pyrite S burial ratio (by weight)	Approximate normal marine value of [27]

Table A.4: Box model equations.

Equation	Description	Reference / Notes
$\frac{d[^{12}C]_{ocean}}{dt} = \frac{F_{C,in} - F_{org} - F_{carb}}{V_{ocean}}$	Isotopic mass balance for ^{12}C in the ocean reservoir	
$\frac{d[^{13}C]_{ocean}}{dt} = \frac{F_{C,in} * \left(\frac{\delta^{13}C_{in}}{1000}+1\right) * {}^{13}R_{VPDB} - F_{org} * \left(\frac{\Delta\delta^{13}C}{1000}+1\right) * \frac{[^{13}C]_{ocean}}{[^{12}C]_{ocean}} - F_{evap} * \frac{[^{13}C]_{ocean}}{[^{12}C]_{ocean}}}{V_{ocean}}$	Isotopic mass balance for ^{13}C in the ocean reservoir	
$\frac{d[^{12}C]_{geo-carb}}{dt} = F_{carb} - (1 - f_{OWOM}) * F_{C,in}$	Isotopic mass balance for ^{12}C in the geologic carbonate reservoir	
$\frac{d[^{13}C]_{geo-carb}}{dt} = F_{carb} * \frac{[^{13}C]_{ocean}}{[^{12}C]_{ocean}} - (1 - f_{OWOM}) * F_{C,in} * \frac{[^{13}C]_{geo-carb}}{[^{12}C]_{geo-carb}}$	Isotopic mass balance for ^{13}C in the geologic carbonate reservoir	
$\frac{d[^{12}C]_{geo-org}}{dt} = F_{org} - f_{OWOM} * F_{C,in}$	Isotopic mass balance for ^{12}C in the geologic organic carbon reservoir	
$\frac{d[^{13}C]_{geo-org}}{dt} = F_{org} * \frac{[^{13}C]_{ocean}}{[^{12}C]_{ocean}} * (\frac{\Delta\delta^{13}C}{1000} + 1) - f_{OWOM} * F_{C,in} * \frac{[^{13}C]_{geo-org}}{[^{12}C]_{geo-org}}$	Isotopic mass balance for ^{13}C in the geologic organic carbon reservoir	
$\frac{d[^{32}S]_{ocean}}{dt} = \frac{F_{S,in} - F_{py/org} - F_{evap}}{V_{ocean}}$	Isotopic mass balance for ^{32}S in the ocean reservoir	
$\frac{d[^{34}S]_{ocean}}{dt} = \frac{F_{S,in} * \left(\frac{\delta^{34}S_{in}}{1000}+1\right) * {}^{34}R_{VCDT} - F_{py/org} * \left(\frac{\Delta\delta^{34}S}{1000}+1\right) * \frac{[^{34}S]_{ocean}}{[^{32}S]_{ocean}} - F_{evap} * \frac{[^{34}S]_{ocean}}{[^{32}S]_{ocean}}}{V_{ocean}}$	Isotopic mass balance for ^{34}S in the ocean reservoir	
$\frac{d[^{32}S]_{geo-evap}}{dt} = F_{evap} - (1 - f_{OWP}) * F_{S,in}$	Isotopic mass balance for ^{32}S in the geologic evaporite reservoir	
$\frac{d[^{34}S]_{geo-evap}}{dt} = F_{evap} * \frac{[^{34}S]_{ocean}}{[^{32}S]_{ocean}} - (1 - f_{OWP}) * F_{S,in} * \frac{[^{34}S]_{geo-evap}}{[^{32}S]_{geo-evap}}$	Isotopic mass balance for ^{34}S in the geologic evaporite reservoir	
$\frac{d[^{32}S]_{geo-py/org}}{dt} = F_{py/org} - f_{OWP} * F_{S,in}$	Isotopic mass balance for ^{32}S in the geologic pyrite + organic sulfur reservoir	
$\frac{d[^{34}S]_{geo-py/org}}{dt} = F_{py/org} * \frac{[^{34}S]_{ocean}}{[^{32}S]_{ocean}} * (\frac{\Delta\delta^{34}S}{1000} + 1) - f_{OWP} * F_{S,in} * \frac{[^{34}S]_{geo-py/org}}{[^{32}S]_{geo-py/org}}$	Isotopic mass balance for ^{34}S in the geologic pyrite + organic sulfur reservoir	
$\frac{dO_2}{dt} = \left(\frac{d^{12}C_{org}}{dt} + \frac{d^{13}C_{org}}{dt}\right) + \frac{15}{16} * \left(\frac{d^{32}S_{py/org}}{dt} + \frac{d^{34}S_{py/org}}{dt}\right)$	Estimated mass balance for O_2 assuming no net Fe redox transitions	[26, 191]

Table A.5: Box model initial conditions (at 335 Ma).

Parameter	Value	Units	Description	Reference / Notes
$C_{geo-carb}$	5.2 x 10^{21}	moles C	Initial size of the geologic carbonate C reservoir	[107]
$C_{geo-org}$	1.3 x 10^{21}	moles C	Initial size of the geologic organic C reservoir	[107]
$S_{geo-evap}$	1.08 x 10^{20}	moles S	Initial size of the geologic evaporite S reservoir	[107]
$S_{geo-py/org}$	1.78 x 10^{20}	moles S	Initial size of the geologic pyrite/organic S reservoir	[107]
$\delta^{13}C_{geo-carb}$	0.5	‰	Initial $\delta^{13}C$ of the geologic carbonate C reservoir	Approximated from [107]
$\delta^{13}C_{geo-org}$	-25	‰	Initial $\delta^{13}C$ of the geologic organic C reservoir	Approximated from [107]
$\delta^{34}S_{geo-evap}$	20	‰	Initial $\delta^{34}S$ of the geologic evaporite S reservoir	Approximated from [107]
$\delta^{34}S_{geo-py/org}$	-15	‰	Initial $\delta^{34}S$ of the geologic pyrite/organic S reservoir	Approximated from [107]
$[C]_{ocean}$	2200	$\frac{mol}{m^3}$	Initial concentration of C in ocean	
$\delta^{13}C_{ocean}$	2.2	‰	Initial $\delta^{13}C$ of the ocean C reservoir	Estimated from carbonate $\delta^{13}C$ curve of [123]
$\delta^{34}S_{ocean}$	13.6	‰	Initial $\delta^{34}S$ of the ocean S reservoir	Estimated from smoothing spline through $\delta^{34}S_{in}$ data from this study
O_2	3.79 x 10^{19}	moles chO2	Initial size of the surface O_2 reservoir	

The carbon and sulfur cycles are coupled within the model via the reduced output fluxes. Berner and Raiswell (1983) noted a characteristic ratio of organic carbon to pyrite sulfur in modern marine sediments close to 3:1 by weight. Here, we force $F_{py/org}$ by imposing a constant burial ratio of organic carbon to pyrite sulfur, $R_{C:S}$, and calculating $F_{py/org}$ at each model time point from the corresponding F_{org} value:

$$F_{py/org} = \frac{F_{org}}{R_{C:S}} \tag{A.4}$$

$R_{C:S}$ is converted to a molar ratio using the molar masses of carbon and sulfur prior to the calculation to ensure unit agreement. $F_{py/org}$ for each isotope of sulfur is calculated assuming that this flux is offset from seawater sulfate in its $\delta^{34}S$ by an amount $\Delta\delta^{34}S$. This offset incorporates the combined effects of isotopic fractionation during sedimentary sulfur cycling (e.g. [125, 176, 365]) and the scavenging of a fraction of the isotopically-fractionated sulfide created through this cycling by iron [23, 271] and organic matter [274, 355] in sediments.

Initial conditions applied to the model have the potential to dramatically affect the model results. Based on relatively stable $\delta^{34}S$ values for the several Myr preceding the time of model initiation (335 Ma), we assume a sulfur cycle in isotopic steady-state at model initiation and calculate a series of possible initial condition parameter values for $\delta^{34}S$ and $\Delta\delta^{34}S$ given a $\delta^{13}C$ of 30‰ (Hayes et al., 1999), a $\delta^{13}C_{in}$ of -4.4‰ (estimated based on the values of Garrels and Lerman, 1981), and seawater $\delta^{34}S$ and $\delta^{13}C$ values matching those of smoothed splines through the $\delta^{13}C_{carb}$ and $\delta^{34}S_{in}$ time series at 335 Ma (+2.2‰ and +13.6‰, respectively). Exploring parameter values between -10‰ and +10‰ for $\delta^{34}S_{in}$ and values between 15‰ and 50‰ for $\Delta\delta^{34}S$, we choose an initial steady state with $\delta^{34}S$ = +4‰ and $\Delta\delta^{34}S$ = 35‰ such that the initial $R_{C:S}$ (3:1) was representative of normal marine deposition. The evaporite flux was set at a constant value (1.09 x $_{10}{}^{12}$ $\frac{\text{mol}}{\text{yr}}$) equal to the difference between the riverine input flux (1.5 x $_{10}{}^{12}$ $\frac{\text{mol}}{\text{yr}}$) and the pyrite sulfur burial flux imposed by this steady state. We note that results similar to those that follow may be obtained using a smaller initial $\Delta\delta^{34}S$ if a higher initial $\delta^{34}S$ and/or a lower initial $R_{C:S}$ are imposed to maintain a steady state initial condition.

Fluxes of O_2 to and from the Earth surface reservoir depend on changes in the burial rates of oxidized and reduced sedimentary materials. Here, we initialize the model with a surface O_2 reservoir size equal to the modern (~ 3.79 x 10^{19}

moles) and with geologic reservoir sizes from Garrels and Lerman (1981). Assuming that one mole of O_2 is produced per mole of organic carbon buried and $\frac{15}{16}$ moles of O_2 are produced per mole of pyrite sulfur buried, we estimate the change in the size of the O_2 reservoir at each time step as follows [26, 191]:

$$\frac{dO_2}{dt} = \frac{d^{12}C_{org}}{dt} + \frac{d^{13}C_{org}}{dt} + \frac{15}{16} * \frac{d^{32}S_{py/org}}{dt} + \frac{d^{34}S_{py/org}}{dt} \tag{A.5}$$

This calculation also assumes that the fractional contributions of the oxidized and reduced geologic reservoirs to the riverine input are invariant with time (i.e., changes in weathering exert zero net influence on the size of the O_2 reservoir). Changes in the lithologies exposed at Earth's surface or a potential feedback between O_2 reservoir size and oxidative weathering may render this assumption invalid. We operate under this assumption for simplicity given the uncertainties in these potential influences. The δ value for each reservoir M is calculated by taking a molar ratio of the isotopes within each reservoir and normalizing to the isotope ratio R of the appropriate isotopic standard (i.e., Vienna Canyon Diablo Troilite for sulfur and Vienna Pee Dee Belemnite for carbon):

$$\delta^{34}\mathrm{S}(‰) = \left(\frac{\frac{^{34}M}{^{32}M}}{^{34}R_{VCDT}} - 1\right) * 1000 \quad \delta^{13}\mathrm{C}(‰) = \left(\frac{\frac{^{13}M}{^{12}M}}{^{34}R_{VPDB}} - 1\right) * 1000 \tag{A.6}$$

To evaluate the quality of the match between each model $\delta^{34}S$ time series to our data, we fit a temporally continuous smoothing spline to our $\delta^{34}S_{in}$ time series and calculated the sum of squared differences between the spline $\delta^{34}S$ values and model $\delta^{34}S$ results interpolated to time points matching those of our $\delta^{34}S_{in}$ data between 335 Ma and 270 Ma. Fits with lower sums of the squared differences are considered better fits than those with higher sums. Although this approach biases our best fit model results toward time intervals with a higher frequency of data points per time, we accept this bias given the decreased uncertainty in seawater $\delta^{34}S$ that greater data density provides. Independent tests of fit schemes in which data were interpolated to (1) create a series with an equal number of points per time or (2) create a series with an equal number of points within 325–319 Ma and after 319 Ma yield similar best fit model results (Figure A.4). In what follows, we use these "sum of the squares" values as a guide toward the best model fits, but also consider the plausibility of the imposed parameter values in discussing whether the best quantitative model fits represent realistic behavior of the Earth system.

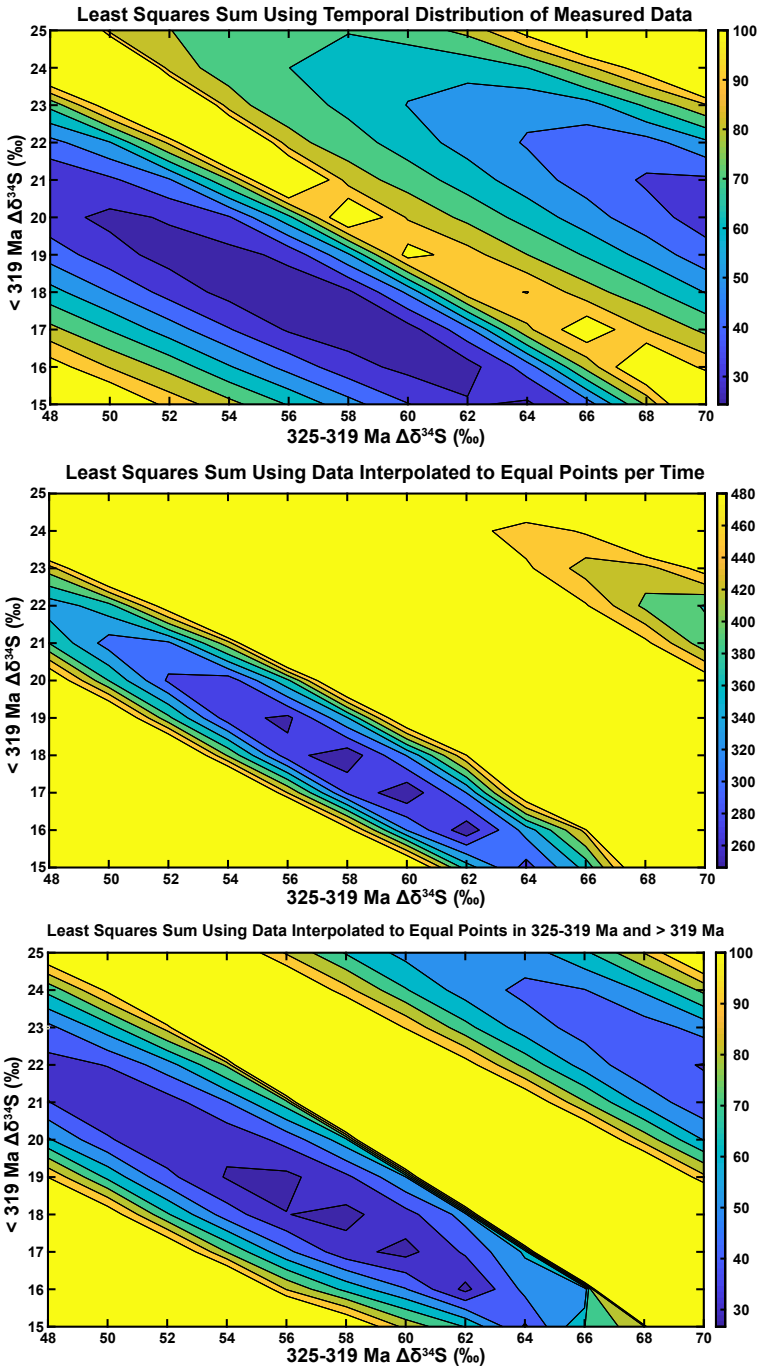

Figure A.4: Example contour plots of least square sum values using model-data pairs matching the temporal distribution of the measured data (top), model-data pairs with data interpolated to a set frequency of one per Myr (middle), and model-data pairs with data interpolated such that the 325-319 Ma and < 319 Ma intervals contain equal numbers of points (bottom). Plots pertain to a run in which only $\Delta\delta^{34}S$ was allowed to vary with time. Best fit parameter values do not shift dramatically with the fit scheme, suggesting that the magnitude of the changes necessary to best fit the data remains similar regardless of which scheme is used.

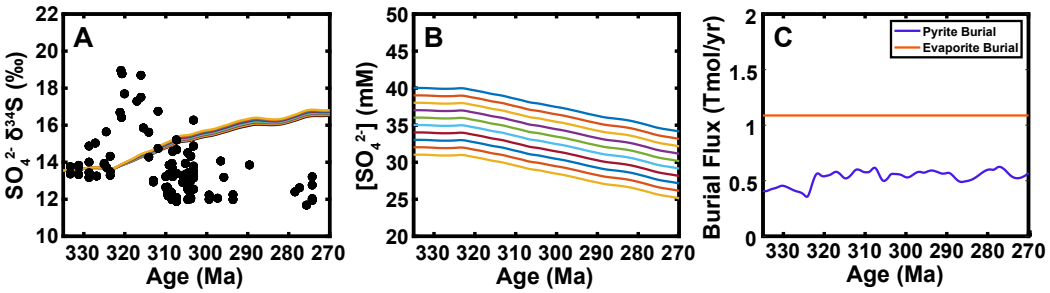

Figure A.5: Plots of (A) SO_4^{2-} $\delta^{34}S$, (B) $[SO_4^{2-}]$, and (C) pyrite and evaporite burial fluxes associated with constant parameter value model runs. Each colored line in the SO_4^{2-} $\delta^{34}S$ and $[SO_4^{2-}]$ plots represents a model run with a different initial $[SO_4^{2-}]$. Shown here are the best 10 model fits based on the sum of the squares fit.

A.7.2 Model run with constant parameter values

To provide an initial baseline, we run the model forward from its initial steady state at 335 Ma to an end point at the Permian-Triassic boundary (252.56 Ma) and let only the $\delta^{13}C_{carb}$-driven $F_{py/org}$ change with time (Figure A.5) with $R_{C:S}$ = 3. We also vary the initial seawater $[SO_4^{2-}]$. In all cases, seawater SO_4^{2-} $\delta^{34}S$ exhibits a large ($\sim$3.5‰) increase starting at $\sim$323 Ma that continues until reaching a plateau at $\sim$270 Ma. However, the increase occurs more gradually than the change indicated by the $\delta^{34}S_{in}$ data, and the model $\delta^{34}S$ fails to decrease back to a stable baseline during the late Carboniferous and early Permian. This behavior is driven by a large increase in pyrite burial imposed by high $\delta^{13}C_{carb}$ during the late Carboniferous and early Permian.

Imposing initial steady-states with higher, more terrestrial-like C:S burial ratios attenuates the $\delta^{34}S$ variations seen in the record and results in slightly better model-data fits. However, all runs ubiquitously fail to replicate our temporal $\delta^{34}S_{in}$ record. These results suggest that a temporal change in one or more model parameters is required to adequately fit the data. Berner and Raiswell (1983) invoked a massive increase in terrestrial organic matter burial to explain the carbon and sulfur isotopic records in this time interval. Based on this idea, we next explore the potential for temporal changes in $R_{C:S}$ to provide better model-data fits. We also test whether changes in $\delta^{34}S_{in}$ or $\Delta\delta^{34}S$ may replicate our data in lieu of changes in $R_{C:S}$.

A.7.3 Model runs with changes in single parameter values

Incorporating temporal changes in parameter values within our model requires an important decision regarding the timing and the magnitude of imposed changes. Here, we model the middle Carboniferous using two step-function changes in parameter values as a means of generating the observed $\delta^{34}S_{in}$ changes. We impose the first of these changes at 325 Ma, a time at which the carbonate $\delta^{13}C$, $\delta^{18}O$, and $\delta^{34}S$ records each show rapid increases and at which sea level begins an estimated $\sim$150 m decrease in association with peak Carboniferous glaciation [232, 291]. The second of these changes is invoked at 319 Ma based on a $\sim$50 meter sea level increase and a moderate lowering of glacial extent [232, 291]. We loop through changes of various magnitudes to find best model fits to our data, but keep the timing of changes consistent throughout model runs. Experimental model runs utilizing different timing for these changes result in lower quality fits while having little effect on the magnitude of changes needed to adequately fit the data. Though step-function changes in parameter values are less realistic than gradual ramped changes, we model the changes as instantaneous to understand the minimum amount of parameter value change needed to generate an adequate model fit to the data. More gradual changes would require an overall change of even greater magnitude to generate seawater $\delta^{34}S$ changes of similar temporal character.

First, we test the ability of step-function changes in $R_{C:S}$ to replicate our data. Specifically, we impose a decrease in $R_{C:S}$ from an initial value of 3.0 to lower values (1.4 to 3.0) at 325 Ma and an increase to higher values (3.0 to 7.0) at 319 Ma. Visual inspection of the model runs (Figure A.6) and sum of the squares results show improvement in model-data fits compared to runs with only $\delta^{13}C_{carb}$-driven $F_{py/org}$ change; the best model fits have sums over an order of magnitude lower than those from the constant $R_{C:S} = 3.0$ model runs. The best 10 model-data fits of the 6500+ iterations indicate that an initial $[SO_4^{2-}]$ of 7–9 mM at 335 Ma, a decrease of $R_{C:S}$ from 3 to 1.9–2.1 at 325 Ma, and an increase of $R_{C:S}$ to 4.6–4.9 at 319 Ma yield results that most closely resemble our data. The size of the O_2 reservoir becomes approximately 3.5x larger than its initial size in each of these runs assuming no change in the fractions of carbon and sulfur input derived from oxidative weathering. Such an O_2 increase would result in an atmosphere with extremely high ($\sim$48 mole %) concentrations of O_2 if all other gas reservoir sizes were constant at modern values. We also note that a decrease

in $R_{C:S}$ at 325 Ma is inconsistent with geologic records suggesting an expansion of terrestrial coal forest vegetation during the Serpukhovian and Bashkirian [73, 236].

Alternatively, step function changes in $\Delta\delta^{34}S$ or in $\delta^{34}S_{in}$ also result in better model-data fits (Figures A.7 & A.8). Best fit scores in each of these cases are again about an order of magnitude better than for the constant $R_{C:S} = 3.0$ model runs, but are approximately 15 to 50% worse than the best fit scores in the variable $R_{C:S}$ case. For $\Delta\delta^{34}S$ runs, the best fit model runs ascribe an increase in $\Delta\delta^{34}S$ of 15 to 21‰ (i.e. $\Delta\delta^{34}S = 50‰$ to 56‰) at 325 Ma and a subsequent decrease to $\Delta\delta^{34}S = 22‰$ at 319 Ma (Figure A.7). For $\delta^{34}S_{in}$ runs, the ten best fit model runs ascribe an increase of 5 to 7‰ in $\delta^{34}Sin$ at 325 Ma (i.e., $\delta^{34}Sin = +9$ to +11‰) and a subsequent decrease in $\delta^{34}Sin$ to -1‰ at 319 Ma (Figure A.8). Initial sulfate concentrations range from 7 mM to 10 mM. Unlike the variable $R_{C:S}$ runs, all $\delta^{34}S_{in}$ and $\Delta\delta^{34}S$ runs exhibit oscillations in seawater $\delta^{34}S$ of up to 2‰ in the Late Carboniferous and Early Permian due to $\delta^{13}C_{carb}$-driven oscillations in $F_{py/org}$. Changes in both of these sets of runs still drive a decrease in $[SO_4^{2-}]$ because high carbonate $\delta^{13}C$ values force $F_{py/org}$ to be relatively high. The combined increases in organic carbon and pyrite burial lead to a large rise in pO_2 that exceeds the pO_2 increase in the variable $R_{C:S}$ runs. The final O_2 reservoir size is 3.8x larger than its initial (modern) value at 335 Ma. A lower final O_2 reservoir size could be achieved through means such as lowering the initial O_2 reservoir size, forcing a temporal increase in oxidative weathering (i.e., f_{OWOM} and/or f_{OWP}), or including an iron oxide O_2 sink (see section 5, "Controls upon O_2 reservoir size"). However, we prefer to turn to other mechanisms to simultaneously improve model-data fits and reduce the extent of this problem.

A.7.4 Model runs with mid-Carboniferous changes in multiple parameter values

To generate model results in better agreement with the geologic record, we turn again to the strong evidence for a massive increase in terrestrial organic carbon burial beginning in the Serpukhovian [73, 236]. We opt to require that $R_{C:S}$ increase to a higher value at 325 Ma and remain unchanged through the end of the model runs. Changes in $\delta^{34}Sin$ and/or $\Delta\delta^{34}S$ are allowed to occur simultaneously with this $R_{C:S}$ change at 325 Ma and independent of $R_{C:S}$ at 319 Ma. Variations in $\delta^{34}Sin$ and $\Delta\delta^{34}S$ are forced to account for a higher proportion of

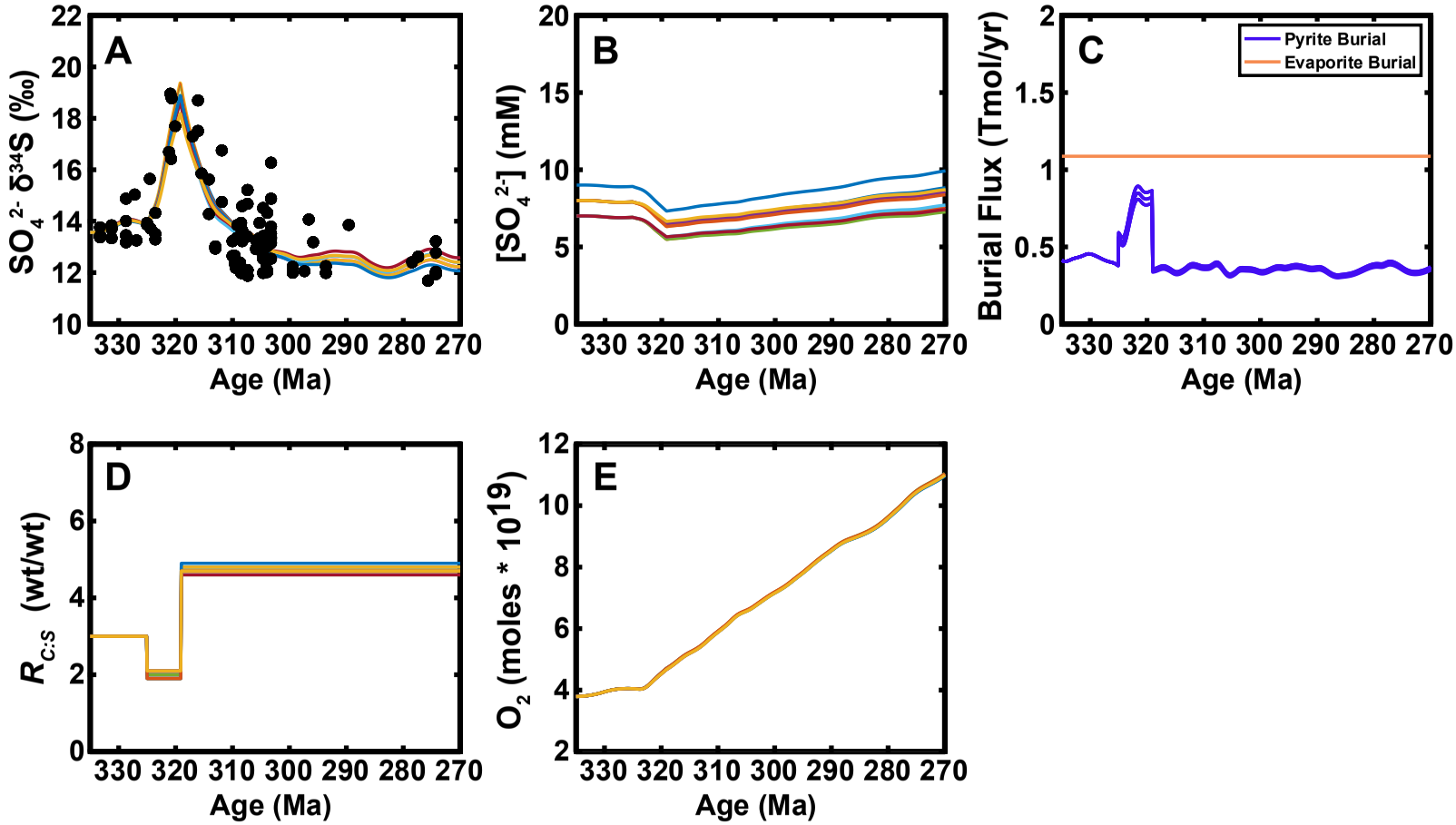

Figure A.6: Plots of (A) SO_4^{2-} $\delta^{34}S$, (B) $[SO_4^{2-}]$, (C) pyrite and evaporite burial fluxes, (D) the reduced C:S burial ratio ($R_{C:S}$), and (E) O_2 reservoir size associated with the single variable parameter model runs in which only $R_{C:S}$ was varied with time. Each colored line in the SO_4^{2-} $\delta^{34}S$ and $[SO_4^{2-}]$ plots represents a different model run; the ten best model-data fit runs are shown. Reasonable fits to the data require a transient $R_{C:S}$ decrease prior to the increase, contrary to expectation set by Berner and Raiswell (1983).

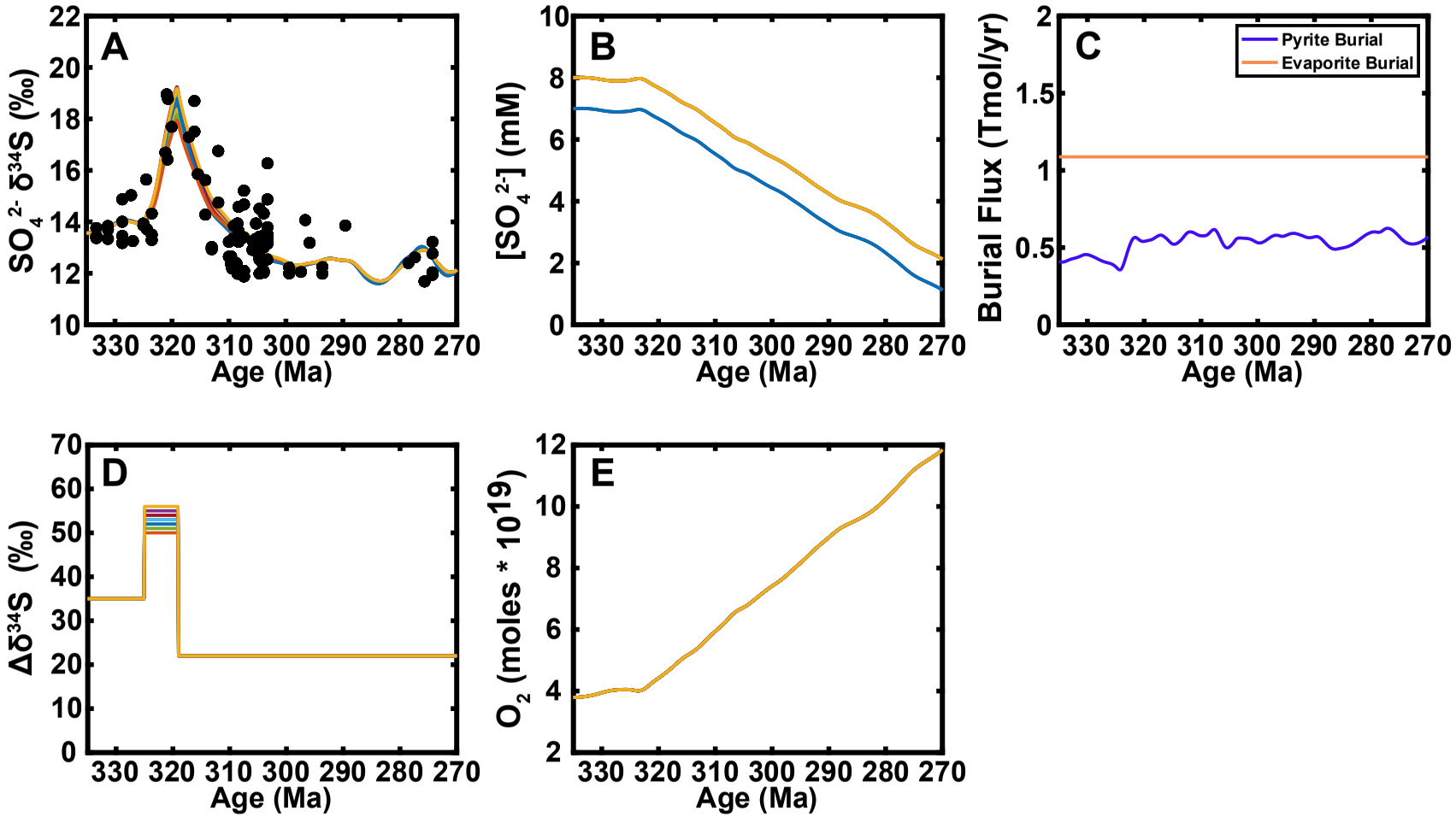

Figure A.7: Plots of (A) SO_4^{2-} $\delta^{34}S$, (B) $[SO_4^{2-}]$, (C) pyrite and evaporite burial fluxes, (D) $\Delta\delta^{34}S$, and (E) O_2 reservoir size associated with the single variable parameter model runs in which only $\Delta\delta^{34}S$ was varied with time. Each colored line in the SO_4^{2-} $\delta^{34}S$ and $[SO_4^{2-}]$ plots represents a different model run; the ten best model-data fit runs are shown.

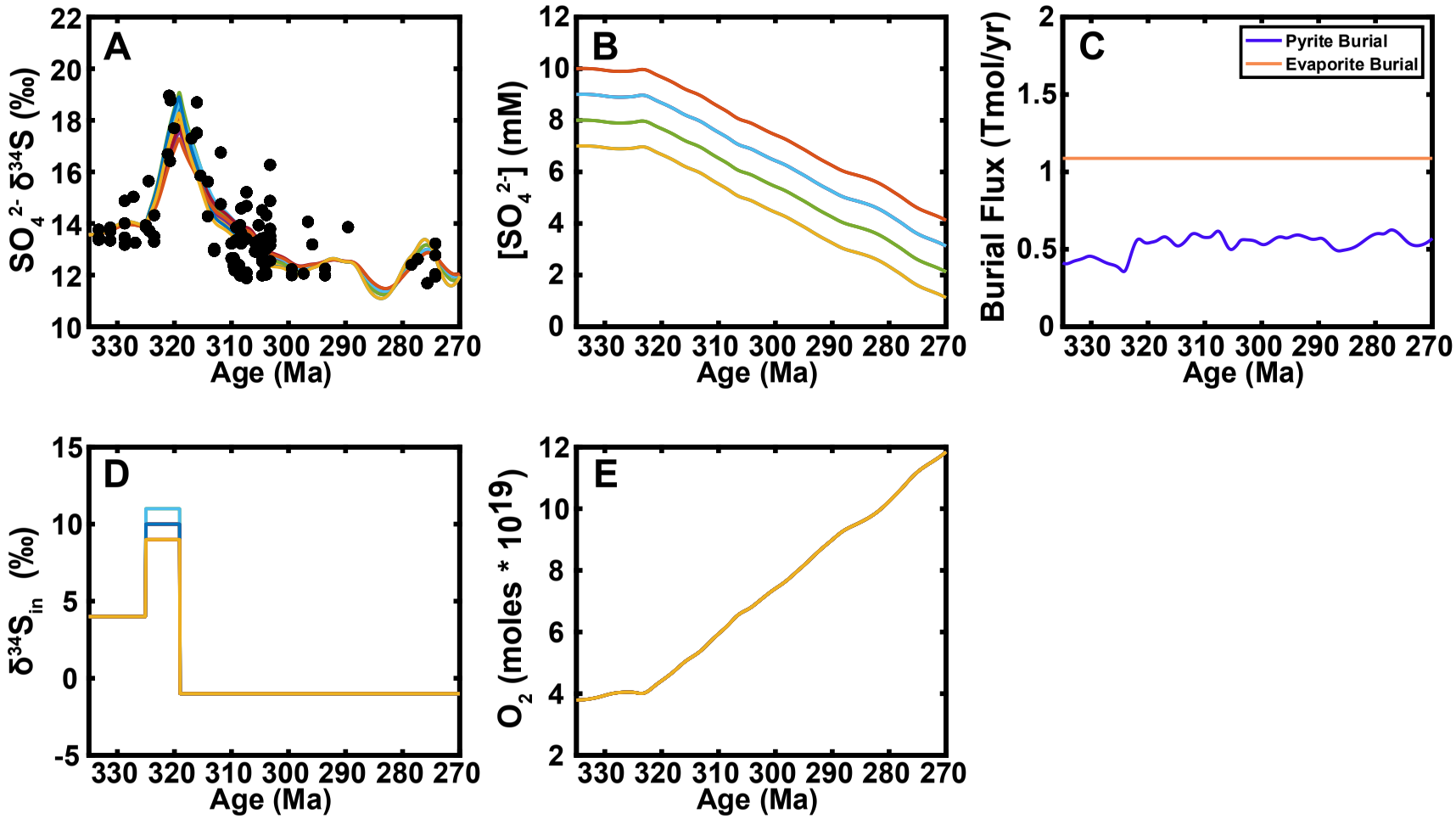

Figure A.8: Plots of (A) SO_4^{2-} $\delta^{34}S$, (B) $[SO_4^{2-}]$, (C) pyrite and evaporite burial fluxes, (D) $\delta^{34}S_{in}$, and (E) O_2 reservoir size associated with the single variable parameter model runs in which only $\delta^{34}S_{in}$ was varied with time. Each colored line in the SO_4^{2-} $\delta^{34}S$ and $[SO_4^{2-}]$ plots represents a different model run; the ten best model-data fit runs are shown.

the temporal variation in seawater $\delta^{34}S$ under this scenario.

We start by testing the ability of changes in $\delta^{34}S_{in}$ to generate acceptable model-data fits while increasing $R_{C:S}$ (Figure A.9). Our ten best fit model runs yield an increase in $R_{C:S}$ to 4.7–7.8 at 325 Ma, an approximately 9 to 12‰ increase in $\delta^{34}S_{in}$ (to +13‰–+16‰) at 325 Ma, and a subsequent decrease in $\delta^{34}S_{in}$ to between +4‰ and +7‰ at 319 Ma. Though sum of the squares values associated with these runs are approximately 5% worse than for runs in which only $R_{C:S}$ was varied, the visual fit between model and data is equally good. Initial $[SO_4^{2-}]$ in these runs varies from 5 mM to 6 mM and remains between the Late Devonian (5 mM at minimum) and Middle Permian (25 mM at maximum) fluid inclusion constraints provided by Lowenstein et al. (2003). However, the potential for such large changes in $\delta^{34}S_{in}$ to occur over such short timescales is questionable. The large increase at 325 Ma in particular would presumably require preferential exposure and weathering of material with a high $\delta^{34}S$ (esp. sulfate evaporites) in response to a tectonic or sea-level perturbation. Shields et al. (2019) have recently invoked such a scenario during the Neoproterozoic, and evidence for mobilization and erosion of Early Carboniferous evaporites within the lower Windsor Group of southeastern Canada [352] suggests that such a scenario could be possible for the mid-Carboniferous. Previous sulfur isotope analyses have measured these evaporites to have a $\delta^{34}S$ of +13.7‰ to +16.5‰ [111, 338]. These values closely match those during our modeled $\delta^{34}S_{in}$ increase, but such a close match is either fortuitous or suggests that dissolution of these evaporites dominated the global S input flux to the ocean during this period. We favor a fortuitous match given that the amount of evaporite loss from this group is uncertain and the timing of mobilization is thought to have occurred more broadly from the late Mississippian into the latest Pennsylvanian [111, 352]. Smaller influxes of sulfate from dissolution of older Early Paleozoic and Neoproterozoic evaporites with higher $\delta^{34}S$ are more plausible. The O_2 reservoir size increases by 3.2x to 3.5x throughout these best fit runs.

Similarly good model-data fits are obtained if the time series is instead simulated with changes in $\Delta\delta^{34}S$ (Figure A.10). Best fit results under this scenario occur when $R_{C:S}$ increases from 3.0 to 3.9–4.3 at 325 Ma. In these same runs, $\Delta\delta^{34}S$ undergoes a 31‰–35‰ increase (to 66‰–70‰) at 325 Ma and a subsequent decrease to 29‰–32‰ at 319 Ma. Fits are about 4% worse than for runs in which only $R_{C:S}$ was varied, and initial $[SO_4^{2-}]$ in the ten best fit runs ranges

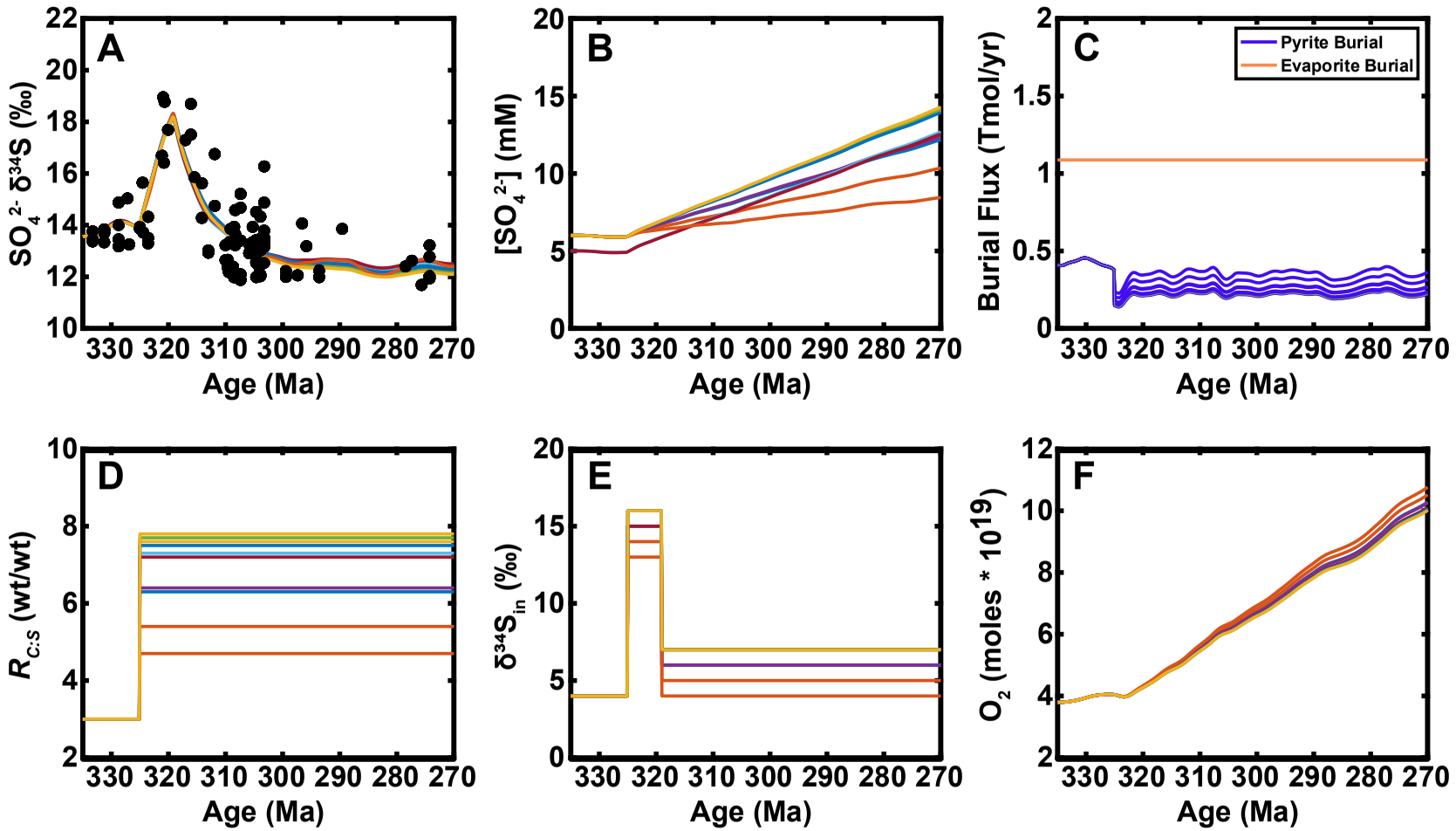

Figure A.9: Plots of (A) SO_4^{2-} $\delta^{34}S$, (B) $[SO_4^{2-}]$, (C) pyrite and evaporite burial fluxes, (D) $R_{C:S}$, (E) $\delta^{34}S_{in}$, and (F) O_2 reservoir size associated with the multi-variable parameter model runs in which $R_{C:S}$ was forced to increase at 325 Ma and $\delta^{34}S_{in}$ was allowed to vary with time. Each colored line in the SO_4^{2-} $\delta^{34}S$ and $[SO_4^{2-}]$ plots represents a different model run; the ten best model-data fit runs are shown.

from 6 to 7 mM. Although these changes in $\Delta\delta^{34}S$ are quite large, previous compilations of sulfur isotopic fractionation between sulfate and sulfide in modern natural environments (e.g. [59]) and in laboratory culture studies (e.g. [195, 313]) have shown that $^{34}\varepsilon$ (i.e., the sulfur isotope fractionation associated with microbial sulfate reduction) may vary dramatically depending on factors such as cell-specific sulfate reduction, temperature, and the availability of different electron donors (e.g. [365]). Larger S isotopic fractionations (e.g. [195, 313]) and lower pyrite $\delta^{34}S$ (e.g. [222, 288]) are expected in the slowly accumulating sediments of the deep ocean where sulfate reduction rates are very slow [43]. Assuming a significant reduction in shelf area with eustatic sea level fall at the Serpukhovian-Bashkirian boundary, we consider an increase in the $\Delta\delta^{34}S$ associated with marine sulfur cycling to be likely given the opportunity for deep marine pyrite formation to become a fractionally greater portion of the total pyrite burial flux. A return toward smaller $\Delta\delta^{34}S$ values in the late Carboniferous is further consistent with sea level rise and a regaining of some of the lost shelf area at that time. However, the requirement that all pyrite sulfur be buried with an isotopic offset near the $\sim$70‰thermodynamic maximum for S isotopic fractionation between SO_4^{2-} and H_2S [95, 157] from 325–319 Ma is unreasonable.

Lastly, we explore the potential for simultaneous changes in both $\delta^{34}S_{in}$ and $\Delta\delta^{34}S$ (Figure II.6). Here, we limit $\Delta\delta^{34}S$ to a minimum value of 25‰ and to a maximum value of 55‰; these values approximately bracket the Phanerozoic minimum and maximum estimates of Wu, Farquhar, and Strauss (2014) for this parameter. Best fits occur when $R_{C:S}$ increases to 4.4–4.8 at 325 Ma with simultaneous increases in $\delta^{34}S_{in}$ to +8‰–+10‰ and $\Delta\delta^{34}S$ to 47‰–55‰. Values of $\delta^{34}S_{in}$ decrease to +6‰ at 319 Ma while $\Delta\delta^{34}S$ decreases to 25‰–27‰. The initial sulfate concentration is 6 mM in all 10 best fit runs, and the O_2 reservoir size increases by 3.4x to 3.5x during each run. Best fit scores are improved by $\sim$4% from the runs in which only $R_{C:S}$ was varied. Model-data fits are further improved by up to 12% if $\Delta\delta^{34}S$ is allowed to decrease below 25‰, and $\delta^{34}S_{in}$ remains at +9‰–+10‰ at 319 Ma. However, we view such low $\Delta\delta^{34}S$ as unlikely given that these values are substantially below literature estimates [195, 369].

We consider the scenario in which $R_{C:S}$ increases and $\delta^{34}S_{in}$ and $\Delta\delta^{34}S$ change simultaneously to be the most plausible mechanism to explain our data. Such a scenario is consistent with an increase in the abundance of terrestrial organic sediments [236] as well as an enhancement of sulfate evaporite erosion [352],

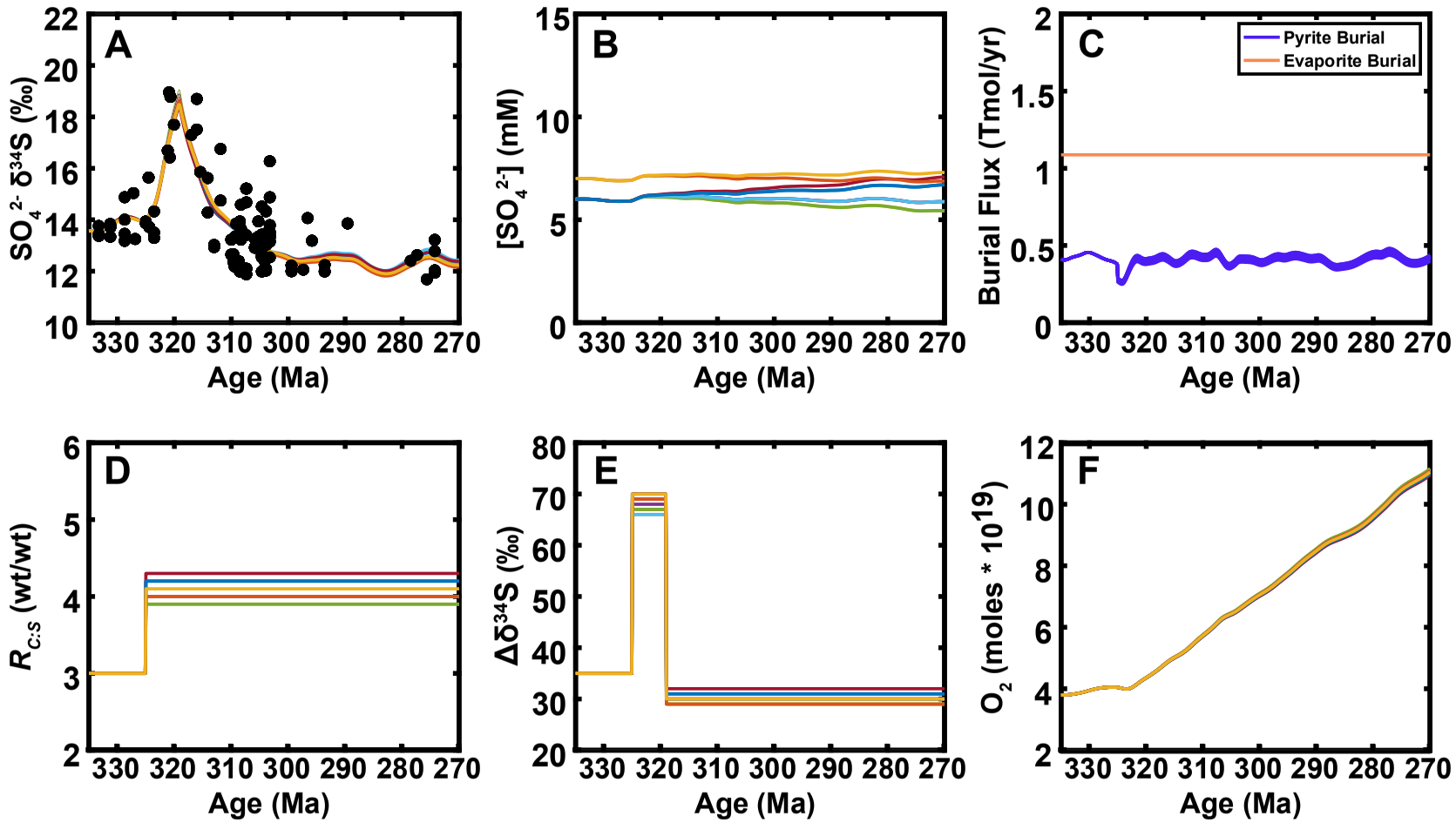

Figure A.10: Plots of (A) SO_4^{2-} $\delta^{34}S$, (B) $[SO_4^{2-}]$, (C) pyrite and evaporite burial fluxes, (D) $R_{C:S}$, (E) $\Delta\delta^{34}S$, and (F) O_2 reservoir size associated with the multi-variable parameter model runs in which $R_{C:S}$ was forced to increase at 325 Ma and $\Delta\delta^{34}S$ was allowed to vary with time. Each colored line in the SO_4^{2-} $\delta^{34}S$ and $[SO_4^{2-}]$ plots represents a different model run; the ten best model-data fit runs are shown.

but does not require this enhanced sulfate evaporite erosion to dominate the global S input flux. This scenario is also consistent with a loss (and later return) of shallow shelf environments due to tectonism and eustatic sea level change. The Macrostrat database of North American strata [**peters_macrostrat_2018**] yields surprisingly few documented occurrences of evaporites (including gypsum and anhydrite) within strata deposited across the 325 Ma–319 Ma interval (Figure A.11) and attests to this temporary loss of shallow shelf environments amenable to evaporite deposition. Additional studies on the relation of sea level change to $\Delta\delta^{34}S$ (e.g. [246]) and the relative timing of sea level change, evaporite erosion, and seawater $\delta^{34}S$ are needed to better attribute seawater $\delta^{34}S$ change to these potential causes.

A.8 Controls upon O_2 reservoir size

Previous box modeling efforts tracking pO_2 change during the Phanerozoic (e.g. [25, 199]) have consistently suggested an increase in pO_2 across the Permo-Carboniferous. However, the > 3x increase in O_2 reservoir size observed in model runs here is very large considering that the model was initiated with a pO_2 equivalent to modern pO_2. We consider the following as viable means of reducing the amount of O_2 accumulation during our model runs:

- Higher f_{OWOM} / f_{OWP} – All model runs displayed here used a time-invariant values of 0.192 for f_{OWOM} and 0.457 for f_{OWP}. Such values were chosen to initialize the model in isotopic steady state for both the C and S cycles given the prescribed isotopic compositions of the oxidized and reduced geologic reservoirs for these elements. However, higher f_{OWOM} and f_{OWP} are possible if more ^{13}C and ^{34}S-enriched isotopic compositions are assumed for the organic carbon and pyrite reservoirs, respectively. To explore potential effects on O_2 reservoir size, we ran a series of model iterations with initial organic C reservoir $\delta^{13}C$ values ranging from -20‰ to -30‰ and pyrite S reservoir $\delta^{34}S$ values ranging from -20‰ to 0‰ (Figure A.12). The initial carbonate C reservoir $\delta^{13}C$ and evaporite S reservoir $\delta^{34}S$ values were left unchanged at +0.5‰ and +20‰, respectively. The results of these model runs show that the final O_2 reservoir size can be reduced by approximately 15% if the pyrite reservoir is assigned a $\delta^{34}S$ value of -5‰ instead of -15‰; a decrease of similar magnitude occurs for each 2‰ increase of the organic C $\delta^{13}C$ above our original value of -25‰.

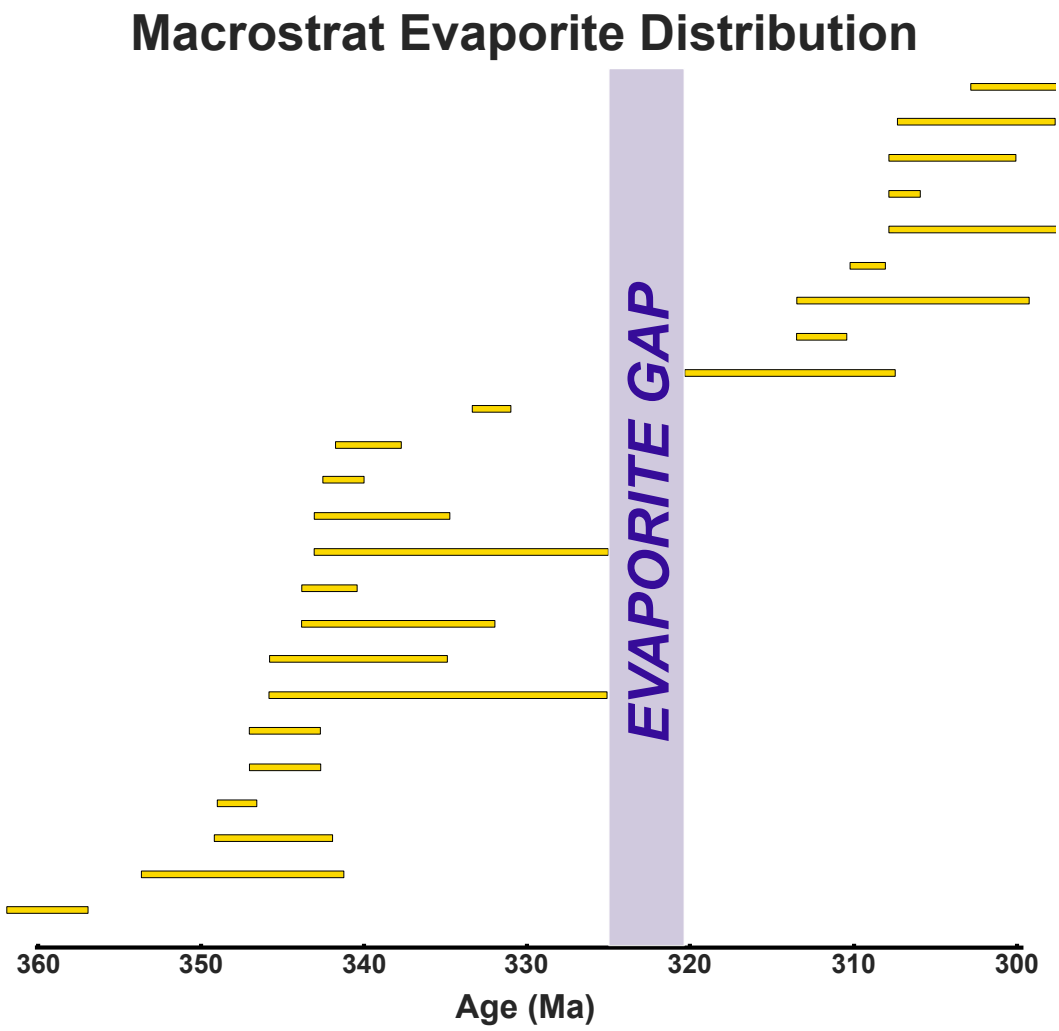

Figure A.11: Plot of duration of Carboniferous units including evaporites among the listed lithologies against age. Information gathered from a query of the Macrostrat database [257]. Each horizontal bar represents a different unit, with the ends of the bar indicating the basal age and top age of the evaporite-containing unit. Notably, there is a gap between 325 Ma and 320 Ma in which no evaporite-containing units are noted in Macrostrat.

Further reductions are possible if higher values are assigned for the initial carbonate C reservoir $\delta^{13}C$ and evaporite S reservoir $\delta^{34}S$.

- Lower organic C burial flux – Our model assumes a steady state carbon cycle with a carbon input flux that is constant in both magnitude and isotopic composition. Given this steady state assumption, reductions in the amount of organic C burial – the primary driver of O_2 reservoir size increases in our model – are possible if (1) the magnitude of the carbon input flux is lowered, (2) the $\delta^{13}C$ of the input flux is increased, (3) the isotopic offset between buried carbonate and organic C ($\delta^{13}C$) is increased, and/or (4) the brachiopod $\delta^{13}C$ curve [123] is biased toward high $\delta^{13}C$ by processes other than organic matter burial (e.g. [110, 297]). Such a lowering of organic C burial would also require reductions in the S input flux to maintain an identical S isotopic steady state. We do not extensively explore changes in these parameters given the good agreement of our chosen values with existing literature. However, we anecdotally note based on model runs excluded here that the final O_2 reservoir size is especially sensitive to the magnitude of the C input flux; the amount of O_2 addition scales linearly with this input flux.

- Inclusion of other reduced sinks for O_2 – The oxidation of mantle-derived ferrous iron to ferric iron has been an important sink for oxidizing power generated by carbon fixation over Earth history (e.g. [137]). Although this net transfer of oxidizing power is thought to have been most active during the Archean and Proterozoic (e.g. [292]), additional transfer during the Phanerozoic may be possible. Macdonald et al. (2019) have recently proposed that arc-continent collisions in the tropics drive the onset of glacial periods, including the Permo-Carboniferous glaciation. Enhanced weathering of mafic and ultramafic rocks exhumed during these collisions, while removing atmospheric carbon dioxide via silicate weathering, could have also presented an opportunity for net removal of O_2 via the oxidation of ferrous iron-bearing minerals within these rocks. However, such net removal relies on the oxidized ferric iron products being buried without reduction back to ferrous iron.

  Further reducing power may be added to Earth's ocean-atmosphere system through the hydrothermal or volcanic addition of reduced materials like H_2, CH_4, H_2S, Fe^{2+}, and CO. Modeling by Laakso and Schrag (2014)

has suggested that order-of-magnitude changes in the fluxes of these materials can lead to substantial (> 0.5 present atmospheric level) reductions in the steady state pO_2 in Earth's surface environments. High reconstructed eustatic sea levels [129, 131] during the Permo-Carboniferous could suggest higher spreading rates (e.g. [139]) and a correspondingly higher flux of these reduced materials to the ocean-atmosphere system through hydrothermal input. A lack of large igneous provinces dating to this time (e.g. [77, 204]) suggests that a large volcanic outgassing flux of reduced gases is unlikely.

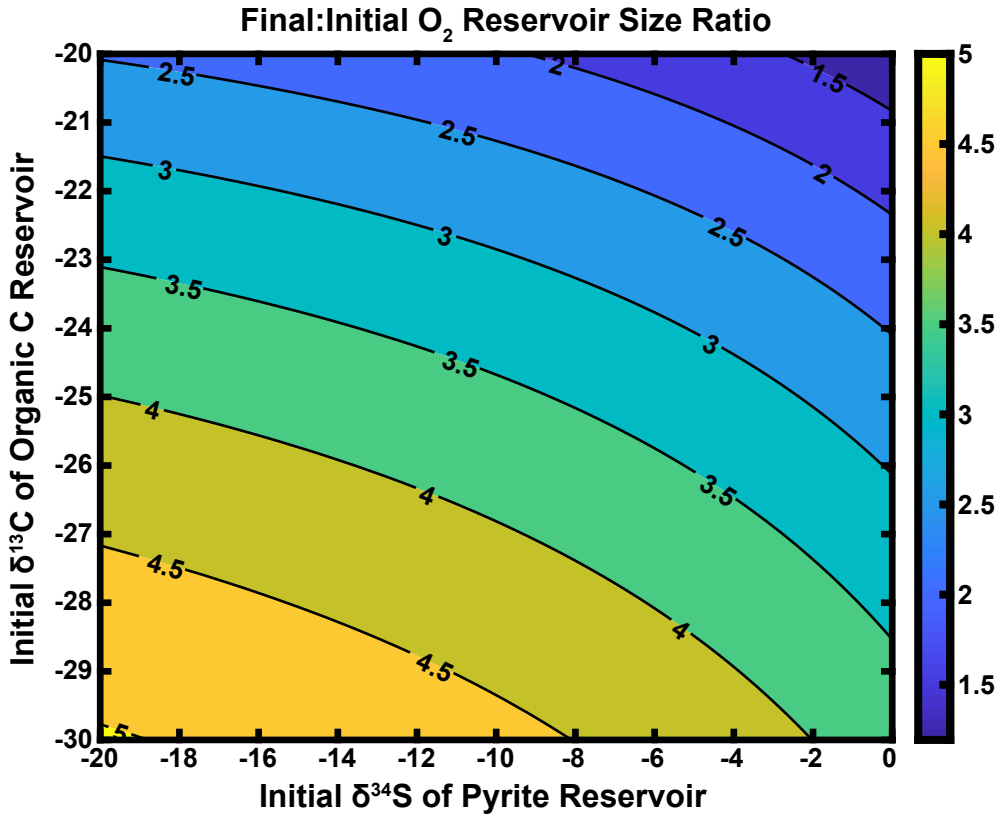

Figure A.12: Contour plot of the ratio of the final O_2 reservoir size to the initial O_2 reservoir size (equivalent to modern) for a series of model runs in which the initial $\delta^{13}C$ of the geologic organic carbon reservoir and the initial $\delta^{34}S$ of the geologic pyrite reservoir were varied. Oxidative weathering fluxes (i.e., f_{OWOM} and f_{OWP}) were modified such that the $\delta^{13}C$ of the carbon input was always -4.4‰ and the $\delta^{34}S$ of the sulfur input was +4‰. Parameters were otherwise left constant with time (as in Figure A.4). These results demonstrate that significant reductions in model O_2 accumulation may be achieved if more ^{13}C- and ^{34}S-enriched compositions are assumed for these two geologic reservoirs.

Appendix B

SUPPLEMENTARY MATERIAL FOR CHAPTER IV

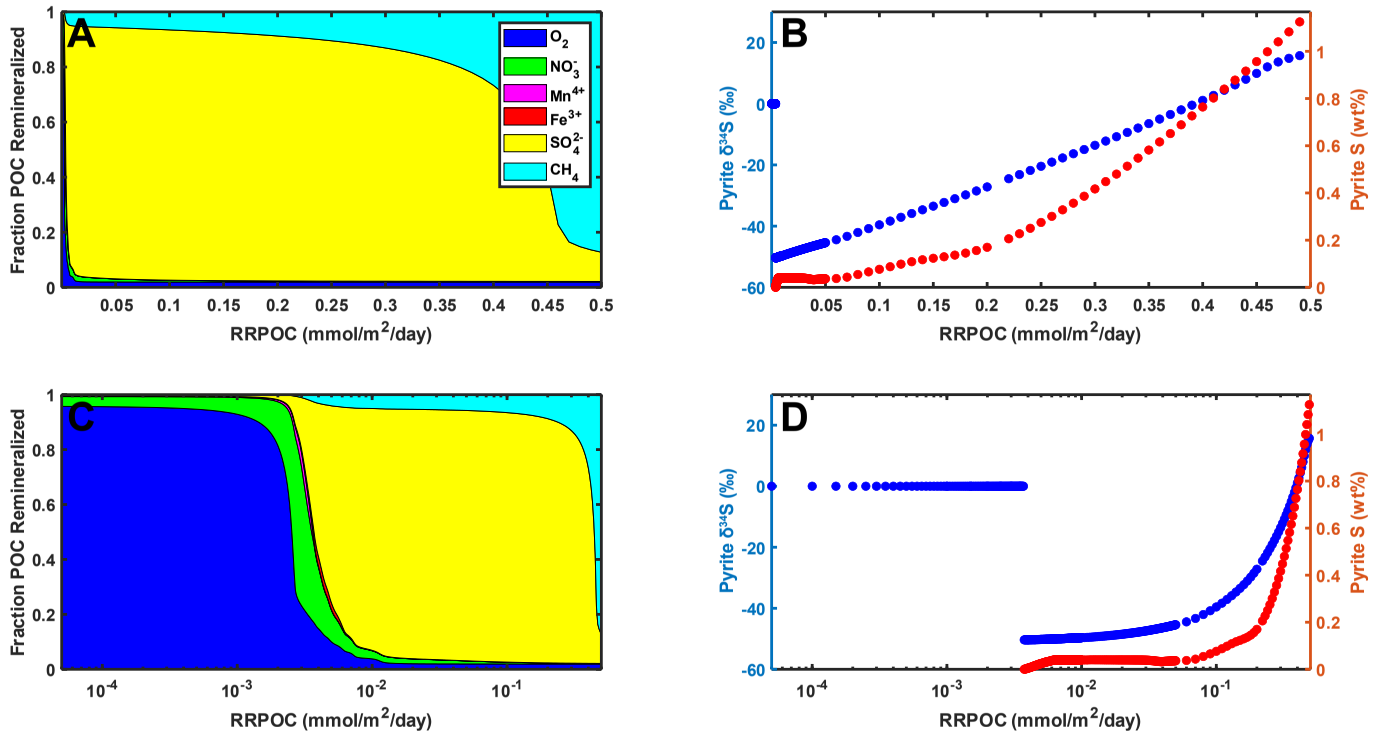

Figure B.1: 5x less Fe input model experiment. (A) Area plot of the fractional contribution of different electron acceptors to organic carbon remineralization at different initial sedimentary POC concentrations for an Fe^{3+} rain rate five times lower than that in the baseline model runs. Shaded areas represent the fractional contributions of oxic respiration (dark blue), denitrification (green), manganese reduction (magenta), iron reduction (red), sulfate reduction (yellow), and fermentation (cyan) to overall POC remineralization. (B) Plot of pyrite $\delta^{34}S$ (left axis; blue circles) and pyrite sulfur concentration (right axis; red circles) for buried pyrite exiting the bottom of the model domain as a funtion of POC rain rate. (C) and (D) are replicate plots of (A) and (B), respectively, with the initial POC plotted on a log scale instead of a linear scale.

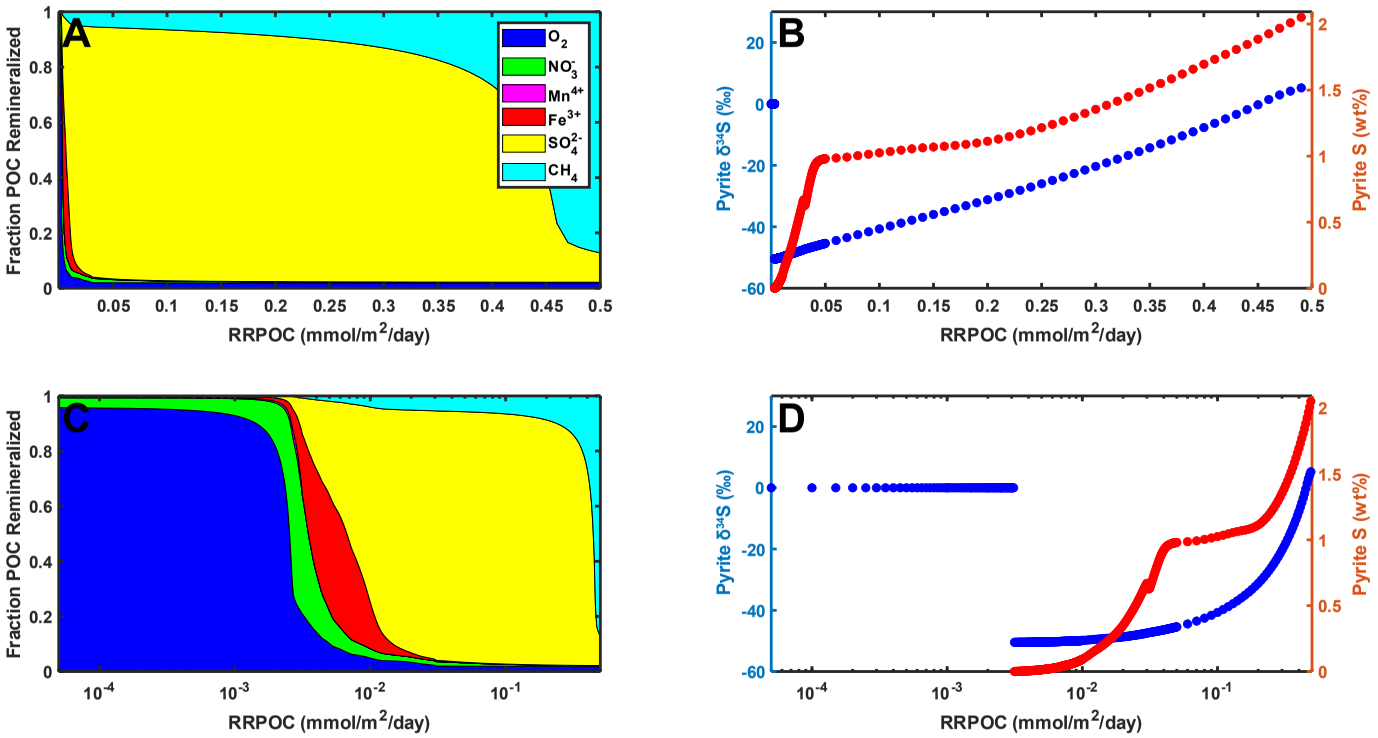

Figure B.2: 5x more Fe input model experiment. (A) Area plot of the fractional contribution of different electron acceptors to organic carbon remineralization at different initial sedimentary POC concentrations for an Fe^{3+} rain rate five times higher than that in the baseline model runs. Shaded areas represent the fractional contributions of oxic respiration (dark blue), denitrification (green), manganese reduction (magenta), iron reduction (red), sulfate reduction (yellow), and fermentation (cyan) to overall POC remineralization. (B) Plot of pyrite $\delta^{34}S$ (left axis; blue circles) and pyrite sulfur concentration (right axis; red circles) for buried pyrite exiting the bottom of the model domain as a funtion of POC rain rate. (C) and (D) are replicate plots of (A) and (B), respectively, with the initial POC plotted on a log scale instead of a linear scale.

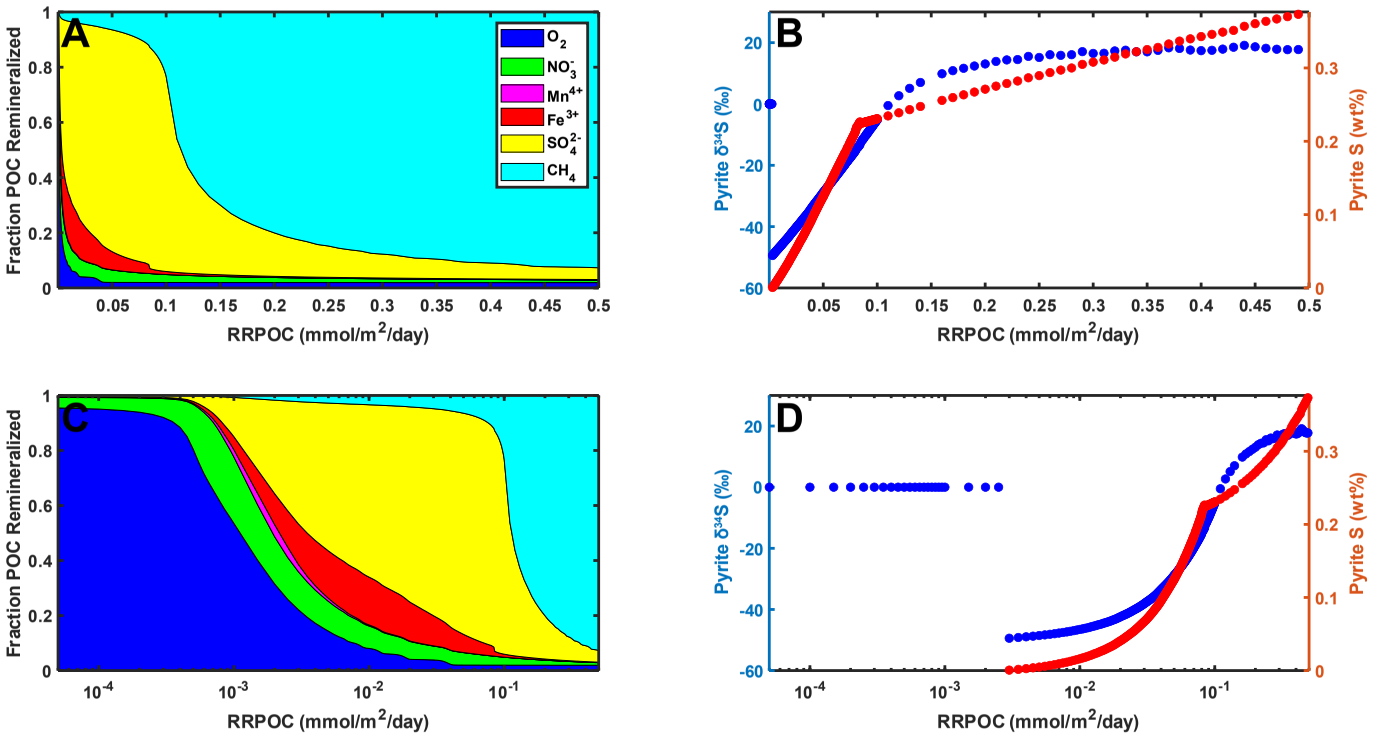

Figure B.3: 10x higher sedimentation rate model experiment. (A) Area plot of the fractional contribution of different electron acceptors to organic carbon remineralization at different initial sedimentary POC concentrations for a sedimentation rate of 10 $\frac{\text{cm}}{\text{kyr}}$ (versus 1 $\frac{\text{cm}}{\text{kyr}}$ for the baseline model runs). Shaded areas represent the fractional contributions of oxic respiration (dark blue), denitrification (green), manganese reduction (magenta), iron reduction (red), sulfate reduction (yellow), and fermentation (cyan) to overall POC remineralization. (B) Plot of pyrite $\delta^{34}S$ (left axis; blue circles) and pyrite sulfur concentration (right axis; red circles) for buried pyrite exiting the bottom of the model domain as a funtion of POC rain rate. (C) and (D) are replicate plots of (A) and (B), respectively, with the initial POC plotted on a log scale instead of a linear scale.

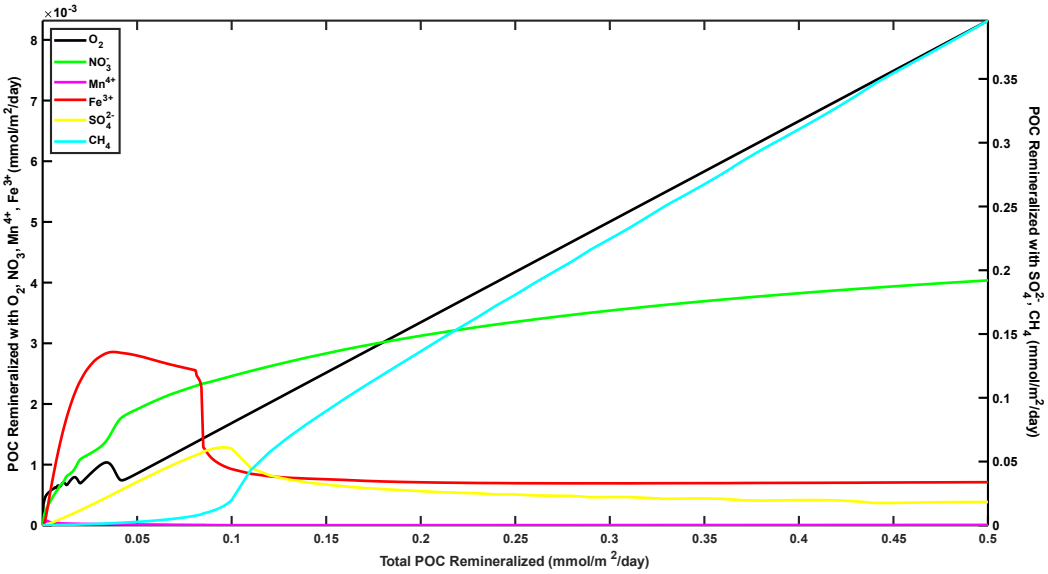

Figure B.4: Line plot of the absolute amount of POC remineralized using different electron acceptors plotted against the total amount of POC remineralized for a 10 $\frac{\text{cm}}{\text{kyr}}$ sedimentation rate. Lines for oxic respiration (black), denitrification (green), mangenese reduction (magenta), and iron reduction (red) are plotted on the left axis, whereas those for sulfate reduction (yellow) and fermentation (cyan) are plotted on the right axis. Note that the rapid switch from a sulfate reduction dominance to a fermentation dominance occurs at a much lower amount of total remineralized POC than in the baseline model runs.

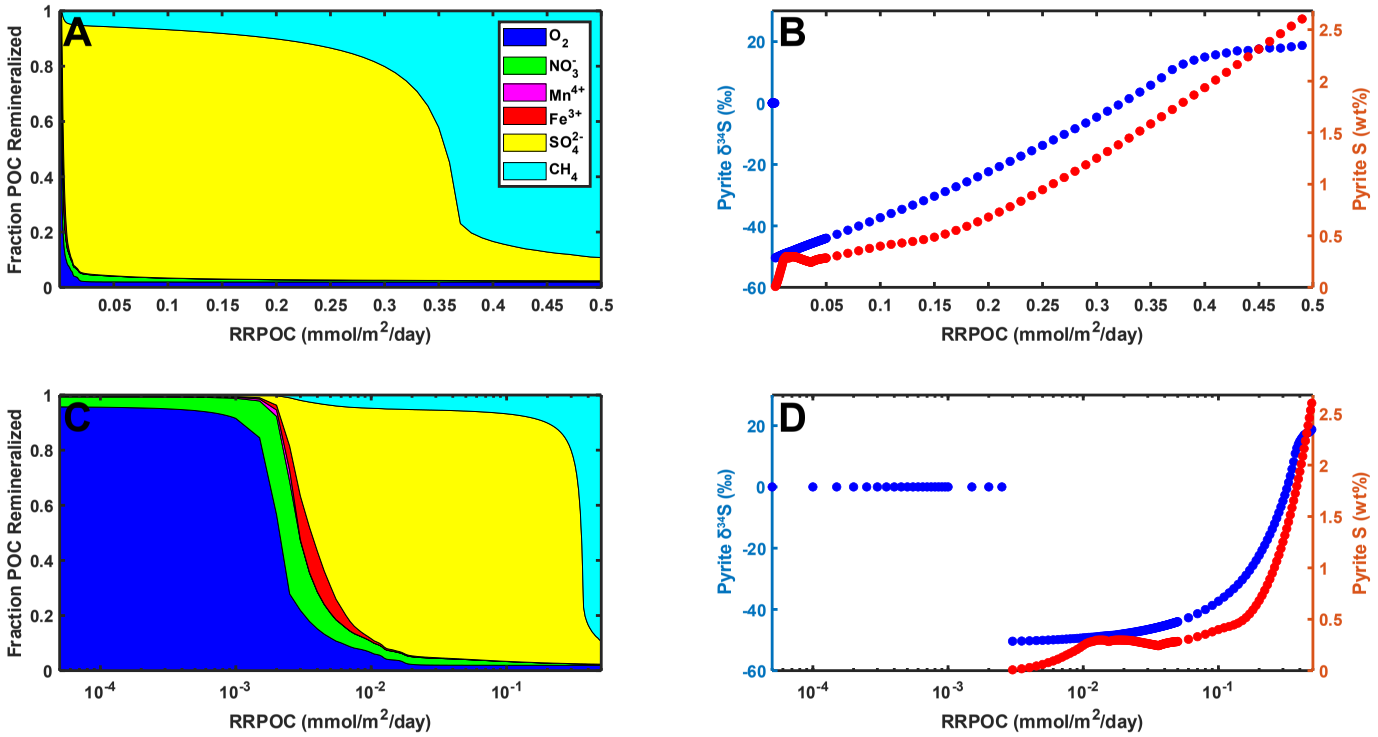

Figure B.5: $\phi_0 = 0.8$, $\zeta = 250$ m model experiment. (A) Area plot of the fractional contribution of different electron acceptors to organic carbon remineralization at different initial sedimentary POC concentrations for $\phi_0 = 0.8$ and $\zeta = 250$ m. Shaded areas represent the fractional contributions of oxic respiration (dark blue), denitrification (green), manganese reduction (magenta), iron reduction (red), sulfate reduction (yellow), and fermentation (cyan) to overall POC remineralization. (B) Plot of pyrite $\delta^{34}S$ (left axis; blue circles) and pyrite sulfur concentration (right axis; red circles) for buried pyrite exiting the bottom of the model domain as a funtion of POC rain rate. (C) and (D) are replicate plots of (A) and (B), respectively, with the initial POC plotted on a log scale instead of a linear scale.

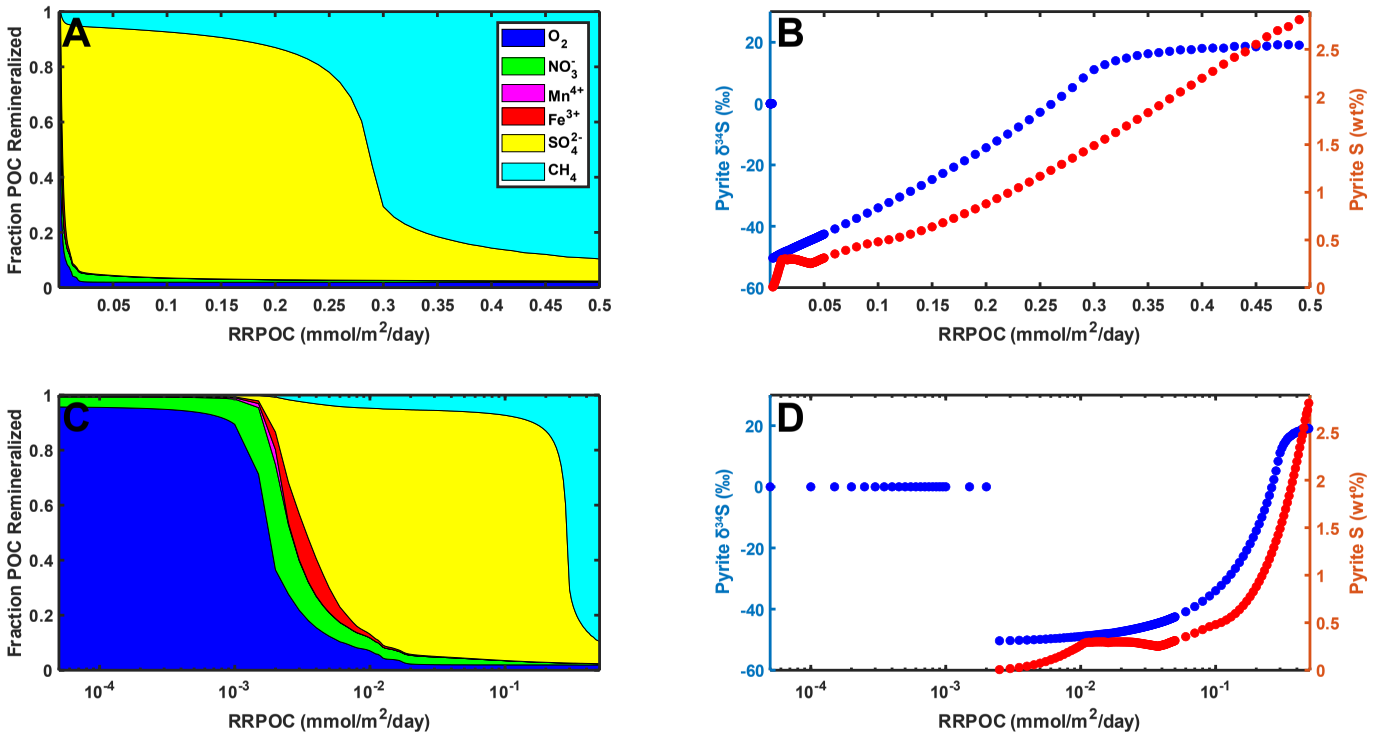

Figure B.6: $\phi_0 = 0.95$, $\zeta = 250$ m model experiment. (A) Area plot of the fractional contribution of different electron acceptors to organic carbon remineralization at different initial sedimentary POC concentrations for $\phi_0 = 0.95$ and a $\zeta = 250$ m. Shaded areas represent the fractional contributions of oxic respiration (dark blue), denitrification (green), manganese reduction (magenta), iron reduction (red), sulfate reduction (yellow), and fermentation (cyan) to overall POC remineralization. (B) Plot of pyrite δ^{34}S (left axis; blue circles) and pyrite sulfur concentration (right axis; red circles) for buried pyrite exiting the bottom of the model domain as a funtion of POC rain rate. (C) and (D) are replicate plots of (A) and (B), respectively, with the initial POC plotted on a log scale instead of a linear scale.

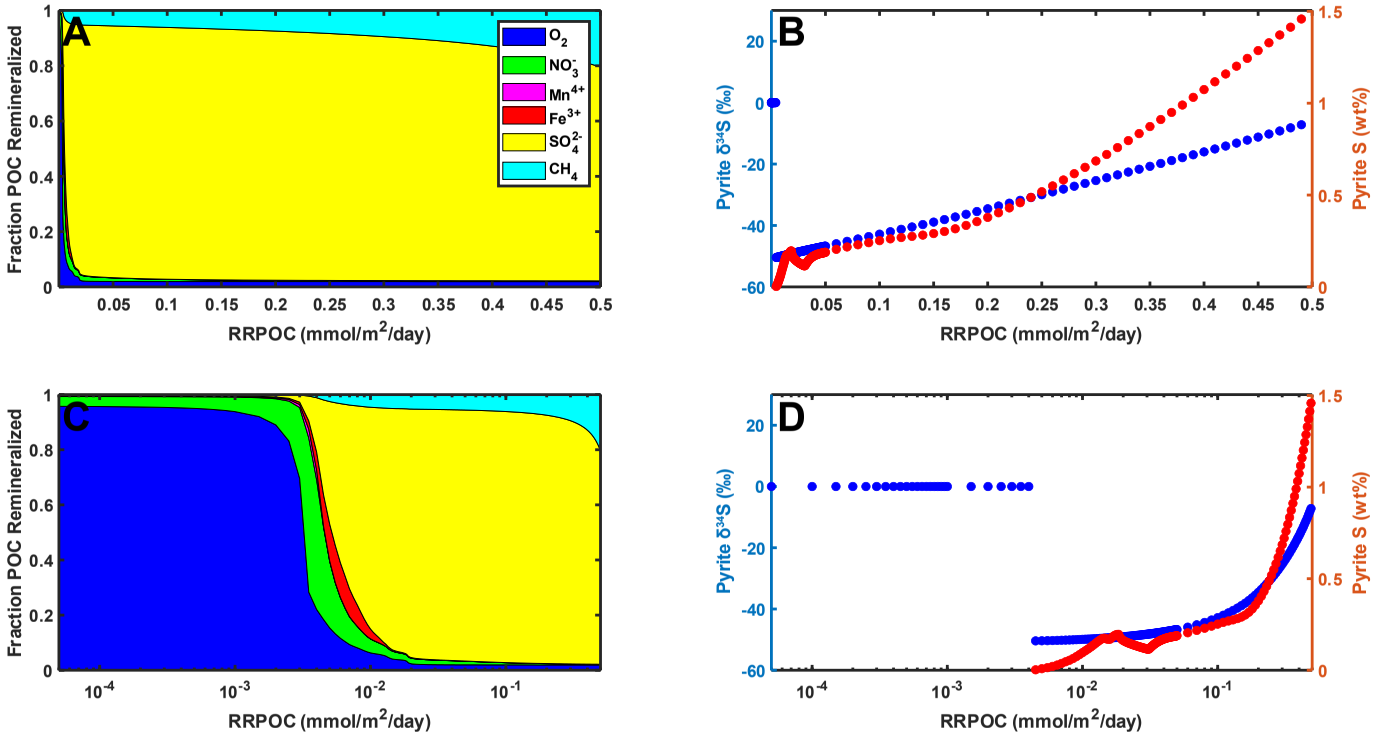

Figure B.7: 10 °C bottom water model experiment. (A) Area plot of the fractional contribution of different electron acceptors to organic carbon remineralization at different initial sedimentary POC concentrations for a bottom water temperature of 10 °C. Shaded areas represent the fractional contributions of oxic respiration (dark blue), denitrification (green), manganese reduction (magenta), iron reduction (red), sulfate reduction (yellow), and fermentation (cyan) to overall POC remineralization. (B) Plot of pyrite $\delta^{34}S$ (left axis; blue circles) and pyrite sulfur concentration (right axis; red circles) for buried pyrite exiting the bottom of the model domain as a funtion of POC rain rate. (C) and (D) are replicate plots of (A) and (B), respectively, with the initial POC plotted on a log scale instead of a linear scale.

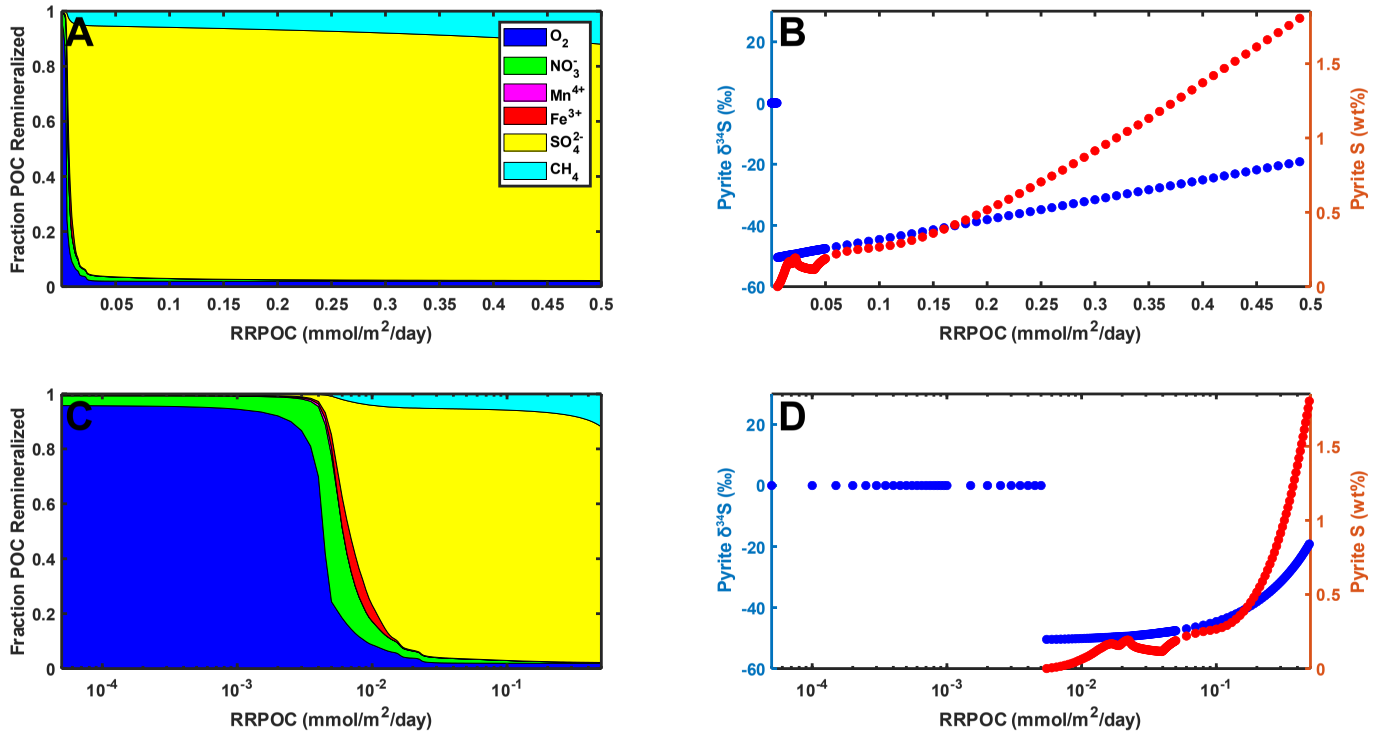

Figure B.8: 20 °C bottom water model experiment. (A) Area plot of the fractional contribution of different electron acceptors to organic carbon remineralization at different initial sedimentary POC concentrations for a bottom water temperature of 20 °C. Shaded areas represent the fractional contributions of oxic respiration (dark blue), denitrification (green), manganese reduction (magenta), iron reduction (red), sulfate reduction (yellow), and fermentation (cyan) to overall POC remineralization. (B) Plot of pyrite δ^{34}S (left axis; blue circles) and pyrite sulfur concentration (right axis; red circles) for buried pyrite exiting the bottom of the model domain as a funtion of POC rain rate. (C) and (D) are replicate plots of (A) and (B), respectively, with the initial POC plotted on a log scale instead of a linear scale.

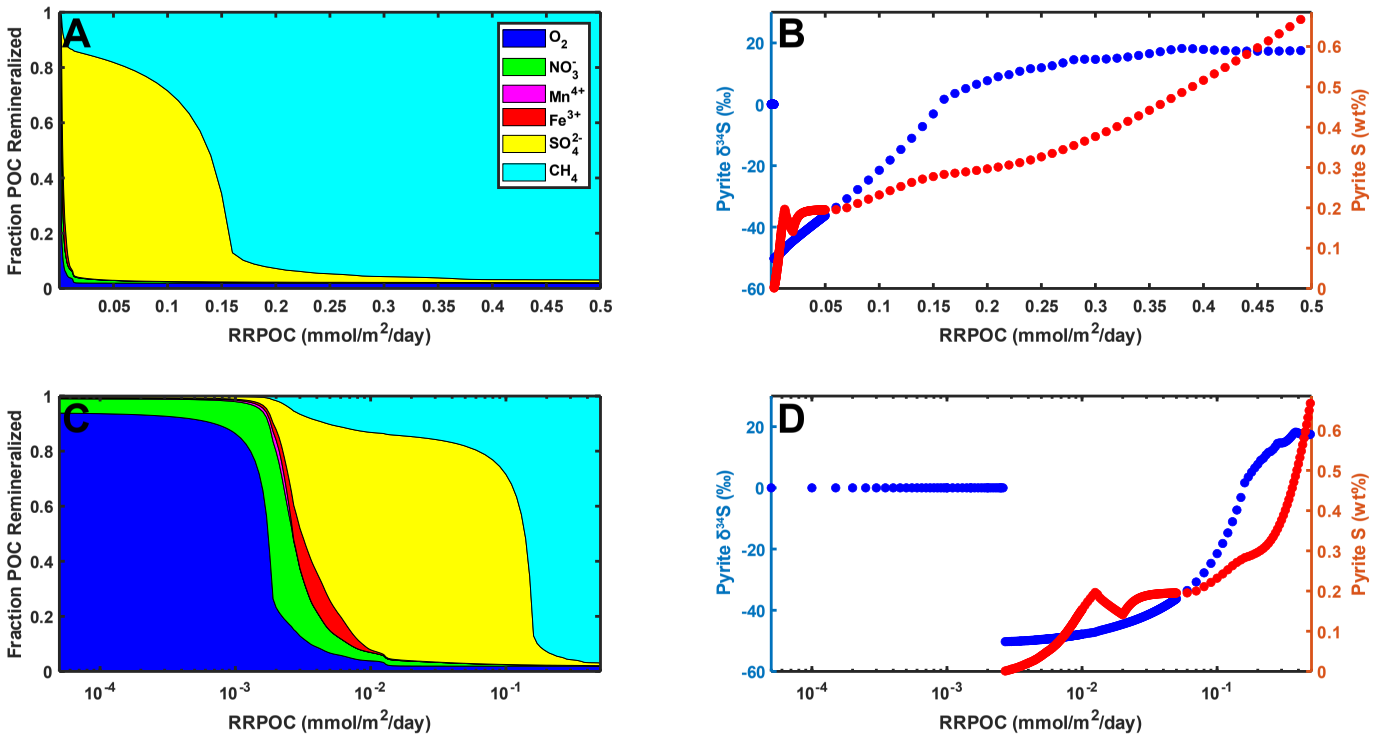

Figure B.9: 10 mM bottom water [SO_4^{2-}] model experiment. (A) Area plot of the fractional contribution of different electron acceptors to organic carbon remineralization at different initial sedimentary POC concentrations for a bottom water sulfate concentration of 10 mM and a bottom water O_2 concentration of 100 μM. Shaded areas represent the fractional contributions of oxic respiration (dark blue), denitrification (green), manganese reduction (magenta), iron reduction (red), sulfate reduction (yellow), and fermentation (cyan) to overall POC remineralization. (B) Plot of pyrite $\delta^{34}S$ (left axis; blue circles) and pyrite sulfur concentration (right axis; red circles) for buried pyrite exiting the bottom of the model domain as a funtion of POC rain rate. (C) and (D) are replicate plots of (A) and (B), respectively, with the initial POC plotted on a log scale instead of a linear scale.

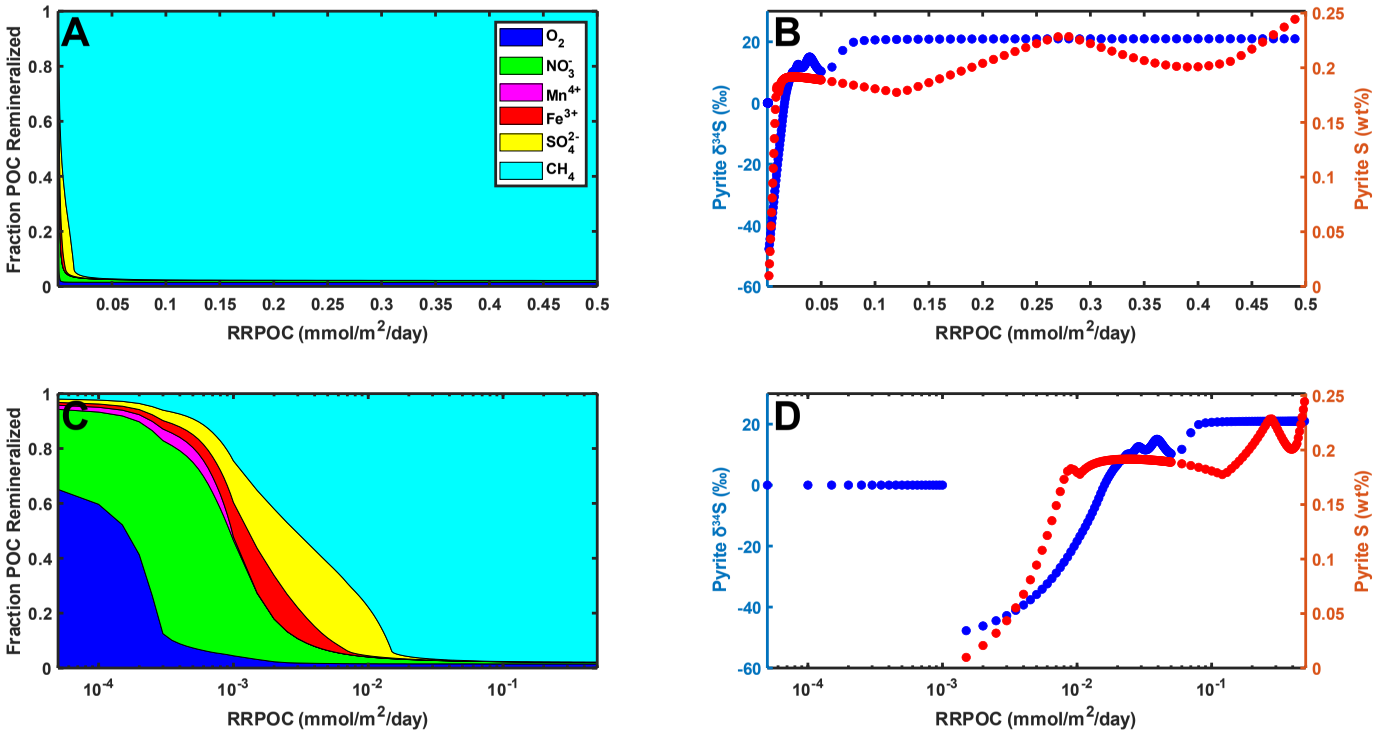

Figure B.10: 1 mM bottom water [SO_4^{2-}] model experiment. (A) Area plot of the fractional contribution of different electron acceptors to organic carbon remineralization at different initial sedimentary POC concentrations for a bottom water sulfate concentration of 1 mM and a bottom water O_2 concentration of 10 μM. Shaded areas represent the fractional contributions of oxic respiration (dark blue), denitrification (green), manganese reduction (magenta), iron reduction (red), sulfate reduction (yellow), and fermentation (cyan) to overall POC remineralization. (B) Plot of pyrite δ^{34}S (left axis; blue circles) and pyrite sulfur concentration (right axis; red circles) for buried pyrite exiting the bottom of the model domain as a funtion of POC rain rate. (C) and (D) are replicate plots of (A) and (B), respectively, with the initial POC plotted on a log scale instead of a linear scale.

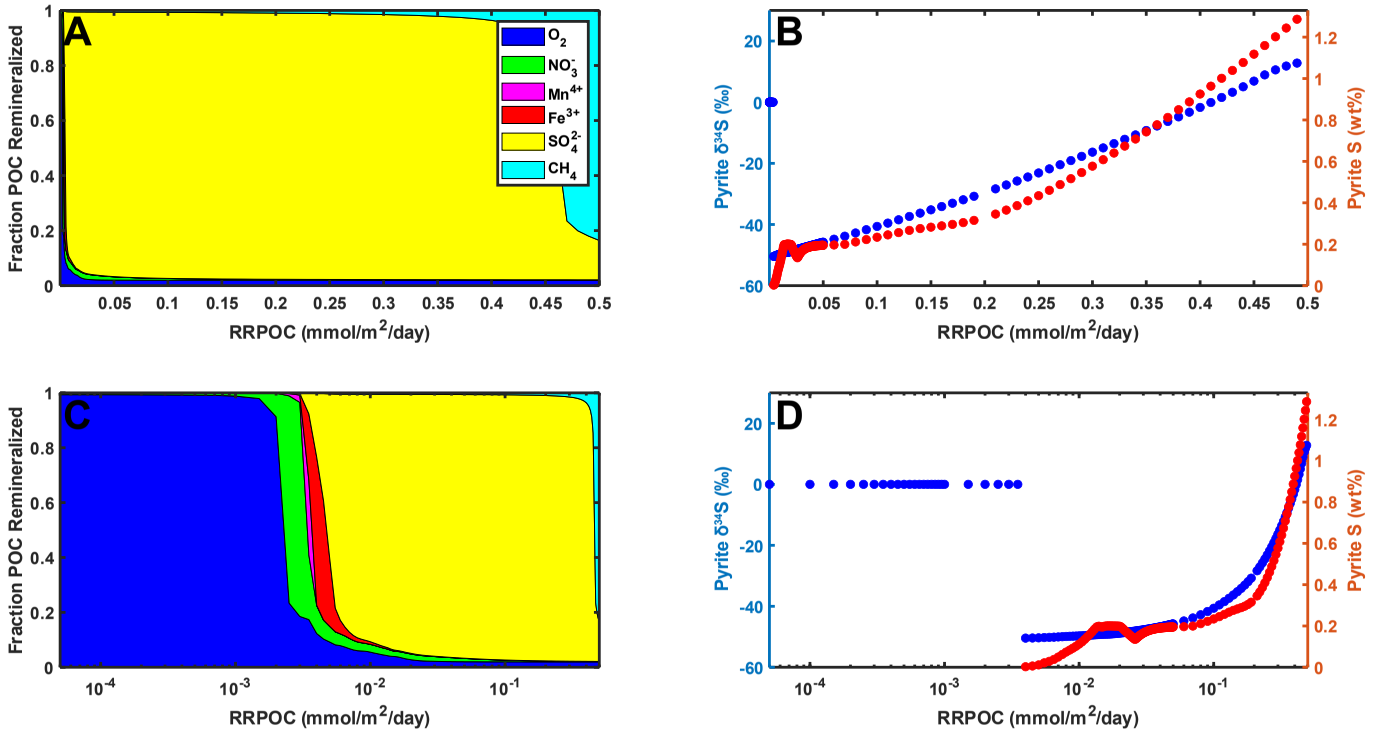

Figure B.11: 10x lower half-saturation and inhibition constants model experiment. (A) Area plot of the fractional contribution of different electron acceptors to organic carbon remineralization at different initial sedimentary POC concentrations for runs in which all half-saturation and inhibition constants were decreased by an order of magnitude. Shaded areas represent the fractional contributions of oxic respiration (dark blue), denitrification (green), manganese reduction (magenta), iron reduction (red), sulfate reduction (yellow), and fermentation (cyan) to overall POC remineralization. (B) Plot of pyrite $\delta^{34}S$ (left axis; blue circles) and pyrite sulfur concentration (right axis; red circles) for buried pyrite exiting the bottom of the model domain as a funtion of POC rain rate. (C) and (D) are replicate plots of (A) and (B), respectively, with the initial POC plotted on a log scale instead of a linear scale.

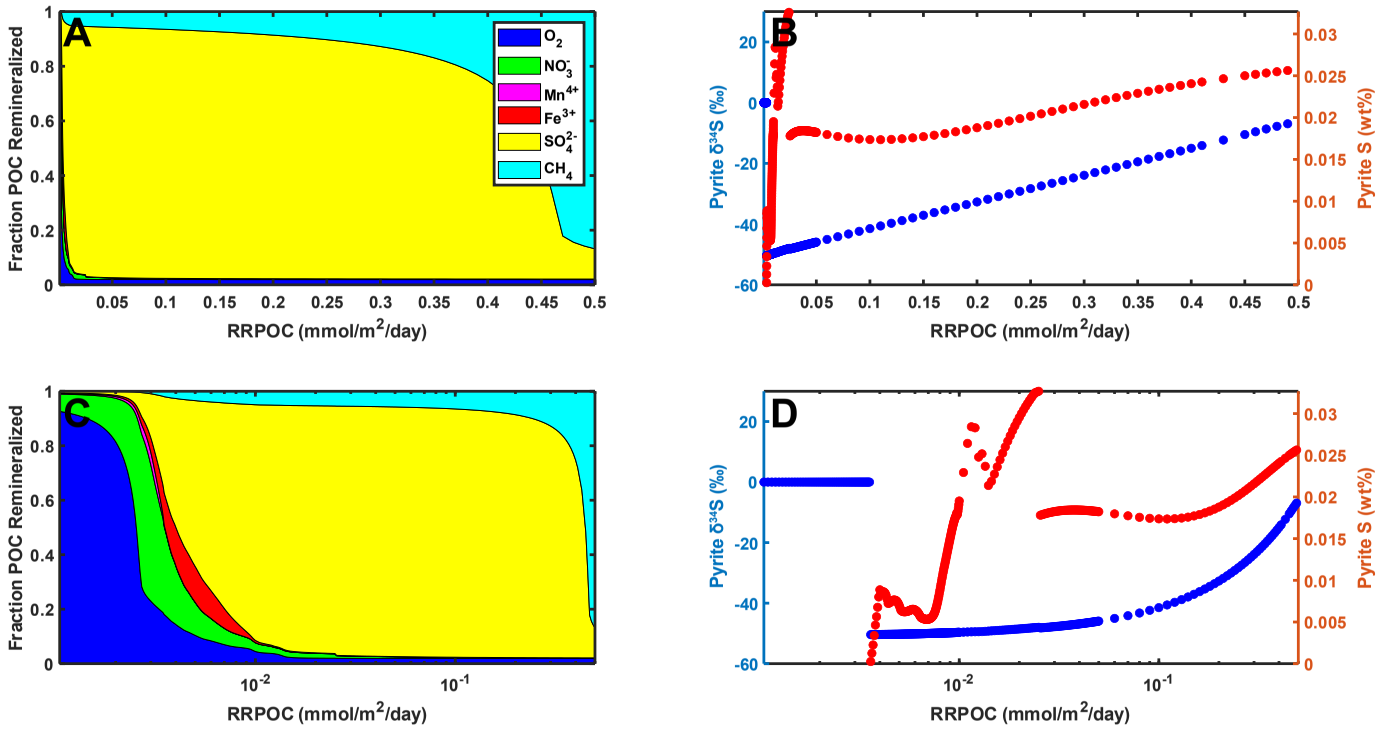

Figure B.12: FeS + S_0 pyrite formation model experiment. (A) Area plot of the fractional contribution of different electron acceptors to organic carbon remineralization at different initial sedimentary POC concentrations for runs in which only the FeS + S^0 pyrite formation mechanism was active. Shaded areas represent the fractional contributions of oxic respiration (dark blue), denitrification (green), manganese reduction (magenta), iron reduction (red), sulfate reduction (yellow), and fermentation (cyan) to overall POC remineralization. (B) Plot of pyrite δ^{34}S (left axis; blue circles) and pyrite sulfur concentration (right axis; red circles) for buried pyrite exiting the bottom of the model domain as a funtion of POC rain rate. (C) and (D) are replicate plots of (A) and (B), respectively, with the initial POC plotted on a log scale instead of a linear scale.

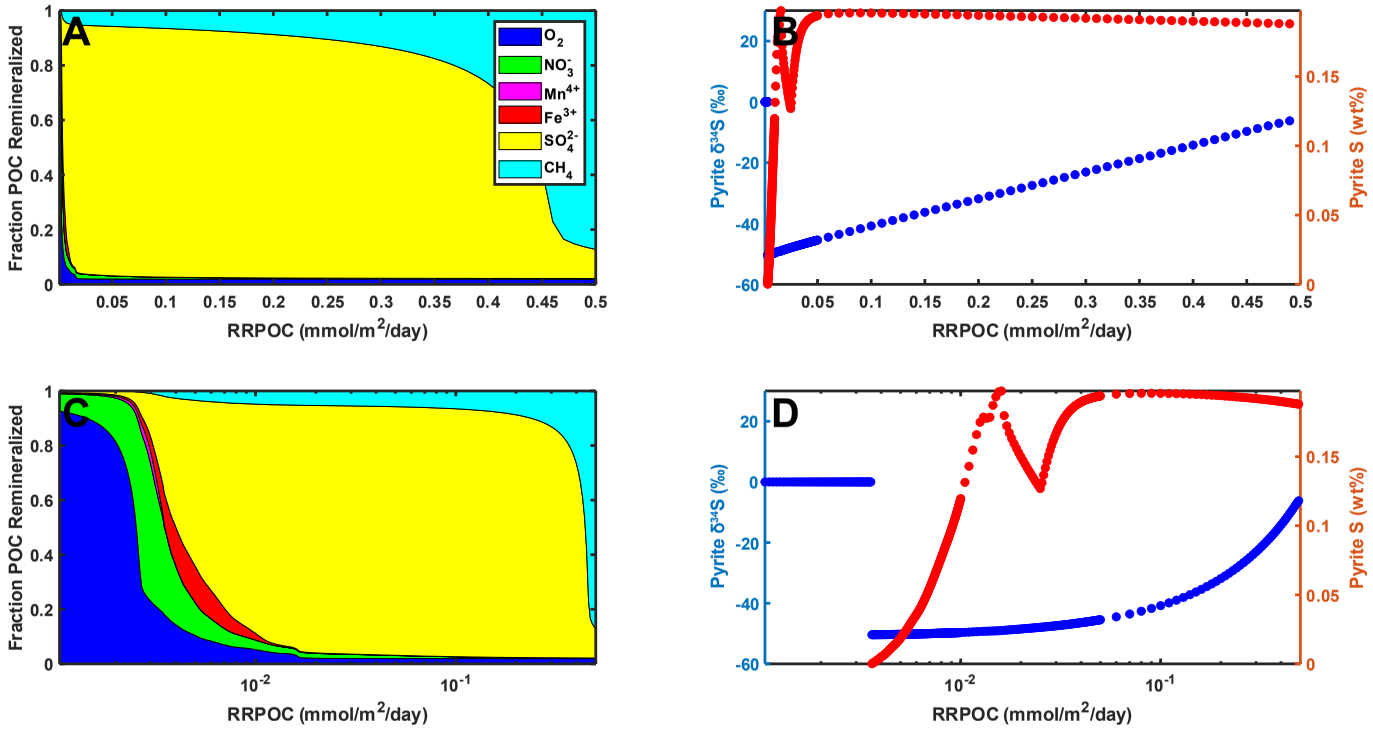

Figure B.13: FeS + H_2S pyrite formation model experiment. (A) Area plot of the fractional contribution of different electron acceptors to organic carbon remineralization at different initial sedimentary POC concentrations for runs in which only the FeS + H_2S pyrite formation mechanism was active. Shaded areas represent the fractional contributions of oxic respiration (dark blue), denitrification (green), manganese reduction (magenta), iron reduction (red), sulfate reduction (yellow), and fermentation (cyan) to overall POC remineralization. (B) Plot of pyrite δ^{34}S (left axis; blue circles) and pyrite sulfur concentration (right axis; red circles) for buried pyrite exiting the bottom of the model domain as a funtion of POC rain rate. (C) and (D) are replicate plots of (A) and (B), respectively, with the initial POC plotted on a log scale instead of a linear scale.

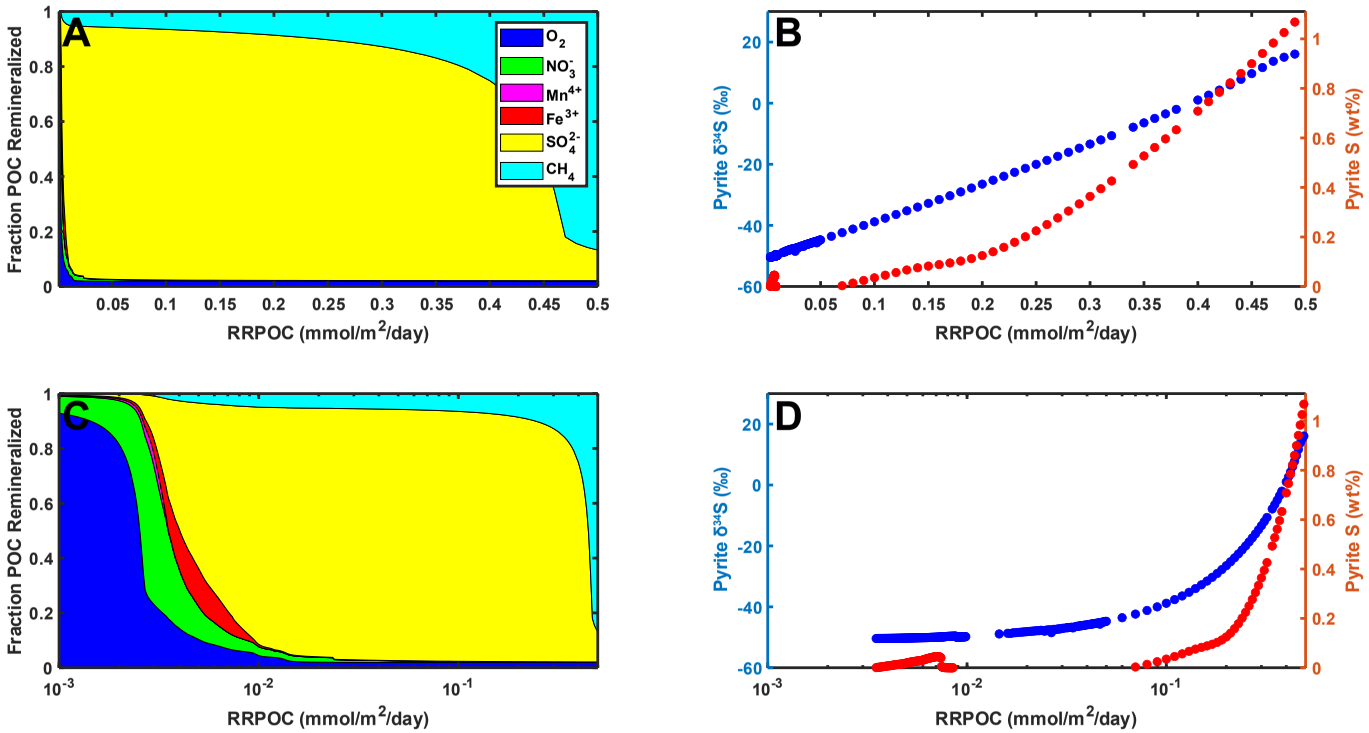

Figure B.14: $FeCO_3 + H_2S$ pyrite formation model experiment. (A) Area plot of the fractional contribution of different electron acceptors to organic carbon remineralization at different initial sedimentary POC concentrations for runs in which only the $FeCO_3 + H_2S$ pyrite formation mechanism was active. Shaded areas represent the fractional contributions of oxic respiration (dark blue), denitrification (green), manganese reduction (magenta), iron reduction (red), sulfate reduction (yellow), and fermentation (cyan) to overall POC remineralization. (B) Plot of pyrite $\delta^{34}S$ (left axis; blue circles) and pyrite sulfur concentration (right axis; red circles) for buried pyrite exiting the bottom of the model domain as a funtion of POC rain rate. (C) and (D) are replicate plots of (A) and (B), respectively, with the initial POC plotted on a log scale instead of a linear scale.

Appendix C

SUPPLEMENTARY MATERIAL FOR CHAPTER V

Table C.1: Aqueous sulfur concentration and $\delta^{34}S$ data. Sample depth and concentration data from [128, 234, 290].

Expedition	Site	Hole	Core	Type	Section	Top offset on section (cm)	Bottom offset on section (cm)	Top depth CSF-A (m)	Shipboard $[SO_4^{2-}]$ (mM)	SO_4^{2-} $\delta^{34}S$ (‰)	Error (1σ)	H_2S $\delta^{34}S$ (‰)	Error (1σ)
361	U1474	B	1	H	1	145	150	1.45		22.14	0.02		
361	U1474	B	1	H	2	145	150	2.9	27.3	23.53	0.13		
361	U1474	A	1	H	3	145	150	3.96	27.0				
361	U1474	B	2	H	1	145	150	6.25		27.01	0.07		
361	U1474	B	2	H	2	145	150	7.75	25.1	28.04	0.05		
361	U1474	B	2	H	3	145	150	9.25		29.07	0.04		
361	U1474	B	2	H	4	145	150	10.75	24.0	30.03	0.10		
361	U1474	B	2	H	6	76	81	13.06		31.56	0.01		
361	U1474	A	2	H	6	116	121	13.32	23.8				
361	U1474	B	3	H	2	145	150	17.25	22.7	32.75	0.02		
361	U1474	B	3	H	3	145	150	18.75	21.9	33.52	0.03		
361	U1474	B	3	H	4	145	150	20.25		34.40	0.14		
361	U1474	B	3	H	5	145	150	21.75		35.09	0.20		
361	U1474	A	3	H	6	95	100	22.82	21.1				
361	U1474	B	3	H	6	145	150	23.25		35.75	0.08		
361	U1474	B	4	H	2	98	103	25.74		37.88	0.09		
361	U1474	A	4	H	6	145	150	33.35	18.5				
361	U1474	B	5	H	1	145	150	34.75		40.92	0.07		
361	U1474	B	5	H	2	145	150	36.25		43.43	0.02		
361	U1474	B	5	H	3	145	150	37.75		44.07	0.03		
361	U1474	B	5	H	6	65	70	41.45		46.00	0.05		
361	U1474	A	5	H	6	145	150	42.85	16.6				
361	U1474	B	6	H	3	145	150	47.25		48.46	0.03		
361	U1474	B	6	H	4	145	150	48.75		49.80	0.10		
361	U1474	B	6	H	5	145	150	50.25		50.59	0.05		
361	U1474	B	6	H	6	145	100	51.25		50.63	0.11		
361	U1474	A	6	H	6	145	150	52.35	14.4				
361	U1474	B	7	H	1	145	150	53.75		50.78	0.07		
361	U1474	B	7	H	2	145	150	55.25		52.94	0.08		
361	U1474	B	7	H	3	145	150	56.75		52.50	0.24		

Expedition	Site	Hole	Core	Type	Section	Top offset on section (cm)	Bottom offset on section (cm)	Top depth CSF-A (m)	Shipboard $[SO_4^{2-}]$ (mM)	SO_4^{2-} $\delta^{34}S$ (‰)	Error (1σ)	H_2S $\delta^{34}S$ (‰)	Error (1σ)
361	U1474	B	7	H	6	145	100	60.75		55.62	0.24		
361	U1474	A	7	H	6	145	150	61.85	12.9				
361	U1474	B	8	H	3	145	150	66.25		58.75	0.22		
361	U1474	B	8	H	6	145	150	70.75		61.35	0.45		
361	U1474	A	8	H	6	145	150	71.35	11.5				
361	U1474	B	9	H	3	145	150	75.75		63.15	0.01		
361	U1474	B	9	H	6	95	100	79.75		66.00	0.01		
361	U1474	A	9	H	6	145	150	80.85	10.0				
361	U1474	B	10	H	1	145	150	82.25		64.27	0.02		
361	U1474	B	10	H	3	140	150	85.25		69.82	0.73		
361	U1474	B	1	H	1	145	150	1.45		22.14	0.02		
361	U1474	B	1	H	2	145	150	2.9	27.3	23.53	0.13		
361	U1474	A	1	H	3	145	150	3.96	27.0				
361	U1474	B	2	H	1	145	150	6.25		27.01	0.07		
361	U1474	B	2	H	2	145	150	7.75	25.1	28.04	0.05		
361	U1474	B	2	H	3	145	150	9.25		29.07	0.04		
361	U1474	B	2	H	4	145	150	10.75	24.0	30.03	0.10		
361	U1474	B	2	H	6	76	81	13.06		31.56	0.01		
361	U1474	A	2	H	6	116	121	13.32	23.8				
361	U1474	B	3	H	2	145	150	17.25	22.7	32.75	0.02		
361	U1474	B	3	H	3	145	150	18.75	21.9	33.52	0.03		
361	U1474	B	3	H	4	145	150	20.25		34.40	0.14		
361	U1474	B	3	H	5	145	150	21.75		35.09	0.20		
361	U1474	A	3	H	6	95	100	22.82	21.1				
361	U1474	B	3	H	6	145	150	23.25		35.75	0.08		
361	U1474	B	4	H	2	98	103	25.74		37.88	0.09		
361	U1474	A	4	H	6	145	150	33.35	18.5				
361	U1474	B	5	H	1	145	150	34.75		40.92	0.07		
361	U1474	B	5	H	2	145	150	36.25		43.43	0.02		
361	U1474	B	5	H	3	145	150	37.75		44.07	0.03		

Expedition	Site	Hole	Core	Type	Section	Top offset on section (cm)	Bottom offset on section (cm)	Top depth CSF-A (m)	Shipboard $[SO_4^{2-}]$ (mM)	SO_4^{2-} $\delta^{34}S$ (‰)	Error (1σ)	H_2S $\delta^{34}S$ (‰)	Error (1σ)
361	U1474	B	5	H	6	65	70	41.45		46.00	0.05		
361	U1474	A	5	H	6	145	150	42.85	16.6				
361	U1474	B	6	H	3	145	150	47.25		48.46	0.03		
361	U1474	B	6	H	4	145	150	48.75		49.80	0.10		
361	U1474	B	6	H	5	145	150	50.25		50.59	0.05		
361	U1474	B	6	H	6	145	100	51.25		50.63	0.11		
361	U1474	A	6	H	6	145	150	52.35	14.4				
361	U1474	B	7	H	1	145	150	53.75		50.78	0.07		
361	U1474	B	7	H	2	145	150	55.25		52.94	0.08		
361	U1474	B	7	H	3	145	150	56.75		52.50	0.24		
361	U1474	B	7	H	6	145	100	60.75		55.62	0.24		
361	U1474	A	7	H	6	145	150	61.85	12.9				
361	U1474	B	8	H	3	145	150	66.25		58.75	0.22		
361	U1474	B	8	H	6	145	150	70.75		61.35	0.45		
361	U1474	A	8	H	6	145	150	71.35	11.5				
361	U1474	B	9	H	3	145	150	75.75		63.15	0.01		
361	U1474	B	9	H	6	95	100	79.75		66.00	0.01		
361	U1474	A	9	H	6	145	150	80.85	10.0				
361	U1474	B	10	H	1	145	150	82.25		64.27	0.02		
361	U1474	B	10	H	3	140	150	85.25		69.82	0.73		
361	U1474	A	10	H	5	145	150	88.85	9.4				
361	U1474	B	10	H	6	95	100	89.25		71.76	0.21		
361	U1474	B	11	H	3	140	150	94.75		74.23	0.02		
361	U1474	B	11	H	6	115	120	98.95		78.19	0.11		
361	U1474	A	11	H	6	66	71	99.06	7.7				
361	U1474	B	12	H	1	145	150	101.25		77.29	0.06		
361	U1474	B	12	H	3	145	150	104.25		78.35	0.12		
361	U1474	B	12	H	6	145	150	108.75		83.65	0.08		
361	U1474	A	12	H	6	146	151	109.42	6.6				

Expedition	Site	Hole	Core	Type	Section	Top offset on section (cm)	Bottom offset on section (cm)	Top depth CSF-A (m)	Shipboard $[SO_4^{2-}]$ (mM)	SO_4^{2-} $\delta^{34}S$ (‰)	Error (1σ)	H_2S $\delta^{34}S$ (‰)	Error (1σ)
361	U1474	B	13	H	3	145	150	113.75		86.55	0.11		
361	U1474	B	13	H	6	115	120	117.95		90.44	0.05		
361	U1474	A	13	H	6	106	111	118.5	5.9				
361	U1474	B	14	H	2	145	150	121.75		90.10	0.15		
361	U1474	B	14	H	6	145	150	127.75		96.26	0.04		
361	U1474	A	14	H	6	145	150	128.36	5.1				
361	U1474	B	15	H	2	145	150	131.25		93.21	0.10		
361	U1474	B	15	H	6	145	150	137.25		102.25	0.12		
361	U1474	A	15	H	6	145	150	137.89	4.6				
361	U1474	B	16	H	3	140	150	142.2		103.38	0.06		
361	U1474	B	16	H	6	140	150	146.24		106.91	0.06		
361	U1474	A	16	H	6	107	112	146.97	4.2				
361	U1474	A	17	H	6	146	151	156.89	3.8				
361	U1474	A	18	H	6	146	151	166.36	3.5				
361	U1474	A	19	H	6	145	150	175.89	3.2				
361	U1474	A	20	H	6	145	150	185.34	3.0				
361	U1474	A	21	H	6	143	148	194.81	2.9				
361	U1474	A	22	H	6	145	150	204.39	2.7				
361	U1474	A	25	H	6	106	111	230.57	2.7				
361	U1475	B	1	H	3	145	150	4.45	27.7				
361	U1475	B	2	H	1	145	150	9.95		24.88	0.04		
361	U1475	B	2	H	6	145	150	15.35	26.1				
361	U1475	B	3	H	6	145	150	24.85	24.8				
361	U1475	B	4	H	1	145	150	25.77		28.70	0.06		
361	U1475	B	4	H	6	145	150	34.36	22.9				
361	U1475	B	5	H	1	145	150	35.45		31.50	0.04		
361	U1475	B	5	H	6	145	150	43.85	20.9				
361	U1475	B	6	H	1	145	150	44.95		32.97	0.04		
361	U1475	B	7	H	1	145	150	49.45		34.68	0.10		
361	U1475	B	6	H	6	145	150	53.35	19.0				

Expedition	Site	Hole	Core	Type	Section	Top offset on section (cm)	Bottom offset on section (cm)	Top depth CSF-A (m)	Shipboard $[SO_4^{2-}]$ (mM)	SO_4^{2-} $\delta^{34}S$ (‰)	Error (1σ)	H_2S $\delta^{34}S$ (‰)	Error (1σ)
361	U1475	B	8	H	1	145	150	58.95		38.06	0.04		
361	U1475	B	7	H	6	97	102	62.37	18.1				
361	U1475	B	9	H	1	140	150	68.4		40.25	0.08		
361	U1475	B	8	H	6	145	150	72.35	17.1				
361	U1475	B	10	H	1	140	150	77.9		42.27	0.08		
361	U1475	B	9	H	6	145	150	81.85	15.7				
361	U1475	B	11	H	1	140	150	87.4		44.99	0.04		
361	U1475	B	10	H	6	145	150	91.35	14.9				
361	U1475	B	12	H	1	140	150	96.9		46.68	0.07		
361	U1475	B	11	H	6	145	150	100.85	13.6				
361	U1475	B	13	H	1	140	150	106.4		49.30	0.04		
361	U1475	B	12	H	6	145	150	110.35	12.9				
361	U1475	B	14	H	1	140	150	115.9		50.05	0.04		
361	U1475	B	13	H	6	145	150	119.85	12.1				
361	U1475	B	14	H	6	145	150	129.35	11.2				
361	U1475	B	16	H	1	140	150	134.9		56.27	0.04		
361	U1475	B	15	H	5	145	150	137.35	10.9				
361	U1475	B	16	H	7	64	74	143.14		58.98	0.08		
361	U1475	B	16	H	6	145	150	148.35	10.0				
361	U1475	B	17	H	6	95	100	157.35	9.3				
361	U1475	B	18	H	6	145	150	167.35	8.8				
361	U1475	B	19	H	6	145	150	176.85	8.1				
361	U1475	B	20	H	6	145	150	186.35	8.0				
361	U1475	B	21	H	6	145	150	195.85	7.6				
361	U1475	B	22	H	6	145	150	205.35	7.1				
361	U1475	B	25	H	6	145	150	233.85	6.3				
361	U1478	B	2	H	1	145	150	2.45		27.58	0.08		
361	U1478	B	2	H	1	140	145	3.9	23.4				
361	U1478	B	2	H	3	145	150	5.45		35.07	0.07		
361	U1478	A	1	H	4	135	140	5.85	22.7				

Expedition	Site	Hole	Core	Type	Section	Top offset on section (cm)	Bottom offset on section (cm)	Top depth CSF-A (m)	Shipboard $[SO_4^{2-}]$ (mM)	SO_4^{2-} $\delta^{34}S$ (‰)	Error (1σ)	H_2S $\delta^{34}S$ (‰)	Error (1σ)
361	U1478	B	2	H	4	145	150	6.95	20.9	37.66	0.12		
361	U1478	B	2	H	5	145	150	8.45		40.33	0.05		
361	U1478	B	2	H	6	98	103	9.48		41.88	0.09		
361	U1478	B	3	H	1	145	150	11.95		45.55	0.06		
361	U1478	B	3	H	2	145	150	13.45	17.2	47.02	0.03		
361	U1478	B	3	H	3	145	150	14.95		48.38	0.00		
361	U1478	A	2	H	6	95	100	15.15	16.8				
361	U1478	B	3	H	4	145	150	16.45	15.9	49.24	0.10		
361	U1478	B	3	H	5	145	150	17.95		50.14	0.04		
361	U1478	B	3	H	6	95	100	18.95		50.70	0.07		
361	U1478	B	4	H	1	145	150	21.45		50.39	0.06		
361	U1478	B	4	H	1	145	150	21.45		50.69	0.19		
361	U1478	B	4	H	2	145	150	22.95	13.8	51.68	0.30		
361	U1478	B	4	H	3	145	150	24.45		52.29	0.05		
361	U1478	A	3	H	6	145	150	25.01	13.4				
361	U1478	B	4	H	4	145	150	25.95	12.9	53.01	0.39		
361	U1478	B	4	H	5	145	150	27.45		53.04	0.08		
361	U1478	B	4	H	6	145	150	28.95		53.58	0.10		
361	U1478	B	5	H	1	140	150	30.9		53.80	0.34		
361	U1478	B	5	H	2	140	150	32.4		52.87	#DIV/0!		
361	U1478	B	5	H	2	140	150	32.4		52.26	0.06		
361	U1478	B	5	H	3	140	150	33.9		54.98	0.18		
361	U1478	A	4	H	6	145	150	34.65	10.7				
361	U1478	B	5	H	4	140	150	35.4		55.87	0.09		
361	U1478	B	5	H	5	140	150	36.9		55.99	0.68		
361	U1478	B	5	H	6	90	100	37.9		56.62	0.19		
361	U1478	B	6	H	1	140	150	40.4		57.13	0.24		
361	U1478	B	6	H	2	140	150	41.9		58.14	0.24		
361	U1478	B	6	H	3	140	150	43.4		59.08	0.11		
361	U1478	A	5	H	6	145	150	44.15	7.3				

Expedition	Site	Hole	Core	Type	Section	Top offset on section (cm)	Bottom offset on section (cm)	Top depth CSF-A (m)	Shipboard $[SO_4^{2-}]$ (mM)	SO_4^{2-} $\delta^{34}S$ (‰)	Error (1σ)	H_2S $\delta^{34}S$ (‰)	Error (1σ)
361	U1478	B	6	H	4	140	150	44.9		59.20	0.51		
361	U1478	B	6	H	4	140	150	44.9		60.67	#DIV/0!		
361	U1478	B	6	H	5	140	150	46.4		60.70	0.24		
361	U1478	B	6	H	6	89	99	47.39		61.64	0.45		
361	U1478	B	7	H	1	140	150	49.9		60.77	0.04		
361	U1478	B	7	H	1	140	150	49.9		60.85	0.08		
361	U1478	B	7	H	2	140	150	51.4		60.10	0.03		
361	U1478	B	7	H	2	140	150	51.4		60.34	0.02		
361	U1478	B	7	H	3	140	150	52.9		63.88	0.08		
361	U1478	B	7	H	4	140	150	54.4		61.17	6.79		
361	U1478	B	7	H	5	140	150	55.9		65.94	0.04		
361	U1478	B	7	H	6	140	150	57.4		66.77	0.14		
361	U1478	B	8	H	3	140	150	62.4		70.35	0.05		
361	U1478	A	7	H	6	145	150	63.15	2.4				
361	U1478	B	8	H	5	140	150	65.4		71.87	0.00		
361	U1478	B	8	H	6	91	101	66.41		72.37	0.15		
361	U1478	B	9	H	1	140	150	68.9		57.82	0.02		
361	U1478	B	9	H	2	140	150	70.4		47.52	0.02		
361	U1478	B	9	H	3	140	150	71.9		22.27	0.05		
361	U1478	A	8	H	6	145	150	72.65	0.4				
361	U1478	B	9	H	6	140	150	76.4		25.15	0.31		
361	U1478	A	9	H	6	146	151	82.16	0.4				
361	U1478	B	10	H	6	90	100	85.4		21.72	0.51		
361	U1478	A	10	H	6	146	151	91.7	0.4				
361	U1478	B	11	H	6	140	150	95.4		21.52	0.62		
361	U1478	A	11	H	6	137	142	100.91	0.4				
361	U1478	B	12	H	6	140	150	104.9		18.94	0.22		
361	U1478	A	12	H	6	145	150	110.65	0.4				
361	U1478	B	13	H	6	100	110	114		22.58	0.33		
361	U1478	B	14	H	6	100	110	123.5		18.93	0.22		

Expedition	Site	Hole	Core	Type	Section	Top offset on section (cm)	Bottom offset on section (cm)	Top depth CSF-A (m)	Shipboard $[SO_4^{2-}]$ (mM)	SO_4^{2-} $\delta^{34}S$ (‰)	Error (1σ)	H_2S $\delta^{34}S$ (‰)	Error (1σ)
361	U1478	A	14	H	6	145	150	129.7	0.4				
361	U1478	A	16	H	6	114	119	148.41	0.4				
361	U1478	A	17	H	6	139	144	157.98	0.4				
361	U1478	A	18	H	6	127	132	167.47	0.4				
361	U1478	A	19	H	5	145	150	175.65	0.4				
361	U1478	A	20	H	6	145	150	186.65	0.4				
361	U1478	A	22	F	3	94	99	200.64	0.4				
361	U1478	A	24	F	3	96	101	210.11	0.4				
361	U1478	A	27	F	3	107	112	214.71	0.4				
361	U1478	A	29	F	3	97	102	224.19	0.4				
361	U1478	A	31	F	3	127	132	233.66	0.4				
363	U1482	A	1	H	1	0	0	0	28.5	21.18	0.06		
363	U1482	A	1	H	1	145	150	1.475		22.25	0.04		
363	U1482	A	2	H	3	145	150	7.375	26.9	25.40	0.09	-44.74	
363	U1482	A	2	H	6	100	105	11.425	25.7	27.87	0.02		
363	U1482	A	3	H	3	145	150	16.875	23.8	29.90	0.05	-41.70	0.15
363	U1482	A	3	H	6	135	140	21.275	23.7	31.56	0.05	-41.92	0.14
363	U1482	A	4	H	2	145	150	24.875	23.3	31.79	0.07	-40.25	
363	U1482	A	4	H	5	145	150	29.375	22.4	33.30	0.04	-39.93	
363	U1482	A	5	H	5	145	150	38.875	19.4	35.32	0.03		
363	U1482	A	6	H	6	145	150	49.875	17.6	37.04	0.27	-36.12	
363	U1482	A	7	H	6	95	100	58.875	15.1	38.82	0.10	-37.96	
363	U1482	A	8	H	6	145	150	68.875	12.8	42.57	0.11	-31.16	0.20
363	U1482	A	9	H	6	145	150	78.415	10.3	46.29	0.12	-27.12	0.28
363	U1482	A	10	H	6	145	150	87.945	7.1	52.00	0.10	-18.00	0.37
363	U1482	A	11	H	6	146	151	97.395	4.4	61.99	0.14	-4.52	0.15
363	U1482	A	12	H	6	145	150	106.915	2.2	77.73	0.21	13.55	0.12
363	U1482	A	13	H	6	145	150	116.415	1.0	61.30	2.10	29.78	
363	U1482	A	14	H	6	145	150	125.905	0.9	38.42	1.86	35.34	0.08
363	U1482	A	15	H	6	145	150	135.355	0.9	22.11	1.08		

Expedition	Site	Hole	Core	Type	Section	Top offset on section (cm)	Bottom offset on section (cm)	Top depth CSF-A (m)	Shipboard $[SO_4^{2-}]$ (mM)	SO_4^{2-} $\delta^{34}S$ (‰)	Error (1σ)	H_2S $\delta^{34}S$ (‰)	Error (1σ)
363	U1483	A	1	H	1	0	5	0.025	29.1	21.05	0.02		
363	U1483	A	1	H	3	145	150	4.475	28.3	22.02	0.02	-39.84	0.00
363	U1483	A	1	H	5	145	150	7.475	27.6	22.94	0.02	-45.80	0.00
363	U1483	A	2	H	3	145	150	13.075	25.3	26.00	0.02	-42.99	0.44
363	U1483	A	2	H	6	145	150	17.575	24.0	28.02	0.02	-41.34	0.38
363	U1483	A	3	H	3	145	150	22.575	22.2	30.98	0.02	-37.09	0.92
363	U1483	A	3	H	6	145	150	27.075	19.7	33.29	0.02	-29.04	0.24
363	U1483	A	4	H	6	142	147	36.145	10.8	47.09	0.02	-7.97	0.27
363	U1483	A	5	H	6	142	147	45.595	3.2	73.93	0.02	14.77	0.06
363	U1483	A	6	H	6	142	147	55.145	0.9	68.10	0.25	28.38	0.07
363	U1483	A	7	H	6	141	146	64.625	0.9	27.17	0.17	28.37	0.19
363	U1483	A	8	H	6	135	140	74.035	0.9	20.98	0.46	28.22	0.06
363	U1483	A	9	H	6	136	141	83.525	0.9	18.68	0.21	24.88	0.08
363	U1483	A	10	H	6	136	141	92.985	0.9	15.90	0.25	21.10	0.06
363	U1483	A	11	H	6	141	146	102.835	0.9	14.72	0.42		
363	U1483	A	12	H	6	143	148	112.455	0.9	14.31	0.37		
363	U1483	A	13	H	6	144	149	121.745	0.9	16.92	0.15		
363	U1483	A	14	H	6	141	146	131.245	0.9	12.86	0.23		
363	U1483	A	15	H	6	140	150	140.795	0.9	11.81	0.38		
363	U1483	A	16	H	6	117	120	149.935	1.2	19.64	0.14		
363	U1483	A	17	H	6	142	147	160.025	0.9	9.47	0.42		
363	U1485	A	1	H	1	0	5	0	28.9	21.10	0.04		
363	U1485	A	1	H	1	145	150	1.45		29.22	0.09		
363	U1485	A	1	H	2	145	150	2.95		38.52	0.04		
363	U1485	A	1	H	3	145	150	4.4	13.5	45.89	0.09		
363	U1485	A	1	H	4	145	150	5.95		50.80	0.04		
363	U1485	A	2	H	1	145	150	8.95		19.82	0.21		
363	U1485	A	2	H	2	145	150	10.45		20.01	0.16		
363	U1485	A	2	H	3	145	150	11.9		21.83	0.11		
363	U1486	A	1	H	1	0	1	0	28.3	21.18	0.12		

Expedition	Site	Hole	Core	Type	Section	Top offset on section (cm)	Bottom offset on section (cm)	Top depth CSF-A (m)	Shipboard $[SO_4^{2-}]$ (mM)	SO_4^{2-} $\delta^{34}S$ (‰)	Error (1σ)	H_2S $\delta^{34}S$ (‰)	Error (1σ)
363	U1486	A	1	H	1	145	150	1.45		24.20	0.01		
363	U1486	A	1	H	2	145	150	2.95		27.94	0.04		
363	U1486	A	1	H	3	140	150	4.4	24.4	30.79	0.09		
363	U1486	A	2	H	1	145	150	7.45		34.82	0.15		
363	U1486	A	2	H	2	145	150	8.95		36.68	0.08		
363	U1486	A	2	H	3	140	150	10.4	22.3	37.64	0.04		
363	U1486	A	2	H	4	145	150	11.95		39.29	0.03		
363	U1486	A	2	H	6	140	150	14.9	21.1	41.32	0.18		
363	U1486	A	3	H	3	135	145	19.8	20.5	44.07	0.05		
363	U1486	A	3	H	6	140	145	24.2	20.2	44.93	0.15		
363	U1486	A	4	H	3	140	150	29.4	20.1	45.04	0.36		
363	U1486	A	4	H	6	140	150	33.9	20.0	45.51	0.14		
363	U1486	A	5	H	6	140	150	43.4	19.8	45.25	0.06		
363	U1486	A	6	H	6	140	150	52.9	19.9	44.91	0.03		
363	U1486	A	7	H	5	140	150	60.9	19.9	43.89	0.41		
363	U1486	A	8	H	6	140	150	71.9	19.8	42.28	0.10		
363	U1486	A	10	H	6	140	150	90.9	20.1	39.79	0.04		
363	U1486	A	11	H	6	140	150	100.4	20.1	37.99	0.19		
363	U1486	A	13	H	6	140	150	114.9	20.1	35.58	0.02		
363	U1486	A	15	H	6	130	140	138.3	19.9	33.54	0.03		
363	U1486	A	17	H	6	140	150	157.4	20.3	31.59	0.09		
363	U1486	A	20	H	6	140	150	185.9	20.2	29.26	0.04		
363	U1486	A	21	H	6	110	120	195.1	20.8	28.60	0.07		
363	U1486	A	22	H	6	112	122	204.62	20.9	28.07	0.10		
363	U1486	A	23	H	3	141	151	209.91	21.0	27.60	0.04		
363	U1487	A	1	H	1	0	1	0	28.6	21.43	0.08		
363	U1487	A	1	H	3	145	150	4.45	24.1	28.67	0.16		
363	U1487	A	2	H	3	145	150	10.85	24.2				
363	U1487	A	2	H	6	110	115	15	24.3				
363	U1487	A	3	H	4	145	150	21.87	24.1	28.46	0.07		

Expedition	Site	Hole	Core	Type	Section	Top offset on section (cm)	Bottom offset on section (cm)	Top depth CSF-A (m)	Shipboard $[SO_4^{2-}]$ (mM)	SO_4^{2-} $\delta^{34}S$ (‰)	Error (1σ)	H_2S $\delta^{34}S$ (‰)	Error (1σ)
363	U1487	A	3	H	6	145	150	24.87	24.3				
363	U1487	A	4	H	6	115	120	34.05	24.1				
363	U1487	A	5	H	6	105	110	43.45	24.2				
363	U1487	A	6	H	6	135	140	53.25	24.4				
363	U1487	A	7	H	6	125	130	62.65	24.4				
363	U1487	A	8	H	6	145	150	72.35	24.2	28.29	0.09		
363	U1487	A	9	H	6	125	130	81.65	24.5				
363	U1487	A	10	H	6	115	120	91.05	24.4				
363	U1487	A	11	H	6	145	150	100.85	24.3				
363	U1487	A	12	H	6	105	110	109.95	24.1	28.34	0.09		
363	U1487	A	13	H	6	115	120	119.55	24.3				
363	U1487	A	14	H	2	140	150	123.3	24.3				
363	U1487	A	15	H	6	140	150	134.1	24.2				
363	U1487	A	16	H	6	140	150	143.6	24.4	28.22	0.04		
363	U1488	A	1	H	1	145	150	1.45	29.4	21.03	0.47		
363	U1488	A	1	H	2	145	150	2.95		21.69	0.08		
363	U1488	A	1	H	3	145	150	4.45	28.8	22.25	0.07		
363	U1488	A	2	H	1	145	150	7.35		22.91	0.08		
363	U1488	A	2	H	2	145	150	8.85		23.82	0.28		
363	U1488	A	2	H	3	140	150	10.3	27.4	23.98	0.09		
363	U1488	A	2	H	4	145	150	11.85		24.25	0.07		
363	U1488	A	2	H	5	145	150	13.35		24.87	0.07		
363	U1488	A	2	H	6	140	150	14.8	26.7	25.22	0.08		
363	U1488	A	3	H	1	145	150	16.85		25.61	0.09		
363	U1488	A	3	H	2	145	150	18.35		25.91	0.07		
363	U1488	A	3	H	3	140	150	19.8	26.2	26.24	0.25		
363	U1488	A	3	H	4	145	150	21.35		26.46	0.06		
363	U1488	A	3	H	5	145	150	22.85		26.46	0.08		
363	U1488	A	3	H	6	140	150	24.3	25.1	26.73	0.07		
363	U1488	A	4	H	1	145	150	26.35		27.08	0.10		

Expedition	Site	Hole	Core	Type	Section	Top offset on section (cm)	Bottom offset on section (cm)	Top depth CSF-A (m)	Shipboard $[SO_4^{2-}]$ (mM)	SO_4^{2-} $\delta^{34}S$ (‰)	Error (1σ)	H_2S $\delta^{34}S$ (‰)	Error (1σ)
363	U1488	A	4	H	2	145	150	27.85		27.37	0.10		
363	U1488	A	4	H	3	140	150	29.3	25.1	27.41	0.07		
363	U1488	A	4	H	4	145	150	30.85		27.52	0.06		
363	U1488	A	4	H	5	145	150	32.35		27.60	0.07		
363	U1488	A	4	H	6	140	150	33.8	24.6	27.81	0.09		
363	U1488	A	5	H	1	145	150	35.85		28.27	0.10		
363	U1488	A	5	H	2	145	150	37.35		28.39	0.07		
363	U1488	A	5	H	3	140	150	38.8	24.5	28.77	13.17		
363	U1488	A	5	H	4	145	150	40.35		28.82	0.14		
363	U1488	A	5	H	5	145	150	41.85		28.72	0.07		
363	U1488	A	5	H	6	140	150	43.3	24.0	28.84	0.07		
363	U1488	A	6	H	1	145	150	45.35		29.37	0.12		
363	U1488	A	6	H	1	145	150	45.35		29.14	0.02		
363	U1488	A	6	H	2	145	150	46.85		29.17	0.09		
363	U1488	A	6	H	3	140	150	48.3	23.6	29.33	0.07		
363	U1488	A	6	H	3	140	150	48.3	23.6	29.66	0.09		
363	U1488	A	6	H	4	145	150	49.85		29.51	0.09		
363	U1488	A	6	H	5	145	150	51.35		29.60	0.08		
363	U1488	A	6	H	6	140	150	52.8	23.4	29.35	0.09		
363	U1488	A	7	H	1	145	150	54.85		30.06	0.09		
363	U1488	A	7	H	2	145	150	56.35		29.53	0.11		
363	U1488	A	7	H	3	140	150	57.8	23.4	30.25	0.07		
363	U1488	A	7	H	4	145	150	59.35		29.81	0.06		
363	U1488	A	7	H	5	145	150	60.85		29.95	0.02		
363	U1488	A	7	H	6	140	150	62.3	23.0	29.77	0.10		
363	U1488	A	8	H	1	145	150	64.35		29.71	0.06		
363	U1488	A	8	H	2	145	150	65.85		29.81	0.12		
363	U1488	A	8	H	3	140	150	67.3	22.6	29.97	0.12		
363	U1488	A	8	H	4	145	150	68.85		30.24	0.09		
363	U1488	A	8	H	5	140	150	70.3	22.9	30.15	0.10		

Expedition	Site	Hole	Core	Type	Section	Top offset on section (cm)	Bottom offset on section (cm)	Top depth CSF-A (m)	Shipboard $[SO_4^{2-}]$ (mM)	SO_4^{2-} $\delta^{34}S$ (‰)	Error (1σ)	H_2S $\delta^{34}S$ (‰)	Error (1σ)
363	U1488	A	9	H	1	145	150	73.85		30.26	0.10		
363	U1488	A	9	H	2	145	150	75.35		30.41	0.08		
363	U1488	A	9	H	3	140	150	76.8	22.2	29.22	0.20		
363	U1488	A	9	H	4	145	150	78.35		30.25	0.10		
363	U1488	A	9	H	5	145	150	79.85		30.28	0.08		
363	U1488	A	9	H	6	140	150	81.3	22.3	30.37	0.09		
363	U1488	A	10	H	1	145	150	83.35		29.95	0.02		
363	U1488	A	10	H	2	145	150	84.85		30.04	0.09		
363	U1488	A	10	H	3	140	150	86.3	22.4	30.31	0.10		
363	U1488	A	10	H	4	145	150	87.85		30.55	0.10		
363	U1488	A	10	H	5	145	150	89.35		30.39	0.11		
363	U1488	A	10	H	6	110	120	90.5	22.4	30.49	0.08		
363	U1488	A	11	H	1	145	150	92.85		30.47	0.11		
363	U1488	A	11	H	2	145	150	94.35		30.23	0.09		
363	U1488	A	11	H	3	140	150	95.8	22.6	30.16	0.07		
363	U1488	A	11	H	4	145	150	97.35		32.84	0.44		
363	U1488	A	11	H	5	145	150	98.85		30.63	0.09		
363	U1488	A	11	H	6	140	150	100.3	21.9	30.62	0.11		
363	U1488	A	12	H	1	145	150	102.35		27.26	0.10		
363	U1488	A	12	H	3	140	150	105.3	22.6				
363	U1488	A	12	H	6	91	101	109.31	23.1				
363	U1488	A	13	H	3	140	150	114.8	22.3				
363	U1488	A	13	H	6	140	150	119.3	21.9				
363	U1488	A	14	H	3	140	150	124.3	21.9				
363	U1488	A	14	H	6	140	150	128.8	21.8				
363	U1488	A	15	H	3	140	150	133.8	22.3				
363	U1488	A	15	H	6	140	150	138.3	22.1				
363	U1488	A	16	H	3	140	150	143.3	22.0				
363	U1488	A	16	H	5	145	150	146.35		29.69	0.10		
363	U1488	A	16	H	6	140	150	147.8	21.9				

Expedition	Site	Hole	Core	Type	Section	Top offset on section (cm)	Bottom offset on section (cm)	Top depth CSF-A (m)	Shipboard $[SO_4^{2-}]$ (mM)	SO_4^{2-} $\delta^{34}S$ (‰)	Error (1σ)	H_2S $\delta^{34}S$ (‰)	Error (1σ)
363	U1488	A	17	H	6	140	150	157.3	23.2				
363	U1488	A	18	H	6	140	150	166.8	22.9				
363	U1488	A	19	H	6	140	150	176.3	22.6	28.49	0.10		
363	U1488	A	20	H	6	140	150	185.8	24.3	29.72	0.27		
363	U1488	A	21	H	6	140	150	195.3	22.4				
363	U1488	A	22	H	6	140	150	204.8	22.7				
363	U1488	A	23	H	6	140	150	214.3	24.0	27.64	0.10		
363	U1488	A	24	H	6	140	150	223.8	22.9				
363	U1488	A	25	H	6	140	150	233.3	22.9				
363	U1488	A	26	H	6	140	150	242.8	23.6	27.31	0.09		
363	U1488	A	27	H	6	140	150	252.3	25.1				
363	U1488	A	28	H	6	140	150	261.8	23.5	26.79	0.10		
363	U1488	A	29	H	6	140	150	271.28	24.0	26.70	0.11		
363	U1488	A	30	H	6	140	150	280.8	24.3	26.98	0.10		
363	U1488	A	31	H	6	140	150	290.3	26.4				
363	U1488	A	32	H	6	140	150	299.8	25.5				
363	U1488	A	34	F	3	100	110	309.1	24.4				
363	U1488	A	35	F	3	110	120	313.9	23.7				
KN223	KN223-02		GC1		1	5	10	0.075	27.5	20.6	0.1		
KN223	KN223-02		GC1		2	5	10	1.575	27.7	21.5	0.2		
KN223	KN223-02		LC1		2	75	80	1.595	26.2	23.5	0.5		
KN223	KN223-02		GC1		3	5	10	3.075	27.3	22.2	0.2		
KN223	KN223-02		LC1		3	70	80	3.125	26.9	22.4	0.1		
KN223	KN223-02		LC1		4	5	10	3.885	26.1	24.1	0.2		
KN223	KN223-02		LC1		4	5	10	3.885	26.1	24.0	0.2		
KN223	KN223-02		LC1		5	5	10	5.415	25.9	24.5	0.1		
KN223	KN223-02		LC1		6	5	10	6.945	25.5	25.9	0.2		
KN223	KN223-02		LC1		7	5	10	8.475	25.1	25.8	0.3		
KN223	KN223-02		LC1		8	5	10	10.005	24.8	27.0	0.2		
KN223	KN223-02		LC1		9	5	10	11.545	24.3	27.6	0.2		

Expedition	Site	Hole	Core	Type	Section	Top offset on section (cm)	Bottom offset on section (cm)	Top depth CSF-A (m)	Shipboard $[SO_4^{2-}]$ (mM)	SO_4^{2-} $\delta^{34}S$ (‰)	Error (1σ)	H_2S $\delta^{34}S$ (‰)	Error (1σ)
KN223	KN223-02		LC1		10	5	10	13.075	24.0	28.1	0.2		
KN223	KN223-02		LC1		12	5	10	16.145	23.2	29.8	0.2		
KN223	KN223-02		LC1		14	5	10	19.205	22.6	31.3	0.4		
KN223	KN223-02		LC1		15	108	113	21.765	22.0	32.1	0.1		
KN223	KN223-16		GC1		1	5	10	0.075	27.3	21.3	0.1		
KN223	KN223-16		LC1		1	5	10	0.075	27.1	21.3	0.1		
KN223	KN223-16		LC1		2	5	10	1.625		25.1	0.1		
KN223	KN223-16		GC1		3	5	10	3.075	22.4	28.8	0.2		
KN223	KN223-16		LC1		4	5	10	3.815	21.5	29.9	0.1		
KN223	KN223-16		LC1		5	5	10	5.355	19.7	33.1	0.2		
KN223	KN223-16		LC1		7	5	10	8.395	15.8	41.0	0.1		
KN223	KN223-16		LC1		8	5	10	9.925	14.0	47.1	0.2		
KN223	KN223-16		LC1		9	5	10	11.46	12.4	51.0	0.2		
KN223	KN223-16		LC1		11	5	10	14.54	9.8	61.0	0.1		
KN223	KN223-16		LC1		12	5	10	16.07	8.5	68.6	0.2		
KN223	KN223-16		LC1		13	5	10	17.6	7.3	71.0	0.2		
KN223	KN223-16		LC1		14	5	10	19.14	6.8	78.8	0.3		
KN223	KN223-16		LC1		15	5	10	20.67	5.8	84.5	0.3		
KN223	KN223-16		LC1		16	5	10	22.2	5.3	88.7	0.3		
KN223	KN223-16		LC1		17	5	10	23.76	4.7	91.5	0.3		
KN223	KN223-16		LC1		18	5	10	25.255	4.0	105.2	0.1		
KN223	KN223-16		LC1		19	5	10	26.795	3.8	99.8	0.2		
KN223	KN223-16		LC1		20	5	10	28.315	3.2	104.5	0.2		
KN223	KN223-16		LC1		22	5	10	31.375	2.1	108.6	0.2		
KN223	KN223-16		LC1		24	5	10	34.435	1.4	113.9	0.1		
KN223	KN223-16		LC1		25	5	10	35.965	0.7	115.9	0.2		
KN223	KN223-16		LC1		27	5	10	39.035	0.0	57.6	0.2		

Table C.2: I-CANDI discretization, sedimentation rate, bottom water concentration, and organic matter details for best fit model runs.

Site	Modeled Depth Range	Modeled Sedimentation Rate ($\frac{cm}{kyr}$)	Total depth boxes	Bottom Water T (°C)	Bottom Water $[O_2]$ (μM)	Bottom Water $[NO_3^-]$ (μM)	Bottom Water $[SO_4^{2-}]$ (mM)	RRPOC ($\frac{mmol}{m^2 day}$)	f_1	f_2	f_3	f_4	Reactive RRPOC ($\frac{mmol}{m^2 day}$)	Notes
U1474	0-300 m	3.7	400	2.2	200	30	28.2	0.0196	0	1	0	0	0.0196	k_2 increased by 50%
U1475	0-250 m	2.8	100	3.0	210	27.5	28.2	0.088	0	0.14	0.02	0.84	0.0141	
U1478	0-100 m	9.2	200	12.0	210	16	28.2	0.558	0.233	0.033	0.027	0.707	0.1635	
U1482	0-130 m	7	260	3.0	120	33	28.55	0.2225	0	0	1	0	0.2225	
U1483	0-60m	10	120	3.0	140	35	29.07	0.315	0	0.333	0	0.667	0.1049	
U1485	0-10m	62.5	200	3.5	100	37.5	28.9	3.41	0.2	0	0	0.8	0.6820	
U1486	0-210m	6	420	3.5	100	39	28.2	0.100	0.76	0.01	0	0.23	0.0770	
U1488	0-320m	3	320	2.0	130	37.5	29.4	0.071	0.237	0.052	0.051	0.66	0.0241	
KN223-02	0-30m	2	400	2.0	250	22.5	28.2	0.0079	0.75	0.22	0.03	0	0.0079	
KN223-16	0-50m	36	400	2.0	260	20	28.2	0.162	0.45	0.34	0.21	0	0.1620	

Table C.3: I-CANDI iron, methane, and sulfur parameters and results for best fit model runs.

Site	**RRFe** ($\frac{\mu mol}{m^2 day}$)	**Mean nSRR** ($\frac{\mu mol}{m^3 yr}$)	$^{34}\epsilon$	**Notes**	**Bottom CH_4 flux** ($\frac{\mu mol}{m^2 day}$)	**Bottom SO_4^{2-} flux** ($\frac{\mu mol}{m^2 day}$)	SO_4^{2-} **flux** $\delta^{34}S$ (‰)	**Final Pyrite Abundance (wt%)**	**Final Pyrite S (wt%)**	**Final Pyrite** $\delta^{34}S$ (‰)	$\delta^{34}S$ (‰)	**Initial** $^{34}\epsilon$ - $\delta^{34}S$ (‰)
U1474	6.1	47.6	88 / 59	Decrease from 88 to 59 at 50 m depth	0	0	-	0.11	0.21	-17	38	50
U1475	2.77	40	57		0	0	-	0.09	0.18	-13.8	34.8	22.2
U1478	40.5	2500	84		4.5	0	-	0.29	0.55	-38.2	59.2	24.8
U1482	3.97	82.4	68		1.6	0	-	0.06	0.11	2.4	18.6	49.4
U1483	3.85	259	75		12.1	0	-	0.04	0.08	1.43	19.57	55.43
U1485	82.5	21100	66		0.0	0	-	0.12	0.23	3.3	17.7	48.3
U1486	24.75	1100	74		-	-	27	0.26	0.49	-41.7	62.7	11.3
U1488	3.3	149	48		0.0	0.3	0	0.12	0.23	-21.7	42.7	5.3
KN223-02	1.65	56.2	57		0	0		0.03	0.06	-30.4	51.4	5.6
KN223-16	29.7	1900	79		0	0	-	0.06	0.12	-13.9	34.9	44.1

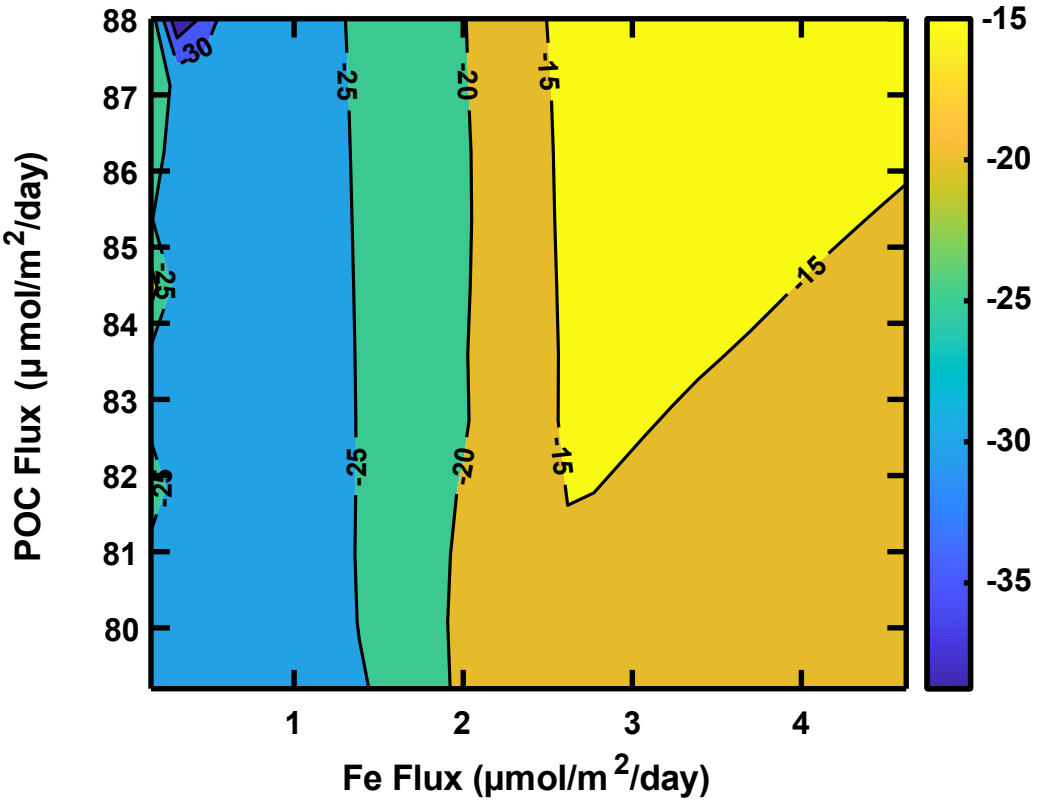

Figure C.1: Contour plot for the $\delta^{34}S$ of pyrite exiting the bottom of the model as a function of POC rain rate (vertical axis) and Fe(III) rain rate (horizontal axis) at Site U1475.

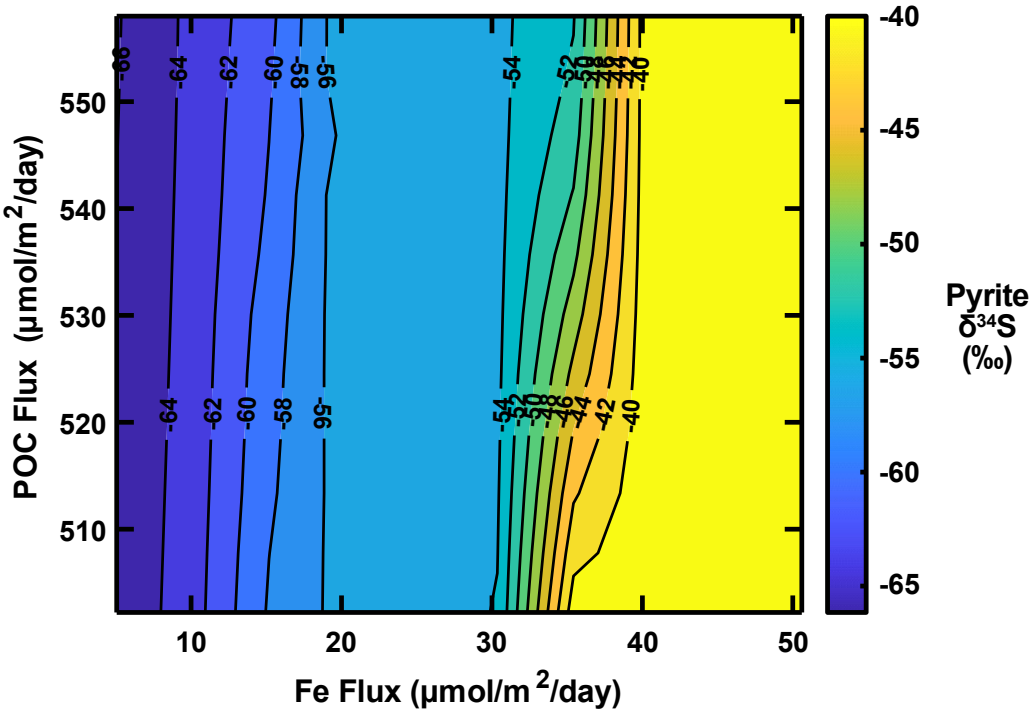

Figure C.2: Contour plot for the $\delta^{34}S$ of pyrite exiting the bottom of the model as a function of POC rain rate (vertical axis) and Fe(III) rain rate (horizontal axis) at Site U1478.

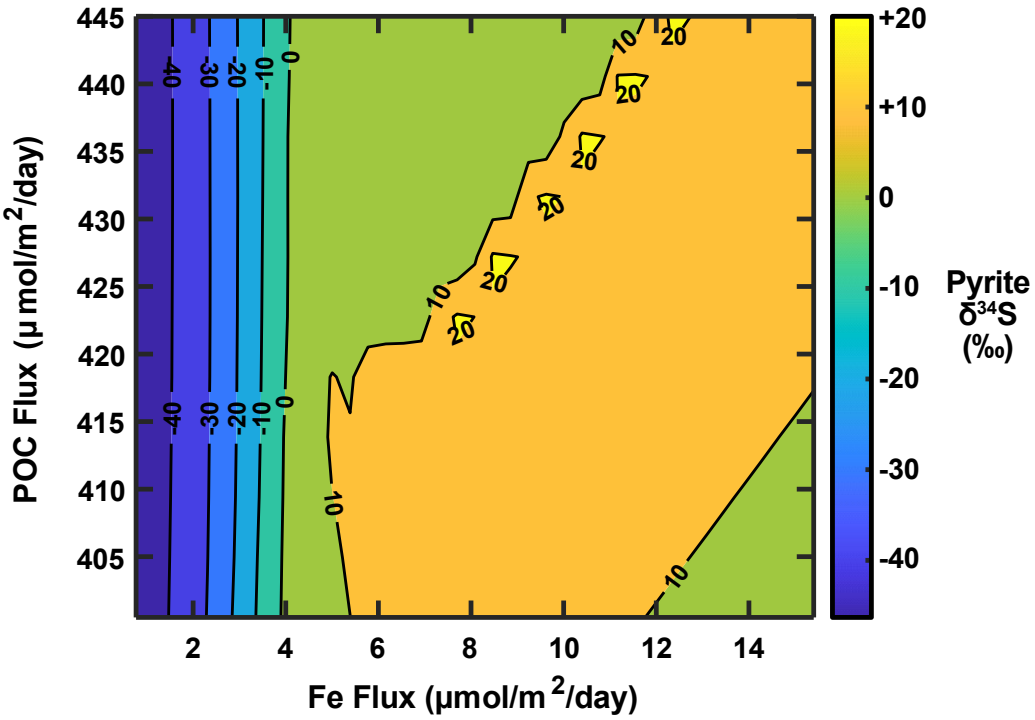

Figure C.3: Contour plot for the $\delta^{34}S$ of pyrite exiting the bottom of the model as a function of POC rain rate (vertical axis) and Fe(III) rain rate (horizontal axis) at Site U1482.

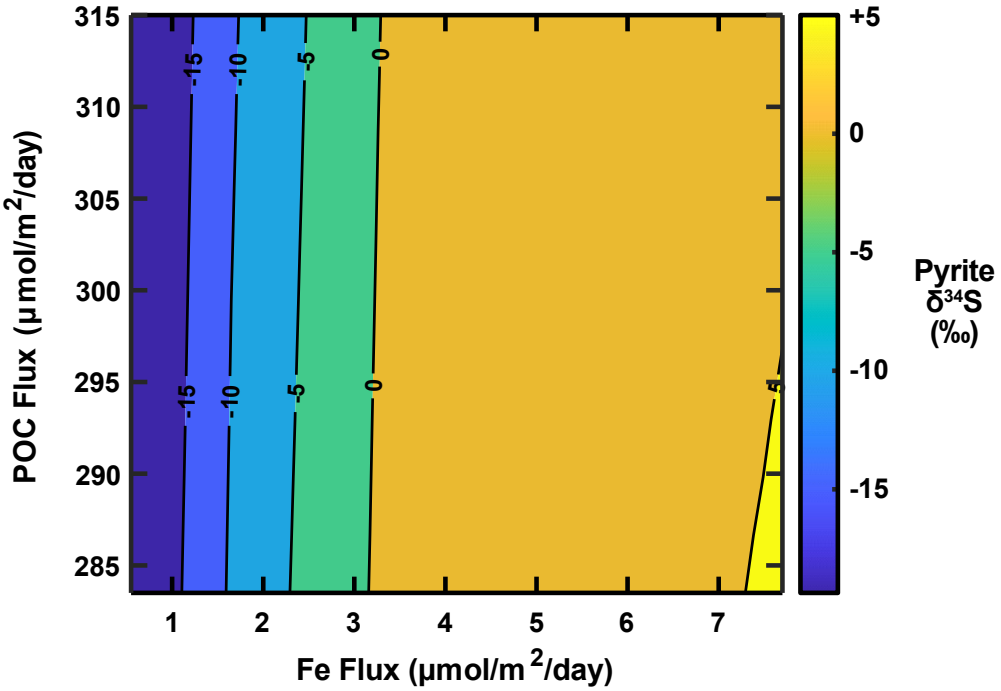

Figure C.4: Contour plot for the $\delta^{34}S$ of pyrite exiting the bottom of the model as a function of POC rain rate (vertical axis) and Fe(III) rain rate (horizontal axis) at Site U1483.

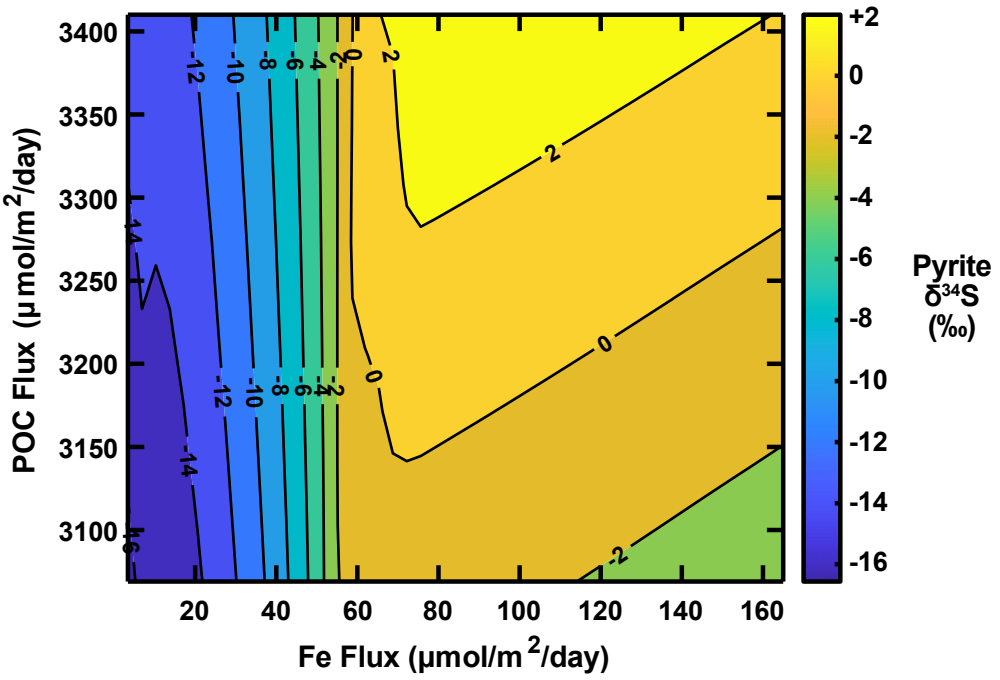

Figure C.5: Contour plot for the $\delta^{34}S$ of pyrite exiting the bottom of the model as a function of POC rain rate (vertical axis) and Fe(III) rain rate (horizontal axis) at Site U1485.

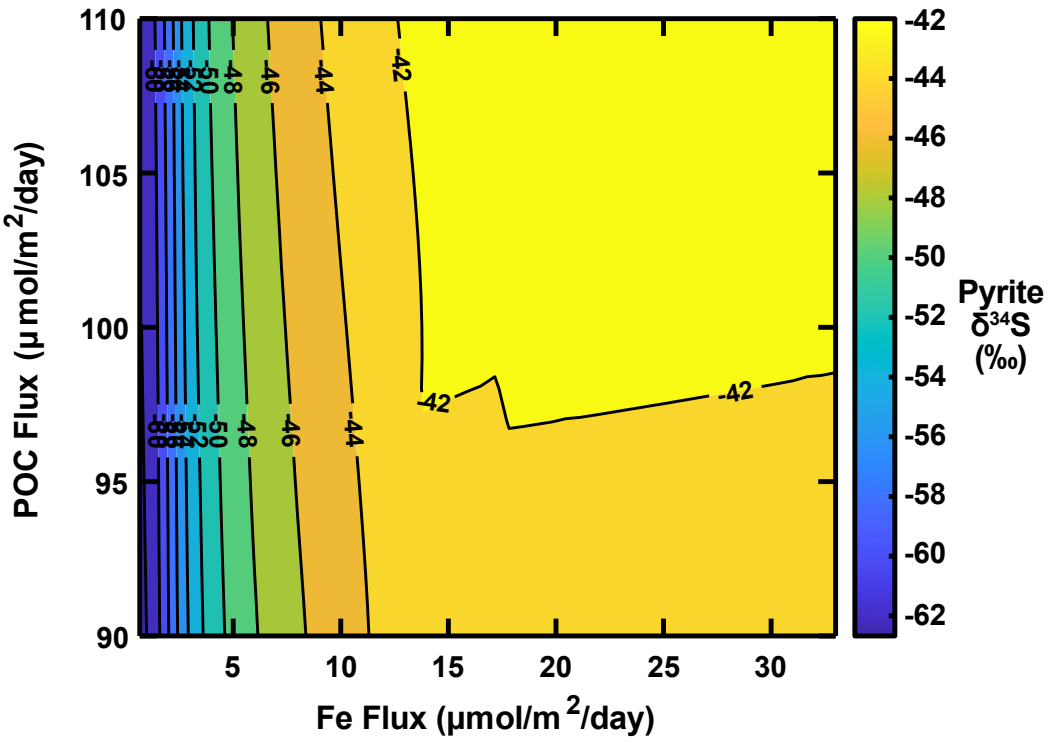

Figure C.6: Contour plot for the $\delta^{34}S$ of pyrite exiting the bottom of the model as a function of POC rain rate (vertical axis) and Fe(III) rain rate (horizontal axis) at Site U1486.

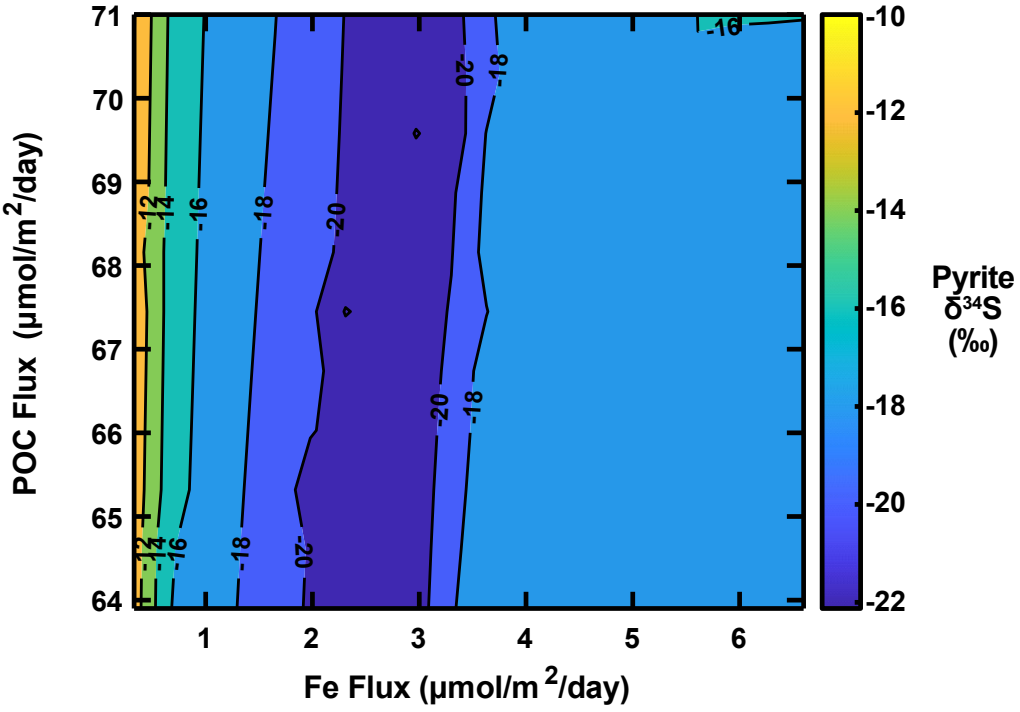

Figure C.7: Contour plot for the $\delta^{34}S$ of pyrite exiting the bottom of the model as a function of POC rain rate (vertical axis) and Fe(III) rain rate (horizontal axis) at Site U1488.

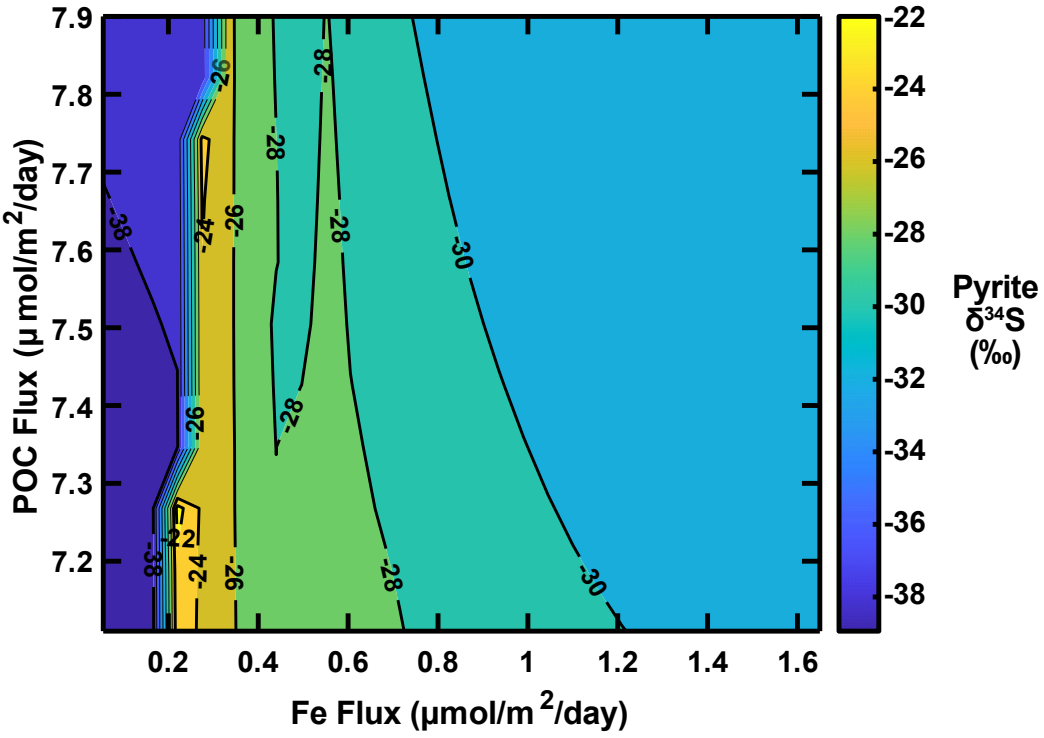

Figure C.8: Contour plot for the $\delta^{34}S$ of pyrite exiting the bottom of the model as a function of POC rain rate (vertical axis) and Fe(III) rain rate (horizontal axis) at Site KN223-02.

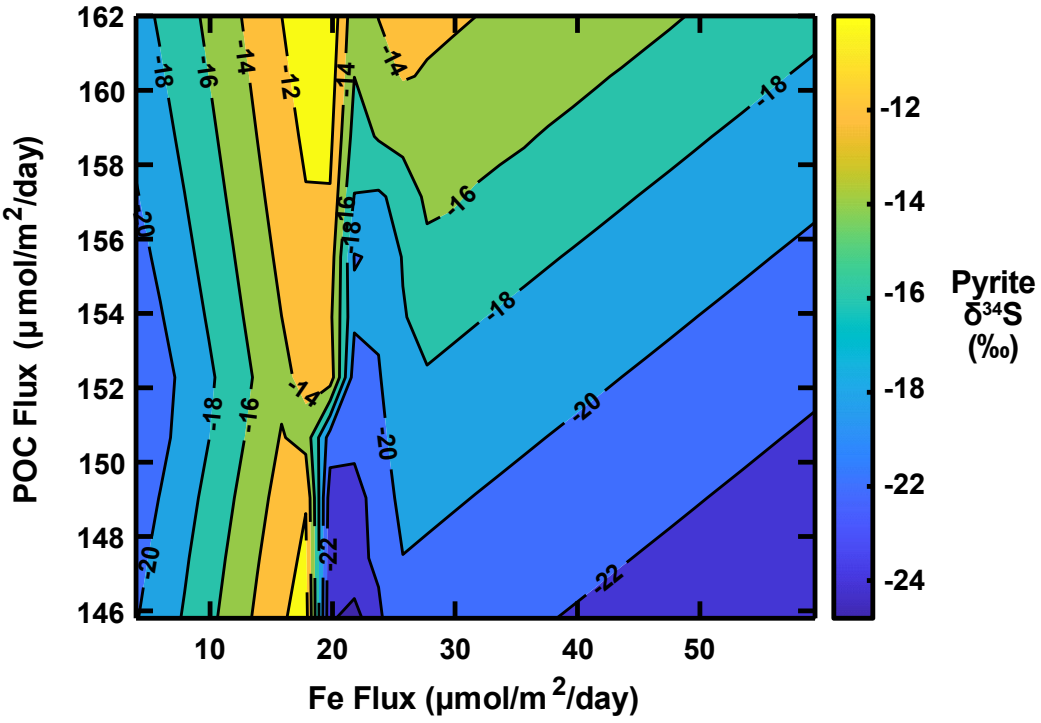

Figure C.9: Contour plot for the $\delta^{34}S$ of pyrite exiting the bottom of the model as a function of POC rain rate (vertical axis) and Fe(III) rain rate (horizontal axis) at Site KN223-16.

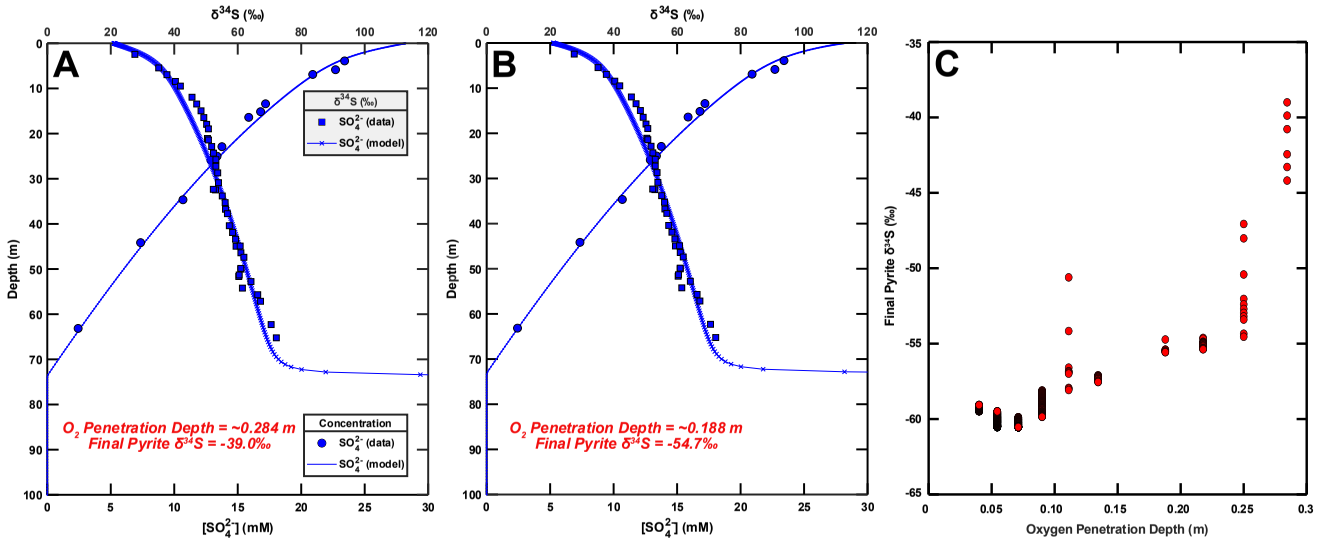

Figure C.10: Effects of oxygen penetration depth on modeled pyrite $\delta^{34}S$. (A) Model depth profiles (blue lines) for SO_4^{2-} concentration (bottom axis) and $\delta^{34}S$ (top axis) with data (filled symbols) overlain at Site U1478. Here, an additional extremely labile organic matter fraction with a 10x higher degradation rate constant than k_1 has been added and assigned a rain rate of 0.0106 $\frac{\text{mmol}}{\text{m}^2\text{day}}$. All other variables have been held constant at the values associated with the best fit model run for Site U1478. The oxygen penetration depth in the run is sim0.284 m and the final pyrite $\delta^{34}S$ is 39.0‰. (B) Model depth profiles for an additional model run in which the extremely labile organic matter rain rate has been increased to 0.2119 $\frac{\text{mmol}}{\text{m}^2\text{day}}$. The oxygen penetration depth decreases to sim0.188 m and the final pyrite $\delta^{34}S$ decreases to -54.7‰ despite very little visible change in the SO_4^{2-} model profiles. (C) Plot of final pyrite $\delta^{34}S$ as a function of oxygen penetration depth for model runs in which Fe(III) was consumed to completion within the depth domain. Although considerable scatter exists, the data show a general trend of lower final pyrite $\delta^{34}S$ as oxygen penetration depth decreases.

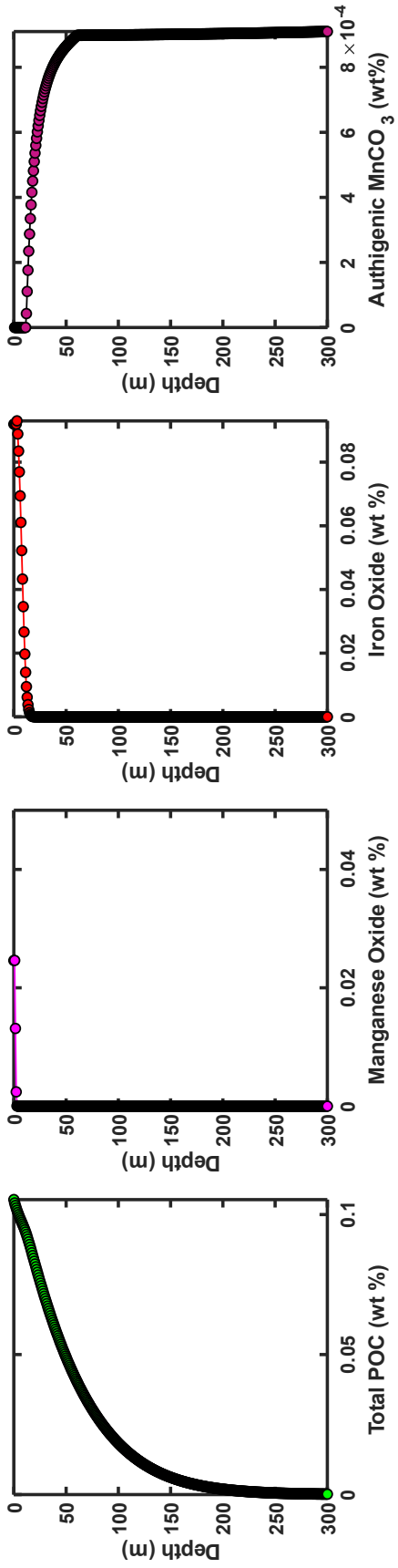

Figure C.11: Depth profiles for solid phases (POC, Mn oxides, Fe oxides, $MnCO_3$, FeS, elemental S, organic S, and pyrite S) for model run with RRPOC = 0.0196 $\frac{\text{mmol}}{\text{m}^2\text{day}}$, RRFe = 3.66 $\frac{\mu\text{mol}}{\text{m}^2\text{day}}$.

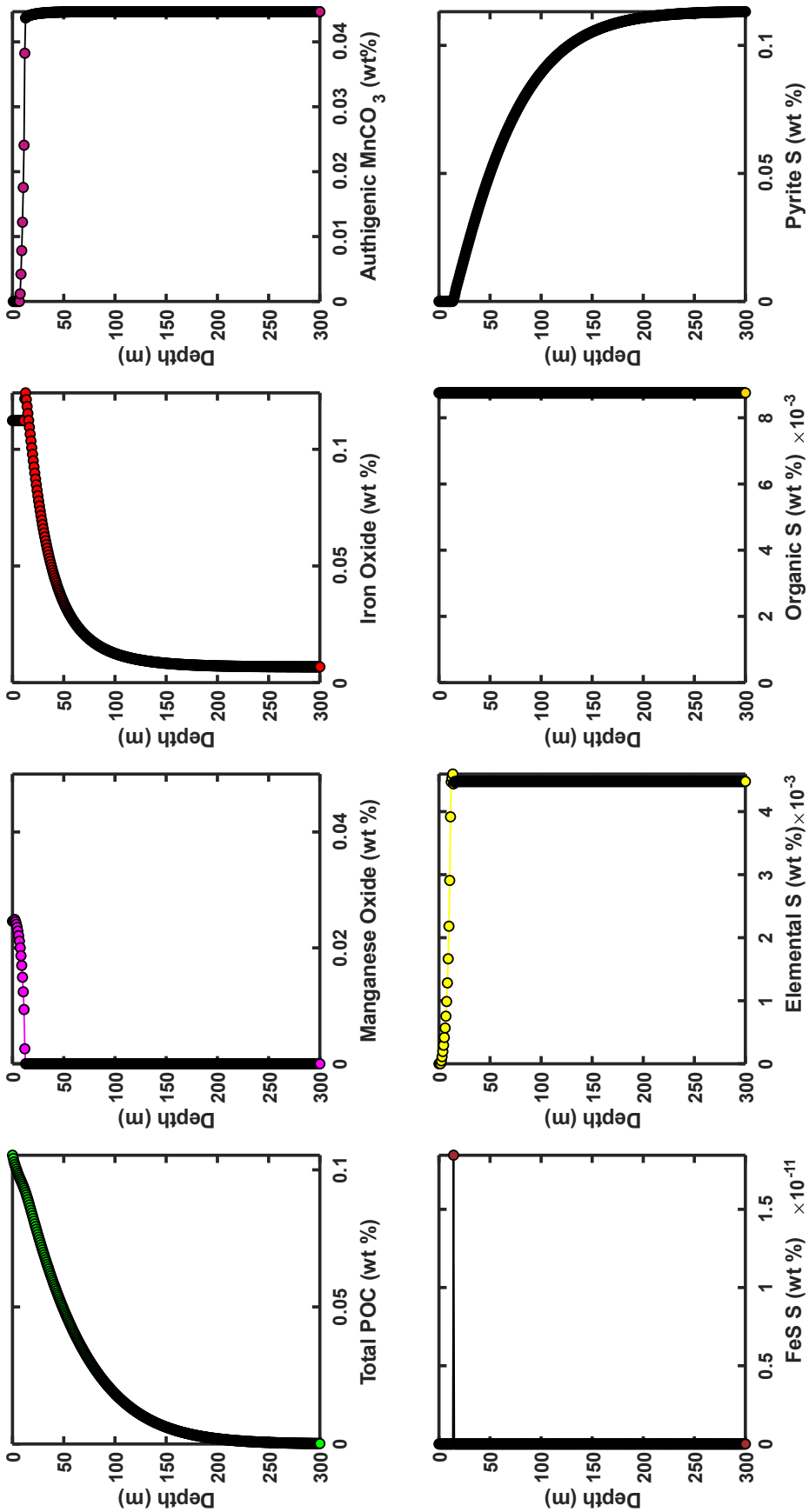

Figure C.12: Depth profiles for solid phases (POC, Mn oxides, Fe oxides, $MnCO_3$, FeS, elemental S, organic S, and pyrite S) for model run with RRPOC = 0.0196 $\frac{\text{mmol}}{\text{m}^2\text{day}}$, RRFe = 4.48 $\frac{\mu\text{mol}}{\text{m}^2\text{day}}$.

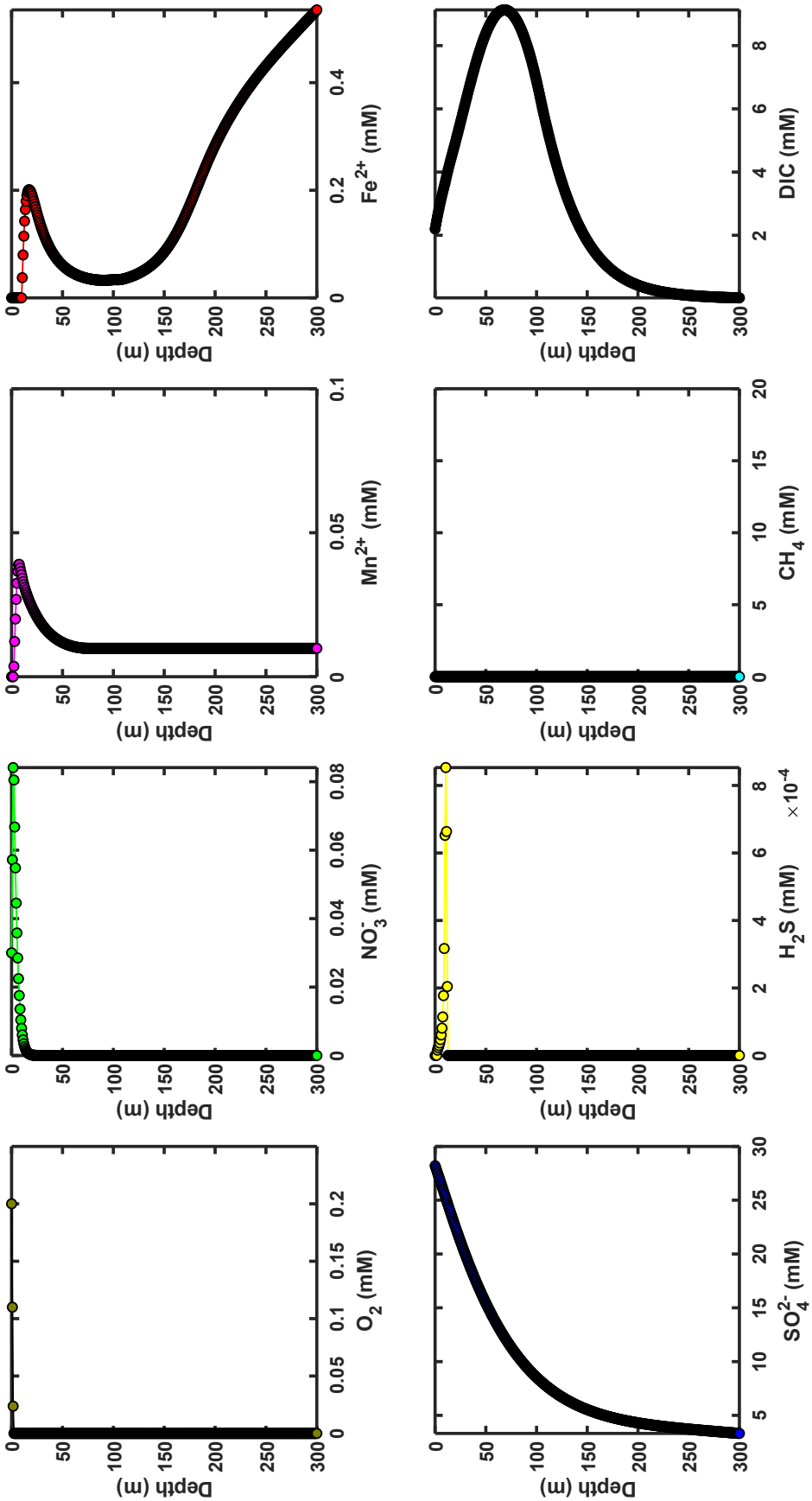

Figure C.13: Depth profiles for dissolved phases (O_2, NO_3^-, Mn^{2+}, Fe^{2+}, SO_4^{2-}, H_2S, CH_4, and dissolved inorganic carbon) for model run with RRPOC = 0.0196 $\frac{\text{mmol}}{\text{m}^2\text{day}}$, RRFe = 12.21 $\frac{\mu\text{mol}}{\text{m}^2\text{day}}$.

Appendix D

SUPPLEMENTARY MATERIAL FOR CHAPTER VI

Table D.1: DSDP, ODP, and IODP site numbers for which data were downloaded from the JANUS and LIMS databases.

1	2	3	4	5	6	7	8
9	10	11	12	13	14	15	16
17	18	19	20	21	22	23	24
25	26	27	28	29	30	31	32
33	34	35	36	37	38	39	40
41	42	43	44	45	46	47	48
49	50	51	52	53	54	55	56
57	58	59	60	61	62	63	64
65	66	67	68	69	70	71	72
73	74	75	76	77	78	79	80
81	82	83	84	85	86	87	88
89	90	91	92	93	94	95	96
97	98	99	100	101	102	103	104
105	106	107	108	111	112	113	114
115	116	117	118	119	120	121	122
123	124	125	126	127	128	129	130
131	132	133	134	135	136	137	138
139	140	141	142	143	144	146	147
148	149	150	151	152	153	154	155
156	157	158	159	160	161	162	163
164	165	166	167	168	169	170	171
172	173	174	175	176	177	178	179
180	181	182	183	184	185	186	187
188	189	190	191	192	193	194	195
196	197	198	199	200	202	203	204
205	206	207	208	209	210	211	212
213	214	215	216	217	218	219	220
221	222	223	224	225	226	227	228

229	230	231	232	233	234	235	236
237	238	239	240	241	242	243	245
246	248	249	250	251	252	253	254
255	256	257	258	259	260	261	262
263	264	265	266	267	268	269	270
271	272	273	274	275	276	277	278
279	280	281	282	283	284	285	286
287	288	289	290	291	292	293	294
295	296	297	298	299	301	302	303
304	305	306	307	308	309	310	311
313	314	315	316	317	318	319	320
321	322	323	324	325	326	327	328
329	330	331	332	333	334	335	336
337	338	339	340	341	342	343	344
345	346	347	348	349	350	352	353
354	355	356	357	358	359	360	361
362	363	364	365	366	367	368	369
370	371	372	373	374	375	376	377
378	379	380	381	382	383	384	385
386	387	388	389	390	391	392	393
394	395	396	397	398	399	400	401
402	403	404	405	406	407	408	409
410	411	412	413	415	416	417	418
419	420	421	422	423	424	425	427
428	429	430	431	432	433	434	435
436	438	439	440	441	442	443	444
445	446	447	448	449	450	451	452
453	454	455	456	457	458	459	460
461	462	463	464	465	466	467	468
469	470	471	472	473	474	475	476
477	478	479	480	481	482	483	484
485	486	487	488	489	490	491	492
493	494	495	496	497	498	499	500
501	502	503	504	505	506	507	508

509	510	511	512	513	514	515	516
517	518	519	520	521	522	523	524
525	526	527	528	529	530	531	532
533	534	535	536	537	538	539	540
541	542	543	544	545	546	547	548
549	550	551	552	553	554	555	556
557	558	559	560	561	562	563	564
565	566	567	568	569	570	571	572
573	574	575	576	577	578	579	580
581	582	583	584	585	586	587	588
589	590	591	592	593	594	595	596
597	598	599	600	601	602	603	604
605	606	607	608	609	610	611	612
613	614	615	616	617	618	619	620
621	622	623	624	625	626	627	628
629	630	631	632	633	634	635	636
637	638	639	640	641	642	643	644
645	646	647	648	649	650	651	652
653	654	655	656	657	658	659	660
661	662	663	664	665	666	667	668
669	670	671	672	673	674	675	676
677	678	679	680	681	682	683	684
685	686	687	688	689	690	691	692
693	694	695	696	697	698	699	700
701	702	703	704	705	706	707	708
709	710	711	712	713	714	715	716
717	718	719	720	721	722	723	724
725	726	727	728	729	730	731	732
733	734	735	736	737	738	739	740
741	742	743	744	745	746	747	748
749	750	751	752	753	754	755	756
757	758	759	760	761	762	763	764
765	766	767	768	769	770	771	772
773	775	777	778	779	780	781	782

783	784	785	786	787	788	789	790
791	792	793	794	795	796	797	798
799	800	801	802	803	804	805	806
807	808	809	810	811	812	813	814
815	816	817	818	819	820	821	822
823	824	825	826	827	828	829	830
831	832	833	834	835	836	837	838
839	840	841	842	843	844	845	846
847	848	849	850	851	852	853	854
855	856	857	858	859	860	861	862
863	864	865	866	867	868	869	870
871	872	873	874	875	876	877	878
879	880	881	882	883	884	885	886
887	888	889	890	891	892	893	894
895	896	897	898	899	900	901	902
903	904	905	906	907	908	909	910
911	912	913	914	915	916	917	918
919	920	921	922	923	924	925	926
927	928	929	930	931	932	933	934
935	936	937	938	939	940	941	942
943	944	945	946	948	949	950	951
952	953	954	955	956	957	958	959
960	961	962	963	964	965	966	967
968	969	970	971	972	973	974	975
976	977	978	979	980	981	982	983
984	985	986	987	988	989	990	991
992	993	994	995	996	997	998	999
1000	1001	1002	1003	1004	1005	1006	1007
1008	1009	1010	1011	1012	1013	1014	1015
1016	1017	1018	1019	1020	1021	1022	1023
1024	1025	1026	1027	1028	1029	1030	1031
1032	1033	1034	1035	1036	1037	1038	1039
1040	1041	1042	1043	1049	1050	1051	1052
1053	1054	1055	1056	1057	1058	1059	1060

1061	1062	1063	1064	1065	1067	1068	1069
1070	1071	1072	1073	1074	1075	1076	1077
1078	1079	1080	1081	1082	1083	1084	1085
1086	1087	1088	1089	1090	1091	1092	1093
1094	1095	1096	1097	1098	1099	1100	1101
1102	1103	1105	1108	1109	1110	1111	1112
1113	1114	1115	1116	1117	1118	1119	1120
1121	1122	1123	1124	1125	1126	1127	1128
1129	1130	1131	1132	1133	1134	1135	1136
1137	1138	1139	1140	1141	1142	1143	1144
1145	1146	1147	1148	1149	1150	1151	1152
1153	1154	1155	1156	1157	1158	1159	1160
1161	1162	1163	1164	1165	1166	1167	1168
1169	1170	1171	1172	1173	1174	1175	1176
1177	1178	1179	1183	1184	1185	1186	1187
1188	1189	1190	1191	1192	1193	1194	1195
1196	1197	1198	1199	1200	1201	1202	1203
1204	1205	1206	1207	1208	1209	1210	1211
1212	1213	1214	1215	1216	1217	1218	1219
1220	1221	1222	1223	1224	1225	1226	1227
1228	1229	1230	1231	1232	1233	1234	1235
1236	1237	1238	1239	1240	1241	1242	1243
1244	1245	1246	1247	1248	1249	1250	1251
1252	1253	1254	1255	1256	1257	1258	1259
1260	1261	1262	1263	1264	1265	1266	1267
1268	1269	1270	1271	1272	1273	1274	1275
1276	1277	1301	1302	1303	1304	1305	1306
1307	1308	1309	1310	1311	1312	1313	1314
1316	1317	1318	1319	1320	1322	1324	1325
1326	1327	1328	1329	U1330	U1331	U1332	U1333
U1334	U1335	U1336	U1337	U1338	U1339	U1340	U1341
U1342	U1343	U1344	U1345	U1351	U1352	U1353	U1354
U1357	U1359	U1363	U1365	U1366	U1367	U1368	U1369
U1370	U1371	U1378	U1379	U1380	U1381	U1382	U1383

U1384	U1385	U1386	U1387	U1388	U1389	U1390	U1391
U1394	U1395	U1396	U1397	U1398	U1399	U1400	U1402
U1403	U1404	U1405	U1406	U1407	U1408	U1409	U1410
U1411	U1412	U1413	U1414	U1417	U1418	U1419	U1420
U1421	U1422	U1423	U1424	U1425	U1426	U1427	U1428
U1429	U1430	U1431	U1432	U1433	U1434	U1435	U1436
U1437	U1438	U1439	U1440	U1443	U1444	U1445	U1446
U1447	U1448	U1449	U1450	U1451	U1452	U1453	U1454
U1455	U1456	U1457	U1459	U1460	U1461	U1462	U1463
U1464	U1465	U1466	U1467	U1468	U1470	U1471	U1472
U1474	U1475	U1476	U1477	U1478	U1479	U1480	U1481
U1482	U1483	U1484	U1485	U1486	U1487	U1488	U1489
U1490	U1491	U1492	U1493	U1494	U1495	U1496	U1497
U1498	U1499	U1501	U1502	U1504	U1505	U1506	U1507
U1508	U1509	U1510	U1511	U1512	U1513	U1514	U1515
U1516	U1517	U1518	U1519	U1520	U1521	U1522	U1523
U1524	U1525	U1526	U1528	U1529	U1530		

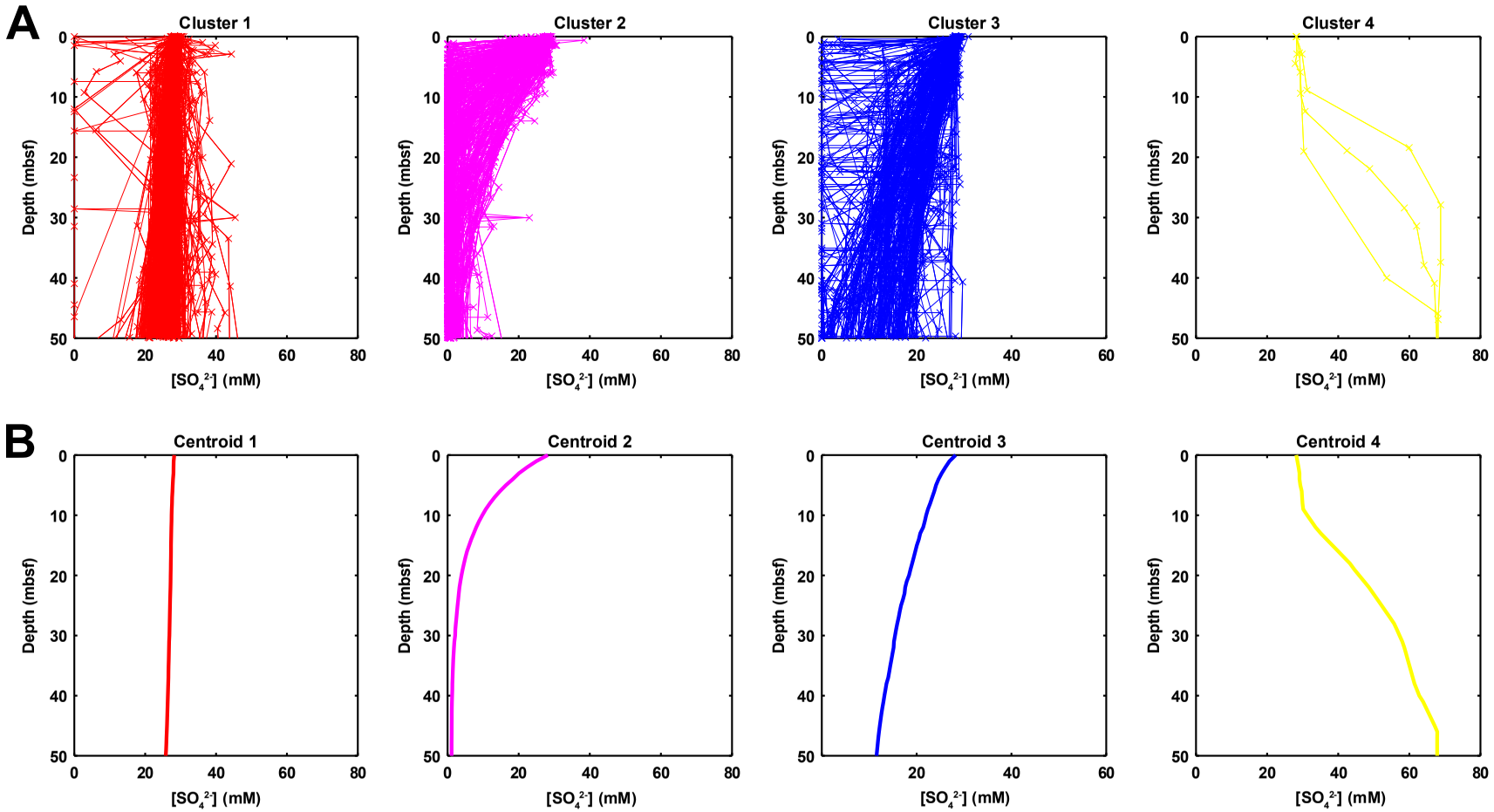

Figure D.1: Cluster analysis results for 50 mbsf bottom boundary, four clusters. (A) Observed $[SO_4^{2-}]$ depth profiles for 0 to 50 mbsf for sites within Clusters 1 (far left) through 4 (far right). (B) Cluster centroids (i.e., the average $[SO_4^{2-}]$ depth profiles for the sites within the cluster) for Clusters 1 (far left) through 4 (far right).

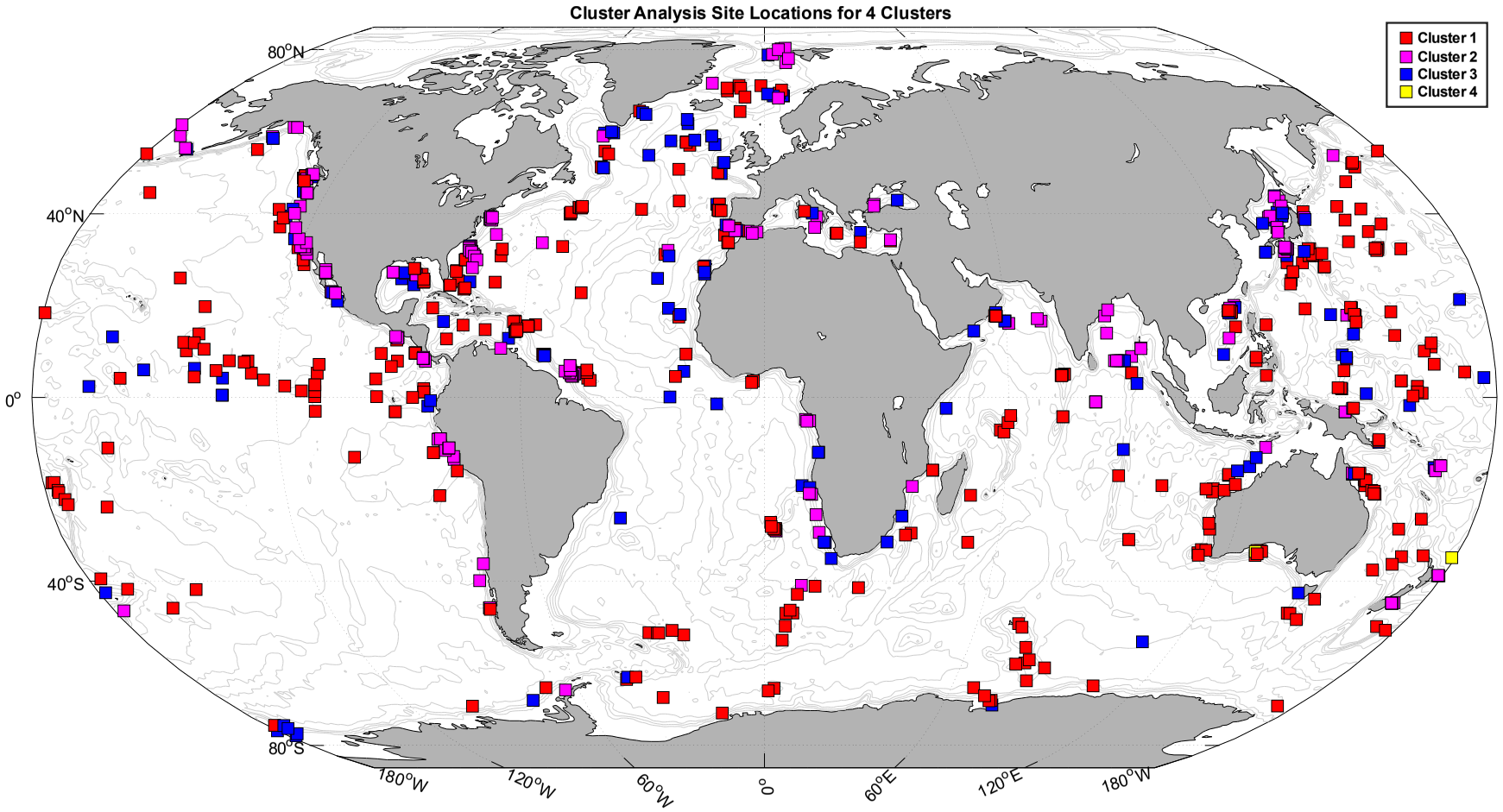

Figure D.2: Global map of the distribution of sites included within the cluster analysis for a bottom boundary depth of 50 mbsf. The color of the symbol denoting site location corresponds to the cluster assignment and matches the colors of the profiles in Figure D.1; i.e., Cluster 1 sites are shown with red squares, Cluster 2 sites with magenta squares, Cluster 3 sites with blue squares, and Cluster 4 sites with yellow squares. Map created using the M _Map mapping package [247].

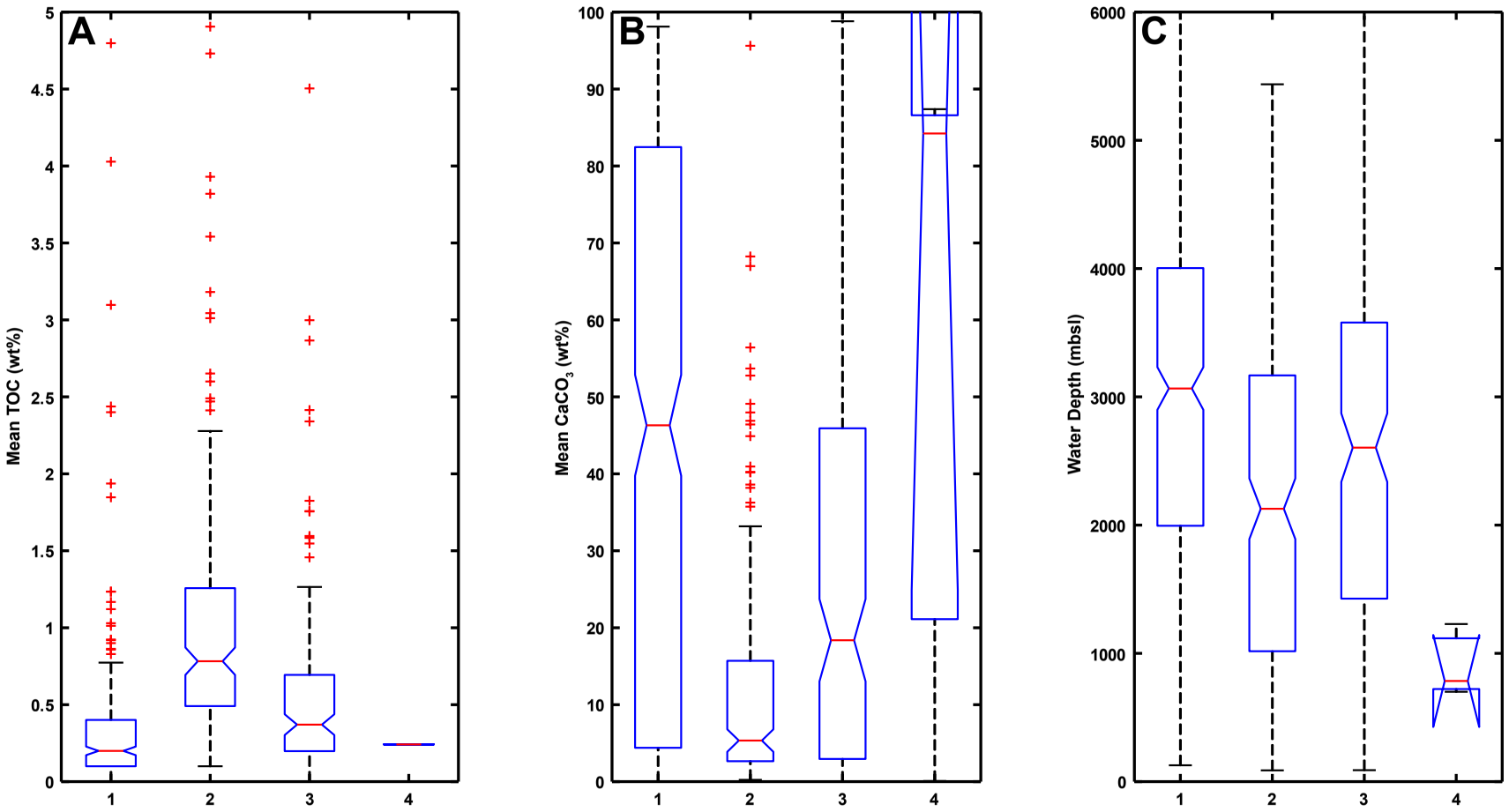

Figure D.3: Box and whisker plots of (A) mean TOC content, (B) mean $CaCO_3$ content, and (C) water depth for the sites included within each cluster for a bottom boundary of 50 mbsf. Red horizontal lines denote the medians for each cluster, and the blue indented notches in the boxes denote the 95% confidence interval bounds for the median value. The top and bottom edges of the blue boxes denote the 25th and 75th percentile ranges for the data within each cluster. Whiskers (capped dashed lines) are depicted with lengths equal to 2σ (95%) coverage of the data within each cluster; outliers are depicted as red "+" symbols.

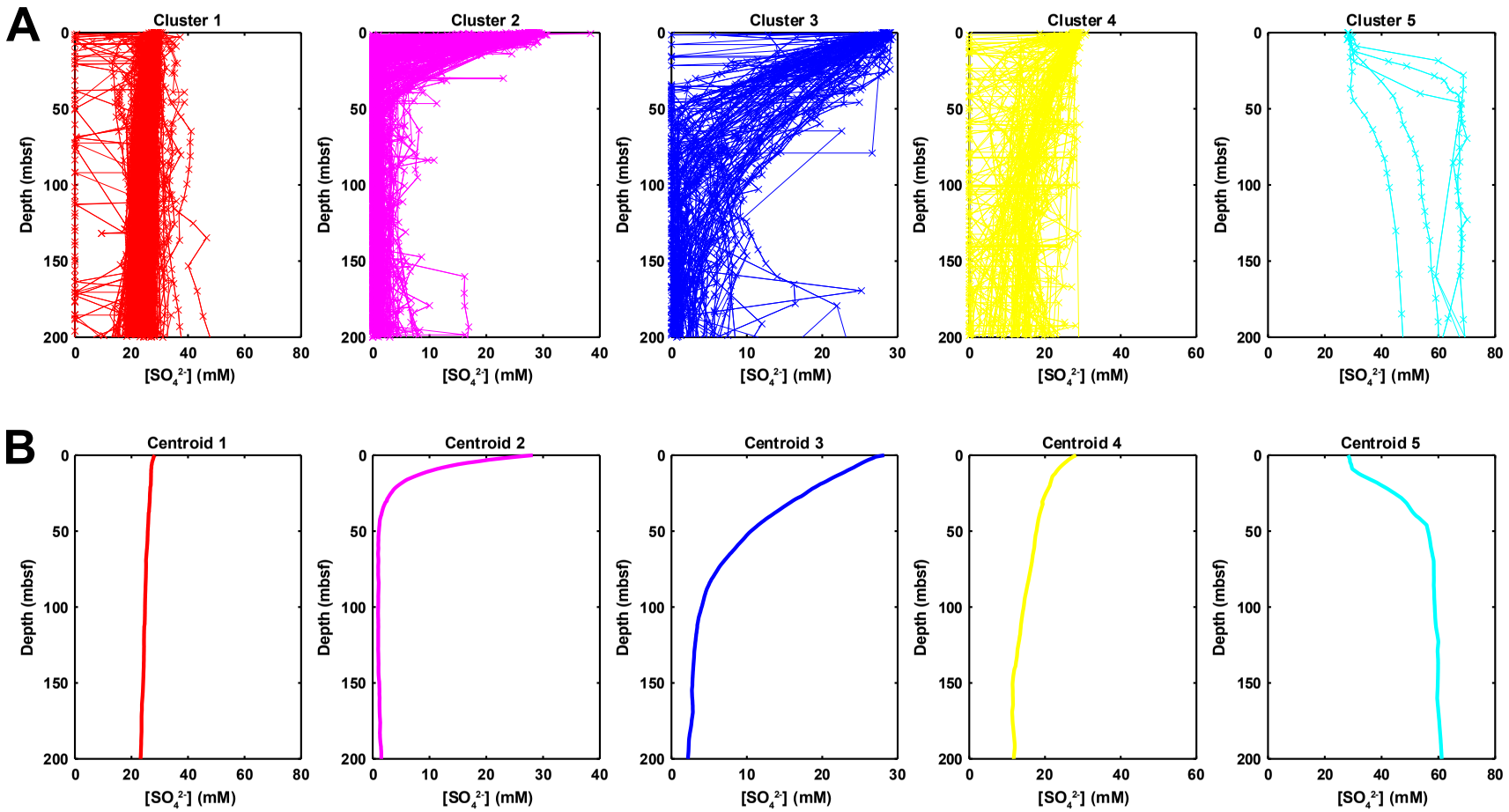

Figure D.4: Cluster analysis results for 200 mbsf bottom boundary, five clusters. (A) Observed $[SO_4^{2-}]$ depth profiles for 0 to 200 mbsf for sites within Clusters 1 (far left) through 5 (far right). (B) Cluster centroids (i.e., the average $[SO_4^{2-}]$ depth profiles for the sites within the cluster) for Clusters 1 (far left) through 5 (far right).

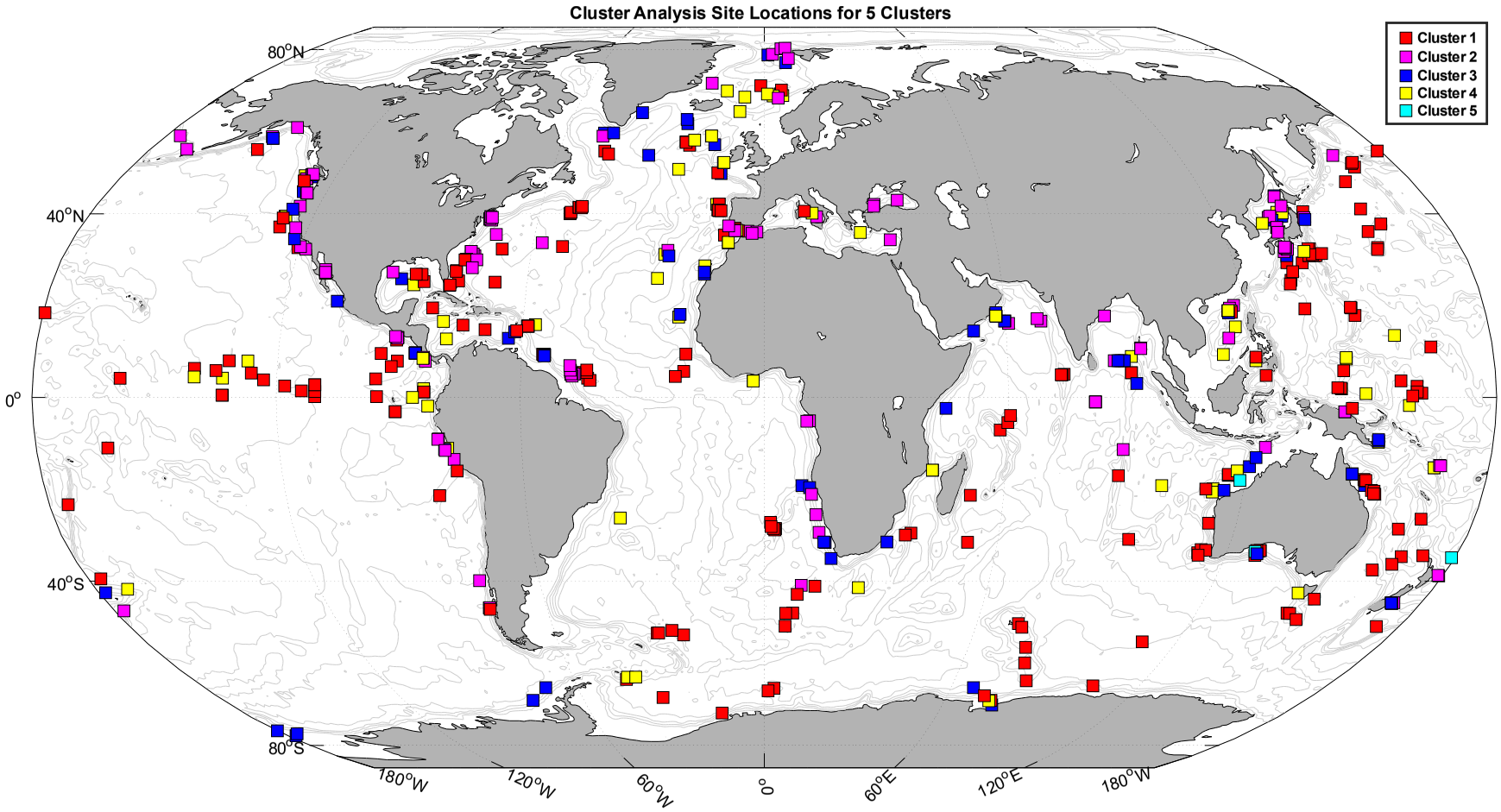

Figure D.5: Global map of the distribution of sites included within the cluster analysis for a bottom boundary depth of 200 mbsf. The color of the symbol denoting site location corresponds to the cluster assignment and matches the colors of the profiles in Figure D.4; i.e., Cluster 1 sites are shown with red squares, Cluster 2 sites with magenta squares, Cluster 3 sites with blue squares, Cluster 4 sites with yellow squares, and Cluster 5 sites with cyan squares. Map created using the M _Map mapping package [247].

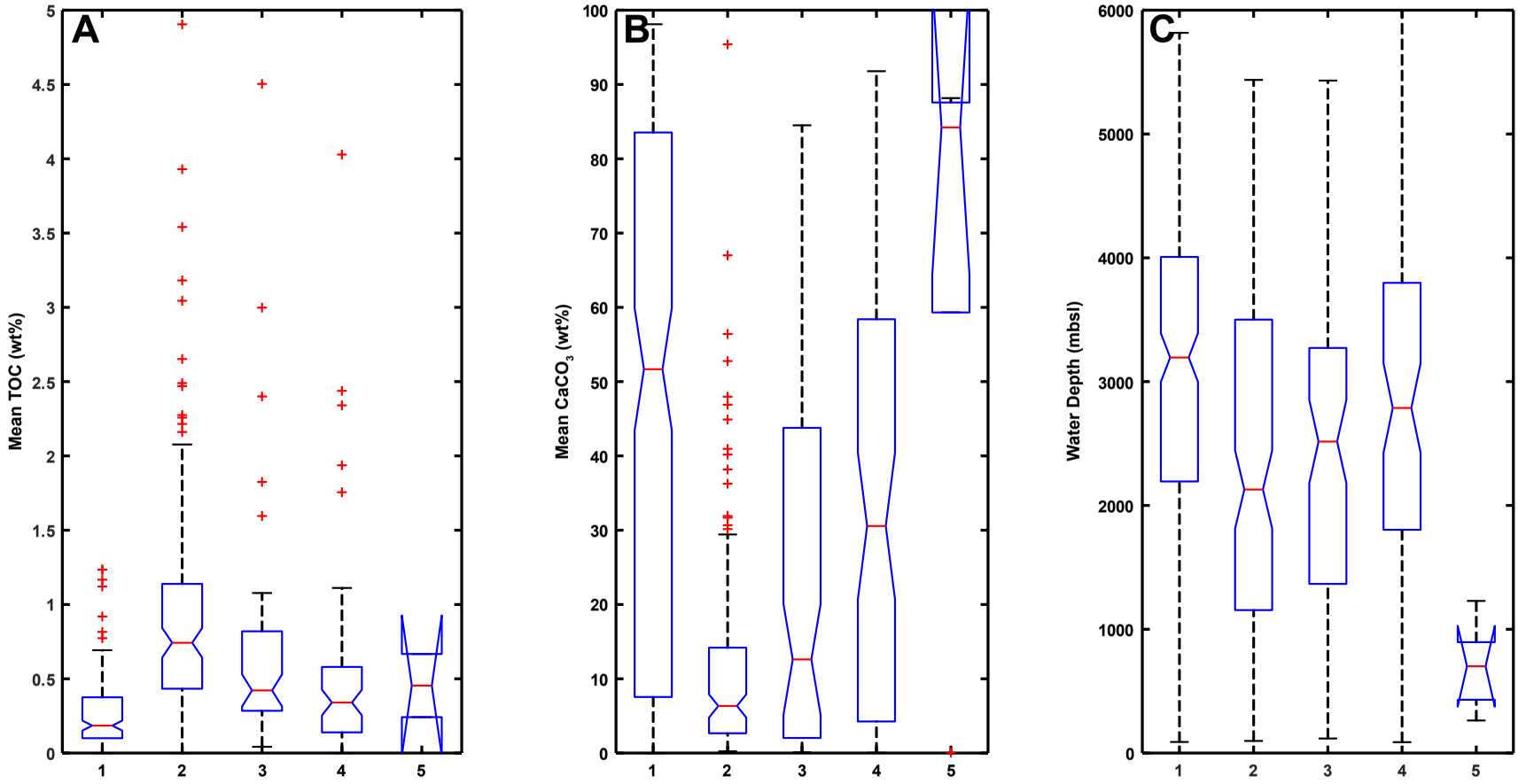

Figure D.6: Box and whisker plots of (A) mean TOC content, (B) mean $CaCO_3$ content, and (C) water depth for the sites included within each cluster for a bottom boundary of 200 mbsf. Red horizontal lines denote the medians for each cluster, and the blue indented notches in the boxes denote the 95% confidence interval bounds for the median value. The top and bottom edges of the blue boxes denote the 25th and 75th percentile ranges for the data within each cluster. Whiskers (capped dashed lines) are depicted with lengths equal to 2σ (95%) coverage of the data within each cluster; outliers are depicted as red "+" symbols.

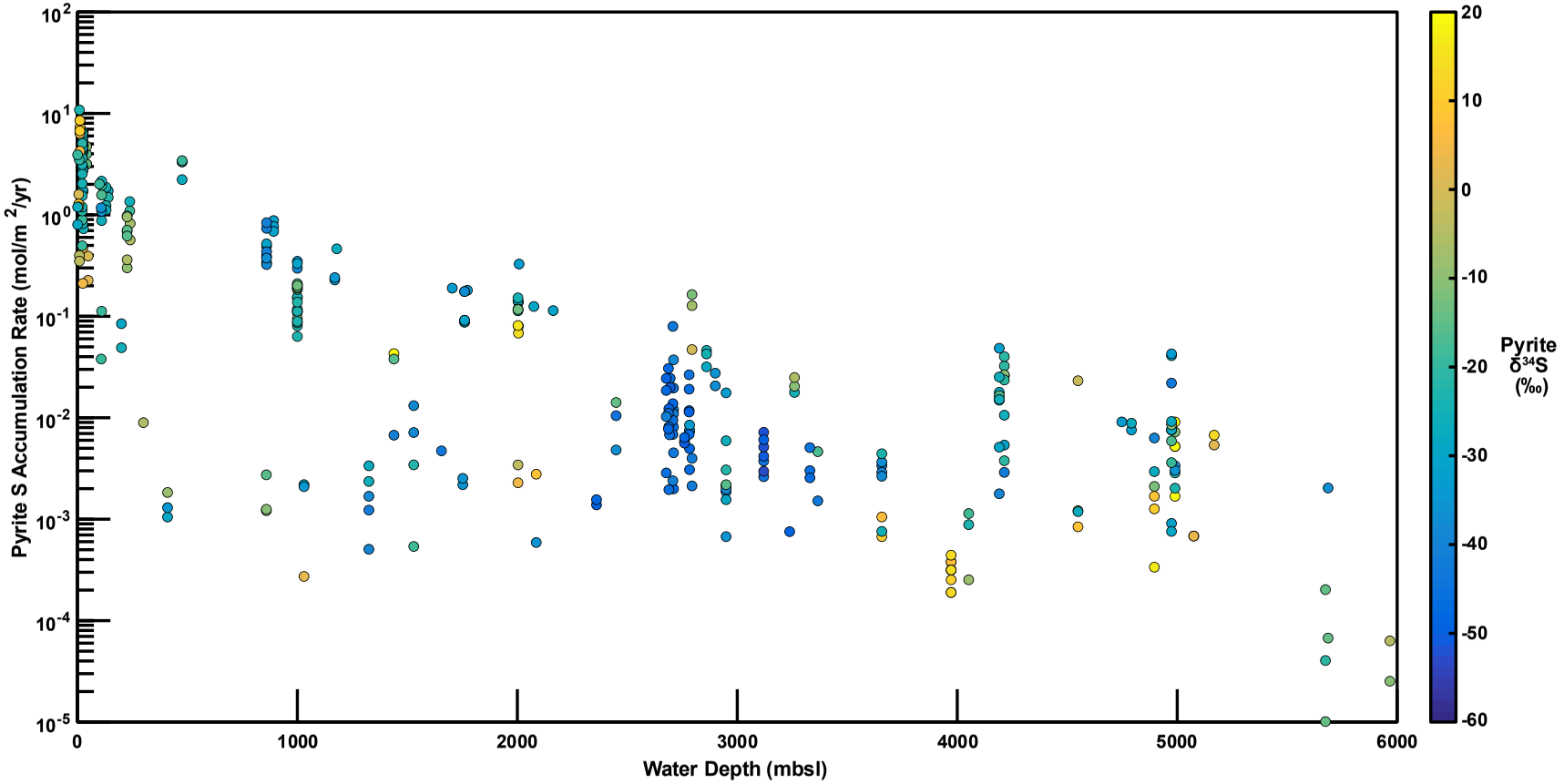

Figure D.7: Literature compilation of 343 measurements (colored circles) of estimated pyrite S accumulation rate plotted against modern water depth (meters below sea level). Color of symbols denotes the measured pyrite $\delta^{34}S$. Sedimentation rates were taken from literature estimates or were estimated from water depth based on the relationship of [219]. Data from [4, 37, 38, 115, 133, 158, 174, 175, 188, 197, 198, 220, 221, 222, 266, 293, 328, 329, 336, 349, 371].

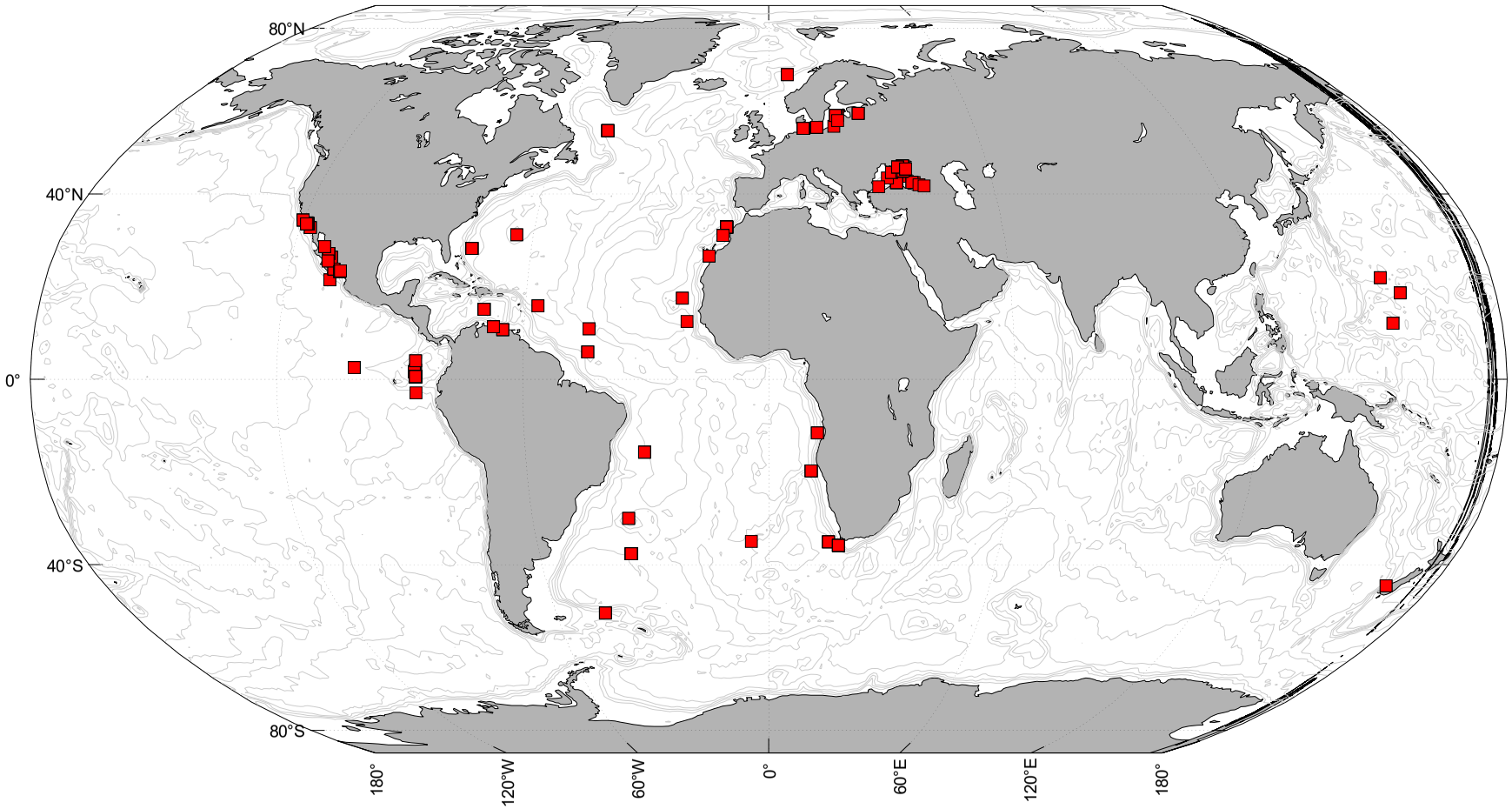

Figure D.8: Locations of sites from which pyrite abundance and $\delta^{34}S$ data ($n = 343$) were compiled. Data points lacking S abundance constraints and/or collected from sediments estimated to be > 40 Ma in age ($n = 151$) have been parsed.

Table D.2: Pyrite compilation data.

Ref.	Site	Lat. (°)	Lon. (°)	Water Depth (mbsl)	Depth (mbsf)	Est. Sed Rate ($\frac{cm}{kyr}$)	Est. Age (Ma)	S (wt %)	Est. Py S Accum. Rate ($\frac{mol\,S}{m^2 yr}$)	Pyrite $\delta^{34}S$ (‰)
[4]	ODP Site 802	12.0963	153.2104	5967	34.34	1.50	2.30	0.005	0.00	-4.8
[4]	ODP Site 802	12.0963	153.2104	5967	91.03	1.50	6.10	0.002	0.00	-10.2
[4]	ODP Site 801	18.6428	156.3595	5674	166.02	1.20	13.80	0.02	0.00	-14.9
[4]	ODP Site 801	18.6428	156.3595	5674	233.55	1.20	19.50	0.004	0.00	-20.7
[4]	ODP Site 801	18.6428	156.3595	5674	263.37	1.20	21.90	0.001	0.00	-13.9
[4]	ODP Site 800	21.923	152.3228	5686	78.28	0.60	13.00	0.402	0.00	-37.1
[4]	ODP Site 800	21.923	152.3228	5686	230.84	2.00	11.50	0.004	0.00	-14.4
[115]		15.8565	-56.8793	5075	237	5.40	4.40	0.015	0.00	3.8
[115]		15.8565	-56.8793	5075	249	5.40	4.60	0.015	0.00	3.7
[133]	Station 2092	54.51667	10.01667	26	0.005	538.00	0.00	0.38	1.72	-20.2
[133]	Station 2094	54.51667	10.01667	24	0.0075	562.00	0.00	0.173	0.82	-23.8
[133]	Station 2096	54.51667	10.01667	22	0.0075	590.00	0.00	0.1	0.50	-19.4
[133]	Station 2092	54.51667	10.01667	26	0.0225	538.00	0.00	0.65	2.94	-22.1
[133]	Station 2094	54.51667	10.01667	24	0.0225	562.00	0.00	0.37	1.75	-27.6

Ref.	Site	Lat. (°)	Lon. (°)	Water Depth (mbsl)	Depth (mbsf)	Est. Sed Rate ($\frac{cm}{kyr}$)	Est. Age (Ma)	S (wt %)	Est. Py S Accum. Rate ($\frac{mol\ S}{m^2 yr}$)	Pyrite $\delta^{34}S$ (‰)
[133]	Station 2096	54.51667	10.01667	22	0.0225	590.00	0.00	0.18	0.89	-20
[133]	Station 2092	54.51667	10.01667	26	0.04	538.00	0.00	1.05	4.76	-23.4
[133]	Station 2094	54.51667	10.01667	24	0.04	562.00	0.00	0.568	2.69	-29
[133]	Station 2096	54.51667	10.01667	22	0.04	590.00	0.00	0.22	1.09	-21.3
[133]	Station 2092	54.51667	10.01667	26	0.06	538.00	0.00	1.09	4.94	-23.4
[133]	Station 2094	54.51667	10.01667	24	0.06	562.00	0.00	0.92	4.36	-27.3
[133]	Station 2096	54.51667	10.01667	22	0.065	591.00	0.00	0.31	1.54	-23.2
[133]	Station 2094	54.51667	10.01667	24	0.08	562.00	0.00	0.94	4.45	-25.9
[133]	Station 2096	54.51667	10.01667	22	0.09	591.00	0.00	0.51	2.53	-24.2
[133]	Station 2094	54.51667	10.01667	24	0.105	562.00	0.00	0.87	4.12	-26.1
[133]	Station 2092	54.51667	10.01667	26	0.115	538.00	0.00	1.05	4.76	-22
[133]	Station 2096	54.51667	10.01667	22	0.115	591.00	0.00	0.41	2.04	-24.2
[133]	Station 2094	54.51667	10.01667	24	0.135	562.00	0.00	0.9	4.26	-27.2
[133]	Station 2092	54.51667	10.01667	26	0.145	538.00	0.00	1.45	6.57	-27.6
[133]	Station 2096	54.51667	10.01667	22	0.145	591.00	0.00	0.63	3.13	-24

Ref.	Site	Lat. (°)	Lon. (°)	Water Depth (mbsl)	Depth (mbsf)	Est. Sed Rate ($\frac{cm}{kyr}$)	Est. Age (Ma)	S (wt %)	Est. Py S Ac-cum. Rate ($\frac{mol\ S}{m^2 yr}$)	Pyrite $\delta^{34}S$ (‰)
[133]	Station 2094	54.51667	10.01667	24	0.1575	562.00	0.00	0.93	4.40	-26.7
[133]	Station 2092	54.51667	10.01667	26	0.175	538.00	0.00	1.45	6.57	-22.4
[133]	Station 2096	54.51667	10.01667	22	0.175	591.00	0.00	0.76	3.78	-22.8
[133]	Station 2094	54.51667	10.01667	24	0.1825	562.00	0.00	0.59	2.79	-26.6
[133]	Station 2096	54.51667	10.01667	22	0.205	591.00	0.00	1.02	5.07	-22.1
[133]	Station 2094	54.51667	10.01667	24	0.215	562.00	0.00	1.08	5.11	-27.1
[133]	Station 2092	54.51667	10.01667	26	0.235	538.00	0.00	1.28	5.80	-20.1
[133]	Station 2096	54.51667	10.01667	22	0.235	591.00	0.00	0.24	1.19	-22.9
[133]	Station 2094	54.51667	10.01667	24	0.245	562.00	0.00	0.98	4.64	-27
[133]	Station 2096	54.51667	10.01667	22	0.26	591.00	0.00	0.73	3.63	-23.5
[133]	Station 2094	54.51667	10.01667	24	0.275	562.00	0.00	1.1	5.21	-25.1
[133]	Station 2092	54.51667	10.01667	26	0.295	538.00	0.00	1.38	6.25	-19.3
[133]	Station 2094	54.51667	10.01667	24	0.305	562.00	0.00	1.11	5.26	-24.9
[133]	Station 2094	54.51667	10.01667	24	0.335	562.00	0.00	0.97	4.59	-26.3
[133]	Station 2094	54.51667	10.01667	24	0.365	562.00	0.00	1.22	5.78	-25.8

Ref.	Site	Lat. (°)	Lon. (°)	Water Depth (mbsl)	Depth (mbsf)	Est. Sed Rate ($\frac{cm}{kyr}$)	Est. Age (Ma)	S (wt %)	Est. Py S Ac-cum. Rate ($\frac{mol\ S}{m^2 yr}$)	Pyrite $\delta^{34}S$ (‰)
[133]	Station 2094	54.51667	10.01667	24	0.395	562.00	0.00	1.34	6.35	-25
[174]	Station A	-44.6333	167.55	200	0.03	146.00	0.00	0.04	0.05	-25.5
[174]	Station G	-44.6333	167.55	200	0.03	146.00	0.00	0.069	0.08	-28.9
[175]		32.73611	-117.55	1030	0.05	0.50	0.01	0.066	0.00	3.1
[175]		32.73611	-117.55	1030	0.95	0.50	0.19	0.53	0.00	-28.8
[175]		32.73611	-117.55	1030	2.45	0.50	0.50	0.506	0.00	-34.6
[175]		33.52778	-118.861	410	0.05	1.10	0.00	0.118	0.00	-29.9
[175]		33.52778	-118.861	410	1.225	1.10	0.12	0.146	0.00	-34
[175]		33.52778	-118.861	410	3.65	1.10	0.35	0.206	0.00	-7.7
[175]		33.74722	-118.819	859	0.05	4.65	0.00	0.031	0.00	-10.7
[175]		33.74722	-118.819	859	0.7	4.65	0.02	0.07	0.00	-15.1
[175]		33.74722	-118.819	859	3.85	4.65	0.08	0.032	0.00	-10.7
[175]		34.35833	-120.108	476	0.05	500.00	0.00	0.529	2.23	-26.6
[175]		34.35833	-120.108	476	0.95	500.00	0.00	0.79	3.33	-17.3
[175]		34.35833	-120.108	476	2.65	500.00	0.00	0.792	3.33	-18.6

Ref.	Site	Lat. (°)	Lon. (°)	Water Depth (mbsl)	Depth (mbsf)	Est. Sed Rate ($\frac{cm}{kyr}$)	Est. Age (Ma)	S (wt %)	Est. Py S Ac-cum. Rate ($\frac{mol\ S}{m^2 yr}$)	Pyrite $\delta^{34}S$ (‰)
[175]		34.35833	-120.108	476	3.65	500.00	0.00	0.814	3.43	-19.9
[175]				1	0.025	501.19	0.00	0.926	3.91	-20
[175]				1	0.325	501.19	0.00	0.283	1.19	-27.1
[175]				1	0.625	501.19	0.00	0.19	0.80	-27.7
[197]		21.4617	-109.232	2900	3.875	6.83	0.06	0.359	0.02	-37
[197]		21.4617	-109.232	2900	5	6.83	0.07	0.479	0.03	-36.1
[197]		23.2317	-107.117	1000	0.9	34.15	0.00	1.036	0.30	-39
[197]		23.2317	-107.117	1000	1.85	34.15	0.01	1.215	0.35	-34
[197]		23.2317	-107.117	1000	2.6	34.15	0.01	1.155	0.33	-31
[197]		23.3833	-106.948	140	0.7	188.31	0.00	1.09	1.73	-27
[197]		23.3833	-106.948	140	2.225	188.31	0.00	0.937	1.49	-22.2
[197]		23.7817	-108.673	2860	0.4	7.04	0.01	0.536	0.03	-28
[197]		23.7817	-108.673	2860	2	7.04	0.03	0.778	0.05	-24
[197]		23.7817	-108.673	2860	2.45	7.04	0.03	0.719	0.04	-24.3
[197]		25.5317	-110.545	1170	0.625	28.45	0.00	0.953	0.23	-35

Ref.	Site	Lat. (°)	Lon. (°)	Water Depth (mbsl)	Depth (mbsf)	Est. Sed Rate ($\frac{cm}{kyr}$)	Est. Age (Ma)	S (wt %)	Est. Py S Accum. Rate ($\frac{mol\ S}{m^2 yr}$)	Pyrite $\delta^{34}S$ (‰)
[197]		25.5317	-110.545	1170	3.3	28.45	0.01	1.006	0.24	-34
[197]		26.3467	-109.93	3260	0.425	5.18	0.01	0.408	0.02	-23.8
[197]		26.3467	-109.93	3260	1.275	5.18	0.02	0.469	0.02	-10.8
[197]		26.3467	-109.93	3260	3.1	5.18	0.06	0.572	0.02	-5.5
[197]		27.1517	-110.867	1760	0.225	16.56	0.00	0.629	0.09	-26.7
[197]		27.1517	-110.867	1760	0.225	16.56	0.00	0.629	0.09	-26.5
[197]		27.1517	-110.867	1760	0.55	16.56	0.00	0.656	0.09	-31
[197]		27.1517	-110.867	1760	0.55	16.56	0.00	0.656	0.09	-30.7
[197]		27.1517	-110.867	1760	2.55	16.56	0.02	1.259	0.18	-33
[197]		27.1517	-110.867	1760	2.55	16.56	0.02	1.259	0.18	-37
[198]	Station 2656	54.75	14	42	0.085	407.96	0.00	0.92	3.16	-18
[198]	Station 2656	54.75	14	42	0.505	407.96	0.00	1.16	3.99	-15.2
[198]	Station 2656	54.75	14	42	1.01	407.96	0.00	0.92	3.16	-14
[198]	Station 2656	54.75	14	42	1.425	407.96	0.00	1.38	4.74	-9
[198]	Station 2682	55	19	110	0.95	222.26	0.00	1.04	1.95	-19.6

Ref.	Site	Lat. (°)	Lon. (°)	Water Depth (mbsl)	Depth (mbsf)	Est. Sed Rate ($\frac{cm}{kyr}$)	Est. Age (Ma)	S (wt %)	Est. Py S Ac-cum. Rate ($\frac{mol\ S}{m^2 yr}$)	Pyrite $\delta^{34}S$ (‰)
[198]	Station 2638	56.33333	20.36667	100	0.05	236.90	0.00	1.01	2.02	-20
[198]	Station 2631a	57.5	19.91667	110	0.035	222.26	0.00	0.47	0.88	-26
[198]	Station 2631a	57.5	19.91667	110	0.11	222.26	0.00	1.15	2.15	-26
[198]	Station 2631a	57.5	19.91667	110	1.6	222.26	0.00	0.84	1.57	-17.2
[198]	Station 2618	57.5	20	238	0.11	127.58	0.00	1.02	1.10	-18.8
[198]	Station 2618	57.5	20	238	1.55	127.58	0.00	1.26	1.35	-26
[198]	Station 2622	57.5	20.5	240	1.575	126.76	0.00	0.77	0.82	-7.4
[198]	Station 2622	57.5	20.5	240	2.45	126.76	0.00	0.53	0.57	-5.2
[198]	Station 2611	58	26.83333	130	0.035	198.28	0.00	1.12	1.87	-24.2
[198]	Station 2611	58	26.83333	130	0.2	198.28	0.00	0.74	1.24	-25
[198]	Station 2611	58	26.83333	130	0.5	198.28	0.00	0.67	1.12	-26
[293]	DSDP Site 329	-50.6535	-46.0955	1529	0.7	0.80	0.09	0.08	0.00	-18.4
[293]	DSDP Site 329	-50.6535	-46.0955	1529	15.9	3.40	0.47	0.12	0.00	-22.1
[293]	DSDP Site 329	-50.6535	-46.0955	1529	45.3	3.40	1.33	0.46	0.01	-37.8
[293]	DSDP Site 329	-50.6535	-46.0955	1529	133.2	3.40	3.92	0.25	0.01	-37.8

Ref.	Site	Lat. (°)	Lon. (°)	Water Depth (mbsl)	Depth (mbsf)	Est. Sed Rate ($\frac{cm}{kyr}$)	Est. Age (Ma)	S (wt %)	Est. Py S Accum. Rate ($\frac{mol\ S}{m^2 yr}$)	Pyrite $\delta^{34}S$ (‰)
[293]	DSDP Site 358	-37.6562	-35.9637	4990	47.6	2.00	2.38	0.2	0.00	-37
[293]	DSDP Site 358	-37.6562	-35.9637	4990	55.5	2.00	2.78	0.31	0.01	-37.7
[293]	DSDP Site 358	-37.6562	-35.9637	4990	123.6	2.00	6.18	0.17	0.00	-24.7
[293]	DSDP Site 358	-37.6562	-35.9637	4990	276.8	2.00	13.84	0.18	0.00	-35.1
[293]	DSDP Site 358	-37.6562	-35.9637	4990	421.2	2.00	21.06	0.54	0.01	22.6
[293]	DSDP Site 358	-37.6562	-35.9637	4990	492.2	2.00	24.61	0.43	0.01	-11.3
[293]	DSDP Site 358	-37.6562	-35.9637	4990	555	2.00	27.75	0.31	0.01	22.2
[293]	DSDP Site 358	-37.6562	-35.9637	4990	592.7	2.00	29.64	0.1	0.00	22.3
[293]	DSDP Site 358	-37.6562	-35.9637	4990	638.6	2.00	31.93	0.12	0.00	-23.4
[293]	DSDP Site 360	-35.8458	18.0965	2949	80.3	1.70	4.72	0.15	0.00	-39.7
[293]	DSDP Site 360	-35.8458	18.0965	2949	81.8	1.70	4.81	0.15	0.00	-32.8
[293]	DSDP Site 360	-35.8458	18.0965	2949	92.7	1.70	5.45	0.13	0.00	-38.5
[293]	DSDP Site 360	-35.8458	18.0965	2949	129.7	5.10	2.54	0.41	0.02	-33.3
[293]	DSDP Site 360	-35.8458	18.0965	2949	137.2	6.40	2.14	0.11	0.01	-26.2
[293]	DSDP Site 360	-35.8458	18.0965	2949	185	1.00	18.50	0.08	0.00	-36.1

Ref.	Site	Lat. (°)	Lon. (°)	Water Depth (mbsl)	Depth (mbsf)	Est. Sed Rate ($\frac{cm}{kyr}$)	Est. Age (Ma)	S (wt %)	Est. Py S Accum. Rate ($\frac{mol\ S}{m^2 yr}$)	Pyrite $\delta^{34}S$ (‰)
[293]	DSDP Site 360	-35.8458	18.0965	2949	224.2	1.80	12.46	0.13	0.00	-40
[293]	DSDP Site 360	-35.8458	18.0965	2949	395.2	3.70	10.68	0.05	0.00	-29.7
[293]	DSDP Site 360	-35.8458	18.0965	2949	793.8	5.20	15.27	0.05	0.00	-15.7
[293]	DSDP Site 360	-35.8458	18.0965	2949	798.7	5.20	15.36	0.07	0.00	-22.3
[293]	DSDP Site 361	-35.0662	15.4485	4549	32	4.80	0.67	0.03	0.00	8.5
[293]	DSDP Site 361	-35.0662	15.4485	4549	179.3	4.70	3.81	0.03	0.00	-26.6
[293]	DSDP Site 361	-35.0662	15.4485	4549	272.8	2.00	13.64	0.05	0.00	8.4
[293]	DSDP Site 361	-35.0662	15.4485	4549	404.2	4.30	9.40	0.64	0.02	-1.3
[293]	DSDP Site 359	-34.985	-4.4805	1655	64	2.00	3.20	0.28	0.00	-43.6
[293]	DSDP Site 357	-30.0042	-35.5598	2086	112.9	1.00	11.29	0.07	0.00	-36
[293]	DSDP Site 357	-30.0042	-35.5598	2086	415.7	5.50	7.56	0.06	0.00	7.9
[293]	DSDP Site 362	-19.7575	10.5325	1325	36.1	0.20	18.05	0.3	0.00	-40
[293]	DSDP Site 362	-19.7575	10.5325	1325	40.6	0.20	20.30	0.73	0.00	-42.3
[293]	DSDP Site 362	-19.7575	10.5325	1325	48.6	0.20	24.30	1	0.00	-38.5
[293]	DSDP Site 362	-19.7575	10.5325	1325	77.1	0.20	38.55	1.4	0.00	-25.8

Ref.	Site	Lat. (°)	Lon. (°)	Water Depth (mbsl)	Depth (mbsf)	Est. Sed Rate ($\frac{cm}{kyr}$)	Est. Age (Ma)	S (wt %)	Est. Py S Ac-cum. Rate ($\frac{mol\ S}{m^2 yr}$)	Pyrite $\delta^{34}S$ (‰)
[293]	DSDP Site 362	-19.7575	10.5325	1325	115.1	0.30	38.37	1.33	0.00	-27.2
[293]	DSDP Site 355	-15.7098	-30.6005	4896	264	5.00	5.28	0.05	0.00	-11.8
[293]	DSDP Site 355	-15.7098	-30.6005	4896	272	5.00	5.44	0.15	0.01	-39
[293]	DSDP Site 355	-15.7098	-30.6005	4896	320.8	5.00	6.42	0.07	0.00	-26.3
[293]	DSDP Site 355	-15.7098	-30.6005	4896	351	5.00	7.02	0.04	0.00	8.1
[293]	DSDP Site 355	-15.7098	-30.6005	4896	390.4	1.00	39.04	0.04	0.00	16.7
[293]	DSDP Site 355	-15.7098	-30.6005	4896	397	5.00	7.94	0.03	0.00	10.1
[293]	DSDP Site 364	-11.572	11.93833	2449	7.7	1.50	0.51	0.83	0.01	-44.8
[293]	DSDP Site 364	-11.572	11.93833	2449	13.1	1.60	0.82	1.05	0.01	-14.2
[293]	DSDP Site 364	-11.572	11.93833	2449	66.2	1.10	6.02	0.52	0.00	-36.6
[293]	DSDP Site 354	5.899167	-44.1963	4052	284.8	1.50	18.99	0.02	0.00	-8.3
[293]	DSDP Site 354	5.899167	-44.1963	4052	403.8	1.50	26.92	0.07	0.00	-22.6
[293]	DSDP Site 354	5.899167	-44.1963	4052	527	1.50	35.13	0.09	0.00	-17.6
[293]	DSDP Site 367	12.48667	-20.0467	4748	68.8	9.00	0.76	0.12	0.01	-33
[293]	DSDP Site 149	15.10417	-70.0925	3972	30.2	0.75	4.03	0.06	0.00	2.3

Ref.	Site	Lat. (°)	Lon. (°)	Water Depth (mbsl)	Depth (mbsf)	Est. Sed Rate ($\frac{cm}{kyr}$)	Est. Age (Ma)	S (wt %)	Est. Py S Ac-cum. Rate ($\frac{mol\ S}{m^2 yr}$)	Pyrite $\delta^{34}S$ (‰)
[293]	DSDP Site 149	15.10417	-70.0925	3972	43.7	0.75	5.83	0.06	0.00	7.35
[293]	DSDP Site 149	15.10417	-70.0925	3972	56.7	0.75	7.56	0.07	0.00	14.5
[293]	DSDP Site 149	15.10417	-70.0925	3972	76.9	0.75	10.25	0.03	0.00	10.2
[293]	DSDP Site 149	15.10417	-70.0925	3972	95	0.75	12.67	0.03	0.00	13.15
[293]	DSDP Site 149	15.10417	-70.0925	3972	117.2	0.75	15.63	0.05	0.00	13
[293]	DSDP Site 149	15.10417	-70.0925	3972	133.6	0.75	17.81	0.05	0.00	14.8
[293]	DSDP Site 149	15.10417	-70.0925	3972	154.2	0.75	20.56	0.05	0.00	-10.1
[293]	DSDP Site 149	15.10417	-70.0925	3972	226.4	0.75	30.19	0.05	0.00	14.7
[293]	DSDP Site 149	15.10417	-70.0925	3972	253.2	0.75	33.76	0.04	0.00	11.8
[293]	DSDP Site 368	17.50667	-21.3533	3366	123.1	2.00	6.16	0.09	0.00	-42.9
[293]	DSDP Site 368	17.50667	-21.3533	3366	270.3	1.00	27.03	0.55	0.00	-16.8
[293]	DSDP Site 369	26.59167	-14.9833	1752	108.5	1.00	10.85	0.26	0.00	-36
[293]	DSDP Site 369	26.59167	-14.9833	1752	118	1.00	11.80	0.3	0.00	-35.2
[293]	DSDP Site 391	28.22683	-75	4974	0.4	9.00	0.00	0.29	0.02	-43.6
[293]	DSDP Site 391	28.22683	-75	4974	33.6	9.00	0.37	0.1	0.01	-36

Ref.	Site	Lat. (°)	Lon. (°)	Water Depth (mbsl)	Depth (mbsf)	Est. Sed Rate ($\frac{cm}{kyr}$)	Est. Age (Ma)	S (wt %)	Est. Py S Accum. Rate ($\frac{mol\ S}{m^2 yr}$)	Pyrite $\delta^{34}S$ (‰)
[293]	DSDP Site 391	28.22683	-75	4974	147.8	0.90	16.42	0.12	0.00	-32.3
[293]	DSDP Site 391	28.22683	-75	4974	203	0.90	22.56	0.1	0.00	-30
[293]	DSDP Site 391	28.22683	-75	4974	261.9	4.30	6.09	0.21	0.01	-26.2
[293]	DSDP Site 391	28.22683	-75	4974	328	4.30	7.63	1.13	0.04	-28.6
[293]	DSDP Site 391	28.22683	-75	4974	357.9	4.30	8.32	0.21	0.01	-28.1
[293]	DSDP Site 391	28.22683	-75	4974	472.4	3.90	12.11	0.26	0.01	-9.1
[293]	DSDP Site 391	28.22683	-75	4974	529.2	3.90	13.57	0.11	0.00	-18.8
[293]	DSDP Site 391	28.22683	-75	4974	565.4	3.90	14.50	0.18	0.01	-16.4
[293]	DSDP Site 391	28.22683	-75	4974	584.6	3.90	14.99	0.28	0.01	-28.3
[293]	DSDP Site 391	28.22683	-75	4974	640.6	3.90	16.43	1.3	0.04	-33.7
[293]	DSDP Site 386	31.18683	-64.249	4792	423.8	3.00	14.13	0.3	0.01	-32.1
[293]	DSDP Site 386	31.18683	-64.249	4792	435.7	3.00	14.52	0.35	0.01	-26.8
[293]	DSDP Site 370	32.83667	-10.7767	4214	1.1	2.00	0.06	0.63	0.01	-26.1
[293]	DSDP Site 370	32.83667	-10.7767	4214	105.7	2.00	5.29	0.32	0.01	-30.7
[293]	DSDP Site 370	32.83667	-10.7767	4214	209.3	0.80	26.16	0.43	0.00	-41.3

Ref.	Site	Lat. (°)	Lon. (°)	Water Depth (mbsl)	Depth (mbsf)	Est. Sed Rate ($\frac{cm}{kyr}$)	Est. Age (Ma)	S (wt %)	Est. Py S Accum. Rate ($\frac{mol\ S}{m^2 yr}$)	Pyrite $\delta^{34}S$ (‰)
[293]	DSDP Site 370	32.83667	-10.7767	4214	221.3	0.80	27.66	0.56	0.00	-20.9
[293]	DSDP Site 370	32.83667	-10.7767	4214	447.2	3.50	12.78	0.88	0.03	-29.5
[293]	DSDP Site 370	32.83667	-10.7767	4214	483.9	3.50	13.83	1.1	0.03	-20.8
[293]	DSDP Site 370	32.83667	-10.7767	4214	542.5	3.50	15.50	1.36	0.04	-20.6
[293]	DSDP Site 370	32.83667	-10.7767	4214	574.3	3.50	16.41	0.9	0.03	-10.4
[293]	DSDP Site 370	32.83667	-10.7767	4214	617.4	3.50	17.64	0.8	0.02	-20.3
[293]	DSDP Site 112	54.01667	-46.604	3657	111.1	2.50	4.44	0.05	0.00	6.7
[293]	DSDP Site 112	54.01667	-46.604	3657	162.6	2.00	8.13	0.04	0.00	10.3
[293]	DSDP Site 112	54.01667	-46.604	3657	202.1	2.00	10.11	0.2	0.00	-42.1
[293]	DSDP Site 112	54.01667	-46.604	3657	278.1	1.50	18.54	0.23	0.00	-40.5
[293]	DSDP Site 112	54.01667	-46.604	3657	289.2	1.50	19.28	0.29	0.00	-37.4
[293]	DSDP Site 112	54.01667	-46.604	3657	446	1.50	29.73	0.21	0.00	-38.3
[293]	DSDP Site 112	54.01667	-46.604	3657	456.2	1.50	30.41	0.06	0.00	-25.9
[293]	DSDP Site 112	54.01667	-46.604	3657	586.7	1.50	39.11	0.35	0.00	-22.8
[293]	DSDP Site 341	67.335	6.110667	1439	29.8	10.00	0.30	0.51	0.04	20.9

Ref.	Site	Lat. (°)	Lon. (°)	Water Depth (mbsl)	Depth (mbsf)	Est. Sed Rate ($\frac{cm}{kyr}$)	Est. Age (Ma)	S (wt %)	Est. Py S Accum. Rate ($\frac{mol\ S}{m^2 yr}$)	Pyrite $\delta^{34}S$ (‰)
[293]	DSDP Site 341	67.335	6.110667	1439	78.3	10.00	0.78	0.45	0.04	-15.7
[293]	DSDP Site 341	67.335	6.110667	1439	241.8	10.00	2.42	0.08	0.01	-40.8
[221]	Location 1990	42.53333	38.41667	2005	0.025	13.56	0.00	1.207	0.14	-29.4
[221]	Location 1990	42.53333	38.41667	2005	0.605	13.56	0.00	0.701	0.08	-20.2
[221]	Location 1990	42.53333	38.41667	2005	1.525	13.56	0.01	0.598	0.07	14.6
[221]	Location 1991	43.86667	36.9	2075	0.025	12.83	0.00	1.158	0.13	-29.2
[221]	Location 1997	45.03333	36.56667	28	0.05	515.79	0.00	0.168	0.73	-25.9
[221]	Location 2001	45.46667	37.33333	9	0.05	945.15	0.00	0.438	3.49	-20.3
[221]	Location 2001	45.46667	37.33333	9	0.235	945.15	0.00	1.361	10.83	-23.6
[221]	Location 2001	45.46667	37.33333	9	0.805	945.15	0.00	0.05	0.40	-4.2
[221]	Location 2001	45.46667	37.33333	9	1.23	945.15	0.00	0.044	0.35	-3.1
[221]	Location 2008	45.9	35.25	11	0.025	853.24	0.00	0.882	6.34	4
[221]	Location 2008	45.9	35.25	11	0.1	853.24	0.00	0.591	4.25	6.5
[221]	Location 2008	45.9	35.25	11	1.61	853.24	0.00	1.187	8.53	10.7
[221]	Location 2008	45.9	35.25	11	2.81	853.24	0.00	0.937	6.73	10.7

Ref.	Site	Lat. (°)	Lon. (°)	Water Depth (mbsl)	Depth (mbsf)	Est. Sed Rate ($\frac{cm}{kyr}$)	Est. Age (Ma)	S (wt %)	Est. Py S Accum. Rate ($\frac{mol\ S}{m^2 yr}$)	Pyrite $\delta^{34}S$ (‰)
[221]	Location 2005	46.15	36.63333	12	0.015	815.74	0.00	1.045	7.18	6.2
[221]	Location 2005	46.15	36.63333	12	0.055	815.74	0.00	0.942	6.47	13.7
[221]	Location 2005	46.15	36.63333	12	0.215	815.74	0.00	1.025	7.04	10.8
[221]	Location 2005	46.15	36.63333	12	0.92	815.74	0.00	1.065	7.32	11
[221]	Location 2005	46.15	36.63333	12	3.395	815.74	0.00	1.246	8.56	0.5
[222]	ODP Site 1041	-2.91667	-86.0333	3238	3.75	5.27	0.07	0.017	0.00	-49.6
[222]	ODP Site 1043	0.5	-86.1667	2760	0.5	7.59	0.01	0.092	0.01	-48.7
[222]	ODP Site 1043	0.5	-86.1667	2760	1.5	7.59	0.02	0.088	0.01	-50.6
[222]	ODP Site 1043	0.5	-86.1667	2760	3	7.59	0.04	0.1	0.01	-48.7
[222]	ODP Site 1046	1.983333	-86.1667	3120	0.5	5.77	0.01	0.077	0.00	-44.7
[222]	ODP Site 1046	1.983333	-86.1667	3120	1.2	5.77	0.02	0.054	0.00	-44.7
[222]	ODP Site 1046	1.983333	-86.1667	3120	1.75	5.77	0.03	0.061	0.00	-53.2
[222]	ODP Site 1046	1.983333	-86.1667	3120	2.5	5.77	0.04	0.086	0.00	-50.5
[222]	ODP Site 1046	1.983333	-86.1667	3120	3	5.77	0.05	0.106	0.01	-51.5
[222]	ODP Site 1046	1.983333	-86.1667	3120	3.2	5.77	0.06	0.148	0.01	-51.5

Ref.	Site	Lat. (°)	Lon. (°)	Water Depth (mbsl)	Depth (mbsf)	Est. Sed Rate ($\frac{cm}{kyr}$)	Est. Age (Ma)	S (wt %)	Est. Py S Accum. Rate ($\frac{mol\ S}{m^2 yr}$)	Pyrite $\delta^{34}S$ (‰)
[222]	ODP Site 1046	1.983333	-86.1667	3120	3.3	5.77	0.06	0.125	0.01	-48.8
[222]	ODP Site 1050	2.533333	-101.083	3330	1.2	4.90	0.02	0.123	0.01	-44
[222]	ODP Site 1050	2.533333	-101.083	3330	2.5	4.90	0.05	0.073	0.00	-45.5
[222]	ODP Site 1050	2.533333	-101.083	3330	3	4.90	0.06	0.062	0.00	-46.4
[222]	ODP Site 1047	4	-86.1667	2360	0.5	10.28	0.00	0.016	0.00	-48.9
[222]	ODP Site 1047	4	-86.1667	2360	4	10.28	0.04	0.018	0.00	-48.7
[220]	ODP Site 415	31.0287	-11.6518	2794	74.59	1.78	4.19	0.142	0.00	-42
[220]	ODP Site 415	31.0287	-11.6518	2794	137.905	1.97	7.00	0.24	0.00	-41.9
[220]	ODP Site 415	31.0287	-11.6518	2794	576.65	20.30	2.84	0.959	0.16	-12.1
[220]	ODP Site 415	31.0287	-11.6518	2794	642.89	20.30	3.17	0.746	0.13	-7.1
[220]	ODP Site 415	31.0287	-11.6518	2794	711.73	20.30	3.51	0.275	0.05	-0.9
[220]	ODP Site 416	32.8363	-10.801	4191	147.275	1.50	9.82	0.141	0.00	-39.7
[220]	ODP Site 416	32.8363	-10.801	4191	300.15	1.50	20.01	0.406	0.01	-29.5
[220]	ODP Site 416	32.8363	-10.801	4191	453.735	6.50	6.98	0.885	0.05	-31.7
[220]	ODP Site 416	32.8363	-10.801	4191	1200.12	6.50	18.46	0.276	0.02	-21.3

Ref.	Site	Lat. (°)	Lon. (°)	Water Depth (mbsl)	Depth (mbsf)	Est. Sed Rate ($\frac{cm}{kyr}$)	Est. Age (Ma)	S (wt %)	Est. Py S Accum. Rate ($\frac{mol\ S}{m^2 yr}$)	Pyrite $\delta^{34}S$ (‰)
[220]	ODP Site 416	32.8363	-10.801	4191	1233.975	6.50	18.98	0.326	0.02	-28.3
[220]	ODP Site 416	32.8363	-10.801	4191	1303.27	6.50	20.05	0.461	0.03	-25.5
[220]	ODP Site 416	32.8363	-10.801	4191	1328.03	6.50	20.43	0.302	0.02	-15.3
[220]	ODP Site 416	32.8363	-10.801	4191	1367.45	6.50	21.04	0.272	0.01	-26.1
[220]	ODP Site 416	32.8363	-10.801	4191	1389.63	6.50	21.38	0.277	0.02	-25.1
[222]	DSDP Site 508	0.5333	-86.1	2783	1.87	7.46	0.03	0.049	0.00	-46.6
[222]	DSDP Site 508	0.5333	-86.1	2783	11.3	7.46	0.15	0.117	0.01	-41.1
[222]	DSDP Site 508	0.5333	-86.1	2783	20.86	7.46	0.28	0.079	0.00	-47.7
[222]	DSDP Site 508	0.5333	-86.1	2783	31.23	7.46	0.42	0.121	0.01	-35.8
[222]	DSDP Site 508	0.5333	-86.1	2783	32.1	7.46	0.43	0.135	0.01	-32.9
[222]	DSDP Site 507	0.5667	-86.09	2710	3.123	7.88	0.04	0.165	0.01	-41.8
[222]	DSDP Site 507	0.5667	-86.09	2695	7.36	7.97	0.09	0.298	0.02	-50.6
[222]	DSDP Site 507	0.5667	-86.09	2695	13.18	7.97	0.17	0.365	0.02	-46.4
[222]	DSDP Site 507	0.5667	-86.09	2692	21.64	7.99	0.27	0.101	0.01	-45.1
[222]	DSDP Site 507	0.5667	-86.09	2689	22.79	8.01	0.28	0.029	0.00	-45.2

Ref.	Site	Lat. (°)	Lon. (°)	Water Depth (mbsl)	Depth (mbsf)	Est. Sed Rate ($\frac{cm}{kyr}$)	Est. Age (Ma)	S (wt %)	Est. Py S Accum. Rate ($\frac{mol\ S}{m^2 yr}$)	Pyrite $\delta^{34}S$ (‰)
[222]	DSDP Site 507	0.5667	-86.09	2689	30.76	8.01	0.38	0.182	0.01	-48.9
[222]	DSDP Site 507	0.5667	-86.09	2689	34.69	8.01	0.43	0.121	0.01	-45.2
[222]	DSDP Site 509	0.589	-86.1315	2677	8.67	8.08	0.11	0.151	0.01	-40.3
[222]	DSDP Site 509	0.589	-86.1315	2677	13.4	8.08	0.17	0.359	0.02	-49.3
[222]	DSDP Site 509	0.589	-86.1315	2687	16.39	8.02	0.20	0.454	0.03	-48.1
[222]	DSDP Site 509	0.589	-86.1315	2677	20.88	8.08	0.26	0.273	0.02	-48.1
[222]	DSDP Site 509	0.589	-86.1315	2687	22.24	8.02	0.28	0.115	0.01	-48.1
[222]	DSDP Site 509	0.589	-86.1315	2677	27.6	8.08	0.34	0.042	0.00	-45.3
[222]	DSDP Site 509	0.589	-86.1315	2687	28.46	8.02	0.35	0.164	0.01	-45.4
[222]	DSDP Site 506	0.607	-86.0913	2707	1.01	7.90	0.01	0.036	0.00	-41.2
[222]	DSDP Site 506	0.607	-86.0913	2707	3.33	7.90	0.04	0.207	0.01	-48.3
[222]	DSDP Site 506	0.607	-86.0913	2707	8.855	7.90	0.11	0.103	0.01	-46.2
[222]	DSDP Site 506	0.607	-86.0913	2707	20.52	7.90	0.26	1.196	0.08	-43.4
[222]	DSDP Site 506	0.607	-86.0913	2707	29.915	7.90	0.38	0.142	0.01	-45.5
[222]	DSDP Site 506	0.6077	-86.0913	2710	23.68	7.88	0.30	0.181	0.01	-42.6

Ref.	Site	Lat. (°)	Lon. (°)	Water Depth (mbsl)	Depth (mbsf)	Est. Sed Rate ($\frac{cm}{kyr}$)	Est. Age (Ma)	S (wt %)	Est. Py S Accum. Rate ($\frac{mol\ S}{m^2 yr}$)	Pyrite $\delta^{34}S$ (‰)
[222]	DSDP Site 506	0.6077	-86.0913	2710	23.74	7.88	0.30	0.296	0.02	-44.8
[222]	DSDP Site 506	0.6077	-86.0913	2710	24.765	7.88	0.31	0.068	0.00	-43.7
[222]	DSDP Site 506	0.6098	-86.0998	2710	22.48	7.88	0.29	0.122	0.01	-46.6
[222]	DSDP Site 506	0.6098	-86.0998	2710	26.75	7.88	0.34	0.561	0.04	-37.6
[222]	DSDP Site 506	0.6098	-86.0998	2710	28.89	7.88	0.37	0.03	0.00	-46.3
[222]	DSDP Site 510	1.6132	-86.41	2781	39.85	7.47	0.53	0.187	0.01	-47.4
[222]	DSDP Site 510	1.6132	-86.41	2781	68.36	7.47	0.91	0.422	0.03	-44.6
[222]	DSDP Site 510	1.6132	-86.41	2781	79.35	7.47	1.06	0.304	0.02	-46.3
[222]	DSDP Site 510	1.6132	-86.41	2781	102.77	7.47	1.38	0.181	0.01	-49
[222]	DSDP Site 510	1.6132	-86.41	2781	112.35	7.47	1.50	0.109	0.01	-46.3
[329]		10.8925	-44.0428	5168	100	32.00	0.31	0.02	0.01	2
[329]		10.8925	-44.0428	5168	478	32.00	1.49	0.025	0.01	13.4
[329]	Core 50G			1000	0.18	34.15	0.00	0.3	0.09	-23.6
[329]	Core 50G			1000	0.25	34.15	0.00	0.22	0.06	-23.2
[329]	Core 50G			1000	0.35	34.15	0.00	0.31	0.09	-23.2

Ref.	Site	Lat. (°)	Lon. (°)	Water Depth (mbsl)	Depth (mbsf)	Est. Sed Rate ($\frac{cm}{kyr}$)	Est. Age (Ma)	S (wt %)	Est. Py S Ac-cum. Rate ($\frac{mol\ S}{m^2 yr}$)	Pyrite $\delta^{34}S$ (‰)
[329]	Core 38G			1000	0.4475	34.15	0.00	0.39	0.11	-18.2
[329]	Core 38G			1000	0.525	34.15	0.00	0.28	0.08	-21.5
[329]	Core 50G			1000	0.55	34.15	0.00	0.39	0.11	-22.7
[329]	Core 38G			1000	0.675	34.15	0.00	0.41	0.12	-17.3
[329]	Core 50G			1000	0.75	34.15	0.00	0.54	0.16	-24
[329]	Core 38G			1000	0.95	34.15	0.00	0.38	0.11	-14.2
[329]	Core 50G			1000	0.95	34.15	0.00	0.48	0.14	-22
[329]	Core 50G			1000	1.05	34.15	0.00	0.71	0.20	-17
[329]	Core 38G			1000	1.15	34.15	0.00	0.33	0.09	-10.9
[329]	Core 50G			1000	1.25	34.15	0.00	0.64	0.18	-16.1
[329]	Core 50G			1000	1.35	34.15	0.00	0.73	0.21	-15.6
[329]	Core 50G			1000	1.45	34.15	0.00	0.66	0.19	-14.6
[329]	Core 38G			1000	1.675	34.15	0.00	0.53	0.15	-7.5
[329]	Core 50G			1000	1.75	34.15	0.01	0.67	0.19	-13.8
[329]	Core 50G			1000	1.95	34.15	0.01	0.7	0.20	-13.6

Ref.	Site	Lat. (°)	Lon. (°)	Water Depth (mbsl)	Depth (mbsf)	Est. Sed Rate ($\frac{cm}{kyr}$)	Est. Age (Ma)	S (wt %)	Est. Py S Ac-cum. Rate ($\frac{mol\ S}{m^2 yr}$)	Pyrite $\delta^{34}S$ (‰)
[329]		28.625	-112.333	226	0	132.74	0.00	0.62	0.69	-20.6
[329]		28.625	-112.333	226	0.09	132.74	0.00	0.873	0.98	-21.9
[329]		28.625	-112.333	226	0.8	132.74	0.00	0.632	0.71	-15.1
[329]		28.625	-112.333	226	0.905	132.74	0.00	0.855	0.96	-8.2
[329]		28.625	-112.333	226	1.43	132.74	0.00	0.554	0.62	-16.1
[329]		28.625	-112.333	226	1.95	132.74	0.00	0.269	0.30	-9.1
[329]		28.625	-112.333	226	3.49	132.74	0.00	0.323	0.36	-6.1
[328]		10.71133	-65.1742	892	2	72.30	0.00	1.443	0.88	-31.8
[328]		10.71133	-65.1742	892	66	72.30	0.09	1.266	0.77	-32.1
[328]		10.71133	-65.1742	892	112	72.30	0.15	1.13	0.69	-30.4
[328]		33.56667	-118.467	860	0.05	166.67	0.00	0.35	0.49	-28
[328]		33.56667	-118.467	860	0.205	166.67	0.00	0.37	0.52	-30.2
[328]		33.56667	-118.467	860	0.425	166.67	0.00	0.279	0.39	-35.1
[328]		33.56667	-118.467	860	1.645	166.67	0.00	0.24	0.34	-39.3
[328]		33.56667	-118.467	860	2.52	166.67	0.00	0.231	0.32	-38.6

Ref.	Site	Lat. (°)	Lon. (°)	Water Depth (mbsl)	Depth (mbsf)	Est. Sed Rate ($\frac{cm}{kyr}$)	Est. Age (Ma)	S (wt %)	Est. Py S Ac-cum. Rate ($\frac{mol\ S}{m^2 yr}$)	Pyrite $\delta^{34}S$ (‰)
[328]		33.56667	-118.467	860	3.18	166.67	0.00	0.309	0.43	-40.1
[328]		33.56667	-118.467	860	3.585	166.67	0.00	0.525	0.74	-40.6
[328]		33.56667	-118.467	860	4.19	166.67	0.00	0.267	0.37	-37.3
[328]		33.56667	-118.467	860	4.375	166.67	0.00	0.597	0.84	-40.1
[336]		11.33333	-67.5	6	6	1155.85	0.00	0.132	1.28	9.9
[336]		11.33333	-67.5	6	6	1155.85	0.00	0.123	1.20	4.6
[336]		11.33333	-67.5	6	6	1155.85	0.00	0.164	1.60	0.3
[336]		11.33333	-67.5	24.4	24.4	557.20	0.00	0.1	0.47	6.3
[336]		11.33333	-67.5	24.4	24.4	557.20	0.00	0.045	0.21	4.1
[336]		11.33333	-67.5	48.8	48.8	372.97	0.01	0.072	0.23	1.35
[336]		11.33333	-67.5	48.8	48.8	372.97	0.01	0.125	0.39	1.2
[349]		41.58333	29.33333	1179	0.05	47.80	0.00	1.15	0.46	-26.3
[349]		41.75	41.5	300	0.125	106.31	0.00	0.01	0.01	-6.1
[349]		42	40.18333	1704	0.05	21.25	0.00	1.06	0.19	-33.7
[349]		42.5	34.3	2003	0.025	13.58	0.00	0.99	0.11	-27.4

Ref.	Site	Lat. (°)	Lon. (°)	Water Depth (mbsl)	Depth (mbsf)	Est. Sed Rate ($\frac{cm}{kyr}$)	Est. Age (Ma)	S (wt %)	Est. Py S Ac-cum. Rate ($\frac{mol\ S}{m^2 yr}$)	Pyrite $\delta^{34}S$ (‰)
[349]		42.5	34.3	2003	0.025	13.58	0.00	1.24	0.14	-27.4
[349]		42.5	34.3	2003	0.175	13.58	0.00	1.33	0.15	-24.9
[349]		42.5	34.3	2003	0.405	13.58	0.00	1.03	0.12	-25.3
[349]		42.5	34.3	2003	1.355	13.58	0.01	1.02	0.12	-13.7
[349]		42.5	34.3	2003	2.515	13.58	0.02	0.71	0.08	15.2
[349]		42.5	34.3	2003	3.745	13.58	0.03	0.02	0.00	4.4
[349]		42.5	34.3	2003	6.8	13.58	0.05	0.03	0.00	-3.4
[349]		42.5	39	2163	0.025	11.97	0.00	1.13	0.11	-30.6
[349]		43.5	32	1773	0.05	16.38	0.00	1.31	0.18	-33.7
[349]		43.83333	33.66667	2008	0.05	47.50	0.00	0.819	0.33	-33.2
[349]		44.7	33.33333	110	0.02	222.26	0.00	0.06	0.11	-19.9
[349]		44.7	33.33333	110	0.175	222.26	0.00	0.58	1.09	-35.4
[349]		44.91667	36.18333	108	0.02	225.02	0.00	0.02	0.04	-20
[349]		44.91667	36.18333	108	0.16	225.02	0.00	0.62	1.17	-35.5

Appendix E

THE $\delta^{34}S_{CAS}$ OF ORDOVICIAN TRILOBITES

Abstract

Carbonate associated sulfate (CAS) has emerged as a valuable proxy for reconstructing the sulfur isotopic composition of seawater sulfate through time. Although brachiopods are considered the most robust target for such reconstructions based on their textural preservation, other archives are needed to reconstruct seawater $\delta^{34}S$ during periods in which brachiopods are rare or absent. Here, we test the potential for trilobite CAS $\delta^{34}S$ (i.e., $\delta^{34}S_{CAS}$) to serve as a proxy for seawater $\delta^{34}S$ using geochemically well-characterized samples from end-Ordovician carbonates at Anticosti Island, Quebec, Canada. We show that trilobite $\delta^{34}S_{CAS}$ is almost universally elevated relative to codepositional brachiopod $\delta^{34}S_{CAS}$, suggesting that the trilobites in this study have been diagenetically altered. Our results are supported by previous studies of the microstructure and geochemistry of trilobite carapace material. In addition, we also test various carbonate cleaning procedures to remove non-CAS sources of SO_4^{2-} and find traditional milliQ water + NaCl rinses to be most effective. We suggest that trilobite $\delta^{34}S_{CAS}$ is unlikely to be a viable proxy for reconstructing seawater $\delta^{34}S$, but may have utility for reconstructing local diagenetic conditions at the time of sediment deposition.

Introduction

Chapter II of this thesis discussed the utility of calcitic brachiopods for constructing records of seawater SO_4^{2-} $\delta^{34}S$ through time. Although calcitic brachiopods are present in the geologic record for most of the Phanerozoic, their rarity during the Cambrian and early Ordovician [300] limits our ability to study the marine sulfur cycle during these periods with brachiopod carbonate associated sulfate (CAS) $\delta^{34}S$. Studies of high temporal resolution (< 1 Myr) require development of a different proxy archive for seawater SO_4^{2-} within this earliest part of the Phanerozoic.

Trilobites are an additional long-lived group of marine animals that evolved in the earliest Cambrian and persisted until the end of the Permian [103]. These

animals formed carapaces that are believed to have had a primary intermediate-Mg calcite composition [214]. Notably, these animals are most abundant during the Cambrian when calcitic brachiopods are rare [300].

Recent work by Present et al. (2015) [262] characterized the sulfur isotopic composition of individual carbonate components within heterogenous bioclastic limestones from Anticosti Island, Quebec, Canada. Although this work measured many ($n = 21$) brachiopods and identified well-preserved brachiopods as the best targets for studies of CAS $\delta^{34}S$ (i.e., $\delta^{34}S_{CAS}$, other components were only measured a limited number of times. Trilobite carapace fragments ($n = 3$) within this study yielded $\delta^{34}S_{CAS}$ values that were 2-5‰ higher than codepositional brachiopod shells [262]. However, these data were not sufficiently numerous to determine the consistency of the offset or — consequently — the potential utility of trilobite carapace $\delta^{34}S_{CAS}$ for reconstructing seawater SO_4^{2-} $\delta^{34}S$.

Here, we probe the ability of trilobite carapace fragments to preserve a primary and/or consistent $\delta^{34}S_{CAS}$ signal by measuring the $\delta^{34}S_{CAS}$ of a large number ($n = 26$) of trilobite carapace samples from well-preserved carbonates from Anticosti Island, Canada — i.e., the same samples studied by Present et al. (2015) [262]. We compare the $\delta^{34}S_{CAS}$ of trilobites to the $\delta^{34}S_{CAS}$ of codepositional brachiopods and find that trilobite carapace fragments are almost universally enriched in ^{34}S relative to codepositional brachiopods. Furthermore, the offset of trilobites toward higher $\delta^{34}S_{CAS}$ than codepositional brachiopods varies by over 15‰, suggesting that the primary seawater $\delta^{34}S$ signature cannot be precisely estimated from trilobite $\delta^{34}S_{CAS}$ data. However, measurements of trilobite $\delta^{34}S_{CAS}$ may have utility for studies of the diagenetic reactions occurring early in the depositional history of the sediments in which carapace fragments are deposited.

Geologic Context

Anticosti Island features an Ordovician-Silurian boundary succession composed of mixed carbonate-siliclastic facies deposited in a storm-dominated tropical setting [84]. A depositional gradient exists from east to west across the island such that near-shore siliclastic-dominated facies predominate in the east and more distal carbonate-dominated facies predominate in the west [84]. The trilobite and brachiopod samples measured in this study come from section 906 of Finnegan et al. (2011) [101] along the banks of the Oil River in the western half of the island and section 908 [101, 161] along the banks of the Salmon

River in the eastern half of the island (Figure 2). Finnegan et al. (2011) [101] found no textural alteration of trilobite fragments from these sections. They also concluded that the fragments' trace metal concentrations and clumped isotope temperatures were consistent with minimal to moderate diagenetic alteration [101].

Methods

Samples analyzed in this study were subjected to a systematic preparation process designed to yield CAS abundance and $\delta^{34}S_{CAS}$ values as uncontaminated with non-CAS sources of SO_4^{2-} as possible. After removal from hand samples using a dental pick or Dremel tool, fragments of *Isotelus* sp. trilobites and brachiopods were viewed under an optical microscope to ensure the absence of excessive micrite. Fragments were rinsed with 18.2 MΩ milliQ water and sonicated for 60 minutes three times, leached for four hours while sonication in a 10% (w/w) NaCl solution, and rinsed again with milliQ water three times. To test the effectiveness of other potential cleaning methods, several trilobite carapace and micrite fragments were ground into homogenous powders and cleaned with only milliQ water rinses, with one or two hydrogen peroxide (H_2O_2) rinses without sonication, or with one or two H_2O_2 rinses with sonication. After cleaning, samples were transferred to acid-cleaned, pre-weighed microcentrifuge tubes and weighed using a microbalance. Carbonate components were dissolved by adding 0.5 N Seastar® HCl using a calibrated pipet to liberate CAS into solution. After centrifugating at 8000 rpm for 10 minutes, solutions were transferred to a chromatography column packed with 0.8 mL of anion exchange resin (Bio-Rad® AG1-X8) preconditioned with 10 column volumes (c.v.) 10% (v/v) reagent grade HNO_3 two times, 10 c.v. 33% (v/v) reagent grade HCl two times, and 10 c.v. 0.5% (v/v) reagent grade HCl two times. Following three 10 c.v. rinses of the column with milliQ water, SO_4^{2-} bound to the resin was eluted with three additions of two c.v. 0.45 N Seastar® HNO_3 and collected in acid-cleaned Teflon vials. The HNO_3 was subsequently evaporated overnight in a PicoTrace hood on a hot plate at 104 °C.

Dried and purified aliquots of samples were subsequently diluted in milliQ water for $[SO_4^{2-}]$ measurements on a Dionex ICS-3000 equipped with an AS4 column. A $Na_2CO_3/NaHCO_3$ buffer was used as the eluent. Concentration measurements on multiple aliquots of the same sample suggest a relative standard

deviation of $< 5\%$. After evaporating the milliQ water, samples were rediluted in 5% (v/v) Seastar® HNO_3 to obtain an $[SO_4^{2-}] \sim 20\ \mu$M. NaOH was subsequently added to attain a $[Na^+]$ of $\sim$40 μM [242]. Sulfur isotope ratios were measured by sample-standard bracketing on a ThermoScientific Neptune Plus MC-ICP-MS equipped with an Aridus II heated spray chamber and desolvating membrane. Each analysis of sample solution consisted of a set of 50 cycles of S isotope ratio measurements, and replicate analyses of each sample solution yielded a typical standard deviation in δ^{34}S of $< 0.1‰$. Deep sea coral and seawater samples served as internal consistency standards to verify the accuracy of the measured sample ratios. All ratios here are reported as δ^{34}S values (in per mil, ‰) relative to the Vienna Canyon Diablo Troilite (VCDT) standard [75].

Results

Cleaning tests

Sulfur isotopic composition results for *Isotelus* trilobite carapace material subjected to different cleaning protocols are shown in Figure E.1, while results for matrix micrite material are shown in Figure E.2. Results are also documented in Table E.1. Trilobite carapace $\delta^{34}S_{CAS}$ measurements vary between +23.9‰ and +29.3‰. CAS abundances within these samples range from 7 ppm to 404 ppm. Matrix micrite $\delta^{34}S_{CAS}$ measurements are less scattered and vary between 23.9‰ and 25.4‰ with CAS abundances between 589 ppm and 1450 ppm.

Fossil $\delta^{34}S_{CAS}$

CAS abundance and $\delta^{34}S_{CAS}$ results for samples are reported in Table E.2; $\delta^{34}S_{CAS}$ values are additionally plotted in histogram form in Figure E.6. Trilobite CAS abundances range from 54 ppm to 298 ppm, and $\delta^{34}S_{CAS}$ values range from 24.7‰ to 41.9‰. In contrast, the brachiopod samples analyzed here ($n = 4$) exhibit elevated CAS abundances ranging from 579 ppm to 1241 ppm, with $\delta^{34}S_{CAS}$ values ranging from 15.5‰ to 25.1‰. Two matrix micrite samples analyzed have CAS abundances of 103 ppm and 193 ppm with $\delta^{34}S_{CAS}$ values of 30.6‰ and 24.0‰, respectively.

Table E.1: Cleaning test results. Samples beginning with "T" are trilobite carapace material, whereas those beginning with "M" are matrix material.

Sample	Treatment	CAS (ppm)	Error (1σ)	$\frac{1}{CAS}$ (ppm^{-1})	$\delta^{34}S_{CAS}$ (‰)	Error (1σ)
T1A	mQ only	25	5	0.040	26.6	0.99
T2A	mQ only	97	6	0.010	26.6	0.88
T3A	mQ only	55	6	0.018	25.8	0.40
TA Blank	mQ only				5.3	
T1B	mQ + NaCl	54	5	0.019	25.1	
T2B	mQ + NaCl	298	9	0.003	24.7	
T3B	mQ + NaCl	6	6	0.175	26.5	0.15
TB Blank	mQ + NaCl				3.8	
T1C	mQ + NaCl + H_2O_2 (1x, no sonication)	23	6	0.044	26.1	0.09
T2C	mQ + NaCl + H_2O_2 (1x, no sonication)	268	7	0.004	26.3	0.11
TC Blank	mQ + NaCl + H_2O_2 (1x, no sonication)				2.9	
T1D	mQ + NaCl + H_2O_2 (2x, no sonication)	62	7	0.016	25.9	
T2D	mQ + NaCl + H_2O_2 (2x, no sonication)	253	9	0.004	29.3	0.75
T3D	mQ + NaCl + H_2O_2 (2x, no sonication)	234	7	0.004	27.0	0.67
TD Blank	mQ + NaCl + H_2O_2 (2x, no sonication)				0.0	
T1E	mQ + NaCl + H_2O_2 (1x, sonication)	248	8	0.004	26.8	0.09
T2E	mQ + NaCl + H_2O_2 (1x, sonication)	286	8	0.003	26.5	0.18
T3E	mQ + NaCl + H_2O_2 (1x, sonication)	267	9	0.004	26.6	0.81
TE Blank	mQ + NaCl + H_2O_2 (1x, sonication)				2.0	
T1F	mQ + NaCl + H_2O_2 (2x, sonication)	237	8	0.004	26.9	0.12
T2F	mQ + NaCl + H_2O_2 (2x, sonication)	335	10	0.003	23.7	
T3F	mQ + NaCl + H_2O_2 (2x, sonication)				24.1	
TF Blank	mQ + NaCl + H_2O_2 (2x, sonication)				6.6	
M1A	mQ only	316	2	0.003	25.4	0.11
M2A	mQ only	226	1	0.004	25.3	0.11
M3A	mQ only	307	2	0.003	25.3	0.20
MA Blank	mQ only				6.8	
M1B	mQ + NaCl	377	2	0.003	25.2	0.09
M2B	mQ + NaCl	341	2	0.003	25.4	0.02
M3B	mQ + NaCl	347	2	0.003	24.2	0.03
MB Blank	mQ + NaCl				7.8	
M1C	mQ + NaCl + H_2O_2 (1x, no sonication)	383	3	0.003	25.1	0.14
M2C	mQ + NaCl + H_2O_2 (1x, no sonication)	422	3	0.002	24.5	0.09
M3C	mQ + NaCl + H_2O_2 (1x, no sonication)	229	2	0.004	25.4	
MC Blank	mQ + NaCl + H_2O_2 (1x, no sonication)				6.4	
M1D	mQ + NaCl + H_2O_2 (2x, no sonication)	267	2	0.004	25.1	0.63
M2D	mQ + NaCl + H_2O_2 (2x, no sonication)	449	3	0.002	24.2	0.13
M3D	mQ + NaCl + H_2O_2 (2x, no sonication)	252	2	0.004	25.4	0.18
MD Blank	mQ + NaCl + H_2O_2 (2x, no sonication)				9.2	
M1E	mQ + NaCl + H_2O_2 (1x, sonication)	312	2	0.003	24.7	
M2E	mQ + NaCl + H_2O_2 (1x, sonication)	381	3	0.003	23.9	0.10
M3E	mQ + NaCl + H_2O_2 (1x, sonication)	425	3	0.002	24.0	0.09
ME Blank	mQ + NaCl + H_2O_2 (1x, sonication)				9.5	
M1F	mQ + NaCl + H_2O_2 (2x, sonication)	426	3	0.002	24.2	0.02
M2F	mQ + NaCl + H_2O_2 (2x, sonication)	406	3	0.002	24.2	0.09
M3F	mQ + NaCl + H_2O_2 (2x, sonication)	510	4	0.002	24.0	0.15
MF Blank	mQ + NaCl + H_2O_2 (2x, sonication)				5.1	
Seawater 1					21.2	0.11
Seawater 2					21.0	
DSC1					22.3	0.12
DSC2					22.5	0.09

Table E.2: $\delta^{34}S_{CAS}$ data for all trilobite, brachiopod, and micrite measurements. Trilobite results generated from the mQ + NaCl treatment group in the cleaning tests have also been included.

Sample	Type	CAS (ppm)	Error (1σ)	$\frac{1}{CAS}$ (ppm^{-1})	$\delta^{34}S_{CAS}$	Error (1σ)
1B	*Isotelus* trilobite material (homogenized)				31.9	0.16
2B	*Isotelus* trilobite material (homogenized)	229	21	0.0044	31.3	0.04
3B	*Isotelus* trilobite material (homogenized)	183	16	0.0055	30.7	0.01
4B	*Isotelus* trilobite material (homogenized)	193	17	0.0052	30.7	0.03
5B	*Isotelus* trilobite material (homogenized)				30.9	0.03
901_xx_02T	*Isoleus* trilobite fragments	257	23	0.0039	30.2	0.18
901_xx_03T	*Isoleus* trilobite fragments	205	18	0.0049	32.1	0.01
901_xx_04T	*Isoleus* trilobite fragments	248	22	0.0040	30.4	0.03
901_xx_05T	*Isoleus* trilobite fragments	263	24	0.0038	30.2	0.04
901_xx_06Ta	*Isoleus* trilobite fragments	194	17	0.0052	33.4	0.02
901_xx_06Tb	*Isoleus* trilobite fragments	217	20	0.0046	32.6	0.14
901_xx_06Tc	*Isoleus* trilobite fragments	208	19	0.0048	32.3	0.00
901_xx_06Td	*Isoleus* trilobite fragments				33.2	0.23
901_xx_06Te	*Isoleus* trilobite fragments	185	17	0.0054	33.2	0.04
T1B	*Isotelus* trilobite material (homogenized; from cleaning test)	54	5	0.0185	25.1	
T2B	*Isotelus* trilobite material (homogenized; from cleaning test)	298	9	0.0034	24.7	
T3B	*Isotelus* trilobite material (homogenized; from cleaning test)	6	6	0.1749	26.5	0.15
906-1 Isotelus	*Isoleus* trilobite fragments	269	11	0.0037	36.8	0.07
906 23-30 Trilo 1	*Isoleus* trilobite fragments	283	18	0.0035	29.1	0.06
906 23-30 Trilo 2	*Isoleus* trilobite fragments	203	9	0.0049	32.7	0.03
906 23-30 Trilo 3a	*Isoleus* trilobite fragments	143	6	0.0070	33.2	
906 23-30 Trilo 3b	*Isoleus* trilobite fragments	133	5	0.0075	28.8	0.01
906 23-30 Trilo 4	*Isoleus* trilobite fragments	283			29.4	0.04
908 T1	*Isoleus* trilobite fragments	96	4	0.0104	39.6	
908 T2	*Isoleus* trilobite fragments	146	6	0.0068	41.9	0.03
908 LCM	*Isoleus* trilobite fragments	147	7	0.0068	39.8	
906 23-30 Brach 1 binoc	Brachiopod fibrous calcite	913	81	0.0011	24.4	0.04
906 23-30 Brach 2 binoc	Brachiopod fibrous calcite	924	71	0.0011	24.3	0.07
906 23-30 Brach 3 binoc	Brachiopod fibrous calcite	1241			15.5	0.07
906 23-30 Brach 4 binoc	Brachiopod fibrous calcite	579	48	0.0017	25.1	0.06
906 23-30 Brach 0	Brachiopod fibrous calcite	1241	88	0.0008	24.3	0.02
906 23-30 Brach 1	Brachiopod fibrous calcite	855	47	0.0012	24.7	0.10
906 23-30 Brach 2	Brachiopod fibrous calcite	662	46	0.0015	24.9	0.08
906 23-30 Brach 3	Brachiopod fibrous calcite	882	69	0.0011	24.4	0.04
906 23-30 Brach 4	Brachiopod fibrous calcite	774	66	0.0013	24.7	
906-1 Micrite	Matrix micrite	193	7	0.0052	24.0	0.02
908 LCM Micrite	Matrix micrite	103	6	0.0097	30.6	0.02

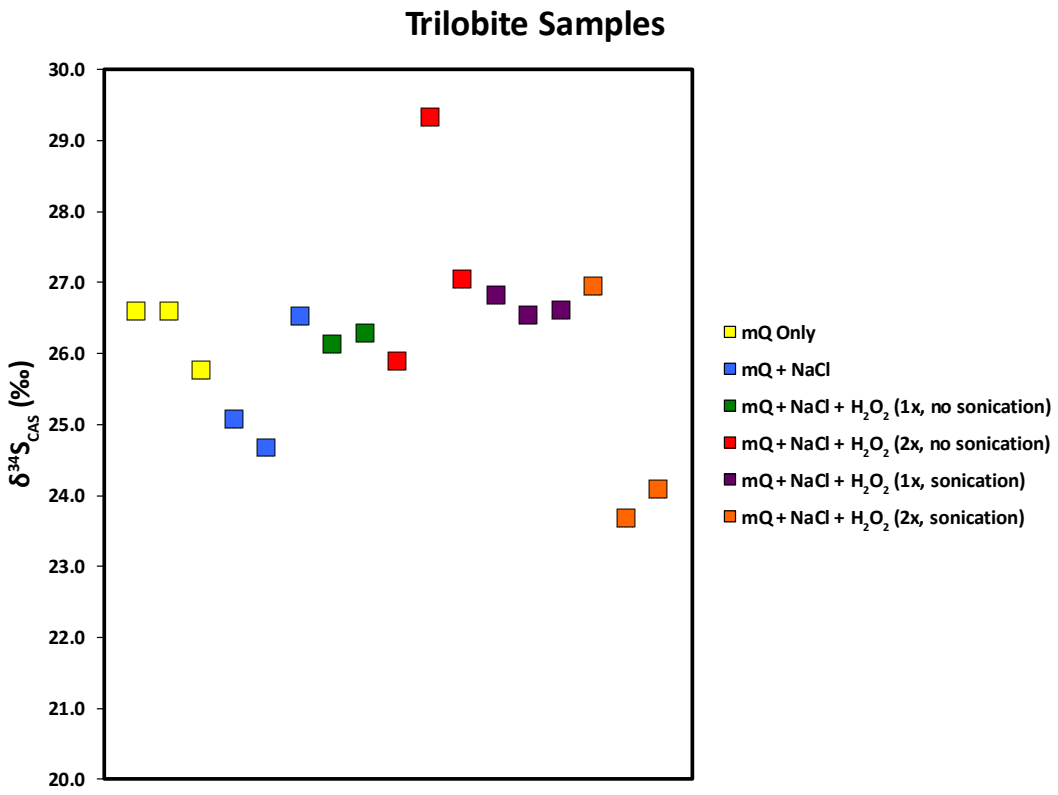

Figure E.1: Plot of $\delta^{34}S_{CAS}$ results for *Isotelus* trilobite carapace samples subjected to various cleaning protocols. Symbol color denotes cleaning protocol used. Horizontal axis simply offsets the results, and distance along the axis has no significance.

Discussion

Cleaning tests

Previous studies of methods for extracting CAS from carbonates [208, 334, 367] have found oxidation of solid phase sulfides to be a potentially significant source of contamination in CAS measurements, particularly when oxidants are used to remove reduced sulfur phases such as organic S and pyrite. The results of our cleaning tests support these findings. Although trilobite carapace material shows no systematic variation in $\delta^{34}S_{CAS}$ with respect to the cleaning protocol applied, matrix micrite material shows a tendency toward lower $\delta^{34}S_{CAS}$ values when protocols utilizing oxidative H_2O_2 rinses are applied. These trends become more clear if our $\delta^{34}S_{CAS}$ data are plotted against the inverse of CAS abundance (Figures E.3 and E.4): trilobite carapace samples shows little to no trend in this space, but matrix material exhibits a clear trend toward lower $\delta^{34}S_{CAS}$ as the inverse of CAS abundance decreases (i.e., as CAS abundance increases). Such a

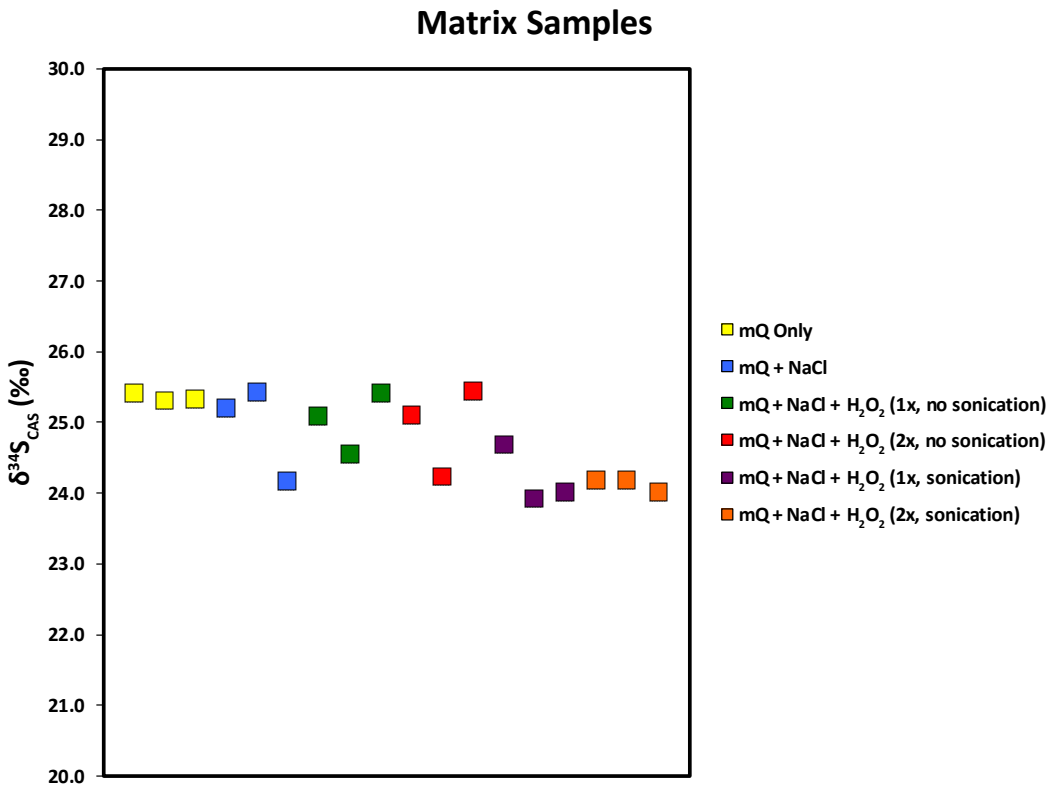

Figure E.2: Plot of $\delta^{34}S_{CAS}$ results for matrix micrite samples subjected to various cleaning protocols. Symbol color denotes cleaning protocol used. Horizontal axis simply offsets the results, and distance along the axis has no significance.

trend suggests mixing between a high CAS abundance, low $\delta^{34}S_{CAS}$ phase and a lower CAS abundance, higher $\delta^{34}S_{CAS}$ phase. Our trilobite carapace material was derived from fragments of relatively pure fossil calcite and presumably contains little to no pyrite. The matrix micrite, on the other hand, included disseminated pyrite grains that were visible under optical microscopy in polished thick sections cut through carapace-bearing matrix material (Figure E.5). Our observation of decreasing $\delta^{34}S_{CAS}$ and increasing CAS abundance in cleaning protocols subjecting this material to oxidative leaches supports previous findings by Wotte et al. (2012) [367] of incomplete reduced S removal and CAS measurement contamination when oxidants were used to clean CAS samples.

Overall, our cleaning test results indicate that milliQ water and NaCl rinses are the most effective method for removing potential sources of CAS contamination. Oxidative steps to remove reduced sulfur do liberate some sulfur from reduced solid phases, but also increase the likelihood of contamination. This

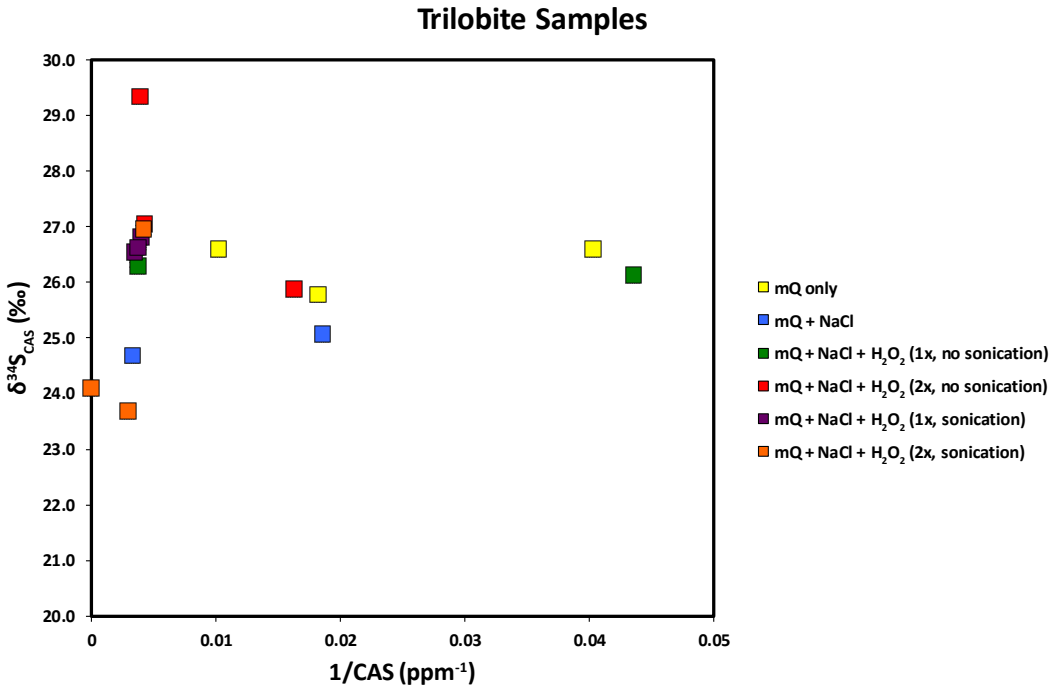

Figure E.3: Plot of $\delta^{34}S_{CAS}$ versus the inverse of CAS abundance for *Isotelus* trilobite carapace samples subjected to various cleaning protocols. Symbol color denotes cleaning protocol used.

same procedure was recommended by Wotte et al. (2012) [367]. Carbonate dissolution under anoxic conditions could further reduce potential contamination from reduced phases, especially in samples that are rich in pyrite; however, the presence of Fe(III) oxidant in many bulk sedimentary samples likely reduces the effectiveness of such efforts [208, 334].

Fossil $\delta^{34}S_{CAS}$

All of our data collected via the mQ + NaCl cleaning protocol for biogenic samples (trilobites and brachiopods) and a few matrix samples are shown in histogram form in Figure E.6. When plotted in this manner, the distinction between the $\delta^{34}S_{CAS}$ exhibited by brachiopod samples and the $\delta^{34}S_{CAS}$ exhibited by trilobite samples becomes very clear: with the exception of two data points from our cleaning tests, all trilobite $\delta^{34}S_{CAS}$ measurements fall above +26‰ and are outside of the 2‰ range (+24‰to +26‰) in which most of the brachipod $\delta^{34}S_{CAS}$ data collected by Present et al. (2015) [262] fall. In contrast, eight of our nine brachiopod $\delta^{34}S_{CAS}$ measurements do fall within this range. These results confirm brachiopod fibrous calcite to be a robust target for studies of past sea-

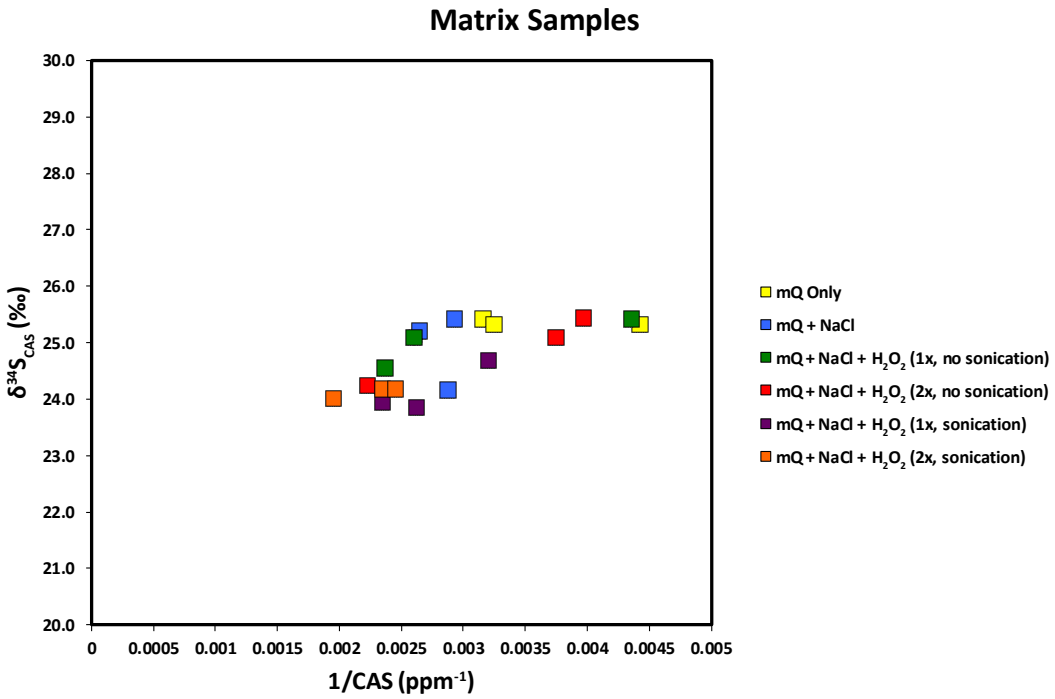

Figure E.4: Plot of $\delta^{34}S_{CAS}$ versus the inverse of CAS abundance for matrix micrite samples subjected to various cleaning protocols. Symbol color denotes cleaning protocol used.

water $\delta^{34}S$. Trilobite $\delta^{34}S_{CAS}$ appears to preserve seawater- and brachiopod-like $\delta^{34}S$ values with low frequency and is not an ideal target for these studies.

A plot of $\delta^{34}S_{CAS}$ versus the inverse of CAS abundance for most of our data (Figure E.7) provides some clues as to *why* our trilobite $\delta^{34}S_{CAS}$ data deviate so strongly from brachiopod $\delta^{34}S_{CAS}$ in the same rocks. Although some scatter in the data exists, both brachiopod $\delta^{34}S_{CAS}$ and trilobite $\delta^{34}S_{CAS}$ show trends of increasing $\delta^{34}S_{CAS}$ as $\frac{1}{CAS}$ increases (i.e., as CAS abundance decreases). As in similar plots from our cleaning tests, such a trend suggests mixing between high CAS abundance, low $\delta^{34}S_{CAS}$ and low CAS abundance, high $\delta^{34}S_{CAS}$ phases. The low $\delta^{34}S_{CAS}$ end member in this case appears to be pristine brachiopod calcite with a $\delta^{34}S_{CAS}$ just below 25‰. Higher $\delta^{34}S_{CAS}$ values can likely be attributed to incorporation of pore water SO_4^{2-} elevated in its ^{34}S content due to microbial sulfate reduction during early diagenesis (e.g. [278]). Observation of similar, but muted trend in our brachiopod data is interesting; this suggests that this incorporation may also have affected brachiopod calcite, but to a lesser degree. The more shallow slope suggests an altered end member with lower $\delta^{34}S_{CAS}$ and/or higher CAS abundance than the altered end member for the trilobite data. The

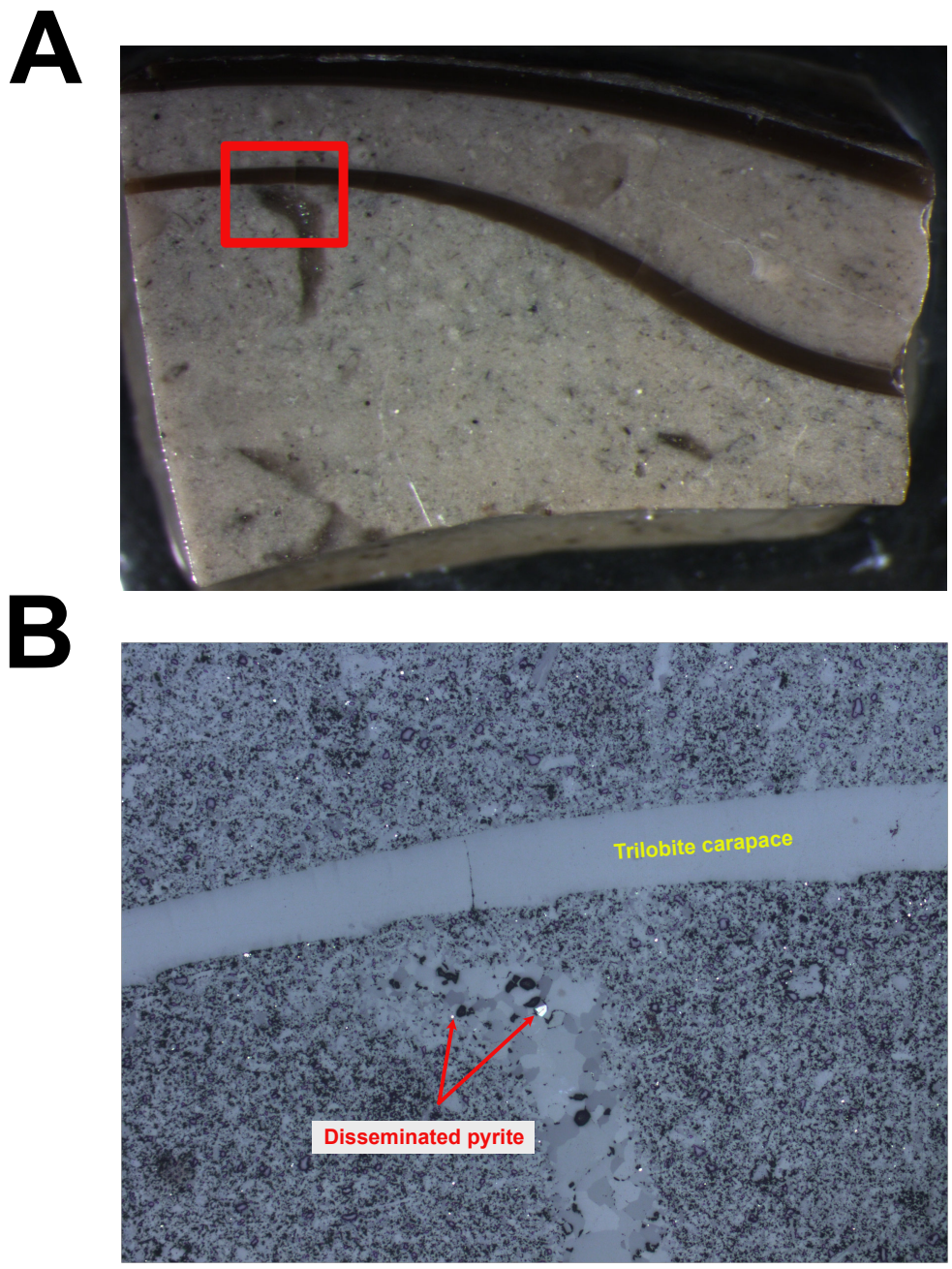

Figure E.5: Thick section images. (A) Binocular microscope image of polished thick section cut from Anticosti 906 hand sample that includes trilobite carapace fragments (brown, horizontally-oriented materials). Red box denotes approximate limits of the region imaged in (B). Image taken under reflected, plane polarized light at 1.25x magnification. (B) Reflected light, plane polarized image of area denoted by red box in (A). Yellow text denotes the trilobite carapace (finely crystalline, horizontal feature). Red text and arrows denote the locations of two highly reflective grains of pyrite disseminated throughout the sample. Note the heterogenous nature of the matrix (e.g., the presence of both micrite and sparry calcite). Image taken at 5x magnification.

brachiopod calcite thus may have been altered within a more shallow, less extensive depth interval than the trilobite calcite.

Additional evidence for a diagenetic influence on our trilobite $\delta^{34}S_{CAS}$ data comes from studies of trilobite carapace microstructure [48, 82, 213, 214, 215, 227, 332, 364]. Unlike the organic-poor, low porosity microstructure of impunctate brachiopods [286, 340], trilobite carapaces include surface cavities [215] up to $\sim$15 microns in diameter and may in some cases be cut by canals similar to those observed in modern arthropod exoskeletons [82, 213, 332]. This porosity may be infilled with diagenetic minerals after death [215]. Teigler and Towe (1975) [332] documented narrow pore canals in *Isotelus* sp. fragments like those analyzed here, suggesting that the inclusion of some diagenetic calcite in our specimens is likely.

Given the high frequency with which the specimens here appear to have been post-depositionally altered, is there any utility to measuring trilobite carapace $\delta^{34}S_{CAS}$? McAllister and Brand (1989) [214] have noted that trilobite fragments collected from shales are often better preserved than similar fragments collected from limestones, as is also the case with brachiopods (e.g. [122]). The specimens measured here were collected exclusively from limestones; future study of the $\delta^{34}S_{CAS}$ of trilobite fragments collected from shales may yield more promise for reconstructions of primary seawater $\delta^{34}S$. In addition, the relatively consistent enrichment of most trilobite samples here in ^{34}S suggests a common degree of alteration among most fragments. Reconstructing the intensity of microbial sulfate reduction in an environment at the time of deposition may be possible if these altered trilobite data are combined with unaltered brachiopod data, constraints on carapace porosity, and sedimentation rate estimates (e.g. [278]). Such a possibility warrants further investigation.

Finally, we briefly call attention to our observation of one brachiopod $\delta^{34}S_{CAS}$ near +15‰. Present et al. (2015) [262] also found one brachiopod to exhibit an anomalously low $\delta^{34}S_{CAS}$ of +16.6‰. Neither this study nor Present et al. (2015) [262] identified the taxonomy of the brachiopods measured for $\delta^{34}S_{CAS}$, preventing us from assessing whether these low $\delta^{34}S_{CAS}$ values are associated with a distinct taxon. However, our observation of a taxon-specific $\delta^{34}S_{CAS}$ effect in Chapter II of this thesis suggests that such a taxon-specific $\delta^{34}S_{CAS}$ offset could be a possibility. The large size of this apparent effect would have significant implications for brachiopod-based reconstructions of the marine sulfur cycle.

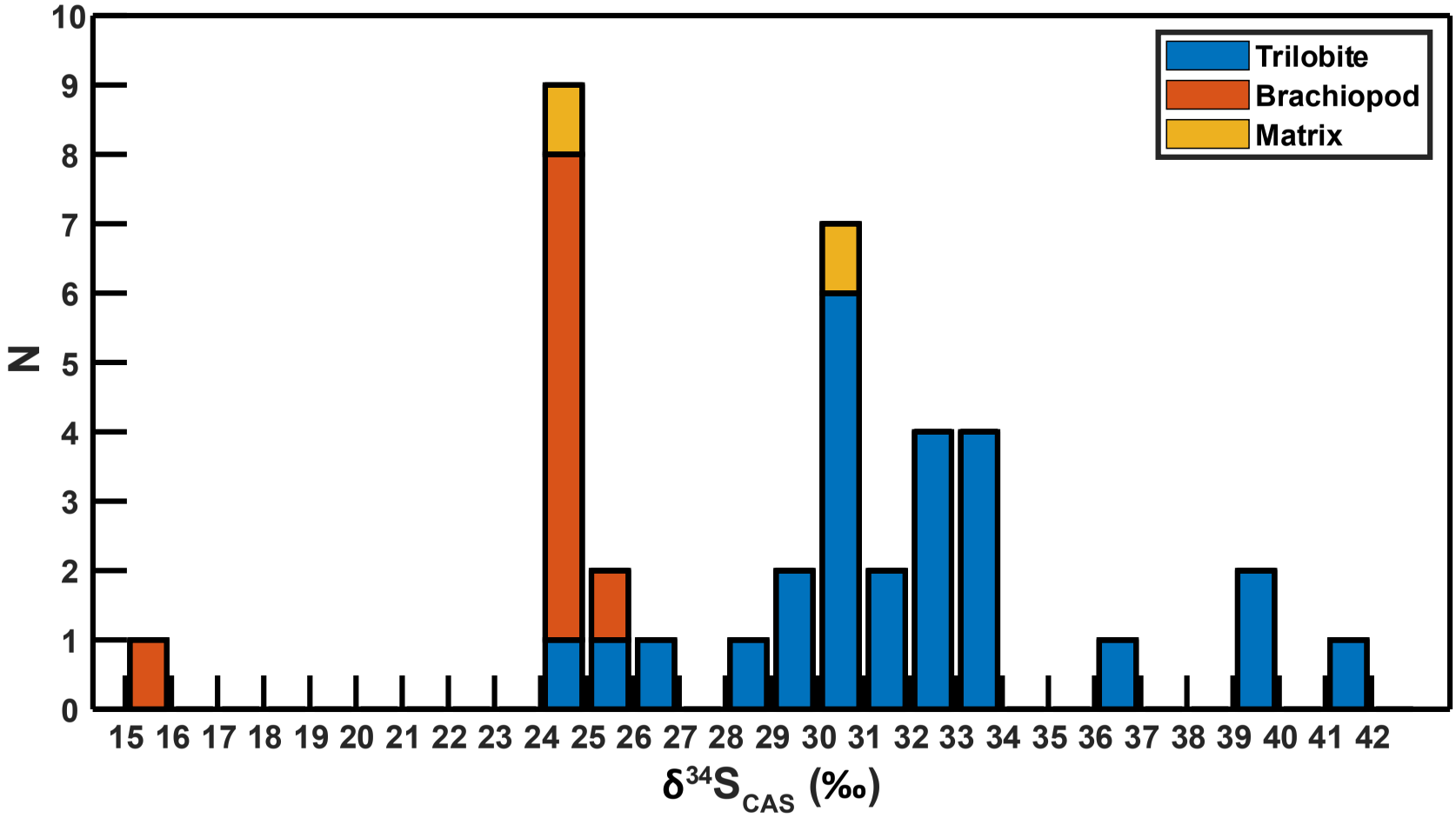

Figure E.6: Histogram of $\delta^{34}S_{CAS}$ values. Bar coloration denotes the fraction of the total number of measurements in a given 1‰ bin (N) that can be attributed to trilobite (blue), brachiopod (orange), or matrix (gold) material.

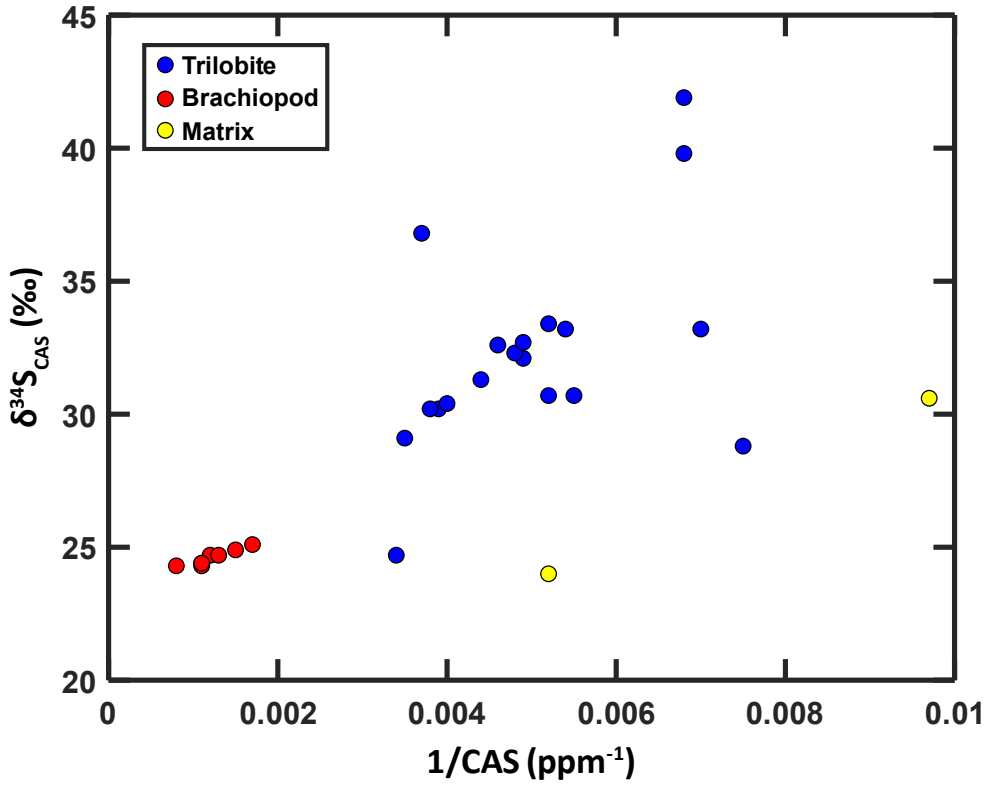

Figure E.7: Plot of $\delta^{34}S_{CAS}$ versus the inverse of CAS abundance for all biogenic carbonate data subjected to the mQ + NaCl cleaning protocol. Two matrix data points also included, and two trilobite data points with unusually low CAS abundance are not shown.

Future studies should probe this possibility in detail.

Conclusions

We have measured the sulfur isotopic composition of carbonate associated sulfate (CAS) in late Ordovician *Isotelus* trilobite fragments and contemporaneous brachiopods from Anticosti Island, Quebec, to test the potential for trilobite $\delta^{34}S_{CAS}$ to serve as a proxy for seawater SO_4^{2-} $\delta^{34}S$. We have also tested the effectiveness of various carbonate cleaning protocols. We find traditional milliQ water + NaCl rinses to be the most appropriate means to clean carbonates without adding CAS contamination from other sulfur phases. Our results show that trilobite $\delta^{34}S_{CAS}$ exceeds brachiopod $\delta^{34}S_{CAS}$ in almost all cases. The degree of this ^{34}S-enrichment varies from sample to sample, preventing trilobite $\delta^{34}S_{CAS}$ from being used to precisely constrain seawater $\delta^{34}S$. A diagenetic origin for the

enrichment is supported by previous microstructural and geochemical studies of trilobite remains. Further investigation into the $\delta^{34}S_{CAS}$ of trilobites collected from shales and other localities is needed to determine if elevated $\delta^{34}S_{CAS}$ is unique to Anticosti Island or is universal among trilobite samples globally. Our results suggest that trilobite $\delta^{34}S_{CAS}$ is unlikely to be a useful proxy for seawater $\delta^{34}S$, but may have utility for reconstructions of the intensity of microbial sulfate reduction in a given locality during sediment deposition.